PREFORMULATION SOLID-STATE SUPRAMOLECULAR BENEFICIATION OF SELECTED ACTIVE PHARMACEUTICAL INGREDIENTS AND A NOVEL DRUG CANDIDATE

Terence James Noonan

Thesis presented for the degree of

DOCTOR OF PHILOSOPHY

In the Department of Chemistry

University of Cape Town

May 2018

Supervisors:

Professor Mino R. Caira

Professor Susan A. Bourne

DEDICATION

Aan my liewe ouers.

Sonder wie dit nie moontlik sou wees nie.

Baie dankie vir jul ondersteuning en liefde.

Conferences and publications:

Parts of this thesis have been presented at the following conferences:

- Poster presentation: *Polymorphism of a nucleoside analogue antiviral drug*, Terence J. Noonan, Susan A. Bourne, Mino R. Caira, Applications in Thermal Analysis Conference, Stellenbosch, South Africa, 17-18 August **2015**.

- Oral presentation: *Novel polymorphs of clevudine: A nucleoside analogue antiviral drug*, Terence J. Noonan, Susan A. Bourne, Mino R. Caira, The Annual SACI and RSC Western Cape Young Chemists Symposium 2015, Cape Town, South Africa, 10 November **2015**.

- Poster presentation: *Supramolecular derivatisation of an antimalarial imidazopyridazine drug lead*, Terence J. Noonan, Susan A. Bourne, Peter M. Cheuka, Kelly Chibale, Mino R. Caira, 9th World Drug Delivery Summit, New Orleans, USA, 30 June – 2 July **2016**.

- Poster presentation: *Supramolecular derivatisation of an antimalarial imidazopyridazine drug lead*, Terence J. Noonan, Susan A. Bourne, Peter M. Cheuka, Kelly Chibale, Mino R. Caira, The Annual SACI and RSC Western Cape Young Chemists Symposium 2016, Stellenbosch, South Africa, 24 October **2016**.

- Poster presentation: *Inclusion of (±)-α-Lipoamide in Native and Methylated Cyclodextrins*, Terence J. Noonan, Susan A. Bourne, Mino R. Caira, 23rd International Conference on the Chemistry of the Organic Solid State (ICCOSS XXIII), Stellenbosch, South Africa, 2-7 April **2017**.

- Poster presentation: *Inclusion of (±)-α-Lipoamide in Native and Methylated Cyclodextrins*, Terence J. Noonan, Susan A. Bourne, Mino R. Caira, The Annual SACI and RSC Western Cape Young Chemists Symposium 2016, Cape Town, South Africa, 6 April **2018**.

Parts of this thesis have been published:

- T. Noonan, B. Mzondo, S. Bourne and M. Caira, *Polymorphism of the antiviral agent clevudine*, *CrystEngComm*, 2016, **18**, 8172-8181.

- T. J. Noonan, S. A. Bourne, P. M. Cheuka, K. Chibale and M. R. Caira, *Supramolecular derivatisation of an antimalarial imidazopyridazine drug lead, J. Pharm. Drug Deliv. Res.*, 2016, **5:3** (Suppl). (Conference abstract)

Abstract:

Terence James Noonan

March 2018

Preformulation solid-state supramolecular beneficiation of selected active pharmaceutical ingredients and a novel drug candidate

The aim from the outset of the project on which this thesis is based was to make use of contemporary methods in the field of supramolecular chemistry to improve the suboptimal physicochemical properties of selected compounds for use in the formulation of pharmaceutical products. The compounds selected were: Clevudine, an established drug that is currently in use for the treatment of chronic hepatitis B infections, 6-(3-(Methylsulfonyl)phenyl)-3-(4-(methylsulfonyl)phenyl)-imidazo[1,2-b]pyridazine (MMV652103), a novel antimalarial drug candidate that displayed good in vitro potency against multidrug resistant and sensitive plasmodial strains and (±)-α-lipoamide, a bioactive antioxidant that is currently in use for the clinical treatment of diabetic neuropathy and has other potential uses e.g. as an antiretroviral agent.

The methods utilised in pursuit of novel solid-state forms of the compounds included a combination of crystal engineering and experimental screening for polymorphs, solvates/hydrates, cyclodextrin (CD) inclusion complexes, pharmaceutical salts and co-crystals. Screening involved grinding and co-precipitation methods. Characterisation of new forms involved thermal analytical methods including hot stage microscopy (HSM), differential thermal analysis (DTA), differential scanning calorimetry (DSC), thermogravimetric analysis (TGA) and variable temperature powder X-ray diffraction (VTPXRD). In all cases where single-crystals of adequate quality and size were successfully prepared, the crystal structures were elucidated by single-crystal X-ray diffraction. Molecular conformations, inter- and intramolecular interactions and packing arrangements of crystals were characterised.

Polymorphism of clevudine was addressed for the first time. Three polymorphs of clevudine were isolated and characterised in terms of crystal structures and thermal behaviour. The solubility and thermodynamic stability ranking of the three forms was established and schematic energy-temperature diagrams were constructed through the use of the thermal methods listed above, solvent-mediated transition experiments and by kinetic solubility experiments. Characterisation by infrared (IR) spectroscopy has made it possible to promptly and effortlessly identify each form.

Multiple novel solid-state forms of the antimalarial drug candidate MMV652103 were produced including four polymorphs, a hydrate, five co-crystals and a salt. The solubility and thermodynamic stability ranking of the polymorphs was established through thermal analysis and kinetic solubility experiments. An amorphous form showed an improvement in dissolution rate, with a concentration 3-4 times that of the crystalline forms after one hour. The designation as co-crystals or salts was accomplished through the use of single crystal X-ray structural analysis and confirmed by IR spectroscopy. Stoichiometry was determined by ^{1}H - nuclear magnetic resonance (NMR) spectroscopy. A customised solubility experiment was carried out to compare the dissolution rates of the various multi-component forms of MMV652103 in an environment simulating the human duodenum. An enhancement of the dissolution rate was observed with a maximum concentration 4.7 times higher for the co-crystal than for the untreated active compound.

Inclusion complexation of (±)-α-lipoamide with native CDs (α-, β-, and γ-CD) was confirmed by comparison of putative PXRD traces with those of known isostructural series. Novel complexes were synthesised with the above mentioned native CDs as well as with three derivatised CDs (TRIMEA, DIMEB and TRIMEB). The crystal structures were characterised by single-crystal X-ray diffraction. Host-guest stoichiometries were determined by ^{1}H-NMR spectroscopy and validated by the ratio of mass loss through TGA. Water composition, melting points and thermal stability in terms of decomposition and guest loss temperatures of the complexes were determined by means of the appropriate thermal methods (DTA, TGA, DSC, HSM). Phase solubility experiments were carried out and showed solubility enhancements for the bioactive compound ranging from a 1.8 fold increase with α-CD to a 7.4 fold increase with randomly methylated β-CD.

Acknowledgements

The author would like to thank:

Professor Mino Caira for his excellent supervision, guidance and the many great opportunities afforded me.

Professor Susan Bourne for her co-supervision, guidance and support.

My colleagues at the Centre for Supramolecular Chemistry Research for their support and assistance.

Professor Kelly Chibale and the H3D Centre for supplying many of the drug leads used in my research.

Dr Liezl Gibhard and her colleagues from the UCT Division of Pharmacology for pharmacokinetic analysis.

The University of Cape Town for financial support.

The role models and friends made along the way for their enthusiastic support and for contributing to my intellectual development: Dr Vaughan Maurel, Dr Dyanne Cruickshank, Dr Lee Hunt, Dr Daniel Otto, Dr Righard Lemmer and Dr Helanie Lemmer.

My partner, Gerda Smits, for moral support, love and inspiration.

Finally, my friends and family for their love, encouragement, support and patience throughout this journey.

Table of contents

Chapter 1: Introduction **4**

Supramolecular chemistry and crystal engineering 4

Polymorphism 7

Solvates and hydrates 13

Cyclodextrin inclusion complexation 18

Active pharmaceutical ingredients (APIs) and bioactive compounds in this study 23

Aims and objectives 25

References 26

Chapter 2 : Materials and experimental methods **35**

Materials 35

Experimental methods 36

Part 1 – General synthetic procedures 36

Part 2 – Analytical methods 38

Additional resources 49

References 49

Chapter 3: Polymorphism of clevudine: a nucleoside analogue antiviral drug **52**

Clevudine Form 1 53

Clevudine Form 2 62

Clevudine Form 3 70

Comparison of the various polymorphs of clevudine 80

Solubility results 82

Isothermal solvent-mediated transformation 83

Energy-temperature diagram 84

Hirshfeld plots 86

Conclusions 89

References 91

Chapter 4: The drug lead 6-(3-(Methylsulfonyl)phenyl)-3-(4-(methylsulfonyl)phenyl)-imidazo[1,2-b]pyridazine (MMV652103): a novel antimalarial drug candidate.

Part one **92**

MMV Form 1 92

MMV Form 2 101

MMV monohydrate 111
MMV Form 3 123
MMV Form 4 127
Comparison of various polymorphs of MMV 132
Solubility experiments 133
Hirshfeld plots 140
Conformations 143
References 144
Chapter 4: Part two 145
MMV-adipic acid co-crystal (MMVADIP) 145
MMV-glutaric acid co-crystal (MMVGLUT) 162
MMV-succinic acid co-crystal (MMVSUCC) 175
MMVSUCC1 176
MMVSUCC2 176
MMVSUCC3 178
MMV-fumaric acid co-crystal (MMVFUM) 206
MMV-malonate salt (MMVMAL) 219
Conformations 232
Hirshfeld plots 233
Comparison of physicochemical properties 240
Solubility comparison 241
Conclusion 243
Future work 244
References 245
Chapter 5: Inclusion of the antioxidant (±)-α-lipoamide in cyclodextrins 247
α-Cyclodextrin inclusion complex with (±)-α-lipoamide (ACDALA) 247
β-Cyclodextrin inclusion complex with (±)-α-lipoamide (BCDALA) 256
γ-Cyclodextrin inclusion complex with (±)-α-lipoamide (GCDALA) 267
TRIMEA inclusion complex with (±)-α-lipoamide (TMAALA) 272
DIMEB inclusion complex with (±) α-Lipoamide (DMBALA) 287
TRIMEB inclusion complex with (±)-α-lipoamide (TMBALA) 293
Phase solubility studies 308

Conclusion 311
Future work 312
References 313
Chapter 6: Conclusion 316
Summary 316
Future work 320
Final comments 321
References 322

Chapter 1

Introduction

The majority of marketed drugs are solid oral dosage forms such as tablets or capsules for the simple reason that these are often more stable during storage, convenient to use and more compact than the alternatives.[1] The variety of solid-state forms in which active pharmaceutical ingredients (APIs) can exist and each potentially having unique physicochemical properties presents an opportunity to discover, characterise and select the solid-state forms with optimal features for the formulation of drug products.

In this chapter, various methods of supramolecular modification are described with a focus specifically on their potential uses in the pharmaceutical field. The specific approaches utilised in this project including the formation of polymorphs, co-crystals, salts, solvates and inclusion complexes will be described.

A brief description of each of the bioactive compounds and APIs explored in this work will also be presented in this chapter.

Supramolecular chemistry and crystal engineering

"What would the properties of materials be if we could really arrange the atoms the way we want them? …when we have some control of the arrangement of things on a small scale we will get an enormously greater range of possible properties that substances can have, and of different things that we can do." These were the words of the famous physicist Richard P. Feynman in a lecture titled, "There's Plenty of Room at the Bottom", given at Caltech to the American Physical Society on December 29, 1959.[2] Though these words are more commonly associated with nanochemistry today, they ring true also for supramolecular chemistry and crystal engineering.

Supramolecular chemistry

The term 'supramolecular chemistry' has been around for over a century with the introduction of a more contemporary meaning ascribed to Lehn (who received a Nobel Prize for work in this field in 1987)[3] namely: "chemistry of molecular assemblies and of the intermolecular bond." The colloquial use of the term at the time of writing this thesis includes countless examples of applications such as in molecular devices and machines, host-guest chemistry, molecular recognition, self-assembly and overlaps with many other fields such as nanochemistry.[4,5] In general this term is used for a wide-ranging variety of interatomic interactions that encompasses virtually every attractive or repulsive effect that does not fall under covalent bonds. The focus of the work presented in this thesis is mainly on organic

supramolecular chemistry and for this reason the descriptions are focused on interactions related to this field. The main forces are hydrogen bonding, van der Waals forces, π-π, C-H···π, dipole-dipole, hydrophobic, ion-dipole and ion-ion interactions. The energies involved in these types of interactions vary greatly, though it is a combination of all these effects on the encompassed components (including solvents and gases) that results in the eventual packing arrangement found in crystals.[6]

The importance of supramolecular chemistry for applications in design of new forms of APIs lies in the fact that the bioactive molecular component retains its inherent medicinal activity while potentially obtaining physicochemical properties differing from the starting components in a beneficial way. The advantageous properties could be for example, improved dissolution rate, solubility enhancement, easier tableting and handling during manufacture because of its improved flow properties, elasticity/plasticity, hardness/softness, lower tendency to convert into a less desirable solid drug form, and improved chemical stability through a reduced tendency to absorb moisture from the atmosphere. These properties can translate into positive effects such as a more rapid onset of action, reduced doses required for the same effect, longer shelf-life and reduced side-effects, among many others. The other important aspect is that the unique multi-component crystals having altered properties can be patented as novel pharmaceutical forms.[7,8]

Crystal engineering

The first use of the term "crystal engineering" in the literature was by Pepinsky in 1955 in an abstract for a meeting of the American Physical Society[9]; however, it is commonly associated with Schmidt's study of photodimerisation related to solid-state reactivity based on topochemical principles in 1971.[10] In his pursuit of understanding the mechanisms driving crystal formation and devising ways to predict or direct the properties of the resulting crystals, Schmidt came to the conclusion that no real progress could be made until such time that protocols were in place for prediction of crystal structures from molecular structures. He referred to this time as "the phase of crystal engineering".[10] In order to describe crystal engineering a comparison can be made to conventional organic synthesis, where the understanding of kinetic control over the forming and breaking of covalent bonds is a prerequisite for success and is even taught in elementary textbooks of organic chemistry. Crystal engineering relies on supramolecular synthesis where the mechanisms and kinetic processes of non-covalent bond formation in crystals are less well understood.[11] The main difference pointed out by Whitesides *et al*.[12] between supramolecular synthesis and conventional covalent synthesis is the energies involved, where product formation in the former is mainly driven by enthalpy and the latter being a result of much weaker interactions and dependent on the interplay between entropy and enthalpy. The outcomes of the

processes in terms of products formed in the case of supramolecular synthesis thus become much harder to predict. Desiraju describes crystal engineering as: "the understanding of intermolecular interactions in the context of crystal packing and in the utilisation of such understanding in the design of new solids with desired physical and chemical properties".[13] Crystal engineering attempts to make use of the understanding of intermolecular interactions to guide molecular recognition, self-assembly and self-organisation to form desired products. The hydrogen bond is a highly useful tool in crystal engineering in that it ranks amongst the strongest intermolecular interactions (after metal-coordination bonds and ionic interactions) and possesses the trait of being directionally specific.[14] The International Union of Pure and Applied Chemistry (IUPAC) definition for a hydrogen bond is as follows: ''The hydrogen bond is an attractive interaction between a hydrogen atom from a molecule or a molecular fragment X–H in which X is more electronegative than H, and an atom or a group of atoms in the same or a different molecule, in which there is evidence of bond formation''.[15] Etter proposed a set of empirical hydrogen bonding "rules" in 1990 for prediction of bonding in crystals and included rules for bonding between specific functional groups.[16] These "rules" are still very useful today and though they are seen more as guidelines, they are used together with a constantly evolving understanding of interaction hierarchies for use in crystal engineering. This means to direct molecular recognition, self-assembly and self-organisation by identifying patterns in intermolecular interactions and determining their occurrence frequency is clearly not a new idea. Ways to simplify this means of prediction includes the use of "supramolecular synthons", a term coined by Desiraju in 1995 for what he describes as "kinetically defined structural units that ideally express the core features or kernel of a crystal structure, and which encapsulate the essence of the crystal in terms of molecular recognition".[17] An important point to note is that even though hydrogen bonds are very useful in crystal engineering they are not the only forces making up synthons, for instance halogen bonding can also be used in cases where no strong hydrogen donor and acceptor groups are present as was shown by Baldrighi *et al.* for the topical antifungal agent haloprogin.[18] These synthons are identifiable units consisting of molecular fragments with specific chemical and geometrical properties that are connected by various supramolecular forces. It is possible to make use of software linked to the Cambridge Structural Database (CSD)[19] that makes hydrogen bond propensity predictions based on occurrence frequencies of particular synthons or bonding motifs in the CSD.[20-22]

A lot of research goes into the establishment of rules for prediction of non-covalent intermolecular interactions and there are countless examples of published papers with a focus on determining hierarchies of specific synthon formation. These hierarchies are usually based on experimental

outcomes and can be aided by statistical analysis of frequency of occurrence in the CSD,[23,24] aided by the calculation of molecular electrostatic potential surfaces,[25-30] accessible surface,[31] focus on charge-assisted hydrogen bonding[32,33] or on halogen bonding[34-36] and a combination of all of these aspects is usually utilised. These are all representative examples and by no means meant to be a comprehensive list. Increasing interest in crystal engineering is also observed nowadays in the previously less studied electrostatic interactions analogous to the halogen bond (related to group 17 elements), namely the chalcogen bond (group 16), pnictogen bond (group 15), tetrel bond (group 14), triel bond (group 13) and the aerogen bond (group 18).[36] The reversible nature and comparatively weak forces involved in intermolecular interactions limit the cogency of comprehensive rules for synthon and hydrogen bond hierarchies. This is compounded by the fact that for even a small increase in the molecular functionality in a system the number of potential supramolecular synthons increases greatly and these molecular functionalities can interfere with the predicted formations in various ways. The competing synthons in cases of multi-component systems can also undergo what is referred to by Aakeröy *et al.* as "synthon crossover"[37] or can undergo "synthon polymorphism" [38,39] (described in a subsequent section). Apart from the interactions involving relatively strong hydrogen bonds, another often overlooked functionality is that of hydrocarbon cores of organic molecules that often affect the expected outcomes.[14,40]

Crystal engineering thus has inherent limitations, but is continuously evolving with guidelines for non-covalent synthetic strategies becoming ever more reliable and reproducible as knowledge in the field grows.

Polymorphism

The term polymorphism, from the Greek words "poly" meaning many and "morph" meaning form, is used to describe the diversity that can be found in nature. In chemistry specifically, the term is used for the occurrence of at least two different possible arrangements of solid-state crystal structures from the same molecule/molecules in three-dimensional space.[41,42] Polymorphism is primarily subcategorised into packing and conformational polymorphism. The former is more common for rigid molecules and is used to describe different ways that molecules pack in three-dimensional space to form crystals where no variation in their conformation occurs. In the case of the latter subcategory, the molecules in question have some level of flexibility and there are dissimilarities in the conformations of the molecules making up the various conformational polymorphs.[43] Another type of polymorphism is referred to as synthon polymorphism where the primary synthons are different for the various polymorphs.[44] The

various conformations, packing arrangements and non-covalent interactions connecting molecules in different polymorphs can result in differences in their physicochemical properties.[45]

The importance of polymorphism in the pharmaceutical field lies in these differing physicochemical properties. Examples include stability during storage or handling, melting points, heat capacity, density, flowability and hardness for tableting, dissolution rate and solubility. The knowledge of both the existence, as well as the specific variables required to produce, each form of an API is of great importance, not only for the obvious conceivable benefits but also to avoid unexpected transitions to other forms during processing or storage with potentially detrimental outcomes. A classic example of such a scenario is that of the anti-HIV agent ritonavir (Norvir™).[46] In summary, this drug underwent a transition during processing and storage from the marketed polymorphic form to a more stable, less soluble form that resulted in a drastic decrease in bioavailability of the API. The product was temporarily withdrawn from the market and the estimated loss in sales for Abbott was $250 million in 1998 alone.[47]

In order to avoid or control the transitions from one form to another it is crucial to have knowledge of the thermodynamic stability relationships of these polymorphs. A useful way to describe these relationships is by defining pairs of polymorphs either as enantiotropic or monotropic, where in the case of enantiotropic polymorphs, which form is more stable will depend on the specific temperature and pressure while for monotropic polymorphs one form will be more stable at any given temperature.[48] It is possible to differentiate between monotropic and enantiotropic polymorphs by considering the correlation between the free energy and the temperature of the various forms. The Gibbs energy of a phase is represented in definition 1.1.

$$G = H - TS \tag{1.1}$$

where G is the Gibbs energy, H is the enthalpy, T the absolute temperature and S the entropy of a phase.[42] A visual representation of the summarised information in the form of a qualitative energy *vs* temperature diagram is presented in Fig. 1.1. The temperature termed T_t in Fig. 1.1. depicts the temperature at which both enantiotropic forms will have the same free energy and be in equilibrium (i.e. $G_A = G_B$) and this temperature will be below the melting point of both forms. These lines only cross once and this shows that at any other temperature it will either be the one or the other form that has the higher stability. In the case of monotropy the free energy of one form will be lower at any temperature and the isobars do not cross before the melting point. This means that one form, that with

the higher free energy (A) will always be metastable when compared to the other form (B) with the lower free energy and form A will thus be energetically driven to transform into form B ($G_A > G_B$).[49]

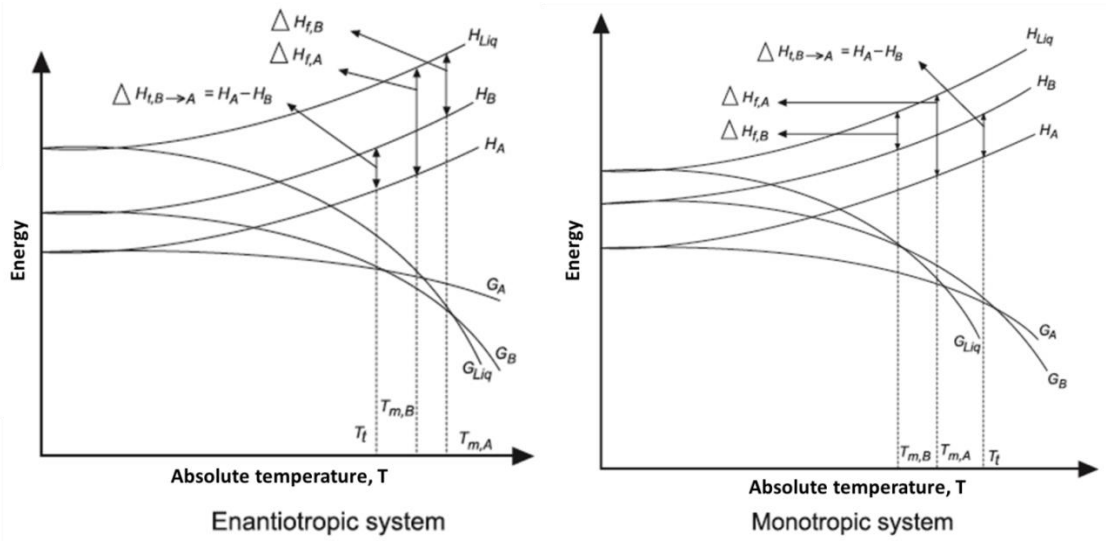

Fig. 1.1 Energy-temperature plots for enantiotropic (left) and monotropic (right) systems. G is the free energy, H is the enthalpy, T is the temperature, subscripts A, B and Liq denote polymorph A, polymorph B and the liquid phase respectively. Subscripts f, t and m, refer to fusion, transition point, and melting point, respectively (Adapted from Lohani and Grant, 2006).[45]

A set of rules for characterisation of polymorphs as either enantiotropic or monotropic was compiled by Burger and Ramberger in 1979 and these are summarised in the following section.[50,51]

- The heat of transition rule states that if an endothermic phase transition takes place, a thermodynamic transition point can be found below this temperature and the two polymorphs will be enantiotropically related. If an exothermic phase transition takes place, there will not be a thermodynamic transition point below this temperature, indicating monotropy or that the transition temperature is higher than what was experimentally observed.
- The heat of fusion rule states that in the case of enantiotropically related polymorphs the higher melting form has a lower heat of fusion, if not they are monotropically related.
- The density rule suggests that a crystal modification with the highest packing density will be the most stable form at absolute zero.
- The infrared rule applies to hydrogen-bonded molecular crystals and states that the polymorph with the higher value for its first absorption band in the infrared spectrum will have a higher entropy value and consequently, lower stability at absolute zero.

In certain cases it is possible that polymorphic conformational flexibility can render the heat of transition rule invalid, though the rule was experimentally shown to be accurate in 99 % of the circumstances tested by Burger and Ramberger[50,51] and this rule along with the heat of fusion rule is considered a reliable and essential means of stability ranking. There are many exceptions to the density and infrared rules and these are considered more useful as guidelines.

The crystallisation of a certain polymorphic form takes place in a combination of steps that include nucleation, crystal growth and Ostwald ripening.[45] The latter, otherwise known as Ostwald's step rule describes the phenomenon where a material that leaves a certain state to transform into a more stable one will not always transform into the most stable state under the current ambient conditions, but rather into the state that is formed with the smallest loss of free energy, or in other words the closest state of energy into which it can transform.[52] In the process of crystallisation there is always a combination of thermodynamic and kinetic influences, the idealised extremes of which duly appear contradictory. If only thermodynamic factors played a role, the system would be able to select the arrangement with the lowest free energy from all possible multimolecular clusters in solution. The clusters would then aggregate into larger clusters by following the path that will lead to the lowest energy through each step of this process and dynamically self-correct if global minima exist with lower energies than that of the local clusters. On the other hand, if kinetics were the only force driving crystal formation, a hydrogen bond would form between the strongest hydrogen bond donor and acceptor and then with the second and so on and so forth. These bonds would not be able to be broken and thus no dynamic changes would occur during further growth. Neither of these extremes is the reality and a competition between thermodynamic and kinetic factors results in the final product of what can be seen as a supramolecular chemical reaction, with different polymorphs being different reaction products.[14]

Crystal structure prediction has already been mentioned in the section describing crystal engineering and the following segment focuses specifically on polymorph prediction. The methods of polymorph prediction are continuously becoming more sophisticated.[21,44,53-58] At present these methods can produce a short list of computer-generated potential crystal structures that frequently contain the observable structures in the case of small rigid molecules.[59] The limitations become apparent when larger, more conformationally flexible molecules with a variety of functional groups are considered. How the nucleation and growth of the predicted structures would be accomplished or whether they would even be possible is another question altogether. The understanding of the kinetics and thermodynamics influencing the formation of crystals i.e. why some predicted structures will be observed and others not,

is possibly the greatest limitation of current predictive methods.[57] At present these methods are useful in conjunction with experimental methods following a logical strategy and applying due diligence. A well-known statement by McCrone[60] made in 1965, that the number of polymorphic forms of a particular compound that one will discover is directly proportional to the time and money spent on it, is likely equally as applicable today.

Metastable and glassy/amorphous states

The most thermodynamically stable polymorph is usually selected for the formulation of drug products as this should result in the longest shelf life, and circumvent the possibility of transitions to a more stable form during storage or processing. The use of metastable crystalline or amorphous forms can, however, be considered in cases where these forms provide a sufficient medical benefit, for instance an improvement in dissolution rate or solubility while being stable enough under standard storage and processing conditions to resist phase transitions.[61]

What defines a solid as being amorphous is a lack of long-range order in its molecular packing arrangement. It is important to note that in most cases there will exist some degree of disorder in any crystalline substance and *vice versa* for amorphous solids.[62] The terms crystalline and amorphous exist as a continuum with potential mesophases found between the extremes of absolute seamless long-range order and complete lack thereof.[63] If most of the substance in question is in a disordered state, the substance can be termed amorphous and if this form exists below the glass transition temperature (T_g) (defined in following section) it is termed a glass.[64]

The changes observed while gradually cooling a supercooled liquid and a melt are identical. This is true down to a certain temperature referred to as the glass transition temperature (T_g) where further cooling will result in an increase in the rate at which viscosity increases per unit drop in temperature.[65] The increase in viscosity will cause the liquid to transform into a syrup-like substance, then into a viscoelastic state and eventually into a brittle state. This brittle state is termed a glass. A glass can therefore be defined as a liquid with an exceptionally high viscosity (± 1014 Pa. s).[66] Large amplitude motions still take place in glasses, but simply at a much slower time scale. Glasses behave like solids mechanically and under most experimental time scales even though their molecular structures are similar to that of liquids.[67] The large amplitude molecular motion taking place could result in what is known as “structural relaxation”, where transition to a more stable form occurs if the activation energy required is reached for molecular coordinational changes.[68]

The Gibbs energy (described previously and defined in 1.1) of amorphous forms will be higher than in the case of crystalline forms. This difference drives the amorphous phases to reach a thermodynamic equilibrium by means of crystallisation or structural relaxation.[63,69] A schematic comparison of the energy-temperature relationship between crystalline and amorphous phases is presented in Fig. 1.2. In this example only one crystalline phase and one amorphous phase is shown, but this does not necessarily have to be the case. There can exist multiple crystalline and amorphous phases, the former instance is termed polymorphism and the latter polyamorphism.[70]

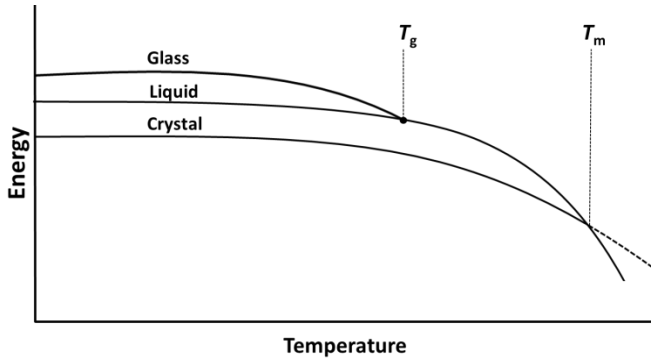

Fig. 1.2 Energy-temperature plot (in arbitrary units) for a single-component system showing a comparison of the Gibbs energy of a glass and a crystalline phase. T_g and T_m represent the glass transition and melting temperatures respectively (Adapted from relations developed by Shalaev and Zografi).[70]

The glass transition, unlike the melting point, is kinetically driven and influenced by heating/cooling rates. This is because slower heating rates will allow more time for molecular motions to result in relaxations.[65] It is however thermodynamically necessary to prevent amorphous solids from having lower enthalpies than crystalline solids. This occurrence is known as the Kauzmann paradox.[63] The T_g can thus be influenced by the thermal history of a sample.[71]

Strict regulatory requirements for maintaining the stability of pharmaceutical products are in place and a thorough understanding of the relationships of the amorphous and crystalline forms is a requirement in the development of new drugs.[70] It is however possible for amorphous forms of APIs to reach the market as drug products. Examples include rosuvastatin calcium (Crestor®), quinapril hydrochloride (Accupril®), and cefuroxime axetil (Ceftin®).

Solvates and hydrates

A solvate is a solid in which a solvent is incorporated into, or accommodated within, the crystal structure. If the solvent in question is water this structure is called a hydrate. In some cases the solvent molecules merely fill voids formed by the packing of other molecules. These voids can be in the shape of channels or closed off three-dimensional cages. These cage-like structures are called clathrates.[72] In other cases the solvent molecules can be strongly bound to other molecules within the crystal structure and play a major role in maintaining the integrity of the structure. Desolvation/dehydration can result in collapse of the crystal structure in these cases resulting in the formation of amorphous products.[73]

Solvates of APIs often show an improvement in the aqueous solubility compared to a crystalline form of the API alone, whereas hydrates are more prone to decrease the aqueous solubility.[72] In the absence of general rules, these simple guidelines are handy, but prudent analysis demands the determination of the relevant properties for each solvate and hydrate individually.[67]

The use of a solvate for the formulation of a completed drug product is complicated by its difficulty in storage in that a solvate is most stable in an environment of its solvent and when taken out of this solvent the partial pressure of the latter essentially becomes zero. The solvate will tend to transform into a more stable form.[72]

Some APIs have the capability to form solvates with a great number of different solvents. One example is the sulfadrug sulfathiazole that has over a hundred known solvates.[74] The large number of solvates does not, however, necessarily equate to useful products for drug formulation due to the limited number of non-toxic solvents that can safely be administered. Even those solvents considered safe, for example ethanol, will only be considered if this form shows a significant improvement over the API alone. Hydrates have however been selected and developed for use in drug products.[75]

Pharmaceutical salts and co-crystals

Finding an all-inclusive and clear definition for co-crystals that everyone will agree on, like many terms in chemistry, will be challenging given that even the spelling (co-crystal/cocrystal) is subject to debate. A recent definition used in a draft of industry guidelines for the regulatory classification of pharmaceutical co-crystals by the United States Food and Drug Administration (FDA) for co-crystals is as follows: “Co-crystals are crystalline materials composed of two or more different molecules, typically drug and co-

crystal formers (coformers), in the same crystal lattice". In this draft a distinction is made between salts and co-crystals by the components of a co-crystal interacting non-ionically. A distinction is made between co-crystals and solvates/hydrates in that the coformer is required to be non-volatile and not a solvent (including water).[76]

This definition was originally proposed in a similar set of FDA guidelines in December 2011. A panel of 46 scientists that were at the time involved in co-crystal research proposed two alternative definitions in 2012 in response to the proposed FDA definition.[77] Problems originally found with the FDA definition were that there often exists overlap between what is defined by the FDA as either polymorphs, salts, co-crystals and/or solvates/hydrates. Complications in classification also arose when considering the full range of readily available potential coformers, for example in cases such as nonvolatile solvents (e.g. diols), other APIs (i.e. for drug-drug co-crystals) and for inorganic salts (ionic co-crystals). The term "ionic co-crystals", coined by Braga *et al.* is an example of new terms arising to define these materials that fall within overlapping classifications,[78] where ionic co-crystals is a term used to describe a co-crystal composed of an organic molecule and an inorganic salt, such as an alkali or alkaline earth halide.[79] An example presented by Aitipamula *et al.*[77] where classification was not possible with the FDA definition was that of a marketed drug, escitalopram oxalate,[80] where a single crystal structure is made up of protonated escitalopram cations, water molecules, oxalate dianions, and diprotonated oxalic acid molecules. The first of the proposed definitions is broader and according to Aitipamula *et al.*[77] more consistent with the scientific literature than the FDA definition was at the time and is as follows: "Co-crystals are solids that are crystalline single phase materials composed of two or more different molecular and/or ionic compounds generally in a stoichiometric ratio". This definition attempted to deal with a problem posed with the FDA definition of the components needed to be in a neutral state in an older draft of guidelines. The second definition adds that the materials "are neither solvates nor simple salts" and thus differentiates between co-crystals and solvates/salts without providing any clear boundaries.

A common boundary that is described by Aakeröy *et al.* as being contoversial, used to distinguish between solvates/clathrates/inclusion compounds and co-crystals is that the reactants used to prepare the material need to be solid at ambient conditions in order to be labeled as co-crystals.[81] Bacchi *et al.* produced solid forms of the anaesthetic, propofol, (a liquid at ambient conditions) by solution crystallisation with 4,4'-bipyridine and phenazine respectively and argue that these should be labeled as co-crystals and not solvates.[82] Steed suggests that the distinction is subjective and does not require to

be part of a formal definition and that hydrates and solvates can be seen as subcategories of co-crystals.[83]

Setting cut-off values for what constitutes a salt or co-crystal based on proton location, bond lengths and bond angles through methods including single-crystal X-ray (or neutron) diffraction, infrared or solid state NMR spectroscopy might seem trivial and will in most cases be routine. Complications can however arise in cases where proton locations are ambiguous. Childs *et al.* describe a continuum existing between the extremes of salts and co-crystals that exemplifies these ambiguous cases. Disorder as a result of partial occupancy of protons can be observed in certain cases where multiple protonation states exist or where protons are being "shared".[84] In some cases changing variables such as temperature may even cause changes in proton bond distances in what is referred to as thermally induced proton migration.[85-87]

With boundaries of distinction seeming somewhat blurred for what constitutes a co-crystal and odd cases existing that do not perfectly fit either classification, there still appears to be no clear consensus on an exact definition. In order to not get bogged down by the vital, yet non-trivial task of defining the term, an expedient classification is proposed for purposes of this thesis. A feature that will be used to distinguish between solvates and salts/co-crystals in cases of crystalline single-phased materials will be that if the coformer is a liquid at standard temperature and pressure the crystal will be considered a solvate and if solid will be considered either a salt or a co-crystal. Further distinction will be made between salts and co-crystals at the discretion of the author on the basis of whether or not protonation occurs, components are in a charged or neutral state and whether interactions are ionic or non-ionic.

The differentiation between salts and co-crystals is important not only for the fact that salts and co-crystals have differences in stability and solubility, but it is also imperative for patentability.[88-90]

The potential benefits and pharmaceutical applications of co-crystals include everything described in the preceding sections and many more. Co-crystals can impart much greater changes in dissolution rates and solubility[91-95] to APIs than what is conferred by various polymorphic forms. Membrane permeability is another parameter that can be altered while simultaneously improving solubility by the formation of co-crystals.[92,96-100] The resultant impacts on pharmacokinetic parameters such as bioavailability[101-106] can be utilised to reduce required dosages or shorten onset times of effect or create extended release dosage forms in cases where dissolution rates are increased or decreased respectively.[107,108] Salts and co-crystals can improve solubilities of APIs by 100-1000 and 4-160 times respectively.[109,110] The intrinsic crystallinity of co-crystals (they are by definition crystalline) grants them higher stability than

amorphous forms of the API. In cases where APIs are hygroscopic, co-crystallisation can be used as a tool to improve the stability to hydration and reduce the chances of occurrence of phase changes.[111] APIs are considered highly polymorphic when they have more than four forms.[1] Salts and co-crystals greatly increase the number of potential forms, with some APIs having more than a dozen crystalline salt forms.[112,113] Unlike in the case of salts, co-crystals do not require ionisable groups and the possibility of making tertiary or quaternary co-crystals and not being limited to one ionisable target functional group (as is usually the case for salts) renders an even greater number of possible forms in the case of co-crystals.[114] In a study by Childs *et al*., twenty-four co-crystals were prepared with the anti-epileptic drug, carbamazepine.[115] The number of potential coformers is further expanded if inorganic salts are added to the list for the formation of ionic co-crystals[78,79,116] or salt co-crystals (neutral molecule with its molecular salt).[117,118] Co-crystals tend to have an advantage over solvates/hydrates in stability. The production of salts or co-crystals can also be used as a means of purification or to effect enantioselectivity. [112,119-121] Crystal engineering strategies can be applied to logically select appropriate coformers from a library of thousands of potential coformers (at least hundreds if only organic molecules from the Generally Recognized as Safe or GRAS list[122] are considered).[8] Prediction of co-crystals is considered non-obvious and this holds a very valuable advantage in terms of intellectual property in that patent protection is considered significantly easier for co-crystals than for other solid forms.[88] Co-crystals are seen in the same light as polymorphs of APIs when it comes to regulatory requirements and not as new APIs.[76] This greatly reduces the time and money required to have a co-crystal approved for use as the rigorous clinical trials required for new APIs are not required in the case of co-crystals.

The utilisation of statistics from the CSD[19] as well as the amassed collective knowledge of synthon hierarchies can be of great use in selecting coformers with a high likelihood of forming co-crystals. There are countless examples to be found in the literature of such hierarchies and statistics of synthon occurrence used for aiding prediction of co-crystal formation, some of which have already been mentioned in the supramolecular chemistry and crystal engineering section of this thesis.[103,114,123-127] Physical experimentation is however still required for screening. The use of *ab initio* virtual screening for the prediction of chances of formation can save time, money and effort in reducing the number of physical experiments required.[22,128-134] Predetermining the resultant physicochemical properties of these products can, however, be a lot less straightforward. One example of a useful guideline in predicting whether a particular combination will result in the formation of a co-crystal or a salt is by examining the differences in pK_a values. It is suggested that if the difference pK_a(base)-pK_a(acid) is higher than 3, a salt

will form; if the difference is less than 0, a co-crystal will form; anything in between will be either a salt or a co-crystal.[84,135] No rules exist for prediction of properties, though logic can be applied in selecting coformers to guide properties by considering general trends, for example melting points, by selection of higher melting coformers.[108,136-138] There are numerous examples of cases that do not follow these observed trends and for this reason they should only be considered as guidelines.

Isostructurality is the phenomenon where similar molecules with comparable unit cell dimensions have identical or close to identical packing motifs and this occurrence is inversely related to polymorphism.[139,140] Isostructurality is a fairly common occurrence in pharmaceutical salts and is also observed in the case of pharmaceutical co-crystals.[141,142] Co-crystals and salts can also exist as polymorphs and these, as in the case of polymorphism of APIs, are differentiated into packing, conformational, or synthon polymorphs.[44,143,144]

Nearly half of the drugs currently on the market are in the form of pharmaceutical salts and this number is rising, among other reasons, due to the potentially lucrative patentability of these forms. [112,145,146] Co-crystals on the other hand are at the moment still a bit of a gray area in terms of regulations due to the conundrum of classification alluded to in a previous section of this thesis. There are many contradictory claims to be found in the literature of what was the first pharmaceutical co-crystal to reach the market. This will depend entirely on one's definition of a co-crystal. The first drug-drug co-crystal was a combination of the tranquiliser/sedative drug, pyrithyldione, and the nonsteroidal anti-inflammatory drug propyphenazone, reported as early as 1937.[147] Wood *et al.*[22] claim that the first API marketed as a co-crystal is dapagliflozin propylene glycol monohydrate.[148] This drug is marketed in Europe as Forxiga™, [149] and approved for use by the FDA in the US as Farxiga™.[150] In this example the coformer in question is propylene glycol, which is a liquid at standard temperature and pressure and the product is considered to be a solvate by some. Novartis launched a novel drug used for the treatment of chronic heart failure called Entresto™.[151] This drug is a pharmaceutical ionic (drug-drug) co-crystal hydrate composed of monosodium sacubitril, disodium valsartan, and water. A co-crystal of the anti-diabetic drug ertugliflozin with 5-oxo-proline/L-pyroglutamic acid was very recently approved by the FDA and is marketed under the name Steglatro™.[152]

A consensus might not be reached any time soon on an exact definition of what constitutes a pharmaceutical co-crystal. Something that everyone will surely agree on however is that co-crystals hold great potential for improvement of the physicochemical properties of APIs in the solid-state. The potential to predictably and reproducibly modify the properties of APIs in a controlled way is becoming

a reality. The first pharmaceutical co-crystals have already been approved and have reached the market and surely many more will follow.

Cyclodextrin inclusion complexation

The IUPAC definition for an inclusion complex is a complex in which a host component forms a cavity or channel within which a second chemical species termed the guest component is located, with the condition that these components are not covalently connected.[153]

Native cyclodextrins

Cylcodextrins (CDs) are cyclic oligosaccharides built up from glucopyranose subunits connected by α-1,4-glycosidic bonds. The glucopyranose subunits have $^4C_1$ chair conformations resulting in what is described as conical cylinder- or truncated cone-shaped macrocycles (Fig. 1.3). Two distinct faces are formed with secondary hydroxyl groups on C2 and C3 placed on the wider rim (known as the secondary hydroxyl face) and primary hydroxyl groups on C6 on the narrower rim (known as the primary hydroxyl face). The most common CDs are made up of 6, 7 and 8 of these glucopyranose units in the cases of α-CD, β-CD and γ-CD respectively (Fig. 1.3) and are referred to as native CDs. The inner cavities of the torus-shaped macrocycles are lined with lone pairs of the O4 oxygen atoms forming the α-1,4-glycosidic bridges as well as hydrogen atoms on C3 and C5 resulting in the cavities being hydrophobic. The hydroxyl groups found on the primary and secondary rims of the CDs cause the exterior of these macrocycles to be hydrophilic. Intramolecular hydrogen bonding can take place between the secondary hydroxyl groups of contiguous glucopyranose units (O3-H···O2'). This results in stabilisation of the CD molecules and causes a decline in their aqueous solubility. In the case of β-CD, these hydrogen bonds form a continuous secondary belt that makes this CD the most rigid of the native CDs and consequently the least water-soluble (water solubility values are 145, 18.5 and 232 mg ml^{-1} at 25 °C for α-, β- and γ-CD respectively).[154] The constrained nature of the secondary hydroxyl groups arising from these hydrogen bonds results in this rim being wider than the comparatively narrower primary rim, where the free rotation of these hydroxyl groups effectively reduces the cavity diameter.[154-157] The cavity diameters for α-, β- and γ-CD are 4.7-5.3, 6.5-6.5 and 7.5-8.3 Å and the cavity volumes are 174, 262 and 427 $Å^3$ respectively.[156]

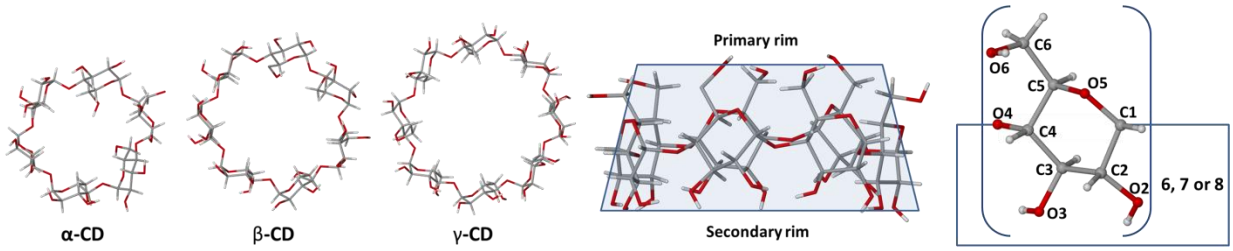

Fig. 1.3 Macrocyclic α-, β- and γ-CD rings (left); side view of β-CD displaying its truncated cone-shape (centre); structure and numbering scheme of an α-D-glucopyranose unit (right).

Derivatised cyclodextrins

Many other chemically modified cyclodextrins have been developed over the years and are available today. These usually have the hydroxyl functional groups at the 2- and 6- or 2-, 3- and 6-positions of the CD changed to different functionalities such as methyl groups. These changes can have considerable effects on the physicochemical properties of the host CDs. A fascinating feature of the methylated CDs is that they display negative solubility coefficients in water, with increased solubility at low temperatures and a tendency to crystallise at higher temperatures. This feature is ascribed to the hydrophobic effect. This phenomenon is hypothesised to be due to the water molecules becoming more mobile at higher temperatures while the CD molecules become more flexible. Hydration networks are broken down and the CDs are found to either have their hydrophobic cavities closed off by some of the flexible O6 methylated groups directed toward the inside of the cavity (also reducing the cavity size) or in some cases the O6 methyl groups of adjacent CD molecules are "self-included" into the CD cavities. Eventual aggregation and crystallisation follows.[158,159] The effect is greatly improved solubility of hydrophobic guest molecules at room temperature as well as the capability of including more bulky guest molecules due to a larger cavity. Other derivatised forms used in this study include hydroxypropyl-β-CD (HP-β-CD) and sulfobutyl ether β-CD (SE-β-CD). (HP-β-CD) and (SE-β-CD) generally improve the solubility of poorly water-soluble guest molecules by an even greater extent, are non-toxic, can effect improvement of permeability across biological membranes, but are amorphous and usually used as solubilisers.

Driving forces of CD inclusion complexation

As per the description of inclusion complexation defined earlier, no covalent bonding takes place between the host CD and the guest molecules. A common feature found in inclusion complexes of CDs with APIs is that the less polar moieties of the APIs are usually found within the hydrophobic CD cavity. The more hydrophilic moieties of the API are usually found either near the hydrophilic secondary hydroxyl rim of the CD or even protruding beyond the rim to interact with water or potentially interacting with other API or CD molecules outside the cavity. An interplay of various driving forces is known to contribute to host-guest inclusion in CDs. Among these are hydrogen bonding, electrostatic-, van der Waals- and hydrophobic interactions, as well as the release of energy as a result of exclusion of water from the cavity or reducing conformational strain.[160,161] The release of conformational strain on the macrocyclic structure is thought to be more a consequence of inclusion than a major driving force.[160] The role of water in the thermodynamics of binding was explored by Todorova and Schwarz[162] and it was determined that there was a larger effect in the case of β-CD than for γ-CD. It has been shown that all of the above-mentioned effects have a role to play in CD host-guest inclusion, but that the contribution of each will depend on the particular system in question. The relatively weak interactions typically result in low binding constants, with the complexes readily dissociating in aqueous solutions. This dissociation has been found to occur even more readily in biorelevant media such as intestinal fluids due to components such as lipids and bile acids having a higher affinity for the CD cavities and displacing the guest APIs as they compete for the cavities.[163]

Geometrical parameters used to describe CDs

Some useful parameters have been proposed and over the years become convention for describing the conformation of CD molecules.[164-166] These structural parameters are utilised for the comparison of the geometry of the CD host in the case of inclusion complexes with that of the uncomplexed forms (usually hydrated to some extent) to determine the effect of complexation on host conformation.

The parameters make use of the O4 atoms that link the contiguous glucopyranose subunits to establish polygons that serve as references from which distances and angles are measured. The specific parameters (Fig. 1.4) are the distance from O4 atoms to a generated centroid of the O4 polygon (*l*); the glycosidic O4···O4' distance (*D*); the O4···O4'···O4''angle (ϕ); the O4···O4'···O4''···O4''' torsion angle (*d*) and tilt angles between the mean plane through all the O4 atoms of the host and the plane through the atoms O4, C4, C1 and O4' of each respective glucopyranose residue (τ_2). Another useful parameter is the

O5-C5-C6-O6 dihedral angle (ω). This torsion angle indicates whether the C6-O6 bonds are pointed towards or away from the CD cavity.

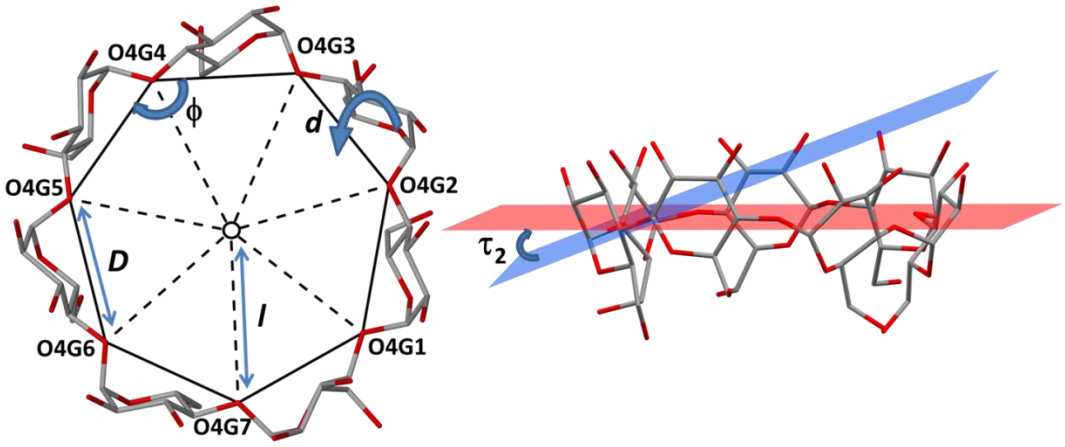

Fig. 1.4 Geometrical parameters used to describe CD conformation (*l, D,* ϕ, *d* and τ_2). β-CD was used as representative of the native CDs and hydrogen atoms are omitted for clarity. The plane in red represents the O4 mean plane and blue represents the plane through the atoms O4, C4, C1 and O4' of a single glucopyranose unit.

Packing and isostructurality of CD inclusion complexes

The phenomenon of isostructurality is very common in CD inclusion complexes.[139,167] Whether inclusion complexes will be isostructural depends primarily on the host CD molecules as these are relatively much larger than the guest molecules and also in most cases have a low degree of conformational flexibility. CD inclusion complexes are ordinarily monomeric or dimeric and can be classified as either being packed in cage- or channel-type modes. Continuous channels are formed when the cavities of the CD macrocycles line up in the case of channel-type packing. Cage-type packing occurs when the alignment of channels is imperfect and the CD cavities are closed off by other CD molecules to form cages. These cages can then be categorised as being herringbone- or brickwork-type arrangements based on whether or not the CD macrocycles in the same layer are tilted in relation to the others.[156,168] A schematic example of each of the broad categories of CD packing arrangements is presented in Fig. 1.5. Several other well-known CD packing arrangements occur including layer, zigzag, helical channel, intermediate, screw channel and chessboard arrangements that will not be discussed in detail here, but are presented in the relevant result sections of this thesis.

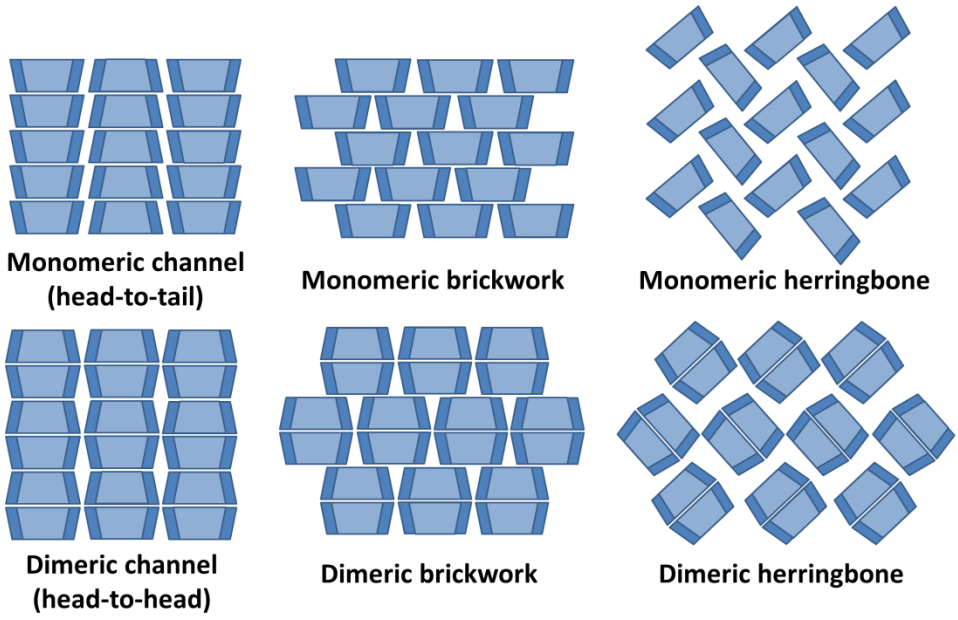

Fig. 1.5 Common packing arrangements of CDs.

The commonality of packing and isostructurality observed in different inclusion complexes has a very useful application in that reference libraries of isostructural series can be assembled. The experimental powder X-ray diffraction (PXRD) pattern of a putative inclusion complex can then be compared to that of an isostructural series. A match indicates isostructurality and this method can be used as a quick means of determining whether or not an inclusion complex was formed. Information regarding the space group, approximate unit cell dimensions and the packing arrangement of the host can also be deduced from a single PXRD experiment.[167]

Pharmaceutical applications of CDs

Cyclodextrins were discovered over a century ago by Villiers, with the first mention made in a publication in 1981 of what was later confirmed to be cyclodextrins.[169] It was, however, not until the 1970s that industrial scale production and widespread use of cyclodextrins caught on. At the time of writing this thesis, cyclodextrins are available at low cost and produced in industrial scales of over ten thousand metric tons per year of which roughly 30 % is used in pharmaceutics. Over 2200 research articles were published in peer-reviewed journals on the topic of CDs and more than 2300 patents/patent applications mentioned CDs in 2016 alone.[170] The numerous pharmaceutical applications are apparent from the number of reviews available on the topic as well as the ever growing list of more

than 50 pharmaceutical products currently on the market that contain cyclodextrins.[170-179] The uses include improvement of the solubility, dissolution rates and bioavailability of APIs.[180,181] Inclusion with CDs can effect improved thermal stability as well as stability against oxidation, hydrolysis and photodegradation.[182-185] CDs can also play a role as a carrier of volatile drugs, to mask unpleasant tastes or odours,[186] reduce adverse side effects such as ophthalmic irritation,[187] irritation at injection sites,[188,189] gastrointestinal ulceration[190] or control the rate at which a drug is released.[191] Cyclodextrins can be used to formulate different dosage forms for other routes of administration such as sublingual, nasal, pulmonary,[192] topical, ocular or injections via intramuscular/parenteral/intravenous routes.[171] Other technologies are often combined with the use of CDs to diversify the potential applications.[193,194] CDs are also used in targeted drug delivery[191,195] and even in gene therapy.[196] CDs are routinely used for chiral discrimination for example in GC columns to effect enantio-separations.[161,197]

The availability, low cost, proven safety and ever expanding list of potential applications of CDs in the pharmaceutical field illustrate the limitless potential of these highly useful and versatile compounds.

Active pharmaceutical ingredients (APIs) and bioactive compounds in this study

Clevudine

Clevudine [1-(2-deoxy-2-fluoro-β-L-arabinofuranosyl)-5-methyl-2,4-(1H,3H)-pyrimidinedione] is an L-nucleoside with potent activity against hepatitis B virus (HBV) infection, which is a major cause of morbidity and mortality,[198] with particularly high incidence in Asia (8-10 % of the adult population is chronically infected with HBV in China and other parts of Asia), the Western Pacific Region (6.2 % of adult population) and Africa (6.1 % of adult population).[199,200] According to the European Association for the Study of the Liver (EASL), roughly a third of the world's population has serological evidence of past or present infection with HBV.[201] Chronic HBV infection causes liver inflammation and damage leading to cirrhosis and liver cancer,[202] and it has been estimated that 350 million people are affected worldwide, with approximately one million deaths reported annually.[198] It has been established that the mechanism whereby clevudine inhibits DNA synthesis of HBV differs significantly from that generally associated with nucleoside reverse transcriptase inhibitors (NRTIs), with the advantage that its coadministration with other NRTIs results in a synergistic inhibitory effect on the virus.[203,204] Long-term monotherapy with clevudine has been reported to cause myopathy (muscle disease) in a number of patients and cases of resistance were observed.[205,206] As a result of myopathy the marketed drug was temporarily withdrawn after being approved in Korea in 2006, but was subsequently reinstated for use in that country when it

was determined that the myopathy is fully reversible following discontinuation of the treatment.[206] Clevudine was launched under the tradename Revovir® in the Philippines by the Tokyo-based company Eisai in 2010.[207] Eisai has also applied for market approval in other Asian countries including India, Indonesia, Malaysia, Singapore, Thailand, Vietnam and China. The potential market for future use of this drug to combat chronic HBV is therefore considerable.

A literature survey on clevudine revealed that an X-ray crystal structure of this drug at 'room-temperature' had been reported in 1996[208] with, however, no reference to crystal polymorphs, solvatomorphs or other solid-state forms of the drug, such as co-crystals, appearing at that time or since. Given the potential for significant widespread use of the drug, understanding of its solid-state chemistry was considered a worthy topic of investigation.

MMV652103

A novel antimalarial drug candidate 6-(3-(Methylsulfonyl)phenyl)-3-(4-(methylsulfonyl)phenyl)-imidazo[1,2-b]pyridazine (MMV652103) was synthesised by the University of Cape Town's Drug Discovery and Development Centre (H3D) after being identified as a "hit" from screening a BioFocus SoftFocus kinase library.[209] A global decline in malaria-related morbidity and mortality rates has been observed over the past 15 years; however malaria remains one of the leading global causes of death and disproportionately affects countries with high poverty indices.[210,211] The World Health Organization (WHO) empirical estimates of malaria cases and deaths were ~216 million and ~445 000 respectively in 2016.[211] Another worrying fact is that the incidence of resistance and reduced sensitivity to first-line artemisinin-based combination therapy is on the rise, with limited chemotherapeutic alternatives available at present.[212-215] MMV652103 displayed good in vitro potency (IC_{50}: K1 = 6.3 nM, NF54 = 7.3 nM) against multidrug resistant (K1) and sensitive (NF54) plasmodial strains and exhibited 98 % activity in the in vivo Plasmodium berghei mouse model in a 4-day test at 4 × 50 mg/kg po and high potency (ED_{90} = 1.5 mg/kg) in a SCID mouse model[216] against Plasmodium falciparum, comparable to marketed antimalarial drugs. The drug lead did however show poor aqueous solubility (< 5 µM at pH 6.5).[209,217] The aim was thus to produce new solid-state forms of this compound with improved aqueous solubility.

α-Lipoamide

(±)-α-Lipoamide (1,2-dithiolane-3-pentanamide) is a bioactive compound and is converted to unbound lipoic acid within the body. Though α-lipoamide does not occur naturally, α-lipoic acid is an endogenous

fatty acid that is produced in mitochondria of living organisms and consequently also found in certain fruits, vegetables and meat products that form part of the human diet.[218,219] α-Lipoic acid plays a major role in energy metabolism of mitochondria by serving as a cofactor for mitochondrial α-keto acid dehydrogenases.[220] This compound is of interest for its use as a nutritional supplement and potential therapeutic agent with wide ranging indications. The most apparent and exploited biological role is that of a potent antioxidant with an ability to scavenge various reactive oxygen species as well as the synergistic ability to induct other endogenous antioxidants.[219,221] It is currently in use for the clinical treatment of diabetic neuropathy[222] and has displayed beneficial effects as metal chelating agent,[223] immunomodulatory,[221] hypotensive,[224] anti-inflammatory, anti-aging,[225] antidiabetic,[226] neuro-cognitive enhancing,[227] antiretroviral[228] and is believed to hold promise for the treatment of Alzheimer's disease.[229] (±)-α-Lipoamide is more stable than α-lipoic acid, but the utility of this compound is drastically hindered by its poor solubility profile and its thermal and metabolic stabilities are not ideal.[222,230] Cyclodextrin inclusion could provide improvement in the aqueous solubility and stability of this compound and this avenue will be explored in this study.

Aims and objectives

The ultimate aim of the project on which this thesis is based was to produce novel solid-state forms of each of the three selected bioactive compounds with improved physicochemical properties for use in the formulation of completed products. This goal can be subdivided into the following steps that are each considered an objective in its own right:

1. Planning:

The first step is to devise logical screening strategies based on combining existing information on physicochemical and structural properties of the selected compounds with crystal engineering principles.

2. Experimental screening:

Kneading, neat grinding, liquid-assisted grinding and co-precipitation methods are used in empirical screening for polymorphs, solvates/hydrates, co-crystals/salts and CD inclusion complexes.

3. Synthesis of novel solid-state forms:

Once a screening experiment has proven the formation of novel solid-state forms, a method for the synthesis or purification of such forms is developed.

4. Characterisation of novel forms:

Thermal, spectroscopic and crystallographic methods are used to characterise the novel solid-state forms. Determination of stability during storage, solubility, dissolution rate, pharmacokinetics and ultimately efficacy will be determined and compared to that of the starting materials.

The knowledge gained in each of these steps will be used when these steps are repeated.

The materials and methods used in this study are described in chapter 2.

References:

1. S. L. Morissette, Ö. Almarsson, M. L. Peterson, J. F. Remenar, M. J. Read, A. V. Lemmo, S. Ellis, M. J. Cima and C. R. Gardner, *Adv. Drug Delivery Rev.*, 2004, **56**, 275-300.
2. E. Hutchings Jr, *Eng. Sci.*, 1960, **23:5**, 22-36.
3. J. -M. Lehn, *Angew. Chem., Int. Ed.*, 1988, **27**, 89-112.
4. J.-M. Lehn, *Proc. Natl. Acad. Sci. U. S. A.*, 2002, **99**, 4763-4768.
5. J. W. Steed and J. L. Atwood, *Supramolecular Chemistry*, John Wiley & Sons, Ltd.©, Chichester, United Kingdom, 2nd edn, **2009**, pp. 1-48.
6. G. W. Gokel, in *Comprehensive Supramolecular Chemistry II*, ed. J. L. Atwood, L. J. Barbour and G. W. Gokel, Elsevier, London, United Kingdom, **2017**, vol. 1, pp. 1-10.
7. J. Bernstein, *Polymorphism in Molecular Crystals*, Oxford University Press, Oxford, **2002**, pp. 297-308.
8. N. K. Duggirala, M. L. Perry, Ö. Almarsson and M. J. Zaworotko, *Chem. Commun.*, 2016, **52**, 640-655.
9. R. Pepinsky, *Phys. Rev.*, 1955, **100**, 971.
10. G. Schmidt, *Pure Appl. Chem.*, 1971, **27**, 647-678.
11. G. R. Desiraju, M. A. Johnson and W. Sander, *ChemPhysChem*, 2013, **14**, 631-633.
12. G. M. Whitesides, E. E. Simanek, J. P. Mathias, C. T. Seto, D. Chin, M. Mammen and D. M. Gordon, *Acc. Chem. Res.*, 1995, **28**, 37-44.
13. G. R. Desiraju, *Crystal Engineering: The Design of Organic Solids*, Elsevier, Amsterdam, New York, 1989, pp. 1-26.
14. G. R. Desiraju, *Angew. Chem., Int. Ed.*, 2007, **46**, 8342-8356.
15. E. Arunan, G. R. Desiraju, R. A. Klein, J. Sadlej, S. Scheiner, I. Alkorta, D. C. Clary, R. H. Crabtree, J. J. Dannenberg and P. Hobza, *Pure Appl. Chem.*, 2011, **83**, 1637-1641.
16. M. C. Etter, *Acc. Chem. Res.*, 1990, **23**, 120-126.
17. G. R. Desiraju, *Angew. Chem., Int. Ed.*, 1995, **34**, 2311-2327.
18. M. Baldrighi, D. Bartesaghi, G. Cavallo, M. R. Chierotti, R. Gobetto, P. Metrangolo, T. Pilati, G. Resnati and G. Terraneo, *CrystEngComm*, 2014, **16**, 5897-5904.
19. Cambridge Structural Database and Cambridge Structural Database System, Version 5.39 (February 2018 update), Cambridge Crystallographic Data Centre, University Chemical Laboratory, Cambridge, England, 2018.
20. P. T. Galek, L. Fábián, W. S. Motherwell, F. H. Allen and N. Feeder, *Acta Crystallogr., Sect. B: Struct. Sci.*, 2007, **63**, 768-782.
21. P. T. Galek, L. Fábián and F. H. Allen, *CrystEngComm*, 2010, **12**, 2091-2099.
22. P. A. Wood, N. Feeder, M. Furlow, P. T. Galek, C. R. Groom and E. Pidcock, *CrystEngComm*, 2014, **16**, 5839-5848.

23. J. A. Bis, P. Vishweshwar, D. Weyna and M. J. Zaworotko, *Mol. Pharmaceutics*, 2007, **4**, 401-416.
24. S. Aitipamula, P. S. Chow and R. B. Tan, *Cryst. Growth Des.*, 2014, **14**, 6557-6569.
25. C. B. Aakeröy, T. K. Wijethunga and J. Desper, *New J. Chem.*, 2015, **39**, 822-828.
26. C. B. Aakeröy, K. Epa, S. Forbes, N. Schultheiss and J. Desper, *Chem. - Eur. J.*, 2013, **19**, 14998-15003.
27. M. Perera, J. Desper, A. Sinha and C. Aakeröy, *CrystEngComm*, 2016, **18**, 8631-8636.
28. C. B. Aakeröy, D. J. Salmon, M. M. Smith and J. Desper, *CrystEngComm*, 2009, **11**, 439-443.
29. P. A. Wood, T. S. Olsson, J. C. Cole, S. J. Cottrell, N. Feeder, P. T. Galek, C. R. Groom and E. Pidcock, *CrystEngComm*, 2013, **15**, 65-72.
30. M. Gryl, S. Cenedese and K. Stadnicka, *J. Phys. Chem. C*, 2014, **119**, 590-598.
31. P. A. Wood and P. T. Galek, *CrystEngComm*, 2010, **12**, 2485-2491.
32. P. Kavuru, D. Aboarayes, K. K. Arora, H. D. Clarke, A. Kennedy, L. Marshall, T. T. Ong, J. Perman, T. Pujari and Ł. Wojtas, *Cryst. Growth Des.*, 2010, **10**, 3568-3584.
33. B. Lou, S. R. Perumalla and C. C. Sun, *Cryst. Growth Des.*, 2014, **15**, 24-28.
34. C. B. Aakeröy, T. K. Wijethunga and J. Desper, *J. Mol. Struct.*, 2014, **1072**, 20-27.
35. B. K. Saha, A. Nangia and M. Jaskólski, *CrystEngComm*, 2005, **7**, 355-358.
36. L. C. Gilday, S. W. Robinson, T. A. Barendt, M. J. Langton, B. R. Mullaney and P. D. Beer, *Chem. Rev.*, 2015, **115**, 7118-7195.
37. C. B. Aakeröy, P. D. Chopade and J. Desper, *Cryst. Growth Des.*, 2011, **11**, 5333-5336.
38. A. Mukherjee and G. R. Desiraju, *Chem. Commun.*, 2011, **47**, 4090-4092.
39. B. Sarma, P. Sanphui and A. Nangia, *Cryst. Growth Des.*, 2010, **10**, 2388-2399.
40. L. Loots and L. J. Barbour, in *The Importance of Pi-Interactions in Crystal Engineering*, ed. E. R. T. Tiekink and J. Zukerman-Schpector, John Wiley & Sons, Chichester, United Kingdom, **2012**, pp. 109-124.
41. J. Bernstein, *Polymorphism in Molecular Crystals*, Oxford University Press, Oxford, **2002**, pp. 1-28.
42. M. R. Caira, in *Comprehensive Supramolecular Chemistry II*, ed. J. L. Atwood, L. J. Barbour and G. W. Gokel, Elsevier, London, United Kingdom, **2017**, vol. 7, pp. 127-160.
43. A. J. Cruz-Cabeza and J. Bernstein, *Chem. Rev.*, 2013, **114**, 2170-2191.
44. N. J. Babu, S. Cherukuvada, R. Thakuria and A. Nangia, *Cryst. Growth Des.*, 2010, **10**, 1979-1989.
45. S. Lohani and D. J. W. Grant, in *Polymorphism: in the pharmaceutical industry*, ed. R. Hilfiker, Wiley-VCH verlag GmbH & Co. KGaA., Weinheim, Germany, **2006**, pp, 21-42.
46. D. J. Kempf, K. C. Marsh, J. F. Denissen, E. McDonald, S. Vasavanonda, C. A. Flentge, B. E. Green, L. Fino, C. H. Park and X.-P. Kong, *Proc. Natl. Acad. Sci. U. S. A.*, 1995, **92**, 2484-2488.
47. S. R. Chemburkar, J. Bauer, K. Deming, H. Spiwek, K. Patel, J. Morris, R. Henry, S. Spanton, W. Dziki and W. Porter, *Org. Process Res. Dev.*, 2000, **4**, 413-417.
48. D. Q. M. Craig, in *Polymorphism: in the pharmaceutical industry*, ed. R. Hilfiker, Wiley-VCH verlag GmbH & Co. KGaA., Weinheim, Germany, **2006**, pp.43-80.
49. D. Q. M. Craig, in *Thermal analysis of pharmaceuticals*, ed. D. Q. M. Craig and M. Reading, CRC Press, Boca Raton, Florida, **2007**, pp. 53-100.
50. A. Burger and R. Ramberger, *Microchim. Acta*, 1979, **2**, 259-271.
51. A. Burger and R. Ramberger, *Microchim. Acta*, 1979, **2**, 273-316.
52. J. Bernstein, *Polymorphism in Molecular Crystals*, Oxford University Press, Oxford, **2002**, pp. 66-93.
53. S. L. Price, *Phys. Chem. Chem. Phys.*, 2008, **10**, 1996-2009.
54. P. T. Galek, F. H. Allen, L. Fábián and N. Feeder, *CrystEngComm*, 2009, **11**, 2634-2639.
55. S. L. Price and S. M. Reutzel-Edens, *Drug Discov. Today*, 2016, **21**, 912-923.

56. P. T. Galek, E. Pidcock, P. A. Wood, N. Feeder and F. H. Allen, in *Computational Pharmaceutical Solid State Chemistry*, ed. Y. A. Abramov, John Wiley & Sons, Inc., Hoboken, New Jersey, USA, **2016**, 15-35.
57. S. L. Price, *Chem. Soc. Rev.*, 2014, **43**, 2098-2111.
58. S. L. Price, D. E. Braun and S. M. Reutzel-Edens, *Chem. Commun.*, 2016, **52**, 7065-7077.
59. G. M. Day and W. S. Motherwell, *Cryst. Growth Des.*, 2006, **6**, 1985-1990.
60. W. C. McCrone, in *Physics and Chemistry of the Organic Solid-State*, ed. D. Fox, M. M. Labes and A. Weisemberg, Interscience, New York, New York, **1965**, vol. 2, pp. 725-769.
61. D. Singhal and W. Curatolo, *Adv. Drug Delivery Rev.*, 2004, **56**, 335-347.
62. B. C. Hancock and G. Zografi, *J. Pharm. Sci.*, 1997, **86**, 1-12.
63. S. Petit and G. Coquerel, in *Polymorphism: in the pharmaceutical industry*, ed. R. Hilfiker, Wiley-VCH verlag GmbH & Co. KGaA., Weinheim, Germany, **2006**, pp. 259-286.
64. M. Saunders and P. Gabbott, in *Solid State characterization of pharmaceuticals*, ed. R. A. Storey and I. Ymén, Blackwell publishing ltd., Chichester, United Kingdom, **2011**, pp. 135-186.
65. I. Ymén, in *Solid State characterization of pharmaceuticals*, ed. R. A. Storey and I. Ymén, Blackwell publishing ltd., Chichester, United Kingdom, **2011**, pp. 1-34.
66. J. K. Guillory, in *Polymorphism in Pharmaceutical Solids*, ed. H. G. Brittain, Marcel Dekker, New York, New York, 1999, vol. 95, pp. 183-226.
67. Y. Cui, *Int. J. Pharm.*, 2007, **339**, 3-18.
68. C. A. Angell, K. L. Ngai, G. B. McKenna, P. F. McMillan and S. W. Martin, *J. Appl. Phys.*, 2000, **88**, 3113-3157.
69. B. Rodríguez-Spong, C. P. Price, A. Jayasankar, A. J. Matzger and N. R. Rodríguez-Hornedo, *Adv. Drug Delivery Rev.*, 2004, **56**, 241-274.
70. E. Shalaev and G. Zografi, in *Amorphous Food and Pharmaceutical Systems*, vol. 281, The Royal Society of Chemistry, Cambridge, United Kingdom, **2002**, pp. 11-30.
71. U. J. Griesser and J. G. Stowell, in *Pharmaceutical analysis*, ed. D.C. Lee and M. W. Webb, Blackwell Publishing Ltd., Oxford, United Kingdom, **2003**, pp. 240-294.
72. U. J. Griesser, in *Polymorphism: in the pharmaceutical industry*, ed. R. Hilfiker, Wiley-VCH verlag GmbH & Co. KGaA., Weinheim, Germany, **2006**, pp. 211-233.
73. B. Kratochvíl, in *Hot topics in thermal analysis and calorimetry: Glassy, amorphous and nano-crystalline materials*, ed. J. Šesták, J. J. Mareš and P. Hubík, Springer Science+Business Media B.V., Dordrecht, Netherlands, **2011**, vol. 8, pp. 129-140.
74. A. L. Bingham, D. S. Hughes, M. B. Hursthouse, R. W. Lancaster, S. Tavener and T. L. Threlfall, *Chem. Commun.*, 2001, 603-604.
75. M. B. Hickey, M. L. Peterson, E. S. Manas, J. Alvarez, F. Haeffner and Ö. Almarsson, *J. Pharm. Sci.*, 2007, **96**, 1090-1099.
76. https://www.fda.gov/downloads/drugs/guidancecomplianceregulatoryinformation/guidances/ucm281764.pdf, (accessed April 2018).
77. S. Aitipamula, R. Banerjee, A. K. Bansal, K. Biradha, M. L. Cheney, A. R. Choudhury, G. R. Desiraju, A. G. Dikundwar, R. Dubey and N. Duggirala, P. P. Ghogale, S. Ghosh, P. K. Goswami, N. R. Goud, R. R. K. R. Jetti, P. Karpinski, P. Kaushik, D. Kumar, V. Kumar, B. Moulton, A. Mukherjee, G. Mukherjee, A. S. Myerson, V. Puri, A. Ramanan, T. Rajamannar, C. M. Reddy, N. Rodríguez-Hornedo, R. D. Rogers, T. N. G. Row, P. Sanphui, N. Shan, G. Shete, A. Singh, C. C. Sun, J. A. Swift, R. Thaimattam, T. S. Thakur, R. K. Thaper, S. P. Thomas, S. Tothadi, V. R. Vangala, N. Variankaval, P. Vishweshwar, D. R. Weyna and M. J. Zaworotko, *Cryst. Growth Des.*, 2012, **12**, 2147-2152.

78. D. Braga, F. Grepioni, L. Maini, S. Prosperi, R. Gobetto and M. R. Chierotti, *Chem. Commun.*, 2010, **46**, 7715-7717.
79. D. Braga, F. Grepioni, G. I. Lampronti, L. Maini and A. Turrina, *Cryst. Growth Des.*, 2011, **11**, 5621-5627.
80. W. T. Harrison, H. Yathirajan, S. Bindya and H. Anilkumar, *Acta Crystallogr., Sect. C: Cryst. Struct. Commun.*, 2007, **63**, o129-o131.
81. C. B. Aakeröy, M. E. Fasulo and J. Desper, *Mol. Pharmaceutics*, 2007, **4**, 317-322.
82. A. Bacchi, D. Capucci, M. Giannetto, M. Mattarozzi, P. Pelagatti, N. Rodriguez-Hornedo, K. Rubini and A. Sala, *Cryst. Growth Des.*, 2016, **16**, 6547-6555.
83. J. W. Steed, *Trends in Pharmacol. Sci.*, 2013, **34**, 185-193.
84. S. L. Childs, G. P. Stahly and A. Park, *Mol. Pharmaceutics*, 2007, **4**, 323-338.
85. T. Steiner, I. Majerz and C. C. Wilson, *Angew. Chem., Int. Ed.*, 2001, **40**, 2651-2654.
86. J. A. Cowan, J. A. Howard, G. J. McIntyre, S.-F. Lo and I. D. Williams, *Acta Crystallogr., Sect. B: Struct. Sci.*, 2003, **59**, 794-801.
87. C. C. Wilson, *Acta Crystallogr., Sect. B: Struct. Sci.*, 2001, **57**, 435-439.
88. A. V. Trask, *Mol. Pharmaceutics*, 2007, **4**, 301-309.
89. C. B. Aakeröy, M. E. Fasulo and J. Desper, *Mol. Pharmaceutics*, 2007, **4**, 317-322.
90. N. Schultheiss and A. Newman, *Cryst. Growth Des.*, 2009, **9**, 2950-2967.
91. L. Rajput, P. Sanphui and G. R. Desiraju, *Cryst. Growth Des.*, 2013, **13**, 3681-3690.
92. S. P. Gopi, M. Banik and G. R. Desiraju, *Cryst. Growth Des.*, 2017, **17**, 308-316.
93. A. Samie, G. R. Desiraju and M. Banik, *Cryst. Growth Des.*, 2017, **17**, 2406-2417.
94. P. K. Mondal, V. Rao, S. Mittapalli and D. Chopra, *Cryst. Growth Des.*, 2017, **17**, 1938-1946.
95. R. Chadha, A. Saini, D. S. Jain and P. Venugopalan, *Cryst. Growth Des.*, 2012, **12**, 4211-4224.
96. P. Sanphui, V. K. Devi, D. Clara, N. Malviya, S. Ganguly and G. R. Desiraju, *Mol. Pharmaceutics*, 2015, **12**, 1615-1622.
97. Y. Yan, J.-M. Chen and T.-B. Lu, *CrystEngComm*, 2013, **15**, 6457-6460.
98. B. Saikia, P. Bora, R. Khatioda and B. Sarma, *Cryst. Growth Des.*, 2015, **15**, 5593-5603.
99. M. Banik, S. P. Gopi, S. Ganguly and G. R. Desiraju, *Cryst. Growth Des.*, 2016, **16**, 5418-5428.
100. S. P. Gopi, S. Ganguly and G. R. Desiraju, *Mol. Pharmaceutics*, 2016, **13**, 3590-3594.
101. P. Sanphui, S. Tothadi, S. Ganguly and G. R. Desiraju, *Mol. Pharmaceutics*, 2013, **10**, 4687-4697.
102. Y. Chen, L. Li, J. Yao, Y.-Y. Ma, J.-M. Chen and T.-B. Lu, *Cryst. Growth Des.*, 2016, **16**, 2923-2930.
103. M. L. Cheney, D. R. Weyna, N. Shan, M. Hanna, L. Wojtas and M. J. Zaworotko, *J. Pharm. Sci.*, 2011, **100**, 2172-2181.
104. M. K. Stanton, R. C. Kelly, A. Colletti, Y. H. Kiang, M. Langley, E. J. Munson, M. L. Peterson, J. Roberts and M. Wells, *J. Pharm. Sci.*, 2010, **99**, 3769-3778.
105. S. L. Childs, P. Kandi and S. R. Lingireddy, *Mol. Pharmaceutics*, 2013, **10**, 3112-3127.
106. D. R. Weyna, M. L. Cheney, N. Shan, M. Hanna, M. J. Zaworotko, V. Sava, S. Song and J. R. Sanchez-Ramos, *Mol. Pharmaceutics*, 2012, **9**, 2094-2102.
107. J.-M. Chen, S. Li and T.-B. Lu, *Cryst. Growth Des.*, 2014, **14**, 6399-6408.
108. C. B. Aakeröy, S. Forbes and J. Desper, *J. Am. Chem. Soc.*, 2009, **131**, 17048-17049.
109. D. J. Good and N. R. Rodríguez-Hornedo, *Cryst. Growth Des.*, 2009, **9**, 2252-2264.
110. S. Aitipamula, A. B. Wong, P. S. Chow and R. B. Tan, *CrystEngComm*, 2012, **14**, 8515-8524.
111. A. V. Trask, W. S. Motherwell and W. Jones, *Cryst. Growth Des.*, 2005, **5**, 1013-1021.
112. S. M. Berge, L. D. Bighley and D. C. Monkhouse, *J. Pharm. Sci.*, 1977, **66**, 1-19.

113. J. F. Remenar, J. M. MacPhee, B. K. Larson, V. A. Tyagi, J. H. Ho, D. A. McIlroy, M. B. Hickey, P. B. Shaw and Ö. Almarsson, *Org. Process Res. Dev.*, 2003, **7**, 990-996.
114. Ö. Almarsson and M. J. Zaworotko, *Chem. Commun.*, 2004, 1889-1896.
115. S. L. Childs, N. Rodríguez-Hornedo, L. S. Reddy, A. Jayasankar, C. Maheshwari, L. McCausland, R. Shipplett and B. C. Stahly, *CrystEngComm*, 2008, **10**, 856-864.
116. D. Braga, F. Grepioni, L. Maini, D. Capucci, S. Nanna, J. Wouters, L. Aerts and L. Quéré, *Chem. Commun.*, 2012, **48**, 8219-8221.
117. H. G. Brittain, *J. Pharm. Sci.*, 2013, **102**, 311-317.
118. F. Grifasi, M. R. Chierotti, K. Gaglioti, R. Gobetto, L. Maini, D. Braga, E. Dichiarante and M. Curzi, *Cryst. Growth Des.*, 2015, **15**, 1939-1948.
119. P. Billot, P. Hosek and M.-A. Perrin, *Org. Process Res. Dev.*, 2012, **17**, 505-511.
120. S. Chen, H. Xi, R. F. Henry, I. Marsden and G. G. Zhang, *CrystEngComm*, 2010, **12**, 1485-1493.
121. O. Sánchez-Guadarrama, F. Mendoza-Navarro, A. Cedillo-Cruz, H. Jung-Cook, J. I. Arenas-García, A. Delgado-Díaz, D. Herrera-Ruiz, H. Morales-Rojas and H. Höpfl, *Cryst. Growth Des.*, 2015, **16**, 307-314.
122. U.S. Food and Drug Admistration, *FDA Generally Recognized as Safe (GRAS)*, http://www.fda.gov/Food/IngredientsPackagingLabeling/GRAS/ (accessed January 2018).
123. C. B. Aakeröy and D. J. Salmon, *CrystEngComm*, 2005, **7**, 439-448.
124. N. Shan and M. J. Zaworotko, *Drug Discov.Today*, 2008, **13**, 440-446.
125. C. B. Aakeröy, S. V. Panikkattu, B. DeHaven and J. Desper, *Cryst. Growth Des.*, 2012, **12**, 2579-2587.
126. D. R. Weyna, M. L. Cheney, N. Shan, M. Hanna, Ł. Wojtas and M. J. Zaworotko, *CrystEngComm*, 2012, **14**, 2377-2380.
127. J. S. Bhandaru, N. Malothu and R. R. Akkinepally, *Cryst. Growth Des.*, 2015, **15**, 1173-1179.
128. P. T. Galek, E. Pidcock, P. A. Wood, I. J. Bruno and C. R. Groom, *CrystEngComm*, 2012, **14**, 2391-2403.
129. D. Musumeci, C. A. Hunter, R. Prohens, S. Scuderi and J. F. McCabe, *Chem. Sci.*, 2011, **2**, 883-890.
130. H. S. Chan, J. Kendrick, M. A. Neumann and F. J. Leusen, *CrystEngComm*, 2013, **15**, 3799-3807.
131. N. Issa, P. G. Karamertzanis, G. W. Welch and S. L. Price, *Cryst. Growth Des.*, 2008, **9**, 442-453.
132. P. G. Karamertzanis, A. V. Kazantsev, N. Issa, G. W. Welch, C. S. Adjiman, C. C. Pantelides and S. L. Price, *J. Chem. Theory Comput.*, 2009, **5**, 1432-1448.
133. Y. A. Abramov, C. Loschen and A. Klamt, *J. Pharm. Sci.*, 2012, **101**, 3687-3697.
134. C. C. Seaton, *CrystEngComm*, 2011, **13**, 6583-6592.
135. A. Lemmerer, S. Govindraju, M. Johnston, X. Motloung and K. L. Savig, *CrystEngComm*, 2015, **17**, 3591-3595.
136. M. K. Stanton and A. Bak, *Cryst. Growth Des.*, 2008, **8**, 3856-3862.
137. M. R. Caira, S. A. Bourne, H. Samsodien, E. Engel, W. Liebenberg, N. Stieger and M. Aucamp, *CrystEngComm*, 2012, **14**, 2541-2551.
138. C. B. Aakeröy, S. Forbes and J. Desper, *CrystEngComm*, 2014, **16**, 5870-5877.
139. M. R. Caira, in *Encyclopaedia of Supramolecular Chemistry*, ed. J. L. Atwood and J. W. Steed, Marcel Dekker, Inc., **2004**, vol. 1, pp. 767-775.
140. A. Kalman, L. Párkányi and G. Argay, *Acta Crystallogr., Sect. B: Struct. Sci.*, 1993, **49**, 1039-1049.
141. P. A. Wood, M. A. Oliveira, A. Zink and M. B. Hickey, *CrystEngComm*, 2012, **14**, 2413-2421.
142. S. Ebenezer, P. T. Muthiah and R. J. Butcher, *Cryst. Growth Des.*, 2011, **11**, 3579-3592.

143. J. A. Bis, P. Vishweshwar, R. A. Middleton and M. J. Zaworotko, *Cryst. Growth Des.*, 2006, **6**, 1048-1053.
144. S. Li, J.-M. Chen and T.-B. Lu, *CrystEngComm*, 2014, **16**, 6450-6458.
145. P. H. Stahl and M. Nakano, in *Handbook of Pharmaceutical Salts: Properties, Selection, and Use*, ed. P. H. Stahl and C. G. Wermuth, Wiley-VCH/VHCA, IUPAC, New York, USA, 2008.
146. A. Patel, S. A. Jones, A. Ferro and N. Patel, *Br. J. Cardiol.*, 2009, **16**, 281-286.
147. F. Hoffmann-La Roche & Co, Basel (Switzerland) CH 187826, 1937.
148. J. Bronson, A. Black, T. M. Dhar, B. A. Ellsworth and J. R. Merritt, in *Annual Reports in Medicinal Chemistry*, Elsevier, **2013**, vol. 48, pp. 471-546.
149. J. Z. Gougoutas, H. Lobinger, S. Ramakrishnan, P. P. Deshpande, J. T. Bien, C. Lai, C. Wang, P. Riebel, J. A. Grosso, A. A. Nirschl, J. Singh and J. D. Dimarco, WO Pat., 2008002824, 2008.
150. United States Food and Drug Administration, FDA approves Farxiga™ to treat type 2 diabetes, 2014, https://www.accessdata.fda.gov/drugsatfda_docs/nda/2014/202293orig1s000toc.cfm, (accessed April 2018).
151. United States Food and Drug Administration, FDA approves Entresto™ to reduce risk of cardiovascular death and heart failure hospitalization, 2015, https://www.novartis.com/news/media-releases/novartis-new-heart-failure-medicine-lcz696-now-called-entrestotm-approved-fda, (accessed April 2018).
152. United States Food and Drug Administration, FDA approves Steglatro™ as an adjunct to diet and exercise to improve glycemic control in adults with type 2 diabetes mellitus, 2017, https://www.accessdata.fda.gov/drugsatfda_docs/nda/2017/209803,209805,209806Orig1s000TOC.cfm, (accessed April 2018).
153. A.D. McNaught and A. Wilkinson, *IUPAC. Compendium of Chemical Terminology, 2nd edn (the "Gold Book")*, Blackwell Scientific Publications, Oxford, United Kingdom, 1997, XML online corrected version 2.3.3, **2014**, http://www.iupac.org/goldbook/I02998.pdf, (accessed April 2018).
154. J. Szejtli, *Chem. Rev.*, 1998, **98**, 1743-1754.
155. J. Szejtli, *Pure Appl. Chem.*, 2004, **76**, 1825-1845.
156. W. Saenger, J. Jacob, K. Gessler, T. Steiner, D. Hoffmann, H. Sanbe, K. Koizumi, S. M. Smith and T. Takaha, *Chem. Rev.*, 1998, **98**, 1787-1802.
157. H. Dodziuk, in *Cyclodextrins and Their Complexes*, Wiley-VCH Verlag GmbH & Co. KGaA, Warsaw, Poland, **2006**, pp. 1-30.
158. A. Kusmin, R. E. Lechner, M. Kammel and W. Saenger, *J. Phys. Chem. B*, 2008, **112**, 12888-12898.
159. T. Aree, H. Hoier, B. Schulz, G. Reck and W. Saenger, *Angew. Chem., Int. Ed.*, 2000, **39**, 897-899.
160. L. Liu and Q.-X. Guo, *J. Inclusion Phenom. Macrocyclic Chem.*, 2002, **42**, 1-14.
161. M. V. Rekharsky and Y. Inoue, *Chem. Rev.*, 1998, **98**, 1875-1918.
162. N. A. Todorova and F. P. Schwarz, *J. Chem. Thermodyn.*, 2007, **39**, 1038-1048.
163. J. Stappaerts and P. Augustijns, *Int. J. Pharm.*, 2016, **511**, 680-687.
164. K. Harata, *Chem. Rev.*, 1998, **98**, 1803-1828.
165. D. Mentzafos, I. Mavridis, G. Le Bas and G. Tsoucaris, *Acta Crystallogr., Sect. B: Struct. Sci.*, 1991, **47**, 746-757.
166. W. Saenger, in *Inclusion Compounds*, ed. J. L. Atwood, J. E. D. Davies and D. D. MacNicol, Academic Press, London, United Kingdom, 1984, Vol. 2, pp. 231-259.
167. M. R. Caira, *Rev. Roum. Chim.*, 2001, **46**, 371-386.

168. W. Saenger, in *Inclusion Compounds*, ed. J. L. Atwood, J. E. D. Davies, D. D. MacNicol, Academic Press, London, United kingdom, 1984, Vol. 2, pp. 231-260.
169. A. Villiers, *Comptes Rend*us, 1891, **112**, 536-538.
170. P. Jansook, N. Ogawa and T. Loftsson, Int. J. Pharm., 2018, **535**, 272-284.
171. T. Loftsson and M. E. Brewster, *J. Pharm. Pharmacol.*, 2010, **62**, 1607-1621.
172. M. E. Brewster and T. Loftsson, *Adv. Drug Delivery Rev.*, 2007, **59**, 645-666.
173. A. Vyas, S. Saraf and S. Saraf, *J. Inclusion Phenom. Macrocyclic Chem.*, 2008, **62**, 23-42.
174. K. Cal and K. Centkowska, *Eur. J. Pharm. Biopharm.*, 2008, **68**, 467-478.
175. R. Challa, A. Ahuja, J. Ali and R. Khar, *AAPS Pharmscitech*, 2005, **6**, E329-E357.
176. V. J. Stella and R. A. Rajewski, *Pharm. Res.*, 1997, **14**, 556-567.
177. T. Loftsson and M. E. Brewster, *J. Pharm. Sci.*, 1996, **85**, 1017-1025.
178. T. Irie and K. Uekama, *J. Pharm. Sci.*, 1997, **86**, 147-162.
179. T. Loftsson and T. Järvinen, *Adv. Drug Delivery Rev.*, 1999, **36**, 59-79.
180. R. L. Carrier, L. A. Miller and I. Ahmed, *J. Controlled Release*, 2007, **123**, 78-99.
181. M. Cirri, C. Rangoni, F. Maestrelli, G. Corti and P. Mura, *Drug Dev. Ind. Pharm.*, 2005, **31**, 697-707.
182. G. Ragno, E. Cione, A. Garofalo, G. Genchi, G. Ioele, A. Risoli and A. Spagnoletta, *Int. J. Pharm*., 2003, **265**, 125-132.
183. X. Chen, R. Chen, Z. Guo, C. Li and P. Li, *Food Chem.*, 2007, **101**, 1580-1584.
184. J.-H. Kim, S.-K. Lee, M.-H. Ki, W.-K. Choi, S.-K. Ahn, H.-J. Shin and C. I. Hong, Int. J. Pharm., 2004, **272**, 79-89.
185. B. Cwiertnia, T. Hladon and M. Stobiecki, *J. Pharm. Pharmacol.*, 1999, **51**, 1213-1218.
186. J. Szejtli and L. Szente, *Eur. J. Pharm. Biopharm.*, 2005, **61**, 115-125.
187. S. Jóhannsdóttir, J. K. Kristinsson, Z. Fülöp, G. Ásgrímsdóttir, E. Stefánsson and T. Loftsson, Int. J. Pharm., 2017, **529**, 486-490.
188. A. Yoshida, M. Yamamoto, T. Itoh, T. Irie, F. Hirayama and K. Uekama, *Chem. Pharm. Bull.*, 1990, **38**, 176-179.
189. V. Stella, H. Lee and D. Thompson, Int. J. Pharm., 1995, **120**, 197-204.
190. B. Woodcock, D. Acerbi, P. Merz, S. Rietbrock and N. Rietbrock, *Eur. J. Rheumatol. Inflammation*, 1993, **12**, 12-28.
191. F. Hirayama and K. Uekama, *Adv. Drug Delivery Rev.*, 1999, **36**, 125-141.
192. G. Dufour, W. Bigazzi, N. Wong, F. Boschini, P. De Tullio, G. Piel, D. Cataldo and B. Evrard, Int. J. Pharm., 2015, **495**, 869-878.
193. G. Chen and M. Jiang, *Chem. Soc. Rev.*, 2011, **40**, 2254-2266.
194. G. Varan, C. Varan, N. Erdoğar, A. A. Hıncal and E. Bilensoy, *Int. J. Pharm.*, 2017, **531**, 457-469.
195. T. Loftsson and E. Stefánsson, Int. J. Pharm., 2017, **531**, 413-423.
196. L.-Y. Wong, B. Xia, E. Wolvetang and J. Cooper-White, *Biomacromolecules*, 2018, **19**, 353-363.
197. H. Dodziuk, W. Koźmiński and A. Ejchart, *Chirality*, 2004, **16**, 90-105.
198. R. K Rawal, A. K Konreddy and C. K Chu, *Curr. Med. Chem.*, 2015, **22**, 3922-3932.
199. C. J. Hoffmann and C. L. Thio, *Lancet Infect. Dis.*, 2007, **7**, 402-409.
200. World Health Organization (WHO), Global Hepatitis Report 2017, http://apps.who.int/iris/bitstream/handle/10665/255016/9789241565455-eng.pdf, (accessed April 2018.).
201. European Association for the Study of the Liver, *J. Hepatol.*, 2012, **57**, 167-185.

202. European Association for the Study of the Liver, *J. Hepatol.*, 2009, **50**, 227-242.
203. Y. Zhou, J. Wang, Z. Gu, S. Wang, W. Zhu, J. L. Aceña, V. A. Soloshonok, K. Izawa and H. Liu, *Chem. Rev.*, 2016, **116**, 422-518.
204. D. N. Clark and J. Hu, *Antiviral Res.*, 2015, **123**, 132-137.
205. B. K. Kim, J. Oh, S. Y. Kwon, W. H. Choe, S. Y. Ko, K. H. Rhee, T. H. Seo, S. D. Lim and C. H. Lee, *J. Hepatol.*, 2009, **51**, 829-834.
206. B. K. Kim, S. Y. Ko, S. Y. Kwon, E. Park, J. H. Kim, W. H. Choe and C. H. Lee, *Hepatitis Mon.*, 2013, **13**.
207. Eisai announces launch of Revovir® in the Phillipines, 2010, http://www.eisai.com/news/enews201006pdf.pdf, (accessed April 2018).
208. T. Ma, S. B. Pai, Y. L. Zhu, J. S. Lin, K. Shanmuganathan, J. Du, C. Wang, H. Kim, M. G. Newton, Y. C. Cheng and C. K. Chu, J. Med. Chem., 1996, **39**, 2835.
209. C. Le Manach, D. Gonzàlez Cabrera, F. Douelle, A. T. Nchinda, Y. Younis, D. Taylor, L. Wiesner, K. L. White, E. Ryan, C. March, S. Duffy, V. M. Avery, D. Waterson, M. J. Witty, S. Wittlin, S. A. Charman, L. J. Street and K. Chibale, *J. Med. Chem.*, 2014, **57**, 2789-2798.
210. S. Bhatt, D. Weiss, E. Cameron, D. Bisanzio, B. Mappin, U. Dalrymple, K. Battle, C. Moyes, A. Henry and P. Eckhoff, *Nature*, 2015, **526**, 207.
211. World Health Organization (WHO), World Malaria Report 2017, http://www.who.int/malaria/publications/world-malaria-report-2017/report/en/, Geneva, Switzerland (accessed April 2018).
212. A. M. Dondorp, F. Nosten, P. Yi, D. Das, A. P. Phyo, J. Tarning, K. M. Lwin, F. Ariey, W. Hanpithakpong, S. J. Lee, P. Ringwald, K. Silamut, M. Imwong, K. Chotivanich, P. Lim, T. Herdman, S. S. An, S. Yeung, P. Singhasivanon, N. P. Day, N. Lindegardh, D. Socheat and N. J. White, *N. Engl. J. Med.*, 2009, **361**, 455-467.
213. F. Lu, R. Culleton, M. Zhang, A. Ramaprasad, L. von Seidlein, H. Zhou, G. Zhu, J. Tang, Y. Liu and W. Wang, *N. Engl. J. Med.*, 2017, **376**, 991-993.
214. E. A. Ashley, M. Dhorda, R. M. Fairhurst, C. Amaratunga, P. Lim, S. Suon, S. Sreng, J. M. Anderson, S. Mao and B. Sam, *N. Engl. J. Med.*, 2014, **371**, 411-423.
215. J. Okombo and K. Chibale, *MedChemComm*, 2018, **9**, 437-453.
216. M. B. Jiménez-Díaz, T. Mulet, S. Viera, V. Gómez, H. Garuti, J. Ibáñez, A. Alvarez-Doval, L. D. Shultz, A. Martínez and D. Gargallo-Viola and I. Angulo-Barturen, *Antimicrob. Agents Chemother.*, 2009, **53**, 4533-4536.
217. C. Le Manach, T. Paquet, D. Gonzàlez Cabrera, Y. Younis, D. Taylor, L. Wiesner, N. Lawrence, S. Schwager, D. Waterson, M. J. Witty, S. Wittlin, L. J. Street and K. Chibale, *J. Med. Chem.*, 2014, **57**, 8839-8848.
218. J. Liu, in *Lipoic Acid: Energy Production, Antioxidant Activity and Health Effects*, ed. M. S. Patel, L. Packer, CRC Press, Taylor & Francis Group, Boca Raton, Florida, USA, **2008**, pp. 475–494.
219. K. P. Shay, R. F. Moreau, E. J. Smith, A. R. Smith and T. M. Hagen, *Biochimica et Biophysica Acta (BBA)*, 2009, **1790**, 1149-1160.
220. L. Packer and E. Cadenas, *J. Clin. Biochem. Nutr.*, 2010, **48**, 26-32.
221. G. Monastra, S. De Grazia, S. Cilaker Micili, A. Goker and V. Unfer, *Expert Opin. Drug Delivery*, 2016, **13**, 1695-1708.
222. M. Koufaki, *Expert Opin. Ther. Pat.*, 2014, **24**, 993-1005.
223. A. Smith, S. Shenvi, M. Widlansky, J. Suh and T. Hagen, *Curr. Med. Chem.*, 2004, **11**, 1135-1146.

224. T. M. Queiroz, D. D. Guimarães, L. G. Mendes-Junior and V. A. Braga, *Molecules*, 2012, **17**, 13357-13367.
225. L. Li, A. Smith, T. M. Hagen and B. Frei, *Ann. N. Y. Acad. Sci.*, 2010, **1203**, 151-159.
226. L. Rochette, S. Ghibu, A. Muresan and C. Vergely, *Can. J. Physiol. Pharmacol.*, 2015, **93**, 1021-1027.
227. A. Fava, D. Pirritano, M. Plastino, D. Cristiano, G. Puccio, C. Colica, C. Ermio, M. De Bartolo, G. Mauro and D. Bosco, *J. Neurodegener. Dis.*, 2013, **2013**, 1-7.
228. A. Baur, T. Harrer, M. Peukert, G. Jahn, J. Kalden and B. Fleckenstein, *Klin. Wochenschr.*, 1991, **69**, 722-724.
229. M. Venigalla, S. Sonego, E. Gyengesi, M. J. Sharman and G. Münch, *Neurochem. Int.*, 2016, **95**, 63-74.
230. N. Ikuta, H. Sugiyama, H. Shimosegawa, R. Nakane, Y. Ishida, Y. Uekaji, D. Nakata, K. Pallauf, G. Rimbach and K. Terao, *Int. J. Mol. Sci.*, 2013, **14**, 3639-3655.

Chapter 2

Materials and experimental methods

This chapter is divided into two main parts aiming to describe the specifications of materials and experimental methods used throughout this thesis. The second part is subdivided into a section describing general synthetic procedures and a section dedicated to outlining the analytical methods employed.

Materials

Bioactive compounds

The established active pharmaceutical ingredient clevudine (1-(2-deoxy-2-fluoro-β-L-arabinofuranosyl)-5-methyl-2,4-(1H,3H)-pyrimidinedione) or L-FMAU was purchased from DOCHEM (Hong Kong) Co., Limited, (Changzhou, China) and was certified 99.9 % pure by HPLC analysis.

The drug lead MMV652103 or 6-(3-(methylsulfonyl)phenyl)-3-(4-(methylsulfonyl)phenyl)-imidazo[1,2-b]pyridazine ($C_{20}H_{17}N_3O_4S_2$) was synthesised and supplied by the UCT Drug Discovery and Development Centre, H3D (University of Cape Town, South Africa).

The bioactive compound (±) α-lipoamide (1,2-dithiolane-3-pentanamide) was purchased from Sigma-Aldrich (Japan) with a certified purity greater than 99 % and used without further purification.

Cyclodextrins

The cyclodextrin host molecules α-cyclodextrin (α-CD), β-cyclodextrin (β-CD), γ-cyclodextrin (γ-CD), hexakis(2,3,6-tri-*O*-methyl)-α-cyclodextrin (TRIMEA), heptakis(2,6-di-*O*-methyl)-β-cyclodextrin (DIMEB), heptakis(2,3,6-tri-*O*-methyl)-β-cyclodextrin (TRIMEB), hydroxypropyl-β-CD (HP-β-CD), sulfobutylether β-CD (SE-β-CD) and randomly methylated β-CD (RAMEB) were purchased from Cyclolab (Budapest, Hungary).

Co-crystal formers

The co-crystal formers methylparaben, succinic acid, 4-hydroxybenzoic acid, adipic acid, glutaric acid, fumaric acid, malonic acid, L-malic acid, D-tartaric acid, maleic acid, oxalic acid and resorcinol were purchased from Sigma-Aldrich Chemie GmbH (Steinheim, Germany) with purity greater than 98 % and used without further purification.

Solvents

The solvents used were anhydrous acetonitrile (99.8 %) purchased from Sigma-Aldrich Chemie GmbH (Steinheim, Germany), acetone (analytical grade), ethanol (99.9 %), ethyl acetate (analytical grade), methanol (99.5 %) and propan-2-ol (99.7 %) obtained from KIMIX Chemical and Lab Supplies CC (Cape Town, South Africa) and 1, 4-dioxane (99 %) and propan-1-ol (99.5 %) were purchased from Merck (Pty) Ltd South Africa (South Africa). The deuterated solvents deuterium oxide (D_2O) and deuterated dimethyl sulfoxide (DMSO-d_6) that were used for ^{1}H NMR spectroscopy studies were purchased from Sigma-Aldrich (USA).

Fasted state simulated intestinal fluid was prepared from FaSSIF/FeSSIF/FaSSGF powder that was purchased from Biorelevant.com Ltd. (London, UK). The powder was dissolved in a phosphate buffer with a pH of 6.5 and used within 24 h after preparation.

Experimental methods

Part 1 – General synthetic procedures

In the following section the general synthetic procedures used are described. The deviations from these methods to obtain specific products are explained in the relevant chapters.

Screening for polymorphs, solvates and hydrates

A general method employed for recrystallisation was to dissolve the compound of interest in a solvent by stirring at elevated temperatures with a heating magnetic stirrer and filtering while hot through a 0.45 µm nylon filter into clean vials. The vials were then left on a benchtop for recrystallization of the compounds to occur.

Variation of cooling rate, solvents used and rate of solvent evaporation were applied in attempts to produce new solid-state forms of these compounds such as polymorphs, solvates or hydrates.

Co-crystal screening

Suitable co-crystal formers (coformers) were selected from a list of compounds on the United States Food and Drug Administration's list of chemicals that are generally recognized as safe (GRAS)[1]. The coformers were selected on the basis that they possess functional groups with a high potential to form intermolecular synthons with the functional groups of the compound in question. The Cambridge

Crystallographic Database[2] and its related software were used to compare the frequency of occurrences of various synthons to aid in selecting coformers.

The first screening step involved neat or dry grinding of 5 mg of the selected compound with an equimolar amount of the chosen coformer for 15 min in a mortar with a pestle. The product was then analysed by means of powder X-ray diffractometry (PXRD) (described in the analytical methods section below) to determine if a new phase had been formed.

Equimolar amounts of the selected compound and coformer were also ground with a mortar and pestle with dropwise addition of solvent in what is known as liquid-assisted grinding (LAG). The products were analysed in a similar fashion to that described for the neat grinding products.

In cases where new traces were produced by the LAG experiments, attempts were made to grow single crystals of the new products. Equimolar amounts of the selected compound and coformer were dissolved together in a range of solvents by stirring at elevated temperatures. The solutions were then filtered through 45 µm nylon filters into clean vials and was either left to cool at room temperature or placed in Dewar flasks for slow cooling. In some cases the vials were placed in a dessicator to minimise the uptake of moisture from the surrounding environment. This general method is known as co-precipitation.

Cyclodextrin inclusion complexation

The first screening step for inclusion complexation is the process of kneading which is usually done with a mortar and pestle. The cyclodextrins were added first and gently triturated after the addition of a small drop of water. The selected guest compound was then added incrementally until an equimolar amount had been added to that of the host cyclodextrin. Small drops of water were added throughout the process to maintain a paste-like consistency. The total kneading time was around 20 minutes. The product of this process was analysed by PXRD to determine if complexation had occurred. This was done by comparing the PXRD traces with traces for available isostructural series calculated from the crystal structures of known CD complexes.[3]

The method for complex synthesis *via* co-precipitation with the native cyclodextrins (α-, β- and γ-cyclodextrins) was similar to that used for co-precipitation with coformers. For the derivatised cyclodextrins (DIMEB, TRIMEA, TRIMEB) the host cyclodextrins and guest compounds were dissolved by stirring during a temperature cycling up to 80 °C and down to -8 °C. The products were filtered through 45 µm nylon filters into clean vials and placed in an oven at 60 °C.

Experimental methods

Part 2 – Analytical methods

The standard operational procedures and setup of each analytical method are described in the following section. Deviations from these methods to obtain specific outcomes are explained in the relevant chapters.

Hot stage microscopy (HSM)

Hot stage microscopy (HSM) was used as a means to visually observe any changes taking place during the heating of samples or to view solvent-mediated transformations. The results are used in conjunction with other methods such as DSC or TGA to compare or identify relevant events.

To view the results a Nikon SMZ-10 stereoscopic microscope was used and micrographs were collected with a Sony Digital Hyper HAD colour video camera fitted to the microscope. The software used was the Soft Imaging System program analySIS[4]. A Linkam THMS600 hot stage was employed and a Linkam TP92 control unit was used to control the temperature.

Differential scanning calorimetry (DSC)

Differential scanning calorimetry (DSC) was used to measure heat gained or lost by a sample as a result of thermal changes taking place during its controlled heating. This is done by having an inert reference without the sample in the same environment and the difference in energy inputs between the reference and sample i.e. differential heat flow, is measured as a function of temperature. Enthalpies, onset temperatures and the ranges of thermal events such as melting, loss of solvent, phase transitions and decomposition can be measured with this instrument.

Either a Q200 or a TA Discovery 25 instrument (TA Instruments) was used with sample masses in the range 1-2 mg. These samples were placed in vented aluminium pans. The heating rates were in the range 2-10 K min^{-1} unless otherwise specified. All DSC runs were performed under dry nitrogen purge gas with a flow rate of 60 ml min^{-1} in the case of the Q200 and 40 ml min^{-1} for the TA Discovery 25. The software used for the analysis of the DSC curves was TA instruments Universal Analysis 2000[5] for the Q200 and TRIOS[6] for the TA Discovery 25.

Differential thermal analysis (DTA)

Differential thermal analysis (DTA) is similar to DSC, the difference being that DSC measures heat flow differences between sample and reference pans with the temperatures held constant while DTA measures the difference in temperature with heat flow kept constant. DTA was used to determine temperatures at which certain thermal events like melting of samples occurred.

DTA measurements were performed on a THASS XP-10 apparatus (Friedberg, Germany). With sample masses ranging from 1-2 mg placed in vented aluminium pans. Heating rates of 20 K min^{-1} were used with a dry nitrogen purge gas flow rate of 40 ml min^{-1}. Analyses were carried out by making use of the program DSC XP-10.[7]

Modulated differential scanning calorimetry (MDSC)

Modulated differential scanning calorimetry (MDSC) adds the additional ability to separate conventional DSC signals into reversing (heating-rate dependent thermodynamic heat flow) and non-reversing (absolute temperature dependent, kinetically-limited heat flow) events as well as directly measure heat capacity. The same cell arrangement as with conventional DSC is used, but where conventional DSC heats the sample and reference pans in a linear fashion, MDSC uses controlled sinusoidal heating ramps that on average follow an underlying heating rate. This adds extra experimental variables to the underlying heating rate, namely modulation amplitude and frequency. The added information obtained by this method can simplify the interpretation and provide greater insight and understanding of thermal events.

A TA Discovery 25 instrument (TA Instruments) was used for all MDSC experiments and the results were analysed by making use of the TA software TRIOS.[6]

Thermogravimetric analysis (TGA)

Thermogravimetric analysis (TGA) is a means of measuring the change in mass of a sample as a function of temperature when subjected to controlled heating or cooling. This can be used to determine the mass of solvent loss as well as the temperature at which this takes place or the mass of a guest lost if this mass loss occurs as a distinct process. Multi-step loss can also be quantified in the case of host-guest inclusion complexes. These data can be used to determine the stoichiometry of components in crystals.

The instrument used was a TA-Q500 (TA Instruments). Sample masses ranged from 1-4 mg. For all experiments the heating rate was 10 K min^{-1} and the flow rate of dry nitrogen was 60 ml min^{-1}. The software used for the analysis of the results was TA instruments Universal Analysis 2000[5].

Powder X-ray diffraction (PXRD) and variable-temperature PXRD

Powder X-ray diffraction patterns were collected at constant or variable temperature on a BRUKER D8 Advance diffractometer equipped with a Lynxeye detector and using Cu$K\alpha_1$ radiation (λ = 1.5406 Å). Samples were placed on a zero background holder with a rotating stage for samples at constant temperature and for variable-temperature collections the samples were placed in a modular temperature chamber (Materials Research Instruments, Karlsruhe, Germany). The standard scanning range was 4–40 2θ° with 2260 steps, step sizes of 0.016° 2θ and exposure time of 20 minutes. X-ray settings were 40 mA and 30 kV.

This method gives a two-dimensional representation of detected intensity of diffracted X-rays as a function of the 2θ angle. This will offer a unique trace for different crystalline phases or packing arrangements of structures, but will result in a similar trace in cases where the crystalline phases in question are isostructural (having identical or close to identical packing motifs of molecules with comparable unit cell dimensions).[3]

PXRD was used to identify any changes occurring during various experiments such as neat grinding, LAG or kneading. Variable-temperature collections were done to observe the changes occurring during controlled heating of the samples. In cases where no changes take place, the traces collected match that of a combination of the starting components and simply indicate a physical mixture. In cases where new traces were observed, they were compared with all the generated patterns from known forms of the components including solvates, hydrates and polymorphs. In the case of cyclodextrin inclusion complexes, the traces are compared to libraries of isostructural series of previously discovered inclusion complexes.[8,9] PXRD is also used to verify that the bulk of scaled up products obtained by methods such as LAG are of the desired phase and can be compared to traces calculated from the solved crystal structures of the desired products.

The program Mercury 3.9[10,11] (Cambridge Crystallographic Data Centre, UK) was used to calculate PXRD traces from known structures. It calculates a Lorentz-polarisation corrected PXRD pattern. The program assumes a laboratory X-ray source (with the default set to Cu$K\alpha_1$ radiation) with fixed slit widths. Non-hydrogen atoms are assumed to have isotropic atomic displacement parameters (U_{iso}) of 0.05 $Å^2$ and

hydrogen atoms are included in the calculation with U_{iso} values of 0.06 $Å^2$. The simulator takes site-occupancy factors into account in cases where structures are disordered and experimental displacement parameters, either isotropic or anisotropic, are taken into account in the calculation if available. Pseudo-Voigt peak shapes with a full width at half maximum of 0.1° 2θ are used for all reflections. The traces are calculated for structures whose intensity data are usually collected at much lower temperatures than that used in routine PXRD experiments (usually collected at ambient temperature). It is a known fact that the *d*-spacings of crystallographic planes can differ with changes in temperature. This can have a significant impact on 2θ peak positions. In certain cases where the crystals in question are plate-like or needle-like in shape, crystals tend to become aligned in a 'preferred orientation' where a PXRD trace will show a diffraction pattern that is representative of a singular crystal face of this orientation and not a good representation of the whole. The result will be that some peaks are more intense than they would be if the crystals had no preferred orientation.

Single crystal X-ray diffraction

Data-collection

Single crystal X-ray diffraction was used to elucidate the structures of crystals produced by the methods described earlier. Crystals were inspected under a polarising microscope and selected based on size, clarity and ability to uniformly extinguish plane-polarised light. The selected crystals were placed under Paratone oil (Exxon Chemical Company, Houston,Texas) to avoid loss of solvent from the crystals. The Paratone oil also doubles as a means to hold a crystal on a nylon cryoloop during a low temperature data-collection. In cases where complexes were formed with derivatised cyclodextrins (TRIMEA, DIMEB or TRIMEB), the crystals were kept at an elevated temperature and surface-dried with filter paper and placed directly into heated Paratone oil to avoid dissolution due to the increased solubility of these cyclodextrins in water at low temperature and minimise thermal shock.

Single crystal X-ray intensity data collections were performed on a Bruker Kappa Apex II Duo diffractometer (Madison, Wisconsin)[11] with graphite-monochromated MoKα radiation (λ = 0.71073 Å). A Bruker K780 generator running at 50 kV and 20 mA was used to produce the radiation. A Cryostream cooler (Oxford Cryosystems, Oxford, UK) was used to maintain low temperatures during collections. An initial cell check was performed at 294(2) K (representing ambient temperature) followed by a cell check at 173(2) K (used as standard temperature for data-collection) to determine if any changes occurred during cooling of the crystal. Data-reduction and unit cell refinement were carried out with the program

SAINT[13]. All intensity data were corrected for Lorentz-polarisation effects and multi-scan absorption corrections were applied with SADABS[14].

Space groups were identified by inspecting the systematically absent reflections and comparing these to those of known space groups.[15]

Structural solution and refinement

The program XPREP[15] was used to prepare SHELXS[16] input files to be used for structure solution. During this setup with XPREP the $|E^2-1|$ value (E being the normalised structure factor) is used to verify the correct assignment of space groups by distinguishing between centrosymmetric and non-centrosymmetric space groups.

Structures were either solved by direct methods or by isomorphous replacement[3] where the atomic coordinates of isostructural complexes are used as a trial model for initial refinement. Structures were solved and then refined by full-matrix least-squares by making use of the X-seed interface[17] to operate the SHELX suite of programs.[17]

SHELXS

The program SHELXS[17] uses direct methods or the Patterson function to solve structures. In all the cases where only relatively small structures needed to be solved i.e. for the various polymorphs of small molecules as well as co-crystals, salts and hydrates, this program was used.

SHELXD

In cases where isomorphous replacement was not possible and the structures were too large to be solved by SHELXS, the program SHELXD[17] was used for solving structures by *ab initio* methods. This program makes use of dual-space iteration algorithms to solve a structure by alternating the data between real and reciprocal spaces. The Patterson function is used to generate starting phases and the largest independent peaks are assigned in real space while the phases are refined by using a tangent expansion formula[18] for refinement in reciprocal space.

SHELXL

After the initial refinement with SHELXS or SHELXD, further refinement was carried out with SHELXL.[17] SHELXL makes use of the full-matrix least-squares technique to minimise the function $\sum w (F_o^2 - F_c^2)^2$.

The residual index (R_1) (expression 2.1) indicates the agreement between the observed (F_o) and calculated (F_c) structure factors. A low R_1 value thus indicates a satisfactory model.

$$R_1 = \frac{\sum||F_o|-|F_c||}{\sum|F_o|} \quad (2.1)$$

Another residual index parameter, wR_2, indicates the agreement between the observed and calculated intensities F^2 (expression 2.2).

$$wR_2 = \sqrt{\frac{\sum w\,(F_o^2-F_c^2)^2}{\sum w\,(F_o^2)^2}} \quad (2.2)$$

The default weighting scheme (w) in expression 2.2 as well as the parameters a and b are refined for each structure by making use of expressions 2.3 and 2.4 so that the selected values for a and b give a constant distribution of [$w\,(F_o^2 - F_c^2)^2$] with sin θ and $\sqrt{F_o/F_{max}}$.

$$w = \frac{1}{\sigma^2(F_o^2)+(aP)^2+bP} \quad (2.3)$$

$$P = \frac{2F_c^2+\max(0,F_o^2)}{3} \quad (2.4)$$

The goodness-of-fit (S) is defined by expression 2.5 where n is the number of reflections and p is the total number of parameters refined.

$$S = \sqrt{\sum\frac{w\,(F_o^2-F_c^2)^2}{n-p}} \quad (2.5)$$

When considering non-centrosymmetric crystal structures, their inversion will result in changes in the structural image and this necessitates the determination of absolute structure in such cases. This is also relevant in the case of chiral molecules where determination of the absolute configuration is necessary. The principle is based on the fact that resonant scattering/anomalous dispersion occurs (due to absorption of X-ray photons via excitation of core electrons of atoms in a crystal) where the absolute structures will display small differences in the intensities of h and $\bar{h}$. The magnitude of this effect depends on the atoms present with the effect being relatively weak if no atoms heavier than oxygen are present. The methods used today rely on what is referred to as the Flack parameter[19] that represents a crystal as an inversion twin with the current refinement model having the absolute structure as a reference domain and the other "twin" as the inverted domain. The measured intensities are modelled according to the following expression.

$$I_{model}(h) = (1-x)\left|F_{single}(h)\right|^2 + x\left|F_{single}(\bar{h})\right|^2 \quad (2.6)$$

In expression 2.6 the reference domain is represented by $\left|F_{single}(h)\right|^2$ and $\left|F_{single}(\bar{h})\right|^2$. The two absolute configurations are then refined while refining the twin scale factor, (*x*), known as the Flack parameter. The Flack parameter will have a value ranging from 0 to 1, with 0 representing the correctly assigned absolute configuration with no fraction of the inverted structure present and 1 demonstrating that the twin is the correct configuration. Intermediate values point to inversion twinning. When interpreting these values the standard uncertainty needs to be taken into consideration as these values are sometimes large enough to make the Flack parameter statistically ambiguous or meaningless.[20,21] Another method used for determining Flack parameters with higher precision is Parsons' method that makes use of selected quotients to estimate a Flack parameter post-refinement.[21,22]

Fourier transform infrared (FTIR) spectroscopy

Fourier transform infrared (FTIR) spectroscopic studies were carried out using either a Bruker Alpha spectrometer with an attenuated total reflectance (ATR) platinum Diamond 1 reflectance accessory for solid samples or a PerkinElmer Spectrum One FTIR spectrometer using attenuated total reflectance (ATR). Scans spanned the range 4000–400 cm^{-1}. The data were analysed using the programs OPUS[23] or Spectrum.[24]

This method of characterisation has numerous uses in the field of supramolecular chemistry and in this study proved useful for multiple procedures. It was used as a means of quick differentiation between various polymorphs by characterising the infrared spectra of each form. Another use was as an aid in detection of salt or co-crystal formation by determination of whether or not proton transfer had taken place by inspection of absorption bands that are characteristic for certain basic and acidic functional groups.

Nuclear magnetic resonance (NMR) spectroscopy

This method of characterisation was used as a means to determine stoichiometric ratios of the various components making up the multi-component systems presented in this thesis. The standard method involved recording the ^{1}H-NMR spectrum of a selected system with a Bruker 300 MHz spectrometer after dissolving crystals of this system in an appropriate deuterated solvent. The program MestReNova[25] was used to integrate proton signals of the respective components for a direct comparison of the signals and to plot the results.

Ultraviolet-visible (UV-Vis) spectrophotometry

In order to determine concentrations of bioactive compounds in solution, ultraviolet-visible light (UV-Vis) spectrophotometry was used. For UV active materials one can make use of the Beer-Lambert law (expression 2.7) to calculate concentrations from the absorbance of the compounds in solution.

$$A = \varepsilon_0 cl \qquad (2.7)$$

This is because of the linear relationship that exists between the absorbance (*A*) and concentration (*c*) of a compound in solution if the path length (*l*) and the extinction co-efficient (ε_0) are kept constant.

The instrument used was either a Cintra-20 UV-Vis spectrophotometer with GBC spectral software[26] or an Agilent Cary 60 UV-Vis spectrophotometer. Spectra were recorded over the wavelength range 200-800 nm.

This method of analysis was used to determine concentrations of solutions for kinetic solubility experiments involving the various forms of clevudine, MMV652103 and to carry out phase solubility experiments with (±)-α-Lipoamide.

Kinetic solubility experiments

In order to compare the solubilities of various polymorphs of clevudine a calibration curve was set up for clevudine dissolved in water. The concentrations were recorded with a Cintra-20 UV-Vis spectrophotometer at a wavelength of 266.2 nm and a temperature of 25 ± 0.5 °C. The calibration curve obtained can be described by $y = 0.0394x - 0.0041$ ($R^2 = 0.9998$) and is shown in appendix A (Fig. A2.1). The actual experiment involved placing an excess (125 mg) of each form of clevudine in a vial with 0.75 ml of water and stirring at 1000 rpm at a temperature of 25 ± 0.5 °C for 72 h. The resulting solutions were filtered through 0.45 µm nylon filters and diluted to a suitable concentration for triplicate absorbance measurements.

Similar methods were set up for kinetic solubility experiments with MMV652103 polymorphs. The calibration curves are presented in appendix A (Figs. A2.2 and A2.3). The pertinent specifications are described in the relevant result sections.

Phase solubility experiments

A phase-solubility experiment similar to the method described by Higuchi and Connors[27] was carried out to test the effects of various cyclodextrins on the solubility of (±) -α-Lipoamide.

Phase-solubility diagrams are broadly categorised as being either A- or B-types.[27-29] A-types show an increase of solubility when increasing the cyclodextrin concentration due to a soluble complex forming between the host and guest. These A-types are then further classified as either a linear increase (A_L), showing a negative (A_N) or positive (A_P) deviation with higher concentrations of CD. B-types show a decrease in the solubility of the guest with an increase of CD concentration due to less soluble complexes forming. These can be further classified as B_S types forming complexes with limited solubility or B_I forming insoluble complexes. A schematic depiction of these typologies is shown in Fig. 2.1.

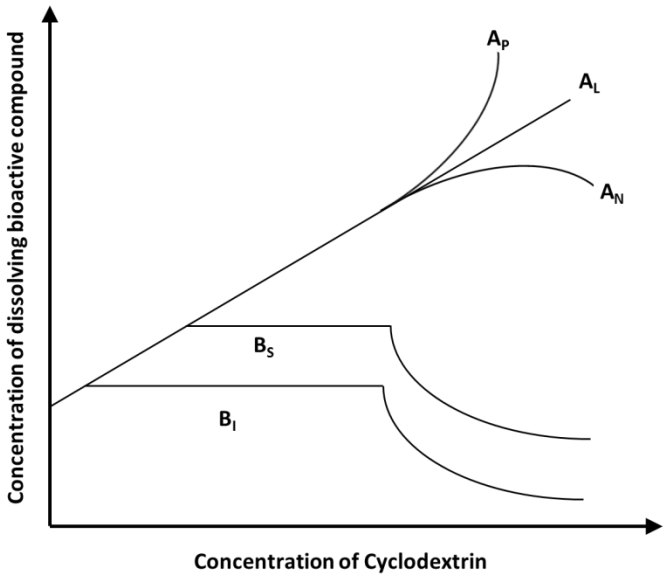

Fig. 2.1 Phase solubility typologies according to Higuchi and Connors.[27]

Due to the poor dissolution and wettability of (±) -α-Lipoamide in pure water, the compound was dissolved in ethanol first and water was subsequently added to make a 50 % ethanol solution by volume. All of the following measurements were carried out on 50 % ethanol solutions. A calibration curve described by $y = 0.5617x$ ($R^2 = 0.998$) was composed by plotting the known concentrations of a prepared stock solution against the measured absorbance at a wavelength of 332 nm (Appendix A, Fig. A2.4).

A range of solutions with different concentrations of each host cyclodextrin (2.5-30 x 10^{-3} M) were added to an excess of guest and stirred for 72 h at a rate of 500 rpm at a temperature of 25 ± 0.5 °C. The

solution was filtered through a 0.45 μm nylon filter and ethanol was then added to make up a 50 % ethanol solution. The concentrations were then calculated by making use of UV-Vis spectrophotometry and the calibration curve mentioned earlier. The instrument used in this case was an Agilent Cary 60 UV-Vis spectrophotometer with a scan range of 200 to 800 nm and a scan rate of 600 nm min^{-1} and 1 nm data intervals. Further dilutions were done in cases where the concentrations did not fall within the range of the calibration curve.

To determine the solubility of (±) -α-Lipoamide in the absence of cyclodextrin i.e. the S_0 value, an excess of the compound was added to pure water and exposed to the same conditions as with the CD-containing vials. S_0 was determined to be 3.101 x 10^{-3} M at 25 ± 0.5 °C.

Relationships and slopes of the phase-solubility diagrams were used to calculate the association constants (K_C) of complexes formed (expression 2.8), where the host-guest ratio is assumed to be 1:1.[27-30]

$$K_C = \frac{\text{slope}}{S_0\,(1-\text{slope})} \qquad (2.8)$$

High-performance liquid chromatography (HPLC)

High-performance liquid chromatography (HPLC) is an analytical method used to separate mixtures into individual components. This is accomplished by using a pressurised mobile phase made up of selected solvents to force a mixture through a column possessing adsorbent properties resulting in individual components exiting the other end of the column at different rates.

The instrumentation used was an Agilent 1220 HPLC system (Agilent Technology, USA), equipped with a binary pump and DAD detector. The HPLC unit was equipped with a 3.0 x 50 mm Poroshell 120 EC-C18 column (Agilent Technology, USA) containing 2.7 μm packing. The software used for peak integration was Agilent OpenLAB CDS.[31]

Powder dissolution rate study in simulated intestinal fluid

HPLC was employed to carry out a customised powder dissolution test to compare the dissolution rate and solubility of various derivatised forms of MMV652103 to that of the unaltered starting material. It was necessary to use HPLC for these experiments because of the composition of the dissolution media

and various derivatised forms consisting of multiple components, some of which were UV active in the same region as the component of interest.

When determining the solubility of drugs, the most common solvent used is water. In cases where the drugs are not sufficiently soluble in water, other organic solvents can often be used. When comparing the solubilities of polymorphs of drugs, for instance, the choice of solvent is of little consequence as the relative solubilities should be the same, independent of the solvent used. The solubility of co-crystals however, is highly dependent on the solvent used. In order to most closely mimic the conditions in which a drug needs to be soluble, namely those of the gastro-intestinal tract, fasted state simulated intestinal fluid (FaSSIF) was used. The aim of the supramolecular derivatisation of MMV652103 was to increase its bioavailability by improving its solubility. The compound has a reported partition coefficient (log D) value of 2.5,[32] theoretically placing it in class 2 of the Biopharmaceutics Classification System[33] (having poor solubility and high permeability). The limiting factor in the uptake of this drug would thus be the rate and extent of its solubility. In theory the drug should be taken up rapidly as soon as it is released. The drug has a reported pK_a of 2.7,[32] indicating that it will most likely be protonated in the acidic environment of the stomach and unionized in the environment of the intestines. Due to the fact that only the unionized form will be able to permeate the walls of the gastro-intestinal tract, it is reasonable to conclude that the rapid dissolution of this drug in the intestine is a desired outcome. A customised experiment was set up in order to compare the solubility and dissolution rate of the co-crystal and salt forms to those of the pure compound in a simulated environment of the small intestine (duodenum).

Samples were sieved to obtain a particle size range of 53-150 µm. A total of 25 mg of the pure MMV652103 or the equivalent amount of MMV652103 in the form of the co-crystal/salt was added to 50 ml of FaSSIF that was kept at a constant temperature of 37.5 ± 0.5 °C while being stirred at 500 rpm. Aliquots were withdrawn at selected intervals (1, 5, 10, 15, and 30 min, 1 h, 1.5 h, 2 h, 3 h, 4 h, and 6 h) and filtered through 0.22 µm nylon filters. The concentration of free MMV652103 dissolved in each sample was measured using HPLC. The flow rate was set to 0.500 ml min^{-1} with the column temperature maintained at 37.5 ± 0.8 °C. The injection volume was set at 5 µl with a draw and eject speed of 200 µl min^{-1} and the detector wavelength was set at 310 nm. A mobile phase containing water and acetonitrile (7:3 v/v) was used. The total retention time at each interval was 3 min with the retention time of MMV652103 being $\pm$ 1.15 min. A representative chromatogram of such an experiment with a

single peak representing MMV652103 visible at 1.147 min and multiple peaks due to FaSSIF around 0.5 min, is presented in Appendix A (Fig. A2.5).

A calibration curve described by y = 4.6062x (R^2 = 0.9979) was composed by plotting the known concentrations of a prepared stock solution against the measured area under the curve of absorbance at a wavelength of 310 nm at retention times spanning the range 1.144-1.149 min (Appendix A Fig. A2.6).

Additional resources

The program CS ChemDraw Pro[34] was used to produce line drawing diagrams of molecules and interactions.

CheckCIF[35] is a program available online that was used for the validation of solution and refinement details of reported crystal structures.

The program LAYER[36] was used to graphically represent intensity data as simulated precession photographs which were then used for determination of space groups by inspection of systematic absences which indicated specific symmetry elements.

The program PLATON[37] was used for the calculation of geometrical parameters of molecules (bond distances and angles as well as torsion angles) and of interactions (hydrogen-bonds, π-π or C-H$\cdots\pi$) for the various crystal structures obtained.

The program POV-Ray[38] was used to generate figures such as those showing interactions, packing diagrams or representations of molecular conformations found in crystal structures.

The CSD[2] and its related software such as ConQuest and Mercury[39] were used to search for isostructural cyclodextrin complexes, co-crystal formers with a high chance of forming supramolecular interactions, as well as known forms of relevant compounds such as polymorphs, solvates or hydrates.

The program CrystalExplorer[40] was used to generate two-dimensional fingerprint plots from three-dimensional Hirshfeld surfaces.

Electronic supplementary data including crystallographic data can be found in Appendix B under the relevant folders. The various file types and information they contain is listed in Table 2.1.

Table 2.1 File types in Appendix B.

File extensions	Data contained
.HTML	Nreport – Crystal structure report
.HKL	Reflection data
.FCF	Structure factor tables
.RES	SHELX co-ordinate data
.CIF	Crystallographic information file with embedded structure factor tables and SHELX co-ordinate data (embedded .RES and .FCF)
.LIS	Platon output
.XL	SHELX output file

References

1. U.S. Food and Drug Admistration, *FDA Generally Recognized as Safe (GRAS)*, http://www.fda.gov/Food/IngredientsPackagingLabeling/GRAS/ (accessed January 2018).
2. Cambridge Structural Database and Cambridge Structural Database System, Version 5.39 (February 2018 update), Cambridge Crystallographic Data Centre, University Chemical Laboratory, Cambridge, England, 2018.
3. M. R. Caira, *Rev. Roum. Chim.*, 2001, **46**, 371-386.
4. Program AnalySIS. Version 3.1 for Windows, Soft Imaging System GmbH, Digital Solutions for Imaging and Microscopy, Münster, Germany.
5. TA instruments, Universal Analysis 2000 for Windows. Version 4.7A, TA Instruments – Waters LLC, New Castle, Delaware, © 1998-2009.
6. TA instruments, TRIOS. Version 4.1.0.31739, TA Instruments – Waters LLC, New Castle, Delaware, © 2016.
7. THASS GmbH, DSC XP-10. Version 3.3.0.7(D), Thermal Analysis & Surface Solutions GmbH, Friedberg, Germany, © 2003.
8. S. Lubhelwana, MSc Dissertation, *Crystal Isostructurality and X-ray Diffraction studies of Cyclodextrin Inclusion Compounds*, University of Cape Town, South Africa, **2005**.
9. L. E. Hunt, Doctoral dissertation, *The supramolecular modification of trans-resveratrol and related antioxidant molecules,* University of Cape Town, South Africa, **2017**.
10. C. F. Macrae, P. R. Edgington, P. McCabe, E. Pidcock, G. P. Shields, R. Taylor, M. Towler and J. v. d. Streek, *J. Appl. Crystallogr.*, 2006, **39**, 453-457.
11. C. F. Macrae, I. J. Bruno, J. A. Chisholm, P. R. Edgington, P. McCabe, E. Pidcock, L. Rodriguez-Monge, R. Taylor, J. v. Streek and P. A. Wood, *J. Appl. Crystallogr.*, 2008, **41**, 466-470.
12. APEX2. Version 1.0-27, Bruker AXS Inc., Madison, Wisconsin, USA.
13. Program SAINT, Version 7.60a, Bruker AXS Inc., Madison, Wisconsin, USA, **2008**.
14. G. M. Sheldrick, SADABS, *program for empirical absorption correction of area detector data*, University of Göttingen, Göttingen, Germany, **1997**.
15. International Tables for Crystallography, Vol II: Mathematical Tables, ed. J.S. Kasper and K. Lonsdale, Kynoch Press, Birmingham, England, 1967, 291.
16. XPREP, *Data Preparation and Reciprocal Space Group Exploration*, Version 2008/2, © Bruker AXS Inc., Madison, Wisconsin, USA, **2008**.
17. G. M. Sheldrick, *Acta Crystallogr., Sect. A: Found. Crystallogr.*, 2008, **64**, 112-122.
18. L. J. Barbour, *J. Supramol. Chem.*, 2001, **1**, 189-191.

19. J. T. Karle and H. Hauptman, *Acta Crystallogr.*, 1956, **9**, 635-651.
20. H. Flack, *Acta Crystallogr., Sect. A: Found. Crystallogr.*, 1983, **39**, 876-881.
21. S. Parsons, H. D. Flack and T. Wagner, *Acta Crystallogr., Sect. B: Struct. Sci., Cryst. Eng. Mater.*, 2013, **69**, 249-259.
22. S. Parsons, *Tetrahedron: Asymmetry*, 2017, **28**, 1304-1313.
23. Bruker Optik GmbH, OPUS. Version 7.2, Bruker Optik GmbH, Ettlingen, Germany, © 2012.
24. PerkinElmer Spectrum. Version 10.03.02, PerkinElmer, Inc., © 2011.
25. Program MestreNova. Version 6.0.2-5475, Mestrelab Research S.L., Santiago de Compostela, Spain © 2009.
26. GBC Spectral. Version 1.70, LabControl® GmbH, © 1993-1998.
27. T. Higuchi and A. Connors, Adv. Chem. Instrum., 1965, **4**, 212–217.
28. M. E. Brewster and T. Loftsson, *Adv. Drug Delivery Rev.*, 2007, **59**, 645-666.
29. T. Loftsson and M. E. Brewster, *J. Pharm. Pharmacol.*, 2010, **62**, 1607-1621.
30. K.A. Connons, in *Comprehensive Supramolecular Chemistry*, ed. J. Szejtli and T. Osa, Elsevier, Oxford, UK, 1996, vol. 3, pp. 205–241.
31. Agilent Technology, OpenLAB CDS ChemStation Edition. Version A.01.06.111, Agilent Technology, Santa Clara, CA, USA, © 1999-2018.
32. C. Le Manach, D. Gonzàlez Cabrera, F. Douelle, A. T. Nchinda, Y. Younis, D. Taylor, L. Wiesner, K. L. White, E. Ryan, C. March, S. Duffy, V. M. Avery, D. Waterson, M. J. Witty, S. Wittlin, S. A. Charman, L. Street and K. Chibale, *J. Med. Chem.*, 2014, **57**, 2789-2798.
33. U.S. Food and Drug Admistration, *FDA Biopharmaceutics Classification System (BCS)*, https://www.fda.gov/aboutfda/centersoffices/officeofmedicalproductsandtobacco/cder/ucm128219.htm (accessed March 2018).
34. S. Rubenstein, CS ChemDraw Pro™, Version 4.0.1, CambridgeSoft Corporation, Massachusetts, USA, © 1985-1997.
35. http://checkcif.iucr.org/ (accessed 2014-2018).
36. L. J. Barbour, *J. Appl. Crystallogr.*, 1999, **32**, 351-352.
37. A. L. Spek, PLATON, A Multipurpose Crystallographic Tool, Version 20604, © 1980-2004.
38. POV-Ray for Windows, Version 3.1e, The persistence of vision team, © 1991-1999.
39. I. J. Bruno, J. C. Cole, P. R. Edgington, M. Kessler, C. F. Macrae, P. McCabe, J. Pearson and R. Taylor, *Acta Crystallogr., Sect. B: Struct. Sci.*, 2002, **58**, 389-397.
40. CrystalExplorer, Version 3.1, S. K. Wolff, D. J. Grimwood, J. J. McKinnon, M. J. Turner, D. Jayatilaka and M. A. Spackman, University of Western Australia, Perth, Australia, **2012**.

Chapter 3

Polymorphism of clevudine: a nucleoside analogue antiviral drug

In this chapter the solid-state modification of the antiviral agent clevudine (Scheme 3.1) will be presented, firstly, by describing each form individually, followed by comparisons of the various forms.

A crystal structure for clevudine that was based on intensity data collected at 'room-temperature' was published in 1996[1] (refcode TEYDAC, Cambridge Crystallographic Database)[2] and another polymorphic form was discovered by an M.Sc student (B. Mzondo) from the same Centre as the author of this thesis (i.e. UCT's Centre for Supramolecular Chemistry Research) but its crystal structure was not published prior to commencement of this study due to the limited characterisation data available at the time.[3]

The initial aim was to fully characterise each form and compare their structural relationships, thermal stabilities, and aqueous solubilities while concurrently developing more solid-state forms of this compound that may be used in pharmaceutical formulations. Fruitless attempts were made to produce co-crystals of this compound with selected coformer molecules. In the process of characterisation of the known forms a new polymorphic form was discovered.

The results of solid-state characterisation of each of the polymorphs will be presented followed by comparisons of the three forms. The polymorphs are numbered chronologically by the dates of their discovery from Form 1 to Form 3.

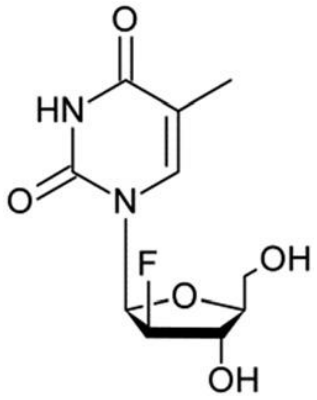

Scheme 3.1 Chemical structure of clevudine

Clevudine Form 1

Preparation of Form 1 single crystals

The raw material, as purchased, matched the crystal form that was reported in 1996[1] (refcode TEYDAC, Cambridge Crystallographic Database)[2] when analysed using FTIR (Fig. 3.1) and PXRD (Fig. 3.2). This form is henceforth referred to as Form 1. In order to obtain a better refined structure than the reported structure collected at 'room temperature',[1] the structure was re-determined at low temperature (173(2) K).

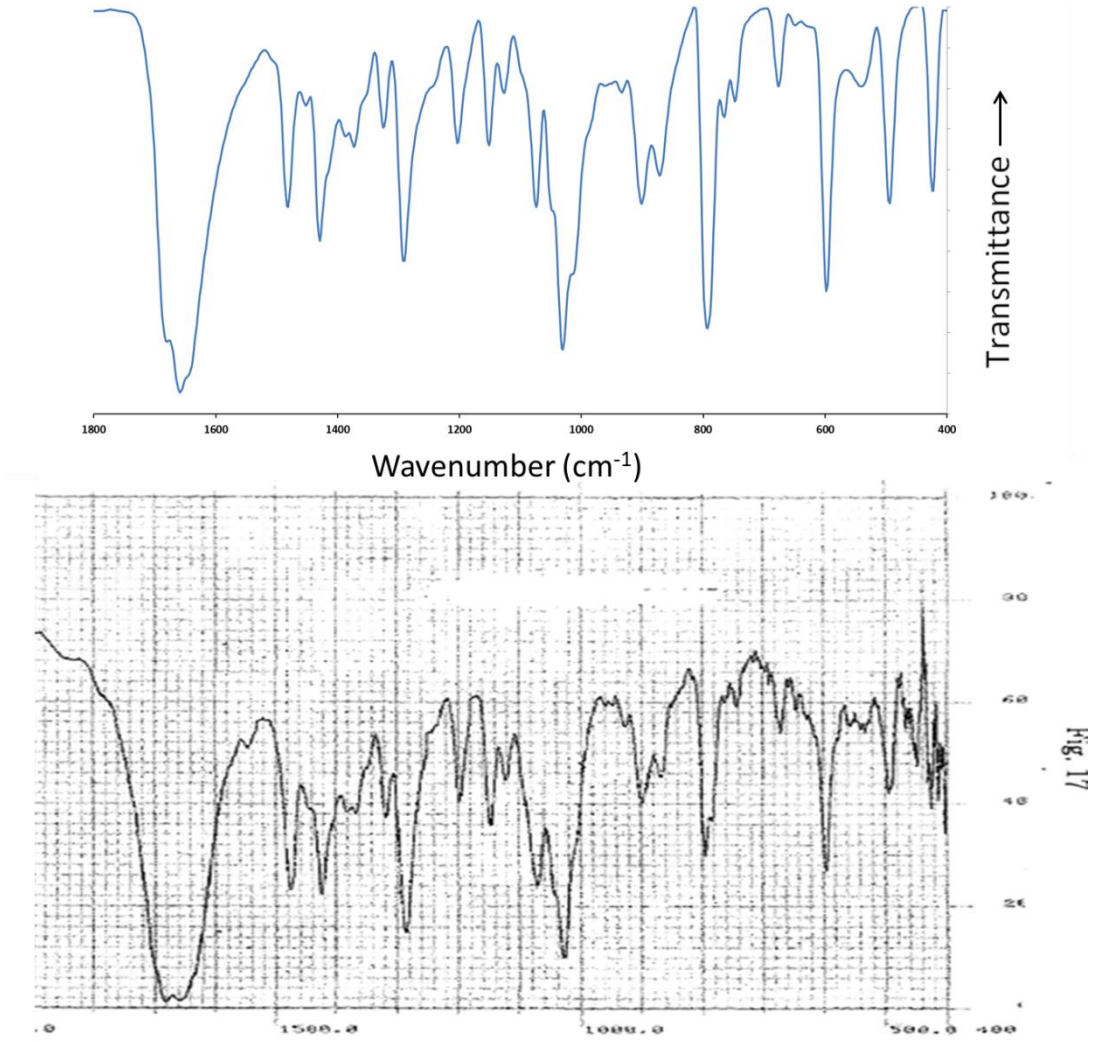

Fig. 3.1 Experimental FTIR spectrum of clevudine Form 1 (top) and reported spectrum from the literature[4] (bottom).

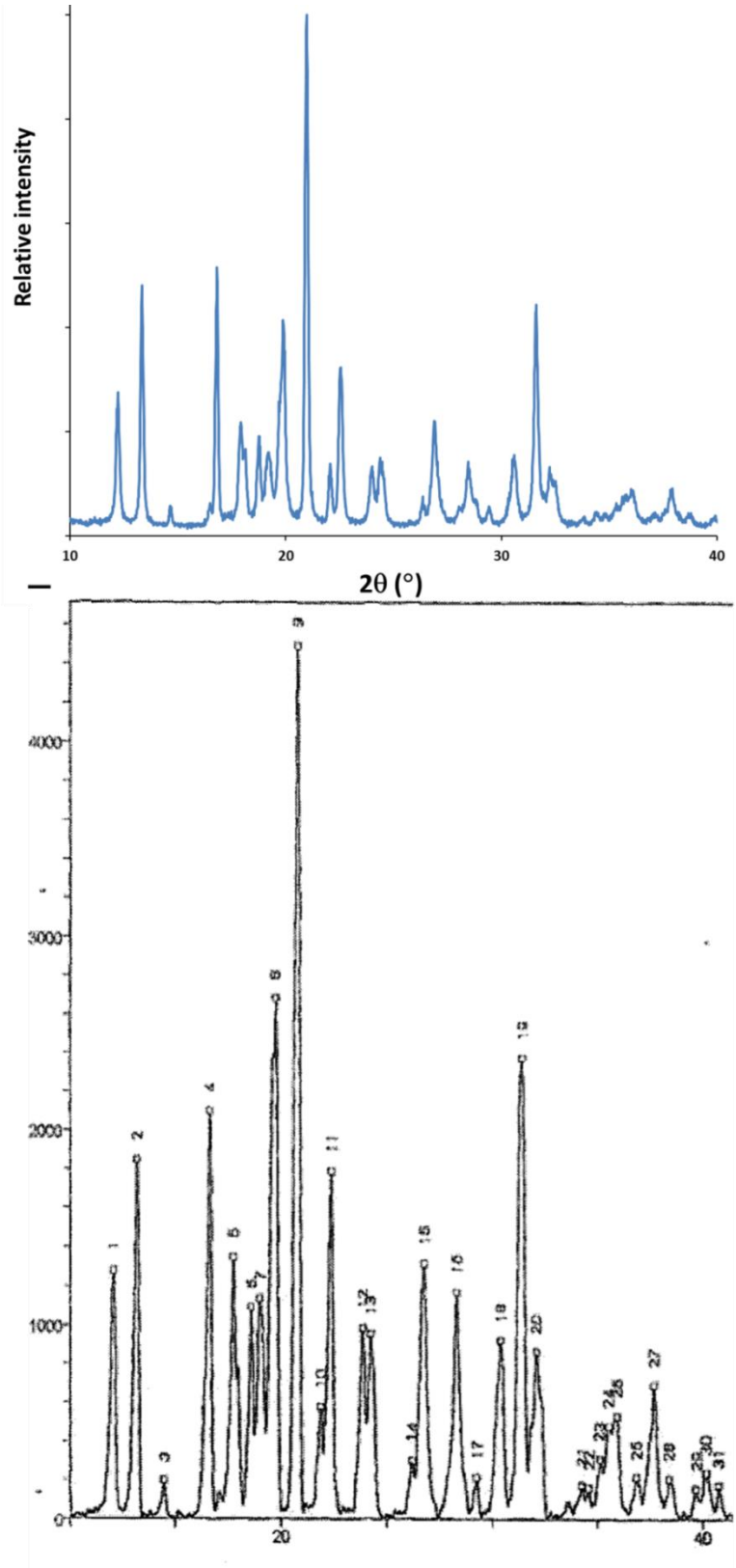

Fig. 3.2 Experimental PXRD trace of the starting material (top) and a reported trace from the literature[4] (bottom).

Method of preparation of single crystals

Single crystals of Form 1 were prepared by dissolving 10 mg of the raw material in 2 cm^3 of ethyl acetate while stirring at a temperature of 50 – 60 °C, filtering through a 0.45 µm nylon filter into a clean vial, covered with Parafilm™, and left on a benchtop for slow evaporation. Crystals started forming after a few days. In this case the crystal data were collected and the structure was determined at a low temperature of 173(2) K (as opposed to the one done at 'room-temp').[1]

Crystal structure analysis

Data-collection and space group determination

The single-crystal X-ray intensity data collection was performed on a Bruker Kappa Apex II Duo diffractometer with graphite-monochromated MoKα radiation (λ = 0.71073 Å). The collection was carried out at 173(2) K. Data reduction was done with the program SAINT[5] and multi-scan absorption corrections were applied with SADABS.[6] The X-ray diffraction pattern showed 2/*m* Laue symmetry, representative of the monoclinic crystal system. The $|E^2-1|$ was determined by making use of XPREP[7] and its value of 0.792 indicated non-centrosymmetry. The systematic absences observed were *hkl: none, h0l: none, 0k0: k = 2n*. The possible space groups matching these limiting conditions were restricted to $P2_1$ or $P2_1/m$. $P2_1$ was selected for analysis due to the chirality of the compound in question. This form has Z = 4 molecules per unit cell and Z′ = 2 molecules per asymmetric unit.

Structure solution and refinement

Crystallographic data and parameters for collection of intensity data are shown in Table 3.1. The X-seed interface[8] was used to operate the SHELX suite of programs[9] in order to solve the structure by direct methods and refine it by full-matrix least-squares. At first all the non-hydrogen atoms were placed and isotropically refined. A hydroxyl group at O9 was found to be disordered over two positions. The site-occupancy factor (s.o.f.) of the major component was refined as *x* while the minor component was refined as 1-*x*. The s.o.f. of the major component settled at x = 0.85. The non-hydrogen atoms, apart from the disordered hydroxyl group, were then refined anisotropically. All hydrogen atoms were found in difference electron density maps and placed in idealised positions in a riding model and refined with thermal parameters 1.2 - 1.5 times the U_{iso} values of their parent atoms. Though the Flack parameter[10] was somewhat dubious due to the lack of heavy-atoms, the absolute structure was proven to be correctly assigned by polarimetry. A PerkinElmer PE-343 polarimeter (Waltham, Massachusetts) was

used at 20 °C and λ = 589 nm to confirm enantiopurity. The reported $[\alpha]_D^{25}$ value for clevudine is -111.77° (c = 0.23, methanol).[11] The absolute configuration described here corresponds to that of the reported structure.[1]

Table 3.1 Data-collection and refinement parameters for clevudine Form 1.

Molecular formula	$C_{10}\,H_{13}\,F\,N_2\,O_5$
Formula weight (g mol^{-1})	260.22
Crystal system	Monoclinic
Space group	$P2_1$
a (Å)	10.3584(10)
b (Å)	10.8540(10)
c (Å)	10.4469(10)
α (°)	90
β (°)	108.403(2)
γ (°)	90
V ($Å^3$)	1114.48(18)
Z	4
D_c (g cm^{-3})	1.551
μ (Mo Kα) (mm^{-1})	0.135
F(000)	544
Data-collection temp. (K)	173(2)
Crystal size (mm^3)	0.50 x 0.48 x 0.45
Range scanned θ (°)	2.05–28.34
Index ranges ±*h*, ±*k*, ±*l*	h: -13, 13; k: -14, 14; l: -13, 13
Reflections (total)	10 821
Independent reflections	5492
Reflections with I>2σ(I)	5291
Number of parameters	335
R_{int}	0.0189
S	1.041
R_1 [*I*>2σ(*I*)]	0.0418
Reflections omitted	8
wR_2	0.1062
a, b in $w = 1/[\sigma^2(F_o^2)+(aP)^2+(bP)]$	a = 0.0493; b=0.6369
$(\Delta/\sigma)_{mean}$	< 0.001
$\Delta\rho_{min,max}$ (e $Å^{-3}$)	-0.519, 0.694
Flack parameter	Flack x = -0.252(899) by classical fit to all intensities; -0.128(419) from 2355 selected quotients (Parsons' method)[12]

Molecular structure

The asymmetric unit of clevudine Form 1 is presented in Fig. 3.3 and the relevant symmetry information is listed in Table 3.2.

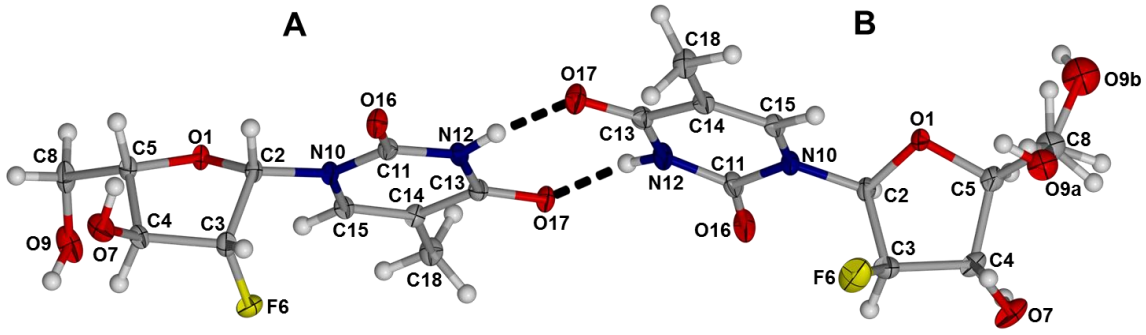

Fig. 3.3 The asymmetric unit of clevudine Form 1 displaying the numbering scheme used as well as the disordered components of atom O9. Displacement ellipsoids are shown at the 50% probability level and hydrogen atoms are drawn with arbitrary radii.

Crystal packing and hydrogen bonding

Table 3.2 Hydrogen bonds in clevudine Form 1[a]

D – H···A	*d*(D – H), Å	*d*(H ···A), Å	*d*(D ···A), Å	∠(DHA), deg.
O7A - H7A···O16B^{i}	0.84	2.09	2.884(3)	158
O7B - H7B···O16A^{ii}	0.84	2.02	2.803(3)	155
O9A - H9A···O7B^{iii}	0.84	2.00	2.804(3)	159
O9B - H9B···O9A^{iv}	0.84	1.98	2.794(4)	165
N12A - H12A··· O17B	0.88	1.94	2.810(3)	171
N12B - H12B···O17A	0.88	1.98	2.851(3)	169
C8B - H8B2···O17A	0.99	2.59	3.441(4)	144
C2A - H2A···O16B^{i}	1.00	2.28	3.122(3)	141
C2B - H2B···O16A^{ii}	1.00	2.35	3.154(3)	137
C15A - H15A···O9B^{vi}	0.95	2.42	3.366(4)	172
C15B - H15B···O9A^{iv}	0.95	2.52	3.450(4)	165

[a]Symmetry transformations used to generate equivalent atoms: *[i]: x,-1+y,z; [ii]: x,1+y,z; [iii]: 1-x,-3/2+y,2-z; [iv]: -1+x,1+y,-1+z; [v]: 1-x,1/2+y,1-z; [vi]: 1+x,-1+y,1+z;*

In the following section, hydrogen bonding motifs are described with individual intermolecular hydrogen bonds written as A–H···B′; the prime symbol is generic and refers to the symmetry operator for atom B listed in Table 3. This notation will be used in all subsequent sections describing H-bonding motifs.

This form of clevudine packs in layers. The distinct layers and interactions between them are visible in Figs. 3.4, 3.5 and 3.6. The interactions connecting the layers are the following:

O7B–H7B···O16A′, O9A–H9A···O7B′, and O9B–H9B···O9A′. Another interaction between the layers is formed by the minor disorder component O9 of molecule B namely O9C–H9C···O17A′ H-bonds.

Each of these layers consists of molecules A and B (colour coded for clarity in Fig. 3.6) hydrogen-bonded via five individual ring motifs, as can be seen in Fig. 3.4. The following section describes these rings by graph-set designators and constituent hydrogen bonds.

There exists an almost symmetrical $R_2^2(8)$ ring between the methylpyrimidine-dione rings of molecules A and B formed by the two N12–H12···O17′ H-bonds. Two pairs of hydrogen bonds, O7–H7···O16′ and C2–H2···O16′, form the ring described by $R_4^2(16)$. A ring formed by C15B–H15B···O9A′ and O9B–H9B···O9A′ is defined by $R_2^1(10)$. Another ring, $R_2^2(10)$, is formed by almost symmetrical C2–H2···O16′ hydrogen bonds. The final ring, $R_2^1(7)$, consists of O7B–H7B···O16A′ and a C2B–H2B···O16A′ H-bonds.

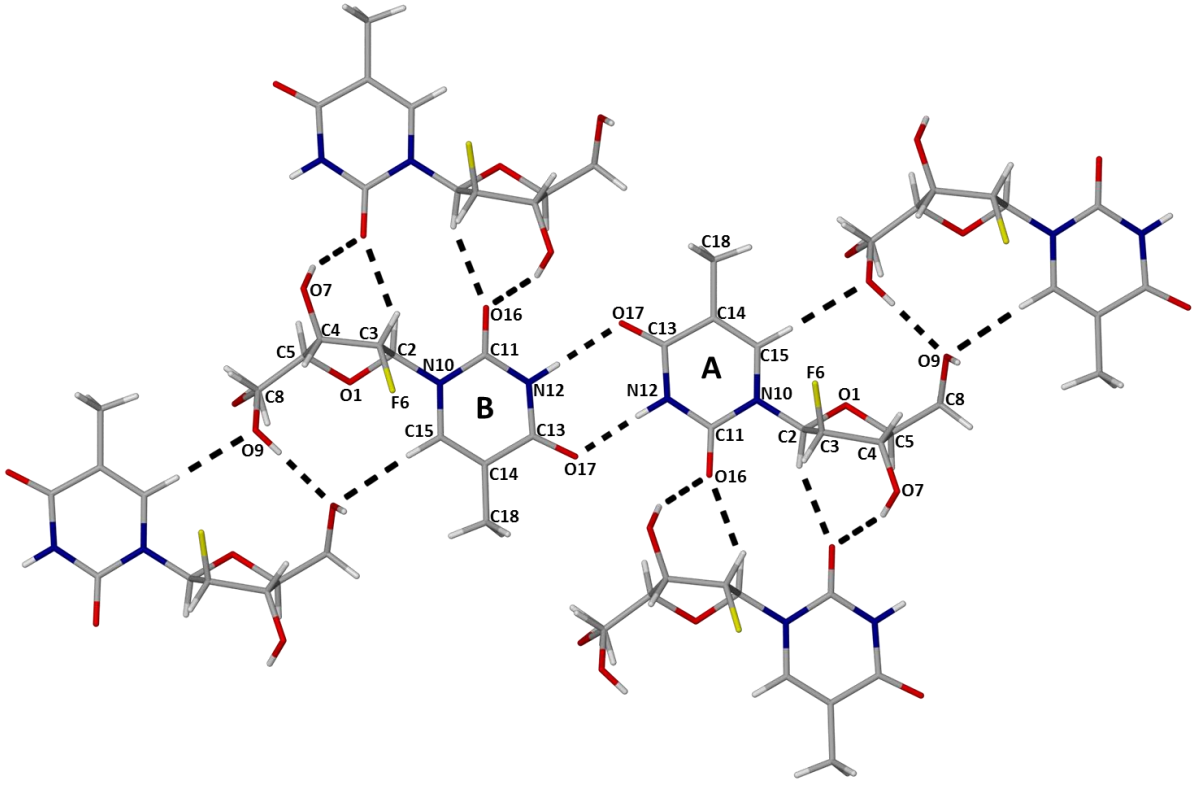

Fig. 3.4 Representative H-bonds in a layer of clevudine Form 1.

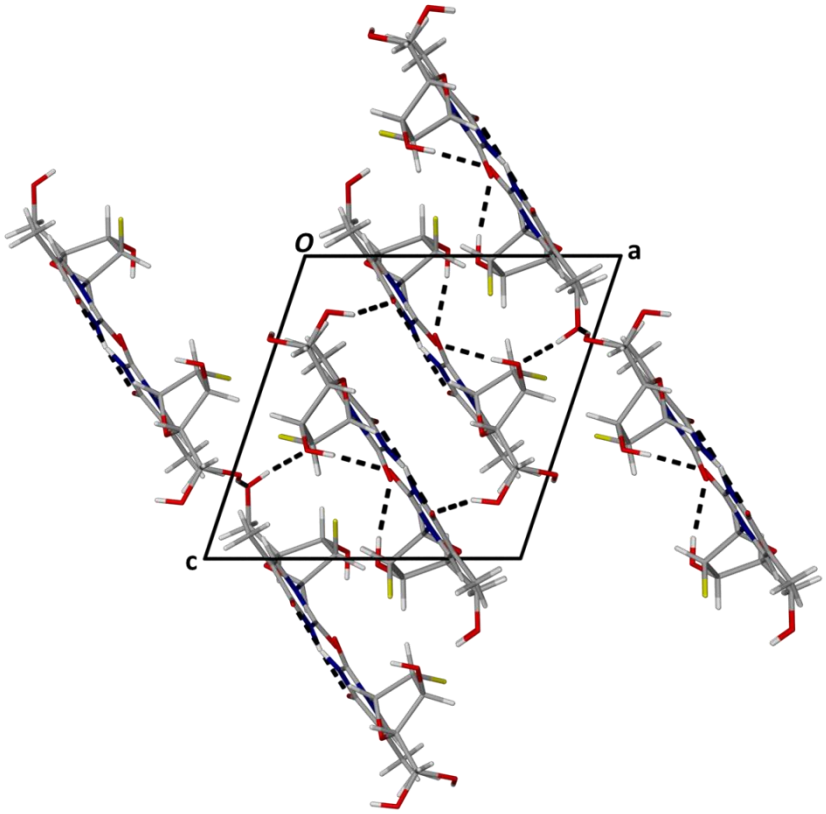

Fig. 3.5 Side view of layers showing the packing and interactions between stacked layers viewed along [010].

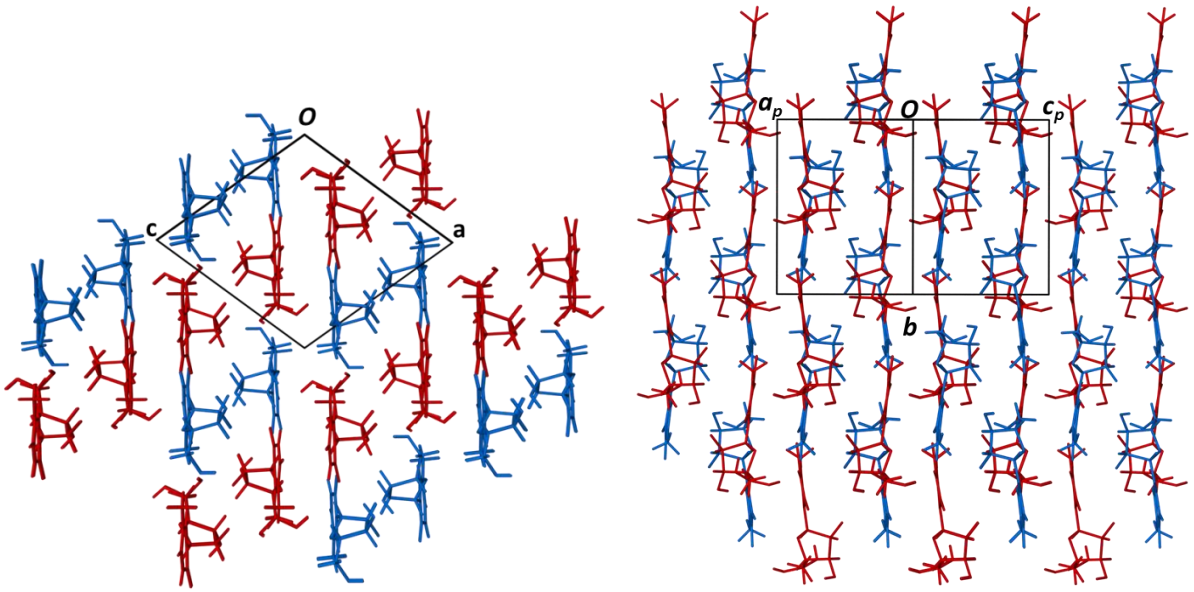

Fig. 3.6 Packing of clevudine Form 1 (A in blue and B in red) viewed along [010] (left) and [101].

The experimentally produced PXRD trace of the starting material of clevudine and the trace calculated from the solved crystal structure are compared in Fig. 3.7. The highest intensity peak is observed at 21°2θ and corresponds to the (2 0 -2) planes with a d-spacing of 4.219 Å. These planes correspond with the layers visible in Figs. 3.5 and 3.6. Another peak with relatively high intensity at 31.8°2θ corresponds to the (3 0 -3) planes with a d-spacing of 2.812 Å and also relates to the layered packing of this form.

The calculated and experimental traces indicate that the starting material matches the form produced by recrystallization from various solvents. The raw material (RM) was used without any further processing for subsequent experiments where clevudine Form 1 was used.

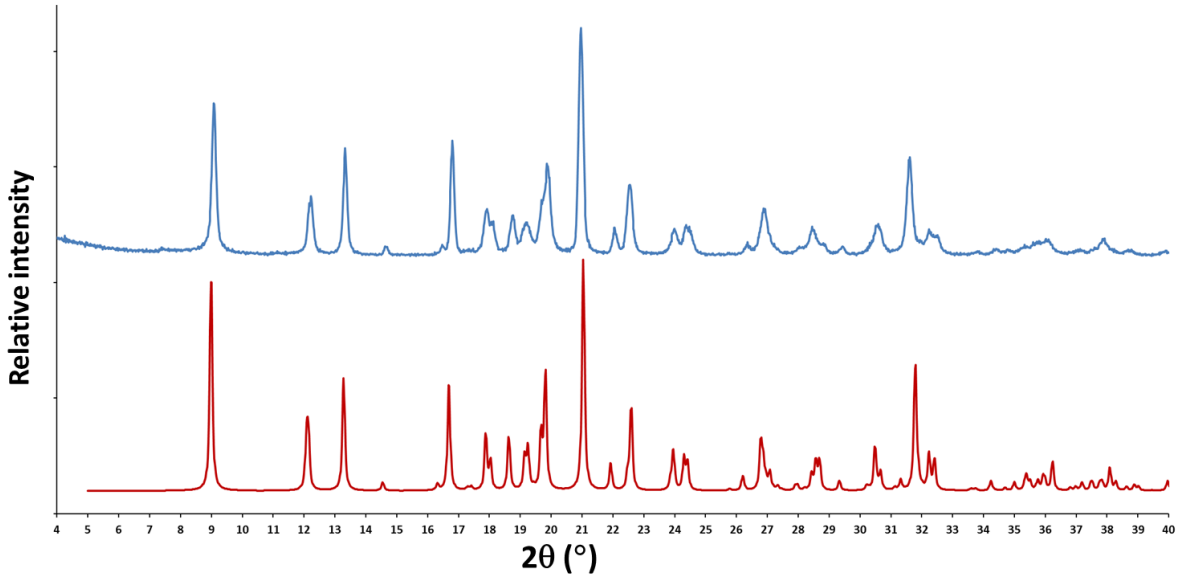

Fig. 3.7 Calculated (bottom) and experimental (top) PXRD traces of clevudine Form 1.

Thermal results

The HSM result (Fig. 3.8) at a heating rate of 10 °C min^{-1}, displays melting of the crystal above 190 °C, with melting being complete above 200 °C. During DSC experiments carried out at the default heating rate used of 10 °C min^{-1}, clevudine Form 1 showed a single endotherm (Fig. 3.9) with onset at 188.5 ± 0.1 °C (n = 3), peak at 189.3 ± 0.1 °C (n = 3) and enthalpy of fusion 212.6 ± 4.7 kJ mol^{-1} matching the HSM result. The TGA result (Fig. 3.10) exhibited no mass loss until well past the melting point. The mass loss starting around 300 °C was due to decomposition.

Hot stage microscopy

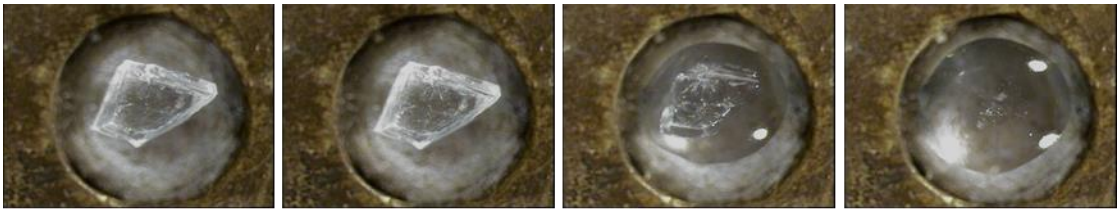

Fig. 3.8 Representative HSM photographs of clevudine Form 1 heated at 10 °C min^{-1}.

Differential scanning calorimetry

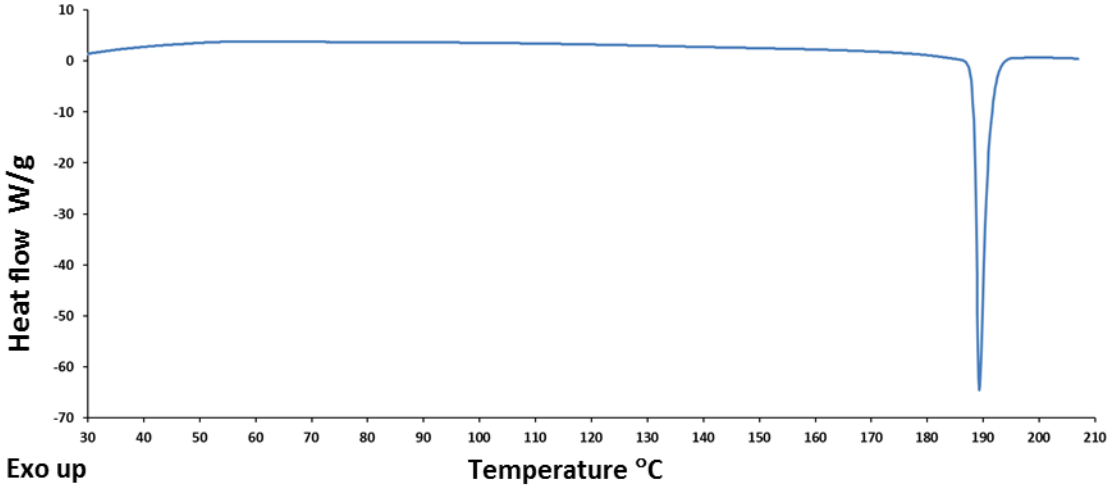

Fig. 3.9 DSC trace of clevudine Form 1 at 10 °C min^{-1}.

Thermogravimetric analysis

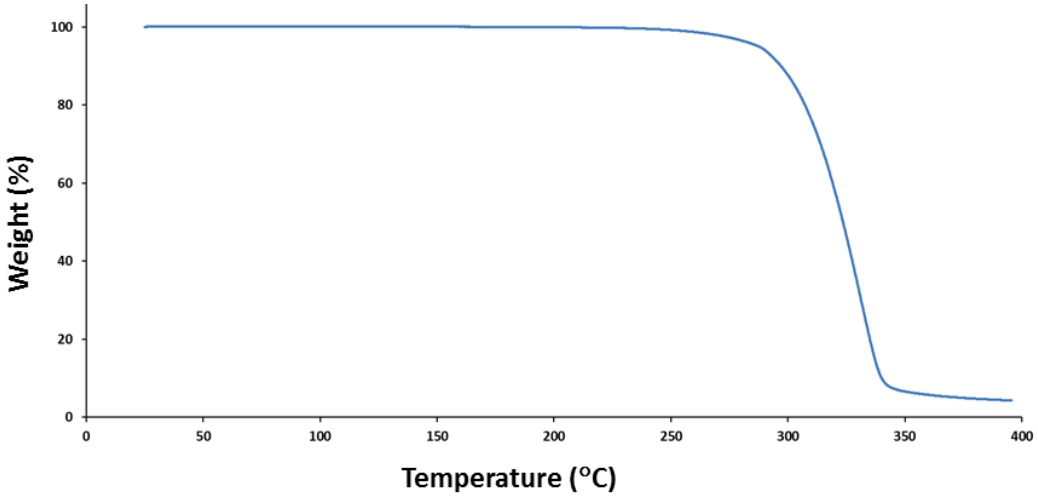

Fig. 3.10 Representative TGA of clevudine Form 1.

Clevudine Form 2

Preparation of Form 2 single crystals

A new polymorphic form of clevudine was serendipitously discovered by B. Mzondo in an attempt to obtain a co-crystal with the coformer cinnamamide.[4] The method followed was to dissolve 10 mg of clevudine with an equimolar quantity of cinnamamide in 3 cm^3 of ethyl acetate while stirring at 60 °C. The solution was filtered through a 0.45 µm nylon filter into a clean vial and kept at an elevated temperature for slow cooling by placing the vial in a Dewar flask containing water that was maintained at 70 °C for one week. The vial was then placed on a benchtop and after one week crystals of pure cinnamamide and crystals of the new API form were present in the same vial. This new form was labelled as Form 2.

Crystal structure analysis

Data-collection and space group determination

The structure was re-determined with new data collected. All the specifications of the X-ray intensity data collection for the Form 2 single crystal were the same as for the Form 1 collection. The X-ray diffraction pattern also showed 2/*m* Laue symmetry, representative of the monoclinic crystal system. The $|E^2-1|$ value of 0.741 indicated non-centrosymmetry. Observed systematic absences were *hkl: none, h0l: none, 0k0: k = 2n*. As was the case for clevudine Form 1 the possible space groups matching these limiting conditions were restricted to $P2_1$ or $P2_1/m$ and due to the known chirality of the compound $P2_1$ was selected for analysis.

A notable difference between Form 1 and Form 2 is that for Form 1, Z = 4 (Z′ = 2) while for Form 2, Z = 2 (Z′ = 1).

Structure solution and refinement

Table 3.3 displays the crystallographic data and parameters of collection for a single crystal of this form. The method employed was the same as for Form 1, though in this case no disordered atoms were present.

Table 3.3 Data-collection and refinement parameters for clevudine Form 2

Molecular formula	$C_{10}\,H_{13}\,F\,N_2\,O_5$
Formula weight (g mol^{-1})	260.22
Crystal system	Monoclinic
Space group	$P2_1$
a (Å)	8.9716(9)
b (Å)	5.3099(5)
c (Å)	11.8624(11)
α (°)	90
β (°)	105.980(2)
γ (°)	90
V $(Å)^3$	543.27(9)
Z	2
D_c (g cm^{-3})	1.591
μ (Mo Kα) (mm^{-1})	0.139
F(000)	272
Data-collection temp. (K)	173(2)
Crystal size (mm^3)	0.55 x 0.51 x 0.48
Range scanned θ (°)	2.361–28.373
Index ranges ±*h*, ±*k*, ±*l*	h: -11, 11; k: -7, 7; l: -15, 15
Reflections (total)	11 600
Independent reflections	2705
Reflections with I>2σ(I)	2677
Number of parameters	166
R_{int}	0.0223
S	1.053
R_1 [I>2σ(I)]	0.0293
Reflections omitted	0
wR_2	0.0767
a, b in $w = 1/[\sigma^2(F_o^2)+(aP)^2+(bP)]$	a = 0.0542; b = 0.0843
$(\Delta/\sigma)_{mean}$	< 0.001
$\Delta\rho_{min,max}$ (e $Å^{-3}$)	-0.290, 0.295
Flack parameter	Flack x = 0.153(663) by classical fit to all intensities; 0.294(236) from 1192 selected quotients (Parsons' method)[12]

Molecular structure

The asymmetric unit of clevudine Form 2 is presented in Fig. 3.11.

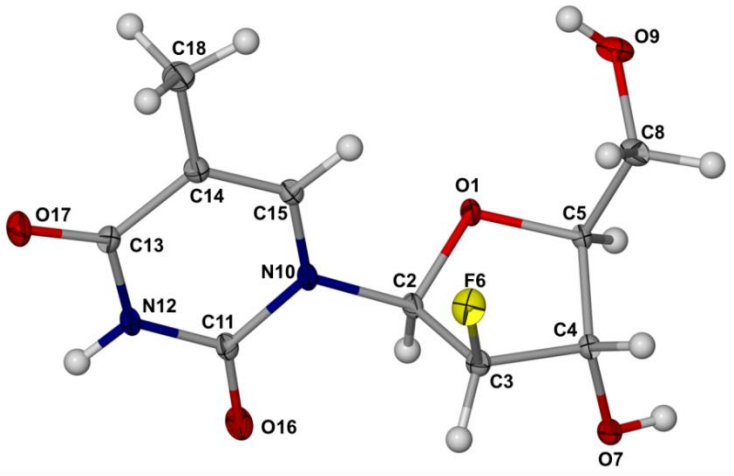

Fig. 3.11 The asymmetric unit of clevudine Form 2 comprised of a single molecule with labelling scheme shown. Displacement ellipsoids are shown at the 50% probability level and hydrogen atoms are drawn with arbitrary radii.

Crystal packing and hydrogen bonding

The relevant symmetry information for clevudine Form 2 is listed in Table 3.4.

Table 3.4 Hydrogen bonds in form 2[a]

D – H···A	*d*(D – H), Å	*d*(H ···A), Å	*d*(D ···A), Å	∠(DHA), deg.
O9 - H9···O9^{i}	0.84	2.23	3.000(2)	153
N12 - H12···O7^{ii}	0.88	2.10	2.9492(17)	162
C3 - H3···O16^{ii}	1.00	2.42	2.9824(19)	115
C5 - H5···F6^{iii}	1.00	2.34	3.0558(19)	128
C5 - H5···O17^{iv}	1.00	2.59	3.144(2)	115'
C15 - H15···O9^{v}	0.95	2.54	3.4616(19)	165

[a]Symmetry transformations used to generate equivalent atoms: *[i]: 1-x,-1/2+y,-z; [ii]: 2-x,-1/2+y,1-z; [iii]: x,1+y,z; [iv]: -1+x,1+y,z; [v]: 1-x,-1/2+y,-z.*

The H-bonding motifs present in Form 2 are different from those seen in Form 1 in that instead of being of a cyclic nature they are packed in infinite helices propagating in the y-direction, one such helical association consisting of 2_1-related clevudine molecules centred on a screw axis found at ½, y, ½. These helices are formed by N12–H12···O7′ and O7–H7···O17′ hydrogen bonds between the clevudine methylpyrimidine-dione rings and incorporated O7–H hydroxyl groups of other sets of 2_1-related clevudine molecules. These interactions make up an elongated 'ring' motif that can be seen in the

middle of the unit cell in Fig. 3.12 as viewed along [010]. Another helical arrangement, more clearly visible when the view is normal to the unique axis b, as seen in Fig. 3.13, is formed by O9–H9···O9′ and this results in an infinite chain centred on ½, y, 1. A helical arrangement centred on the 2_1-axis at 0, y, ½ formed by the hydrogen bond, C3–H3···O16′ is also present in this structure.

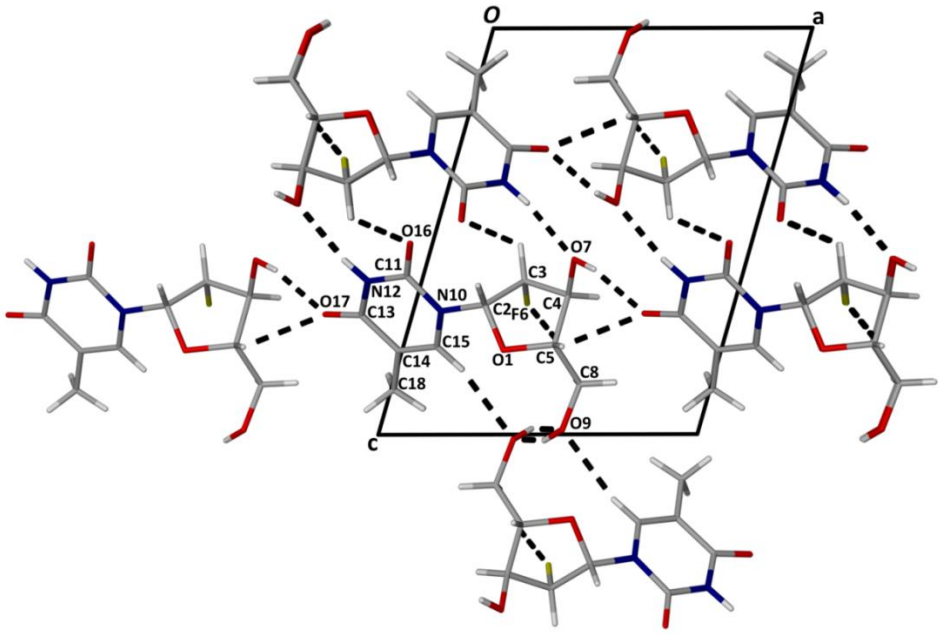

Fig. 3.12 Hydrogen bonding interactions found in the structure of clevudine Form 2 viewed along [010].

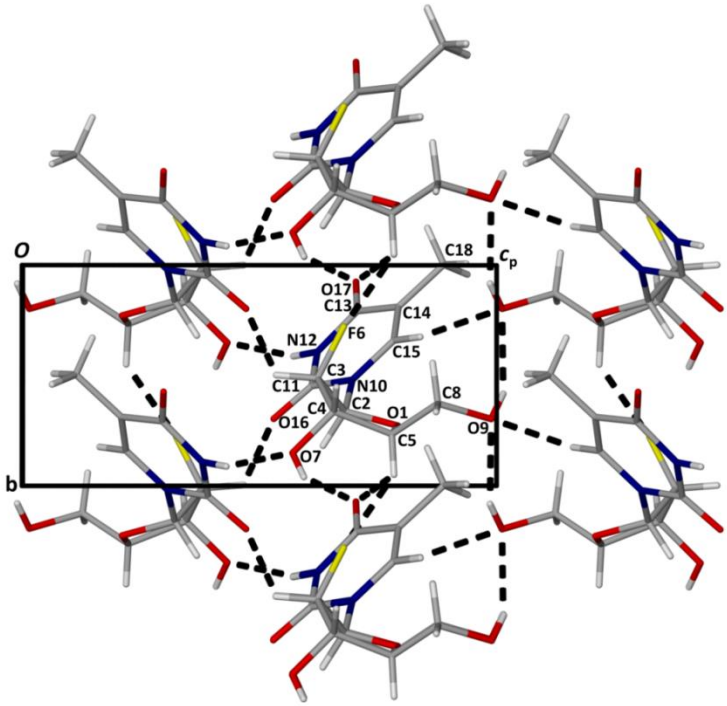

Fig. 3.13 Hydrogen bonding interactions found in the structure of clevudine Form 2 viewed along [100].

Method for scaling up phase pure clevudine Form 2

To scale up Form 2 for further experimentation, a LAG method was used. Small drops of acetonitrile were added while the clevudine raw material (Form 1) was gently ground in a mortar with a pestle. After about two hours of grinding, complete conversion from Form 1 to Form 2 had taken place. The gradual conversion can be seen in the PXRD traces recorded at 5 min of grinding intervals displayed in Fig. 3.14. The gradual disappearance of peaks and the formation of new ones that can be seen in this Fig. indicate the transition from Form 1 to Form 2. This continues until complete conversion to Form 2 has taken place.

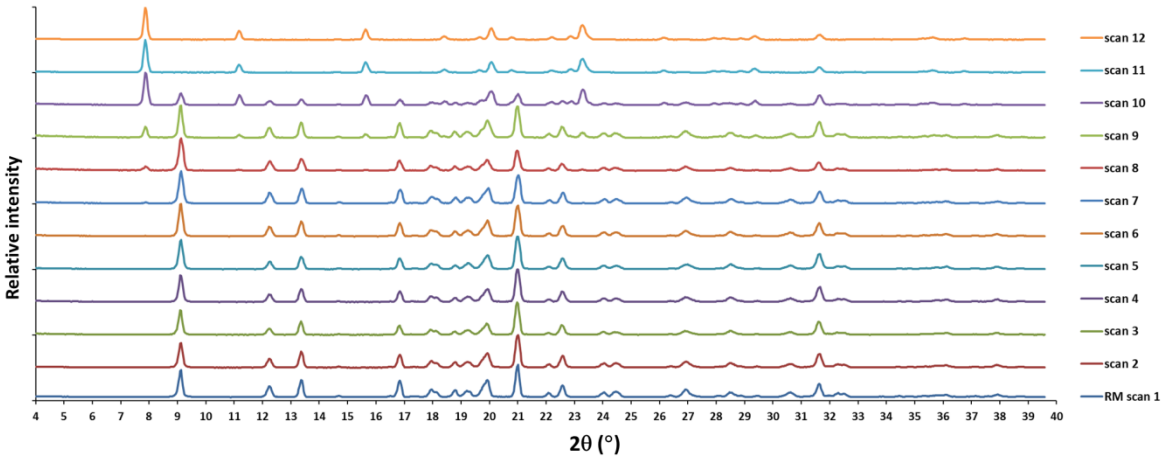

Fig. 3.14 PXRD traces recorded after intervals of LAG showing gradual transition from Form 1 to Form 2.

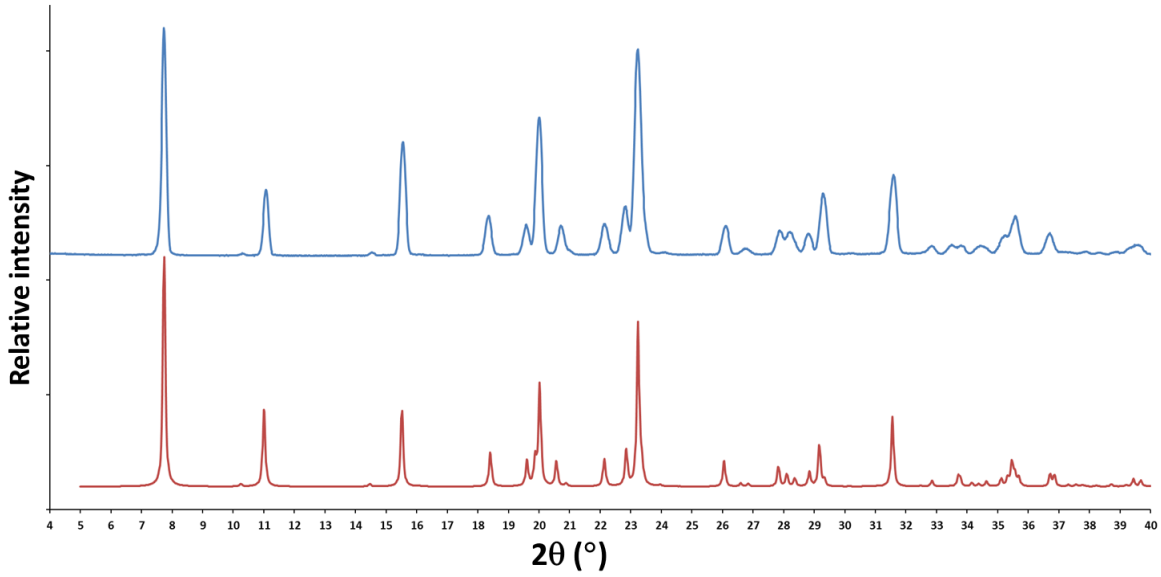

Fig. 3.15 Calculated (bottom) and experimental (top) PXRD traces of clevudine Form 2.

Thermal analysis

The HSM result visible in Fig. 3.16, like the DSC result for clevudine Form 2 at 10 °C min^{-1} (Fig. 3.17), shows three separate events in the temperature range 160 – 205 °C. The event labelled A in Fig. 3.17 has an onset temperature of 175.3 ± 0.6 °C (n = 2) and corresponds to the HSM result visible in Fig. 3.16 at the same temperature. The crystal goes from being clear to opaque as heating continues. The result shows that a phase transition is taking place and was confirmed by variable-temperature powder X-ray diffraction (VTPXRD) at a later stage that the transition is from Form 2 to Form 1 (Fig. 3.18). The endothermic nature of the transition would suggest that the two forms are enantiotropically related according to the heat-of-transition rule.[13] Due to the incongruent nature of this transition, its enthalpy was not reproducibly measurable. The next event visible in the DSC trace, labelled B, has an onset of 188.1 ± 0.5 °C (n = 2). This event also appears to overlap with another. This causes the peak temperatures and enthalpy values to differ from run to run and for this reason the values will be of limited use. The onset is comparable to the value seen for pure Form 1, substantiating the hypothesis that a transition to Form 1 has taken place. It is believed that incomplete conversion from Form 2 to Form 1 takes place at this heating rate and that recrystallization from the melt of Form 1 to another form takes place. This was later proven true by VTPXRD and can be seen in Fig. 3.18 and 3.20. A likely explanation for this is that Form 2 partially transitions to Form 3 and the trace amounts of Form 3 present serve as seeds from which the recrystallization after the onset of the melt of Form 1 originates. The third event seen in the DSC trace, labelled C, was unexpected. This event has an onset at 195.5 ± 0.5 °C (n = 2) and a peak at 196.4 ± 0.5 °C (n = 2). The possibility of the formation of another phase was realised and further investigation was considered warranted. Upon re-examination of the pure Form 1 it was noticed that by lowering the heating rate, it was possible to separate out two distinct events, as can be seen in Fig. 3.19.

A variable temperature PXRD experiment was carried out starting with clevudine Form 2. The results are displayed in Fig. 3.18. When comparing the traces at 30 °C with that at 170 °C one can see the peaks slightly shift to lower angles due to thermal expansion of the unit cells. The changes visible from 170 to 175 °C are more drastic with new peaks visible around 20, 22, and 24 °2θ and the disappearance of peaks near 15 and 23 °2θ. Another clear change is observable from 180 to 190 °C. A new large peak is visible at 21 °2θ and peaks have vanished at 19 and 22 °2θ. It is important to note that the scans are carried out over periods exceeding 10 minutes at each temperature and more time is allowed for transitions to occur than in the case of a DSC experiment carried out at 10 K min^{-1}. A VTPXRD experiment

was also carried out starting with clevudine Form 1 (Fig. 3.20). In this case, the transition to a new phase (Form 3) was also observed. The notable difference being that the peak intensities were much lower in this case than when starting with Form 2. This result fits the explanation that apart from the time required for a complete transition to occur (due to kinetic hindrance at higher heating rates) the possible presence of 'seeds' of Form 3 present in the case of Form 2 will speed up the transition to Form 3 by nucleation.

The TGA result (Fig. 3.21) showed no significant weight loss until the onset of decomposition at 315.1 ± 0.1 °C (n=2).

Hot stage microscopy

Fig. 3.16 Representative HSM photographs of clevudine Form 2.

Differential scanning calorimetry

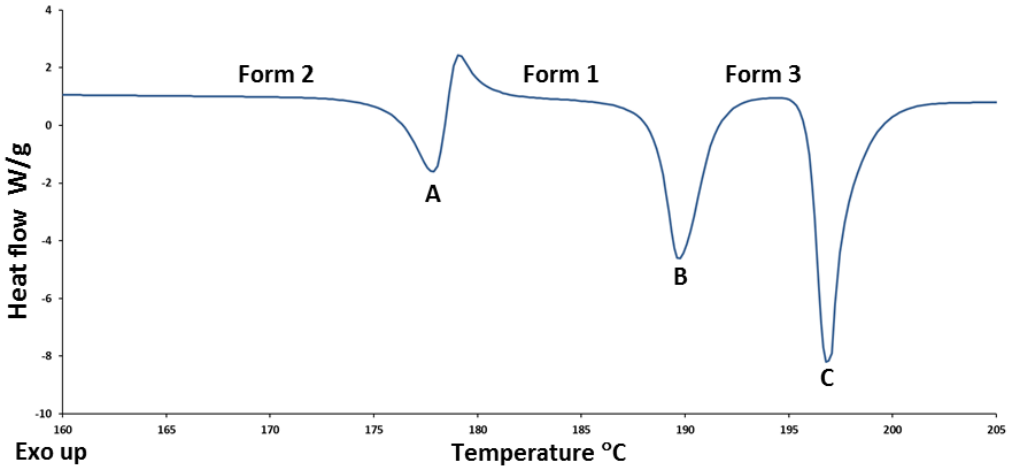

Fig. 3.17 Representative DSC trace of clevudine Form 2.

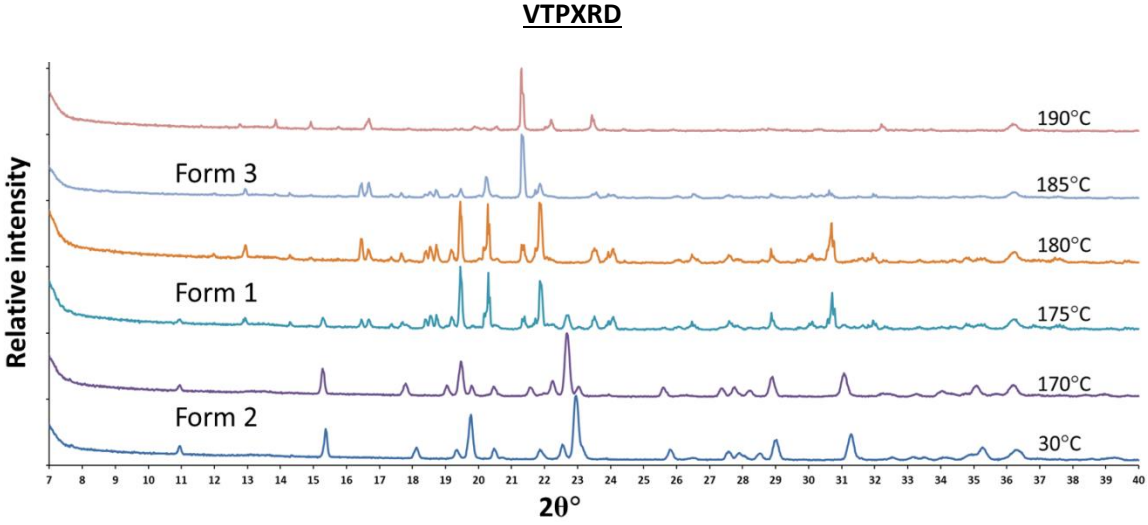

Fig. 3.18 Variable-temperature PXRD showing the sequence of events starting with clevudine Form 2.

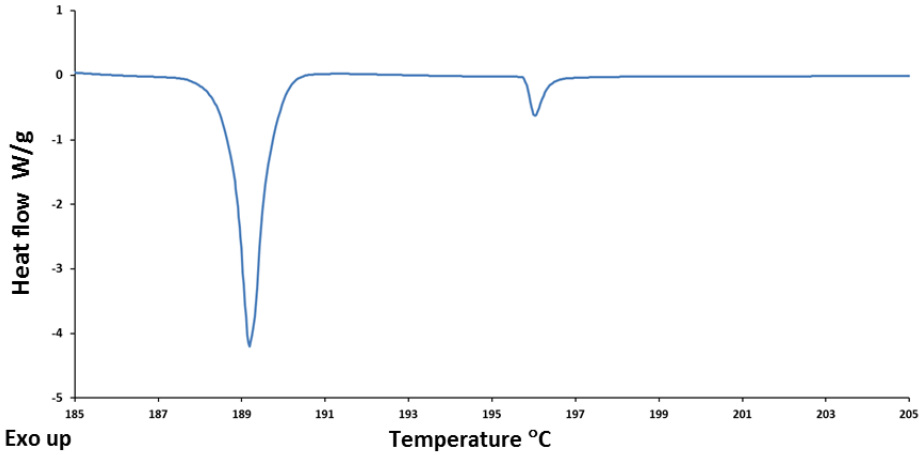

Fig. 3.19 DSC trace of clevudine Form 1 at 2 °C min^{-1}.

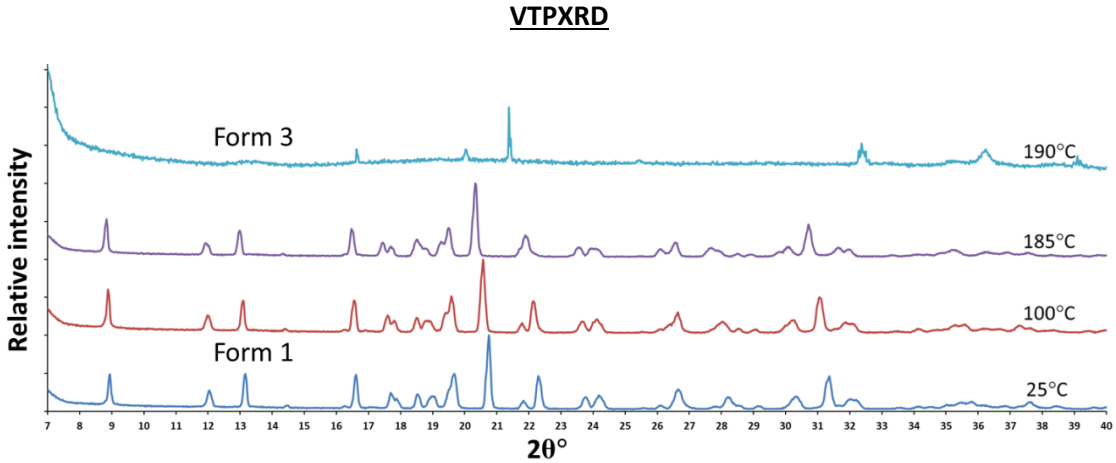

Fig. 3.20 Variable-temperature PXRD showing the sequence of events starting with clevudine Form 1.

Thermogravimetric analysis

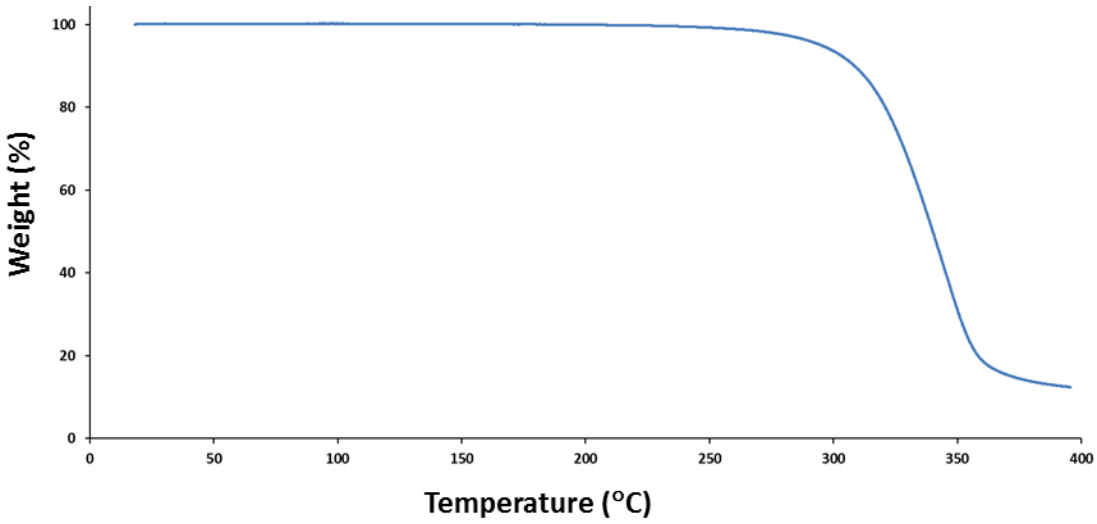

Fig. 3.21 Representative TGA trace of clevudine Form 2.

Clevudine Form 3

Preparation of clevudine Form 3 single crystals

After noticing a phase transition occurring during the heating of Form 1 at lower heating rates, an attempt was made to produce crystals of a new form of this compound by heating single crystals of Form 1. At first it was thought that a single crystal to single crystal transition might be possible. A large single crystal of clevudine Form 1 was maintained at 190 °C for 30 minutes and observed under a microscope (Fig. 3.22). This result shows that the crystal becomes opaque with time, indicating a possible transition, though the transformed crystals would not be useful as single crystals for data-collection on a diffractometer. In Fig. 3.23 the result is shown where a single crystal of Form 1 was melted and left to cool after melting. In this case there are smaller clear crystals visible that exist as a conglomerate mass. A large single crystal of Form 1 was placed in an open DSC pan, rapidly heated to 183 °C and then heated to 192 °C at a rate of 1 K min^{-1}. The product was not a single crystal, but many smaller crystals. These turned out to be of the polymorphic form referred to as Form 3.

Fig. 3.22 HSM photographs of Form 1 held at 190 °C for 30 min.

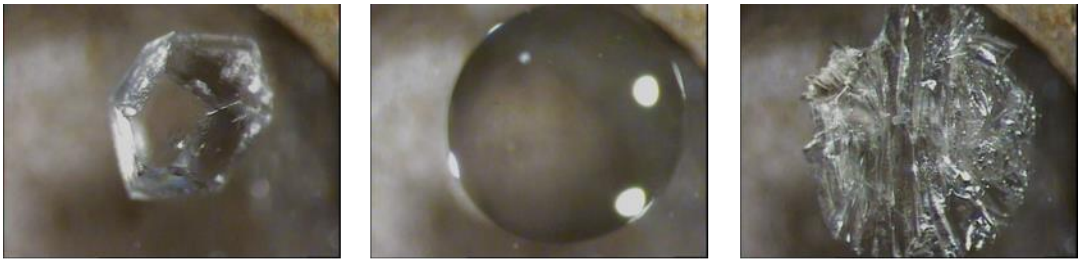

Fig. 3.23 HSM result to illustrate the formation of Form 3 crystals from the melt of Form 1.

Crystal structure analysis

Data-collection and space group determination

The single-crystal X-ray intensity data-collection was performed at 173(2) K on a Bruker Kappa Apex II Duo diffractometer with graphite-monochromated MoKα radiation (λ = 0.71073 Å). Data reduction was performed with the program SAINT[5] and multi-scan absorption corrections were applied with SADABS.[6] The X-ray diffraction pattern, as in the cases of clevudine Forms 1 and 2, showed 2/*m* Laue symmetry. This is characteristic of the monoclinic crystal system. The space group and the $|E^2-1|$value of 0.813 were determined by making use of XPREP.[7] The available options posed by the program XPREP were $P2_1$ and $P2_1/m$ and these were shown to be correct from the systematic absences *hkl: none, h0l: none, 0k0: k = 2n*. Due to the known chirality of the compound the space group was determined to be $P2_1$. This polymorph has Z′ = 4 molecules per asymmetric unit and Z = 8 molecules per unit cell.

Structure solution and refinement

Table 3.5 displays the crystallographic data and parameters of collection for a single crystal of this form. The method employed was the same as that described for Form 1 with the exception that there were no disordered atoms in this instance.

Table 3.5 Data-collection and refinement parameters for clevudine Form 3.

Molecular formula	$C_{10}\ H_{13}\ F\ N_2\ O_5$
Formula weight (g mol^{-1})	260.22
Crystal system	Monoclinic
Space group	$P2_1$
a (Å)	10.4391(13)
b (Å)	16.017(2)
c (Å)	13.8687(18)
α (°)	90
β (°)	101.604(2)
γ (°)	90
V $(Å)^3$	2271.4(5)
Z	8
D_c (g cm^{-3})	1.522
μ (Mo Kα) (mm^{-1})	0.133
F(000)	1088
Data collection temp. (K)	173(2)
Crystal size (mm^3)	0.38 x 0.35 x 0.29
Range scanned θ (°)	1.499–28.447
Index ranges ±*h*, ±*k*, ±*l*	h: -13, 13; k: -21, 21; l: -18, 18
Reflections (total)	42 390
Independent reflections	11 355
Reflections with I>2σ(I)	10 137
Number of parameters	661
R_{int}	0.0259
S	1.031
R_1 [*I*>2σ(*I*)]	0.0355
Reflections omitted	1
wR_2	0.0831
a, b in $w = 1/[\sigma^2(F_o^2)+(aP)^2+(bP)]$	a = 0.0484; b = 0.1585
$(\Delta/\sigma)_{mean}$	< 0.001
$\Delta\rho_{min,max}$ (e $Å^{-3}$)	-0.216, 0.283
Flack parameter	Flack x = 0.180(490) by classical fit to all intensities; 0.172(217) from 4224 selected quotients (Parsons' method)[12]

Molecular structure

The asymmetric unit of clevudine Form 3 is presented in Fig. 3.24.

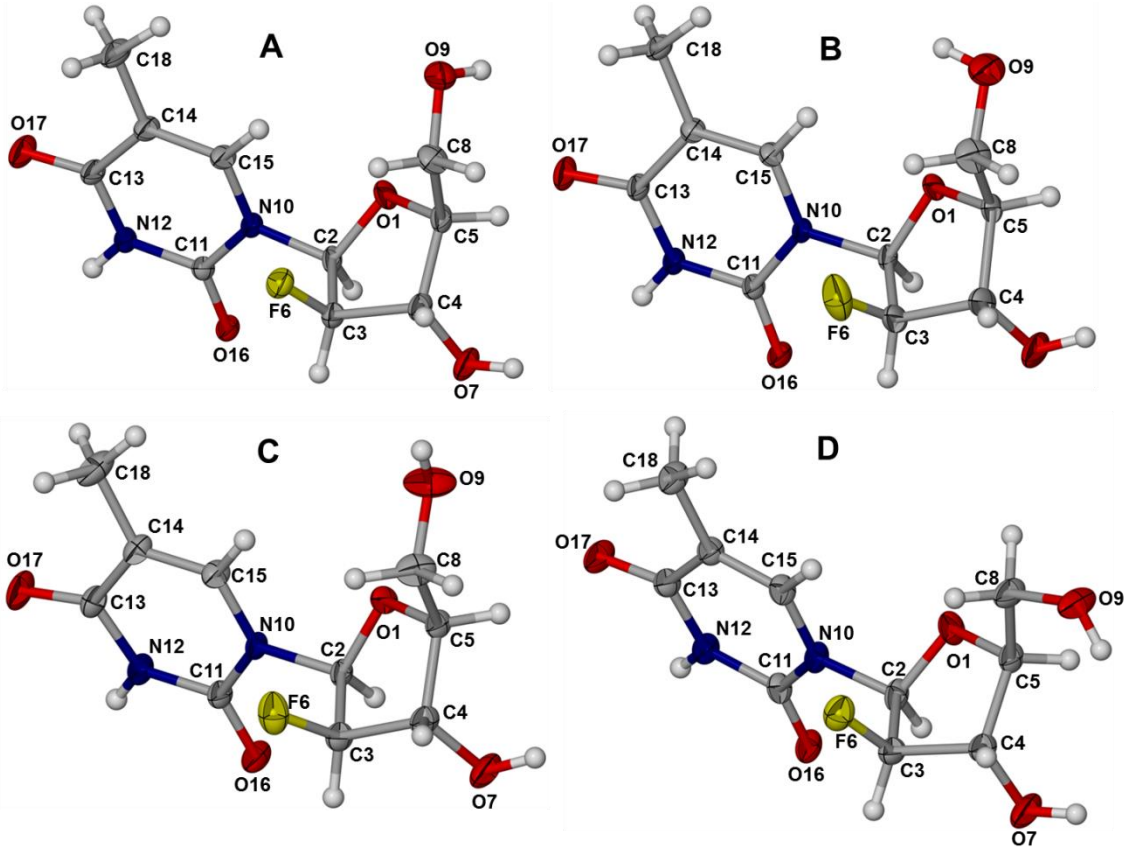

Fig. 3.24 The molecules that comprise the asymmetric unit of clevudine Form 3. The four unique molecules have been orientated in a similar way to enable ease of comparison while avoiding overlap. The numbering scheme is shown. Thermal ellipsoids are shown at the 50% probability level.

Crystal packing and hydrogen bonding

The relevant hydrogen bonds and their symmetry information for clevudine Form 3 are listed in Table 3.6.

Table 3.6 Hydrogen bonds in clevudine Form 3[a].

D – H···A	*d*(D – H), Å	*d*(H ···A), Å	*d*(D ···A), Å	∠(DHA), deg.
O7B - H7B···O17B[i]	0.84	1.96	2.758(3)	158
O7C - H7C···O17C[i]	0.84	2.33	3.073(3)	147
O7D - H7D···O16C[ii]	0.84	2.31	2.873(2)	125
O7D - H7D···O17D[iii]	0.84	2.33	2.998(3)	137
O9A - H9A···O9C[i]	0.84	1.95	2.782(3)	171
O9B - H9B···O9A[iv]	0.84	1.97	2.784(3)	162
O9C - H9C···O9D	0.84	1.84	2.675(3)	172
O9D - H9D···O17D[iii]	0.84	1.86	2.700(2)	178
N12A - H12A···O16B[v]	0.88	1.92	2.796(2)	175
N12B - H12B···O16A[vi]	0.88	1.91	2.776(2)	167
N12C - H12C···O16D[vii]	0.88	1.91	2.776(3)	167
N12D - H12D···O16C[viii]	0.88	1.91	2.757(2)	162
C2C - H2C···O1B[ix]	1.00	2.53	3.020(3)	110
C18D - H4···F6A[iv]	0.98	2.45	3.228(3)	137
C5B - H5B···O17B[i]	1.00	2.56	3.240(3)	125
C5C - H5C···O17C[i]	1.00	2.45	3.105(3)	123
C18A - H18A···O9B[x]	0.98	2.45	3.402(4)	163

[a]Symmetry transformations used to generate equivalent atoms: *[i]: 1+x,y,z; [ii]: x,y,-1+z; [iii]: -1+x,y,z; [iv]: 2-x,1/2+y,1-z; [v]: 1-x,-1/2+y,-z; [vi]: 1-x,1/2+y,-z; [vii]: -1+x,y,1+z; [viii]: 1+x,y,-1+z; [ix]: 1-x,-1/2+y,1-z; [x]: 2-x,-1/2+y,1-z.*

The third polymorphic form of clevudine packs in stacked layers, resembling those seen in Form 1. The asymmetric unit in this instance consists of 4 unique molecules (labelled A-D in Fig. 3.24). Alternating distinct layers are formed by hydrogen-bonds connecting molecules A with B (Fig. 3.25) and C with D (Fig. 3.26) respectively. These layers have a spacing between them of ~b/4 and are stacked in the sequence (AB)(CD)(AB)(CD)…, as is visible in Fig. 3.27 and the unique confomers are colour-coded to show how they are packed in Fig. 3.28.

Another similarity between the packing of this form and that of Form 1 is in the nearly symmetrical $R_2^2(8)$ rings between the methylpyrimidine-dione rings present in the layers of (AB) as well as (CD), as was the case for Form 1. The difference lies in that the ring in Form 1 was formed by H-bonds N12–H12···O17′ but in the case of Form 3 for (AB) and (CD) it is formed by the complementary H-bonds N12–H12···O16′.

A bifurcated H-bonded ring described by $R_2^1(6)$ is formed by the H-bonds C5B–H5B···O17B′ and O7B–H7B···O17B′ with an analogous synthon present in the layer (CD) formed by C5C–H5C···O17C′ and O7C–H7C···O17C′ H-bonds. Another ring connecting molecules in the layer (AB) with descriptor $R_2^2(12)$ is

formed by O9B–H9B···O9A′ and C18A–H18A···O9B′ H-bonds. A ring in layer (CD) with the descriptor $R_2^1(8)$ is formed by the H-bonds O9D–H9D···O17D′ and O7D–H7D···O17D′ (Fig.3.25 and 3.26).

The interactions connecting the alternating layers are O9A–H9A···O9C′, C2C–H2C···O1B′, and C18D–H4···F6A′ (Fig. 3.27).

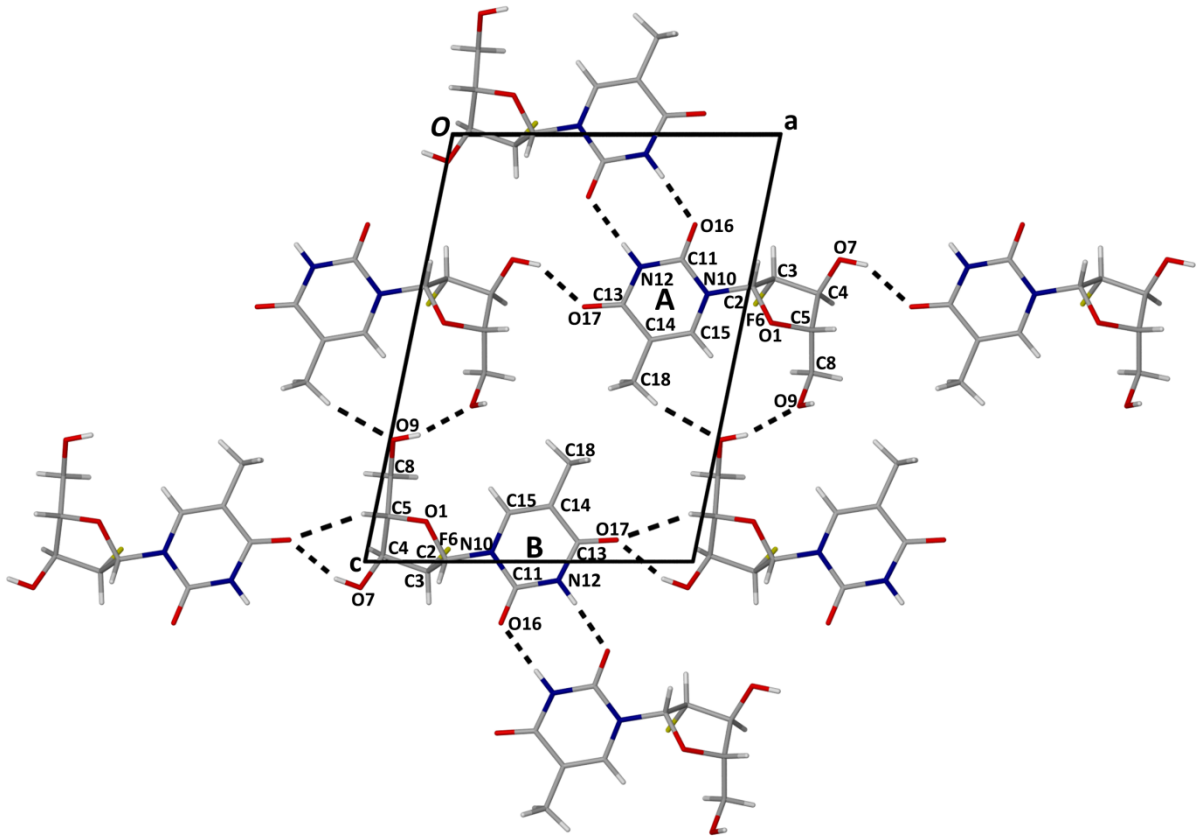

Fig. 3.25 Topology of the layer containing A and B molecules showing hydrogen bonding in clevudine Form 3.

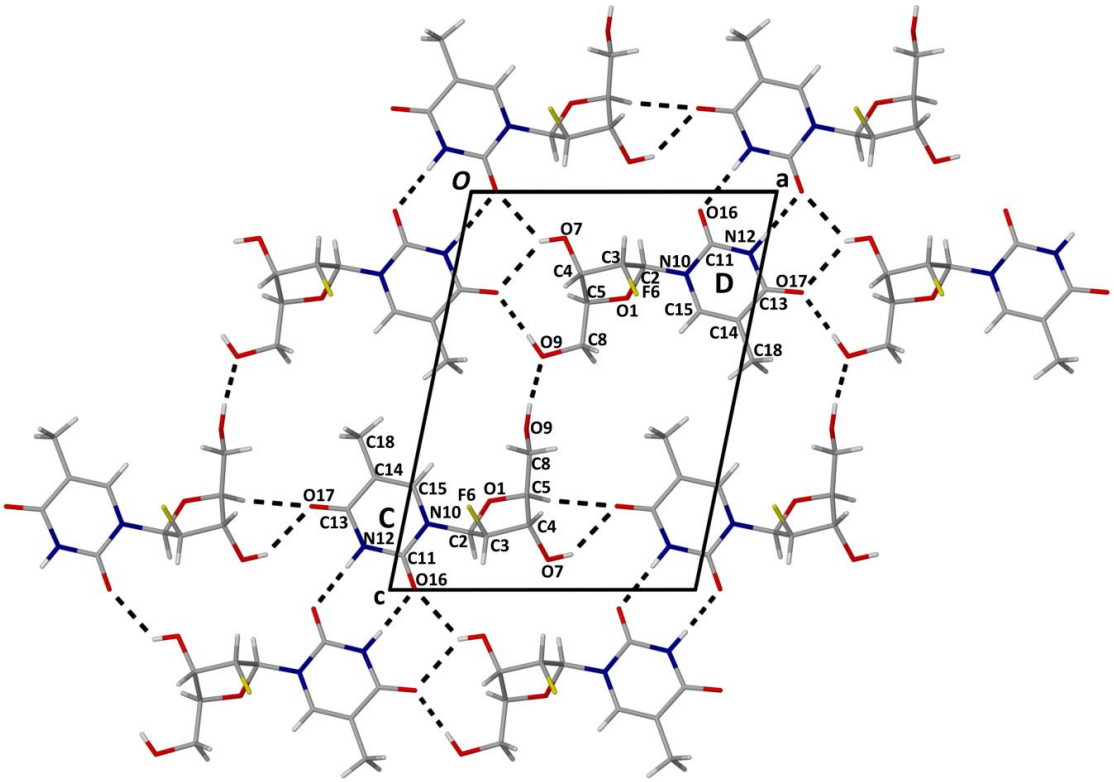

Fig. 3.26 Topology of the layer containing C and D molecules showing hydrogen bonding in clevudine Form 3.

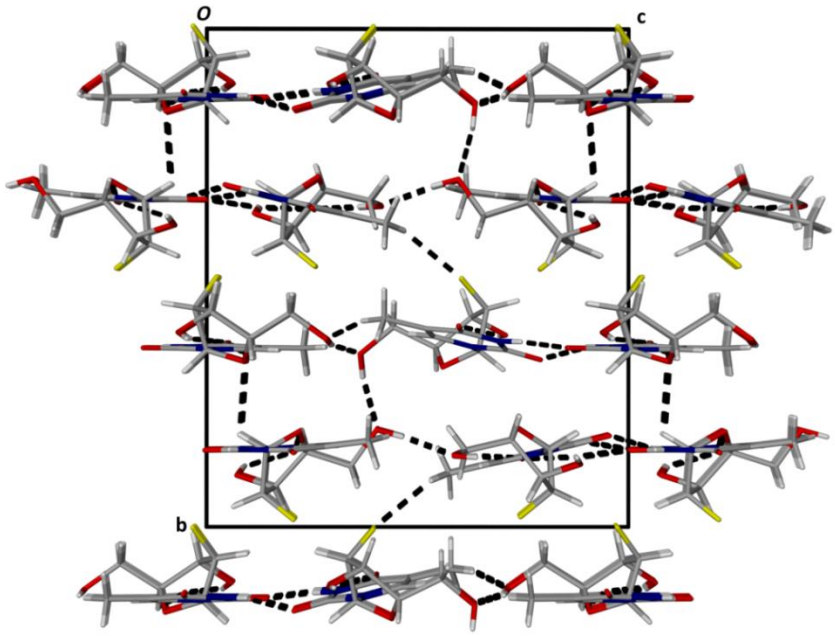

Fig. 3.27 Packing diagram showing the layers in clevudine Form 3 as well as the interactions connecting them viewed along [100].

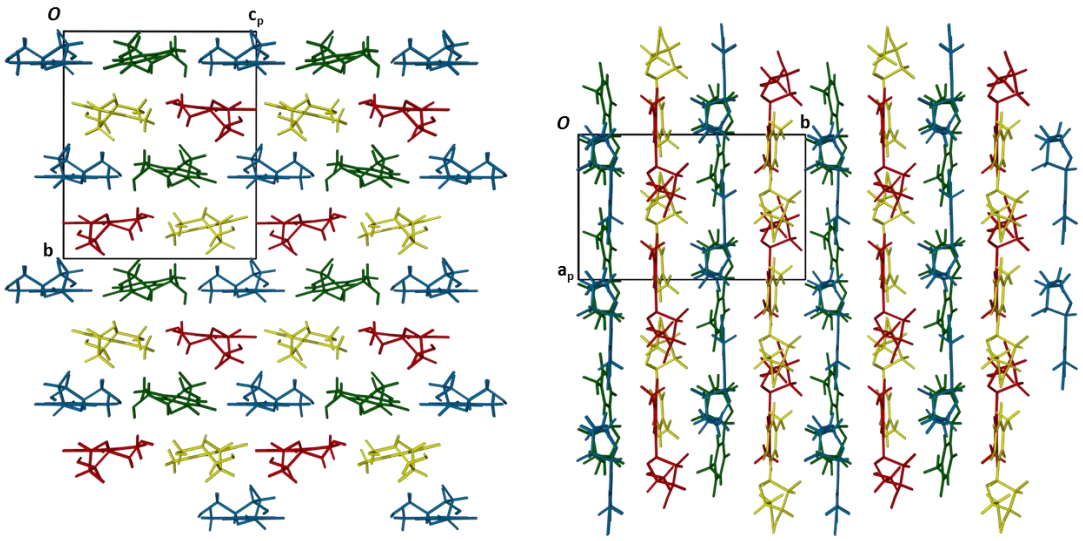

Fig. 3.28 Packing of clevudine Form 3 viewed along [100] (left) and [001] (right) illustrating the arrangement of unique molecules (A-green, B-blue, C-red, D-yellow)

The experimental PXRD trace is compared to that of the trace generated from the solved crystal structure of clevudine Form 3 in Fig. 3.29. The highest intensity peak at 22.2 °2θ corresponds to reflection from the (0 4 0) planes with d-spacing 4.004 Å and is a result of the layered packing described in the previous section and displayed in Figs. 3.27 and 3.28. The good match between the calculated and experimental PXRD patterns shows that the method employed to produce this polymorph was successful and hence it was used for scaling up this form for further experimentation and characterisation.

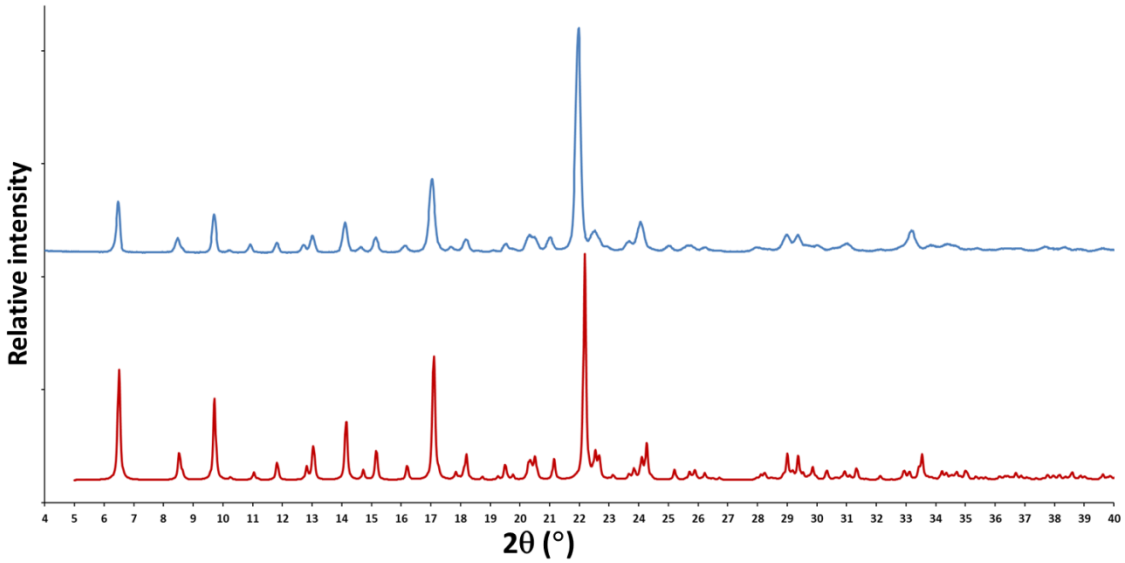

Fig. 3.29 Calculated (bottom) and experimental (top) PXRD traces of clevudine Form 3.

Thermal analysis

The HSM results are presented in Fig. 3.30. The sample visibly starts to melt at 200 °C. The portion of the sample situated on the glass slide above the window melts later than the sample directly above the heating block due to its being at a slightly lower temperature. The sample has completely melted by 210 °C.

The DSC result for clevudine Form 3 is shown in Fig. 3.31. There is a single sharp endotherm visible with an onset at 195.7 ± 0.1 °C (n = 3), a peak at 197.0 ± 0.2 °C (n = 3) and an enthalpy related to this event of 102.1 ± 1.3 J g^{-1} or 26.6 ± 0.3 kJ mol^{-1} (n = 3). This event correlates with the HSM result and would indicate that this is the melting endotherm of Form 3.

A DSC result going from a high to a lower temperature is presented in Fig. 3.32. The sample was taken to a temperature above its melting point and cooled at a controlled rate. The experiment presented in the Fig. was carried out with a cooling rate of 10 K min^{-1}. A single exothermic event is visible in this trace, the onset of which is dependent on the rate of cooling due to a hysteresis effect. The onset temperature was 177.8 ± 0.6 °C (n = 3), with a peak at 175.1 ± 0.9 °C (n = 3), and an enthalpy related to this event of -101.0 ± 8.6 J g^{-1} or -26.3 ± 2.2 kJ mol^{-1} (n = 3). The previous thermal results have shown that Form 3 crystallises from the melt and this result shows that the magnitudes of the enthalpies of recrystallization and melting of Form 3 are practically the same, as expected.

The TGA result is presented in Fig. 3.33. Similar to the results of Forms 1 and 2, there is no significant mass loss before the onset of decomposition above 300 °C.

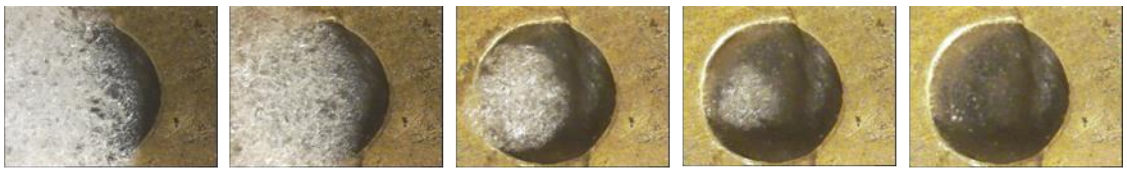

Fig. 3.30 Representative HSM photographs of clevudine Form 3.

Differential scanning calorimetry

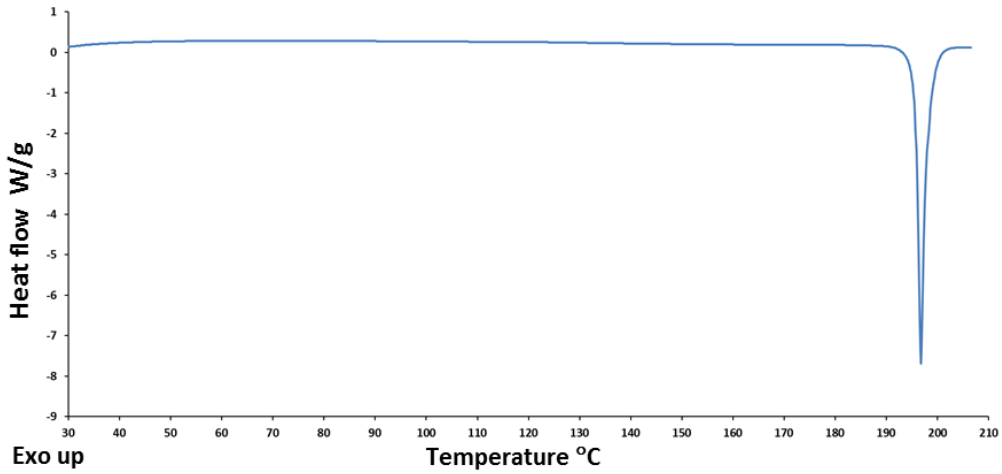

Fig. 3.31 Representative DSC trace of clevudine Form 3.

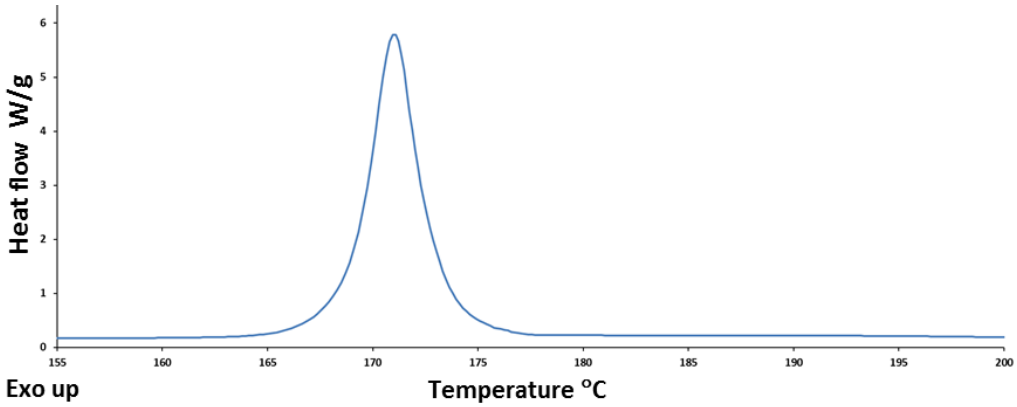

Fig. 3.32 A representative DSC trace for the cooling of clevudine after melting at 10 °C min^{-1}.

Thermogravimetric analysis

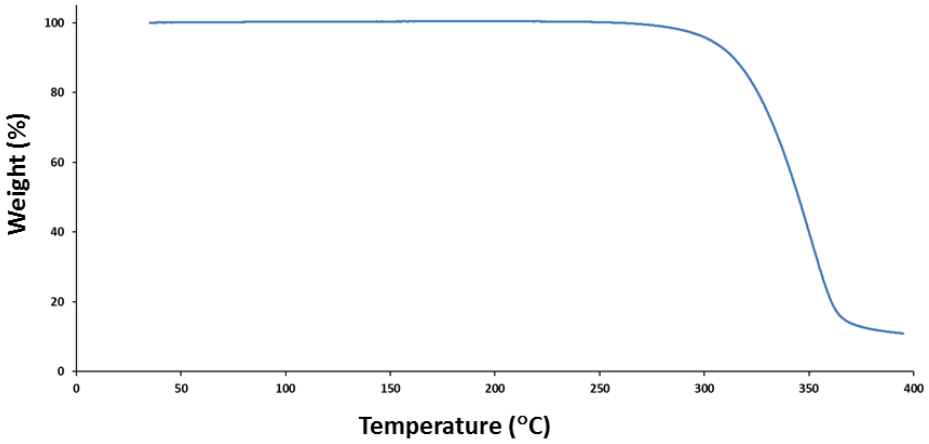

Fig 3.33 Representative TGA of clevudine Form 3.

Comparison of the various polymorphs of clevudine

Infrared spectroscopy

The FTIR spectra for the different polymorphs of clevudine are presented in Fig. 3.34. The spectra show numerous dissimilarities in the fingerprint regions as well as the C–H, O–H, and N–H stretching regions concerning wavenumbers and multiplicity of peaks. A distinctive feature of the spectrum of clevudine Form 2 is that there are two separate peaks in the carbonyl stretching region (1600–1800 cm^{-1}). An explanation for this feature is that in the case of Form 2 there are two chemically distinct carbonyl groups in the crystal due to its having a Z′ = 1. The considerably different lengths of 1.214(2) and 1.233(2) Å, result in a clear separation of wavenumbers for these peaks. The other forms, having higher Z′ values (Z′ = 2 and 4 for Forms 1 and 3 respectively), have more different symmetry-independent C=O bonds. One might expect to see a wider spread of bond lengths in these cases, but interestingly in both instances the ranges are narrower, resulting in smaller differences with narrower and less conspicuous splitting of peaks. These unique aspects make it possible to distinguish between and identify the respective forms from the appearance of the spectra.

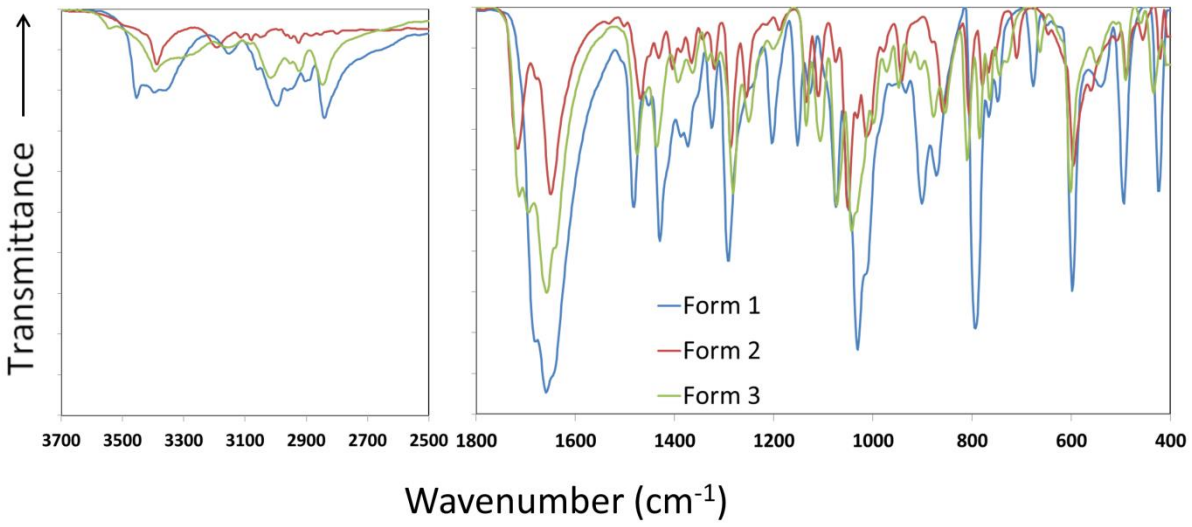

Fig. 3.34 FTIR spectra of the various forms of clevudine.

Comparison of thermal results

The stacked DSC results for the various forms are presented in Fig. 3.35 and the related data are summarised in table 3.7.

As was discussed in the thermal results section for clevudine Form 2, there is a transition from Form 2 to Form 1 at a temperature just above 170 °C. The transition is endothermic and when considering the heat-of-transition rule,[13] this indicates that Forms 1 and 2 are enantiotropically related. Due to this form undergoing a transition before the onset of melting, no melting temperature was recorded and the incongruent nature of the transition from Form 2 to Form 1 made the reproducibility of measurements of enthalpy of transition problematic.

Forms 1 and 3 had distinct melting onsets when heated at 10 K min^{-1}. Form 1 displayed the lower melting onset and the higher enthalpy of fusion of the two forms. According to the heat-of-fusion rule,[13] this indicates that Forms 1 and 3 are also enantiotropically related. As mentioned in the thermal results section of Form 3, it was possible to effect a transition from Form 1 to Form 3 at lower heating rates due to the transition being kinetically delayed. The measured enthalpies are not however comparable to that of the measurements taken at higher heating rates and even at the lower rates of 2 K min^{-1} the transition was incomplete. The enthalpy of transition from Form 1 to Form 3 was measured during the DSC experiments with Form 2. Though these values showed good reproducibility the actual enthalpies recorded do not give a clear portrayal of the events. The total heat flow measured is caused by the overlapping melting and recrystallizing events. The theoretical enthalpy of transition calculated from $\Delta H_{t,3} = \Delta H_{f,1} - \Delta H_{f,3}$ will thus differ from the measured value.

None of the transitions observed in the DSC results proved to be reversible when the samples were cooled at the standard rates used for cooling. This does not necessarily mean that the transitions are irreversible, but simply that the transitions are kinetically hindered and may take more time to occur.

The occurrence of multiple thermal events in a narrow range (~25 °C) and the fact that some of these events overlap at the typically used heating rates make the DSC results inadequate for complete quantitative characterisation. Further experimentation involving different methods were thus considered necessary to determine the thermodynamic relationships of the various forms.

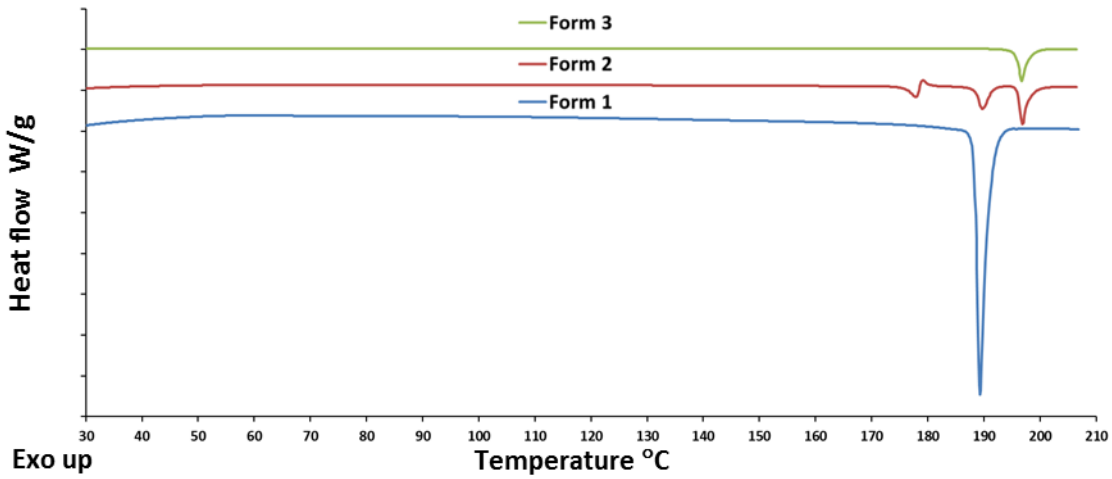

Fig. 3.35 Stacked DSC results for the various forms of clevudine at 10 K min^{-1}.

Table 3.7 Thermal data for different forms of clevudine obtained by DSC.

Datum	Form 1	Form 2	Form 3
Melting point onset [°C]	188.5 ± 0.1	*b*	195.7 ± 0.1
Enthalpy of fusion [kJ mol^{-1}]	212.6 ± 4.7	*b*	26.6 ± 0.3
Entropy of fusion[a] [J K^{-1} mol^{-1}]	461	*b*	57
Transition temperature onset [°C]	188.8 ± 0.1	175.3 ± 0.6	-

[a] Calculated from $\Delta S_f = \Delta H_f/T_m$. [b] Unobservable.

Solubility results

Kinetic solubility experiments were carried out to determine if the novel polymorphic forms showed improvements in the rates of dissolution while simultaneously aiding in determination of the thermodynamic stability ranking. The experiments were carried out in pure water at a temperature of 25 ± 0.5 °C and the duration of stirring before determination of the concentrations was 72 h.

The result at 72 h is presented in Fig. 3.36. At 72 h the measured concentrations for the various forms were comparable, namely 124.5 ± 2.6 mg ml^{-1}, 129.4 ± 4.6 mg ml^{-1}, and 146.8 ± 3.4 mg ml^{-1} for Form 1, Form 2, and Form 3 respectively. The difference between Forms 1 and 2 was inconsequential, with a slight improvement for Form 3. The relatively high solubility of the unaltered starting material (matching Form 1) made the differences in solubility between the forms less significant.

In order to determine which form was most abundant in each vial after 72 h of stirring, PXRD experiments were carried out on each sample (each was done in triplicate). The samples tested from the

Form 1 vials had undergone complete conversion to Form 2 in all three vials. The samples from the Form 2 vials remained unchanged. The samples from the Form 3 vials had all incompletely converted to the more stable Forms 1 and 2, with various ratios of all three forms present in each of the vials. This indicates that at 25 °C Form 2 is the most stable form.

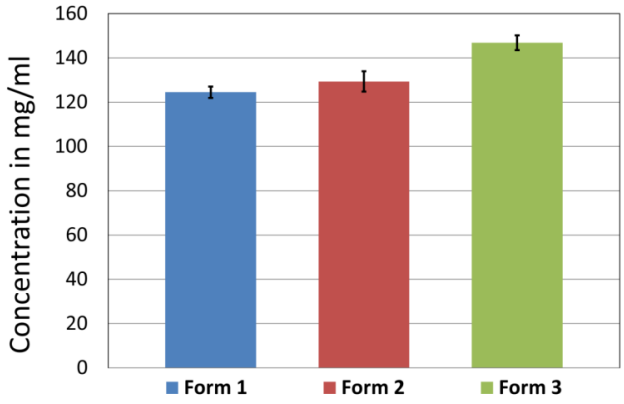

Fig. 3.36 Chart displaying clevudine concentrations in water at 25 ± 0.5 °C after 72 h of stirring.

Isothermal solvent-mediated transformation

As a means of confirmation of the stability ranking at 25 °C, an isothermal solvent-mediated transformation experiment was carried out. The method involved placing crystals of each form of clevudine in a solution that is close to saturation with the starting material at a set temperature of 25 °C. The crystals were observed under the microscope and micrographs were recorded at several intervals. The results are presented in Fig. 3.37. The micrographs show a clear change in sizes of the crystals over the first 6 h. The Form 3 crystals had undergone near complete dissolution, the Form 1 and Form 2 crystals also having shrunk, but the Form 1 crystals shrank to a noticeably greater degree than the Form 2 crystals. In the interval from 6 h to 24 h all the crystals had experienced growth. The products were all characterised by either checking the unit cells of the crystals or in the case where this was not possible the sample was analysed by PXRD. All the samples matched Form 2. This result serves as corroboration of the stability ranking that was found in the experiment where the final products of the solubility experiments were identified. This result confirms that Form 2 is the most stable form at 25 °C and would imply that this will be the case up to the temperature at which the enantiotropic transition was observed (175 °C).

Fig. 3.37 Micrographs showing the results of an isothermal solvent-mediated transformation experiment carried out with the various forms of clevudine at 25 °C over a period of 24 h.

Energy-temperature diagram

The results of the experiments mentioned prior to this section were used to construct an energy-temperature diagram (Fig. 3.38). It was observed that during heating, Form 2 undergoes an endothermic transition to Form 1 and that Form 3 has the higher melting point with a lower enthalpy of fusion. These results show that these forms are enantiotropically related and that the free energy (G) isobars will inevitably cross during heating before melting commences. The stability ranking of the various forms at room temperature was determined to be Form 2 > 1 > 3. These results were shown in the solubility and isothermal solvent-mediated transformation experiments and also match the ranking of highest calculated crystal densities (Form 2 > 1 > 3). According to the density rule the polymorph with the highest density should have the highest thermal stability at absolute zero.[13] It is assumed that these G isobars will only cross once and it is expected that the stability ranking will remain the same from absolute zero up to the respective transition temperatures as is visualised in the energy-temperature diagram. Form 2 will thus be the most stable form from absolute zero to its transition temperature ($T_{t,2\rightarrow1}$) of 175 °C or 448 K. Form 1 will be the most stable form from this temperature up to the temperature where, depending on the heating rate, it will either melt or undergo transition to Form 3. At a heating rate of 10 K min^{-1} Form 1 will melt before this transition will have enough time to occur and the onset of fusion ($T_{f,1}$) is at 188.5 °C or 461 K, represented as the crossing of the G-T isobar of Form 1 and that of the liquid. The observed transition temperature from Form 1 to Form 3 ($T_{t,1\rightarrow3}$) when heating the sample at lower heating rates is essentially at the same temperature, with a measured value of 188.8 °C. This is represented in the energy-temperature diagram as the G isobars of the two forms crossing. Form 3 will thus be the most stable form above 461 K up to its melting point ($T_{f,3}$) at 195.7 °C or 468 K.

By inspecting the energy-temperature diagram one can infer some other values that were not experimentally obtained. For instance the enthalpy of fusion and the melting point of Form 2 ($T_{f,2}$) were not experimentally observed, but the diagram will give a temperature range and an idea of the magnitude of the enthalpy involved for these events.

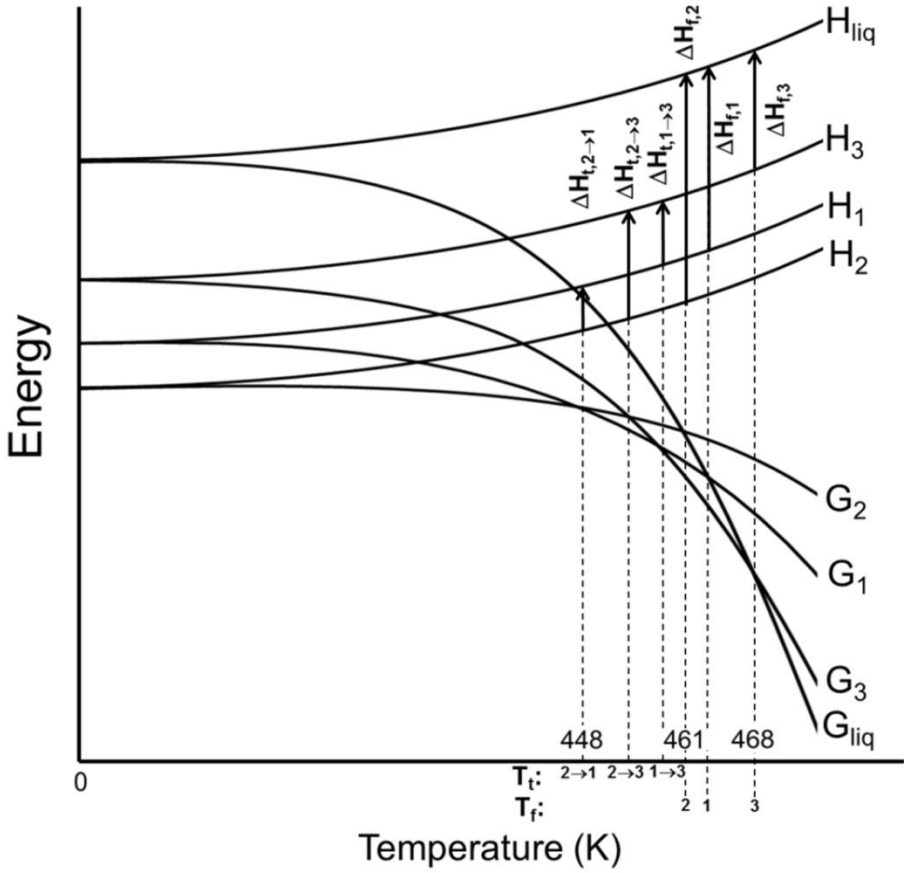

Fig. 3.38 A schematic energy-temperature diagram for the various polymorphs of clevudine.

Hirshfeld plots

The program CrystalExplorer[14] was used to generate 2D fingerprint plots from Hirshfeld surfaces of the variety of molecules making up the packing arrangements of the different polymorphic forms of clevudine (Fig. 3.39). At a glance these plots show a striking resemblance. This should not be surprising as the strongest intermolecular interactions are common to all three forms, one example of which is the O···H interactions, being the shortest interactions for all the molecules (indicated on the bottom left of the plot of Form 1, mol. A(1) of Fig. 3.39). Minor differences in H-bond geometries are evident in the small variations in sharpness and length of the spikes representing the respective interactions. More obvious differences are the so-called 'wings' noticeable in Form 1 [mol. A(2) in Fig. 3.39] that are not visible in molecules 1B, 2 and less prominent in 3A, B, C and D. These wings are a result of C-H···π interactions and the most prominent being that between O7A-H7A and the carbon and nitrogen atoms forming part of the six-membered ring in molecule A. Longer contact distances are portrayed by a spread to the top right corner of the plots. This occurrence is noticeable in the majority of the plots, with Form 2 being the anomaly. This signifies a denser/ more efficient packing arrangement of Form 2, which correlates with the calculated densities where Form 2 showed the highest density. A few sharp spikes due to individual close H···H distances, such as the one pointed out in the plot of Form 3, mol. A (H4A and H18E) are visible. Other H···H interactions that appear less pointed are also seen in the plots with those of Form 1 being shorter in general than those of Form 2 and Form 3 molecules. Due to overshadowing, some features are not visible when showing plots of all the interactions and will only be seen when looking at specific interactions. An example of this is F···H interactions as highlighted in the plot of Form 1, mol. B(2). In the case of Form 2 the F···H interaction is not even discernible.

Another indication of the similarities between the interactions involved in the various forms of clevudine is visible in the relative contributions to the Hirshfeld surface for the close intermolecular contacts of the various forms presented in Fig. 3.40. The lack of diversity in contributions between the various forms is self-evident and indicative of comparable connective forces being involved.

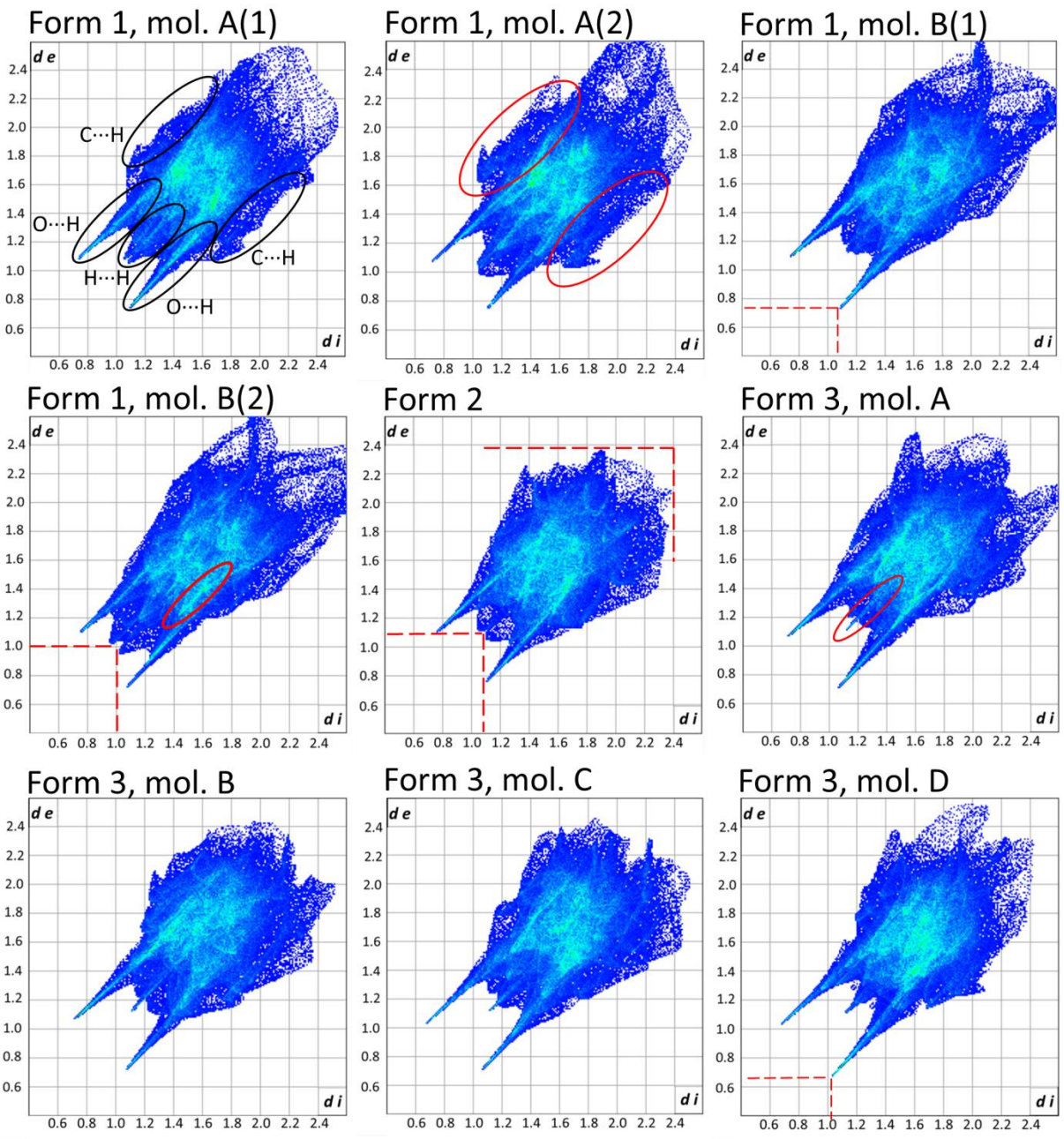

Fig. 3.39 Two-dimensional fingerprint plots for the unique molecules in the crystal structures of each form of clevudine. Parameters d_e and d_i are the distances from a point on the surface to the nearest atom nucleus exterior and interior to the surface. The first image is used to highlight characteristic interactions and other features of note are shown where appropriate. Separate plots were generated for the disordered molecules of Form 1. Form 1 A(1) and B(1) are a pair and Form 1 A(2) and B(2) are a pair.

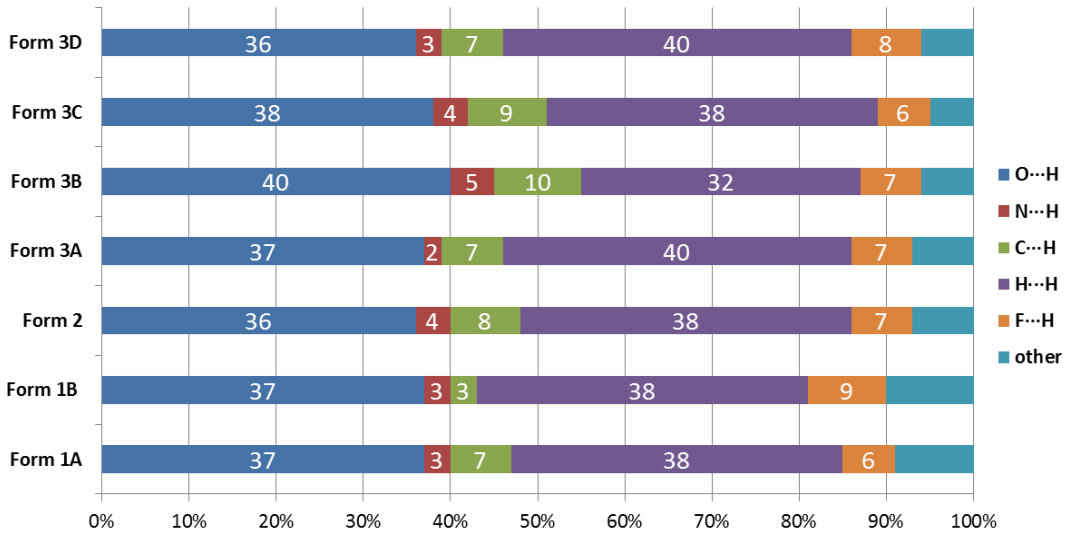

Fig. 3.40 Relative contributions to the Hirshfeld surface for the close intermolecular contacts of the various forms of clevudine.

Conformations

Various conformers exist in the different polymorphs of clevudine, as shown in Fig. 3.41. The five-membered ring conformations displayed some variation, namely Form 1, A (twisted), B (twisted); Form 2 (twisted); Form 3, A, B, C (envelope on atom C3), D (twisted). Torsion angles relating to some selected rotatable bonds are presented in Fig 3.42 and Table 3.7.

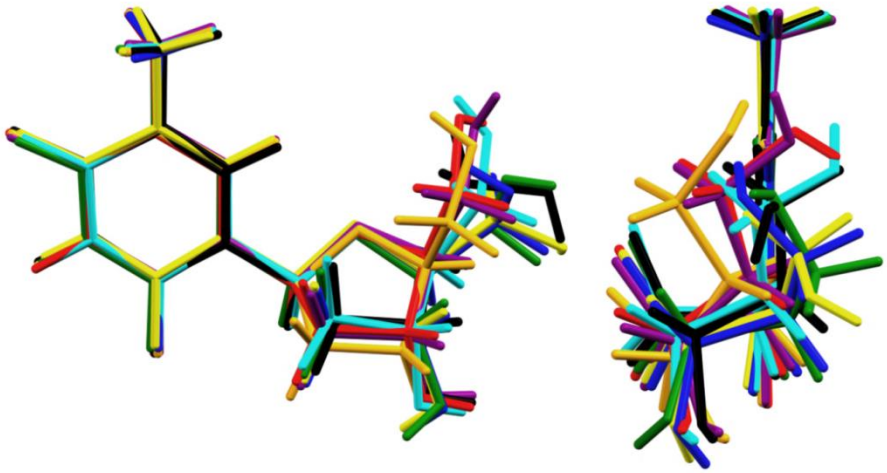

Fig. 3.41 Overlay of all seven (8 with disordered 1B) conformers of clevudine occurring in the three crystal forms viewed approximately normal (left) and parallel (right) to the methylpyrimidine-dione ring [Form 1: A-green, B (1)-blue, B (2)-yellow; Form 2: cyan; Form 3: A-red, B-orange, C-purple, D-black].

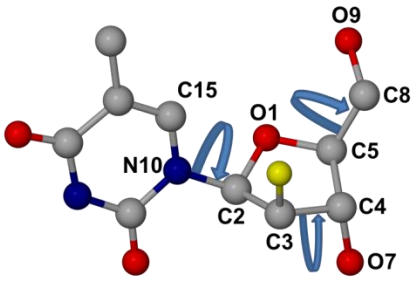

Fig. 3.42 Structural diagram showing selected torsion angles of clevudine.

Table 3.7 Torsion angles for the various forms of clevudine.

Structure	Torsion angle C15-N10-C2-O1 (°)	Torsion angle O1-C5-C8-O9 (°)	Torsion angle C2-C3-C4-O7 (°)
Form 1 – A	-38.9(3)	67.5(3)	-112.4(3)
Form 1 – B	-31.4(4)	74.2 and -69.5[a]	-112.3(3)
Form 2	-39.9(2)	-53.8(2)	-88.1(1)
Form 3 - A	-35.9(3)	-52.5(3)	-85.8(2)
Form 3 - B	-15.1(3)	-64.8(3)	-84.2(2)
Form 3 - C	-24.7(3)	-59.9(3)	-85.4(2)
Form 3 - D	-41.0(3)	-167.8(2)	-85.4(2)

[a]Minor disordered component

Conclusions

The aim from the onset of this study was multifaceted. The main goal was to prepare new solid-state forms of the chiral antiviral drug clevudine that could potentially be used in the formulation of new completed products. The other aim was to fully characterise a novel polymorph (discovered by another member of the research group at an earlier date) and determine the relative thermodynamic stabilities of the different forms. To our knowledge no indications of potential polymorphism had been reported prior to the commencement of this study. Any new pharmaceutically relevant information regarding clevudine should be of value given that it is indicated in the treatment of hepatitis B virus infections and is currently in widespread and ongoing use. The positive outcome of this study was that yet another new polymorph was identified and the full structural characterisation of all three distinct forms and comprehensive evaluation of the spectroscopic, thermal and solubility data were carried out.

DSC results alone were not adequate to confidently assign the stability ranking of the various forms due to multiple thermal events occurring in a narrow temperature range (~175 – 200 °C). A variety of

complementary methods including HSM, VTPXRD, and solvent-mediated phase transformation experiments were employed to facilitate the construction of an energy-temperature diagram. The solubility results did not indicate any major differences between the various forms. Clevudine is known to have good aqueous solubility and is well absorbed after oral administration,[15] making the differences seen in the solubility experiments less significant. The thermal stability ranking at 25 °C was determined to be Form 2 > Form 1 > Form 3. The importance of this stability ranking is that the starting material as purchased corresponds to a metastable form at room temperature. It was also shown that this form undergoes a transition during LAG with acetonitrile. This means that the drug products hold the possibility of potential phase transitions occurring during storage over extended periods or in the course of manufacturing processes. Other properties that might be influenced by the packing of the different forms include shear properties that could be considerably different when comparing the lamellar packing arrangements of Forms 1 and 3 with that of Form 2. This in turn could show benefits in tabletting ability, though this aspect was not pursued in the present study.

All three polymorphs crystallise in the second most popular Sohncke space group $P2_1$ (No. 4)[16] with Z′ values of 2, 1, and 4 for Forms 1, 2, and 3 respectively. The series of polymorphs could be of great value in the context of crystal structure prediction[17] in that compounds with multiple Z′ values pose a considerable challenge for prediction and this series can serve as an instrumental test case. The polymorphs are extensively connected by intermolecular hydrogen bonding as was observed by X-ray diffraction. The small degree of conformational flexibility results in Form 1 and Form 3 forming layered structures and Form 2 forming helical hydrogen bonded motifs.

It was also shown that PXRD and FTIR spectroscopy could be used as a means of rapid and simple differentiation between the different forms.

References

1. T. Ma, S. B. Pai, Y. L. Zhu, J. S. Lin, K. Shanmuganathan, J. Du, C. Wang, H. Kim, M. G. Newton, Y. C. Cheng and C. K. Chu, J. Med. Chem., 1996, **39**, 2835.
2. Cambridge Structural Database and Cambridge Structural Database system, Version 5.39, Cambridge Crystallographic Centre, University Chemical Laboratory, Cambridge, England, **2018**.
3. B. Mzondo and M.R. Caira, Private communication.
4. S.-J. Woo, H. Park, K.-H. Song, T.-H. Han and C.-H. Koo, PCT Int. Appl. WO 2008069451 A1 20080612, 2008.
5. Program SAINT, Version 7.60a, Bruker AXS Inc., Madison, Wisconsin, USA, **2008**.
6. G. M. Sheldrick, SADABS, *program for empirical absorption correction of area detector data*, University of Göttingen, Göttingen, Germany, **1997**.
7. XPREP, *Data Preparation and Reciprocal Space Group Exploration*, Version 2008/2, © Bruker AXS Inc., Madison, Wisconsin, USA, **2008**.
8. L. J. Barbour, J. Supramol. Chem., 2001, **1**, 189.
9. G. M. Sheldrick, *Acta Crystallogr., Sect. A: Found. Crystallogr.*, 2008, **64**, 112-122.
10. H. Flack, *Acta Crystallogr., Sect. A: Found. Crystallogr.*, 1983, **39**, 876-881.
11. T. Ma, S. B. Pai, Y. L. Zhu, J. S. Lin, K. Shanmuganathan, J. Du, C. Wang, H. Kim, M. G. Newton, Y. C. Cheng and C. K. Chu, *J. Med. Chem.*, 1996, **39**, 2835.
12. S. Parsons, H. D. Flack and T. Wagner, *Acta Crystallogr., Sect. B: Struct. Sci., Cryst. Eng. Mater.*, 2013, **69**, 249-259.
13. A. Burger and R. Ramberger, *Microchim. Acta*, 1979, **2**, 259-271.
14. CrystalExplorer, Version 3.1, S. K. Wolff, D. J. Grimwood, J. J. McKinnon, M. J. Turner, D. Jayatilaka and M. A. Spackman, University of Western Australia, Perth, Australia, **2012.**
15. E. Paintsil and Y.-C. Cheng, Pathogenesis, Antiviral Agents, in *Encyclopedia of Microbiology*, ed. M. Schaechter, Academic Press, San Diego, CA, USA, 3rd edn, 2009, vol. 4, pp. 223-257.
16. H. D. Flack, *Helv. Chim. Acta*, 2003, **86**, 905-921.
17. S. L. Price, *Chem. Soc. Rev.*, 2014, **43**, 2098-2111.

Chapter 4

The drug lead 6-(3-(Methylsulfonyl)phenyl)-3-(4-(methylsulfonyl)phenyl)-imidazo[1,2-b]pyridazine (MMV652103): a novel antimalarial drug candidate.

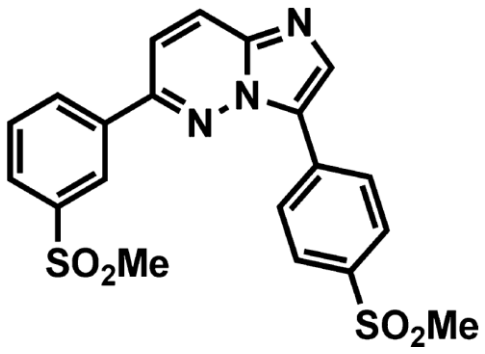

Scheme 4.1.1 Structure of MMV652103

In this section a variety of new solid-state forms of the compound shown in the Scheme above, including polymorphs, a hydrate, co-crystals and a salt is presented along with the physicochemical characterisation and the methods used for synthesis. The chapter is divided into two parts, the first of which focuses on various polymorphs and a hydrated form of the compound and the second part focuses on multi-component systems consisting of the drug and various co-crystal formers.

Part one

MMV Form 1

The polymorph that was isolated first will be discussed in this section and will be referred to as MMV Form 1 hereafter.

Preparation of single crystals

Single crystals were obtained by recrystallisation from solution. 5 mg of the raw material (RM) was dissolved in 1 cm^3 of acetone while being stirred and heated to 45-50 °C with a heating magnetic stirrer. The hot solution was filtered through a 0.45 µm nylon filter into a clean vial. The vial was capped and placed on a benchtop. After a few days the crystals had formed. The same product was obtained on subsequent occasions by the same method when using ethanol as solvent. If, however, there is too much water present in the solvents, a hydrate is predominantly formed. The calculated PXRD trace from the solved crystal structure of this form matches the trace produced by PXRD analysis of the RM.

Crystal structure analysis

Data-collection and space group determination

The single-crystal X-ray intensity data-collection was performed on a Bruker Kappa Apex II Duo diffractometer at 173(2) K. The X-ray diffraction pattern showed *mmm* Laue symmetry, indicative of the orthorhombic crystal system. The mean $|E^2-1|$ value obtained by making use of the software XPREP[1] was 0.720, which corresponds to non-centrosymmetry. The space group was determined from the conditions limiting possible reflections (*hkl: none, h00: h = 2n, 0k0: k = 2n, 00l: l = 2n)* to be $P2_12_12_1$.

Structure solution and refinement

Crystallographic data, parameters for collection of intensity data, and refinement parameters are reported in Table 4.1.1. Data reduction and unit cell refinement were performed with the program SAINT.[2] The structure was solved by direct methods through the use of SHELXS.[3] All non-hydrogen atoms were placed and then refined isotropically by full-matrix least-squares with SHELXL.[3] The non-hydrogen atoms were then refined anisotropically. All hydrogen atoms were found in difference electron density maps and placed in idealised positions in a riding model and refined with thermal parameters 1.2-1.5 times the U_{iso} values of their parent atoms. The absolute structure of this non-centrosymmetric crystal was shown to be correctly assigned from the Flack parameter value that is very close to zero with a small e.s.d. (as was described in the experimental chapter).[4,5]

Table 4.1.1: Data-collection and refinement parameters for MMV Form 1

Molecular formula	$C_{20}H_{17}N_3O_4S_2$
Formula weight (g mol^{-1})	427.48
Crystal system	Orthorhombic
Space group	$P2_12_12_1$
a (Å)	5.4811(5)
b (Å)	16.5034(16)
c (Å)	20.9563(19)
α (°)	90
β (°)	90
γ (°)	90
V $(Å)^3$	1895.6(3)
Z	4
D_c (g cm^{-3})	1.498
μ (Mo Kα) (mm^{-1})	0.315
F(000)	888
Data-collection temp. (K)	173(2)
Crystal size (mm^3)	0.04 x 0.06 x 0.48

Range scanned θ (°)	1.57 – 28.37
Index ranges ±*h*, ±*k*, ±*l*	-7, 7; -22, 21; -27, 27
Reflections (total)	24 852
Independent reflections	4746
Reflections with I>2σ(I)	3715
Number of parameters	264
R_{int}	0.0719
S	1.020
R_1 [*I*>2σ(*I*)]	0.0420
Reflections omitted	1
wR_2	0.0957
a, b in w = $1/[\sigma^2(F_o^2)+(aP)^2+(bP)]$	a = 0.0447; b = 0.2128
$(\Delta/\sigma)_{mean}$	< 0.001
$\Delta\rho_{min,max}$ (e Å^{-3})	-0.335, 0.242
Flack parameter	0.018(96) by classical fit to all intensities; 0.031(51) from 1309 selected quotients (Parsons' method)

Molecular structure

The asymmetric unit and labelling scheme of MMV Form 1 are shown in Fig. 4.1.1.

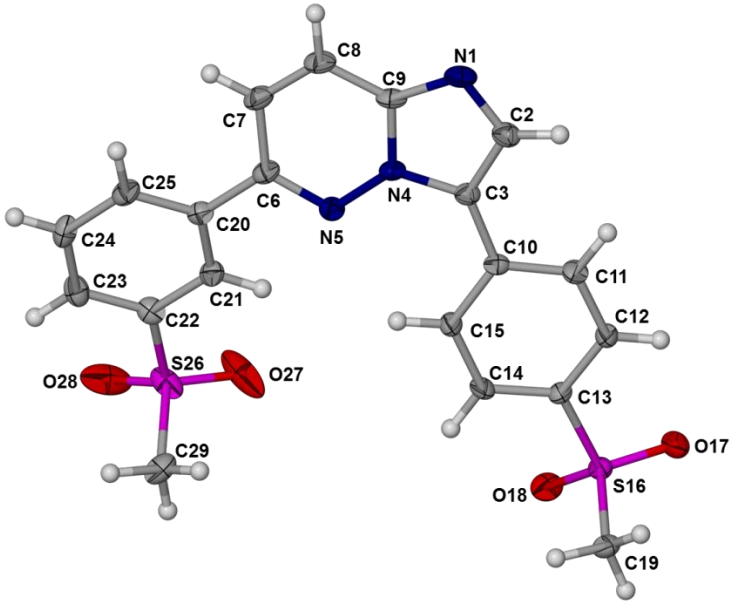

Fig. 4.1.1 The asymmetric unit and numbering scheme of MMV Form 1 with thermal ellipsoids shown at the 50 % probability level.

Crystal packing and hydrogen bonding

A summary of H-bonds and their parameters present in MMV Form 1 is presented in Table 4.1.2. No classical H-bonds are present as this compound only has hydrogen acceptor atoms and no strong hydrogen donor atoms. For the most part the cut-off values used were: donor atom to acceptor atom distances of less than the sum of the van der Waals radii of the donor and acceptor atoms + 0.50 Å; hydrogen to acceptor atom distances of less than the sum of the van der Waals radii of the hydrogen and acceptor atoms -0.12 Å; donor atom to hydrogen atom to acceptor atom angles of greater than 100°. Exceptions were made in cases where the interactions were deemed appropriate to be added.

Table 4.1.2 Hydrogen bonds in Form 1[a]

	D–H···A	***d*(D–H), Å**	***d*(H···A), Å**	***d*(D···A), Å**	**∠(DHA), deg.**
	C7-H7···O18^{i}	0.95	2.37	3.223(4)	150
Intra	C12-H12···O17	0.95	2.53	2.896(4)	103
Intra	C15-H15···N5	0.95	2.33	2.973(4)	124
	C19-H19A···O27^{ii}	0.98	2.50	3.350(5)	144
	C19-H19B···O17^{iii}	0.98	2.51	3.456(4)	163
Intra	C21-H21···O27	0.95	2.53	2.901(4)	103
	C24-H24···O28^{iv}	0.95	2.50	3.367(4)	153
	C29-H29A···O27^{iii}	0.98	2.32	3.279(5)	166
	C29-H29C···N1^{v}	0.98	2.46	3.412(4)	164
Intra	C21-H21···N5	0.95	2.46	2.771(4)	99
Intra	C14-H14···O18	0.95	2.72	2.989(4)	97
Intra	C23-H23···O28	0.95	2.68	2.979(4)	99
	C14-H14···O17^{iii}	0.95	2.61	3.330(4)	133

[a]Symmetry transformations used to generate equivalent atoms: *[i]: 1/2-x,1-y,1/2+z;*

[ii]: 1-x,-1/2+y,1/2-z; [iii]: -1+x,y,z; [iv]: -1/2+x,3/2-y,1-z; [v]: 1/2-x,1-y,-1/2+z.

The same notation as described in Chapter 3 is used in the following section.

This form of MMV packs in a herringbone arrangement that is visible when viewed down [001] as is shown in Figs. 4.1.3 and 4.1.8. Infinite ribbons propagating in the *z*-direction are formed by MMV molecules stacked in a head-to-tail manner. These ribbons are formed by the interactions C29-H29C···N1′ and C7-H7···O18′. These interactions form rings that can be described as $R_2^2(21)$ and are visible in Figs. 4.1.2 and 4.1.6.

Infinite columns that propagate in the *x*-direction are formed by the following interactions (with graph-set designators in parentheses): C19-H19B···O17′, C29-H29A···O27′ ($R_2^2(32)$), and C14-H14···O17′ (Fig. 4.1.7). A bifurcated H-bond consisting of C19-H19B···O17′ and C14-H14···O17′ forms a ring that can be described by $R_2^1(7)$ (Fig. 4.1.4).

The MMV molecules are also connected to almost perpendicularly orientated surrounding molecules that appear to be in different layers by the H-bonds, C19-H19A···O27′ and C24-H24···O28′.

Various elongated 'ring' motifs can be observed that play a role in the packing of this form. An $R_4^4(30)$ ring formed by the interactions C7-H7···O18′ and C14-H14···O17′, an $R_4^4(32)$ ring formed by the interactions C7-H7 ···O18′ and C19-H19B···O17′, a ring $R_4^4(48)$, formed by the interactions C7-H7···O18′ and C29-H29A···O27′, and C19-H19A···O27′ with C14-H14···O17′R_4^4 (38) connects molecules stacked in the x-direction with other stacked molecules in the y-direction. These are shown in Fig. 4.1.4.

The packing arrangement of this form is shown viewed along [100] in Fig. 4.1.5 and along [001] in Fig. 4.1.8.

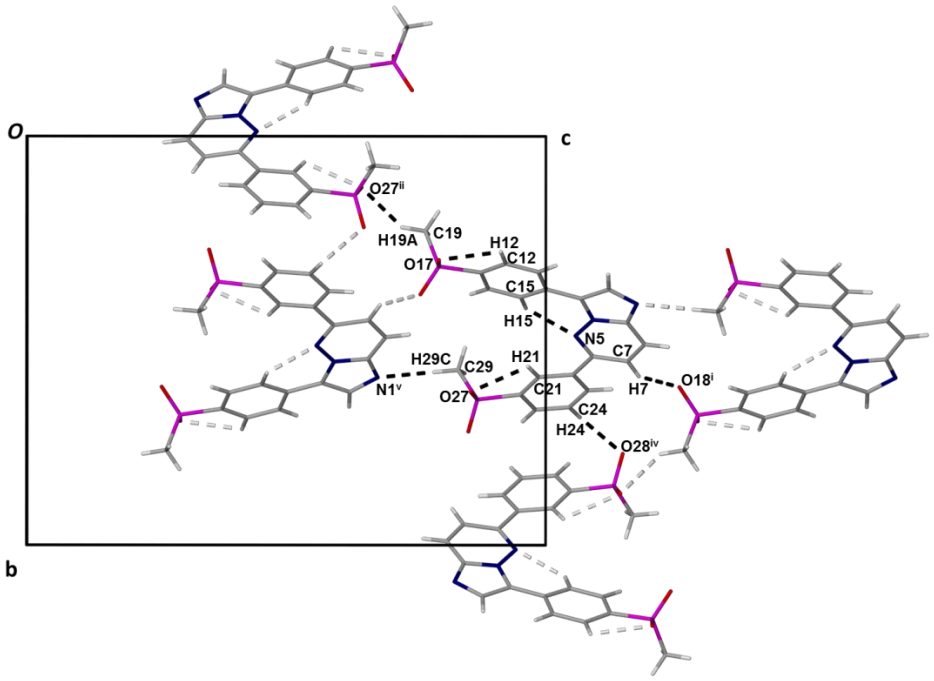

Fig. 4.1.2 Hydrogen bonding interactions found in the structure of MMV Form 1 viewed along [100].

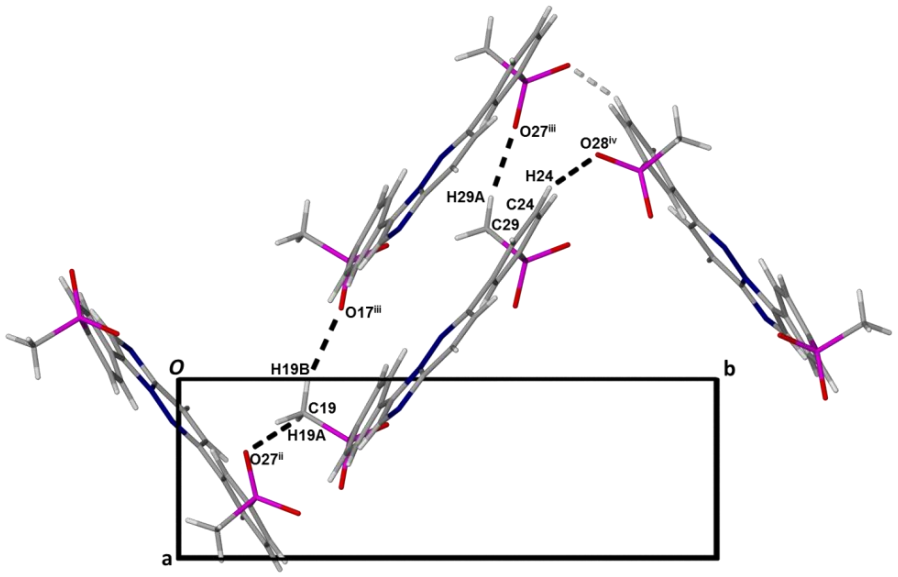

Fig. 4.1.3 Hydrogen bonding interactions found in the structure of MMV Form 1 viewed along [001].

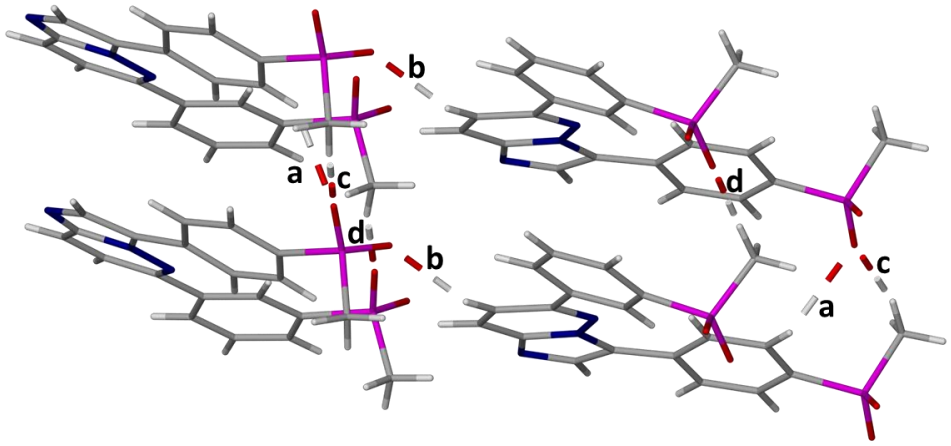

Fig. 4.1.4 Ring motifs connecting MMV Form 1 molecules where (a), (b), (c) and (d) represent C14-H14···O17′, C7-H7···O18′ , C19-H19B···O17′ and C29-H29A···O27′ respectively, where (a) with (b) forms $R_4^4(30)$; (c) with (d) $R_2^2(32)$; (b) with (c) forms $R_4^4(32)$; (b) with (d) forms $R_4^4(48)$ and a bifurcated H-bond (a) with (c) forms a ring $R_2^1(7)$.

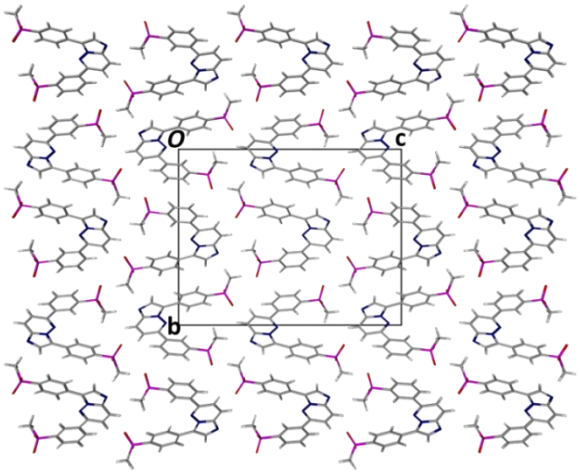

Fig. 4.1.5 Packing of MMV Form 1 viewed along [100].

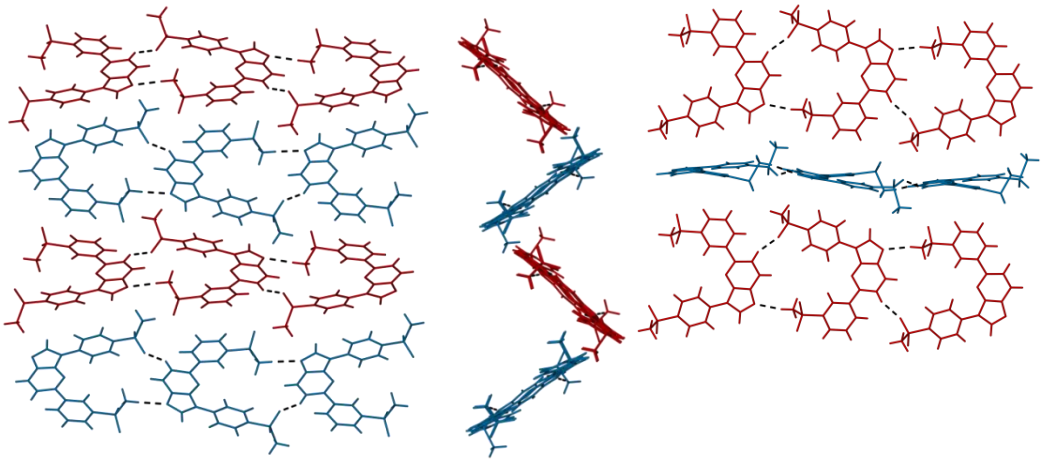

Fig. 4.1.6 A layer of MMV Form 1 highlighting the infinite ribbons propagating in the *y*-direction viewed from different perspectives.

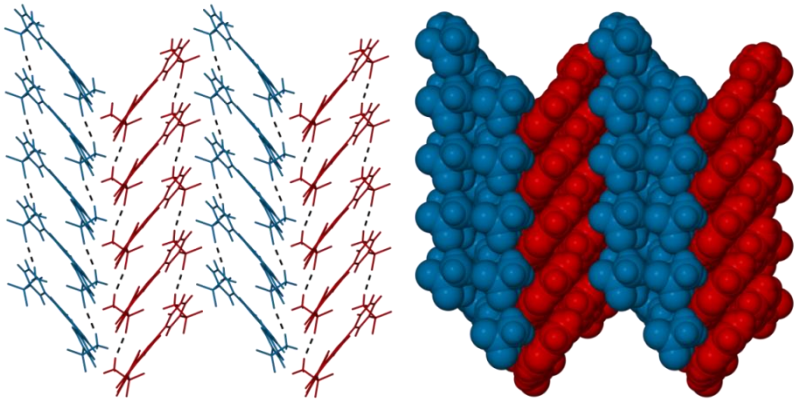

Fig. 4.1.7 Packing of MMV Form 1 showing infinite stacked columns propagating in the *x*-direction from a side view as stick and space-filling models respectively.

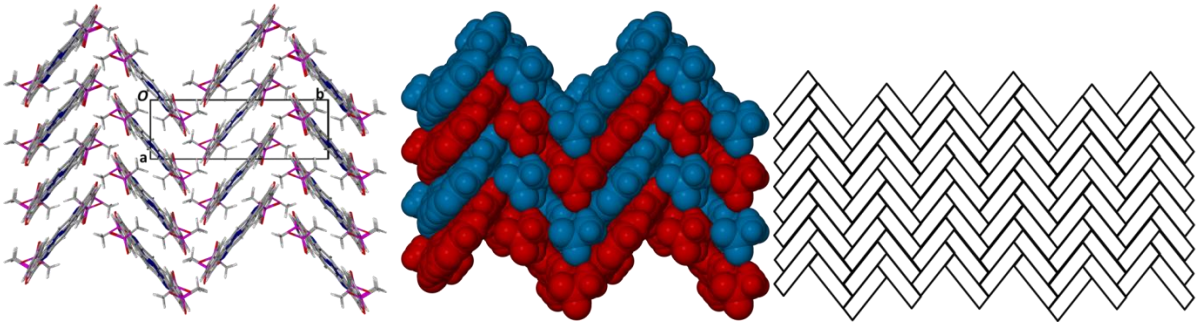

Fig. 4.1.8 Packing of MMV Form 1 in a herringbone pattern viewed along [001] shown as stick and space-filling models.

A comparison of the PXRD traces obtained experimentally with MMV (RM) and calculated from the solved crystal structure of MMV Form 1 is presented in Fig. 4.1.9. The traces match well and from this result it is clear that the RM is the same polymorphic form as MMV Form 1.

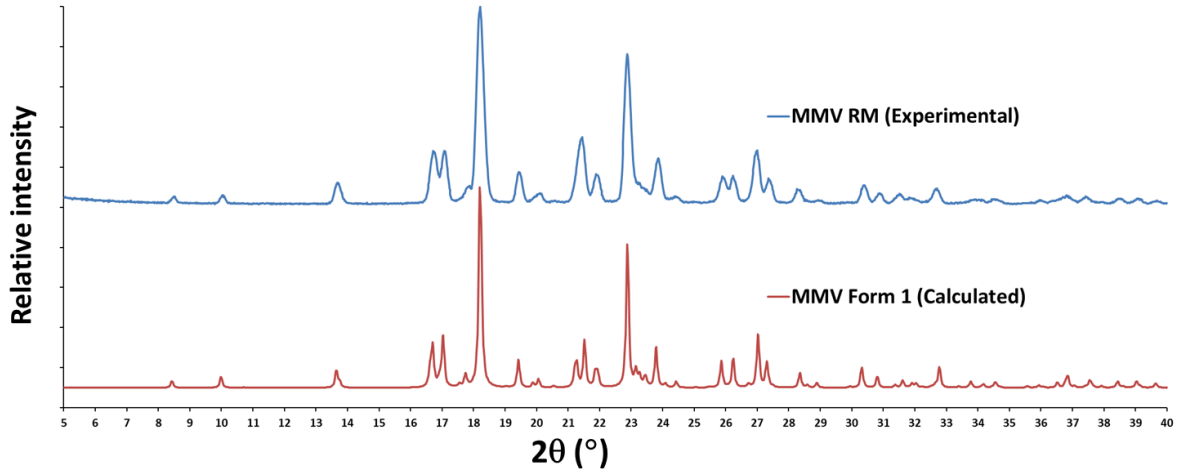

Fig. 4.1.9 Comparison of the calculated PXRD trace of MMV Form 1 with the experimental trace for the RM.

Thermal analysis

The needle-like crystals of MMV Form 1 visible in the HSM images (Fig. 4.1.10) started to melt around 250 °C and were completely melted by 270 °C. In the DSC trace of MMV Form 1 (Fig. 4.1.11) there is a single sharp endotherm visible with an onset temperature of 245.0 ± 0.5 °C (n = 3), a peak at 247.0 ± 0.3 °C (n = 3), and an enthalpy related to the event of 111.8 ± 6.6 J g^{-1} (n = 3). The temperature matches that seen with HSM and could be accepted as being a melting endotherm. The TGA result (Fig. 4.1.12) shows no significant mass loss until the onset of decomposition far above the melting temperature at 397.7 ± 2.9 °C (n = 2).

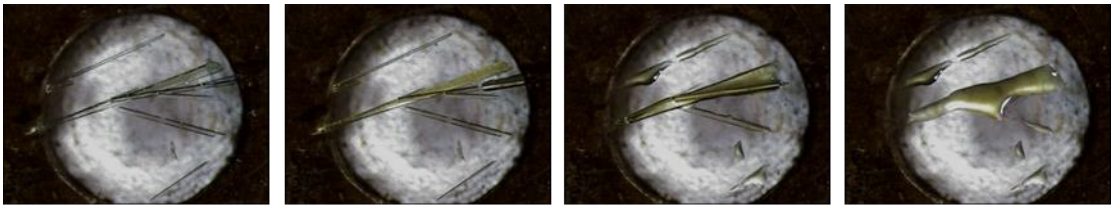

Fig. 4.1.10 HSM micrographs of MMV Form 1 crystals at various temperatures.

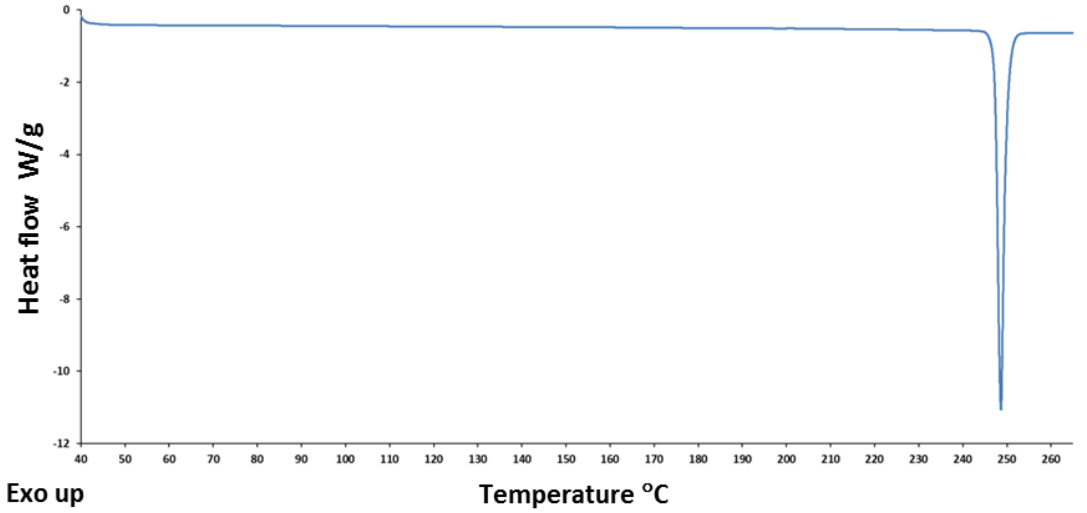

Fig. 4.1.11 Representative DSC trace for MMV Form 1.

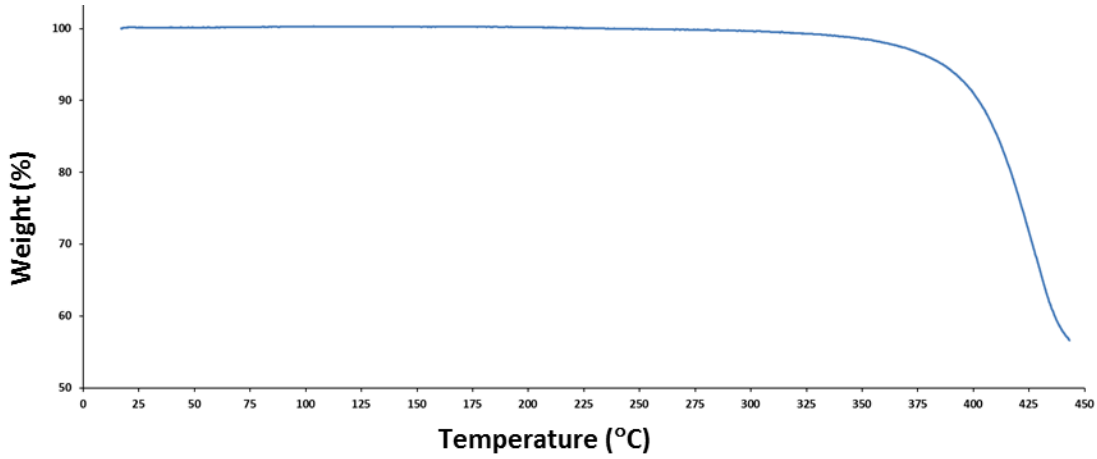

Fig. 4.1.12 Representative TGA trace for MMV Form 1.

MMV Form 2

A new polymorph of MMV was serendipitously discovered in an attempt to grow co-crystals from solution. The conditions under which these crystals were first obtained were as follows. 5 mg of MMV RM and an equimolar amount of succinic acid were dissolved in 5 cm^3 of ethyl acetate at 60 °C while being stirred. The solution was filtered through a 0.45 µm nylon filter into a clean vial and placed in a desiccator. These conditions were found not to be necessary for this form to crystallise as on subsequent occasions the crystals formed from ethyl acetate and acetonitrile solutions in the absence of the co-crystal former.

Crystal structure analysis

Data-collection and space group determination

The single-crystal X-ray intensity data-collection was performed on a Bruker Kappa Apex II Duo diffractometer at 173(2) K. The X-ray diffraction showed *2/m* Laue symmetry, indicative of the monoclinic crystal system. The mean $|E^2-1|$ value obtained by making use of the software XPREP[1] was 0.930 and corresponds to centrosymmetry. The space group was determined from the conditions limiting possible reflections (*hkl: none, h0l: l = 2n, 0k0: k = 2n*) to be $P2_1/c$.

Structure solution and refinement

Crystallographic data, parameters for collection of intensity data, and refinement parameters are reported in Table 4.1.3. The procedure followed was the same as that described for Form 1.

Table 4.1.3 Data-collection and refinement parameters for MMV Form 2

Molecular formula	$C_{20}H_{17}N_3O_4S_2$
Formula weight (g mol^{-1})	427.48
Crystal system	Monoclinic
Space group	$P2_1/c$
a (Å)	9.7617(12)
b (Å)	8.5070(10)
c (Å)	23.799(3)
α (°)	90
β (°)	97.621(2)
γ (°)	90
V $(Å)^3$	1958.9(4)
Z	4

D_c (g cm^{-3})	1.449
μ (Mo Kα) (mm^{-1})	0.305
F(000)	888
Data-collection temp. (K)	173(2)
Crystal size (mm^3)	0.30 x 0.17 x 0.03
Range scanned θ (°)	1.73 – 28.34
Index ranges ±*h*, ±*k*, ±*l*	-13, 13; -11, 11; -31, 31
Reflections (total)	38 374
Independent reflections	4873
Reflections with I>2σ(I)	3623
Number of parameters	264
R_{int}	0.0642
S	1.011
R_1 [*I*>2σ(*I*)]	0.0966
Reflections omitted	2
wR_2	0.1078
a, b in w = 1/[σ^2(F_o^2)+(aP)^2+(bP)]	a = 0.0447; b = 1.1654
$(\Delta/\sigma)_{mean}$	< 0.001
$\Delta\rho_{min,max}$ (e Å^{-3})	-0.380, 0.404

Molecular structure

The asymmetric unit and labelling scheme of MMV Form 2 are shown in Fig. 4.1.13.

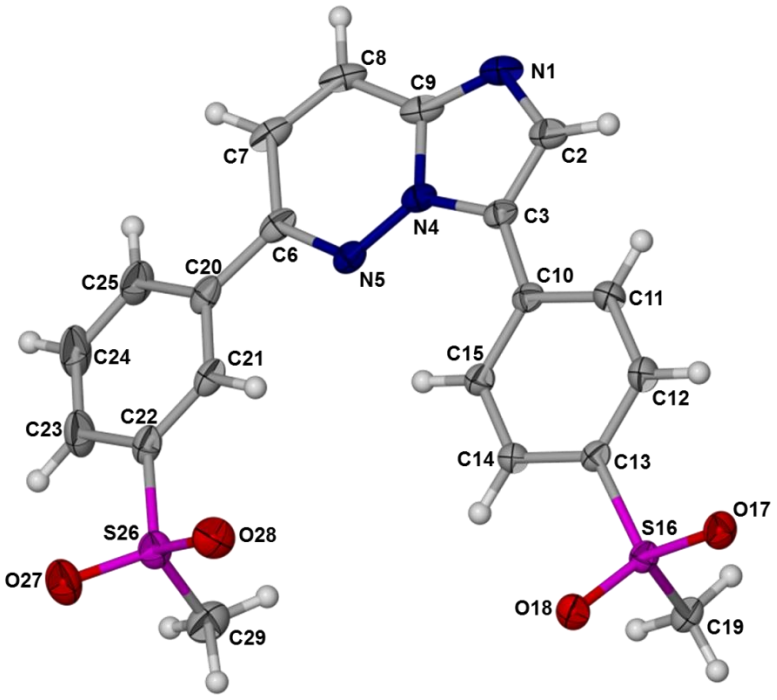

Fig. 4.1.13 The asymmetric unit and numbering scheme of MMV Form 2 with thermal ellipsoids shown at the 50 % probability level.

Crystal packing and hydrogen bonding

A summary of H-bonds and their parameters present in MMV Form 2 is presented in Table 4.1.4. The cut-off parameters used in this instance are the same as those used for Form 1.

Table 4.1.4 Hydrogen bonds in Form 2[a]

	D–H···A	*d*(D–H), Å	*d*(H···A), Å	*d*(D···A), Å	∠(DHA), deg.
	C8-H8···N1^{i}	0.95	2.56	3.325(3)	137
Intra	C12-H12···O17	0.95	2.49	2.888(3)	105
Intra	C15-H15···N5	0.95	2.33	2.985(2)	126
	C19-H19A···O28^{ii}	0.98	2.52	3.440(3)	156
	C19-H19B···O27^{iii}	0.98	2.46	3.406(3)	163
	C19-H19C···O18^{ii}	0.98	2.48	3.372(3)	151
Intra	C21-H21···O28	0.95	2.53	2.920(2)	105
	C23-H23···O17^{iv}	0.95	2.50	3.321(3)	144
	C29-H29A···N1^{v}	0.98	2.59	3.546(3)	165
	C29-H29C···O17^{ii}	0.98	2.41	3.219(3)	140
Intra	C21-H21 ···N5	0.95	2.42	2.724(3)	98
	C29-H29B···O27^{vi}	0.98	2.64	3.463(3)	142

[a] Symmetry transformations used to generate equivalent atoms: *[i]: -x,-y,-z; [ii]: 2-x,1-y,-z; [iii]: x,1/2-y,-1/2+z; [iv]: x,1/2-y,1/2+z; [v]: 1-x,-y,-z; [vi]: -x,-1/2+y,1/2-z.*

Infinite ribbons (shown in Fig. 4.1.21) propagating in two different directions (Fig. 4.1.23) are formed by the following interactions: C8-H8···N1′ $R_2^2(8)$ (Fig. 4.1.14 and 4.1.16), C19-H19A···O28′ $R_2^2(32)$, C19-H19C···O18′ $R_2^2(8)$, and C29-H29C···O17′ $R_2^2(32)$ (Fig. 4.1.15). All of these interactions are formed around inversion centres. Unlike in the case of Form 1, these ribbons are formed by MMV molecules connected head-to-head and tail-to-tail.

Interactions that form the connections between stacked ribbons are the following: C29-H29A···N1′ $R_2^2(22)$ (Fig. 4.1.17) as well as the π-π interactions at an inversion centre between the rings C10-C11-C12-C13-C14-C15 and N4-N5-C6-C7-C8-C9, generated by the symmetry operator 1-x,1-y,1-z, with an offset face-to-face centroid-to-centroid distance of 3.837 Å. The shortest interatomic distance between these rings is 3.328 Å (C8···C14) (Fig. 4.1.18). The distance between these π-stacked molecules and the next ones generated by the symmetry operator 1-x,2-y,1-z would suggest that they are not connected by π-π interactions and are thus not continuously π-stacked and the sequence is interrupted in this direction to form alternating stacks (Figs. 4.1.18, 4.1.22, and 4.1.23).

The alternating stacks form ribbons and these are connected by C23-H23···O17′ and C19-H19B···O27′ $R_2^2(9)$ (Fig. 4.1.14). A bifurcated H-bond is present that consists of C19-H19B···O27′ and C29-H29B···O27′ and forms a ring, $R_4^2(36)$, that connects alternating stacked ribbons (Fig. 4.1.19).

The packing arrangement of this form is shown in Fig. 4.1.20 as viewed along [010] and [100].

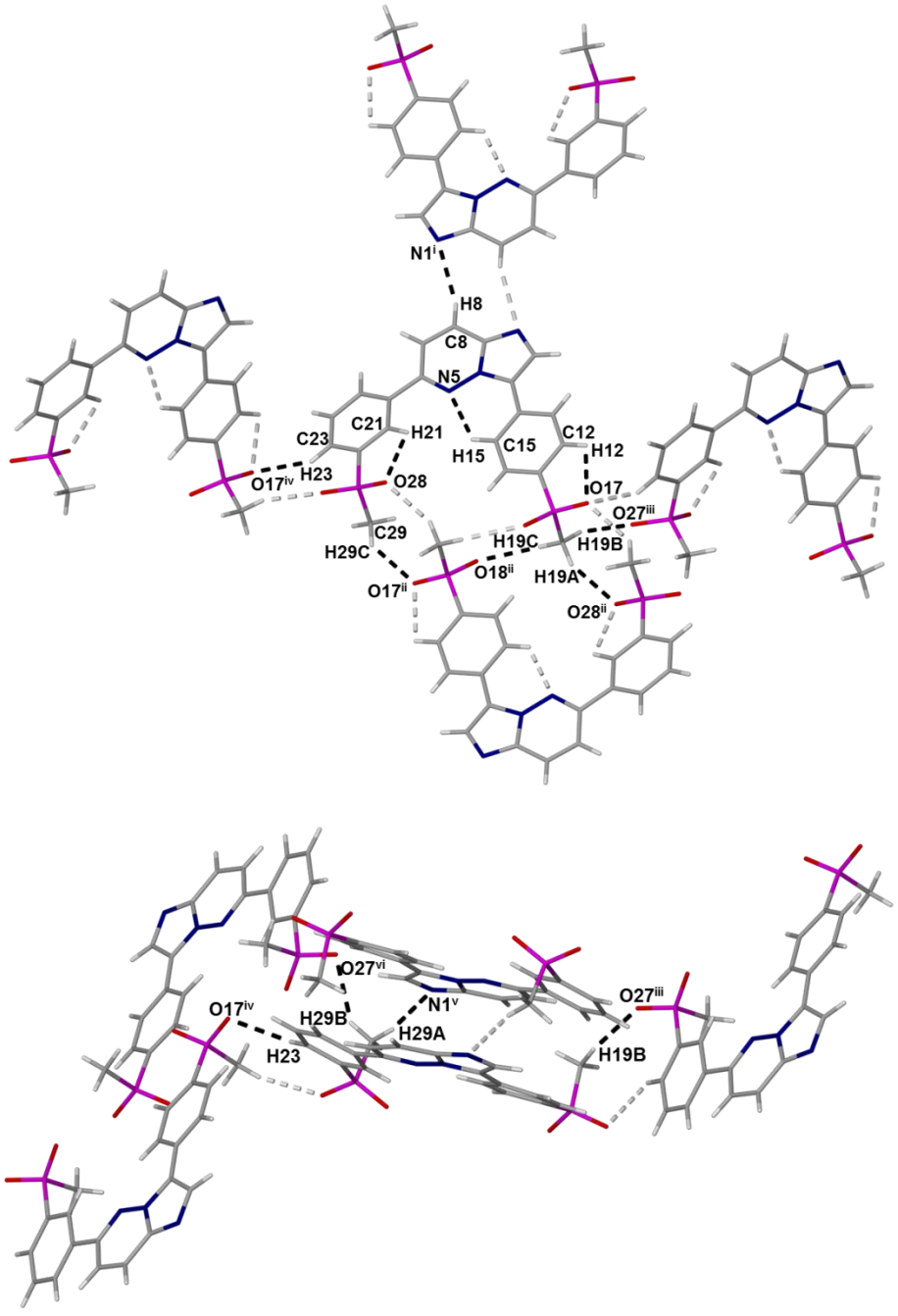

Fig. 4.1.14 Hydrogen bonding interactions found in the structure of MMV Form 2 from different perspectives.

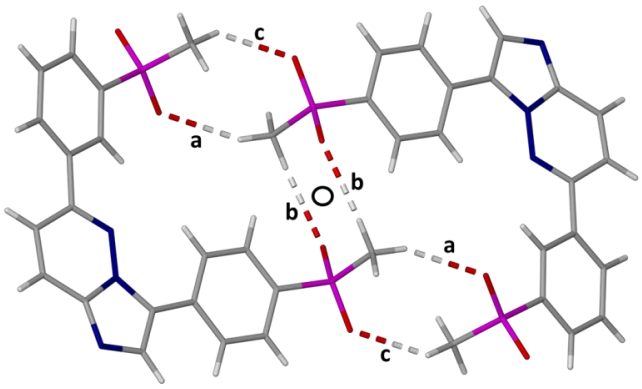

Fig. 4.1.15 Various ring motifs formed by intermolecular interactions in MMV Form 2: C19-H19A···O28′ is labelled (a), C19-H19C···O18′ is labelled (b), and C29-H29C···O17′ is labelled (c). (a) forms a ring that can be described by $R_2^2(32)$; (b) forms $R_2^2(8)$; (c) forms $R_2^2(32)$; (a) with (c) forms $R_2^2(8)$.

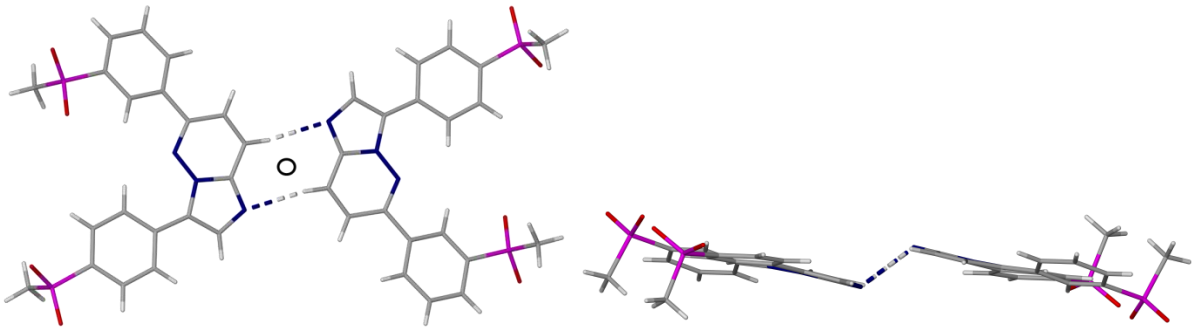

Fig. 4.1.16 C8-H8···N1′ $R_2^2(8)$ viewed roughly normal (left) and parallel (right) to the imidazopyridazine ring.

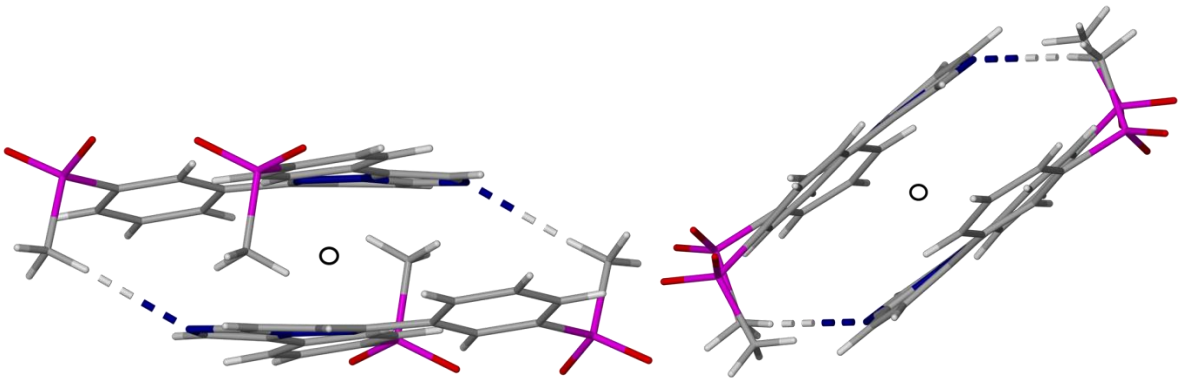

Fig. 4.1.17 Interactions between molecules that form the stacking of ribbons propagating in the same direction. C29-H29A···N1′ $R_2^2(22)$-(viewed from different perspectives)

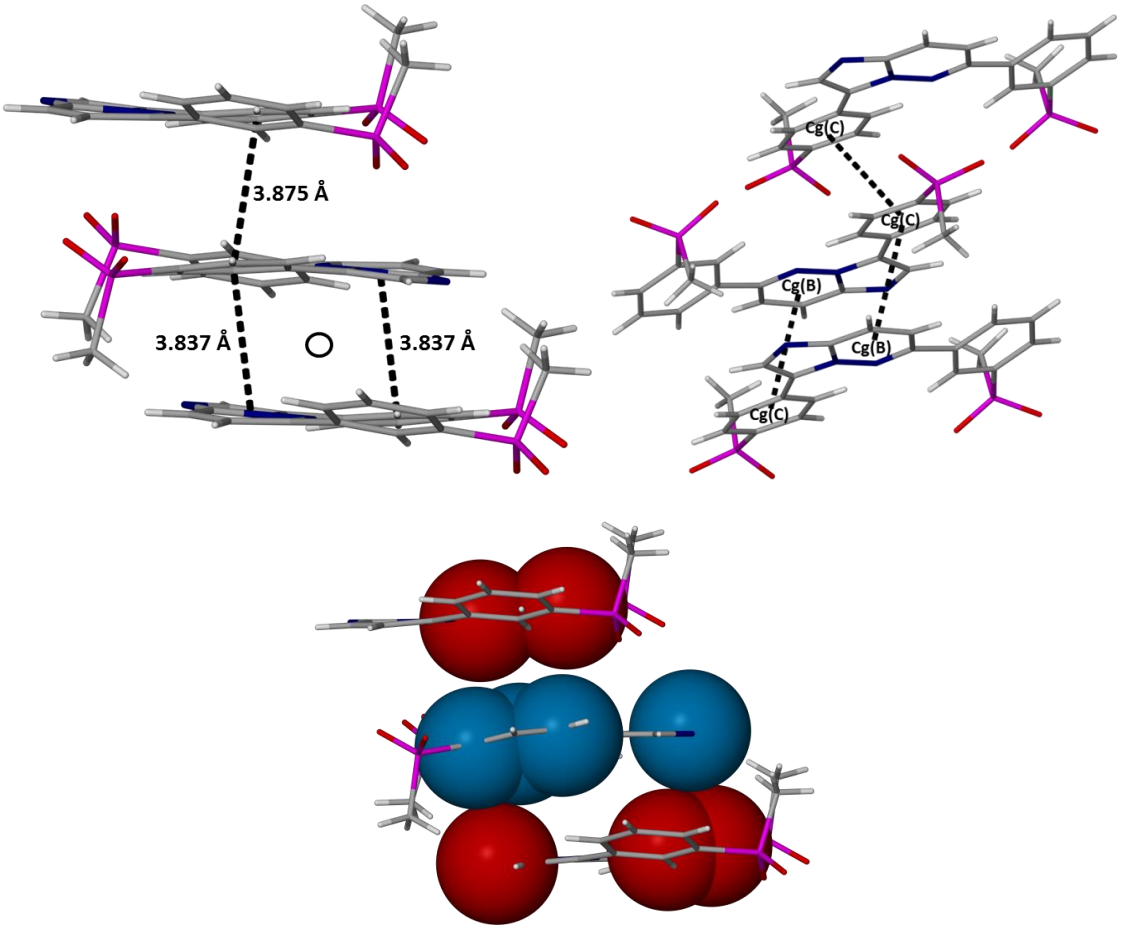

Fig. 4.1.18 π-π interactions connecting layers of ribbons viewed from different perspectives showing centroids and offset centroid-to-centroid distances between them (top). Selected atoms drawn with van der Waals radii to illustrate the overlap in the case of Cg(B)···Cg(C) and the lack thereof in the case of Cg(C)···Cg(C) (bottom).

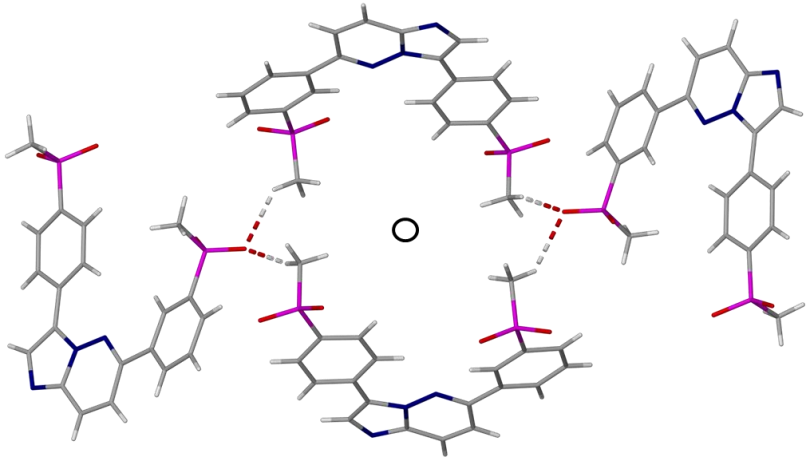

Fig. 4.1.19 Interactions connecting ribbons propagating in different directions to form a ring: C19-H19B···O27′ and C29-H29B···O27′, R_4^2 (36).

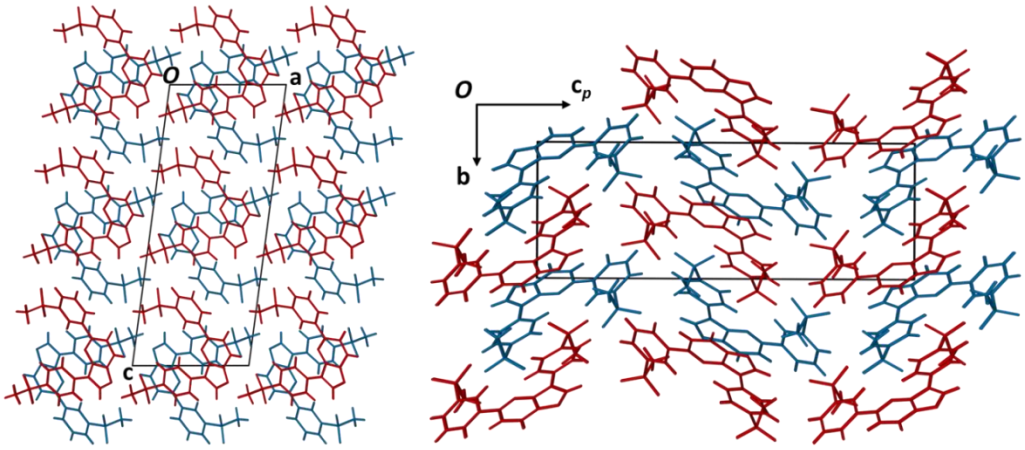

Fig. 4.1.20 Packing of MMV Form 2 viewed along [010] (left) and along [100] (right).

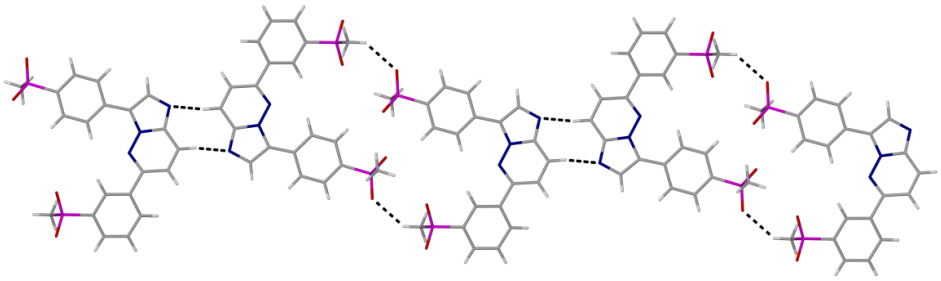

Fig. 4.1.21 Infinite ribbon, assembled head-to-head and tail-to-tail, viewed roughly normal to the imidazopyridazine ring.

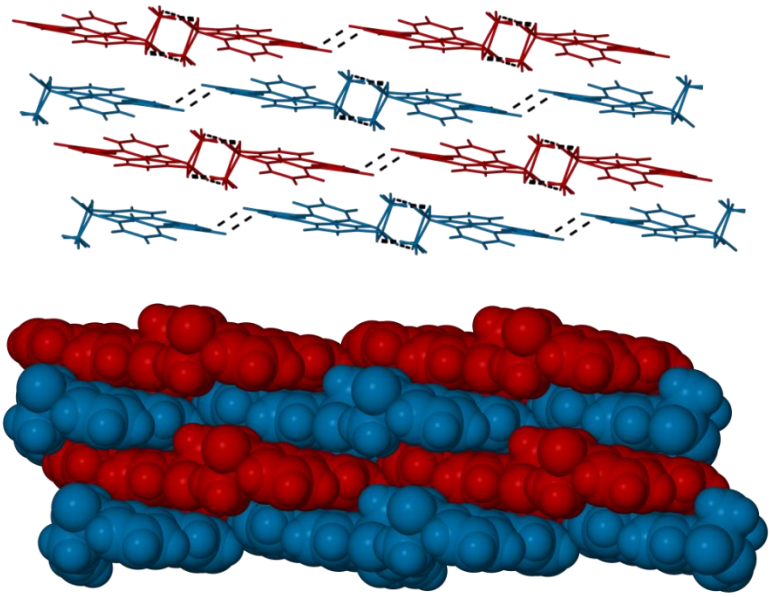

Fig. 4.1.22 Stacked infinite ribbons viewed roughly parallel to the imidazopyridazine ring presented as stick (top) and space-filling models (bottom).

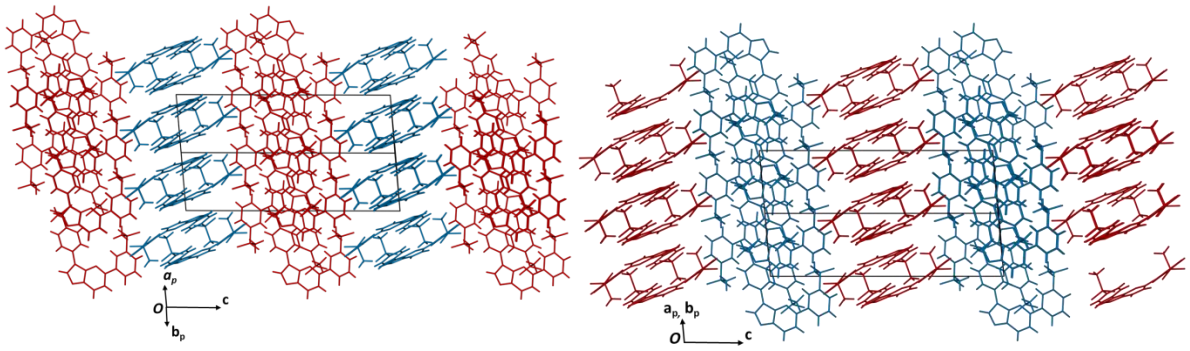

Fig. 4.1.23 Packing diagram showing stacked infinite ribbons propagating in different directions viewed from different viewpoints.

Powder X-ray diffraction

Crystals were obtained from recrystallisation by slow evaporation of MMV RM from anhydrous acetonitrile. These crystals were gently ground and the experimental PXRD result is compared to the calculated trace obtained for the solved crystal structure of MMV Form 2 and displayed in Fig. 4.1.24. The traces are a good match and this showed that this method could be used to prepare this form for further experimentation.

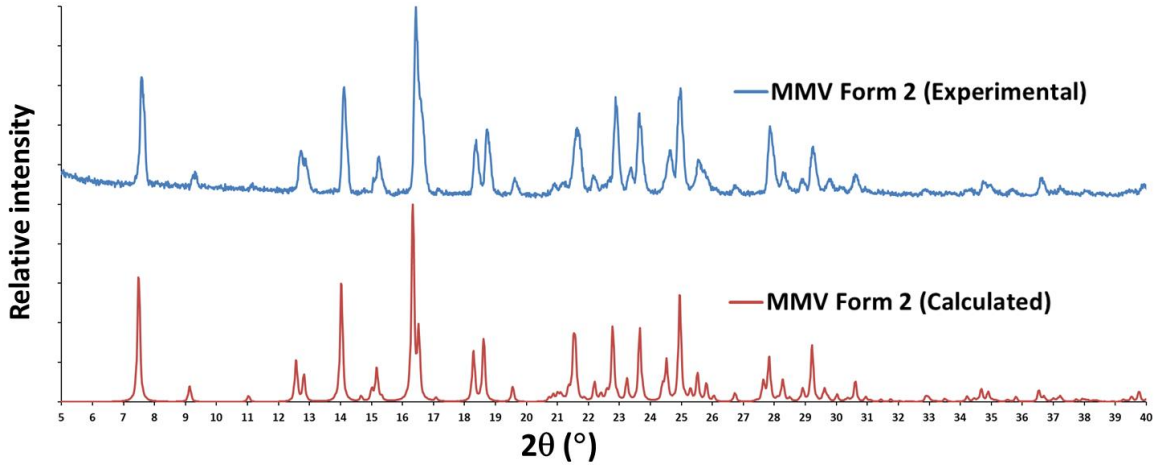

Fig. 4.1.24 Comparison of experimental and calculated PXRD traces of MMV Form 2.

Thermal analysis

The HSM images (Fig. 4.1.25) show a very small plate-like crystal of MMV Form 2 that starts to melt around 240 °C and has mostly melted by 250 °C. The DSC results for MMV Form 2 (Fig. 4.1.26) show a single sharp endotherm with an onset of 233.5 ± 0.1 °C (n = 3), a peak at 235.6 ± 0.1 °C (n = 3) and an enthalpy of 114.7 ± 1.9 J g^{-1} (n = 3). This endotherm relates to the melting of MMV Form 2 seen in the HSM results. On other occasions the DSC results showed an endothermic peak that is interrupted by an exothermic peak, as is visible in Fig. 4.1.27. The tendency of the various forms to crystallise concomitantly under non-ideal conditions can lead to the possibility of varying amounts of Form 1 being present in each sample. The fact that the pure Form 2 melts without recrystallisation at a heating rate of 10 K min^{-1}, but shows significant recrystallisation and a second endotherm correlating to the melt of Form 1 would suggest that the presence of 'seeds' of Form 1 results in nucleation that facilitates the recrystallisation of the melt to the higher melting Form 1. Similar results are not uncommon and one such case was observed with the nonsteroidal anti-inflammatory drug indomethacin.[6] The TGA results show no substantial mass loss before the onset of decomposition at 400.0 ± 4.9 °C (n = 2) (Fig. 4.1.28).

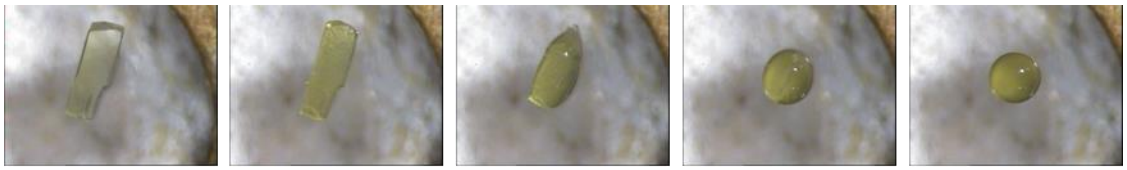

Fig. 4.1.25 HSM photographs of an MMV Form 2 crystal at various temperatures.

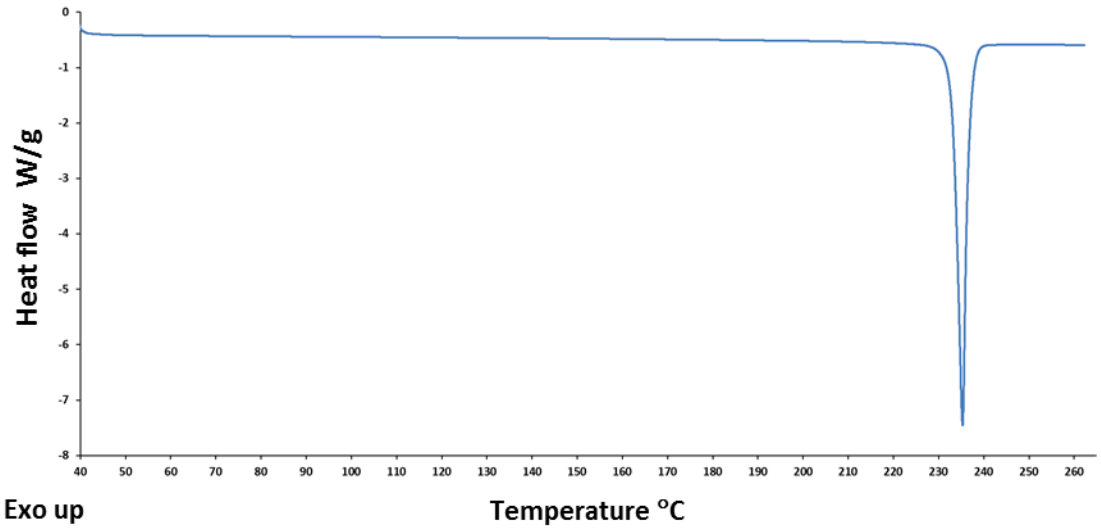

Fig. 4.1.26 Representative DSC trace for MMV Form 2.

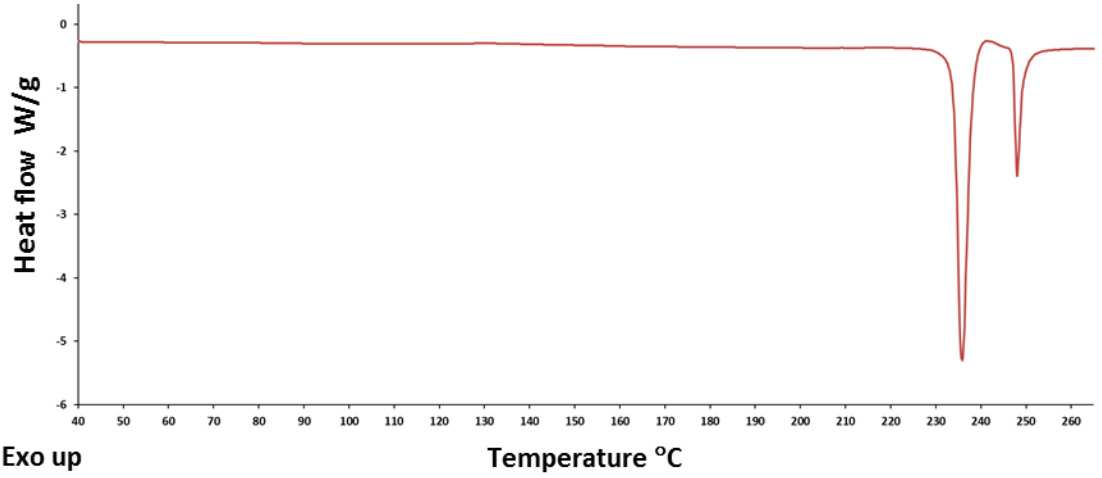

Fig. 4.1.27 Representative DSC trace for MMV Form 2 where traces of Form 1 were present.

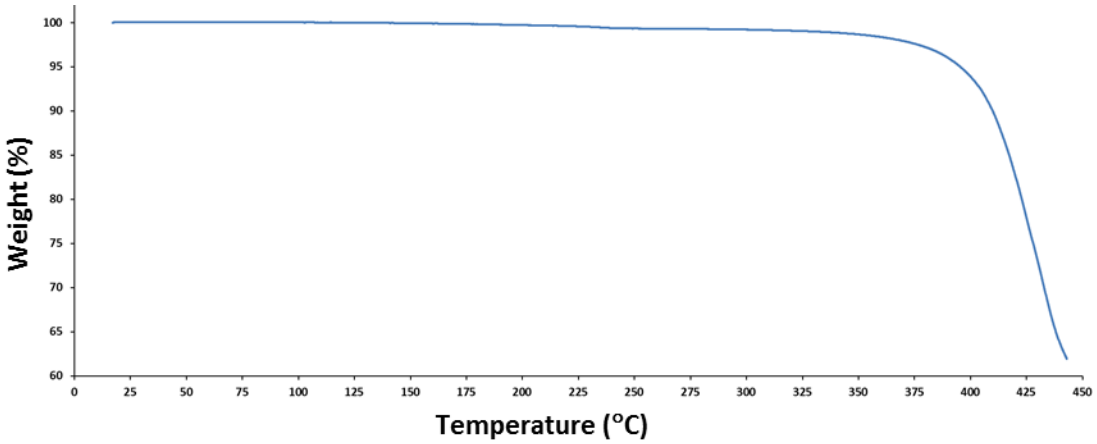

Fig. 4.1.28 Representative TGA of MMV Form 2.

MMV monohydrate

Single crystals of this form were first observed in a recrystallisation experiment where 5 mg of MMV was dissolved in 6 cm^3 of ethyl acetate, heated to 70 °C while being stirred and filtered through a 0.45 µm nylon filter into a clean vial and placed on a benchtop. In the same vial needle-like single crystals of MMV Form 1 appeared first and the hydrated crystals with a more plate-like habit formed later. Subsequently the method used to obtain purely the hydrated form was as follows: 10 mg of MMV was dissolved in about 5 cm^3 of acetone that was heated to 50 °C while being stirred and then filtered through a 0.45 µm nylon filter into a clean vial with 2 cm^3 of water added to the already filtered solution and the mixture was placed on a benchtop. After a few days the plate-like crystals had formed.

Crystal structure analysis

Data-collection and space group determination

The single-crystal X-ray intensity data collection was performed on a Bruker Kappa Apex II Duo diffractometer at 173(2) K. The X-ray diffraction pattern showed $\bar{1}$ Laue symmetry, indicative of the triclinic crystal system. The mean $|E^2-1|$ value obtained by making use of the software XPREP[1] was 0.959 and corresponds to centrosymmetry. The centrosymmetry definitively indicates that from the two possible options in the triclinic system the space group has to be $P\ \bar{1}$.

Structure solution and refinement

Crystallographic data and parameters for collection of intensity data are reported in Table 4.1.5. A DFIX command was used to restrain the O-H bond lengths of the water molecule in the asymmetric unit to a length of 0.84(2) Å. Apart from this the procedure used was the same as for Forms 1 and 2.

Table 4.1.5 Data-collection and refinement parameters for MMV monohydrate

Molecular formula	$(C_{20}H_{17}N_3O_4S_2)\cdot(H_2O)$
Formula weight (g mol^{-1})	445.50
Crystal system	Triclinic
Space group	$P\bar{1}$
a (Å)	8.2805(6)
b (Å)	9.8729(7)
c (Å)	12.4456(9)
α (°)	101.036(2)
β (°)	96.554(2)
γ (°)	90.363(2)
V (Å)^3	991.70(12)
Z	2
D_c (g cm^{-3})	1.492
μ (Mo Kα) (mm^{-1})	0.308
F(000)	464
Data-collection temp. (K)	173(2)
Crystal size (mm^3)	0.18 x 0.09 x 0.06
Range scanned θ (°)	1.68 – 28.31
Index ranges ±*h*, ±*k*, ±*l*	-11, 11; -13, 13; -16, 16
Reflections (total)	29 794
Independent reflections	4920
Reflections with I>2σ(I)	3798
Number of parameters	284
R_{int}	0.0507
S	1.015
R_1 [*I*>2σ(*I*)]	0.0385
Reflections omitted	5
wR_2	0.0989
a, b in w = 1/[$\sigma^2(F_o^2)$+(aP)^2+(bP)]	a = 0.0450; b = 0.4001
$(\Delta/\sigma)_{mean}$	< 0.001
$\Delta\rho_{min,max}$ (e Å^{-3})	-0.338, 0.410

Molecular structure

The asymmetric unit and labelling scheme of MMV monohydrate are shown in Fig. 4.1.29.

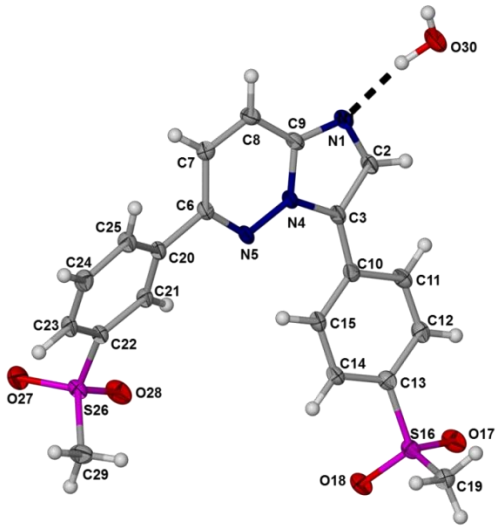

Fig. 4.1.29 The asymmetric unit and numbering scheme of MMV monohydrate with thermal ellipsoids shown at the 50% probability level.

Crystal packing and hydrogen bonding

The H-bonds present in MMV monohydrate are presented in Table 4.1.6 with their related parameters. The cut-off parameters used are the same as those described for Form 1.

Table 4.1.6 Hydrogen bonds in MMV monohydrate[a]

	D–H···A	*d*(D–H), Å	*d*(H···A), Å	*d*(D···A), Å	∠(DHA), deg.
	O30-H30A···N1	0.86(2)	1.98(2)	2.828(2)	167(2)
	O30-H30B···O17^{i} (1)	0.83(3)	2.10(3)	2.905(2)	164(2)
	C11-H11···O27^{ii} (1)	0.95	2.50	3.326(2)	146
Intra	C12-H12···O17	0.95	2.56	2.928(2)	103
	C14-H14···O18^{iii} (1)	0.95	2.56	3.360(2)	143
Intra	C15-H15···N5	0.95	2.29	2.955(2)	126
	C19-H19B···O28^{iv} (1)	0.98	2.42	3.356(2)	161
Intra	C21-H21···O27	0.95	2.53	2.919(2)	105
	C23-H23···O30^{v} (2)	0.95	2.55	3.479(2)	164
	C29-H29B···O30^{v} (2)	0.98	2.33	3.301(2)	169
	C29-H29C···O30^{vi} (2)	0.98	2.51	3.441(2)	158
Intra	C21-H21···N5	0.95	2.50	2.777(2)	97
Intra	C14-H14···O18	0.95	2.69	3.006(2)	100

[a]Symmetry transformations used to generate equivalent atoms: *[i]: -1+x,1+y,z; [ii]: 2-x,1-y,1-z; [iii]: 2-x,-y,1-z; [iv]: x,y,1+z; [v]: x,-1+y,-1+z; [vi]: 1-x,1-y,1-z.*

This form of MMV packs in slightly sloped layers that are stacked in an alternating fashion in terms of the direction in which the molecules are orientated. Each layer is formed by similarly orientated molecules that are arranged in a head-to-tail manner. The various interactions connecting molecules in the same layers are presented in Fig. 4.1.30 and the topology of these layers is presented in Fig. 4.1.37. Water molecules play the role of linkers connecting the molecules in the same layers, though the distinct layers are interwoven by other interactions as well. The water molecules are found in isolated sites (Fig. 4.1.38 and 4.1.39) and are highly H-bonded, playing a key role in holding the structure as a whole together. The interactions connecting the water molecules in the crystal structure are the following: O30-H30A···N1′; O30-H30B···O17′; C23-H23···O30′; C29-H29B···O30′; C29-H29C···O30′ (Fig. 4.1.30). Due to these interactions, these crystals are relatively stable and do not show water loss upon storage at ambient conditions when kept out of the mother liquor. This is also seen in the thermal results presented in a following section.

The layers are connected through interactions between MMV molecules with other MMV molecules as well as through water molecules serving as linkers to form several ring motifs. A ring centred around an inversion centre formed by the interactions C11-H11···O27′ can be described as $\mathrm{R}_2^2(24)$ (Fig. 4.1.32) and connects different layers. A series of rings formed around an inversion centre is presented in Fig. 4.1.33 and can be described by the following: C14-H14···O18′ $\mathrm{R}_2^2(10)$; C19-H19C···O27′ $\mathrm{R}_2^2(32)$; C19-H19A···O18′ $\mathrm{R}_2^2(8)$; C14-H14···O18′ and C19-H19A···O18′ $\mathrm{R}_2^1(7)$ and $\mathrm{R}_2^2(9)$. Other interactions connecting stacked molecules of different layers are the π-π interactions listed in Table 4.1.7 and Fig. 4.1.31. The rings (C20-C21-C22-C23-C24-C25) labelled Cg(D) have a centroid-to-centroid distance of 3.666(1) Å with the closest contacts being between C23 and C25′ (3.383(3) Å) and they are connected at a centre of inversion.

Various ring motifs are formed with water playing a role as a linker. The interactions C29-H29B···O30′ and C23-H23···O30′ $\mathrm{R}_2^1(7)$ are visible in Fig. 4.1.30. Other rings, formed by interactions C29-H29C···O30′ and C23-H23···O30′ $\mathrm{R}_4^2(14)$ and C29-H29C···O30′ and C29-H29B···O30′ $\mathrm{R}_4^2(8)$, are presented in Fig. 4.1.34; more rings are formed by the interactions C29-H29C···O30′ and O30-H30A···N1′ $\mathrm{R}_4^4(26)$ (Fig. 4.1.35) C29-H29C···O30′ and O30-H30B···O17′ $\mathrm{R}_4^4(36)$ (Fig. 4.1.36).

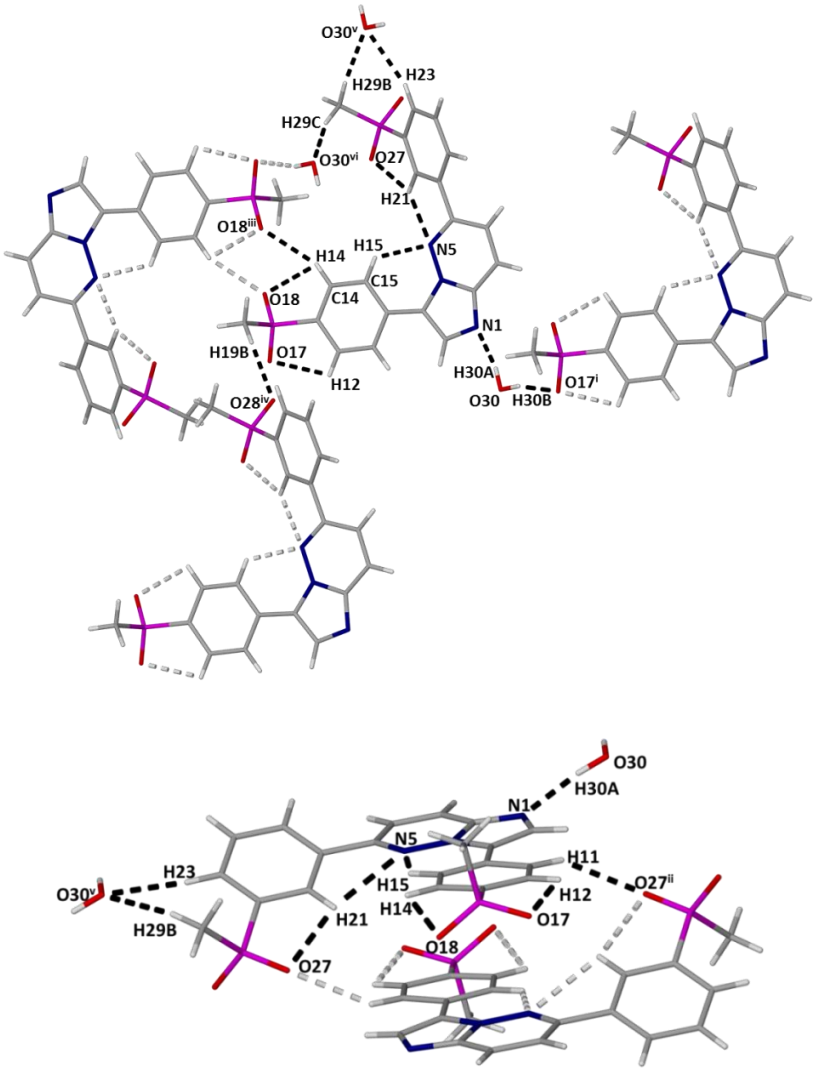

Fig. 4.1.30 Hydrogen bonding interactions found in the structure of MMV monohydrate from different perspectives.

Table 4.1.7 π-π interactions found in MMV monohydrate.

Ring interaction	Centroid-centroid distance, Å	Shortest atom to atom distance	Symmetry operator (refers to second Cg listed in column 1)
Cg(B)···Cg(C)	3.781(1) offset face-to-face	(C8···C15) 3.341(2) Å	2-x,1-y,1-z
Cg(D)···Cg(D)	3.666(1) offset face-to-face	(C23···C25) 3.383(3) Å	1-x,1-y,-z

Ring B: N4-N5-C6-C7-C8-C9

Ring C: C10-C11-C12-C13-C14-C15

Ring D: C20-C21-C22-C23-C24-C25

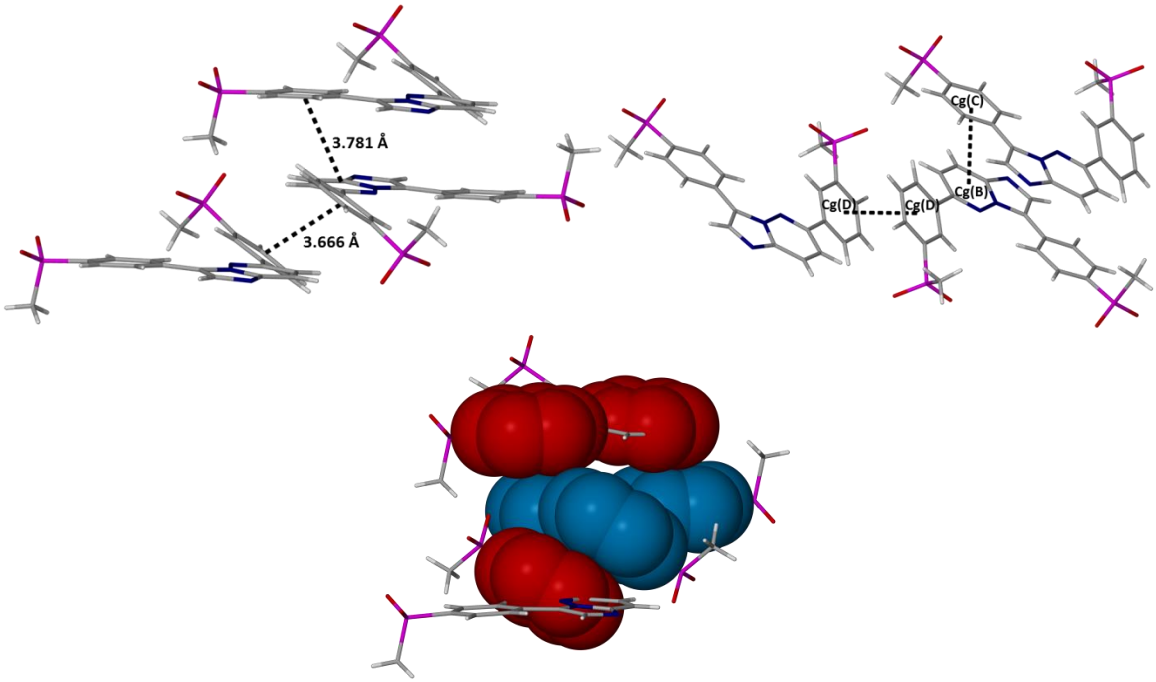

Fig. 4.1.31 π-π interactions connecting layers viewed from different perspectives showing the centroids mentioned in Table 4.1.7 as well as the distances between them. The van der Waals radii of the atoms of the π-stacked rings are shown.

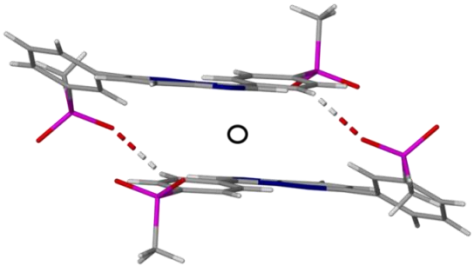

Fig. 4.1.32 Hydrogen bonding pattern $R_2^2(24)$ formed by C11-H11···O27′ around an inversion centre.

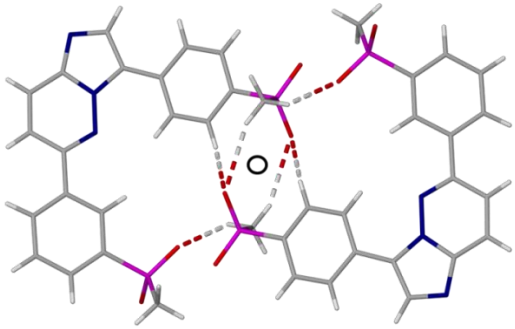

Fig. 4.1.33 Diagram showing various rings connecting MMV molecules in different layers formed around an inversion centre (C14-H14···O18′ $R_2^2(10)$; C19-H19C···O27′ $R_2^2(32)$; C19-H19A···O18′ $R_2^2(8)$; C14-H14···O18′ and C19-H19A···O18′ $R_2^1(7)$ and $R_2^2(9)$.)

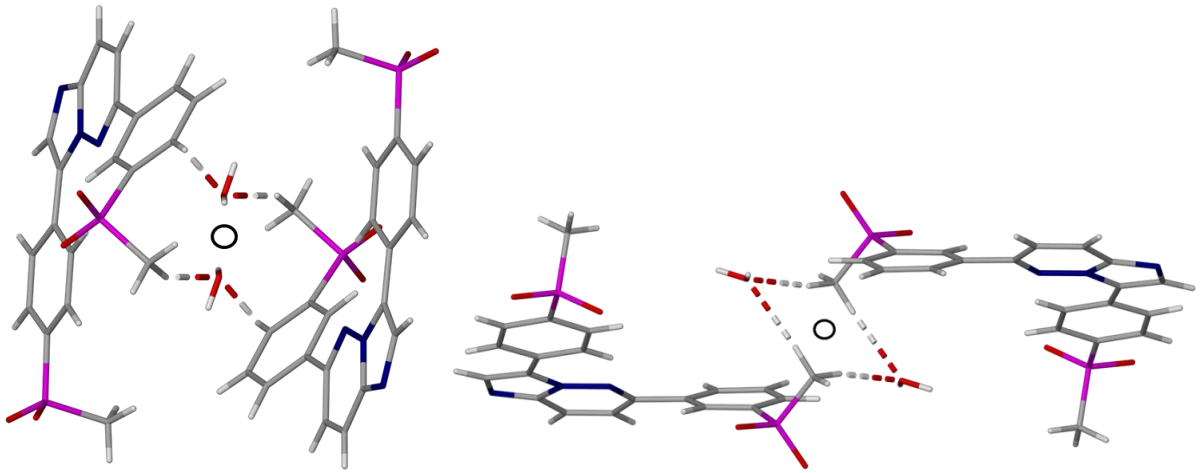

Fig. 4.1.34 Diagram showing rings connecting layers where water molecules serve as linkers. C29-H29C···O30′ and C23-H23···O30′ $R_4^2(14)$(left); C29-H29C···O30′ and C29-H29B···O30′ $R_4^2(8)$(right).

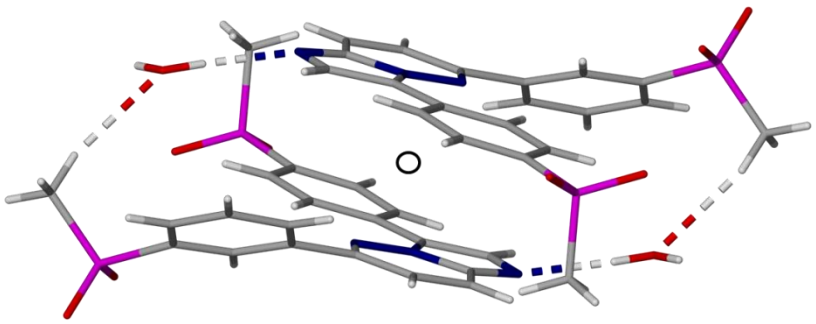

Fig. 4.1.35 C29-H29C···O30′ and O30-H30A···N1′ $R_4^4(26)$

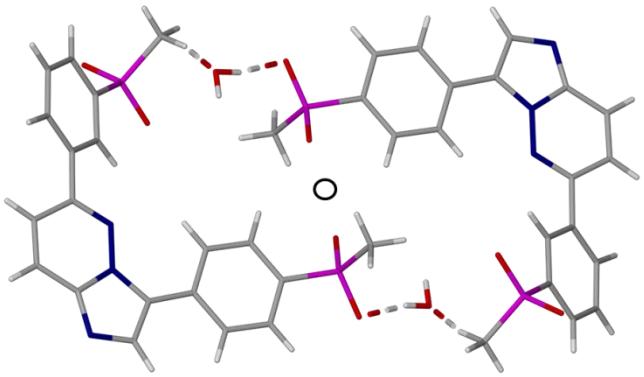

Fig. 4.1.36 C29-H29C···O30′ and O30-H30B···O17′ $R_4^4(36)$

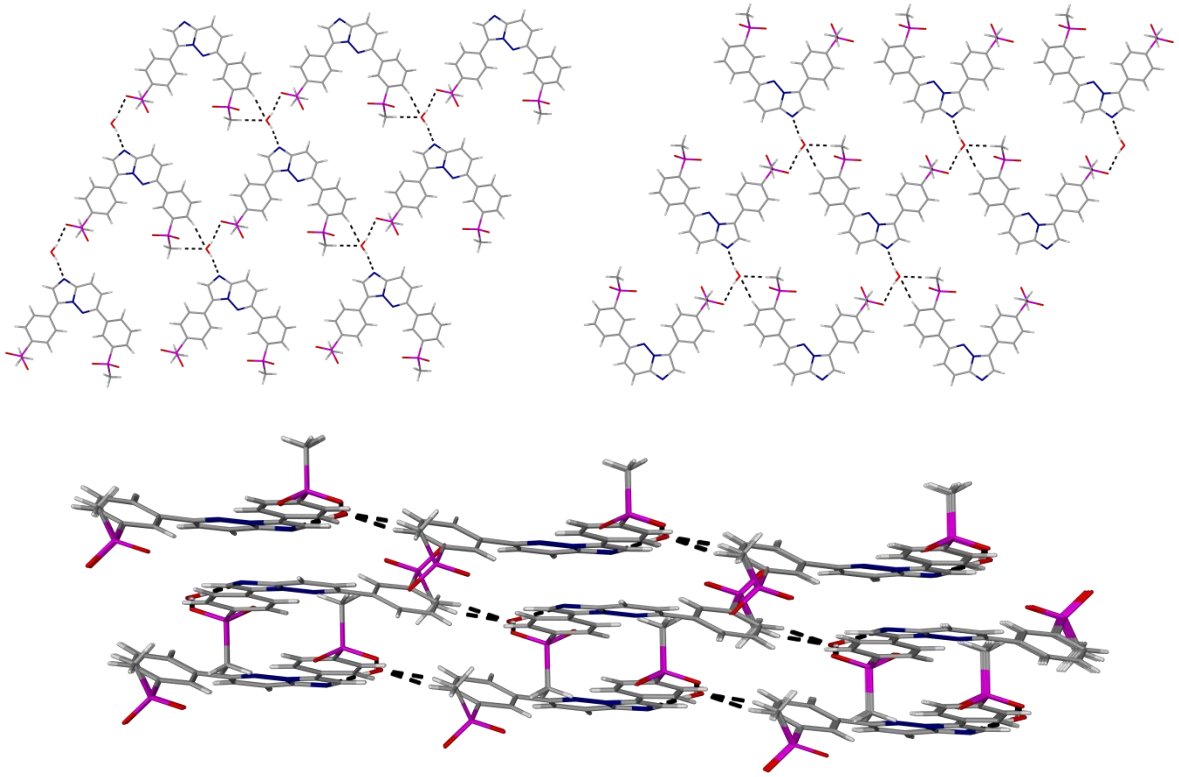

Fig. 4.1.37 Diagram showing individual alternating sloped layers of MMV monohydrate viewed roughly normal (top) to the imidazopyridazine ring and a roughly parallel view of stacked layers (bottom).

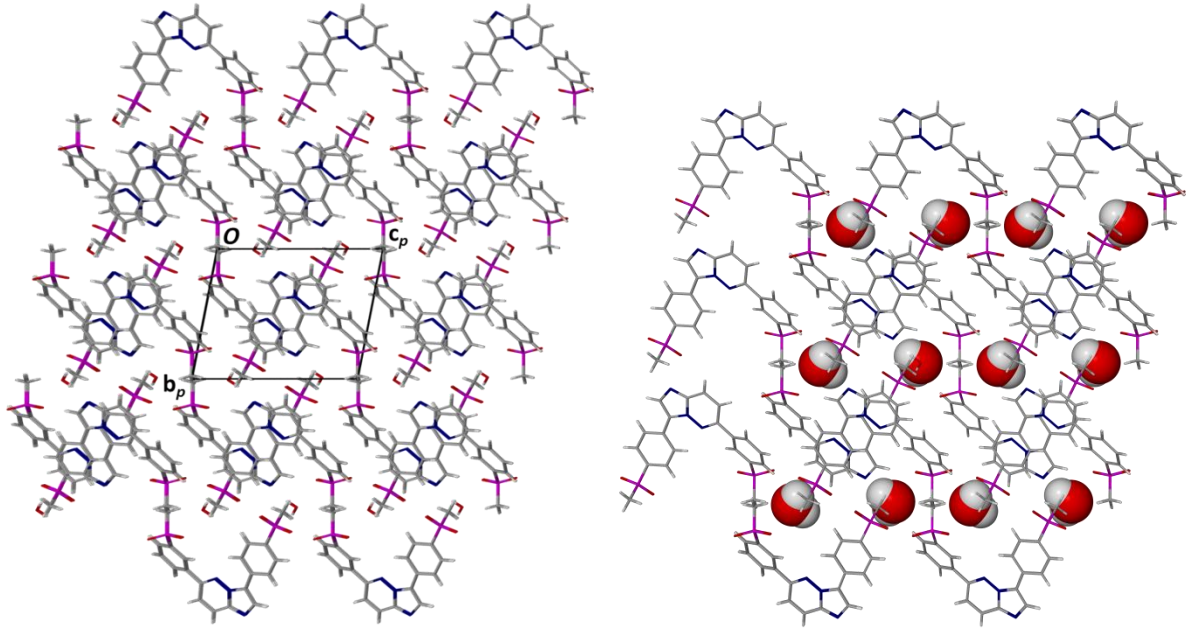

Fig. 4.1.38 Packing of MMV Hydrate viewed along [100] showing water as space-fill model.

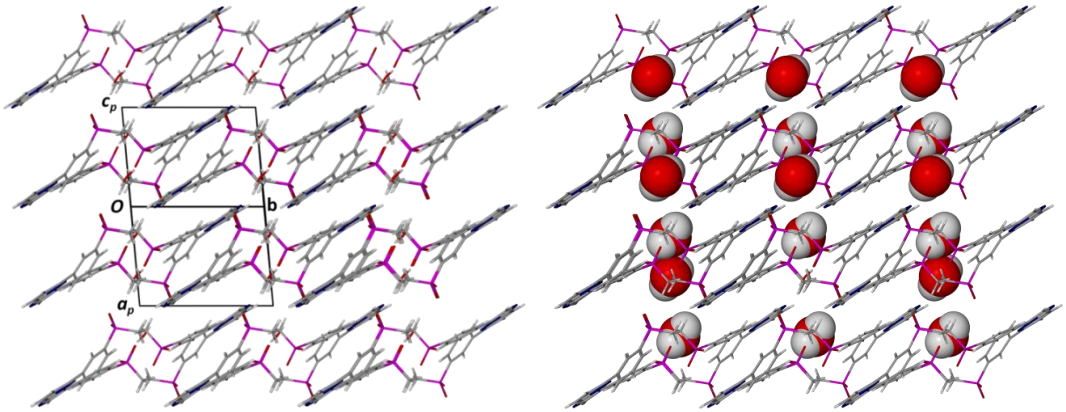

Fig. 4.1.39 Packing of MMV monohydrate showing water as space-fill model.

Powder X-ray diffraction

The following describes the method used to produce MMV monohydrate crystals in bulk. MMV RM was dissolved in acetone by heating the solution to around 40 °C while continuously stirring. The hot solution was then filtered through a 0.45 µm nylon filter into a clean vial and a small volume of water was subsequently added to the filtered solution. The vial was covered with parafilm™ with holes poked in it and left on a benchtop. The resulting crystals were gently ground and the PXRD trace was collected. The experimental PXRD trace is compared to the trace produced by generating a PXRD trace from the solved crystal structure of MMV monohydrate in Fig. 4.1.40. The matching traces show that this method successfully produced MMV monohydrate and it was subsequently used to produce this form for further experimentation.

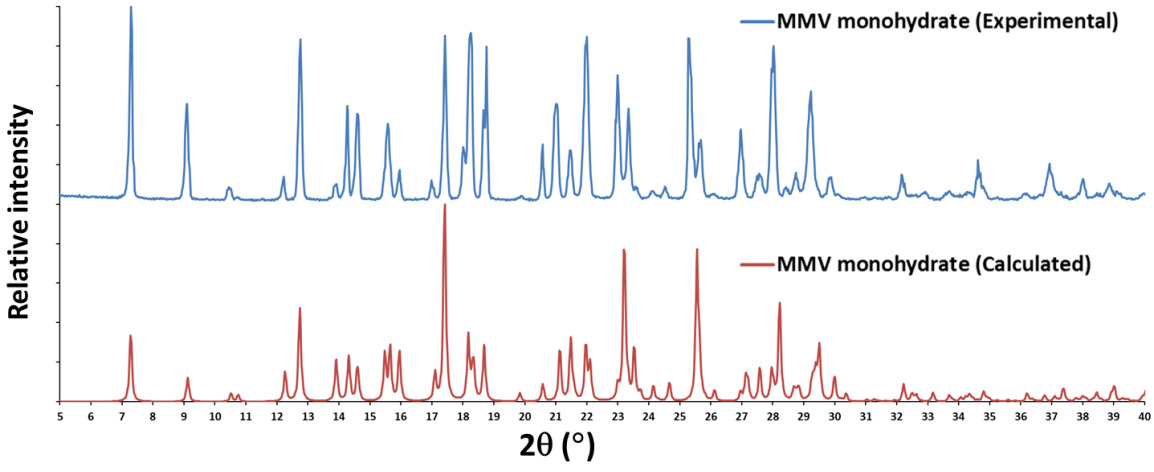

Fig. 4.1.40 Comparison of experimental and calculated PXRD traces of MMV monohydrate.

Thermal analysis

The HSM results (Fig. 4.1.41) show the crystals going opaque from roughly 100 °C with deformation and bubbling at higher temperatures (above 160 °C). By 255 °C it appears as though melting has started with thin needle-like crystals (visible at the bottom of the HSM image at 255 °C, Figs. 4.1.41 and 4.1.42) simultaneously forming. By 265 °C the crystals are mostly melted. In the DSC trace (Fig. 4.1.43) there are at least four distinct events visible. The first event (labelled A in Fig. 4.1.43) shows a broad endotherm spanning a range from roughly 70 to 120 °C and agrees with the temperature range where mass loss is visible in the TGA trace (Fig. 4.1.44). The mass loss, broad endotherm as well as bubbling occurring serve as evidence of solvent loss. The events occurring around the boiling point of water and being present in crystals obtained from different solvents would suggest that water is the most likely possibility. The mass loss of 3.8 $\pm$ 0.2 % (n = 3) observed through TGA equates to 1 molecule of water for every molecule of MMV (the calculated percentage is 4.0). This matches the ratio seen in the SCXRD results. The way in which the water molecules are highly H-bonded and play a significant role in the structural integrity of the crystals, as is apparent from the interactions explained in the crystal packing and hydrogen bonding section, would explain why the some of the water only gets released well above its boiling point.

The second event labelled B in Fig. 4.1.43 starts off as an endothermic event, but appears to be curtailed by an exothermic peak. The temperature at which these overlapping events occur does not match any of those seen with the other forms of MMV and at this point it was assumed that a new phase was present from directly after the water loss of the hydrated form up to this event. A variable-temperature PXRD experiment was carried out on MMV monohydrate and is presented in Fig. 4.1.46. The calculated PXRD traces for each form are presented in Fig. 4.1.45 to facilitate comparison of the VTPXRD results. The VTPXRD experiment was started with unground MMV monohydrate for the reason that there was concern that grinding might result in loss of water from the sample. It is for this reason that the PXRD trace seen at the starting temperature of 25 °C has different peak intensities from those seen in the calculated trace and is due to the effect of preferred orientation. This experiment was repeated with the MMV monohydrate sample ground prior to commencement and the result is to be found in the supplementary section. The trace recorded at 150 °C clearly differs from the trace of the hydrated form, though at first glance resembles the trace for Form 2. Three peaks with high intensity for Form 2 at 14.0, 15.2, and 16.5 °2θ respectively are also visible in the trace of the form seen after dehydration of the hydrate. There were however also new peaks visible at 8.3 and 27.3 °2θ and some of the other peaks seen with Form 2 were not visible. At this stage it was thought that the form present from 130 to 190 °C

was either a new phase or a mixture of phases, likely consisting of a sizeable portion of Form 2. This metastable form of MMV, hereafter referred to as Form 3, is further discussed in a subsequent section of this chapter. The PXRD trace after the event labelled B matches the trace for Form 2 and this indicates that after the event, Form 2 was the most abundant form present and that a transition to this form had occurred.

The third event (labelled C in Fig. 4.1.43) that is visible in the DSC trace is a sharp endotherm leading into an exothermic event. This event matches the melting onset temperature of Form 2 and shows a similar pattern to that observed when heating Form 2 containing traces of Form 1. This is consistent with the variable temperature PXRD experiment.

The fourth event visible (labelled D in Fig. 4.1.43) occurs at the temperature at which Form 1 melts. The formation of small needle-like crystals visible in the HSM results and the PXRD trace at 240 °C matching that of the pure Form 1 is proof that a transition has taken place to Form 1 before the onset of melt for this form.

Hot stage microscopy

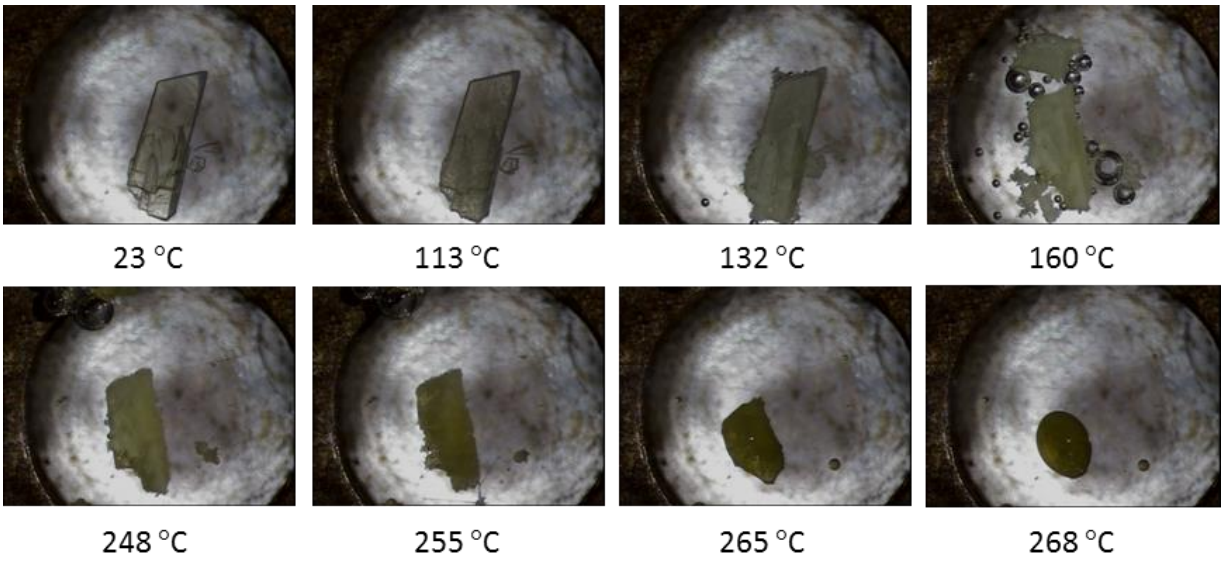

Fig. 4.1.41 HSM photographs of MMV monohydrate crystals at various temperatures.

Fig. 4.1.42 Enlarged image of the HSM photograph taken at 255 °C.

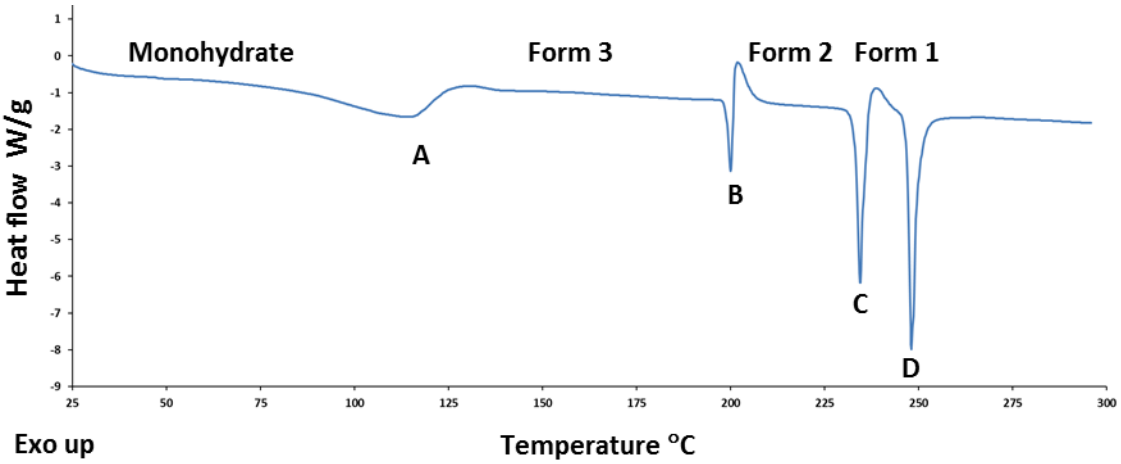

Fig. 4.1.43 Representative DSC trace for MMV monohydrate.

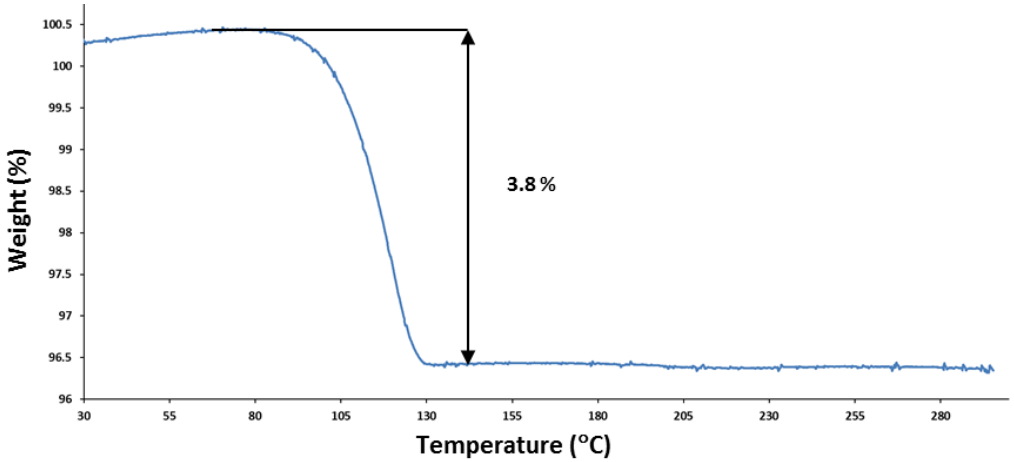

Fig. 4.1.44 Representative TGA of MMV monohydrate.

Powder X-ray diffraction

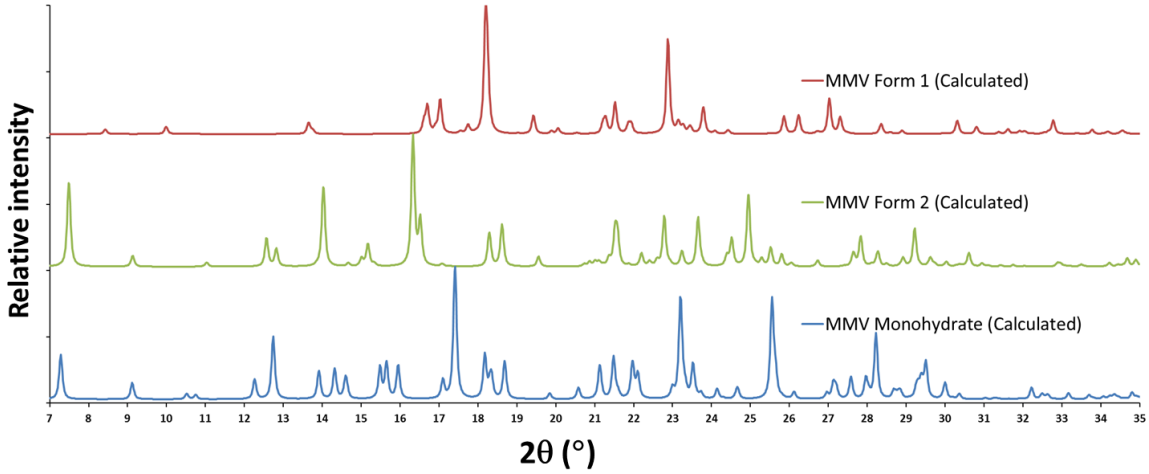

Fig. 4.1.45 Calculated PXRD traces for MMV monohydrate and two polymorphic forms.

Variable temperature powder X-ray diffraction

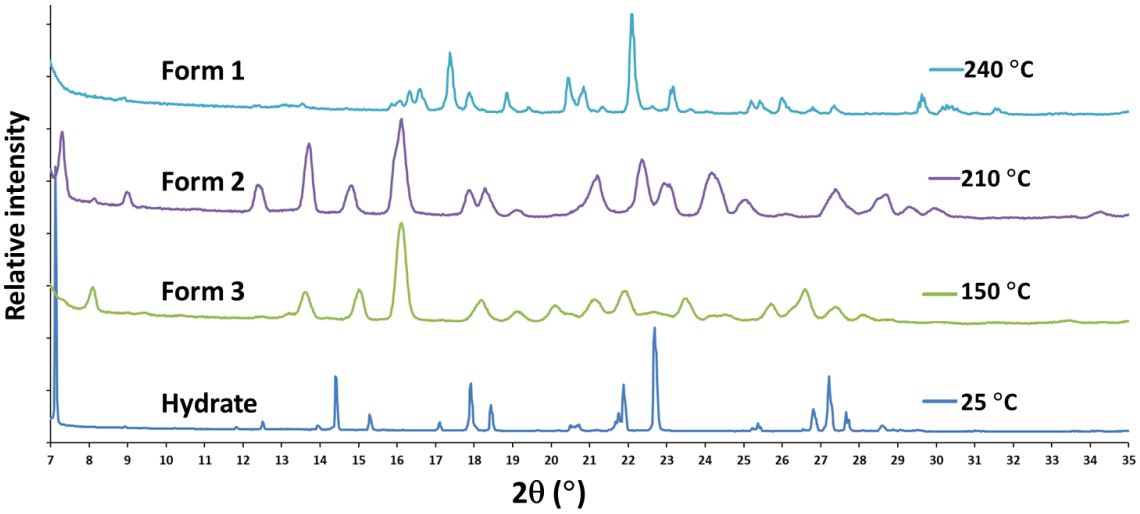

Fig. 4.1.46 Variable-temperature PXRD showing the sequence of events starting with MMV monohydrate.

MMV Form 3

This metastable polymorphic form was serendipitously discovered during a DSC experiment of the monohydrated form as was discussed in the previous section. In attempts to bulk up the quantities of this form for further characterisation, an open DSC pan was used and the monohydrated form was heated to 135 °C at 20 K min^{-1}. This resulted in a mixture consisting of mostly Form 3, but with small

traces of Form 2 being present. It was thought that the heating may have led to some of the hydrate transitioning directly into Form 2. To avoid this thermally induced transition, a freeze-drying method was applied where the sample of the hydrated form was cooled to -60 °C under vacuum with a VirTis® BenchTop™ "K" Series Freeze Dryer (SP Industries, Inc., Warminster, Pennsylvania) to dehydrate the monohydrate without applying heat. This resulted in the formation of pure Form 3 and this method was used from this point onward to produce this form. No single crystals of adequate size and quality were obtained for structure elucidation by single-crystal XRD and PXRD was relied on to determine phase purity.

Thermal results

HSM results are presented in Fig. 4.1.47. At 200 °C the powder appears to start melting on the periphery of the images. The image recorded at 208 °C shows that some of the powder is melted near the centre and the powder on the outside has already solidified. By 215 °C the bulk of the powder has undergone the transition that appeared to be radiating inward in the previous images. (The reason why the visible changes occur from the outside inward is due to the centre of the images being situated on top of a window made for the passage of light from the bottom. The window will thus be at a slightly lower temperature than the heating block surrounding it). By 250 °C the solid has started to melt again starting from the edges and by 260 °C the entirety of the sample has melted.

The DSC results (Fig. 4.1.48) show an event with an onset temperature of 193.8 $\pm$ 0.8 °C (n = 3) that relates to the onset of melting seen in the HSM results. The endotherm appears to be abruptly curtailed by the onset of an exothermic event. The enthalpy of this event could not be accurately measured due to its incongruent nature. A second event, showing a sharp endotherm with an onset of 244.8 $\pm$ 0.2 °C (n = 3) and a peak at 246.9 $\pm$ 0.1 °C (n = 3) matches the temperatures previously noted for the melt of Form 1. The DSC results together with the HSM results indicate an onset of melting of the Form 3 powder leading into the recrystallisation of Form 1. The next event is that of the Form 1 melting. In this case no sign of Form 2 was present in the DSC traces. This serves as additional evidence of Form 3 being a distinct polymorphic form.

The TGA results for this form are shown in Fig. 4.1.49. A small mass loss starting at the commencement of heating up to 100 °C of 0.86 $\pm$ 0.07 % (n = 2) is observed. This could be due to residual water that had not been completely removed by the freeze-drying process or possibly due to adsorption of moisture from the air to the surface of this highly hygroscopic crystalline powder. Determining how much water is

taken up from the atmosphere over time and how this will affect the stability of this form upon storage was not determined and would definitely be vital information to have if this crystalline modification is to be considered a potential form to use in formulation of a completed product.

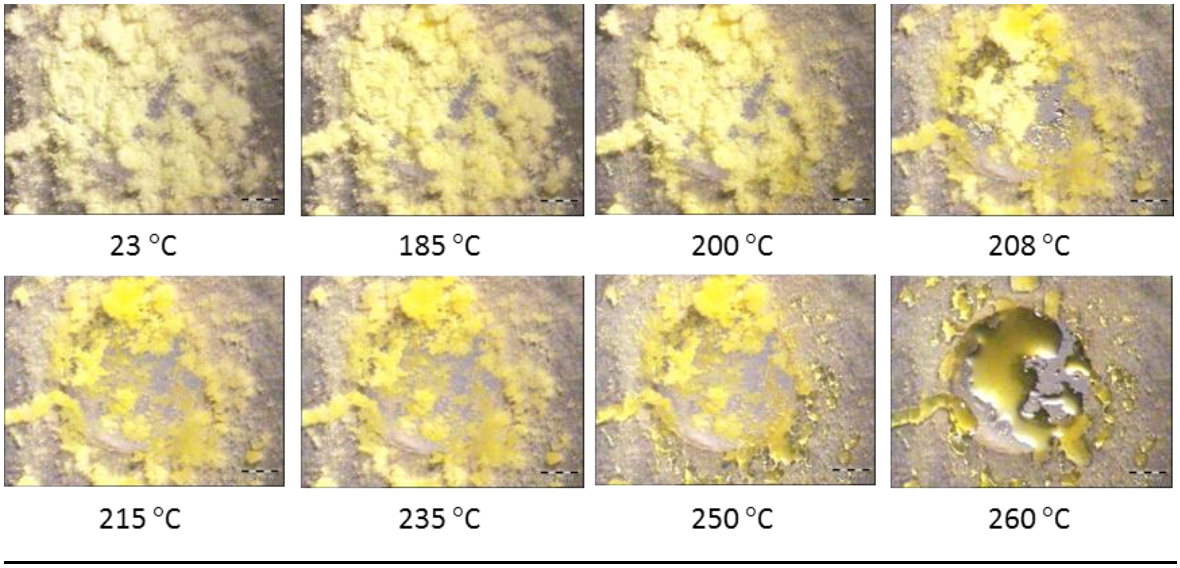

Fig. 4.1.47 HSM photographs of MMV Form 3 as crystalline powder at various temperatures.

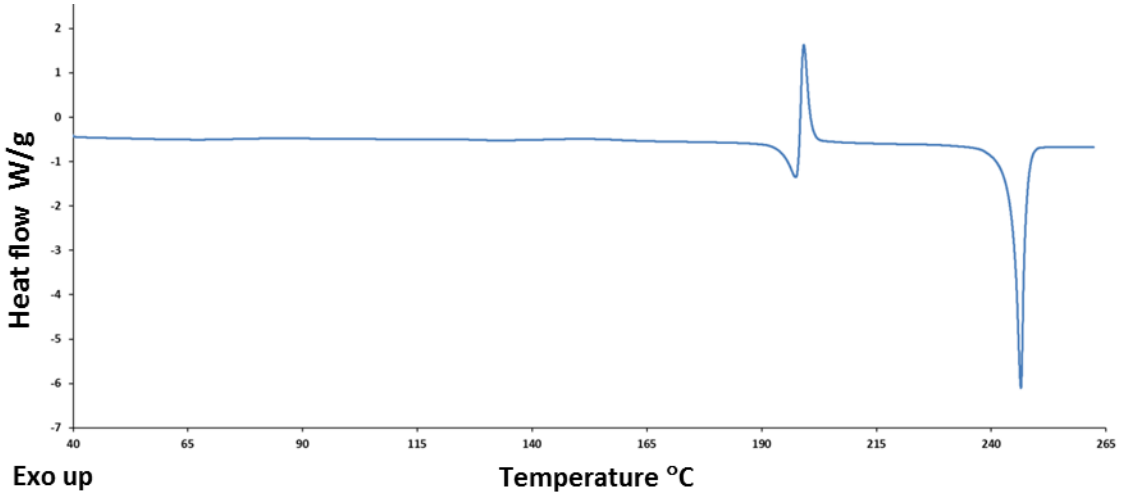

Fig. 4.1.48 Representative DSC trace for MMV Form 3.

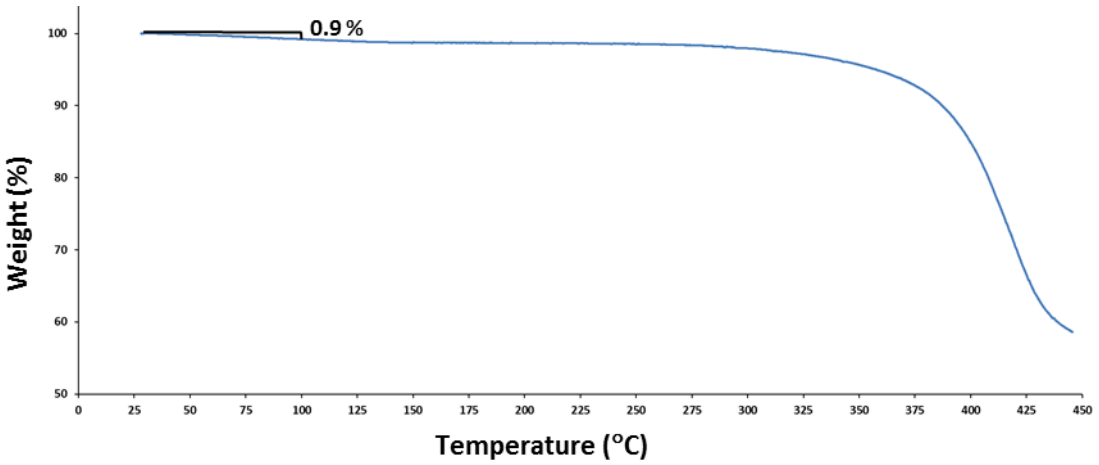

Fig. 4.1.49 Representative TGA of MMV Form 3.

Powder X-ray diffraction

PXRD traces of the various forms of MMV are presented in Fig. 4.1.50. The differences that were pointed out when describing the changes witnessed in the VTPXRD of MMV monohydrate, namely the peaks at 8.3 and 27.3 °2θ, are visible here. The similarities between the PXRD traces of Form 2 and Form 3 with relatively high intensity peaks at 14.0, 15.2, and 16.5 °2θ in both cases are plain to see. With the DSC results showing no trace of Form 2, the possibility of the common features arising from a mixture being present is ruled out. This shows that the similarities are coincidental and assumed to be due to similar packing features.

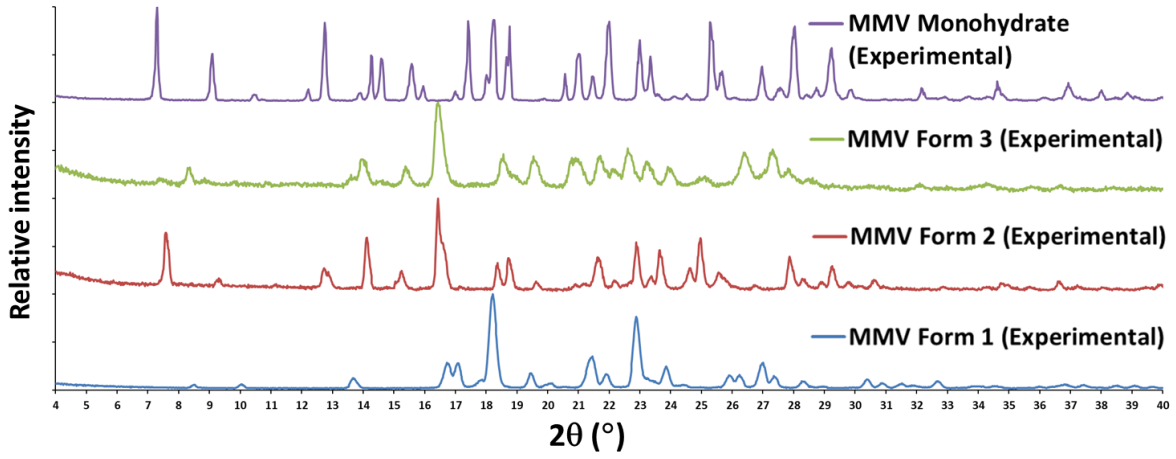

Fig. 4.1.50 Comparison of experimental PXRD traces of the various forms of MMV.

MMV Form 4

After melting and subsequently cooling any of the previously mentioned forms of MMV, a brittle glass is formed by vitrification. This amorphous form is referred to as Form 4 hereafter. This was noticed in a DSC experiment where the sample was cooled after melting with no clearly visible signs of recrystallisation. The TGA results showed that the onset of decomposition is much higher than the melting temperatures of any of the known forms and it was presumed that the product was not a result of decomposition. The method used to prepare this form for further characterisation was by heating the MMV starting material to 255 °C at a heating rate of 50 K min^{-1} in an open DSC pan. The cooling rate was not controlled and the glass-forming ability of this compound was found to be good enough that no extra steps need be taken to exceed the critical cooling rate for the glass to form.

Powder X-ray diffraction

The experimental PXRD trace for MMV Form 4 is presented in Fig. 4.1.51. The featureless trace with a broad low intensity hump, also known as the diffuse "halo" effect, is indicative of an amorphous form that lacks long-range crystalline order.

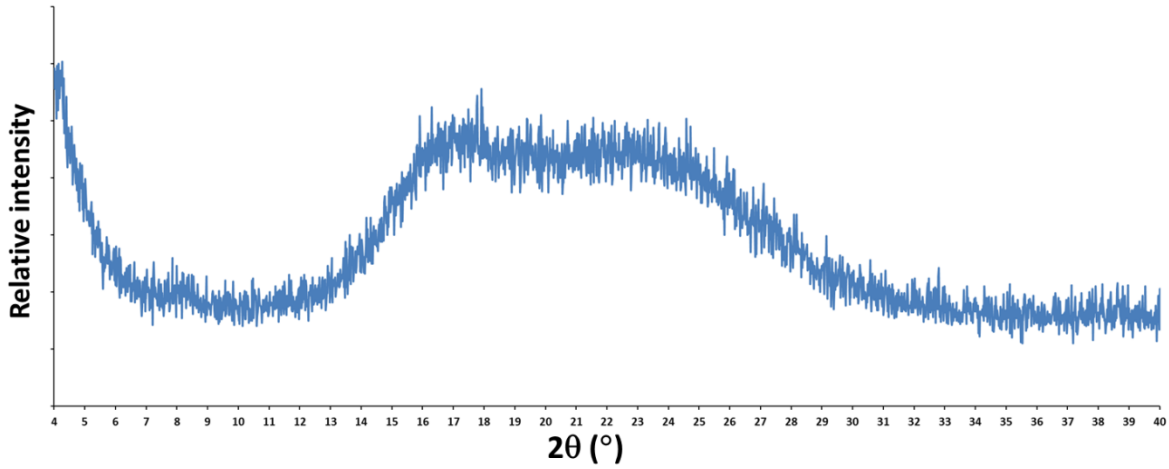

Fig. 4.1.51 Experimental PXRD trace of MMV Form 4.

Thermal results

HSM results for MMV Form 4 are presented in Fig. 4.1.52. The glass appears to undergo a phase change from a brittle solid to a fluid state as is visible in the micrographs at 140 °C. The next observable change is resolidification starting around 150 °C and in the micrograph taken at 200 °C the sample has

completely solidified. At 250 °C the onset of melting is observed and by 258 °C the sample has completely melted.

Hot stage microscopy

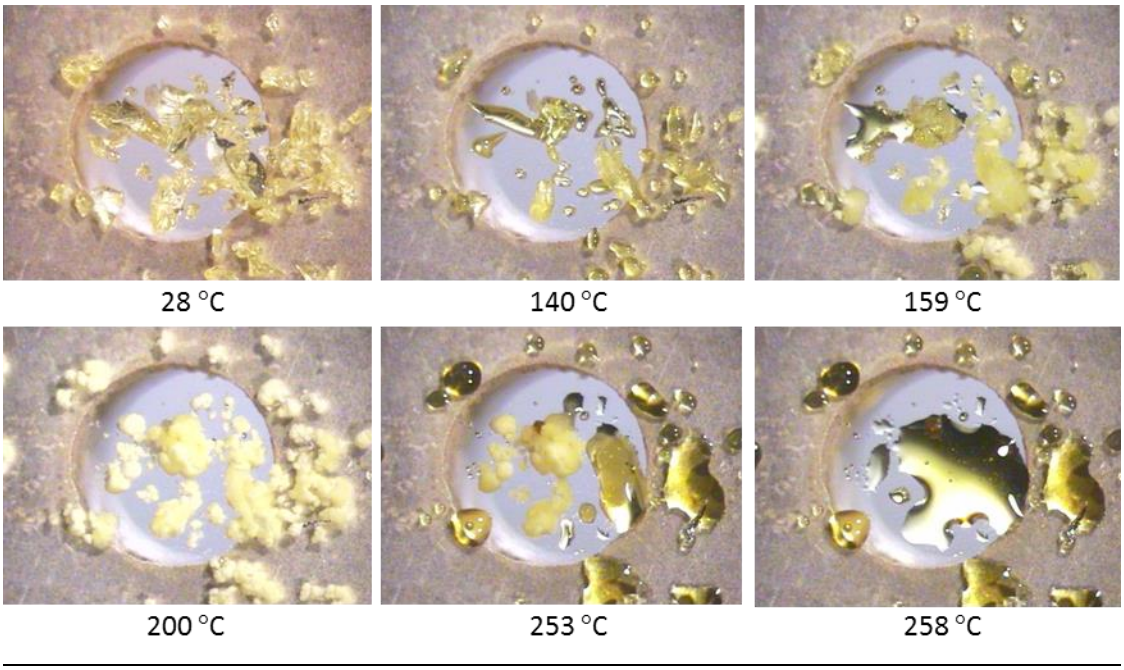

Fig. 4.1.52 HSM photographs of MMV Form 4 at various temperatures.

The DSC result for MMV Form 4 is presented in Fig. 4.1.53. An event labelled A in Fig. 4.1.53 has the signature appearance of a glass transition (T_g) with a midpoint calculated at half height of 103.6 ± 2.5 °C (n = 3). This event correlates with the visual changes observed in the HSM result.

The enthalpy of this event will be dependent on the thermal history of the sample as a glass will undergo enthalpic relaxation over time as it moves closer to equilibrium and energy is released as the system becomes more ordered. This process will occur at a greater rate the closer the storage temperature is to T_g. The Kauzmann temperature (T_K)[7,8] denotes the temperature below which most translational molecular motion will be reduced to a point where physical and chemical changes in pharmaceutical products can be considered negligible over experimental timescales. It is assumed that molecular motion will continue to decrease as temperature is reduced further below T_g until it reaches a minimum at T_K. There are numerous proposed methods to calculate this value, the simplest approximation of which is possibly T_g - 50 K.[9] The relatively high T_g of this glass should lend a degree of thermal stability to it and if kept at room temperature the processes of enthalpy relaxation should be

relatively slow. Another factor that could speed up the rate of transition to more stable forms is humidity.

The T_g value will depend on the heating rate used as the macro-molecular motion of the sample is time-dependent and slower heating rates would result in more time spent at temperatures closer to T_g where more motion and also enthalpic relaxation will be possible.

Substances showing large heat capacity changes at T_g are termed fragile, while smaller and consequently harder to detect changes are associated with strong glasses.[9] The fragility of MMV Form 4 is determined to be relatively high from the "rule of thumb" described by Kaushal and Bansal[9] (The calculated T_m/T_g ratio for MMV Form 4 is lower than 1.5).

An exothermic event (labelled B in Fig. 4.1.53) is seen with an onset temperature of 160.7 ± 7.1 °C (n = 3), a peak at 173.6 ± 9.4 °C (n = 3), and an enthalpy related to the event of -73.2 ± 1.6 J g^{-1}. This matches the temperature at which the HSM sample recrystallised. An endothermic event (labelled C in Fig. 4.1.53) is seen with an onset at 242.6 ± 1.8 °C (n = 3), a peak at 246.0 ± 1.0 °C (n = 3), and enthalpy of 95.4 ± 3.7 J g^{-1}. This matches the temperature in the HSM micrographs where the sample melts and the melting temperature of MMV Form 1. An explanation of the events is that the amorphous solid undergoes T_g at A, recrystallises into the higher melting Form 1 at B and finally melts at C.

Differential scanning calorimetry

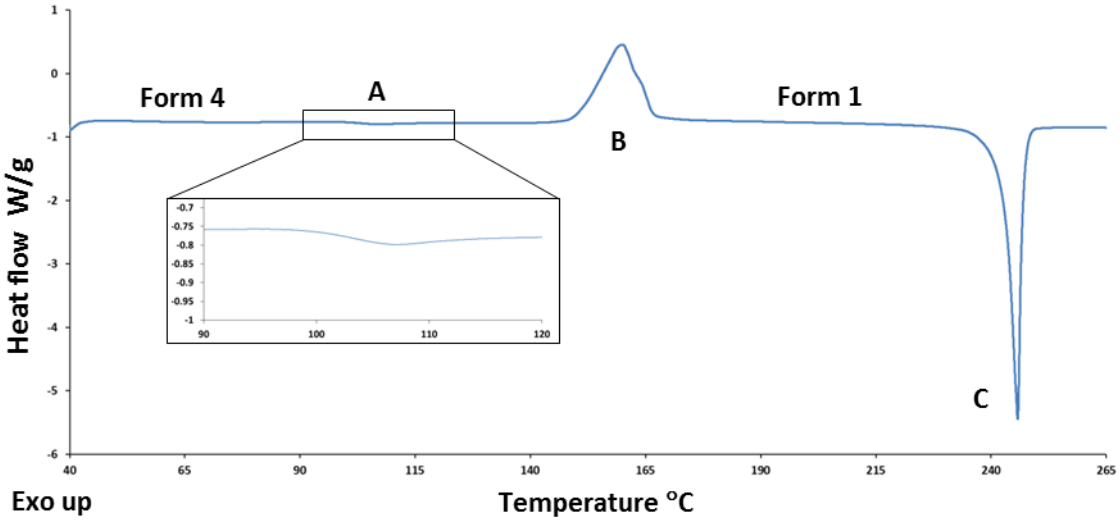

Fig. 4.1.53 Representative DSC trace for MMV Form 4.

The explanation for the difference in the enthalpy of crystallisation (ΔH_{CR}) and the eventual enthalpy of fusion (ΔH_f) is that for an amorphous material, enthalpy will increase at a higher rate upon heating than for its crystalline counterpart. This is visualised in Fig. 4.1.54. This will inevitably result in the ΔH_{CR} being less than the ΔH_f, because the temperature of crystallisation (T_{CR}) is between the T_g and the melting point (T_f). Lefort *et al*. have shown how these values can be experimentally quantified.[10]

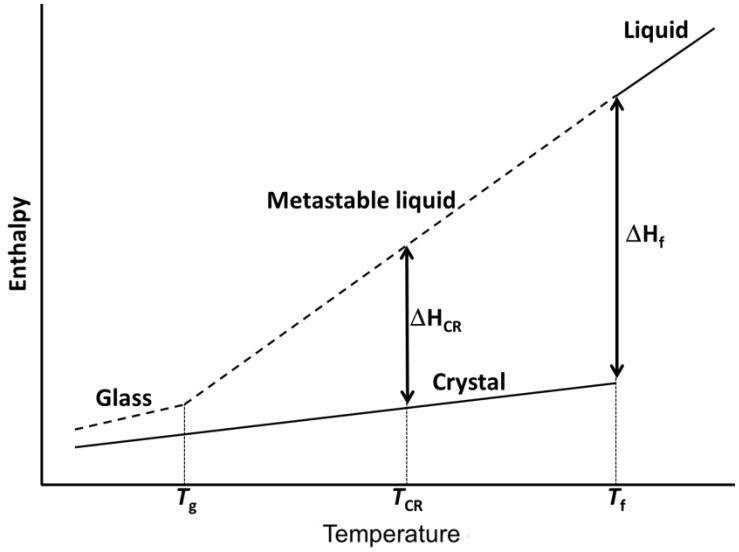

Fig. 4.1.54 Schematic representation of enthalpy/temperature for crystalline and amorphous forms of the same material (Adapted from Lefort *et al*., 2004)[10]

A modulated DSC result for MMV Form 4 is presented in Fig. 4.1.55. Measurements were done by conventional MDSC with an underlying heating rate of 3 K min^{-1}, modulation period of 60 s, an amplitude of $\pm$ 1 K, and sample masses ranging from 1.78-2.64 mg. When considering the trace for total heat flow the first visible event is the T_g with a midpoint at half height at 103.4 °C $\pm$ 0.8 °C (n = 3), that was also visible in the DSC result. This heat flow resembles that of the DSC experiment and shows an endothermic dip after the glass transition that is due to enthalpy recovery where the energy lost during enthalpy relaxation is recovered. The next visible event in the total heat flow trace is that of crystallisation at 176 °C $\pm$ 18 °C (n = 3). MDSC makes it possible to deconvolute the signal into reversing and non-reversing heat flow to separate the concomitantly occurring thermodynamic events namely the T_g and enthalpy relaxation. The reversing heat flow signal shows only the T_g and another change in heat capacity at a higher temperature as a result of crystallisation whereas the non-reversing heat flow signal shows the enthalpy recovery and the enthalpy involved in crystallisation. The normalised reversing C_p

signal displays a relatively large step increase at T_g. This is common for glasses with high fragility.[9] A stepped drop to a C_p value slightly lower than that seen for the glass occurs during recrystallisation. The small difference in the C_p values when comparing Form 4 and Form 1 (an unstable amorphous and a highly stable crystalline form respectively) during this experiment would show why it is often difficult to measure different C_p for forms that have similar thermodynamic stabilities.

The TGA result (Fig. 4.1.56) shows a small mass loss between the starting temperature and 100 °C of 0.80 ± 0.06 % (n = 2). This could be due to some moisture adsorbed on the surface of the amorphous powder. The onset of decomposition starts at 389.4 ± 0.3 °C (n = 2). This value is very close to the decomposition onset seen for the other forms.

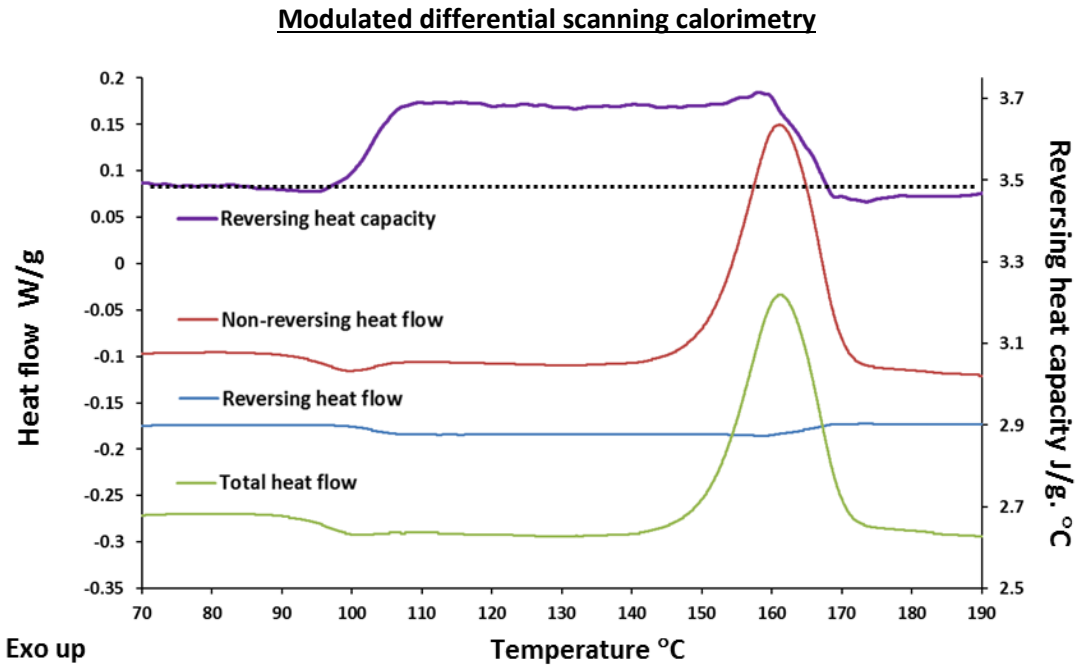

Fig. 4.1.55 Representative MDSC trace for MMV Form 4 showing total, reversing and non-reversing heat flow and reversing heat capacity.

Thermogravimetric analysis

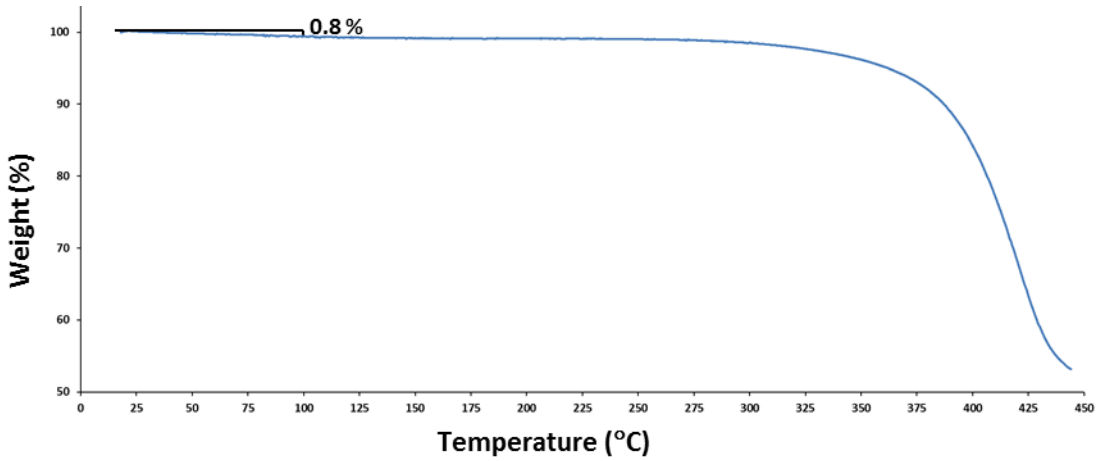

Fig. 4.1.56 Representative TGA of MMV Form 4.

Comparison of various polymorphs of MMV

The stacked DSC results are presented in Fig. 4.1.57 to facilitate comparison. The thermal data are summarised in Table 4.1.8.

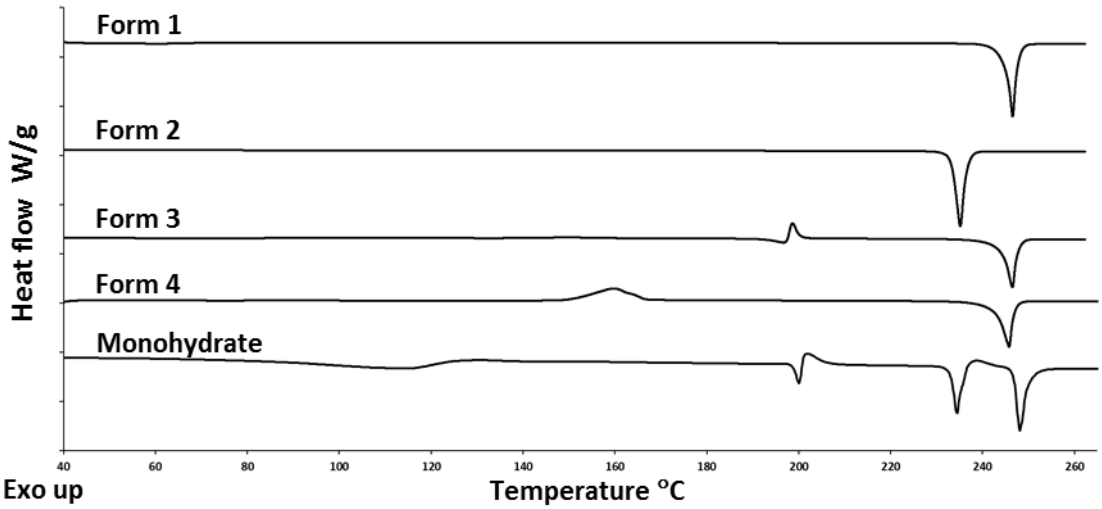

Fig. 4.1.57 Stacked DSC traces for different forms of MMV obtained by DSC.

Table 4.1.8 Thermal data for different forms of MMV obtained by DSC and MDSC.

Datum	Form 1	Form 2	Form 3	Form 4
Melting point onset [°C]	245.0 ± 0.5	233.5 ± 0.1	193.8 ± 0.8	-
Enthalpy of fusion [kJ mol^{-1}]	47.8 ± 2.8	49.0 ± 0.8	*b*	-
Entropy of fusion[a] [J K^{-1} mol^{-1}]	92.3 ± 10.3	96.8 ± 1.6	*b*	-
Glass transition (midpoint MDSC) [°C]	-	-	-	103.4 ± 0.8

[a] Calculated from $\Delta S_f = \Delta H_f/T_m$. [b] Unobservable.

Calculating thermodynamic transition points (T_t)

Many examples[11-14] can be found in the literature that show how one can successfully approximate the order of transition points and determine whether different forms are monotropically or enantiotropically related by making use of expression (4.1.1), given that one has sufficiently accurate thermochemical data. The data required are melting points, heat capacities, and enthalpies of fusion.

$$\boldsymbol{T_t} = \frac{\boldsymbol{\Delta H_{f,2} - \Delta H_{f,1} + (C_{p,liq} - C_{p,1})(T_{f,1} - T_{f,2})}}{\frac{\boldsymbol{\Delta H_{f,2}}}{\boldsymbol{T_{f,2}}} - \frac{\boldsymbol{\Delta H_{f,1}}}{\boldsymbol{T_{f,1}}} + \boldsymbol{(C_{p,liq} - C_{p,1}) ln}(\frac{\boldsymbol{T_{f,1}}}{\boldsymbol{T_{f,2}}})} \qquad (4.1.1)$$

In the absence of highly-accurate heat capacity values the difference in heat capacities for the higher melting form and the liquid ($C_{p,liq}$-$C_{p,1}$) can be substituted with an empirical correction term $k\Delta_{fus}H_1$ resulting in the simplified expression (4.1.2). Yu[13] states that the value for *k* typically ranges from 0.001 to 0.007 K^{-1} with a maximum of 0.005 K^{-1} according to Burger and Ramberger.[11,12] A *k* value of 0.003 K^{-1} is used for the following calculations.

$$\boldsymbol{T_t} = \frac{\boldsymbol{\Delta H_{f,2} - \Delta H_{f,1} + k\Delta H_{f,1}(T_{f,1} - T_{f,2})}}{\frac{\boldsymbol{\Delta H_{f,2}}}{\boldsymbol{T_{f,2}}} - \frac{\boldsymbol{\Delta H_{f,1}}}{\boldsymbol{T_{f,1}}} + \boldsymbol{k\Delta H_{f,1} ln}(\frac{\boldsymbol{T_{f,1}}}{\boldsymbol{T_{f,2}}})} \qquad (4.1.2)$$

where T_t is the transition temperature (K), T_f is the melting point (K), ΔH_f is the enthalpy of fusion (kJ mol^{-1}), and C_p is the heat capacity (kJ K^{-1} mol^{-1}).

Solubility experiments

A solubility experiment was carried out to compare the aqueous solubilities of the various polymorphic forms of MMV at room temperature. Due to the hydrophobic nature of the compound, a solvent medium of 25 % v/v of ethanol was used for this experiment. A standard curve was set up by making use of ultraviolet-visible (UV-vis) spectrophotometry as described in Chapter 2 by making use of a 50 % v/v ethanol solution, where the compound was dissolved in pure ethanol and incrementally diluted with

water to 50 % v/v to prevent precipitation of the drug. The experiment was set up so that three separate vials containing an excess of the respective phase pure samples were stirred at 500 rpm at 25 ± 0.5 °C to be assayed at intervals of 1.5, 24, and 72 hours. The results are presented in Fig. 4.1.58. The solubility ranking was constant throughout this experiment, with Form 1 surprisingly having a much higher solubility than the other forms and Form 3 having the lowest solubility. This result was unexpected as the stability ranking information obtained from thermal experiments of the various forms would suggest very different results. A possible explanation was that solvent-mediated transformations may have had an effect on the outcome. The products of the various vials were analysed by PXRD to determine which phases were present at each stage of the experiment. The products of the Form 1 and Form 2 vials had remained phase-pure throughout the experiment up to 72 hours. Unsurprisingly Form 3, which is a metastable dehydrated form of the monohydrate, transitioned back to the hydrated form in this mostly aqueous medium. What was surprising though is that near complete conversion from Form 3 to the hydrate had taken place by the 1.5 hour mark, with traces of Form 2 present as well. It was thus deemed necessary to repeat the experiment in a solvent medium where water is absent to prevent the formation of the hydrated form. At the time this experiment was carried out Form 4 had not been discovered and for this reason was not added to the results.

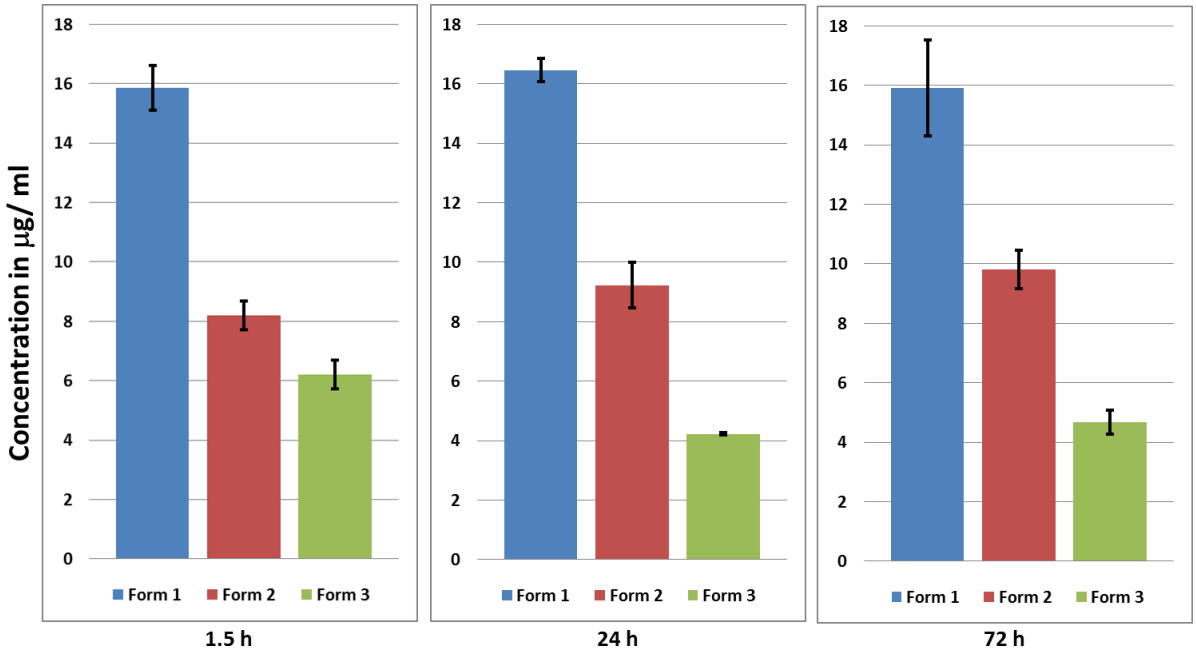

Fig. 4.1.60 Chart displaying MMV concentrations in 25% ethanol at 25 ± 0.5 °C after 1.5, 24, and 72 h of stirring.

The experiment described in the preceding paragraph was repeated with methanol (99.5 %) as solvent medium and the results are presented in Fig. 4.1.59, the only other differences being that the first time interval was taken at one hour instead of one and a half hours and the third was after five days instead of three. Form 4 was added to the list of forms tested in this experiment.

The amorphous form unsurprisingly had the highest concentration after being stirred for one hour. The concentration was much higher at 4.0, 4.9, and 3.1 times those of Forms 1, 2, and 3 respectively. The concentrations were unfortunately not recorded at time intervals shorter than one hour and the high energy amorphous form could have already started to recrystallise by this interval. By 24 hours of stirring the concentration of the amorphous form had dropped to a value closer to those of the other forms and by 5 days had dropped to a concentration just above those for Forms 1 and 2, and even slightly lower than that of Form 3.

Form 3 had the highest concentrations of the three crystalline forms at each of the intervals assessed (factors of roughly 1.3 and 1.5 higher than those of Forms 1 and 2 respectively), Form 1 had the second highest solubility at each of the intervals, with Form 2 having the lowest. The actual measured concentrations were higher after stirring for 24 hours than after one hour as could be expected. The ratio of solubility stayed fairly constant throughout this experiment for the crystalline forms. The products of each vial were checked with PXRD after being stirred for five days to determine if any solvent-mediated phase transitions had occurred. The contents of the Form 1 vials had undergone near complete conversion to Form 2. The contents of the Form 2 vials had remained unchanged. Forms 3 and 4 also appeared to have undergone near complete conversion to Form 2. The transition from Form 1 to Form 2, as well as Form 2 having the lower solubility, would indicate that at this temperature Form 2 is the more stable form of those tested.

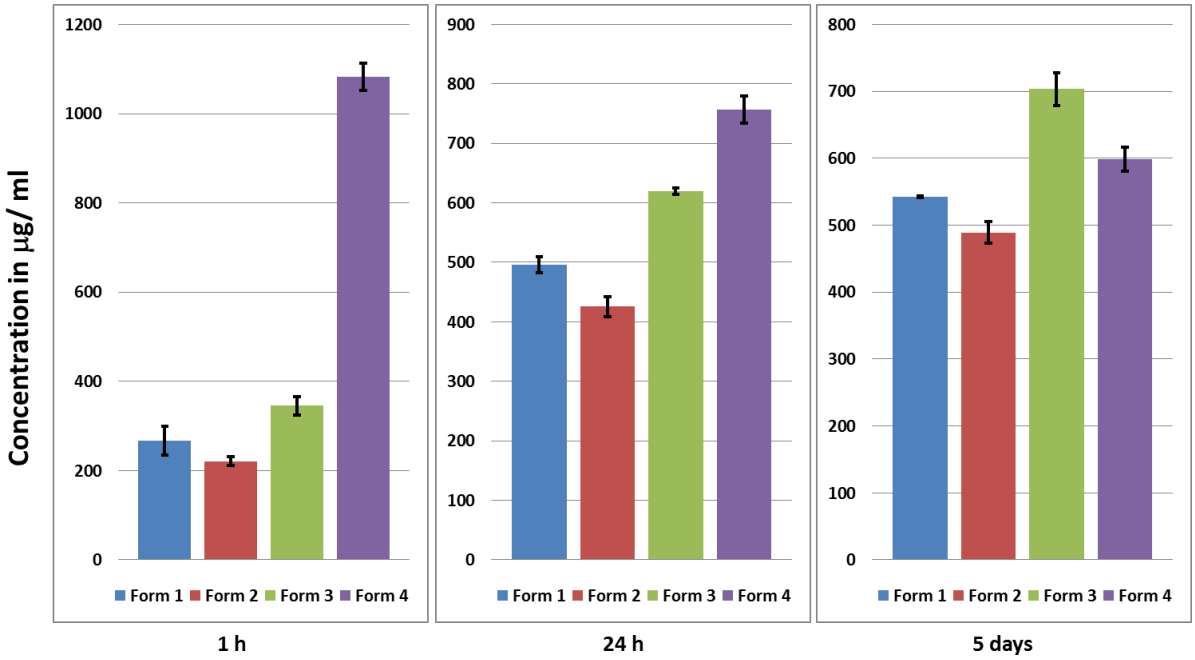

Fig. 4.1.59 Chart displaying MMV concentrations in methanol at 25 ± 0.5 °C after 1 h, 24 h, and 5 days of stirring.

Solvent-mediated transformation experiments

In order to determine the stability ranking of Form 1 and Form 2 at different temperatures, the phase-pure samples were placed in vials with selected solvents (methanol/1-butanol) and left to stir at 500 rpm over five days. The solid products were then inspected with PXRD to determine which form was present. The products from the solubility experiments described in the preceding section were characterised by PXRD. These experiments were carried out at 25 ± 0.5 °C with methanol as solvent. The same setup was used for the experiment carried out at 50 ± 0.5 °C. Higher temperatures required a different solvent with a higher boiling point and for this reason 1-butanol was used to carry out the experiments at 75 ± 0.5 °C and 100 ± 0.5 °C.

The results after stirring at 25 °C, as mentioned earlier, were that Form 1 had fully converted into Form 2 while Form 2 remained unchanged. The same result was observed at 50 °C. The experiment carried out at 100 °C resulted in complete conversion of Form 2 to Form 1 and Form 1 remained unchanged.

At 75 °C Form 1 changed into Form 2 after 5 days of stirring and Form 2 remained unchanged. This shows that the temperature at which Form 1 and Form 2 will have equal free energy lies between 75 and 100 °C. Form 2 will thus be the stable form up to at least 75 °C and the temperature at which Form 1 becomes the more stable form lies above this temperature.

Energy/temperature diagram

A schematic energy/temperature diagram was constructed from the information obtained by the various methods of characterisation and is presented in Fig. 4.1.60. The solvent-mediated transition and kinetic solubility experiments carried out at different temperatures indicated that at 25 °C the thermodynamic stability ranking from highest to lowest is as follows: Form 2 > Form 1 > Form 3 > Form 4. This stability ranking is assumed to remain unchanged below this temperature down to 0 K. Form 4 being a glass and thus naturally having the higher free energy is the least stable at all temperatures. The reason why the free energy isobar for Form 4 is higher than that of the liquid below T_g is due to an excess of enthalpy and configurational entropy due to drastically reduced molecular motion making the sample unable to reach an equilibrium at experimental rates. At T_g the molecular mobility rapidly rises upon heating; this can be up to a 10-fold increase for an increase of temperature of only 3 to 5 K just above T_g.[15] The isobars merge at T_g as at this point the molecular motion will be sufficient for the glass to reach an equilibrium with its surroundings and above this point will possess properties of a supercooled liquid. It is important to keep in mind however that T_g is a kinetic process and will depend on the crossing of timescales of molecular rearrangement and experiments performed.

Form 3 was found to be less stable than Forms 1 and 2 at 25 °C and had the lowest T_f of the crystalline polymorphic forms. The exact ΔH_f of Form 3 was not measurable due to the incongruent nature of this event and this value is presented as an estimation in the E/T diagram. The lack of any observed transitions to this form and the lower melting temperature would suggest that Form 3 is monotropically related to Forms 1 and 2 and there is thus no crossing of the G isobars. The similar ΔH_f for Forms 1 and 2 make this value alone inadequate for confident determination of the relationship in terms of enantiotropy/monotropy and calculation of T_t (making use of expressions 4.1.1 and 4.1.2 the calculated T_t values were 73.2 and 77.7 °C respectively). Form 2 having the higher stability at room temperature and a lower T_f than Form 1 would suggest that a crossing of the G isobars would have to occur between these temperatures. The T_t of Form 2 to 1 was found from the solvent-mediated transition experiments to occur between 75 and 100 °C and at this point the G isobars cross.

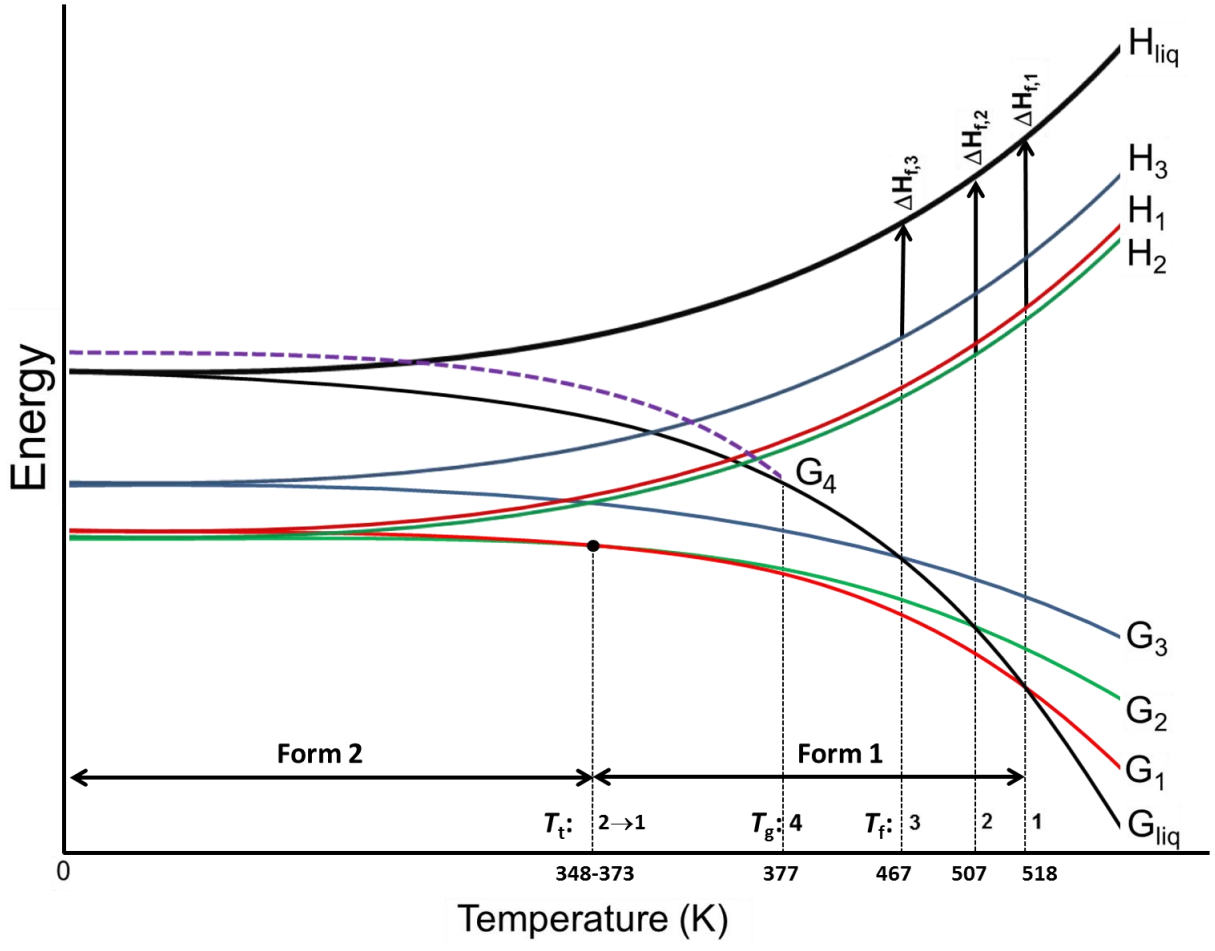

Fig. 4.1.60 A schematic energy/temperature diagram for the various polymorphs of MMV.

Stability ranking of the various forms

The heat of fusion rule states that in the case of enantiotropically related polymorphs the higher melting form has a lower heat of fusion; if not, they are monotropically related.[11] When considering Form 1 and Form 2, the melting points are significantly different, with Form 1 having a melting onset more than 10 °C higher than that of Form 2. The experimental heats of fusion on the other hand are very similar. When taking the standard deviations of the measurements into consideration the difference in the values is not statistically significant. In the case of Form 3 the onset of the melt is much lower than for Forms 1 and 2 (roughly 40 °C lower than that of Form 2). The ΔH_f cannot be measured due to the incongruent nature of the event. The crystallisation to the more stable Forms 1 and 2 overlap with the melting event and it is not possible to accurately separate and quantify the enthalpies involved in the various overlapping events. Heating rates of 150 K min^{-1} were unsuccessfully used in an attempt to prevent recrystallisation by not allowing enough time for it to occur.

A point to note is that the ΔH_f of the recrystallised Form 1 from the melts of either of the other forms (Forms 2, 3, 4, and the monohydrate) is significantly lower than for the pure Form 1. This is most likely due to incomplete crystallisation to this form during heating at the experimental rates. One can calculate the fraction that did recrystallise from the ratio of these enthalpies as illustrated by Lefort *et al*.[10]

Entropy of fusion—In the case of monotropy the higher melting polymorph has the higher entropy of fusion. The same problem arises here in that the differences in these values when considering the standard deviations are not statistically significant.

Density rule— According to Lohani and Grant[16] the rule is based on Kitaigorodskii's principle of closest packing for molecular crystals.[17] It states that numerous van der Waals interactions between molecules will result in the more densely packed form to be the most thermodynamically stable polymorph (having the lowest free energy) at absolute zero. This will be the case for non-hydrogen-bonded systems, because strong hydrogen-bonding could compensate for fewer van der Waals interactions in less closely-packed forms.

Forms 1 and 2 have calculated densities of 1.498 g cm^{-3} and 1.449 g cm^{-3} respectively. This is a difference of 3.38 %. Due to a lack of any strong hydrogen-bonding in either of these forms, another possible explanation for the divergence from the rule is because of the difference in the conformations of these forms.

Fourier transform infrared spectroscopy (FTIR)

The FTIR spectra of the various forms are presented in Fig. 4.1.61. When comparing the spectra there are many visible differences in both the fingerprint region and in the O-H (hydrated form) and C-H stretching (due to C-H stretching of the aromatic rings and the methyl groups) regions in terms of peak positions, intensity, and multiplicity. The most prominent difference is the broad and intense water peaks in the region 3000-3500 cm^{-1} seen in the case of the hydrated form and to a much lesser extent in the spectrum of Form 3, indicating the presence of small amounts of water, as was also seen in the TGA experiments. The spectrum produced by Form 4 has broader peaks with lower intensity, as expected for an amorphous form having a naturally greater spread of differing bond lengths and energies. It would thus be possible to distinguish between these forms by inspecting the FTIR spectra alone.

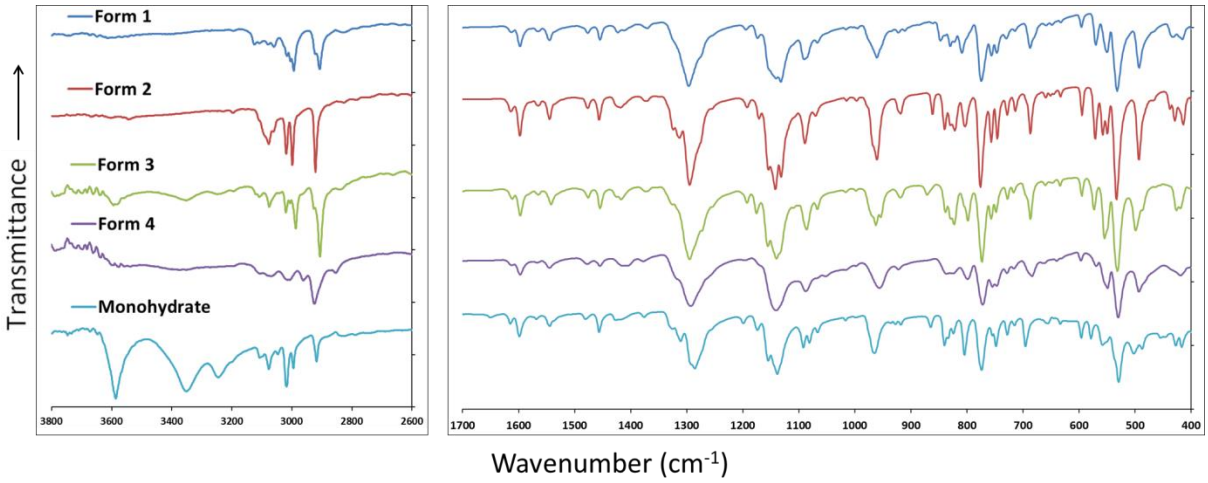

Fig. 4.1.61 FTIR spectra of the various forms of MMV.

Hirshfeld plots

Two-dimensional fingerprint plots[18] are presented in Fig. 4.1.62. Most of the main features are shared by the different forms as is clear from the similarity of the plots. The most prominent features are the spikes pointed out in the plots formed by the shortest contacts for both forms, specifically those of the O···H and N···H bonds with a symmetrical shape in both cases. This feature is commonly seen with cyclic interactions.

The O···H and N···H contact distances are slightly shorter in the case of Form 1 than in Form 2 as is also clear from the values in the H-bond interaction Tables 4.1.2 and 4.1.4. The sharpness of the spikes is similar in both plots and this also agrees with the comparable donor-hydrogen-acceptor angles reported in the tables.

The most obvious difference is also pointed out in the Fig. 4.1.62 where there is a short H···H contact in Form 2, but not for Form 1. The specific interaction involves the atoms labelled H19C and H8 from a different molecule related by the symmetry operator 1-x,1-y,1-z at a distance of 2.64 Å apart. The close proximity of these hydrogen atoms will cause repulsion in the case of Form 2. The relative contributions of various interactions for the two forms of MMV are shown in Fig. 4.1.63. The comparative effects of the O···H and N···H interactions for the two forms are similar as can be seen in Figs. 4.1.62 and 4.1.63. There is however a significant difference in contributions of C···H and H···H, with Form 1 having a higher value for C···H and Form 2 for H···H.

A ratio of interest in the packing of these forms is that of the contributions of C···H/ C···C. This ratio will give a good idea of the nature of π-interactions. In the case of both forms these interactions play a role and in the absence of very strong hydrogen bond donors in the compound these interactions are of even more significance in that they could be the determining factor in how packing ultimately occurs.[19] In the case of Form 1 the C···H/ C···C ratio is 7.9 (26.1 %/3.3 %) and for Form 2 it is 2.6 (16.9 %/6.5 %). Both plots show 'wings' that are a result of C-H···π interactions as these are prominently featured in both polymorphs as can be seen in Figs. 4.1.64 and 4.1.65. Form 2 shows a smaller ratio and this makes sense if one takes into consideration the π···π interactions present in Form 2 (Fig. 4.1.65). Something to keep in mind here is that there are nitrogen atoms in the rings Cg(A) and Cg(B) and this will affect the C···H and C···C contributions. The other noteworthy difference is the way the plot is more compact for Form 1 while that of Form 2 is spread out over the top right corner, which is expected because Form 1 has a higher density than Form 2 and so should be more densely packed.

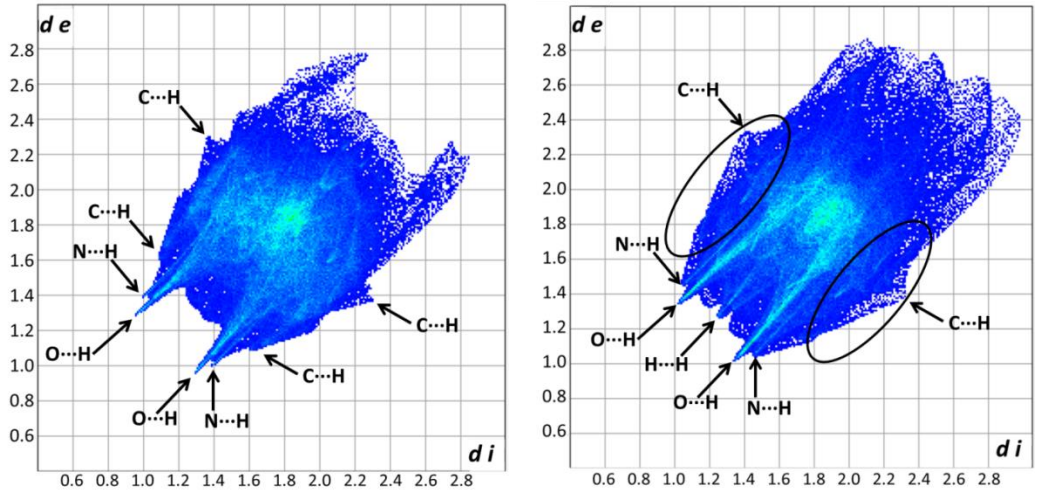

Fig. 4.1.62 Two-dimensional fingerprint plots for MMV Form 1 (left) and MMV Form 2 (right). Parameters d_e and d_i are the distances from a point on the surface to the nearest atom nucleus exterior and interior to the surface.

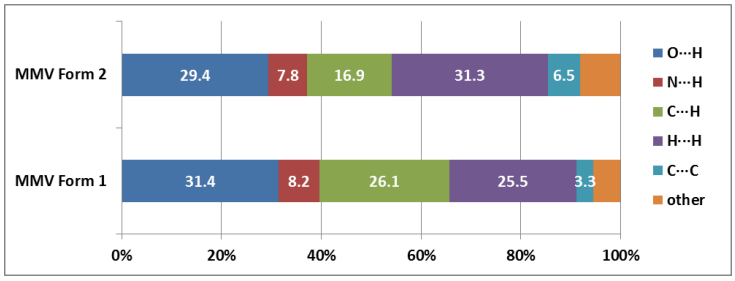

Fig. 4.1.63 Relative contributions to the Hirshfeld surface for the close intermolecular contacts of MMV Form 1 and Form 2.

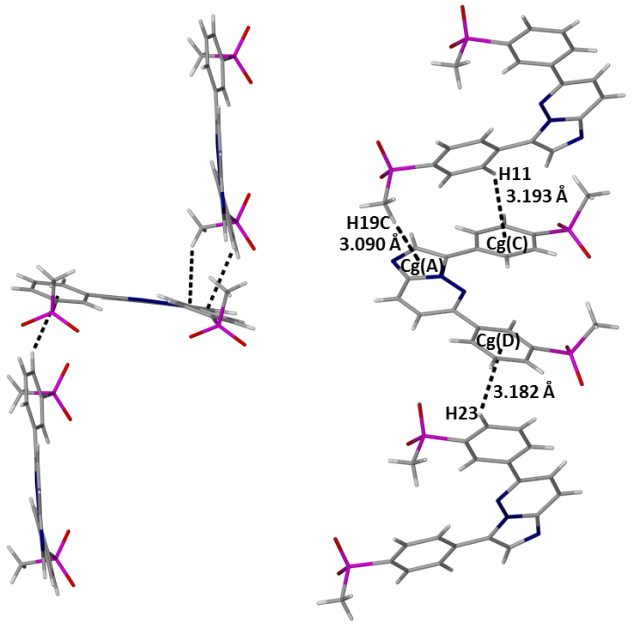

Fig. 4.1.64 X-H···Cg close contacts between adjacent molecules seen from different viewpoints showing X-H···Cg distances present in Form 1.

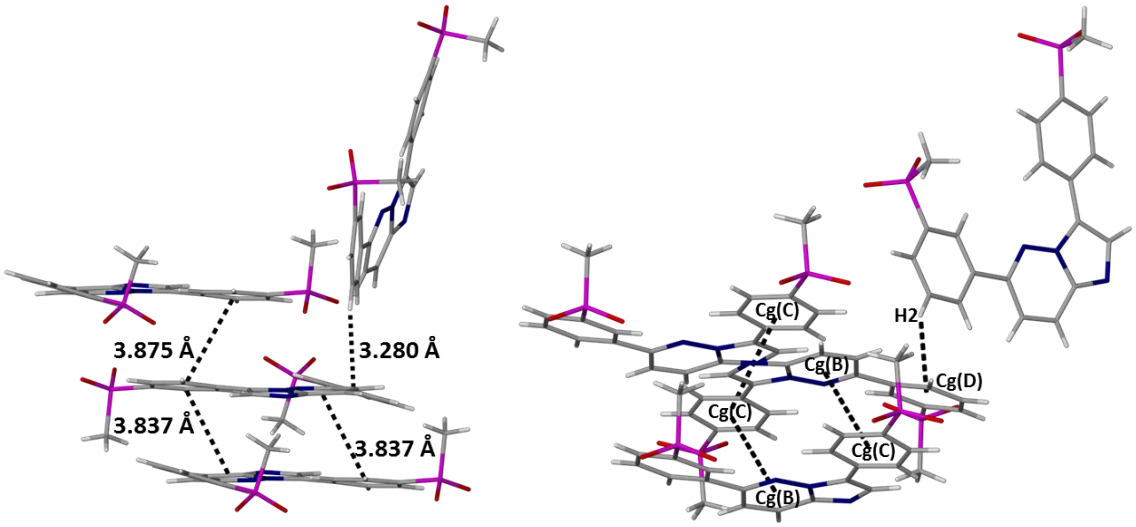

Fig. 4.1.65 π-π close contacts between layers of ribbons and X-H···π close contacts viewed from different perspectives showing Cg···Cg and X-H···Cg distances present in Form 2.

Conformations

The MMV molecule has four freely rotatable bonds and this lends some flexibility to the molecule as can be seen in the various conformers overlayed in Fig. 4.1.66. Torsion angles are listed in Table 4.1.9. The co-planarity of phenyl rings (C10-C11-C12-C13-C14-C15) and (C20-C21-C22-C23-C24-C25) is maintained by the intramolecular H-bonds C15-H15···N5 and C21-H21···N5 for Forms 1, 2 and the hydrate. There are, however, dissimilarities when comparing the forms, the most prominent being that of the (C20-C21-C22-C23-C24-C25) ring of the hydrated form, which is tilted at an angle of 28.7(2)° relative to the imidazopyridazine ring.

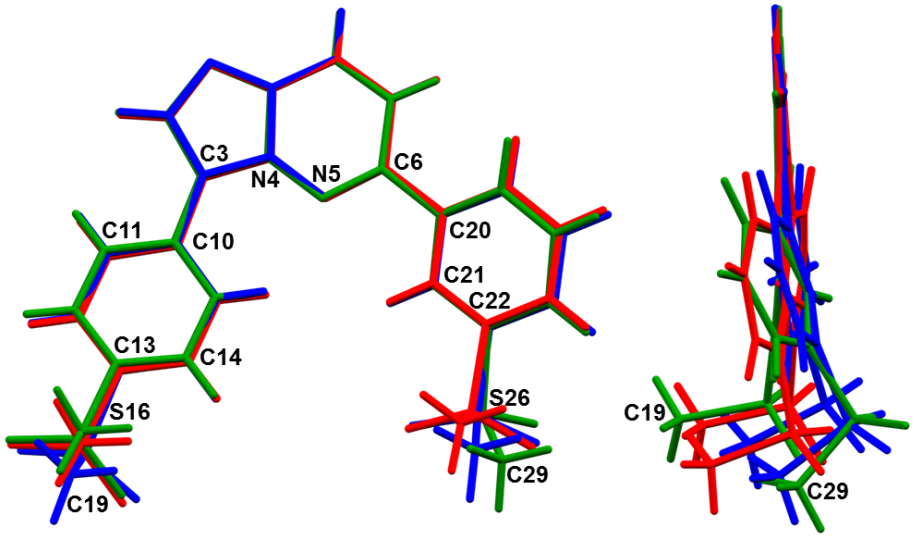

Fig. 4.1.66 Overlay of the different conformers of MMV occurring in the various polymorphs and hydrated form viewed roughly normal (left) and parallel (right) to the imidazopyridazine ring [MMV Form 1: blue; MMV Form 2: red, MMV monohydrate: green]

Table 4.1.9 Torsion angles for the various forms of MMV and the monohydrate.

Structure	Torsion angle N4-C3-C10-C11 (°)	Torsion angle N5-C6-C20-C21 (°)	Torsion angle C14-C13-S16-C19 (°)	Torsion angle C21-C22-S26-C29 (°)
Form 1	-169.3(3)	17.9(4)	82.8(3)	-99.0(3)
Form 2	-172.5(2)	13.3(2)	75.0(2)	-100.3(2)
Monohydrate	-179.9(2)	28.7(2)	82.1(2)	-125.5(2)

References:

1. XPREP, *Data Preparation and Reciprocal Space Group Exploration*, Version 2008/2, © Bruker AXS Inc., Madison, Wisconsin, USA, **2008**.
2. Program SAINT, Version 7.60a, Bruker AXS Inc., Madison, Wisconsin, USA, **2008**.
3. G. M. Sheldrick, *Acta Crystallogr., Sect. A: Found. Crystallogr.*, 2008, **64**, 112-122.
4. H. Flack, *Acta Crystallogr., Sect. A: Found. Crystallogr.*, 1983, **39**, 876-881.
5. S. Parsons, H. D. Flack and T. Wagner, *Acta Crystallogr., Sect. B: Struct. Sci., Cryst. Eng. Mater.*, 2013, **69**, 249-259.
6. S. Qi and D. Q. Craig, *Mol. Pharm.*, 2012, **9**, 1087-1099.
7. W. Kauzmann, *Chem. Rev.*, 1948, **43**, 219-256.
8. B. C. Hancock and S. L. Shamblin, *Thermochim. Acta*, 2001, **380**, 95-107.
9. A. M. Kaushal and A. K. Bansal, *Eur. J. Pharm. Biopharm.*, 2008, **69**, 1067-1076.
10. R. Lefort, A. De Gusseme, J.-F. Willart, F. Danede and M. Descamps, *Int. J. Pharm.*, 2004, **280**, 209-219.
11. A. Burger and R. Ramberger, Microchim. Acta, 1979, **2**, 259-271.
12. A. Burger and R. Ramberger, Microchim. Acta, 1979, **2**, 273-316.
13. L. Yu, *J. Pharm. Sci.*, 1995, **84**, 966-974.
14. D. E. Braun, T. Gelbrich, V. Kahlenberg, R. Tessadri, J. Wieser and U. J. Griesser, *J. Pharm. Sci.*, 2009, **98**, 2010-2026.
15. M. D. Ediger, C. Angell and S. R. Nagel, *J. Phys. Chem.*, 1996, **100**, 13200-13212.
16. S. Lohani and D. J. W. Grant, in *Polymorphism in the Pharmaceutical Industry*, ed. R. Hilfiker, Wiley-VCH Verlag GmbH & Co. KGaA, Weinheim, Germany, **2006**, pp. 21-42.
17. A. I. Kitaigorodskii, *Molecular crystals and molecules*, Academic Press Inc., New York, New York, USA, **1973**, pp.1-133.
18. CrystalExplorer, Version 3.1, S. K. Wolff, D. J. Grimwood, J. J. McKinnon, M. J. Turner, D. Jayatilaka and M. A. Spackman, University of Western Australia, Perth, Australia, **2012.**
19. L. Loots and L. J. Barbour, in *The Importance of Pi-Interactions in Crystal Engineering*, ed. E. R. T. Tiekink and J. Zukerman-Schpector, John Wiley & Sons, Chichester, United Kingdom, **2012**, pp. 109-124.

Chapter 4

Part two

The following section describes the structural and physicochemical characterisation, as well as the methods used to synthesise, multi-component solid-state forms of MMV with selected co-crystal formers that are on the US Food & Drug Administration's (FDA) list of compounds that are generally recognized as safe (GRAS).[1] The first step in the screening for co-crystals after selecting the co-crystal formers with the highest expected likelihood of success is by physically grinding the components together making use of a mortar and pestle in the absence of solvent. This method only resulted in physical mixtures. Another method is to make use of very small volumes of solvent for LAG as described in the experimental chapter of this thesis. The coformers that resulted in new phases in LAG experiments with MMV are the following: methylparaben, succinic acid, 4-hydroxybenzoic acid, adipic acid, glutaric acid, fumaric acid, malonic acid, L-malic acid, D-tartaric acid, maleic acid, oxalic acid, and resorcinol. The table of coformer-solvent combinations that resulted in new phases and the associated PXRD traces are displayed in the supplementary section.

The next step after the LAG screening experiments is to produce single crystals of acceptable size and quality for structural elucidation by X-ray diffractometry. A range of methods are used for this step as was described in the experimental chapter, though the most common method is some variant of co-precipitation. Not all of the coformers that produced hits with LAG screening experiments produced adequate single crystals. The co-crystal and salt forms that were produced by co-precipitation are individually discussed in the following section and this is followed by a comparison of the various multi-component systems.

MMV-adipic acid co-crystal (MMVADIP)

5 mg of MMV was ground with a mortar and pestle with an equimolar amount of adipic acid for 15 min while adding acetone in small drops. The product was then analysed with PXRD and the resulting trace was compared to those of the starting materials of MMV and the coformer. The results are shown in Fig. 4.2.1. There were clear differences visible, with the most prominent new peaks appearing at °2θ of 7.0, 14.5, 16.0, 21.0, and 27.5 for the product of the LAG experiment. This suggested that formation of a new phase had occurred. Further comparisons with other known structures formed with the starting materials ruled out the formation of these forms.

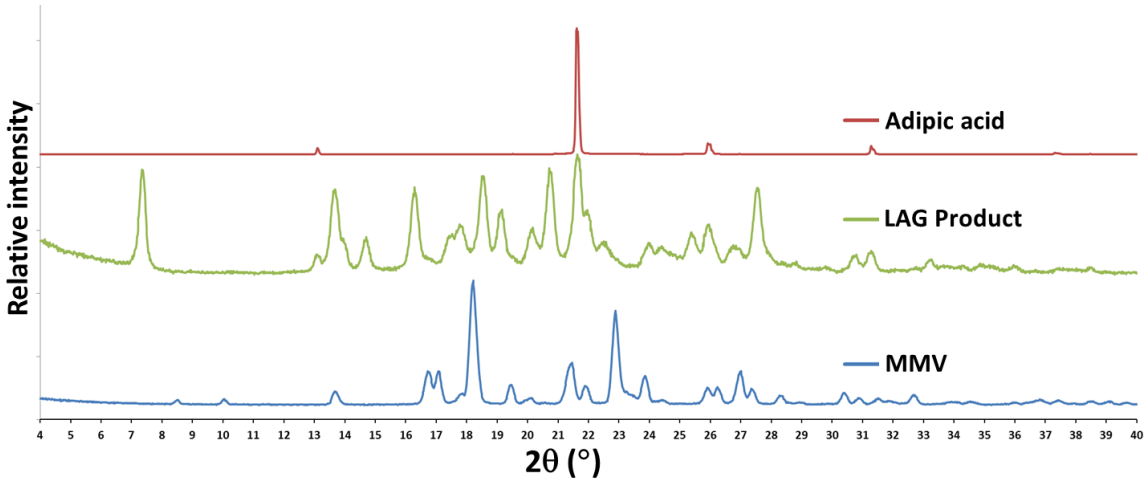

Fig. 4.2.1 Recorded PXRD traces for the product of a LAG experiment and the starting materials, MMV and adipic acid.

Preparation of single crystals

Single crystals of the co-crystals were produced by co-precipitation through dissolving 5.000 mg of MMV together with an equimolar amount of adipic acid (1.709 mg) in 2 cm^3 of acetone while stirring at 50 °C. The resulting solution was then filtered through a 0.45 µm nylon filter into a clean vial and placed on a benchtop after covering the vial with Parafilm™.

Stoichiometry determination by ^{1}H – NMR spectroscopy

Single crystals obtained by co-precipitation of MMV with adipic acid were dissolved in DMSO-d_6 and analysed by ^{1}H-NMR spectroscopy to determine the stoichiometric ratio of the individual components. The proton labelling schemes and the ^{1}H-NMR spectrum are shown in Fig. 4.2.2. The integration values are presented in Table 4.2.1. The ratio was determined to be 2:1 of MMV to adipic acid.

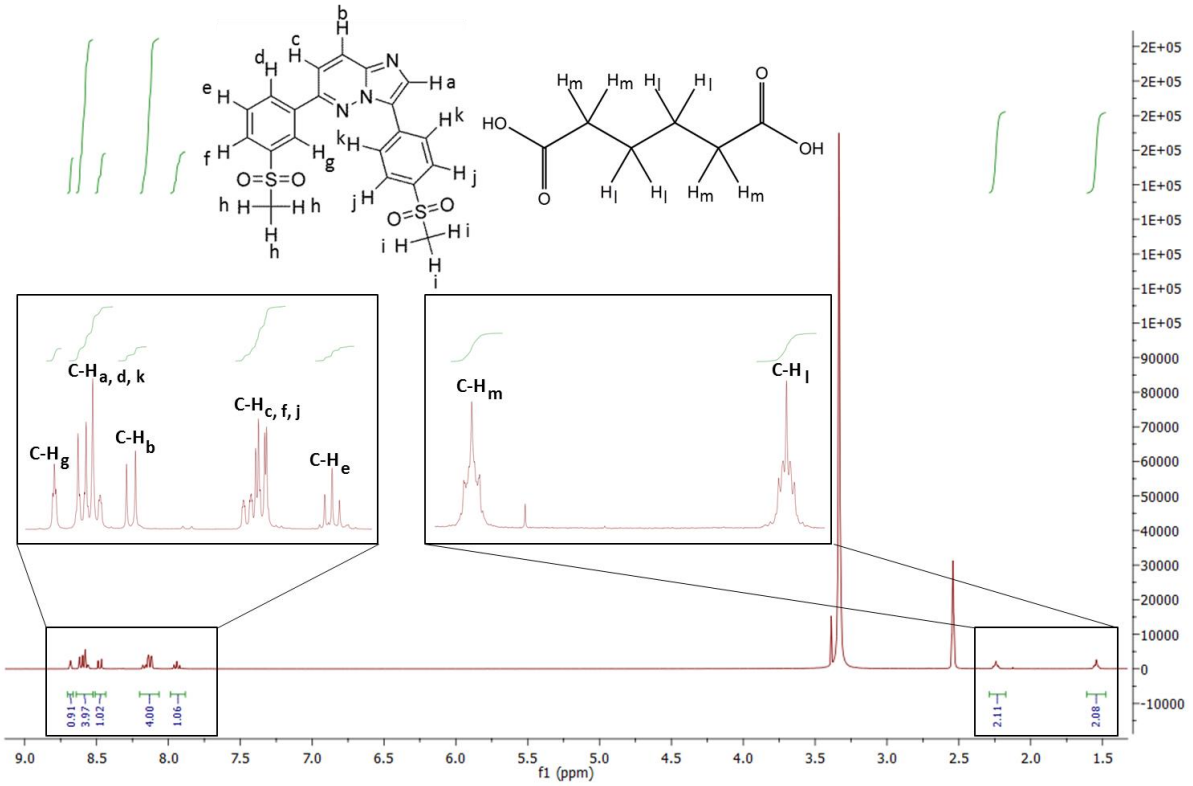

Fig. 4.2.2 ^{1}H-NMR spectrum of MMVADIP in DMSO-d_6 for determination of stoichiometry

Table 4.2.1 Integrals of protons for individual components to determine stoichiometry of MMVADIP.

Proton – [Number of protons]	δ (ppm)	Integration	Experimental/ Theoretical
MMV			
C-$H_{c,f,j}$– [4]	8.07-8.20	4.00*	1.00
C-H_g – [1]	8.66-8.70	0.91	0.91
C-$H_{a,d,k}$– [4]	8.52-8.64	3.97	0.99
C-H_b – [1]	8.44-8.51	1.02	1.02
C-H_e – [1]	7.88-7.99	1.06	1.06
Adipic acid			
C-H_l – [4]	1.48-1.61	2.08	0.52
C-H_m – [4]	2.17-2.29	2.11	0.53

*** Reference integral**

Infrared spectroscopy

Dicarboxylic acids tend to form acid dimers as a result of a common hydrogen bond synthon as depicted in scheme 4.2.1.

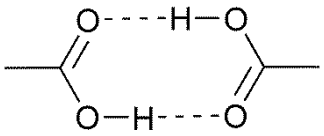

Scheme 4.2.1 Diagrammatic depiction of carboxylic acid homo-dimer.

When looking at the spectrum of adipic acid in Fig. 4.2.3, a broad and relatively intense band can be seen in the region from 2500 to 3400 cm^{-1}. This band is due to the O-H stretching of adipic acid. The in-plane O-H bending band can be seen at 1407 cm^{-1} and a broad band with moderate intensity representing out-of-plane O-H bending has a peak at 919 cm^{-1}. A C-O stretch of the carboxylic acid is indicated by the band at 1273 cm^{-1}. The most intense peak visible in the spectrum of adipic acid is that of the carbonyl stretch at 1683 cm^{-1}.[2-4]

Many features are common for the spectra of MMV and MMVADIP, such as the intense bands observed in the regions 1310-1340 cm^{-1} (asym. SO_2 stretch) and 1135-1165 cm^{-1} (sym. SO_2 stretch) as these are present in both cases, as pointed out in Fig. 4.2.3. The out-of-plane C-H bending vibrations of aromatic molecules (in the *meta*-position) in the range 750-810 cm^{-1} are also observed in MMV and MMVADIP and pointed out in Fig. 4.2.3.[2]

The out-of-plane O-H bending peak that was present in the spectrum of adipic acid at 923 cm^{-1} is absent in the spectrum of MMVADIP. This serves as evidence that the acid homo-dimer interaction is not present.[5] In the spectrum of MMVADIP a broad band centred around 2450 cm^{-1} and another centred around 1920 cm^{-1} are due to the O-H···N stretching of the acid-imidazole absorption. These bands are a result of the proton shuttling between the bonded and transferred states and serve as an indication of co-crystal formation.[5,6] A slightly broad and relatively intense peak visible at 1705 cm^{-1} is due to the asymmetric stretching of the carbonyl group of the coformer. The small shift to a higher energy of this band (from 1683 to 1705 cm^{-1}) is also indicative of the formation of a co-crystal.[5,7,8]

Some other features frequently used to identify co-crystals of this nature are in positions that overlap with bands of the MMV RM, for instance a peak at 1595 cm^{-1}, peaks around 1300 cm^{-1} and a large peak at 500 cm^{-1} caused by proton movement in the acid-imidazole synthon.[4]

The features used to identify co-crystal or salt formation in these FTIR results should serve as a means of screening to save time, but the definitive evidence should be found in the elucidation of the crystal structures by X-ray diffraction.

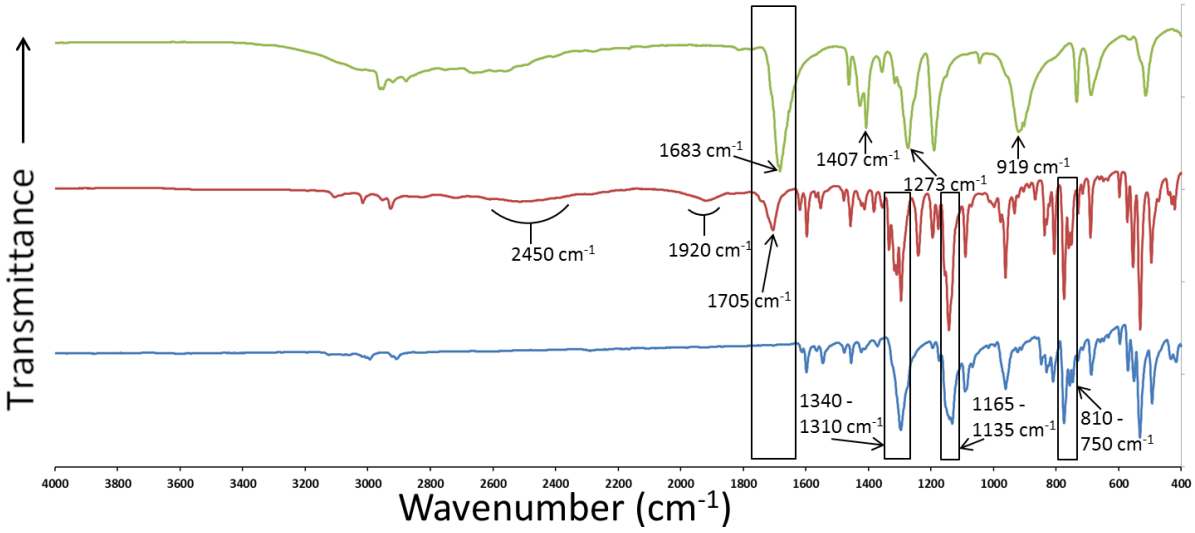

Fig. 4.2.3 FTIR spectra of MMV (Blue), MMVADIP (Red), and adipic acid (Green).

Crystal structure analysis

Data-collection and space group determination

The single-crystal X-ray intensity data collection was performed on a Bruker Kappa Apex II Duo diffractometer at 173(2) K. The X-ray diffraction showed $\bar{1}$ Laue symmetry, revealing the triclinic crystal system. The mean $|E^2-1|$ value obtained by making use of the software XPREP[9] was 0.951 and corresponds to centrosymmetry. This clearly indicated that the space group is $P\ \bar{1}$.

Structure solution and refinement

Crystallographic data, parameters for collection of intensity data and refinement details are reported in Table 4.2.2. Data reduction and unit cell refinement were carried out with the program SAINT.[10] The structure was solved by direct methods through the use of SHELXS.[11] All non-hydrogen atoms were placed and then refined isotropically by full-matrix least-squares with SHELXL.[11] The non-hydrogen atoms were then refined anisotropically. In order to ascertain whether proton transfer had occurred and thereby determining whether the product was a salt or a co-crystal, the positions of the carboxyl hydrogen of the adipic acid moiety and the imidazole nitrogen of the MMV moiety were sought

explicitly. The Fourier difference map clearly showed that the proton was present as the carboxyl hydrogen and the distinct C-O bond lengths of the adipic acid functional groups of 1.318(2) Å and 1.199(2) Å are representative of single and double bonds.[12,13] Both molecules were thus in the neutral state indicating that the structure is a co-crystal. All hydrogen atoms were found in difference electron density maps and placed in idealised positions in a riding model and refined with thermal parameters 1.2-1.5 times the U_{iso} values of their parent atoms.

Table 4.2.2 Data-collection and refinement parameters for MMVADIP.

Molecular formula	$(C_{20}H_{17}N_3O_4S_2) \cdot 0.5(C_6H_{10}O_4)$
Formula weight (g mol^{-1})	500.55
Crystal system	Triclinic
Space group	$P\ \bar{1}$
a (Å)	8.5654(8)
b (Å)	10.9472(11)
c (Å)	13.2987(13)
α (°)	114.125(2)
β (°)	93.811(2)
γ (°)	90.324(2)
V (Å)^3	1134.81(19)
Z	2
D_c (g cm^{-3})	1.465
μ (Mo Kα) (mm^{-1})	0.281
F(000)	522
Data-collection temp. (K)	173(2)
Crystal size (mm^3)	0.20 x 0.05 x 0.04
Range scanned θ (°)	1.68 – 28.36
Index ranges ±*h*, ±*k*, ±*l*	-11, 11; -14, 14; -17, 17
Reflections (total)	32 261
Independent reflections	5672
Reflections with I>2σ(I)	4121
Number of parameters	310
R_{int}	0.0617
S	1.024
R_1 [*I*>2σ(*I*)]	0.0421
Reflections omitted	4
wR_2	0.1050
a, b in w = 1/[$\sigma^2(F_o^2)$+(aP)^2+(bP)]	a = 0.0428; b = 0.4207
$(\Delta/\sigma)_{mean}$	< 0.001
$\Delta\rho_{min,max}$ (e Å^{-3})	-0.328, 0.390

Molecular structure

The asymmetric unit and labelling scheme of MMVADIP are shown in Fig. 4.2.4.

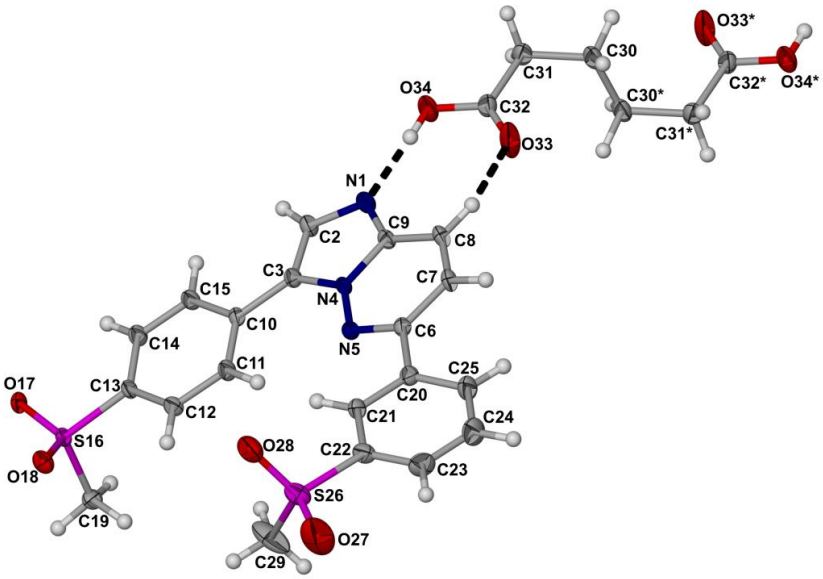

Fig. 4.2.4 The asymmetric unit and numbering scheme of MMVADIP with thermal ellipsoids shown at the 50% probability level. Atoms labelled with an asterisk are symmetry-generated and are not part of the asymmetric unit.

Crystal packing and hydrogen bonding

The relevant symmetry information for MMVADIP is listed in Table 4.2.3.

Table 4.2.3 Hydrogen bonds in MMVADIP[a].

	D–H···A	*d*(D–H), Å	*d*(H···A), Å	*d*(D···A), Å	∠(DHA), deg.
	O34-H34···N1	0.84	1.87	2.703(2)	174
	C8-H8···O33	0.95	2.32	3.114(2)	141
Intra	C11-H11···N5	0.95	2.32	2.985(3)	126
Intra	C14-H14···O17	0.95	2.56	2.941(2)	104
	C19-H19A···O33^{i}	0.98	2.24	3.222(3)	177
	C19-H19B···O17^{ii}	0.98	2.48	3.358(2)	148
	C19-H19C···O28^{iii}	0.98	2.42	3.304(3)	150
Intra	C23-H23···O27	0.95	2.50	2.889(3)	105
	C23-H23···O34^{iv}	0.95	2.57	3.346(3)	139'
intra	C21-H21···N5	0.95	2.48	2.778(2)	98
	C15-H15···O28^{ii}	0.95	2.68	3.336(3)	127

[a] Symmetry transformations used to generate equivalent atoms: *[i]: 1-x,1-y,1-z; [ii]: -x,-y,1-z; [iii]: x,-1+y,z; [iv]: x,1+y,1+z.*

The graph-set designations used in this chapter to describe interactions are those described by Etter *et al.*[14]

A multitude of interactions connect these molecules and the intra- and inter-molecular interactions are listed in Table 4.2.3 and are presented in Figs. 4.2.5 to 4.2.7.

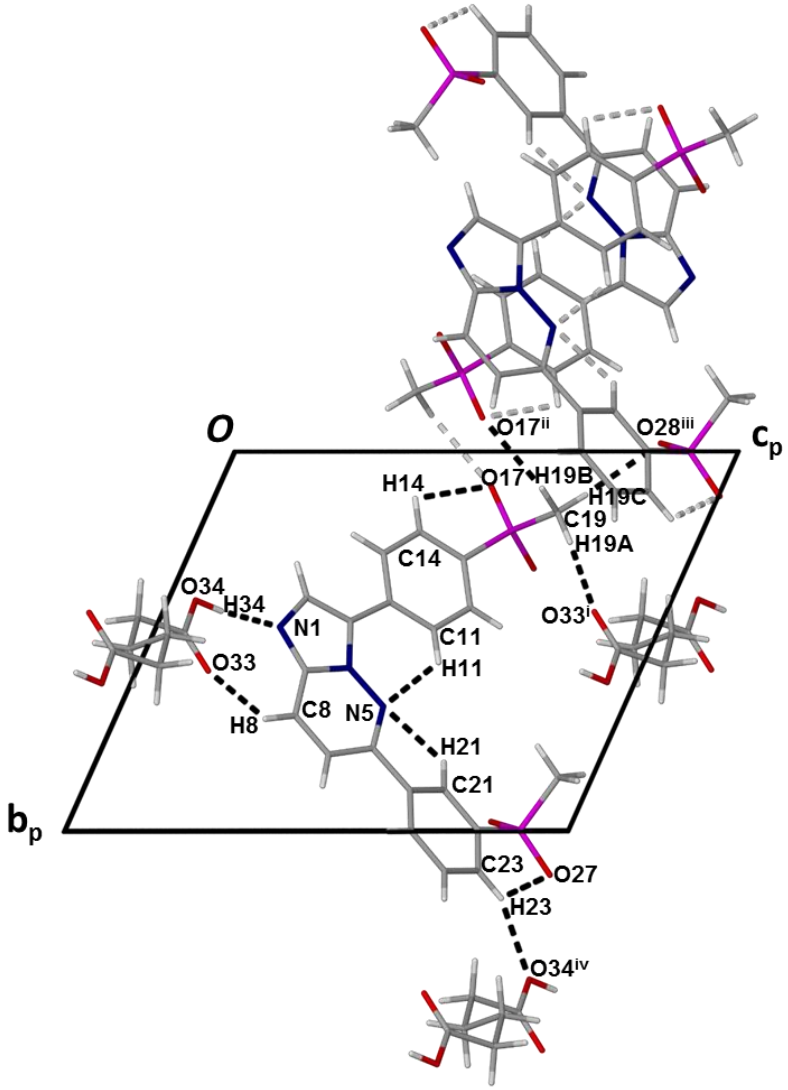

Fig. 4.2.5 Hydrogen bonding interactions found in the structure of MMVADIP viewed along [100].

The molecules of this co-crystal pack in stepped layers as can be seen in Fig. 4.2.6 displaying an interaction linking the stepped layers (C19-H19C···O28').

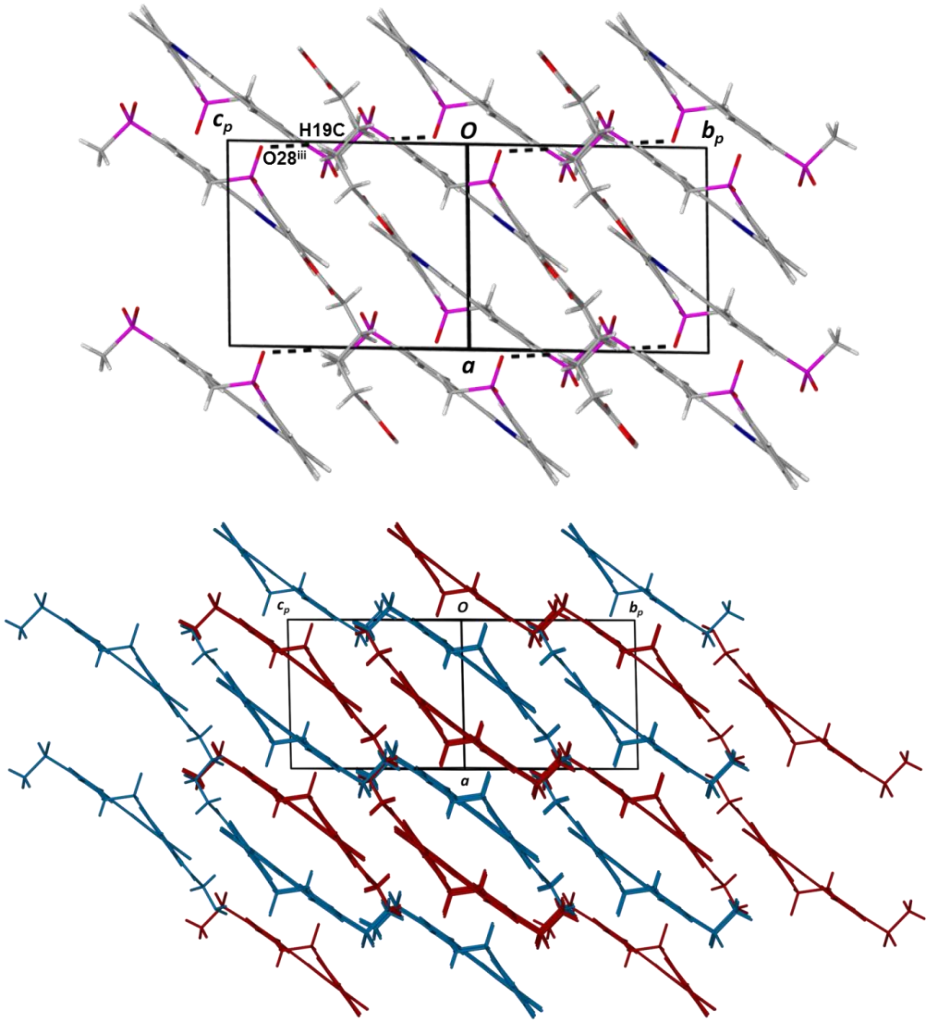

Fig. 4.2.6 The hydrogen bonding connecting the stepped layers (top) and the stepped layers highlighted (bottom).

The topology of a single stepped layer is displayed in Fig. 4.2.7. The stepped layers feature the following interactions: rings are formed by the H-bonds C8-H8···O33 and O34-H34···N1 ($R_2^2(8)$) (Figs. 4.2.5 and 4.2.7) and form discrete ribbons of two MMV molecules attached to opposite ends of an adipic acid molecule (($D_2^2(10)$) (Fig. 4.2.7); these discrete ribbons are linked in parallel directions by C19-H19B···O17' (forming another ring ($R_2^2(8)$) around an inversion centre) (Fig. 4.2.8) and by the interaction

C23-H23···O34′ to form a set of rings described by the graph set designators $R_4^4(34)$ and $R_4^4(38)$ as is shown in Fig. 4.2.9 and 4.2.10.

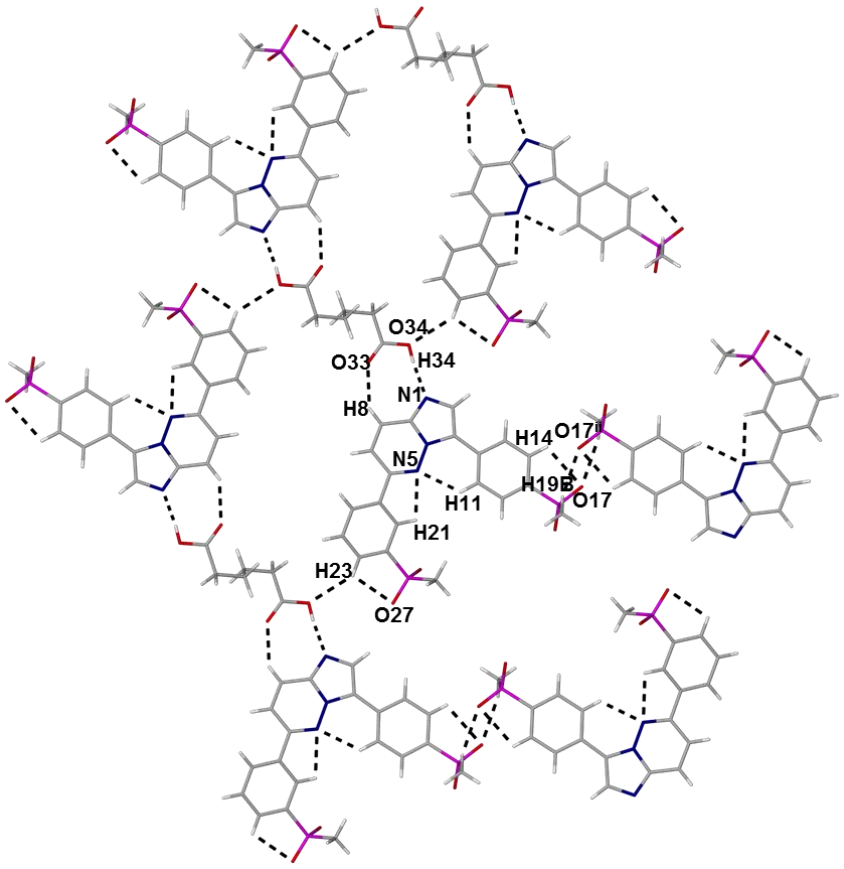

Fig. 4.2.7 The topology of the stepped layer showing some of the hydrogen bonding interactions present in MMVADIP.

There are many interactions connecting the molecules in different layers of MMVADIP that in turn result in numerous rings formed by combinations of these. Among these are C15-H15···O28′ $R_2^2(24)$ (Fig. 4.2.11); C8-H8···O33′ and C19-H19A···O33′ $R_4^2(8)$ (Fig. 4.2.12); C19-H19A···O33′ and C19-H19C···O28′ $R_6^6(54)$.

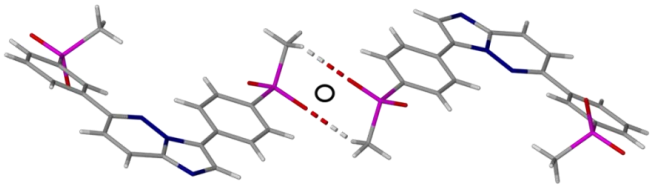

Fig. 4.2.8 Ring interaction connecting adjacent MMV molecules in MMVADIP: C19-H19B···O17′ $R_2^2(8)$.

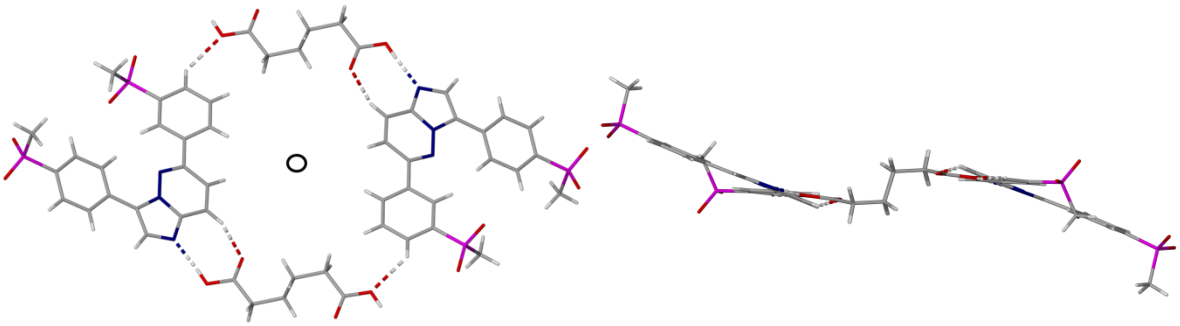

Fig. 4.2.9 Ring interactions in MMVADIP: C8-H8···O33 and O34-H34···N1 $R_2^2(8)$; C8-H8···O33 and C23-H23···O34' $R_4^4(34)$; as well as O34-H34···N1 and C23-H23···O34' $R_4^4(38)$ shown from different views.

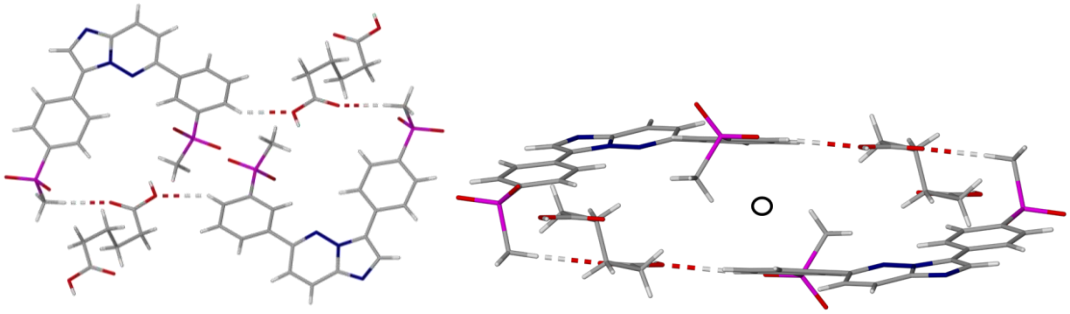

Fig. 4.2.10 Ring interactions found in MMVADIP: C23-H23···O34' and C19-H19A···O33' $\mathrm{R}_4^4(38)$ viewed from different perspectives.

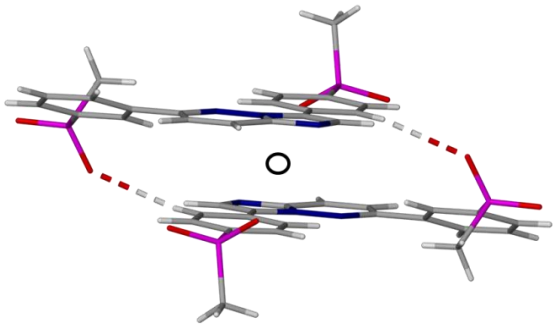

Fig. 4.2.11 Ring interaction connecting stacked MMV molecules in MMVADIP: C15-H15···O28' $\mathrm{R}_2^2(24)$.

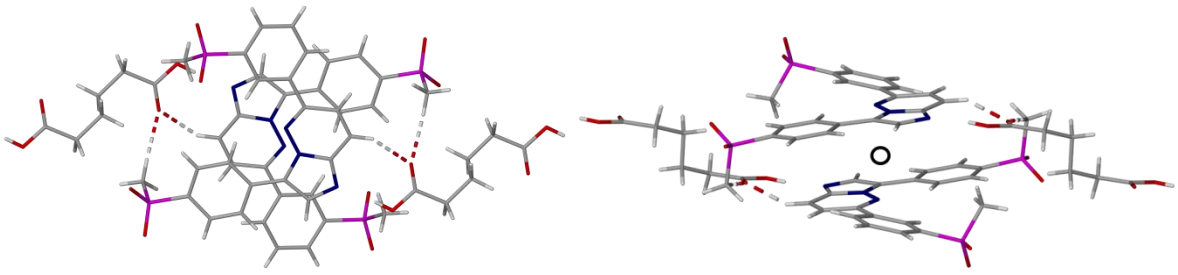

Fig. 4.2.12 The interactions C8-H8···O33' and C19-H19A···O33' $\mathrm{R}_4^2(8)$ from different views.

Offset face-to-face π-stacking interactions are present between the rings N4-N5-C6-C7-C8-C9 (Cg(A)) and C10-C11-C12-C13-C14 (Cg(B)) (where Cg refers to the centroid of a ring) and are related by the symmetry operator 1-x,1-y,1-z (Fig. 4.2.13). The rings have a centroid-to-centroid distance of 3.668(1) Å and the shortest contact distances are 3.384 Å for C12···C8 and 3.385 Å for C8···C11. The distance of 4.000(1) Å between the offset centroids Cg(B)···Cg(B) with the symmetry operator -x,1-y,1-z is too long to be deemed a π-π interaction and this shows that the π-stacking interactions are not continuous but are interrupted to form alternating stacks.

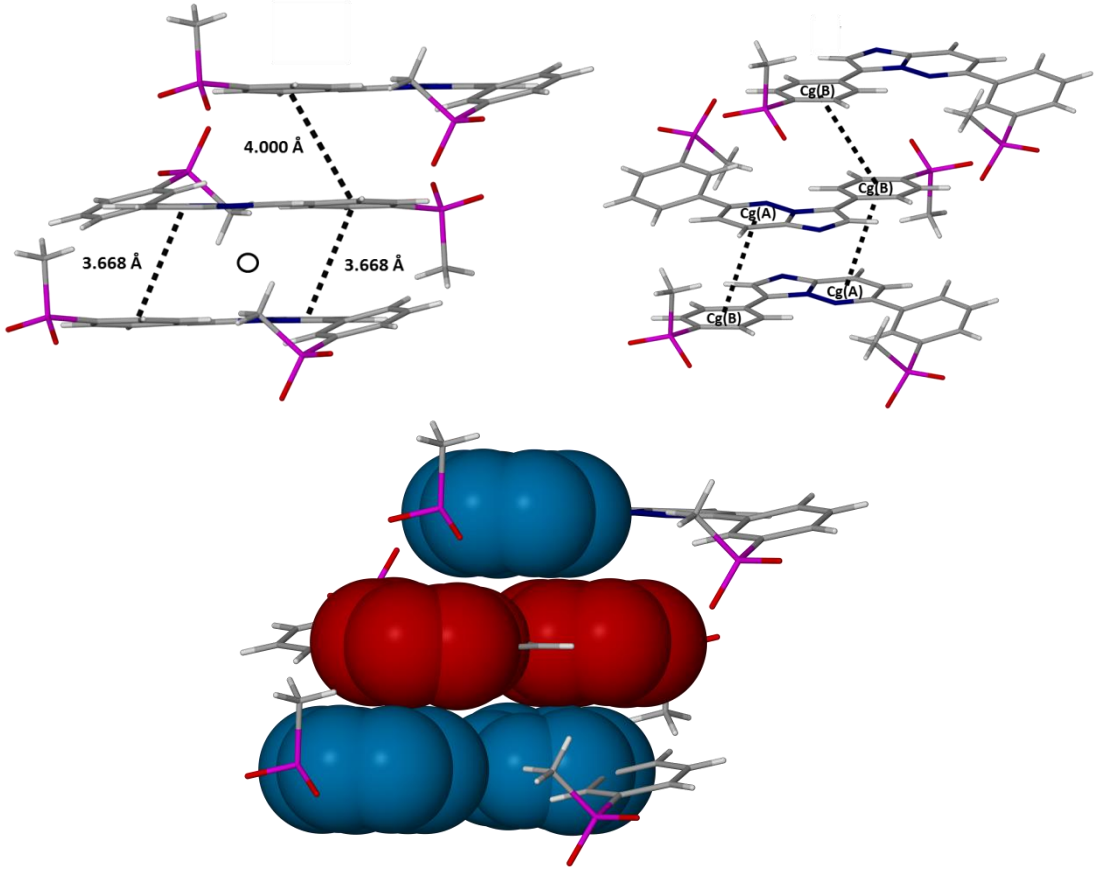

Fig. 4.2.13 π-π interactions connecting layers viewed from different perspectives showing centroids and offset centroid-to-centroid distances between them. Ring atoms are drawn with van der Waals radii to illustrate the overlap in the case of Cg(A)···Cg(B) and the lack thereof in the case of Cg(B)···Cg(B).

The packing arrangements viewed along [100] and [010] are illustrated in Figs. 4.2.14 and 4.2.15 respectively.

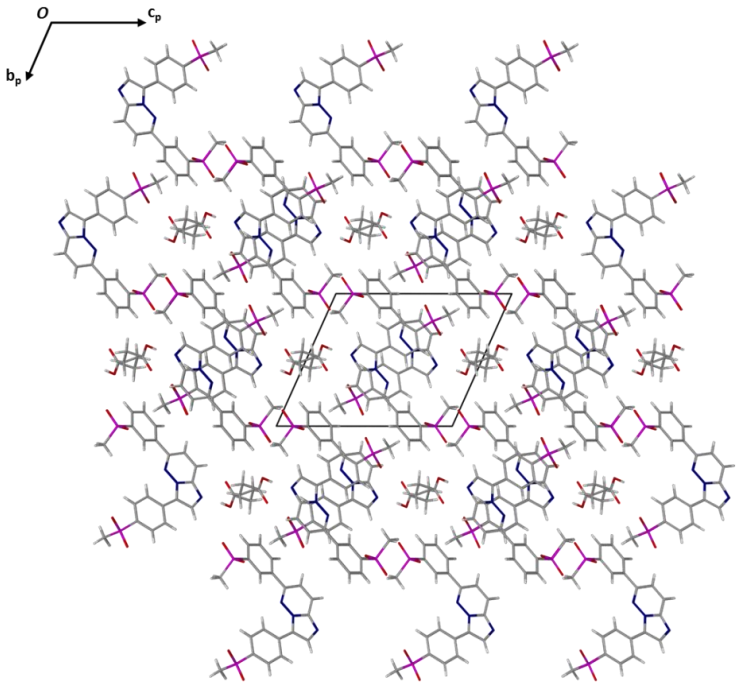

Fig. 4.2.14 Packing of MMVADIP viewed along [100].

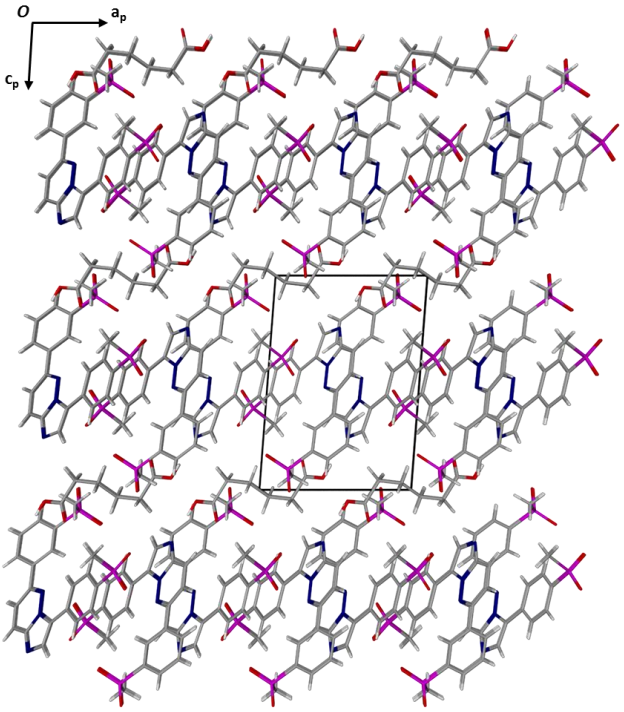

Fig. 4.2.15 Packing of MMVADIP viewed along [010].

PXRD

The PXRD traces of MMVADIP produced by LAG with acetone and the trace computationally generated from the solved crystal structure of MMVADIP are compared in Fig. 4.2.16. The highest intensity peak at 27.87 °2θ corresponds to reflection from the (2 -2 2) planes with a d-spacing of 3.201 Å. These planes coincide with the layers seen in Fig. 4.2.6. The traces match well enough that the method of preparation was considered adequate to produce this form for subsequent experiments.

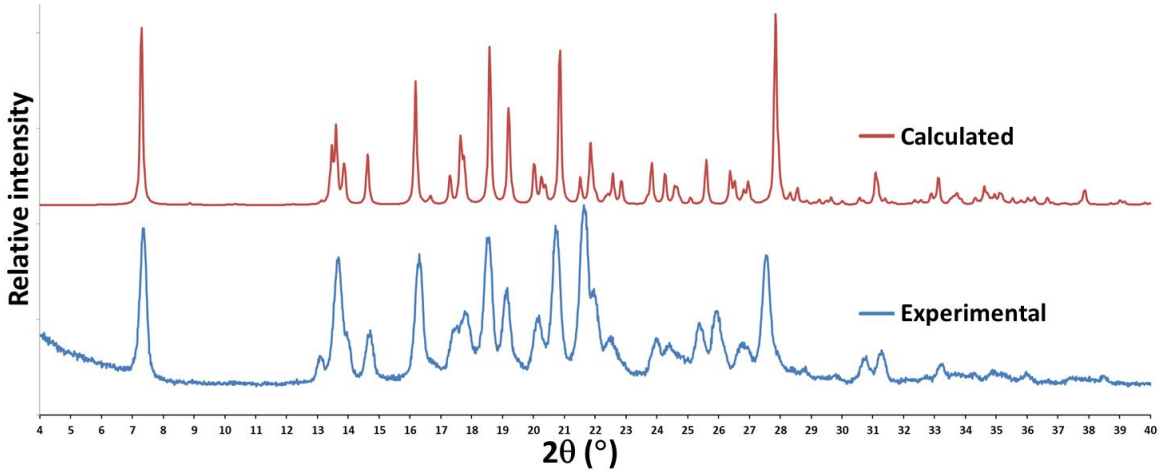

Fig. 4.2.16 PXRD traces collected for the bulk product produced by LAG (MMV, adipic acid and acetone) and a trace computationally generated from the single crystal structure of MMVADIP.

Thermal analysis

The HSM results for MMVADIP are presented in Fig. 4.2.17. The micrographs show that by 210 °C the crystals had started to melt and by 235 °C most of the crystals had melted. Melting was complete by 242 °C.

The experimentally observed onset of melting in the DTA result (Fig. 4.2.18) for the adipic acid starting material near 150 °C with a peak at 152 °C corresponds to the value of 151.5 (0.6) °C found in the literature.[15] The MMV starting material had a melt onset at 245 °C (matching the values reported in Chapter 4 part 1 for MMV Form 1) and a peak near 253 °C. MMVADIP had a melting onset of 215.5 ± 0.99 °C (n = 3) and a peak at 220.9 ± 0.12 °C (n = 3). The clear difference in the temperatures at which the LAG product melted when compared to the starting materials is an indication of a new form having been produced. It does not however, rule out the formation of polymorphs, hydrates, or solvates of the starting components.

The mass loss observed from 100 to 300 °C through TGA (Fig. 4.2.19) of 15.17 ± 0.09 % (n = 3) equates to 1 molecule of adipic acid for every 2 molecules of MMV (the theoretical percentage is 14.6). This matches the ratio seen in the SCXRD and NMR results. The first step had an observed onset of 214.5 ± 0.6 °C (n = 3). This value is very close to the observed melting onset in the DSC result.

Fig. 4.2.17 Representative HSM photographs of MMVADIP at various temperatures.

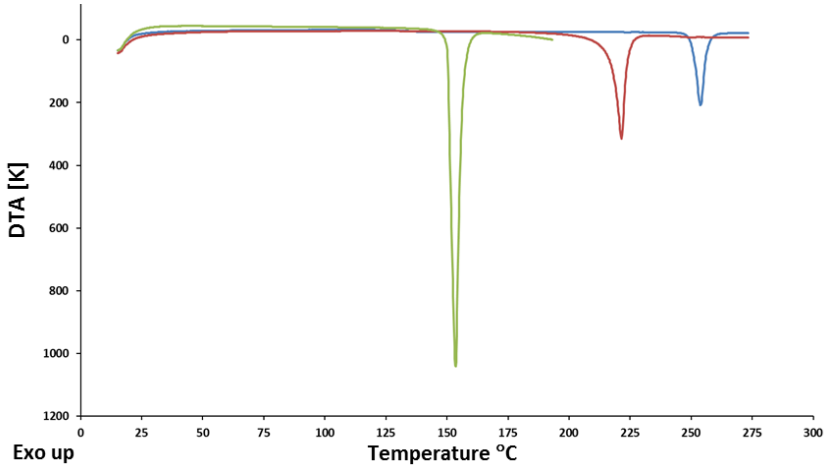

Fig. 4.2.18 Representative DTA thermogram of MMV (Blue) and adipic acid (Green) starting materials and of MMVADIP (Red).

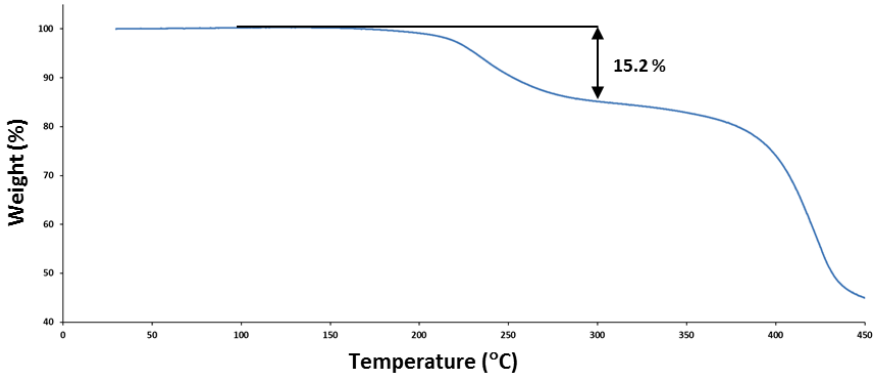

Fig. 4.2.19 Representative TGA trace of MMVADIP.

Solubility test

In order to compare the solubility and dissolution rate of the co-crystal to that of the pure compound, a quantitative kinetic solubility measurement was carried out. A total of 29.27 mg of MMVADIP (equivalent to 25.00 mg of pure MMV) was added to 50 cm^3 of fasted state simulated intestinal fluid (FaSSIF) that was kept at a constant temperature of 37.5 ± 0.5 °C while being stirred at 500 rpm. Aliquots of 0.7 cm^3 were taken at specific time points, filtered through 0.22 µm nylon filters, and diluted to 1 cm^3 by adding pure acetonitrile to prevent precipitation after filtering. The samples were then analysed by HPLC and the concentrations were determined by comparing the mAU (milli-Absorbance Unit) areas to a calibration standard curve (see appendix A, Fig. A2.6).

From Fig. 4.2.20 it is clear that the co-crystal form has a greater solubility and dissolution rate than the unaltered MMV starting material. The highest concentration measured (S_{max}) calculated from the average of two experiments was 16 ± 0.5 µg. cm^{-3} (n = 2). This value was observed 5 minutes after adding the samples to the stirring solution and is more than four times as high as the reference S_0 value (3.5 ± 0.2 µg. cm^{-3} (n = 2)). The concentration of free MMV in solution from the co-crystal is already much higher (15 ± 3 µg. cm^{-3} (n = 2)) after one min of stirring than the maximum reached in the control experiment and reaches a value close to the maximum observed for the co-crystal. After peaking at 5 min, the concentration starts dropping and is already lower at 10 min (12.5 ± 0.6 µg. cm^{-3} (n = 2)). By 15 min of stirring the concentration has dropped to a value comparable to the control and after this interval the concentration is lower than for the control and remains within a range of 1.6 to 2.5 µg. cm^{-3} from the 30 min mark to the final measurement.

The result can be attributed to the high solubility of the coformer in the aqueous solution medium. The MMV molecules should rapidly dissociate from the coformer molecules as the coformer leaches into the aqueous medium and give rise to the spike in concentration right at the start of the experiment. As time progresses, the MMV molecules can reassemble into solid MMV-MMV conglomerates as well as the hydrated solid form of the compound. The effect is commonly seen in co-crystal solubility experiments[16-21] and is referred to by Cheney *et al.* as the "spring and parachute" effect.[19] In this case the product was centrifuged and was determined to be mostly the hydrated form of MMV through PXRD comparison with the known forms. In this case the parachute effect was not as evident, however. The potential implication of this result is that the free drug candidate molecules could be absorbed rapidly through the intestinal epithelium as the co-crystal dissociates, before it has time to interact with other MMV

molecules and precipitate back into a solid that could not be absorbed. This could have a considerable impact on the bioavailability of the drug and through this means greatly improve its efficacy.

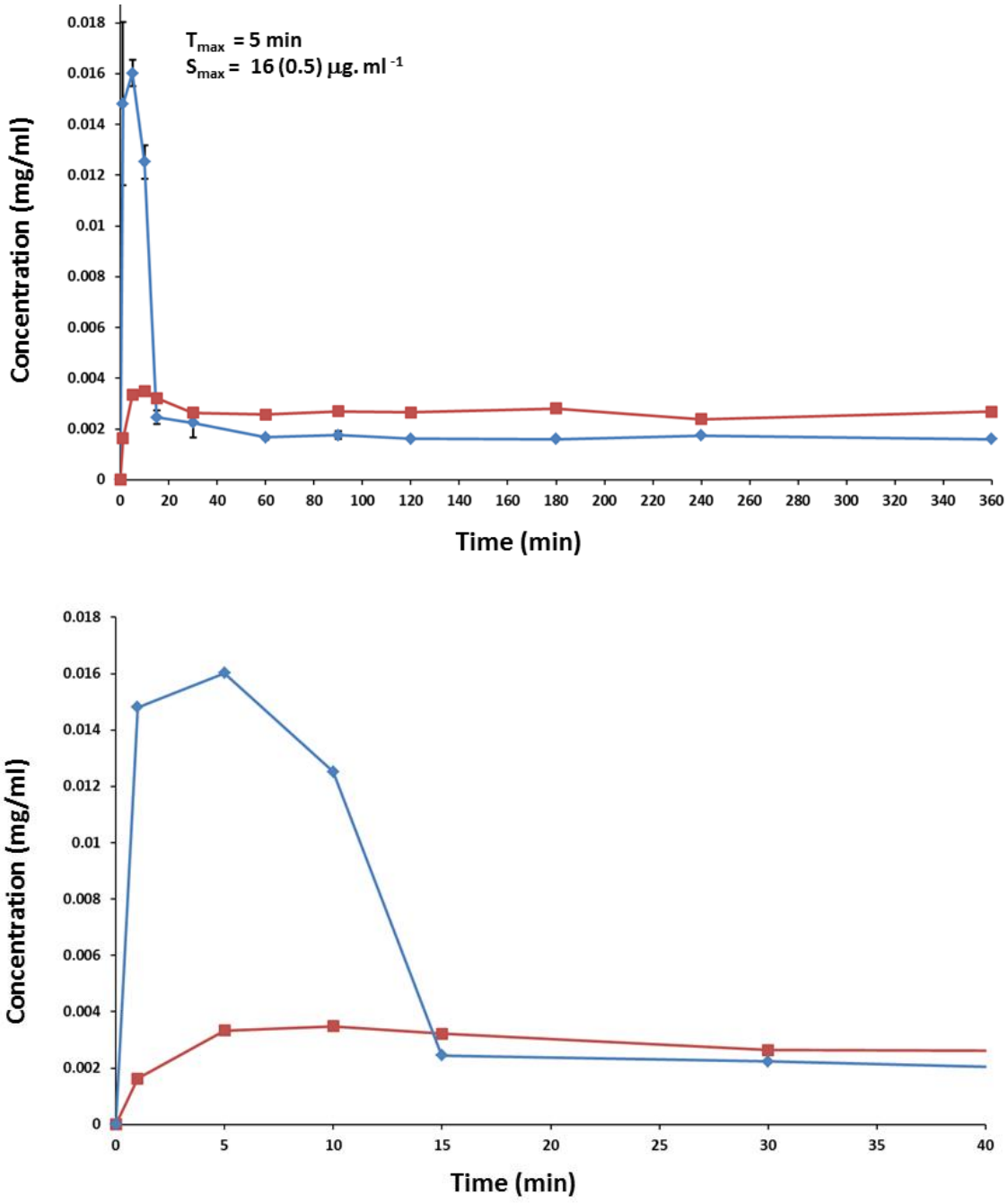

Fig. 4.2.20 Powder dissolution profile of MMV (red) compared to MMVADIP (blue) in FaSSIF at 37.5 ± 0.5 °C (showing the average of two experiments). The top and bottom figures show the concentration measurements over 6 h and 40 min respectively).

MMV-glutaric acid co-crystal (MMVGLUT)

5 mg of MMV was ground with a mortar and pestle with an equimolar amount of glutaric acid for 15 min while adding acetone in small drops. The product was then analysed by PXRD and the resulting trace was compared to the starting materials of MMV and the coformer. The results are shown in Fig. 4.2.21. There were many clear differences visible, the most noticeable of these being at °2θ of 4.0, 16.4, 17.6, 24.7, and 28.0.

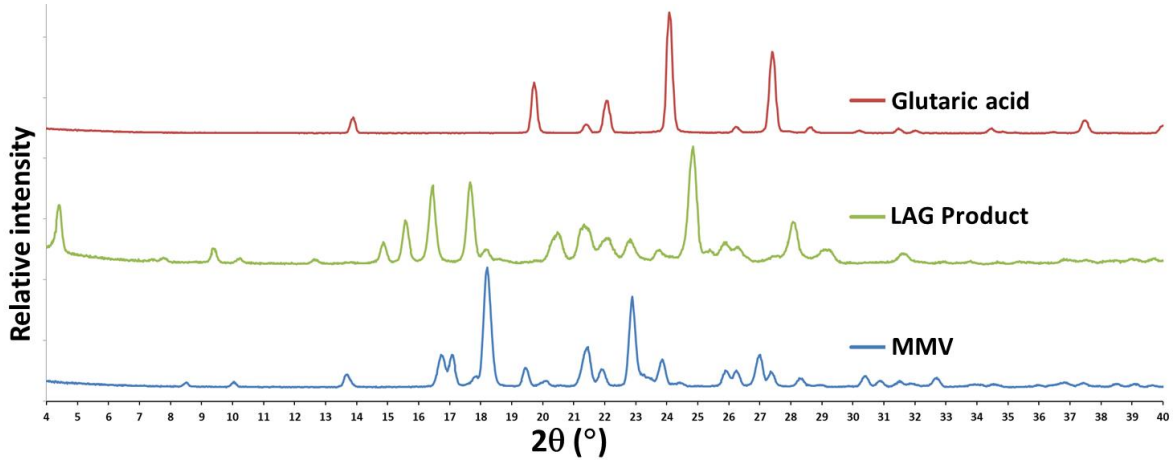

Fig. 4.2.21 Recorded PXRD traces for the product of a LAG experiment and the starting materials, MMV and glutaric acid.

Preparation of single crystals

Single crystals of the co-crystals were obtained by co-precipitation by dissolving 5 mg of MMV with roughly 10 times the molar amount of glutaric acid (15 mg) in 1 cm^3 of acetone while stirring at 50 °C and filtering through a 0.45 µm nylon filter into a clean vial and placing on a benchtop after covering the vial with Parafilm™.

Stoichiometry determination by ^{1}H – NMR spectroscopy

Single crystals of MMVGLUT obtained by co-precipitation were dissolved in DMSO-d_6 and analysed by ^{1}H-NMR spectroscopy to determine the stoichiometric ratio of the individual components. The proton labelling schemes and the ^{1}H-NMR spectrum are shown in Fig. 4.2.22. The integration values are presented in Table 4.2.4. The ratio was determined to be 1:1.15 (~1:1) of MMV to glutaric acid. The ratio being slightly higher for the coformer than MMV is most likely due to some of the pure coformer having precipitated on the surfaces of, or in between, the MMVGLUT crystals as the starting ratio for the co-precipitation had an abundance of coformer present (a 10:1 ratio).

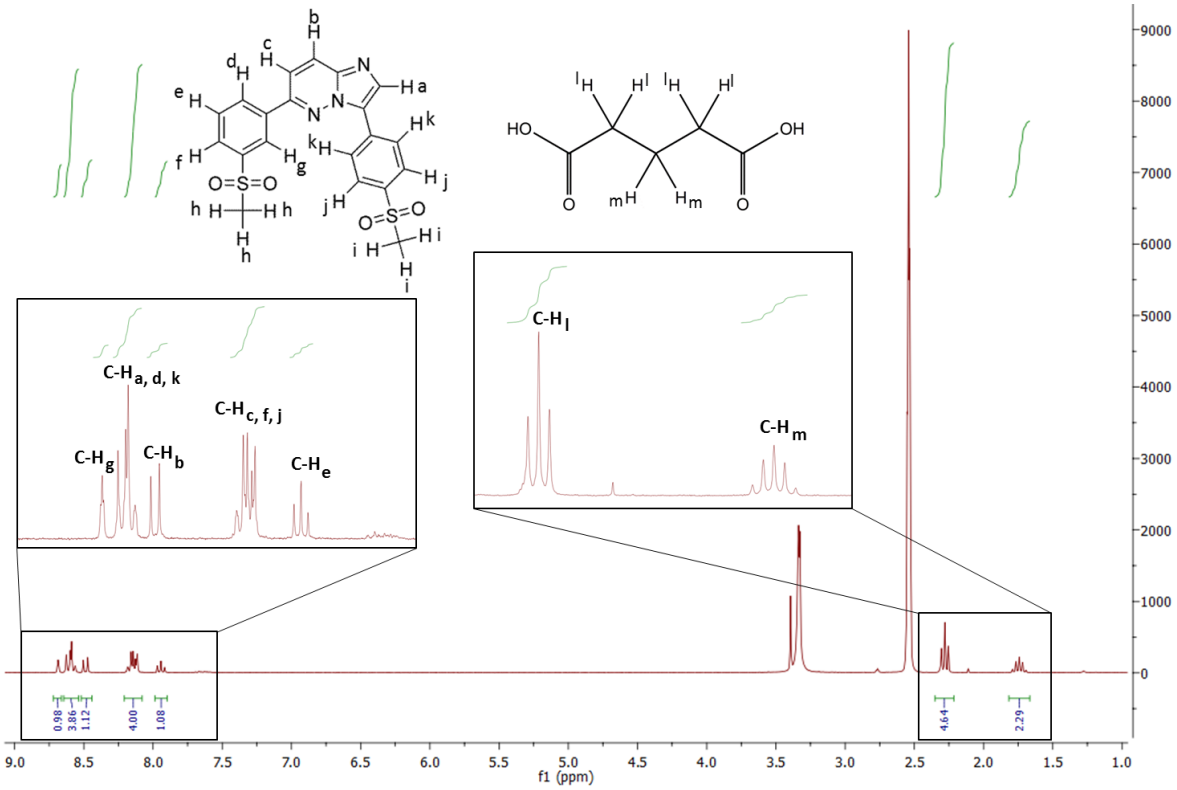

Fig. 4.2.22 ^{1}H-NMR spectrum of MMVGLUT in DMSO-d_6 for determination of stoichiometry.

Table 4.2.4 Integrals of protons for individual components to determine stoichiometry of MMVGLUT.

Proton – [Number of protons]	δ (ppm)	Integration	Experimental/ Theoretical
MMV			
C-$H_{c,f,j}$– [4]	8.079-8.207	4.00*	1.00
C-H_g – [1]	8.662-8.719	0.98	0.98
C-$H_{a,d,k}$– [4]	8.538-8.645	3.86	0.97
C-H_b – [1]	8.441-8.518	1.12	1.12
C-H_e – [1]	7.898-7.985	1.08	1.08
Glutaric acid			
C-H_l – [4]	2.215-2.352	4.64	1.16
C-H_m – [2]	1.665-1.817	2.29	1.15

*** Reference integral**

Infrared spectroscopy

The FTIR spectrum of glutaric acid (Fig. 4.2.23) shows all the same characteristic features described for adipic acid. The broad and relatively intense band due to the O-H stretching of glutaric acid is visible in the region from 2500 to 3400 cm^{-1}. The in-plane and out-of-plane O-H bending bands are visible at 910 cm^{-1} and 1406 cm^{-1} respectively. The carbonyl stretch at 1686 cm^{-1} is the most intense peak in the spectrum.

A broad band centred around 1910 cm^{-1} in the spectrum of MMVGLUT and a less noticeable broad band centred around 2450 cm^{-1} are a result of the O-H···N stretching between the acid and imidazole moieties. These broad bands are generally used as a means of quick screening for co-crystals with dicarboxylic acids before the crystal structure is solved.[7,22]

The shift due to the asymmetric stretching of the carbonyl group of the coformer that was visible in the case of MMVADIP is visible in this case as well (1686 to 1710 cm^{-1}). The peak is however split into two distinct peaks at 1687 and 1710 cm^{-1} respectively. The peak at 1710 cm^{-1} is most probably due to the carbonyl stretching interaction between the coformer and MMV molecules. The other peak seen at 1687 cm^{-1} is possibly due to the carbonyl stretch occurring between two coformer molecules. Both homo- and hetero- interactions can be seen in the crystal structure of this co-crystal (presented in following section (Fig. 4.2.27)). There exist many examples of co-crystals with this coformer and the splitting of the carbonyl band is also observed in other cases where similar homo- and hetero-interactions are observed. An example of this is in the case of a 1:1 co-crystal of Riluzole with glutaric acid reported by Mondal *et al.*[23] The shift to a higher energy of the carbonyl stretch band can serve as a good indication of the formation of a co-crystal though the final proof should be found in the elucidation of the crystal structure by single-crystal X-ray diffraction.

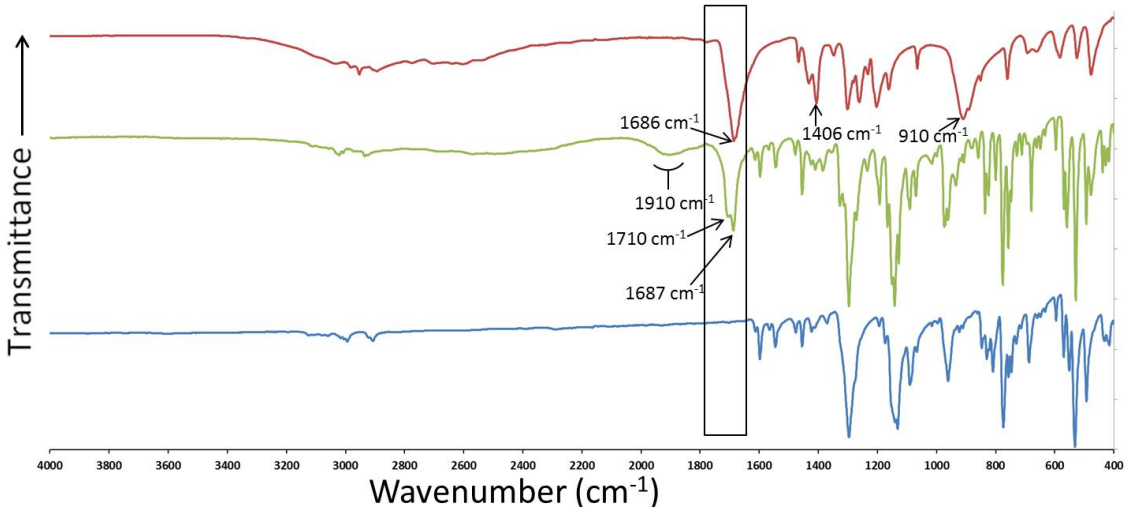

Fig. 4.2.23 FTIR spectra of MMV (blue), MMVGLUT (green), and glutaric acid (red).

Crystal structure analysis

Data-collection and space group determination

The single-crystal X-ray intensity data collection was performed on a Bruker Kappa Apex II Duo diffractometer at 300(2) K. The diffraction turned out to be of improved quality when doing the collection at this higher than usual temperature. $\bar{1}$ Laue symmetry was observed in the X-ray diffraction pattern. This indicates that the crystal belongs to the triclinic crystal system and the mean $|E^2-1|$ value obtained by making use of the software XPREP[9] was 0.981 corresponding to centrosymmetry. The obvious choice of space group was $P\ \bar{1}$.

Structure solution and refinement

Crystallographic data, parameters for collection of intensity data and refinement details are reported in Table 4.2.5. The methods for data reduction, unit cell refinement and structure elucidation were the same as described for MMVADIP.

In order to ascertain if proton transfer had occurred and thereby determining if the product was a salt or a co-crystal, the locations of the carboxyl hydrogens of the glutaric acid molecules and the imidazole nitrogens of the MMV molecules were sought in the Fourier difference map, which clearly showed that both protons were present as the carboxyl hydrogens. The distinct C-O bond lengths of the glutaric acid moiety that forms the hydrogen bond with the MMV nitrogen of the imidazole moieties are 1.310(2) Å and 1.191(2) Å, representing single and double bonds. The C-O bond lengths of the carboxylic acid

moiety forming the dimer interaction at the opposite terminal are 1.232(2) Å and 1.274(2) Å. Both molecules were thus in the neutral state, indicating that the structure is a co-crystal.[12,13] All hydrogen atoms were found in difference electron density maps and placed in idealised positions in a riding model and refined with thermal parameters 1.2-1.5 times the U_{iso} values of their parent atoms.

Table 4.2.5 Data-collection and refinement parameters for MMVGLUT.

Molecular formula	$(C_{20}H_{17}N_3O_4S_2) \cdot (C_5H_8O_4)$
Formula weight (g mol^{-1})	559.60
Crystal system	Triclinic
Space group	$P\ \bar{1}$
a (Å)	5.0654(3)
b (Å)	12.4436(8)
c (Å)	20.7515(13)
α (°)	101.9293(12)
β (°)	90.5518(12)
γ (°)	99.4137(13)
V (Å)^3	1261.24(14)
Z	2
D_c (g cm^{-3})	1.474
μ (Mo Kα) (mm^{-1})	0.267
F(000)	584
Data-collection temp. (K)	300(2)
Crystal size (mm^3)	0.31 x 0.20 x 0.10
Range scanned θ (°)	1.69 – 28.38
Index ranges ±*h*, ±*k*, ±*l*	-6, 6; -16, 16; -27, 27
Reflections (total)	30 036
Independent reflections	6299
Reflections with I>2σ(I)	4809
Number of parameters	345
R_{int}	0.0381
S	1.038
R_1 [*I*>2σ(*I*)]	0.0422
Reflections omitted	3
wR_2	0.1245
a, b in w = 1/[$\sigma^2(F_o^2)$+(aP)^2+(bP)]	a = 0.0633; b = 0.3191
$(\Delta/\sigma)_{mean}$	< 0.001
$\Delta\rho_{min,max}$ (e Å^{-3})	-0.317, 0.444

Molecular structure

The asymmetric unit and labelling scheme of MMVGLUT are shown in Fig. 4.2.24.

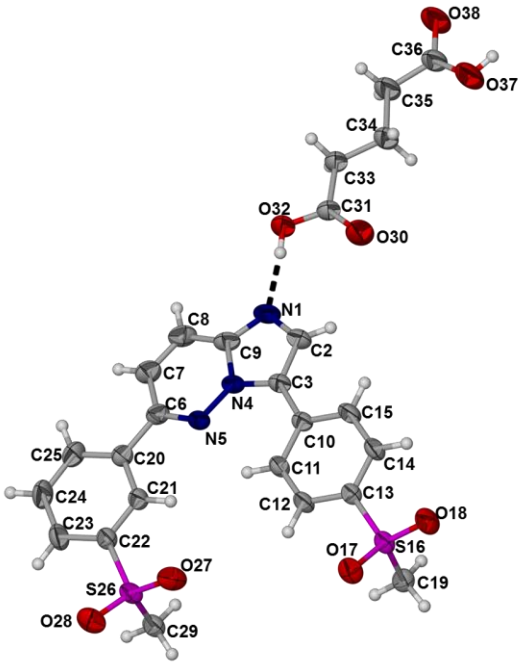

Fig. 4.2.24 The asymmetric unit and numbering scheme of MMVGLUT with thermal ellipsoids shown at the 50% probability level.

Crystal packing and hydrogen bonding

The relevant symmetry information for MMVGLUT is listed in Table 4.2.6.

Table 4.2.6 Hydrogen bonds in MMVGLUT[a].

	D–H···A	*d*(D–H), Å	*d*(H···A), Å	*d*(D···A), Å	∠(DHA), deg.
	O32-H32···N1	0.82	1.85	2.662(2)	173
	O37-H37···O38^{i}	0.82	1.83	2.637(3)	168
	C8-H8···O38^{ii}	0.93	2.47	3.378(3)	165
Intra	C11-H11···N5	0.93	2.31	2.967(2)	127
Intra	C14-H14···O18	0.93	2.57	2.934(2)	104
	C19-H19A···O17^{iii}	0.96	2.59	3.271(2)	128
	C19-H19B···O17^{iv}	0.96	2.50	3.385(3)	153
	C19-H19C···O27^{iv}	0.96	2.48	3.344(3)	149
Intra	C21-H21···O27	0.93	2.51	2.892(2)	105
Intra	C21-H21···N5	0.93	2.36	2.696(2)	101'
	C24-H24···O30^{v}	0.93	2.37	3.204(3)	149
	C29-H29B···O18^{vi}	0.96	2.42	3.334(2)	160
Intra	C23-H23···O28	0.93	2.68	3.001(2)	101
Intra	C12-H12···O17	0.93	2.70	3.020(2)	101

[a] Symmetry transformations used to generate equivalent atoms: *[i]: 4-x,2-y,-z; [ii]: 3-x,1-y,-z; [iii]: 1+x,y,z; [iv]: -1-x,1-y,1-z; [v]: -1+x,-1+y,z; [vi]: x,-1+y,z*

These crystals show a layered packing arrangement. The interactions connecting the molecules are summarised in Table 4.2.6 and Figs. 4.2.25 and 4.2.26.

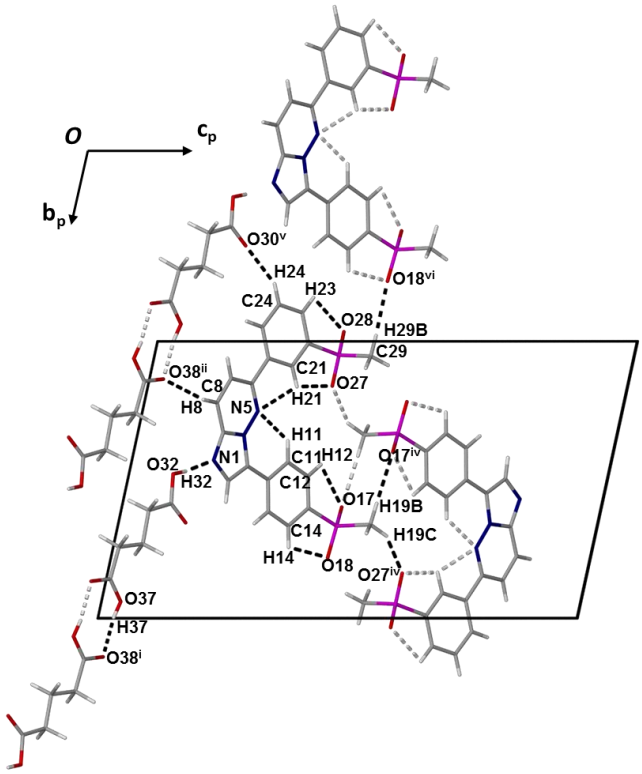

Fig. 4.2.25 Hydrogen bonding interactions found in the structure of MMVGLUT viewed along [100].

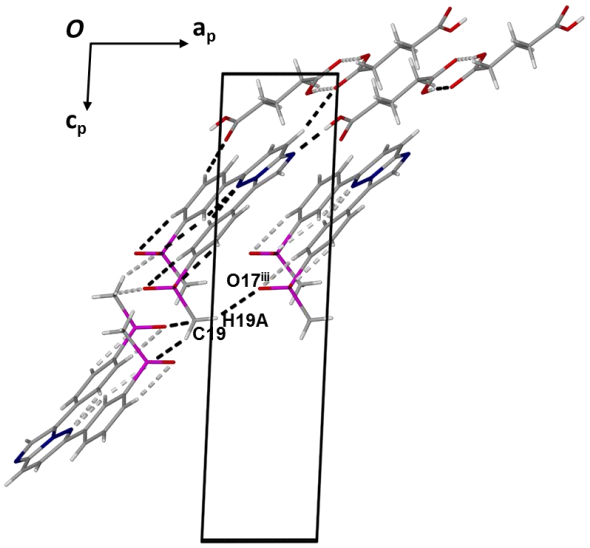

Fig. 4.2.26 Diagram to illustrate hydrogen bonding interactions found in the structure of MMVGLUT viewed along [010].

A discrete ribbon ($D_3^3(19)$) is formed by two MMV molecules being linked by two glutaric acid molecules that are connected by a dimer between carboxylic acid moieties (O37-H37···O38′ $R_2^2(8)$) (Fig. 4.2.27). These discrete ribbons form continuous ribbons through the interactions C19-H19B···O17′ ($R_2^2(8)$) and C19-H19C···O27′ ($R_2^2(32)$) connecting the MMV molecules at the ends of these discrete ribbons with MMV molecules of the following MMV molecules (Fig. 4.2.25 and 4.2.28). The distance separating C2-H2 and O30 indicates that these atoms are not connected via a hydrogen bond.

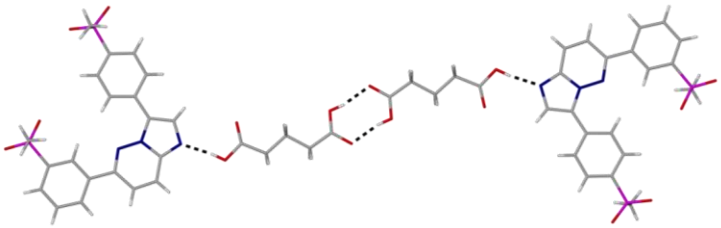

Fig. 4.2.27 Discrete ribbons ($D_3^3(19)$) connected by a ring formed by a dimer between two carboxylic acid moieties of the coformer (O37-H37···O38′ $R_2^2(8)$).

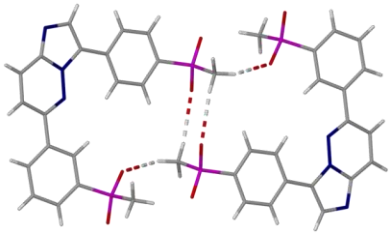

Fig. 4.2.28 Ring interactions connecting discrete ribbons to form continuous ribbons: C19-H19B···O17′ ($R_2^2(8)$) and C19-H19C···O27′ ($R_2^2(32)$).

The ribbons are also repeated diagonally to form the layers mentioned earlier and are connected by the interactions: C8-H8···O38′ and C24-H24···O30′ ($R_4^4(30)$); O32-H32···N1 and C8-H8···O38′ ($R_4^4(24)$) (Fig. 4.2.29). The topology of the layers can be seen in Figs. 4.2.30 and 4.2.31 and the stacked layers are visible in Fig. 4.2.32.

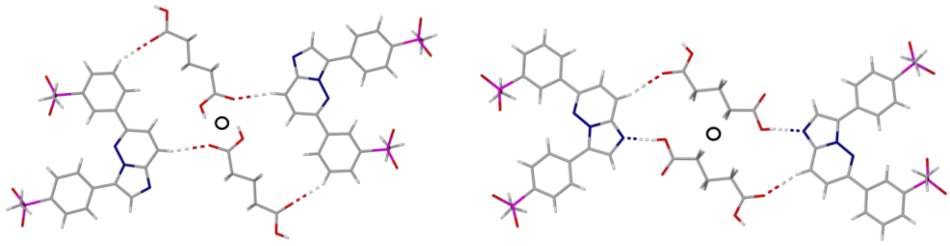

Fig. 4.2.29 Interactions connecting molecules to form layers: C8-H8···O38′ and C24-H24···O30′ ($R_4^4(30)$) (left) and O32-H32···N1′ with C8-H8···O38′ ($R_4^4(24)$) (right).

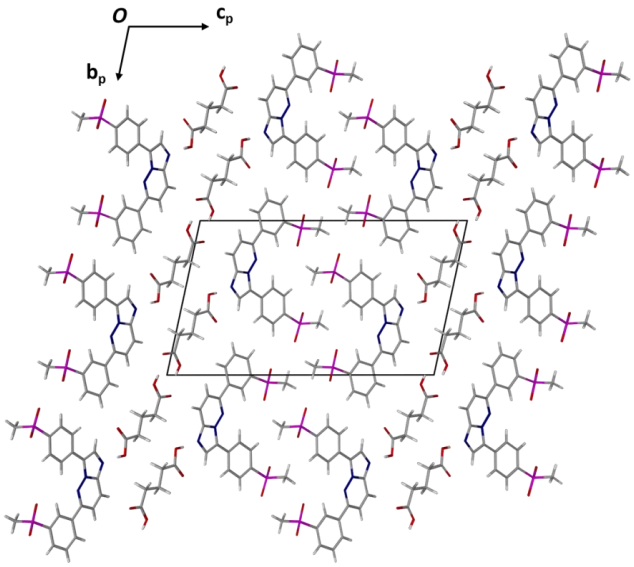

Fig. 4.2.30 Packing of MMVGLUT viewed along [100] showing the topology of the layers.

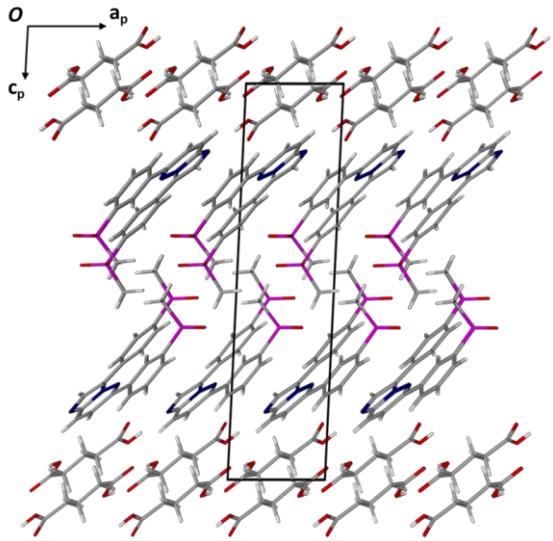

Fig. 4.2.31 Packing of MMVGLUT viewed along [010].

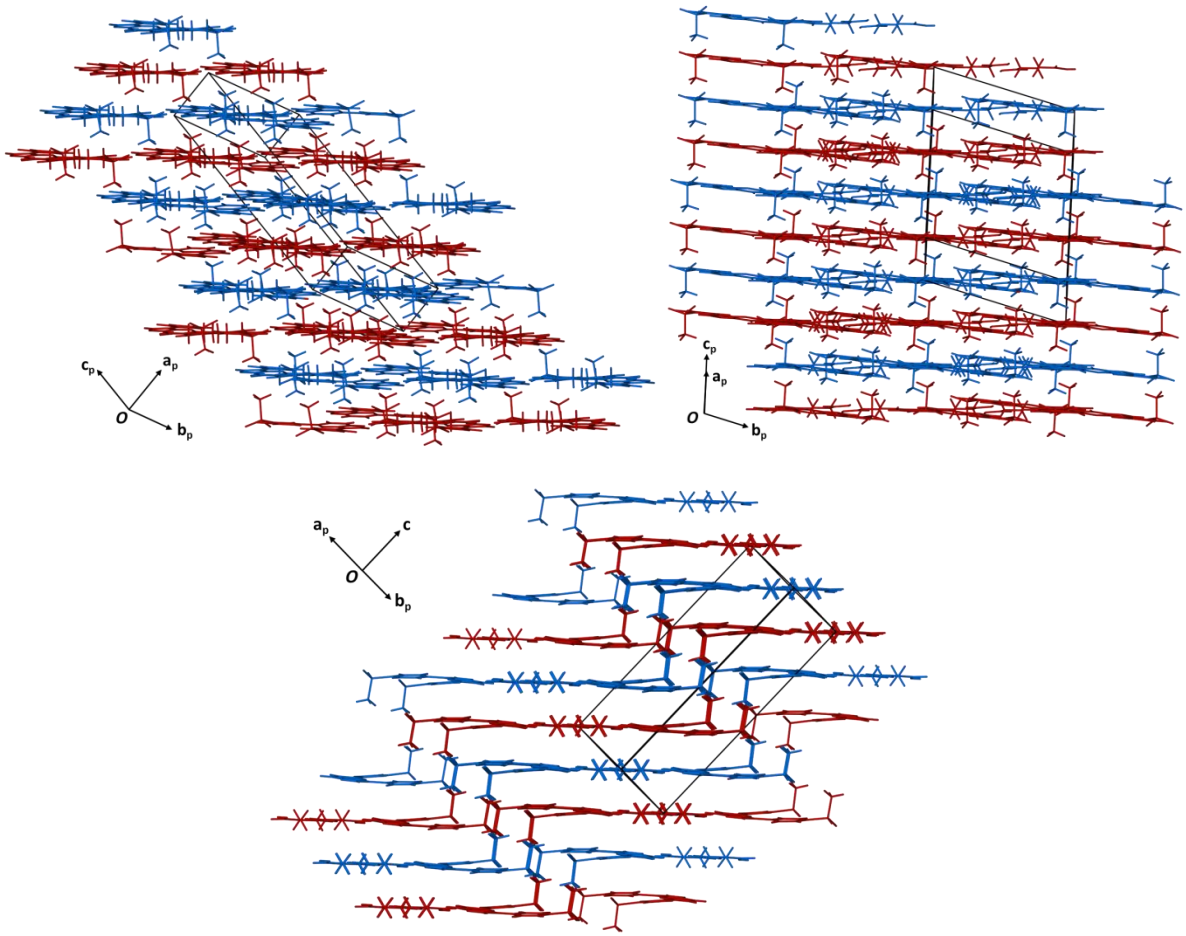

Fig. 4.2.32 Showing the packing of layers of MMVGLUT from different perspectives.

The stacked layers are connected by the following interactions: C19-H19B···O17′ and C19-H19A···O17′ ($R_4^2(8)$ and $R_4^4(16)$) (Fig. 4.2.33); C29-H29B···O18′ and C19-H19B···O17′ ($R_4^4(40)$); C29-H29B···O18′ and C19-H19C···O27′ ($R_4^4(16)$) (Fig. 4.2.34); H19A···O17′ and C19-H19C···O27′ ($R_4^4(36)$); C29-H29B···O18′ and C19-H19A···O17′ ($R_4^4(40)$).

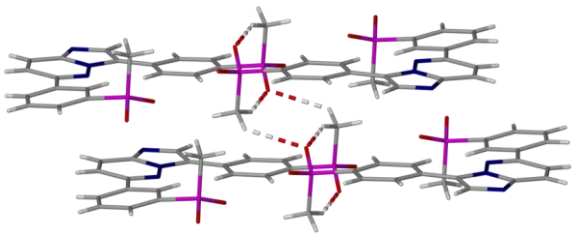

Fig. 4.2.33 Interactions connecting stacked layers: C19-H19B···O17′ and C19-H19A···O17′ ($R_4^2(8)$ and $R_4^4(16)$).

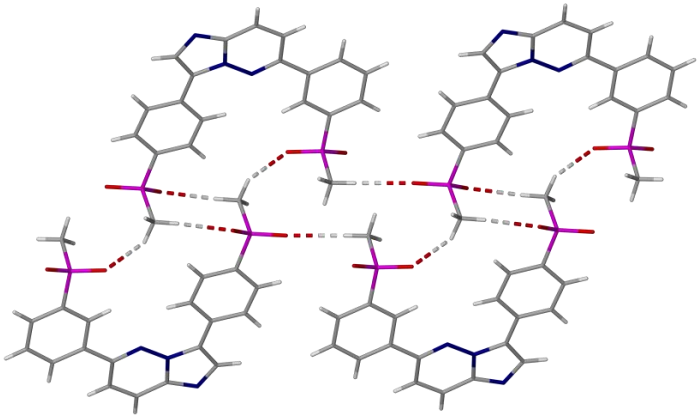

Fig. 4.2.34 Interactions connecting layers: C29-H29B···O18'and C19-H19B···O17' ($R_4^4(40)$); C29-H29B···O18' and C19-H19C···O27' ($R_4^4(16)$).

PXRD

A calculated PXRD trace from the solved crystal structure of MMVGLUT is compared with an experimentally produced trace of MMVGLUT prepared by LAG with acetone in Fig. 4.2.35. The good match between the traces indicates that this method was successfully used to produce the co-crystal form in bulk for further analysis. The peak with the highest intensity is at 24.7 °2θ. This peak is associated with the (1 -1 4) planes and d-spacing of 3.605 Å. These planes correlate with the stacked layers observed in Fig. 4.2.32.

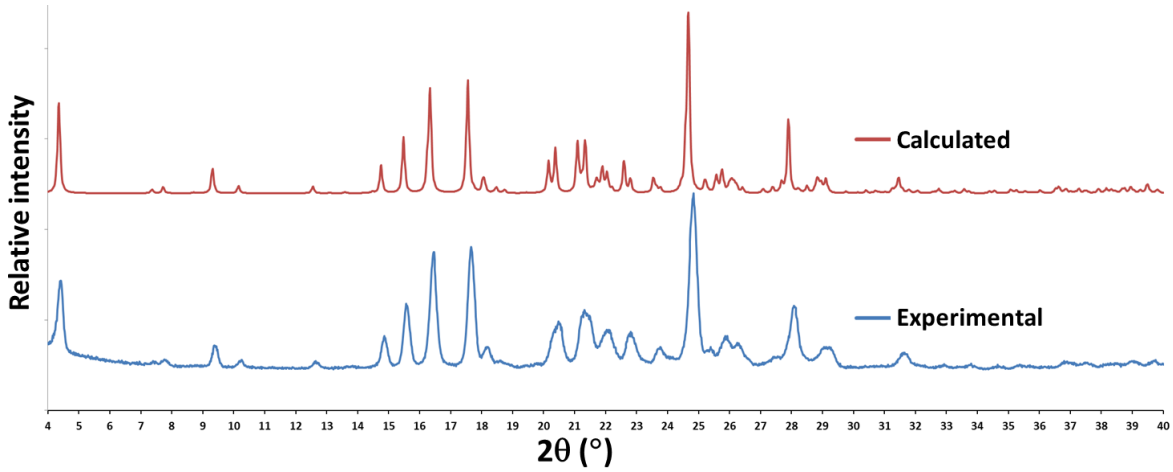

Fig. 4.2.35 PXRD traces collected for the bulk product produced by LAG (using acetone) and a trace computationally generated from the single crystal structure of MMVGLUT.

Thermal analysis

The HSM result for a crystal of MMVGLUT is presented in Fig. 4.2.36. The crystals became more opaque around 175 °C and started to sprout crystallites from within the original specimen at 190 °C. Melting occurred at around 260 °C.

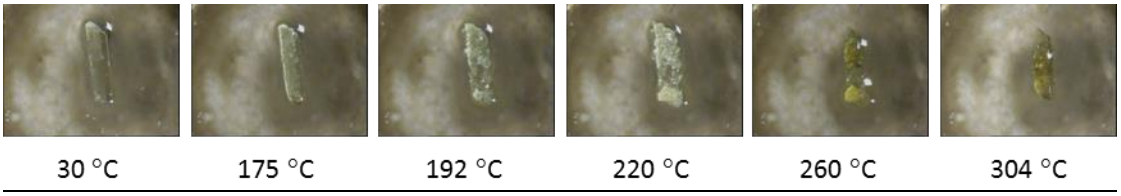

Fig. 4.2.36 Representative HSM photographs of MMVGLUT at various temperatures.

The pure coformer glutaric acid had a melting onset of 91.7 °C and a peak at 93.2 °C when analysed with DTA (Fig. 4.2.37). This is slightly lower than the value reported in literature, namely 97.9(0.3) °C.[15] The LAG product MMVGLUT displayed a thermal event with an onset of 160.2 ± 0.5 °C (n = 3) and a peak at 168.3 ± 0.1 °C (n = 3).

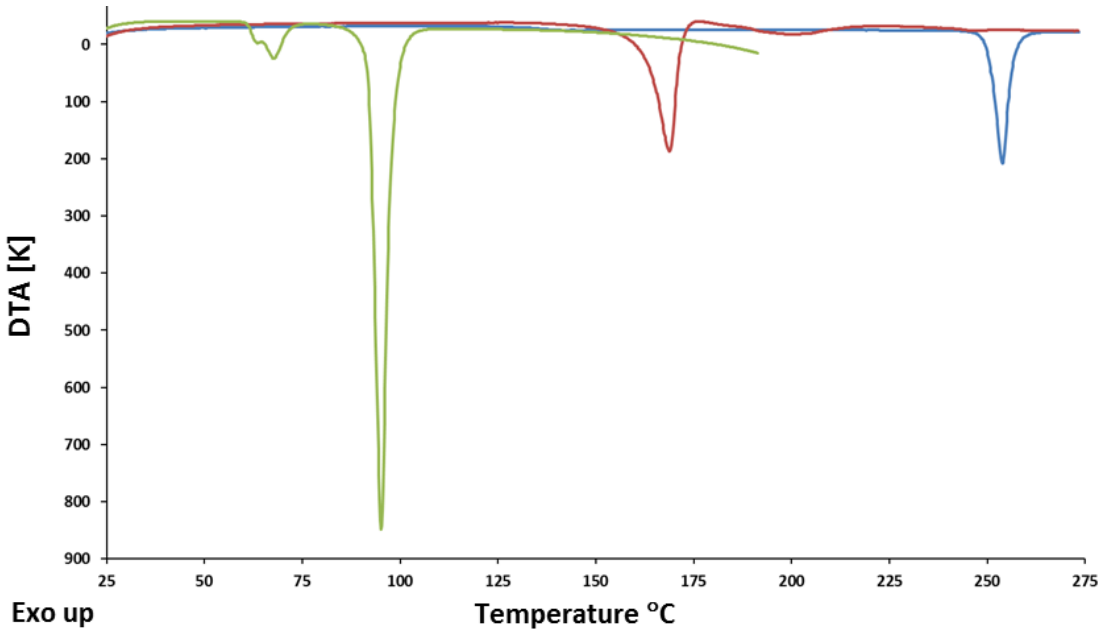

Fig. 4.2.37 Representative DTA thermogram of MMV (Blue) and glutaric acid (Green) starting materials and for MMVGLUT (Red).

The onset of mass loss seen in the TGA trace (Fig. 4.2.38) at 186 ± 3 °C (n = 3) is higher than the temperatures where changes are visible in the HSM and DTA results. The mass loss of 24.8 ± 0.5 % (n = 3) observed from 100 to 300 °C through TGA equates to one molecule of glutaric acid for every molecule of MMV (theoretical percentage 23.6). This matches the ratio seen in the SCXRD and NMR results. The TGA trace indicates that the event observed in the DTA trace as well as the HSM micrographs is a result of the sublimation of glutaric acid as it has a reported boiling point of 200 °C. The co-crystal shows significantly different thermal behaviour from those of the individual starting components.

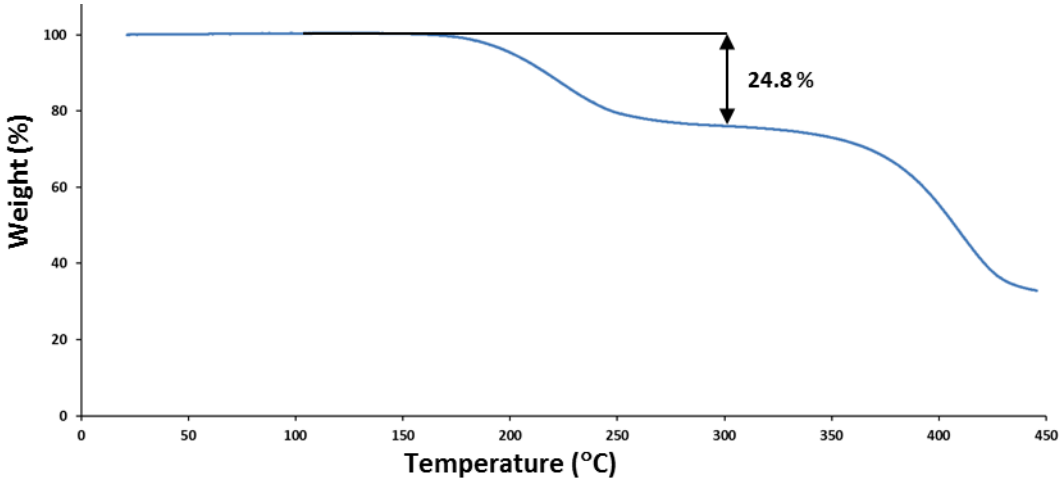

Fig. 4.2.38 Representative TGA trace of MMVGLUT.

Solubility test

32.73 mg of MMVGLUT, equivalent to 25.00 mg of pure MMV, was added to 50 cm^3 of FaSSIF and stirred at a rate of 500 rpm at a temperature of 37.5 ± 0.5 °C with aliquots of 0.7 cm^3 taken at selected time intervals. The concentrations of dissolved MMV were measured by the method described in Chapter 2 and plotted in Fig. 4.2.39. The concentration at time 1 min (6.9 ± 0.3 µg. cm^{-3}; (n = 3)) was already much higher than that measured in the control experiment. The concentration continued rising to an S_{max} of 16.4 ± 1.9 µg. cm^{-3} (n = 3) at 10 min. This value is a factor of 4.7 times that of the reference S_0 value. By 30 min the concentration had started to drop and was down to a concentration lower than at the 5 min mark. When looking at the average of three experiments the concentration steadily decreases from 30 minutes (10 ± 1 µg. cm^{-3} (n = 3)) until it reaches a minimum of 7 ± 2 µg. cm^{-3} (n = 3) at the final aliquot taken after six hours. The mechanism by which this jump and subsequent slower lowering in

concentration occurs can again be attributed to the so-called “spring and parachute” effect[19] mentioned in earlier sections. The theory is that the highly water-soluble coformer molecules leach out of the solid co-crystals and result in a product consisting of a metastable or amorphous assembly of MMV alone. In the absence of the strong interactions keeping the MMV molecules together, the molecules should dissolve much more rapidly (the “spring” effect) and it would take time for the free MMV molecules to reform strong interactions with other molecules in the solution (i.e. other MMV, water or coformer molecules) resulting in the “parachute” effect. In this example the parachute effect is more apparent than in the case of MMVADIP where there was a much quicker drop in concentration following attainment of the peak. The final product was centrifuged after the last aliquot was taken and analysed by PXRD. Its PXRD trace matched that of the MMV monohydrate and this will explain the drop in concentration after the initial spike.

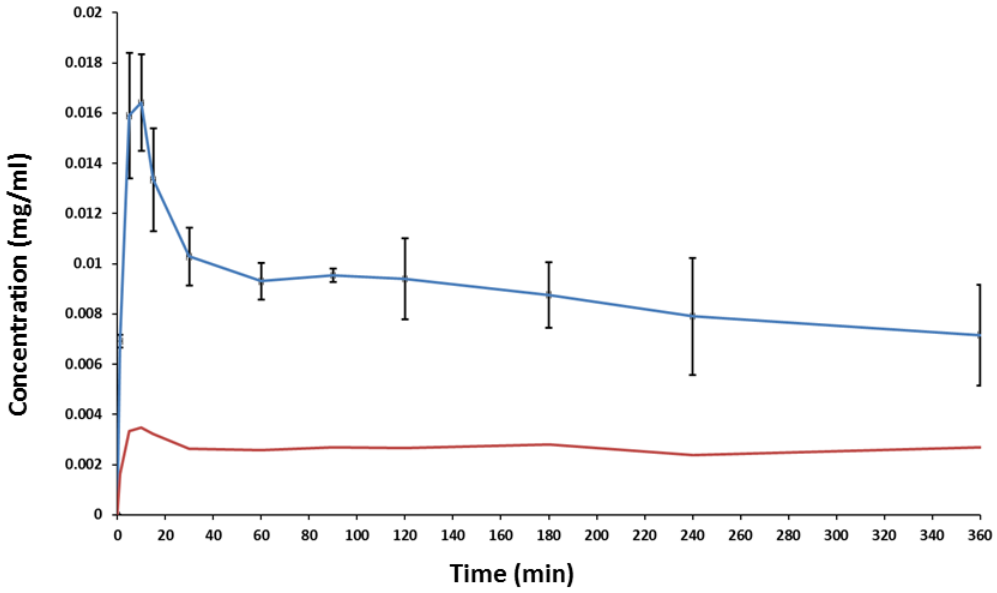

Fig. 4.2.39 Powder dissolution profile of MMV (Red) compared to MMVGLUT (Blue) in FaSSIF at 37.5 ± 0.5 °C.

MMV-succinic acid co-crystal (MMVSUCC)

Multiple multi-component phases were obtained in attempts to form co-crystals with MMV and succinic acid. In this section the various phases are grouped together and the characterisation of each phase and a comparison of the phases are presented in this section.

MMVSUCC1

5 mg of MMV was ground with a mortar and pestle with an equimolar amount of succinic acid for 15 min while adding acetone in small drops. The product was then analysed with PXRD and the resulting trace was compared to the PXRD patterns of the starting materials MMV and the coformer. The results are shown in Fig. 4.2.40. There were clear differences visible with new peaks at °2θ of 8.3, 8.6, 16.2, 21.0, 25.0, 28.0, and 30.7.

MMVSUCC2

The same method as mentioned above was used, the only difference being that the solvent employed in this case was ethanol. The product was analysed with PXRD and the resulting trace was compared to those of the starting materials MMV and the coformer as well as the new trace produced by LAG with acetone. The results are shown in Fig. 4.2.40. There were clear differences visible with new peaks appearing at °2θ values 4.6, 9.3, 15.2, 24.1, and 29.0. This trace did not match that of the trace produced by LAG of acetone either and for expediency this phase is termed MMVSUCC2.

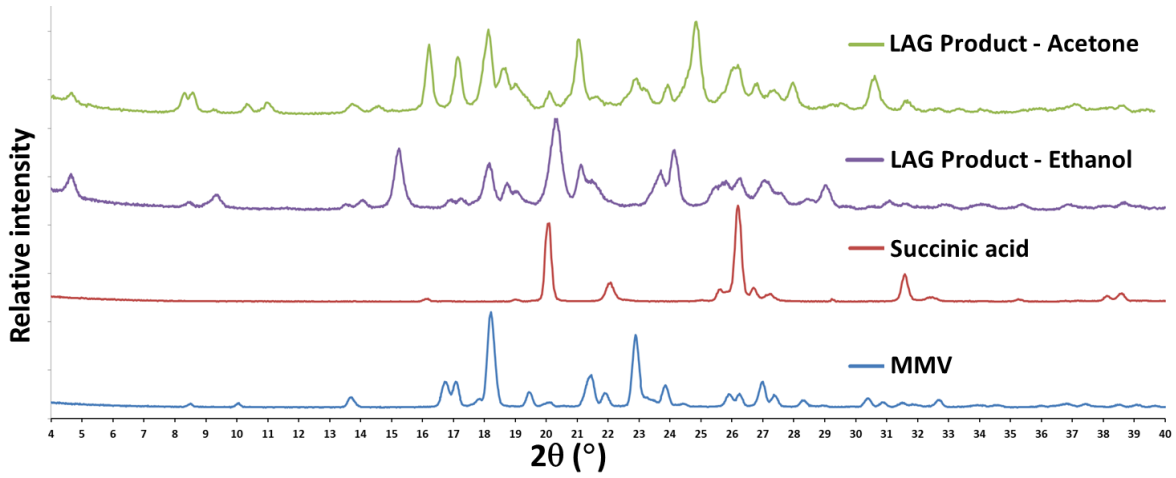

Fig. 4.2.40 Recorded PXRD traces for the product of LAG experiments using acetone and ethanol respectively and the starting materials, MMV and succinic acid.

Infrared spectroscopy

The characteristic FTIR features of dicarboxylic acids mentioned previously are visible in the case of succinic acid as well (Fig. 4.2.41). The O-H stretching band is visible between 2500 and 3400 cm^{-1}, the in-plane O-H bending band at 1410 cm^{-1}, the out-of-plane O-H bending band has a peak at 890 cm^{-1}, and the carbonyl stretch is the most intense peak at 1679 cm^{-1}.

Features very similar to those seen in the spectra of MMVADIP and MMVGLUT (Fig. 4.2.3 and 4.2.23 respectively) are visible in the spectrum of MMVSUCC1 (Fig. 4.2.41). The broad band centred around 1910 cm^{-1} and a much less obvious broad band centred around 2450 cm^{-1} due to the presence of O-H···N stretching between the acid and imidazole moieties are also visible in this case. The shift due to the asymmetric stretching of the carbonyl group of the coformer from 1679 to 1699 cm^{-1} is again indicative of the formation of a co-crystal.

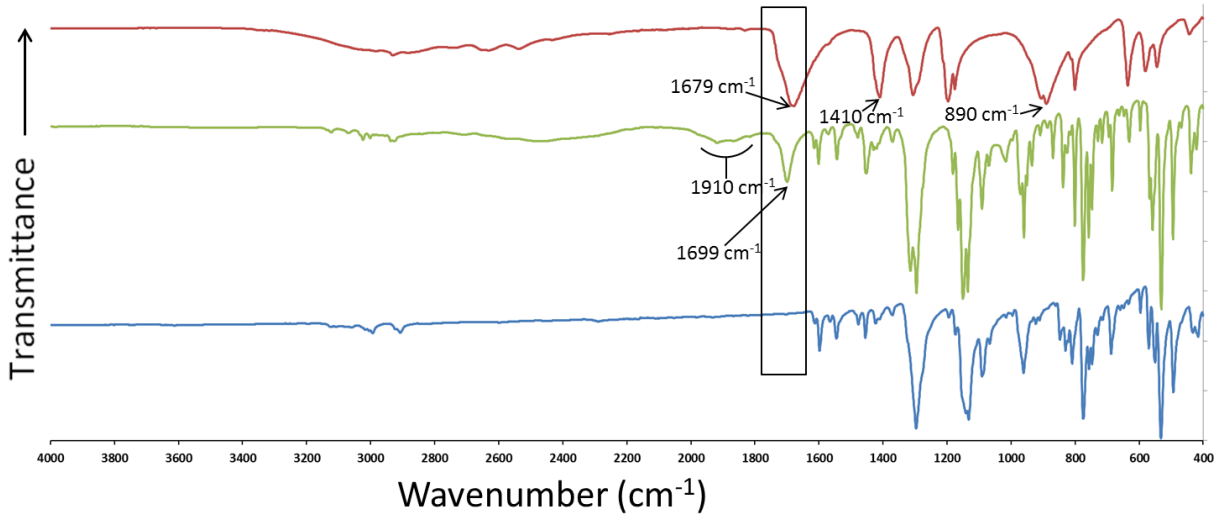

Fig. 4.2.41 FTIR spectra of MMV (Blue), MMVSUCC1 (Green), and succinic acid (Red).

In the FTIR spectrum of MMVSUCC2, as was the case for the MMVSUCC1, broad O-H···N stretching bands centered at 2450 cm^{-1} and 1920 cm^{-1} are visible, though they are slightly less prominent for MMVSUCC2 (Fig. 4.2.42). Here interestingly, the carbonyl stretching band is split into two separate peaks at 1677 and 1699 cm^{-1}, resembling the spectrum of MMVGLUT (Fig. 4.2.23). Keeping in mind that in the case of MMVGLUT the split was due to hetero- and homo- interactions occurring between two glutaric acid molecules and between MMV and glutaric acid respectively, this could indicate that similar interactions are present in MMVSUCC2. A new peak is visible at 1233 cm^{-1} possibly as a result of an imidazole-acid C-O stretch.[4]

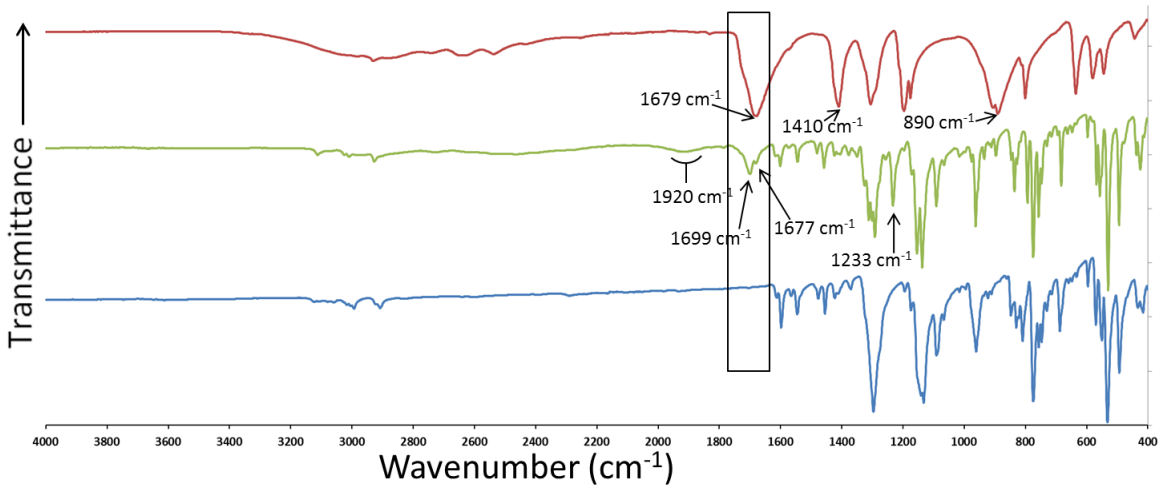

Fig. 4.2.42 FTIR spectra of MMV (Blue), MMVSUCC2 (Green), and succinic acid (Red).

Preparation of single crystals

Single crystals of MMVSUCC1 were obtained by co-precipitation of 5.00 mg of MMV with an equimolar amount of succinic acid (1.38 mg) dissolved in 3 cm^3 of acetone, heated to 50 °C while stirring and filtering through a 0.45 µm nylon filter into a clean vial and placing on a benchtop after covering the vial with Parafilm™.

MMVSUCC3

In an attempt to grow single crystals of adequate size and quality for single-crystal X-ray structural elucidation, some of the crystalline powder obtained by LAG of MMV and succinic acid with ethanol (i.e. MMVSUCC2) was placed in a vial with a saturated solution of MMV dissolved in acetonitrile to serve as 'seeds' to nucleate crystals of this form. After one day some precipitation was visible and a layer of powder had covered the bottom of the vial. The vial was left untouched for a period of more than 2 months, at which time small crystals were visible in the vial. As shown in a subsequent section, it was also determined by PXRD and thermal analysis comparisons of the various products obtained by LAG and co-precipitation experiments with MMV and succinic acid that this phase differed from the others obtained at that stage. For convenience this form was called MMVSUCC3.

Infrared spectroscopy

In the case of the FTIR result of MMVSUCC3 (Fig. 4.2.43) the signs indicating that the sample is a co-crystal that were observed and described earlier for MMVADIP and MMVSUCC1 are also present. The two broad bands signifying O-H···N stretching are present at 1910 cm^{-1} and 2450 cm^{-1}. A shift of the carbonyl stretching band from 1679 to 1705 cm^{-1} serves as a sign that MMVSUCC3 is a co-crystal.

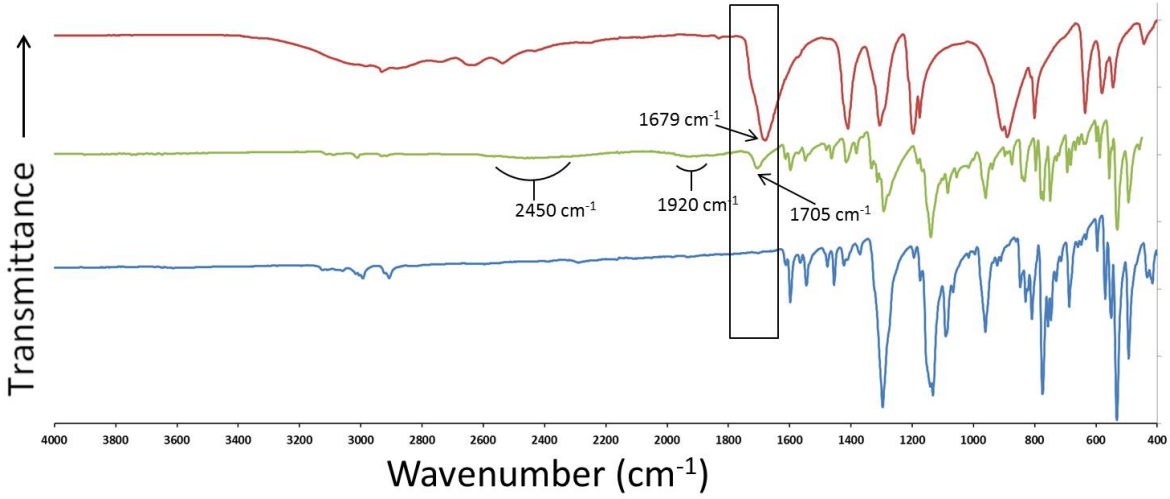

Fig. 4.2.43 FTIR spectra of MMV (Blue), MMVSUCC3 (Green), and succinic acid (Red).

Stoichiometry determination by ^{1}H – NMR spectroscopy

The stoichiometric ratio of the individual components of the single crystals of MMVSUCC1 obtained by co-precipitation were determined by ^{1}H-NMR spectroscopy after the crystals were dissolved in DMSO-d_6. The resulting spectrum is presented together with the proton labelling schemes used in Fig. 4.2.44. The integration values are presented in Table 4.2.7. The ratio was determined to be 2:1 of MMV to succinic acid.

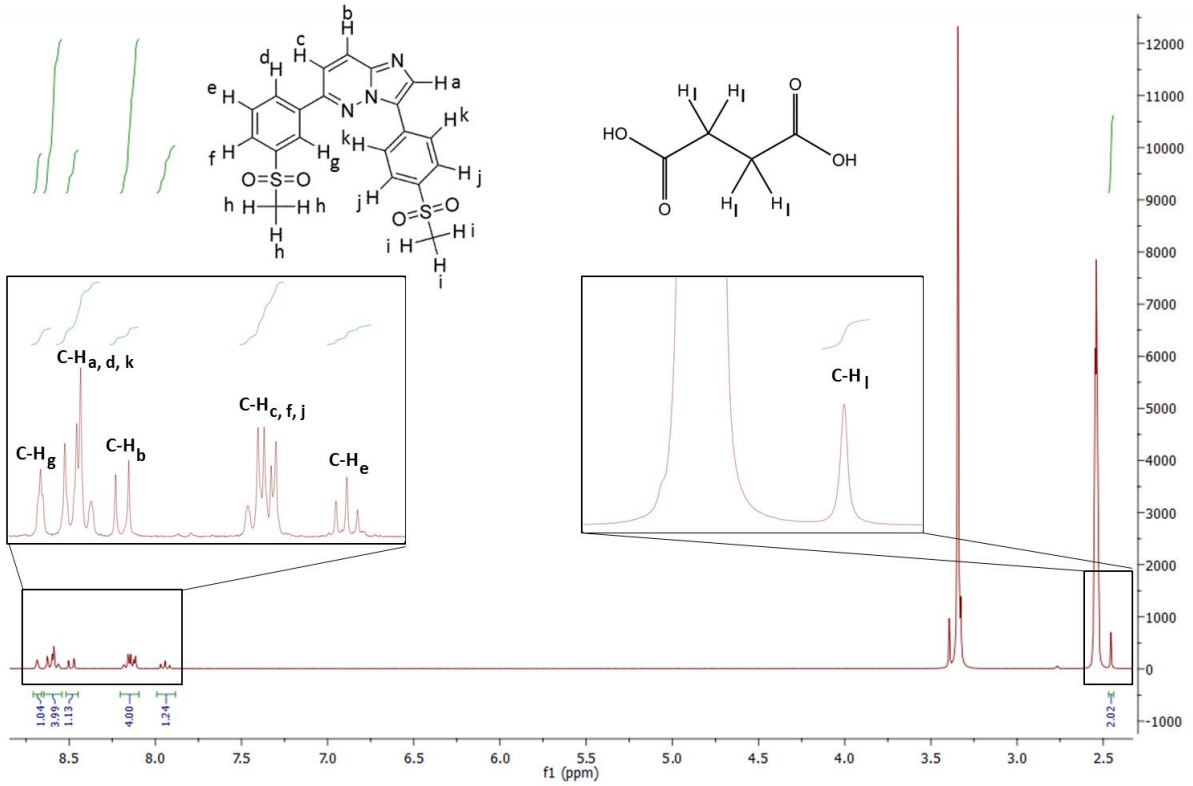

Fig. 4.2.44 ^{1}H-NMR spectrum of MMVSUCC1 in DMSO-d_6 for determination of stoichiometry.

Table 4.2.7 Integrals of protons for individual components to determine stoichiometry of MMVSUCC1.

Proton – [Number of protons]	δ (ppm)	Integration	Experimental/ Theoretical
MMV			
C-$H_{c,f,j}$– [4]	8.09-8.20	4.00*	1.00
C-H_g – [1]	8.66-8.71	1.04	1.04
C-$H_{a,d,k}$– [4]	8.54-8.65	3.99	1.00
C-H_b – [1]	8.45-8.52	1.13	1.13
C-H_e – [1]	7.88-7.99	1.24	1.24
Succinic acid			
C-H_I – [4]	2.44-2.47	2.02	0.51

*** Reference integral**

Following the same procedure as mentioned for MMVSUCC1, MMVSUCC3 crystals were dissolved in DMSO-d_6 and the stoichiometric ratio of the individual components making up the co-crystal were determined by ^{1}H-NMR spectroscopy. The labelling scheme used as well as the ^{1}H-NMR spectrum are

presented in Fig. 4.2.45. The integration values obtained are reported in Table 4.2.8. As was the case for MMVSUCC1, the ratio was determined to be 2:1 of MMV to succinic acid. This shows that MMVSUCC1 and MMVSUCC3 are made up of the same components and in the same stoichiometric ratio, signifying that these crystals are co-crystal polymorphs.

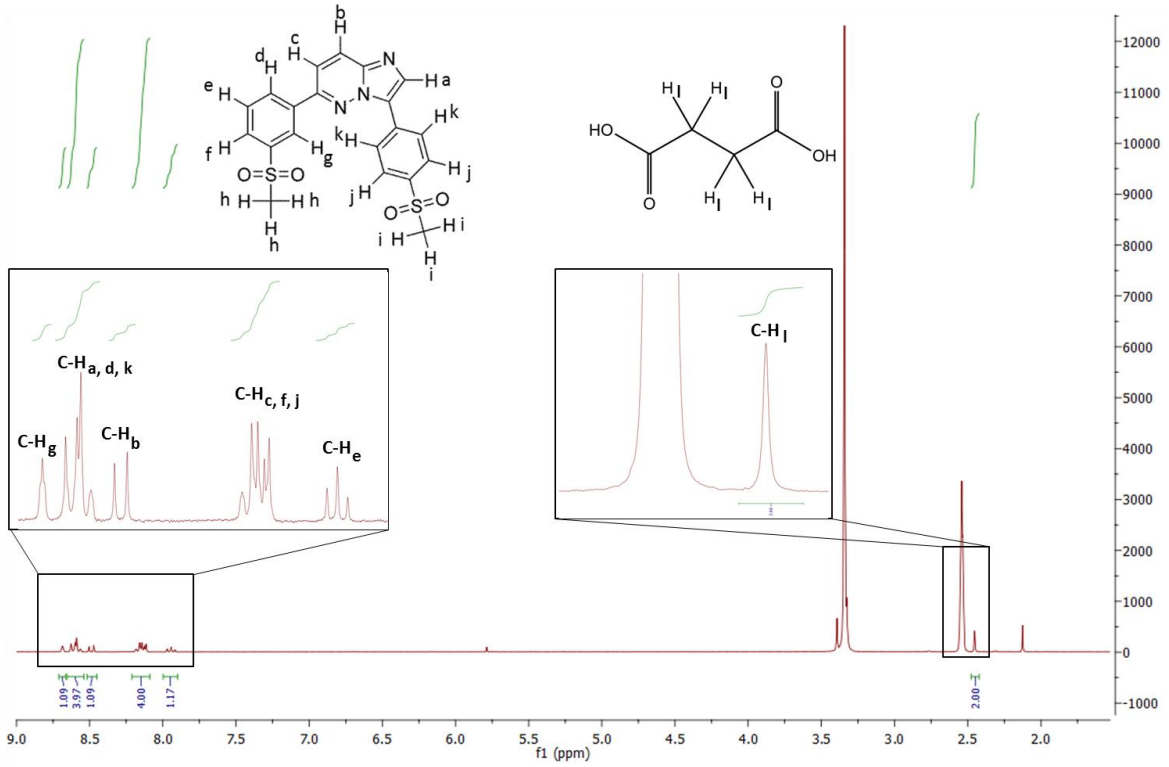

Fig. 4.2.45 ^{1}H-NMR spectrum of MMVSUCC3 in DMSO-d_6 for determination of stoichiometry.

Table 4.2.8 Integrals of protons for individual components to determine stoichiometry of MMVSUCC3.

Proton – [Number of protons]	δ (ppm)	Integration	Experimental/ Theoretical
MMV			
C-$H_{c,f,j}$– [4]	8.09-8.21	4.00*	1.00
C-H_g – [1]	8.66-8.71	1.09	1.09
C-$H_{a,d,k}$– [4]	8.54-8.65	3.97	0.99
C-H_b – [1]	8.45-8.52	1.09	1.09
C-H_e – [1]	7.90-8.00	1.17	1.17
Succinic acid			
C-H_l – [4]	2.42-2.48	2.00	0.50

*** Reference integral**

Crystal structure analysis

Data-collection and space group determination

The single-crystal X-ray intensity data for MMVSUCC1 were collected on a Bruker Kappa Apex II Duo diffractometer at 173(2) K. Similar to MMVADIP and MMVGLUT the X-ray diffraction showed $\bar{1}$ Laue symmetry which indicates that the crystal belongs to the triclinic system. Centrosymmetry was shown by the mean $|E^2-1|$value of 0.968 and it was determined that this crystal can be assigned the space group $P\ \bar{1}$ unequivocally.

Structure solution and refinement

Crystallographic data, parameters for collection of intensity data and refinement details are reported in Table 4.2.9. The method employed for the solution and refinement of this structure was the same as described for MMVADIP. To determine whether the comprising molecules were in the neutral state (suggesting that the crystal is a co-crystal) or if the components were charged (suggesting salt formation) the carboxyl moiety and the imidazole moiety of the respective molecules were inspected. By examination of the Fourier difference map it was deduced that proton transfer had not taken place as the proton was found to be bonded as carboxyl hydrogen and the distinct C-O bond lengths of the succinic acid carboxylic acid functional groups of 1.325(2) Å and 1.209(2) Å are representative of single and double bonds. This clearly shows that both components are in a neutral state and the crystal is thus a co-crystal.[12,13] All hydrogen atoms were found in difference electron density maps and placed in idealised positions in a riding model and refined with thermal parameters 1.2-1.5 times the U_{iso} values of their parent atoms.

Table 4.2.9 Data-collection and refinement parameters for MMVSUCC 1.

Molecular formula	$(C_{20}H_{17}N_3O_4S_2) \cdot 0.5(C_4H_6O_4)$
Formula weight (g mol^{-1})	486.53
Crystal system	Triclinic
Space group	$P\ \bar{1}$
a (Å)	5.0658(4)
b (Å)	11.1784(9)
c (Å)	19.5381(15)
α (°)	101.144(2)
β (°)	94.039(2)
γ (°)	101.070(2)
V $(Å)^3$	1058.67(14)
Z	2
D_c (g cm^{-3})	1.526

μ (Mo Kα) (mm^{-1})	0.299
F(000)	506
Data-collection temp. (K)	173(2)
Crystal size (mm^3)	0.23 x 0.13 x 0.04
Range scanned θ (°)	1.89 – 28.38
Index ranges ±*h*, ±*k*, ±*l*	-6, 6; -14, 14; -26, 25
Reflections (total)	27 551
Independent reflections	5282
Reflections with I>2σ(I)	3982
Number of parameters	301
R_{int}	0.0550
S	1.033
R_1 [*I*>2σ(*I*)]	0.0432
Reflections omitted	1
wR_2	0.1104
a, b in w = $1/[\sigma^2(F_o^2)+(aP)^2+(bP)]$	a = 0.0504; b = 0.2797
$(\Delta/\sigma)_{mean}$	< 0.001
$\Delta\rho_{min,max}$ (e $Å^{-3}$)	-0.396, 0.412

Molecular structure

The asymmetric unit and labelling scheme of MMVSUCC1 are shown in Fig. 4.2.46.

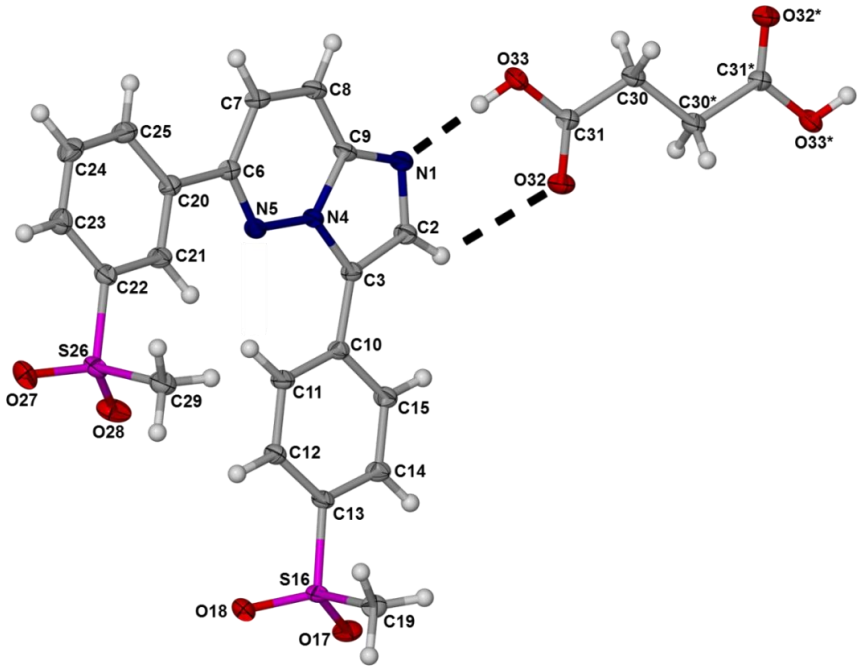

Fig. 4.2.46 The asymmetric unit and numbering scheme of MMVSUCC1 with thermal ellipsoids shown at the 50% probability level. Atoms labelled with an asterisk are symmetry-generated and are not part of the asymmetric unit.

Crystal packing and hydrogen bonding

The relevant symmetry information for MMVSUCC1 is listed in Table 4.2.10.

Table 4.2.10 Hydrogen bonds in MMVSUCC1[a].

	D–H···A	*d*(D–H), Å	*d*(H···A), Å	*d*(D···A), Å	∠(DHA), deg.
	O33-H33···N1	0.84	1.82	2.665(2)	179
Intra	C11-H11···N5	0.95	2.23	2.906(3)	127
Intra	C12-H12···O18	0.95	2.56	2.932(2)	104
	C19-H19C···O27^{i}	0.98	2.43	3.386(3)	165
	C25-H25···O32^{ii}	0.95	2.58	3.326(3)	136
	C29-H29A···O18^{iii}	0.98	2.56	3.411(3)	146
	C29-H29B···O28^{iv}	0.98	2.53	3.250(3)	130
	C2-H2···O32	0.95	2.64	3.195(2)	118
Intra	C21-H21···N5	0.95	2.37	2.704(2)	100
Intra	C14-H14···O17	0.95	2.67	3.007(2)	101
Intra	C21-H21···O28	0.95	2.61	2.951(2)	101
intra	C23-H23···O27	0.95	2.61	2.952(2)	102

[a] Symmetry transformations used to generate equivalent atoms: *[i]: -1+x,-1+y,z; [ii]: 1+x,1+y,z; [iii]:-x,2-y,1-z; [iv]: 1+x,y,z*

The various H-bonds and interactions connecting the molecules in these crystals are summarised in Table 4.2.10 and displayed in Figs. 4.2.47 to 4.2.49.

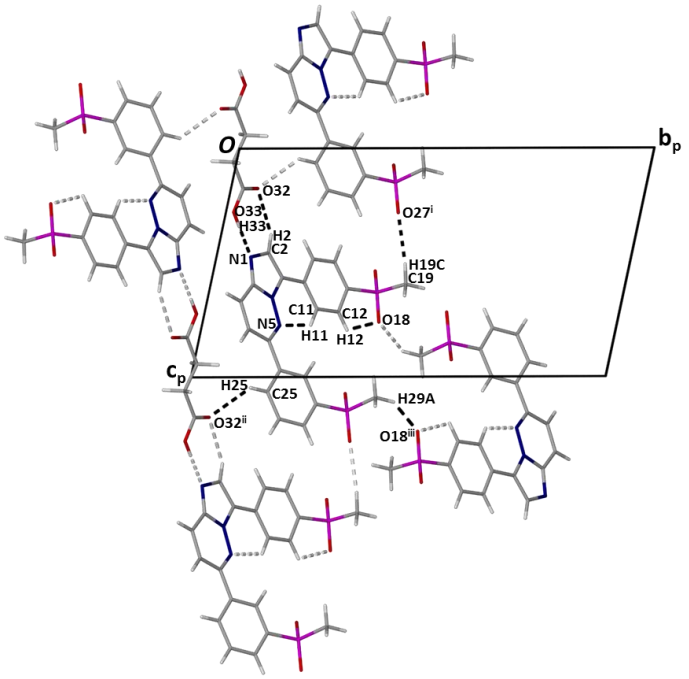

Fig. 4.2.47 Hydrogen bonding interactions found in the structure of MMVSUCC1 viewed along [100].

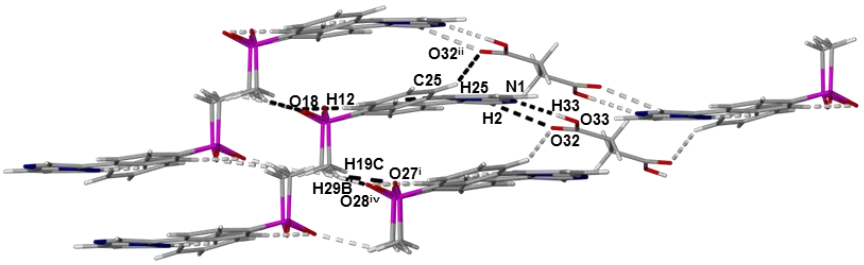

Fig. 4.2.48 Hydrogen bonding interactions found in the structure of MMVSUCC1.

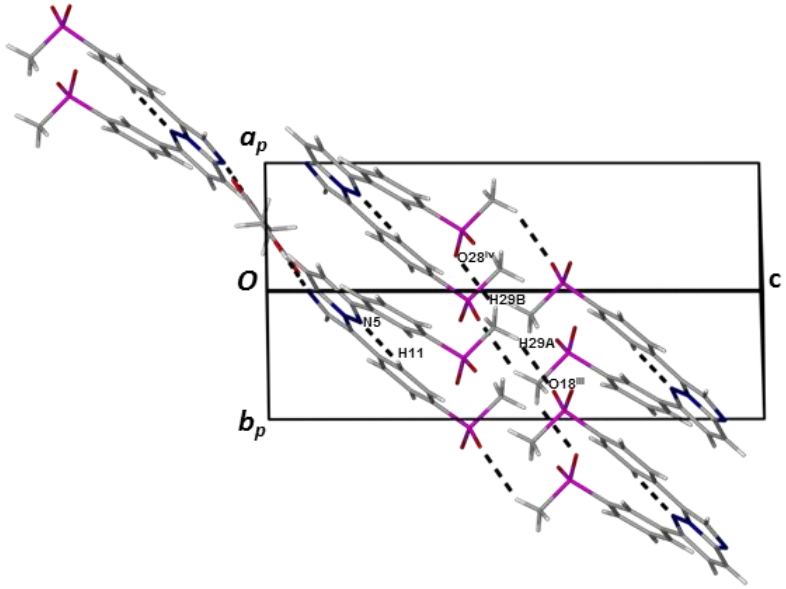

Fig. 4.2.49 Hydrogen bonding interactions found in the structure of MMVSUCC1 viewed along [110].

Discrete ribbons ($D_2^2(10)$ formed by two MMV molecules hydrogen bonded as a dimer ($R_2^2(7)$) to each end of the dicarboxylic succinic acid molecules (Figs. 4.2.48, 4.2.49 and 4.2.50) are linked together by interactions between MMV molecules and other MMV molecules, namely C29-H29A···O18' H-bonds to form $R_2^2(32)$. These interactions result in the formation of infinite planar ribbons as can be seen in Fig. 4.2.50.

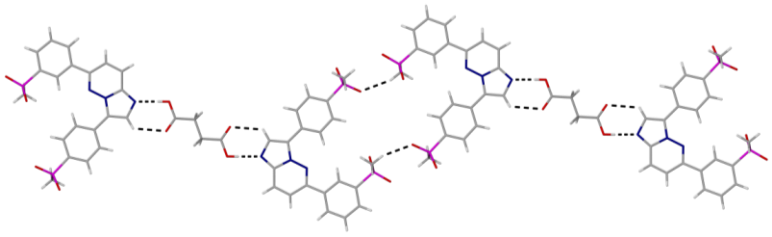

Fig. 4.2.50 Infinite planar ribbons present in MMVSUCC1. The following interactions are visible in this figure: C29-H29A···O18' ($R_2^2(32)$); O33-H33···N1 and C2-H2···O32 ($R_2^2(7)$).

This co-crystal packs in stepped layers as can be seen in Figs. 4.2.51 and 4.2.52. The topology of a single layer can be seen in Figs. 4.2.51 and 4.2.53.

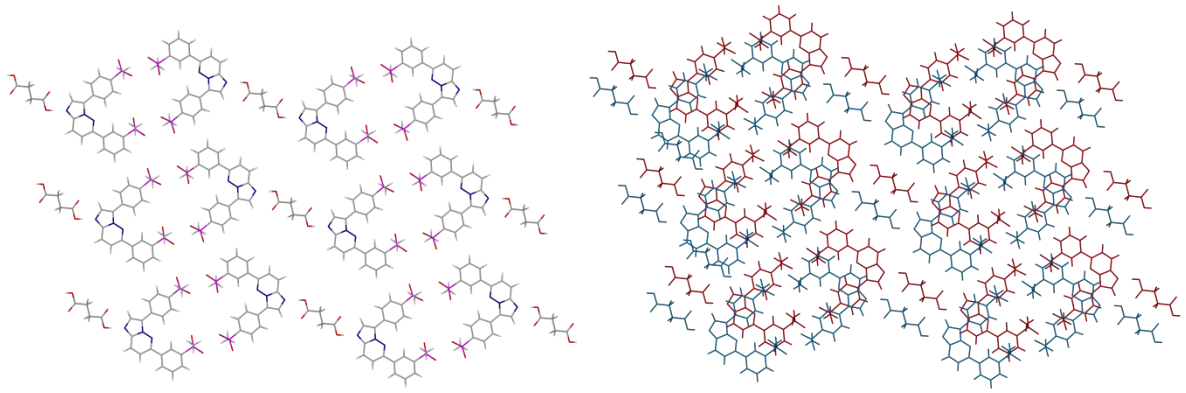

Fig. 4.2.51 The topologies of a single stepped layer of MMVSUCC1 (left) and two stacked stepped layers (right).

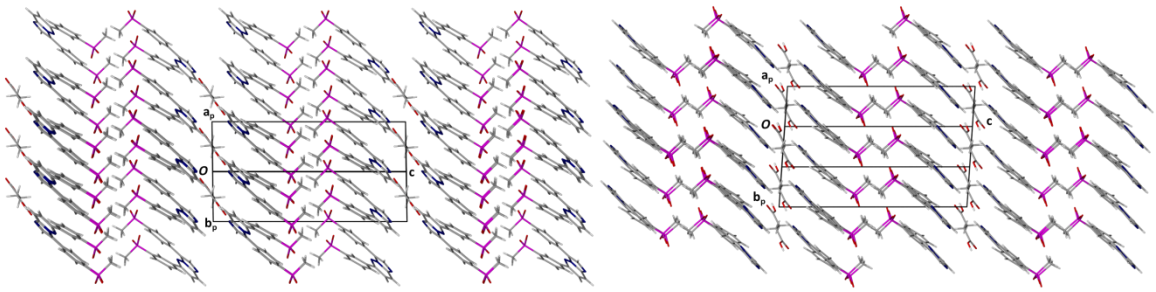

Fig. 4.2.52 Packing of MMVSUCC1 illustrating stepped layer, shown from different perspectives.

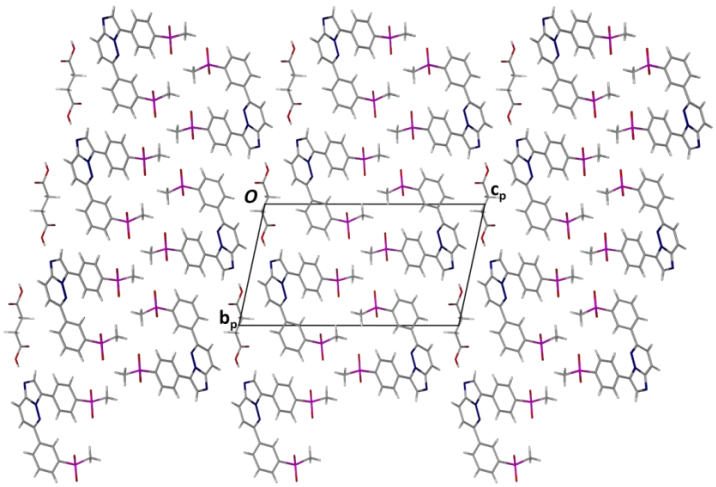

Fig. 4.2.53 Packing of MMVSUCC1 viewed along [100].

The ribbons mentioned previously are packed in a stepwise fashion to form layers. The ribbons forming the separate layers are not directly connected, but are linked by connecting ribbons packed above and below this plane.

The interactions forming these connections are the following: C25-H25···O32'; C29-H29B···O28'; C19-H19C···O27' (Figs. 4.2.47 and 4.2.54). Two elongated rings are formed by the interactions C25-H25···O32' with O33-H33···N1 ($R_4^4(30)$) and C29-H29B···O28' with O33-H33···N1 ($R_6^6(58)$) (Fig. 4.2.54).

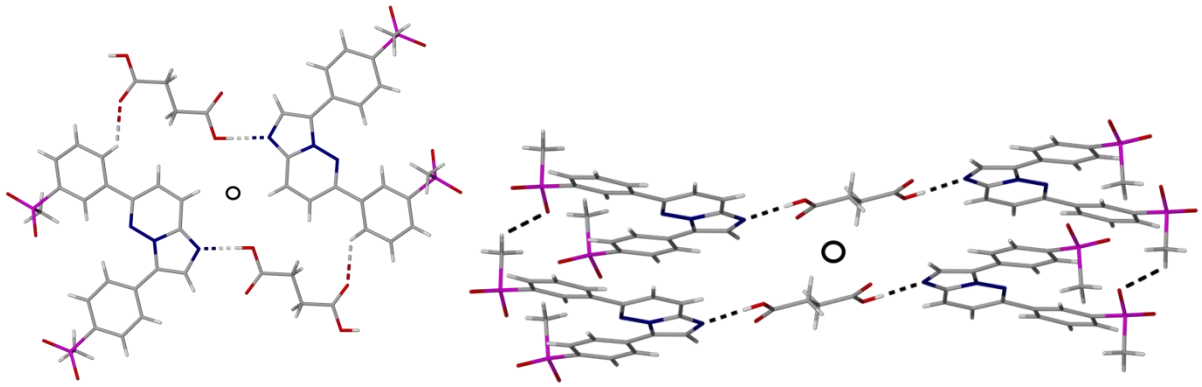

Fig. 4.2.54 Interactions that play a role in linking the infinite ribbons to form stepped layers. The interactions C25-H25···O32' and C29-H29B···O28' connect different layers and together with O33-H33···N1 form rings described by $R_4^4(30)$ (left) and $R_6^6(58)$ (right).

The stacked layers of MMVSUCC1 are also connected by several π-π interactions (Fig. 4.2.55). Two slightly offset face-to-face π-interactions exist between the rings N1-C2-C3-N4-C9 (with centroid Cg(A)) and C10-C11-C12-C13-C14-C15 (with centroid Cg(C)) and the rings N4-N5-C6-C7-C8-C9 (with centroid Cg(B)) and C10-C11-C12-C13-C14-C15 (with centroid Cg(C)). Both are related by the symmetry operator 1+x,y,z. The centroid-to-centroid distances are 3.617(1) Å for Cg(A)···Cg(C) and 3.540(1) Å for Cg(B)···Cg(C), the shortest contact distances between atoms being 3.296 Å (C9···C10) common for Cg(A)···Cg(C) and Cg(B)···Cg(C) and 3.354 Å (C8···C10) for Cg(B)···Cg(C).

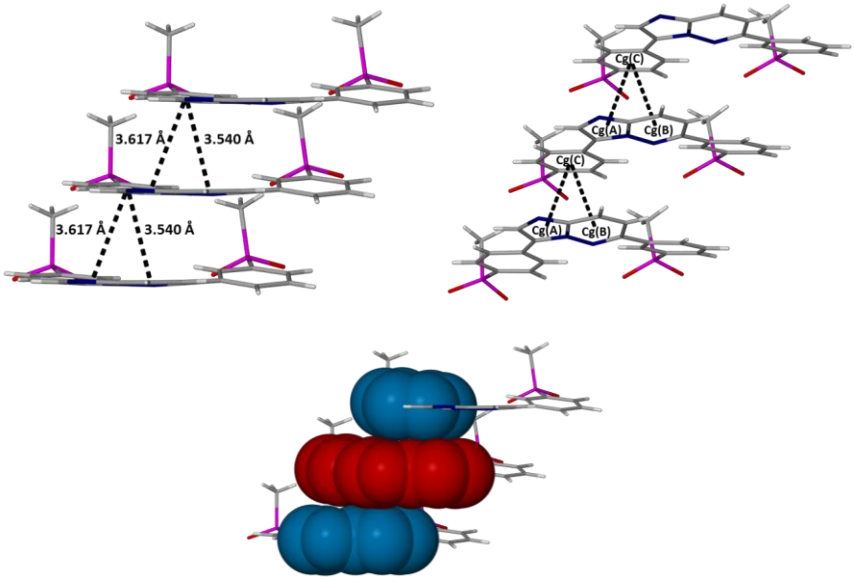

Fig. 4.2.55 π-π interactions connecting layers viewed from different perspectives showing ring centroids and offset centroid-to-centroid distances between them. Ring atoms are drawn with van der Waals radii to illustrate the overlap in the case of Cg(A)···Cg(C) and Cg(B)···Cg(C).

PXRD

A PXRD trace obtained from the product of a LAG experiment with MMV and succinic acid with acetonitrile is compared to a calculated trace from the solved crystal structure of MMVSUCC1 in Fig. 4.2.56. The matching traces are indicative that the same phase was produced by LAG as by the co-precipitation methods and thus the LAG method was used on following occasions to produce this phase for further characterisation. The peak with the highest intensity in the PXRD trace at 25.1 °2θ arises from reflection from the (1 -2 3) planes with d-spacing 3.549 Å and though these planes do not perfectly fall on the layers seen in this crystal structure a relationship can be discerned.

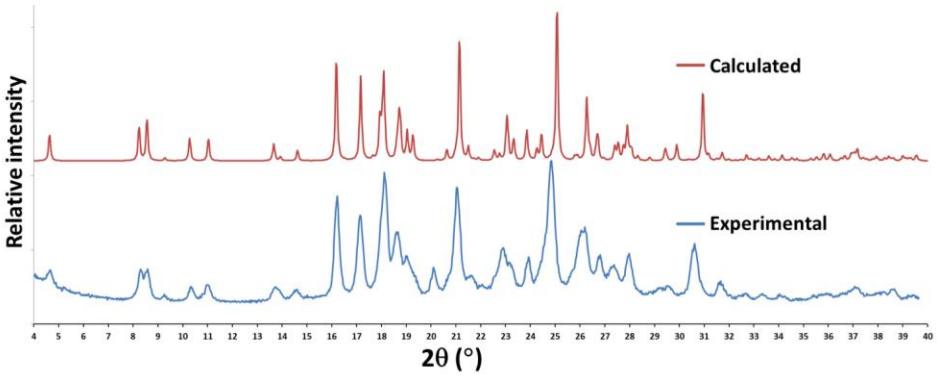

Fig. 4.2.56 PXRD traces collected for the bulk product produced by LAG (with acetonitrile) and a trace computationally generated from the single crystal structure of MMVSUCC1.

Crystal structure analysis MMVSUCC3

Data-collection and space group determination

The single-crystal X-ray intensity data for MMVSUCC3 were collected on a Bruker Kappa Apex II Duo diffractometer at 173(2) K. Similar to the other structures described in this section the X-ray diffraction pattern showed $\bar{1}$ Laue symmetry which indicates the triclinic system. Centrosymmetry was shown by the mean $|E^2-1|$ value of 0.956 and it was determined that this crystal belongs to the space group $P\ \bar{1}$.

Structure solution and refinement

Crystallographic data, parameters for collection of intensity data and refinement details are reported in Table 4.2.11. The method employed for the solution and refinement of this structure was the same as that described for MMVADIP. The same steps of inspection described for MMVSUCC1 were followed to determine whether the comprising molecules were in the neutral state (suggesting that the crystal is a co-crystal) or if the components were charged (suggesting salt formation).

The Fourier difference map showed that proton transfer had not taken place. The proton was found to be bonded as carboxyl hydrogen to the succinic acid molecule with distinct C-O bond lengths of the carboxylic acid functional groups of 1.313(3) Å and 1.221(3) Å. These bond lengths indicate single and double bonds and show that both components are in a neutral state. This serves as unequivocal evidence that the crystal is a co-crystal.[12,13] All hydrogen atoms were found in difference electron density maps and placed in idealised positions in a riding model and refined with thermal parameters 1.2-1.5 times the U_{iso} values of their parent atoms.

Table 4.2.11 Data-collection and refinement parameters for MMVSUCC3.

Molecular formula	$(C_{20}H_{17}N_3O_4S_2) \cdot 0.5(C_4H_6O_4)$
Formula weight (g mol^{-1})	486.53
Crystal system	Triclinic
Space group	$P\ \bar{1}$
a (Å)	10.0972(13)
b (Å)	10.6636(13)
c (Å)	11.1281(13)
α (°)	103.282(2)
β (°)	109.626(2)
γ (°)	97.508(3)
V (Å)^3	1069.8(4)
Z	2
D_c (g cm^{-3})	1.5102
μ (Mo Kα) (mm^{-1})	0.299

F(000)	506
Data-collection temp. (K)	173(2)
Crystal size (mm^3)	0.04 x 0.25 x 0.33
Range scanned θ (°)	2.01 – 28.31
Index ranges ±*h*, ±*k*, ±*l*	-13, 13; -14, 14; -14, 14
Reflections (total)	29 023
Independent reflections	5298
Reflections with I>2σ(I)	3941
Number of parameters	301
R_{int}	0.0568
S	1.037
R_1 [*I*>2σ(*I*)]	0.0448
Reflections omitted	3
wR_2	0.1213
a, b in w = $1/[\sigma^2(F_o^2)+(aP)^2+(bP)]$	a = 0.0568; b = 0.3777
$(\Delta/\sigma)_{mean}$	< 0.001
$\Delta\rho_{min,max}$ (e $Å^{-3}$)	-0.436, 0.624

Molecular structure

The asymmetric unit and labelling scheme of MMVSUCC3 are shown in Fig. 4.2.57.

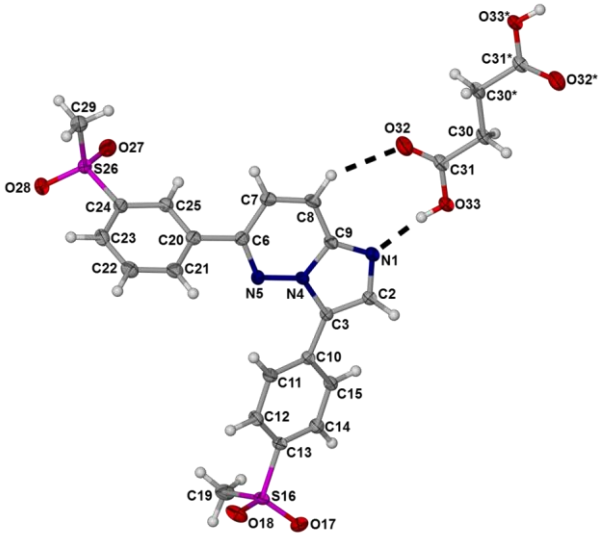

Fig. 4.2.57 The asymmetric unit and numbering scheme of MMVSUCC3 with thermal ellipsoids shown at the 50% probability level. Atoms labelled with an asterisk are symmetry-generated and are not part of the asymmetric unit.

Crystal packing and hydrogen bonding

The relevant symmetry information for MMVSUCC3 is listed in Table 4.2.12 and relevant hydrogen bonds are shown in Fig. 4.2.58.

Table 4.2.12 Hydrogen bonds in MMVSUCC3[a].

	D–H···A	*d*(D–H), Å	*d*(H···A), Å	*d*(D···A), Å	∠(DHA), deg.
	O33-H33···N1	0.84	1.85	2.679(3)	169
	C8-H8···O32	0.95	2.39	3.212(3)	144
Intra	C11-H11···N5	0.95	2.41	2.992(3)	119
Intra	C12-H12···O18	0.95	2.57	2.925(3)	103
	C19-H19B···O33^{i}	0.98	2.45	3.130(3)	126
	C19-H19C···O27^{ii}	0.98	2.43	3.363(3)	159
intra	C21-H21···O27	0.95	2.58	2.931(3)	102
	C29-H29B···O18^{iii}	0.98	2.36	3.333(3)	170

[a] Symmetry transformations used to generate equivalent atoms: *[i]: x,-1+y,z; [ii]: -1+x,-1+y,-1+z; [iii]: 1+x,1+y,1+z.*

This co-crystal polymorph has similarities in structure to MMVSUCC1 in that discrete ribbons are formed by the MMV molecules H-bonded to each end of the dicarboxylic acid coformer molecules (Figs. 4.2.58 and 4.2.59). The difference is that the cyclic H-bonding motif is distinct, the specific interactions being O33-H33···N1 and C8-H8···O32 in the case of MMVSUCC3, forming a ring $R_2^2(8)$, as opposed to the interactions O33-H33···N1 and C2-H2···O32 in MMVSUCC1, which generate a $R_2^2(7)$ motif.

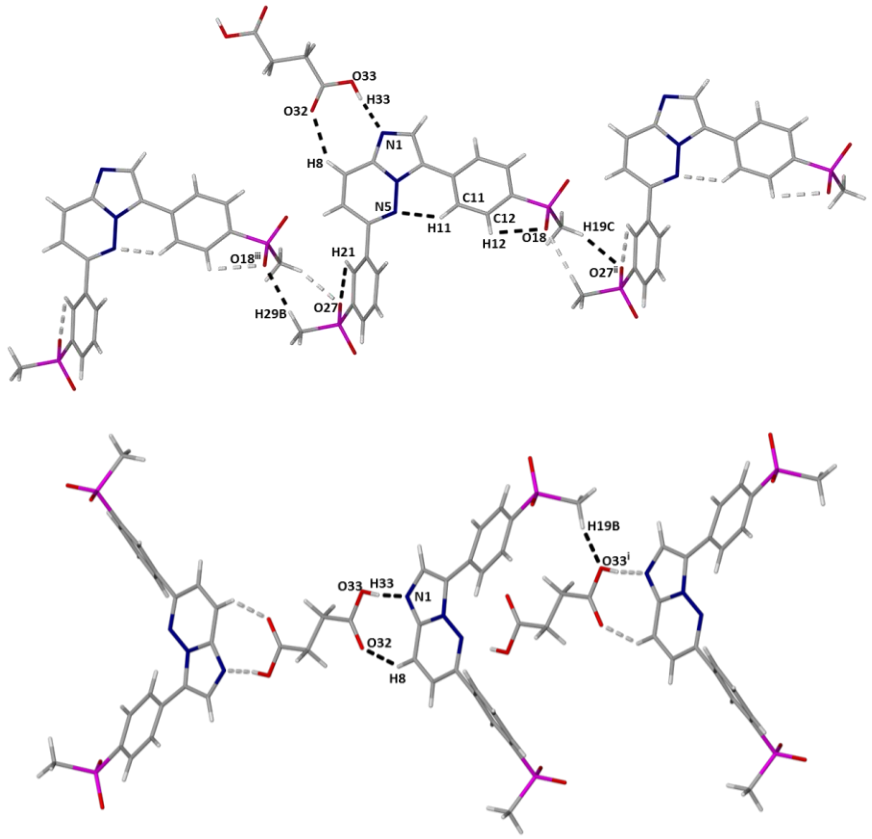

Fig. 4.2.58 Hydrogen bonding interactions found in the structure of MMVSUCC3.

Offset face-to-face π-π interactions occur between MMV molecules to connect the discrete ribbons and form infinite ribbons (Fig. 4.2.60). The atoms C23···C24 of the rings (C20-C21-C22-C23-C24-C25 (Cg(D)) related by the symmetry operator 2-x,-y,1-z are separated by a distance of 3.257 Å.

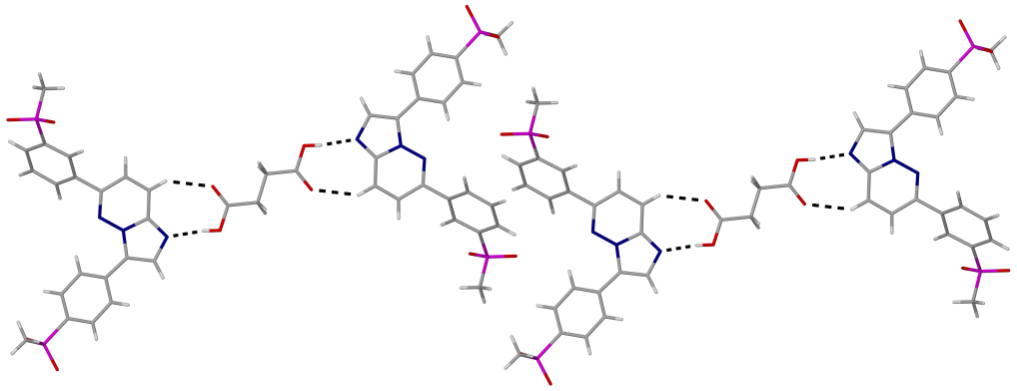

Fig. 4.2.59 Infinite ribbons in the structure of MMVSUCC3.

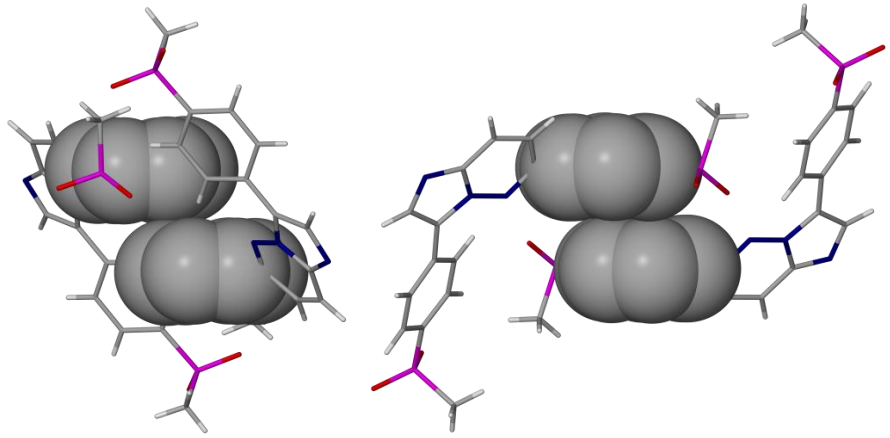

Fig. 4.2.60 π-π interactions connecting MMV molecules to form infinite ribbons viewed from different perspectives. Ring atoms are drawn with van der Waals radii to illustrate the overlap between atoms of Cg(D)···Cg(D) related by the symmetry operator 2-x,-y,1-z.

As was the case with MMVSUCC1, the infinite ribbons are connected to form layers and the layers are in turn stacked in a stepped fashion. The topology of such a layer is shown in Fig. 4.2.61 and another layer is shown to illustrate the stepped fashion in which it is arranged. Fig. 4.2.62 shows another view of these stepped layers. Other interactions connecting molecules in the same layers are C29-H29B···O18′ and C19-H19C···O27′ which form rings that can be described as $R_2^2(8)$ (Fig. 4.2.58).

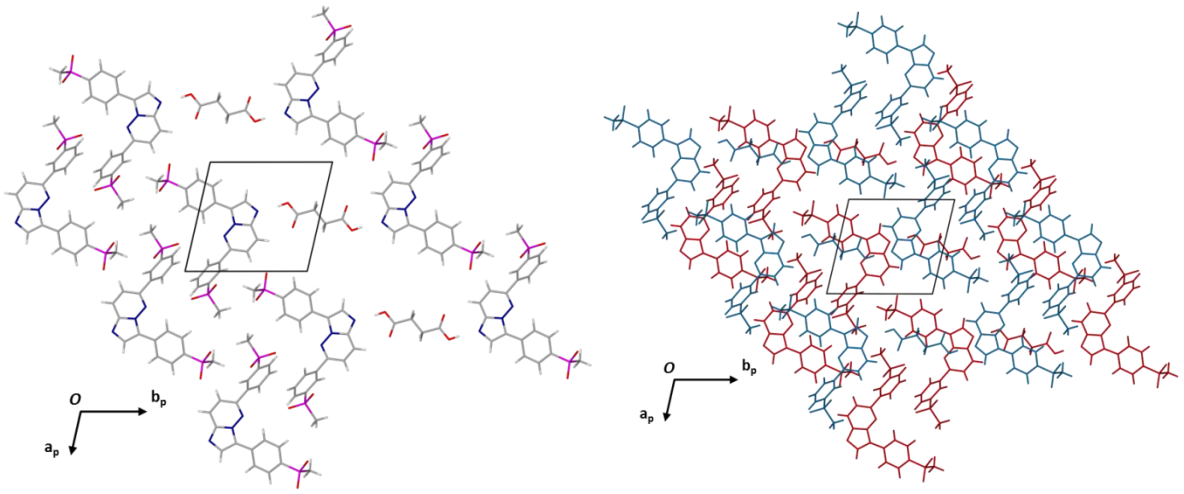

Fig. 4.2.61 The topology of a single layer (left) and stacked layers (right) in MMVSUCC3 viewed along [001].

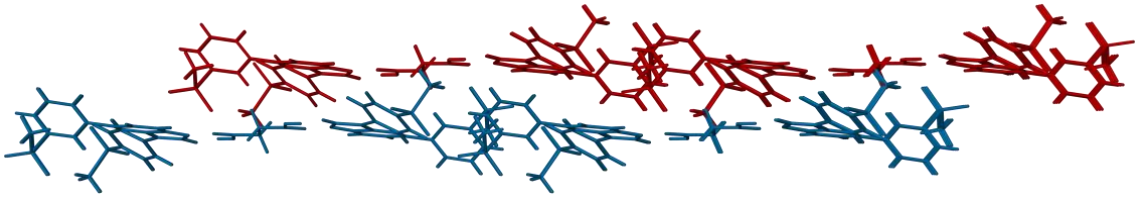

Fig. 4.2.62 Stacked stepped layers of MMVSUCC3 viewed from roughly parallel to the imidazopyridazine ring of the MMV molecules.

Interactions connecting the layers are C19-H19B···O33' (Fig. 4.2.58) and these form another $D_2^2(8)$ discrete ribbon which together with C8-H8···O32 and O33-H33···N1 forms rings $R_4^4(36)$ and $R_4^4(34)$ respectively (Fig. 4.2.63).

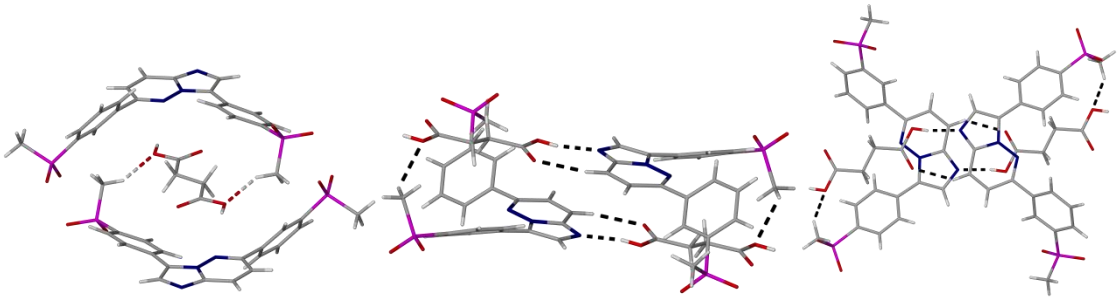

Fig. 4.2.63 Interactions connecting layers in MMVSUCC3: C19-H19B···O33' ($D_2^2(8)$) (left) with C8-H8···O32 and O33-H33···N1 $R_4^4(36)$ and $R_4^4(34)$ viewed from different perspectives (centre and right).

Though there are numerous instances of relatively short X-H···π contacts to be found in the structure of MMVSUCC3, none is short enough and at the correct angles to be considered authentic X-H···π bonds. Examples include C8-H8···Cg(D) with a distance of 3.093 Å; O30-H30B···Cg(C) with a distance of 2.916 Å; O33-H33···Cg(B) with a distance of 3.105 Å (where (Cg(B,C, and D) are the centres of gravity of the rings (N4-N5-C6-C7-C8-C9), (C10-C11-C12-C13-C14-C15), and (C20-C21-C22-C23-C24-C25) respectively). These interactions are shown in appendix A (Fig. A4.2.24).

The packing arrangement of the components making up MMVSUCC3 is displayed in Figs. 4.2.64 and 4.2.65.

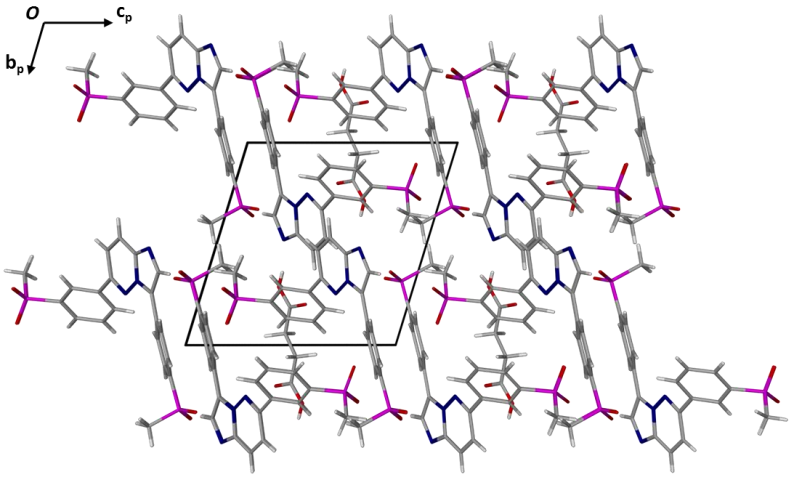

Fig. 4.2.64 Packing of MMVSUCC3 viewed along [100].

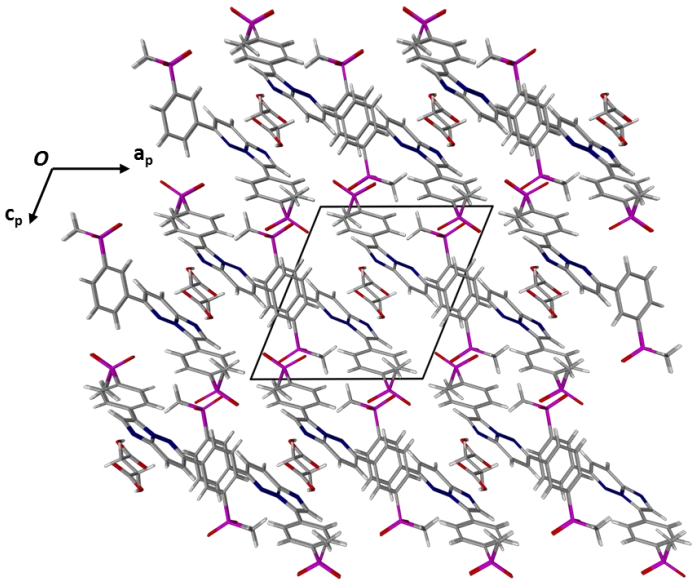

Fig. 4.2.65 Packing of MMVSUCC3 viewed along [010].

PXRD

The PXRD traces of MMVSUCC3 produced by co-precipitation and that calculated from the solved crystal structure are compared in Fig. 4.2.66. The good correlation of the traces was taken as an indication that this product was the same phase and it was utilised for further characterisation.

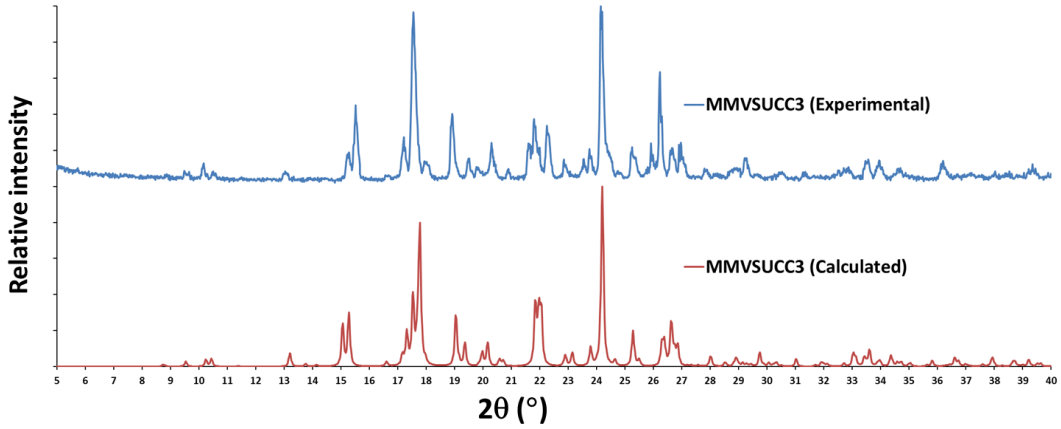

Fig. 4.2.66 PXRD traces collected for MMVSUCC3 and a trace computationally generated from the single crystal X-ray structure of MMVSUCC3.

Thermal analysis

MMVSUCC1 started to melt around 200 °C in the HSM experiment shown in Fig. 4.2.67. The crystals had mostly melted by 215 °C and were completely melted by 228 °C.

The HSM result for MMVSUCC2 is presented in Fig. 4.2.68. A crystalline powder was used for this experiment, as the growth of larger crystals was unfortunately not accomplished. The results show a slight but noticeable change in colour of the sample between the starting temperature of 28 and 175 °C when heated at a rate of 10 °C min^{-1}. A more apparent change occurs around 190 °C where the powder has gone from being completely opaque to partly clear. Some traces of the sample had melted by 200 °C with the bulk remaining unchanged. The sample had started to darken in colour and along the periphery of the image where it is closer to the heating block it started to melt around 249 °C. The sample was completely melted by 260 °C.

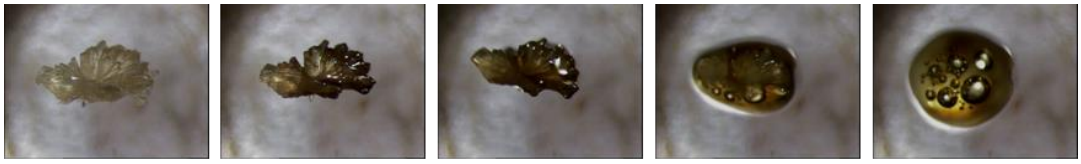

Fig. 4.2.67 Representative HSM photographs of MMVSUCC1 at various temperatures.

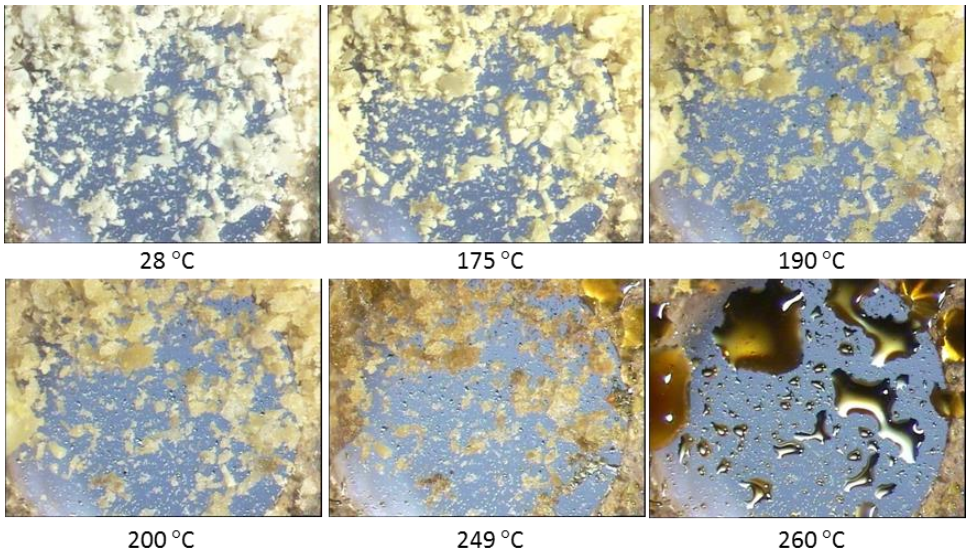

Fig. 4.2.68 Representative HSM photographs of MMVSUCC2 crystalline powder at various temperatures.

In the DTA experiments (Fig. 4.2.69) the succinic acid starting material began to melt with an onset at 188.6 °C and a peak at 190 °C. A melting point of succinic acid reported in the literature is 185(3) °C.[15] Succinic acid is known to have various polymorphic forms and this could explain the spread of reported melting points. MMVSUCC1 displayed two separate events, the first of which had an onset of 205.8 ± 1.1 °C (n = 3) and a peak at 213.4 ± 0.3 °C (n = 3). These values correlate well with what was observed in the HSM experiment. The second onset was at 224.13 ± 1.0 °C (n = 3) and the peak at 226.5 ± 0.8 °C (n = 3). The enthalpy of this second event was much lower than that witnessed in the first event and this could be a result of partial transition to a different phase.

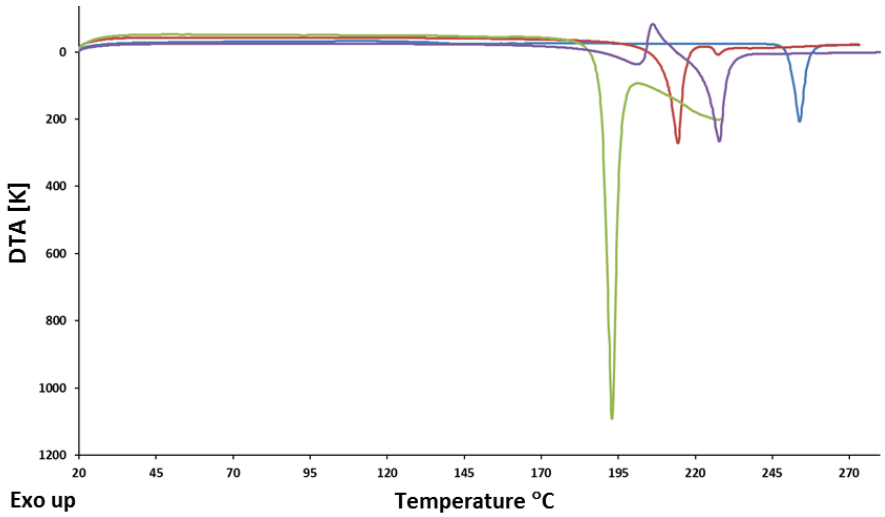

Fig. 4.2.69 Representative DTA thermograms of MMV (blue) and succinic acid (green) starting materials, for MMVSUCC 1 (red) and MMVSUCC2 (purple).

MMVSUCC2 also showed two distinct events, the first of which had an onset at 185.3 ± 0.8 °C (n = 3) and a peak at 201.2 ± 0.1 °C (n = 3). This event appears to be two overlapping events namely a wide endotherm that is curtailed by an exothermic event resembling recrystallization and this matches the temperature in the HSM result where a change in the appearance of the sample was observed. The second onset was seen at 220.2 ± 0.4 °C (n = 3) with a peak at 227.2 ± 0.2 °C (n = 3). The second event matches the temperature of the second event seen in the case of MMVSUCC1. The assumption was made that the transition occurring in the case of MMVSUCC1 might also have been occurring with MMVSUCC2. Variable-temperature PXRD experiments were carried out in an attempt to clarify what was taking place at these temperatures and these are described in a later section.

MMVSUCC3 was discovered after the other thermal characterisation described in the preceding section of MMVSUCC1 and MMVSUCC2 had been carried out and was at first thought to be single crystals of MMVSUCC2. After the structural elucidation of these crystals it was clear that these were not the same phase. In an attempt to resolve the thermal stability ranking of the various forms, DSC experiments were undertaken with all three MMVSUCC phases.

The HSM result for MMVSUCC3 is shown in Fig. 4.2.70. A representative plate-like crystal is seen that remains virtually unchanged up to a temperature of 225 °C, where the edges start to melt. By 235 °C the crystals are completely melted.

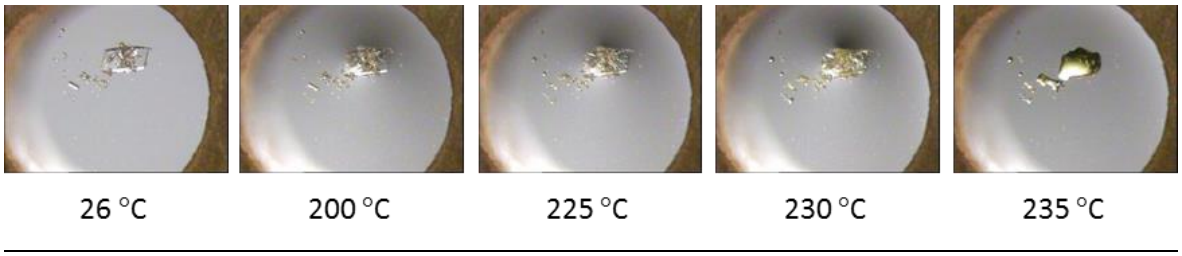

Fig. 4.2.70 Representative HSM photographs of MMVSUCC3 at various temperatures.

The DSC results for MMVSUCC1, MMVSUCC2, and MMVSUCC3 are presented in Fig. 4.2.71. The DSC result of MMVSUCC1, as observed also by DTA, showed two distinct events. The first of these had an onset of 204.2 ± 0.2 °C (n = 3), a peak at 209.3 ± 0.1 °C (n = 3) and an enthalpy related to the event of 96.8 ± 1.8 J g^{-1} (n = 3); the second event had an onset temperature of 219.5 ± 0.4 °C (n = 3), a peak at 222.9 ± 0.2 °C (n = 3) and enthalpy related to the event of 61.1 ± 2.3 J g^{-1} (n = 3). A DSC experiment was carried out on MMVSUCC1 where a heating rate of 100 °C min^{-1} was employed (Appendix A, Fig. A4.2.25). In this case there was a single endothermic event with an onset of 208.8 °C, a peak at 213.7 °C and enthalpy of this event of 103.5 J g^{-1}. This indicates that the transition observed in the DSC experiments carried out at 10 °C min^{-1} can be bypassed at a sufficiently high heating rate.

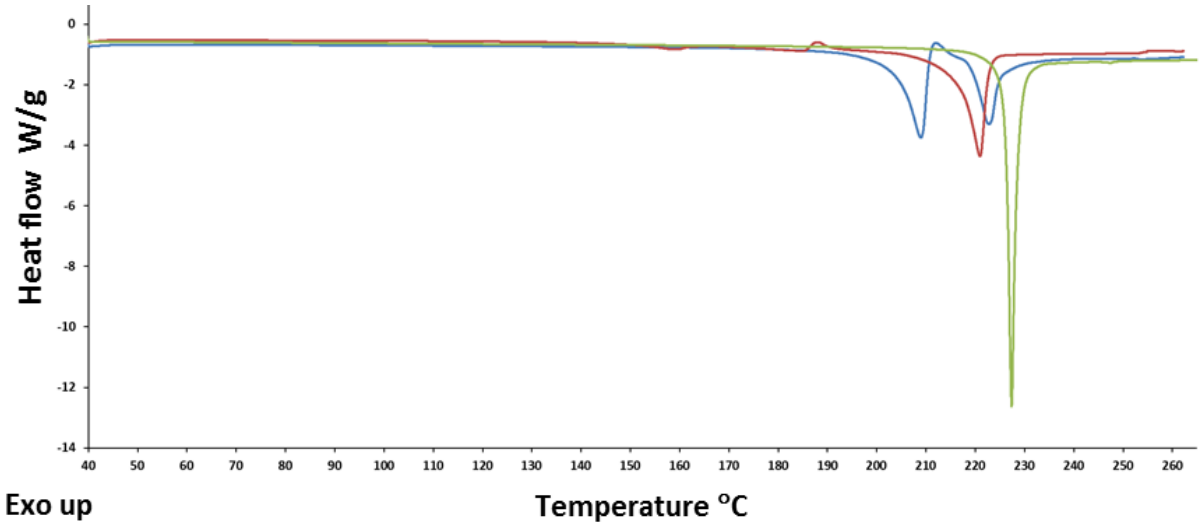

Fig. 4.2.71 Overlayed representative DSC traces for MMVSUCC1 (Blue), MMVSUCC2 (Red), and MMVSUCC3 (Green).

MMVSUCC2 showed three events, the first of which had an onset of 152.2 ± 0.3 °C (n = 3), a peak at 159.7 ± 0.1 °C (n = 3) and an enthalpy related to the event of 5.5 ± 0.3 J g^{-1} (n = 3). This event was not seen in the DTA result and there was no clear sharp change at this temperature in the HSM result. The second event had an onset of 171.3 ± 0.5 °C (n = 3), a peak at 185.0 ± 0.1 °C (n = 3), and enthalpy of 7.0 ± 0.5 J g^{-1} (n = 3). This event, as in the case of the DTA experiment, appears to represent overlapping endothermic and exothermic events. The enthalpy involved will thus not portray the actual energies involved in the individual events. The third event had an onset of 216.8 ± 0.3 °C (n = 3), a peak at 221.4 ± 0.1 °C (n = 3), and enthalpy of 109.3 ± 1.7 J g^{-1} (n = 3). The temperatures are comparable to those at which the corresponding events occurred in the DTA experiments.

MMVSUCC3 showed a single endothermic event in its DSC trace with an onset temperature of 226.7 ± 0.1 °C (n = 3), a peak at 227.8 ± 0.1 °C (n = 3) and an enthalpy of 142.0 ± 12.9 J g^{-1} (n = 3). This result shows a good correlation with the HSM result.

The mass loss observed for MMVSUCC1, between 150 and 250 °C, through TGA (Fig. 4.2.72) of 12.4 ± 0.1 % (n = 3) equates to one molecule of succinic acid for every two molecules of MMV (theoretical percentage 12.0). This matches the ratio seen in the SCXRD and NMR results. The observed onset for the first mass loss step is 203.5 ± 0.8 °C (n = 3) and closely resembles the temperatures in the DTA and DSC results.

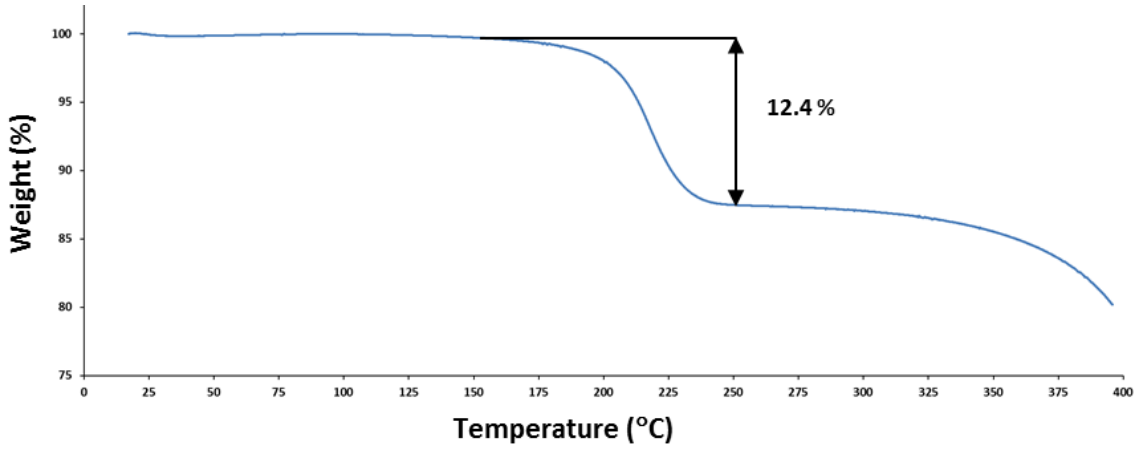

Fig. 4.2.72 Representative TGA trace of MMVSUCC1.

The experimental mass loss seen for MMVSUCC2 occurs in two overlapping, but distinct steps, long before the decomposition of MMV starts (Fig. 4.2.73).

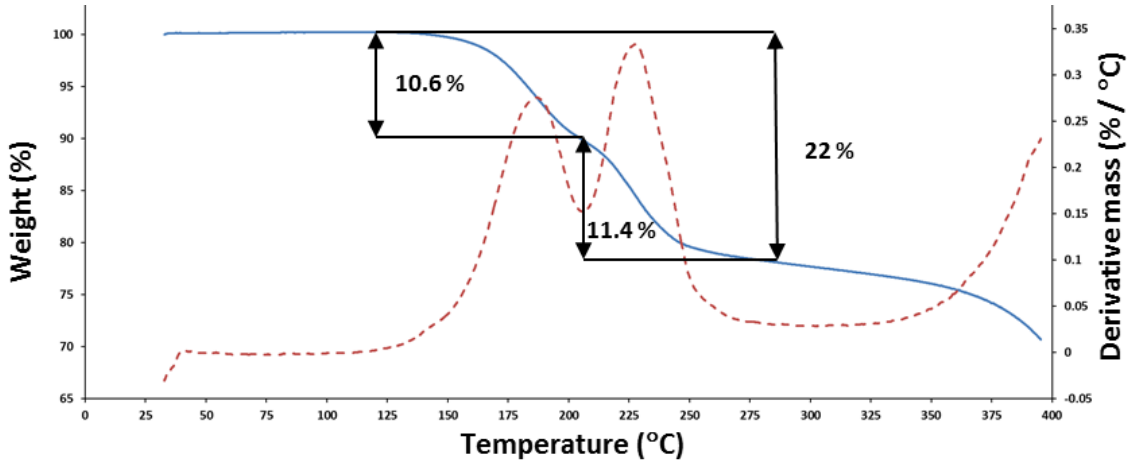

Fig. 4.2.73 Representative TGA trace of MMVSUCC2 showing the derivative of change in respect to mass and temperature (red dotted line).

The total mass loss percentage for both steps combined was 22.0 ± 0.1 % (n = 3). This indicates a ratio of 1:1 of MMV to succinic acid molecules (theoretical percentage 21.6). The individual steps have mass losses of 10.6 ± 0.1 % from 110 to 207 °C and 11.4 ± 0.1 % (n = 3) from 207 to 280 °C. A possible explanation for this result is that succinic acid molecules are released from the crystalline sample in a stepwise fashion with a stoichiometric equivalent of 1 molecule of succinic acid for every two MMV molecules being released in the first step and another in a slightly overlapping yet distinct second step. The calculated onset of the first stepped mass loss is 165.1 ± 0.1 °C (n = 3). This value is lower than the experimental onset of the first event in the DTA result for this sample, though that result showed a gradual onset resembling other traces where guest (in the form of a solvent) loss was observed. The DSC result for this phase had another event visible before this onset of mass loss. The second and third events correspond to the temperatures at which the stepped mass loss is observed (Fig. 4.2.74).

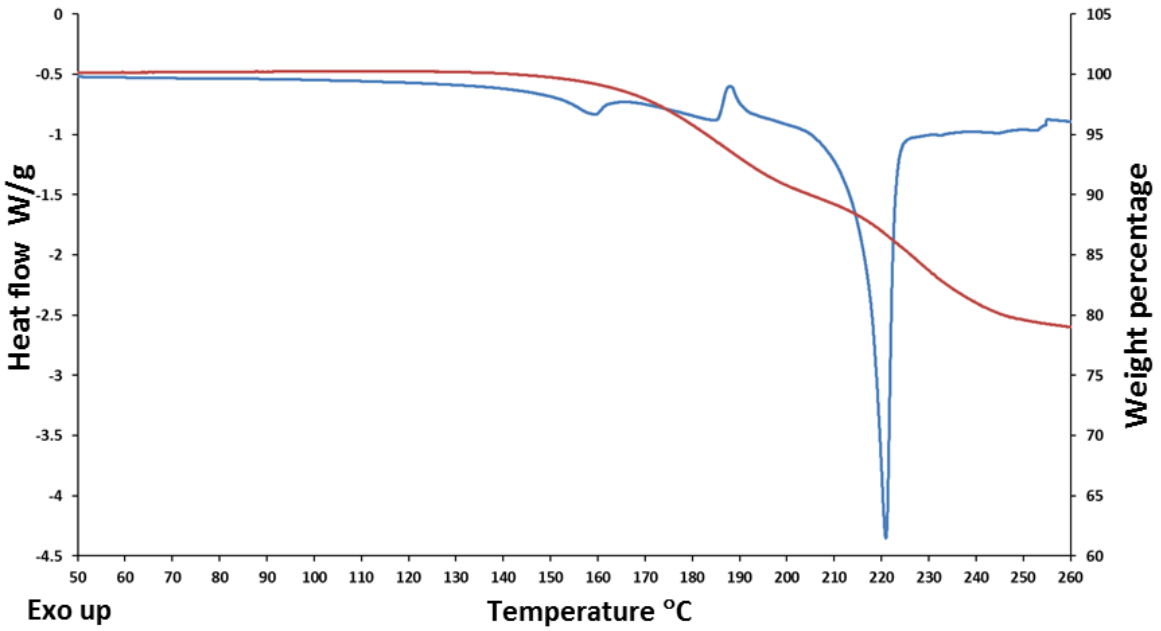

Fig. 4.2.74 Overlayed representative DSC (Blue) and TGA (Red) traces for MMVSUCC2.

The high temperature at which the mass loss starts makes it unlikely that it is due to solvent loss. A variable-temperature PXRD experiment was carried out with MMVSUCC1 and MMVSUCC2 (Figs. 4.2.75 and 4.2.76 respectively). In both cases clear changes in the PXRD traces were observed during heating. A gradual change from MMVSUCC1 to MMV Form 1 was observed for MMVSUCC1 over the temperature range 150 to 190 °C. By 190 °C complete conversion had taken place. The result for MMVSUCC2 was similar with a change from MMVSUCC2 to MMV Form 1 happening from 170 to 190 °C. These results do not match the DSC results where the final melting temperatures were lower by more than 20 °C than the melting temperature seen for pure MMV Form 1. This discrepancy can be explained by the time spent at higher temperatures for these samples. Each scan at a specific temperature requires the sample to be held at this temperature for over 10 min. The TGA results showed a gradual mass loss starting around 165 °C and a reasonable consequence would be that maintaining the samples at temperatures higher than this for extended periods should result in sublimation of the coformer molecules and eventual crystallisation of the form of pure MMV that is stable at high temperatures (i.e. MMV Form 1).

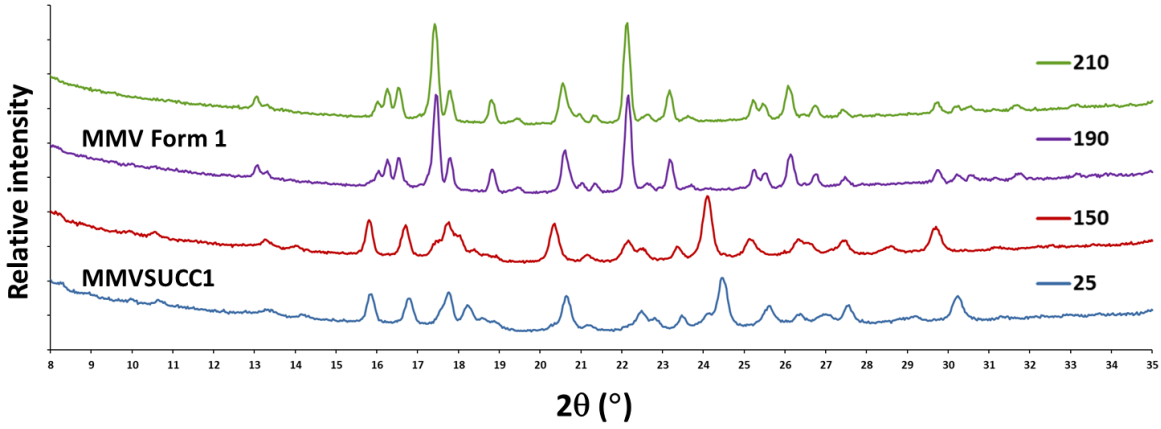

Fig. 4.2.75 Variable-temperature PXRD of MMVSUCC1 (showing temperatures in °C).

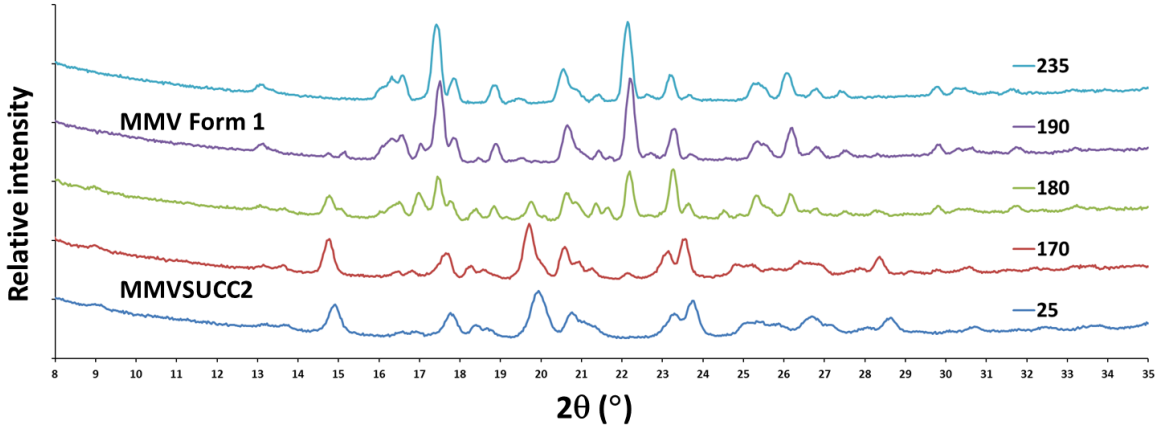

Fig. 4.2.76 Variable-temperature PXRD of MMVSUCC2 (showing temperatures in °C).

The HSM results for MMVSUCC1 and MMVSUCC2 also showed high melting points close to the melting temperature of pure MMV Form 1, possibly due to this same reason. An HSM experiment was carried out at a slightly increased heating rate of 20 °C. min^{-1} to test if this would change the result. The result is presented in Fig. 4.2.77.

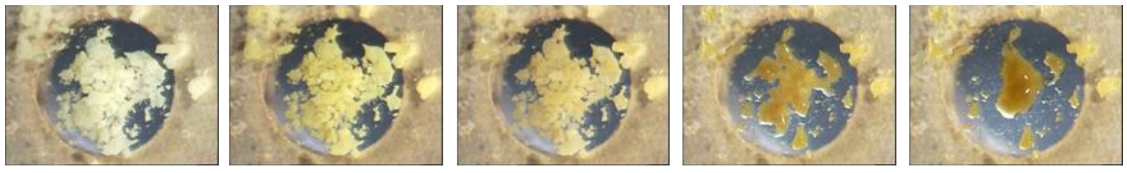

Fig. 4.2.77 Representative HSM photographs of MMVSUCC3 at various temperatures when heated at 20 °C min^{-1}.

The sample melted around 235 °C, matching that observed with MMVSUCC3 and shows that the heating rate does influence which transition will occur (MMVSUCC2 to MMVSUCC3 or MMVSUCC2 to MMV Form 1). A simple experiment was devised to confirm this hypothesis. The samples were heated in open (i.e. non-hermetically sealed) DSC pans and heated to temperatures just exceeding those at which transitions were observed in the other thermal results and the products were then analysed by PXRD at room temperature to avoid possible transitions from being kept at high temperatures for extended periods. The result is presented in Fig. 4.2.78.

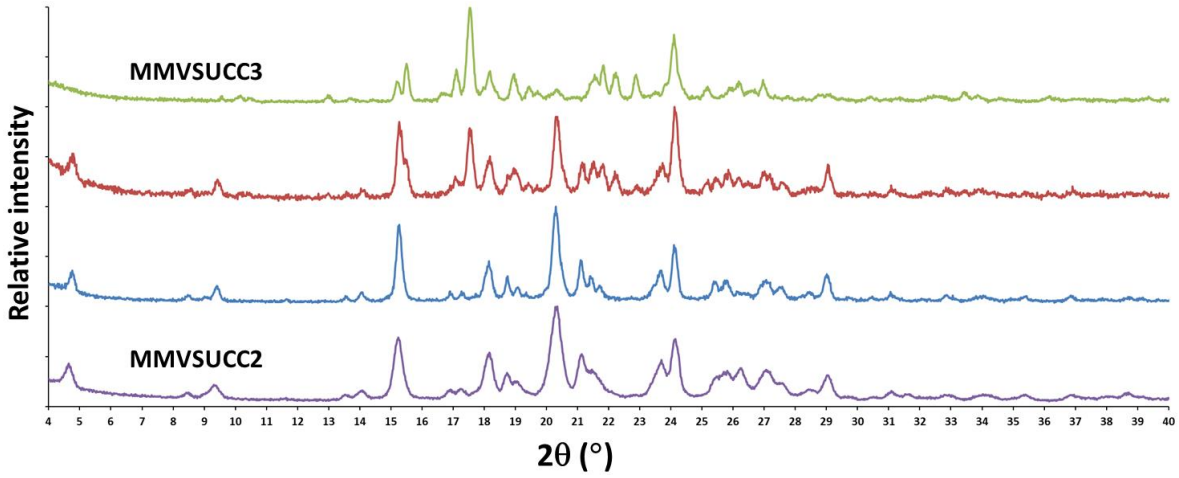

Fig. 4.2.78 PXRD traces starting with MMVSUCC2 (purple), showing the traces of products after being heated to the following temperatures: 160 °C (blue), 190 °C (red), and 205 °C (green).

This result shows that a transition from MMVSUCC2 to MMVSUCC3 had taken place by heating this sample at the same rate as was used in the DSC and DTA experiments (i.e. 10 °C min^{-1}) (a comparison of PXRD traces is presented in appendix A (Fig. A4.2.22)). This result correlates with what was observed in the DSC experiments in that the observed phase transition around 190 °C and the melting temperature of the product matches that of MMVSUCC3 whereas it was much further away from the melting temperature of MMV Form 1.

A similar experiment was carried out with MMVSUCC1, where the sample was heated in an open DSC pan to a temperature above which a transition was observed. The product was analysed by PXRD (Fig. 4.2.79) (a comparison of the various traces is presented in Fig. A4.2.23 in appendix A).

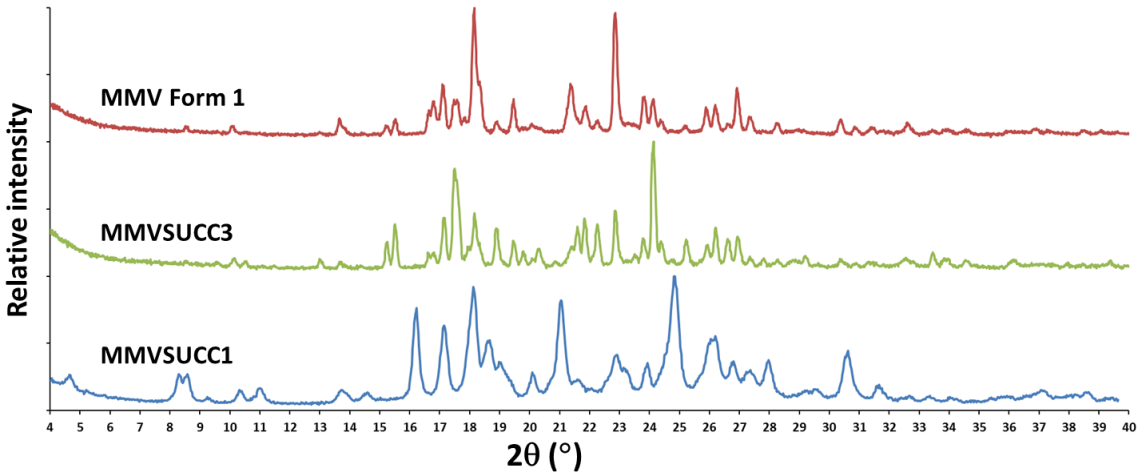

Fig. 4.2.79 PXRD traces starting with MMVSUCC1 (blue), showing the traces of products after being heated to 195 °C at a heating rate of 40 °C min^{-1} and then heated to 215 °C at a heating rate of 10 °C min^{-1} in a closed pan (green) and an open pan (red).

In this case the sample had again transitioned from MMVSUCC1 to MMV Form 1. The mass loss observed in the TGA result for MMVSUCC1 occurs at a similar temperature to where the transition is observed in the DSC experiment and this might lead to the assumption that the transition is to a form of pure MMV. This would agree with the result seen in the variable-temperature PXRD result. The difference in the melting points of MMV Form 1 is however much higher than the melting temperature observed in the DSC result for MMVSUCC1. The obvious difference in the DSC experiment and the other experiments is that in the case of the former the pan was hermetically sealed. An experiment was carried out where the sample was sealed in a pan and heated to 195 °C at a heating rate of 40 °C min^{-1} and then heated to 215 °C at a heating rate of 10 °C min^{-1}. This was done to limit sublimation of the coformer while allowing enough time for the transition to take place. The result is presented in Fig. 4.2.80. In this case the product PXRD trace matched the PXRD pattern of MMVSUCC3 and thus proved that a transition takes place from MMVSUCC1 to MMVSUCC3. This result also shows that these polymorphs are monotropically related as the higher melting MMVSUCC3 also has the higher enthalpy of fusion (MMVSUCC1: 96.8 ± 1.8 J g^{-1} (n = 3) compared to MMVSUCC3: 142.0 ± 12.9 J g^{-1} (n = 3)).

The TGA result for MMVSUCC3 is presented in Fig. 4.2.80. The onset temperature of mass loss was higher in this case than for MMVSUCC1 and MMVSUCC2 and was determined to be 222.0 ± 0.4 °C (n = 2). The mass loss between 170 and 260 °C was 10.9 ± 0.2 % (n = 2). This value equates

to a ratio of approximately 2:1 of MMV to succinic acid (theoretical percentage 12.0), matching the result observed in the NMR and SCXRD results. The higher onset of mass loss compared to the other polymorphic form also confirms that this form has greater stability at high temperatures.

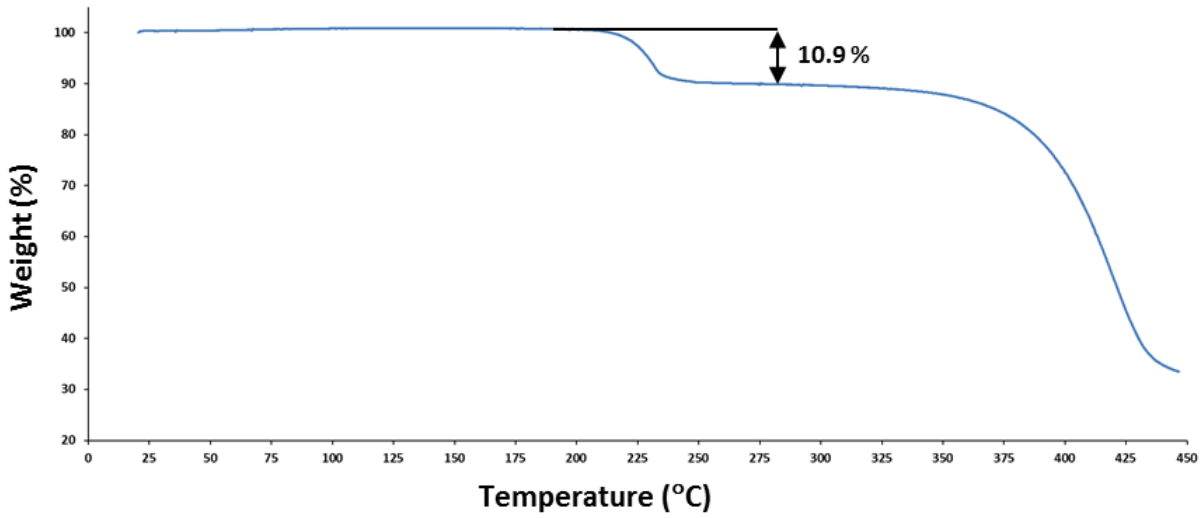

Fig. 4.2.80 Representative TGA trace of MMVSUCC3.

Solubility test

A sample size of 28.45 mg of MMCSUCC1 (equivalent to 25.00 mg of pure MMV) was added to 50 cm^3 of FaSSIF at 37.5 ± 0.5 °C and the resulting solution was stirred at 500 rpm. At specific time intervals aliquots were drawn from the solution, filtered through 0.22 µm nylon filters and diluted from 0.7 to 1.0 cm^3 with pure acetonitrile to prevent precipitation of MMV. The results of the measured concentrations are plotted in Fig. 4.2.81.

In this experiment the result is similar to that of the other co-crystal solubility experiments described thus far in that the concentration peaks at an early stage. The S_{max} of 16.9 ± 1.1 µg. cm^{-3} (n = 3) is reached at 5 min (a factor of 4.8 times S_0) and shows a trend of steady decrease from this point onward. By six hours the concentration has dropped to below the concentration measured after one minute. As is clear from Fig. 4.2.81, the entire range of concentrations measured in the case of the co-crystal was significantly higher than for the control during the course of the experiment.

The resulting solution was centrifuged and the PXRD trace of the solid material recorded. The trace matches that of the Form 1 polymorph of MMV (presented in appendix A Fig. A4.2.27). This result

supports the conjecture that the drop in concentration is due to the precipitation of the less soluble MMV polymorph.

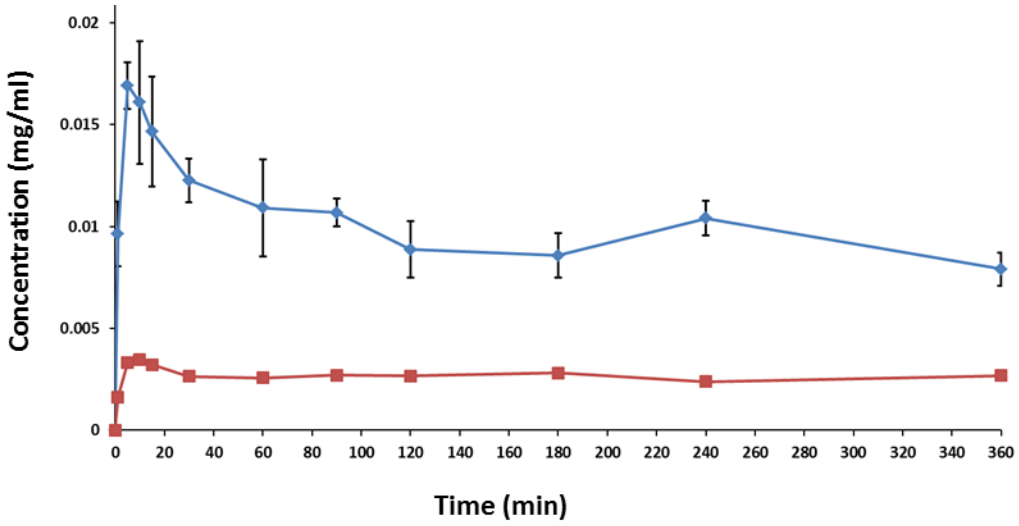

Fig. 4.2.81 Powder dissolution profile of MMV (red) compared to MMVSUCC 1 (blue) in FaSSIF at 37.5 ± 0.5 °C.

The conformational co-crystal polymorphs MMVSUCC1 and MMVSUCC3 have proven to be monotropically related with MMVSUCC3 being the more stable form. Other comparisons are made between these polymorphs and the other multi-component MMV crystal systems in a subsequent section of this chapter.

MMV-fumaric acid co-crystal (MMVFUM)

5 mg of MMV was ground with a mortar and pestle with an equimolar amount of fumaric acid for 15 min while adding acetone in small drops. The product was then analysed with PXRD and the resulting trace was compared to the starting materials MMV and the coformer. The results are shown in Fig. 4.2.82. There are clear differences visible; for example, for the product, new peaks appear at °2θ values 16.5, 21.0, 25.0 and 30.7. Though the trace does not match that of either of the starting materials, it does match the trace recorded for MMVSUCC1 (Fig. 4.2.56). This is due to the occurrence of isostructurality (a phenomenon described in the Introduction chapter) between the two phases.

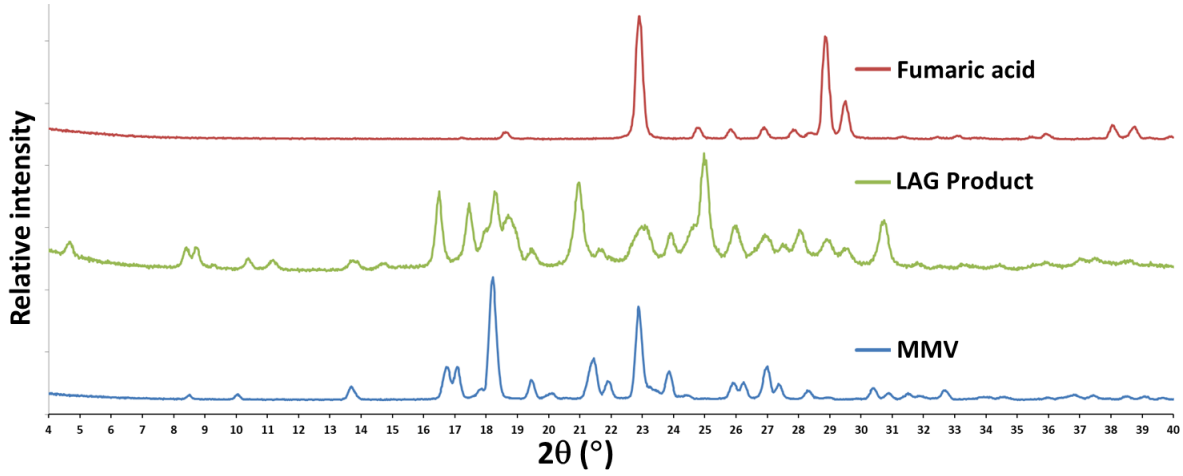

Fig. 4.2.82 Recorded PXRD traces for the product of a LAG experiment and the starting materials, MMV and fumaric acid.

Infrared spectroscopy

The distinguishing FTIR features of dicarboxylic acids described in previous sections are also observable in the case of fumaric acid (Fig. 4.2.83). The O-H stretching band appears between 2500 and 3400 cm^{-1}, the in-plane O-H bending band is visible at 1422 cm^{-1}, the out-of-plane O-H bending band peaks at 889 cm^{-1}, a C-O stretch of the carboxylic acid is indicated by the band at 1271 cm^{-1}, and the carbonyl stretch is very broad and has a high intensity with a peak at 1660 cm^{-1}.

The trends observed in the FTIR results for the other co-crystals in this chapter are visible in the case of MMVFUM as well. The two broad bands around 1910 cm^{-1} and 2450 cm^{-1} are present and indicate acid-imidazole O-H···N stretching. The energy increase of the asymmetric stretching band of the carbonyl moiety of fumaric acid has caused a shift from 1660 to 1697 cm^{-1}. This indicates that MMVFUM is a co-crystal.

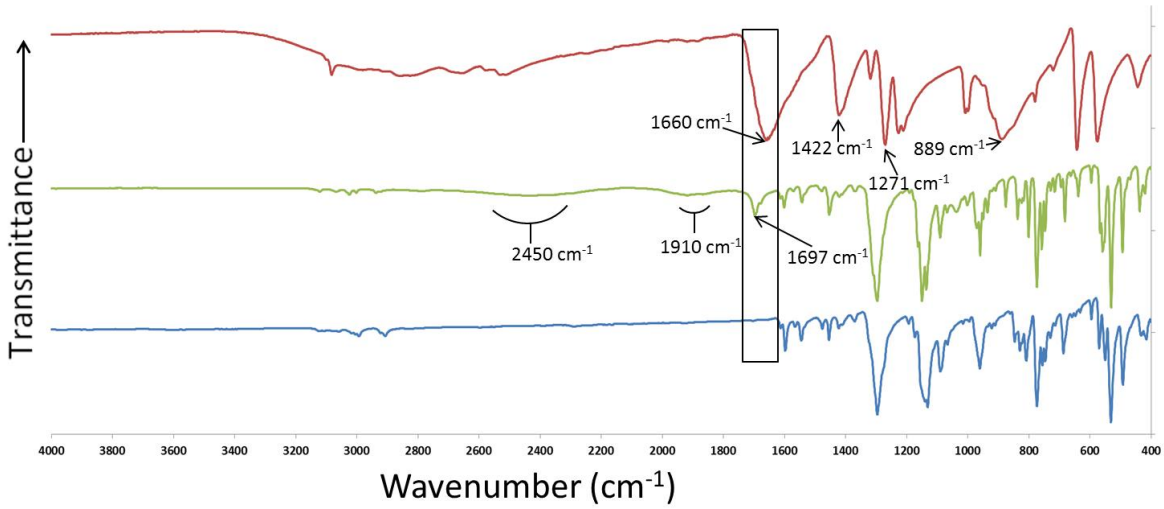

Fig. 4.2.83 FTIR spectra of MMV (Blue), MMVFUM (Green), and fumaric acid (Red).

Preparation of single crystals

Single crystals were obtained by co-precipitation of 5.00 mg of MMV with an equimolar amount of fumaric acid (1.36 mg) dissolved in 2 cm^3 of acetone, heated to 50 °C while stirring and filtering through a 0.45 µm nylon filter into a clean vial and placing on a benchtop after covering the vial with Parafilm™. After a week crystals were observed at the bottom of the vial and these were used for further characterisation.

Stoichiometry determination by ^{1}H – NMR spectroscopy

The stoichiometry of the components making up MMVFUM was determined by ^{1}H-NMR spectroscopy of single crystals of this phase that were dissolved in DMSO-d_6. The proton labelling schemes and the ^{1}H-NMR spectrum are shown in Fig. 4.2.84. The integration values are presented in Table 4.2.13. The ratio was determined to be 2:1 of MMV to fumaric acid.

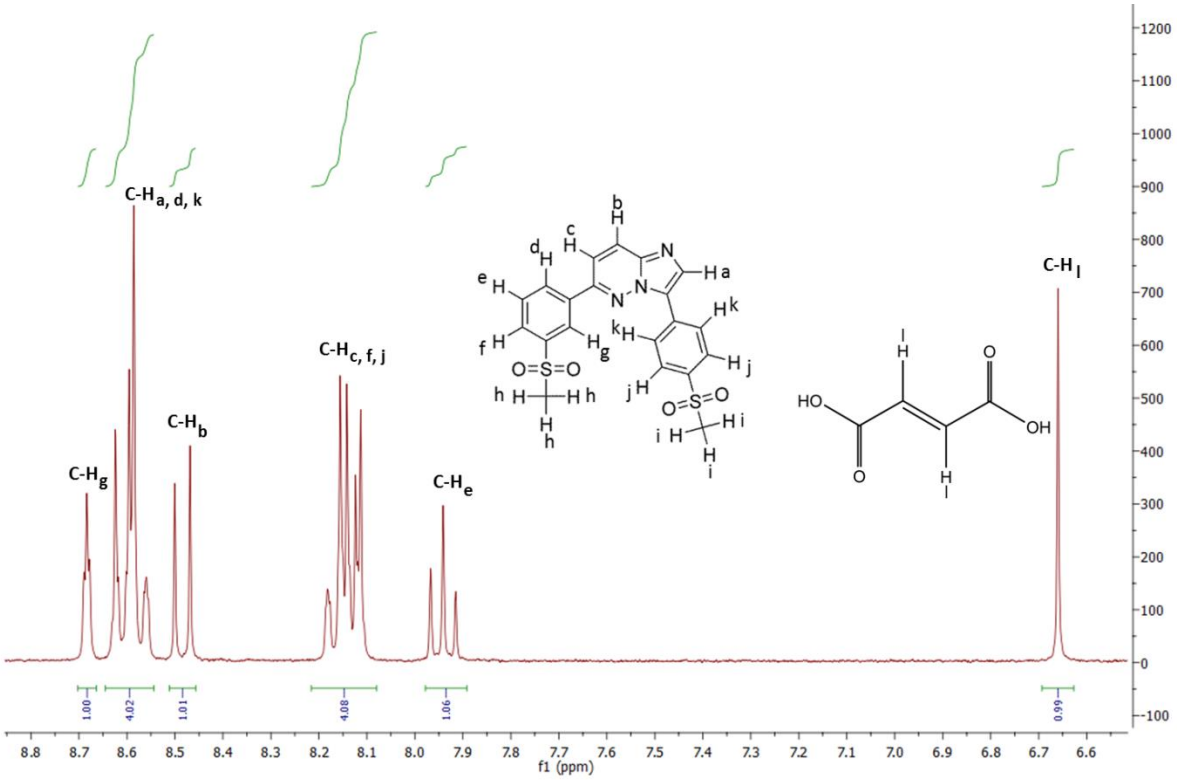

Fig. 4.2.84 ^{1}H-NMR spectrum of MMVFUM in DMSO-d_6 for determination of stoichiometry.

Table 4.2.13 Integrals of protons for individual components to determine stoichiometry of MMVFUM.

Proton – [Number of protons]	δ (ppm)	Integration	Experimental/ Theoretical
MMV			
C-$H_{c,f,j}$– [4]	8.080-8.216	4.08	1.02
C-H_g – [1]	8.664-8.702	1.00*	1.00
C-$H_{a,d,k}$– [4]	8.544-8.645	4.02	1.01
C-H_b – [1]	8.457-8.512	1.01	1.01
C-H_e – [1]	7.892-7.978	1.06	1.06
Fumaric acid			
C-H_l – [2]	6.627-6.693	0.99	0.50

*** Reference integral**

Crystal structure analysis

Data-collection and space group determination

A Bruker Kappa Apex II Duo diffractometer was used to collect single-crystal X-ray intensity data at 173(2) K. $\bar{1}$ Laue symmetry was observed and this indicates that the compound crystallizes in the triclinic crystal system. A mean $|E^2-1|$ value of 0.959, corresponding to centrosymmetry, was found by making use of the software XPREP[9]. *P* $\bar{1}$ was therefore chosen as the space group for this structure.

Structure solution and refinement

Crystallographic data, parameters for collection of intensity data and refinement details are reported in Table 4.2.14. The method for data reduction, unit cell refinement and structure elucidation was the same as that described for MMVADIP. As for the previous co-crystals, the relevant environments of the coformer molecule and the MMV molecule were inspected to ascertain whether proton transfer had occurred. The distinct C-O bond lengths of the fumaric acid functional groups of 1.326(2) Å and 1.221(2) Å are representative of single and double bonds. This detail along with the carboxyl hydrogen being visible in the Fourier difference map indicated that the MMV and fumaric acid molecules are in the neutral state and hence that the structure is a co-crystal.[12,13] The remaining hydrogen atoms were identified through inspection of the difference electron density maps and placed in idealised positions in a riding model and refined with thermal parameters 1.2-1.5 times the U_{iso} values of their parent atoms.

An interesting detail to point out is that the unit cell parameters for MMVFUM closely match those of MMVSUCC1 and, as was mentioned above in the comparison of the LAG results, this is due to the isostructural packing arrangement of the two phases.

Table 4.2.14 Data-collection and refinement parameters for MMVFUM.

Molecular formula	$(C_{20}H_{17}N_3O_4S_2) \cdot 0.5(C_4H_4O_4)$
Formula weight (g mol^{-1})	485.52
Crystal system	Triclinic
Space group	*P* $\bar{1}$
a (Å)	5.0808(4)
b (Å)	11.0323(9)
c (Å)	19.5422(16)
α (°)	100.398(2)
β (°)	93.705(2)
γ (°)	101.228(2)
V (Å)^3	1051.12(15)
Z	2
D_c (g cm^{-3})	1.534

μ (Mo Kα) (mm^{-1})	0.301
F(000)	504
Data-collection temp. (K)	173(2)
Crystal size (mm^3)	0.14 x 0.11 x 0.06
Range scanned θ (°)	1.92 – 28.29
Index ranges ±*h*, ±*k*, ±*l*	-6, 6; -14, 14; -25, 25
Reflections (total)	20 376
Independent reflections	5196
Reflections with I>2σ(I)	4061
Number of parameters	300
R_{int}	0.0527
S	1.028
R_1 [*I*>2σ(*I*)]	0.0403
Reflections omitted	1
wR_2	0.1014
a, b in w = $1/[\sigma^2(F_o^2)+(aP)^2+(bP)]$	a = 0.0409; b = 0.4309
$(\Delta/\sigma)_{mean}$	< 0.001
$\Delta\rho_{min,max}$ (e $Å^{-3}$)	-0.376, 0.342

Molecular structure

The asymmetric unit and labelling scheme of MMVFUM are shown in Fig. 4.2.85.

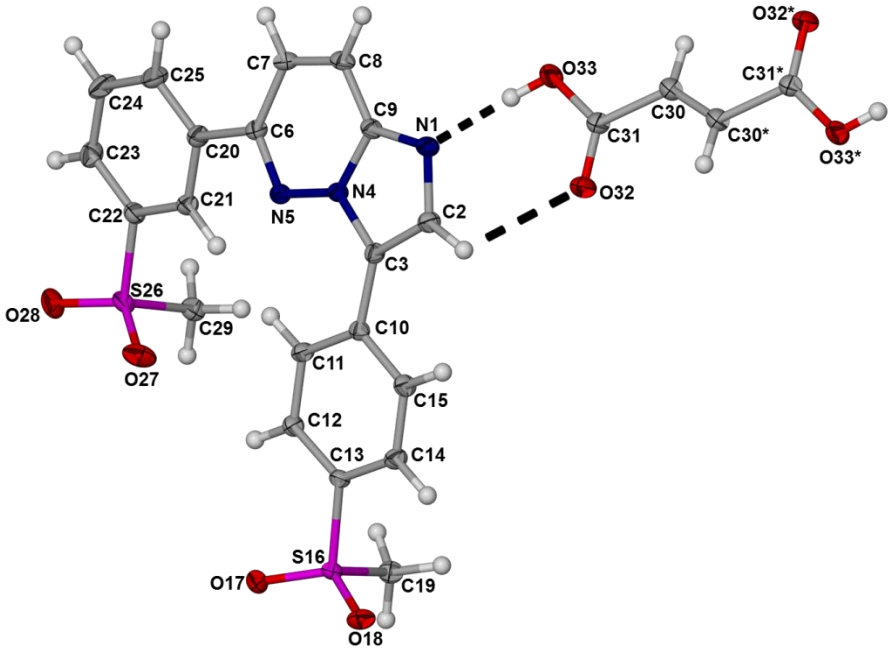

Fig. 4.2.85 The asymmetric unit and numbering scheme of MMVFUM with thermal ellipsoids shown at the 50% probability level. Atoms labelled with an asterisk are symmetry-generated and are not part of the asymmetric unit.

Crystal packing and hydrogen bonding

The relevant symmetry information for MMVFUM is listed in Table 4.2.15.

Table 4.2.15 Hydrogen bonds in MMVFUM[a].

	D–H···A	*d*(D–H), Å	*d*(H···A), Å	*d*(D···A), Å	∠(DHA), deg.
	O33-H33···N1	0.84	1.82	2.653(2)	175
	C2-H2···O32	0.95	2.61	3.191(2)	120
Intra	C12-H12···O17	0.95	2.58	2.945(2)	103
Intra	C11-H11···N5	0.95	2.23	2.905(2)	127
	C19-H19A···O28^{i}	0.98	2.40	3.355(2)	163
Intra	C21-H21···N5	0.95	2.36	2.696(2)	100
	C25-H25···O32^{ii}	0.95	2.54	3.302(2)	137
	C29-H29A···O17^{iii}	0.98	2.59	3.508(2)	157
	C29-H29B···O27^{iii}	0.98	2.53	3.254(3)	131
	C29-H29C···O17^{iv}	0.98	2.57	3.429(2)	146
Intra	C14-H14···O18	0.95	2.67	3.008(2)	102
Intra	C21-H21···O27	0.95	2.61	2.954(2)	102
Intra	C23-H23···O28	0.95	2.62	2.954(2)	101
	C30-H30···O32^{iii}	0.95	2.63	3.462(2)	146
Intra	C30-H30···O32^{v}	0.95	2.59	2.864(2)	97

[a] Symmetry transformations used to generate equivalent atoms: *[i]: 1+x,1+y,z; [ii]: -1+x,-1+y,z; [iii]: -1+x,y,z; [iv]: 2-x,-y,-z; [v]:1-x,2-y,1-z*

The packing of this co-crystal as well as the interactions present are very similar to those reported for MMVSUCC1 for the reason that the respective coformers (fumaric acid and succinic acid) are both dicarboxylic acids with equal chain lengths and this results in isostructurality of the co-crystal structures. Interactions of interest are summarised in Table 4.2.15 and are displayed in Figs. 4.2.86 and 4.2.87.

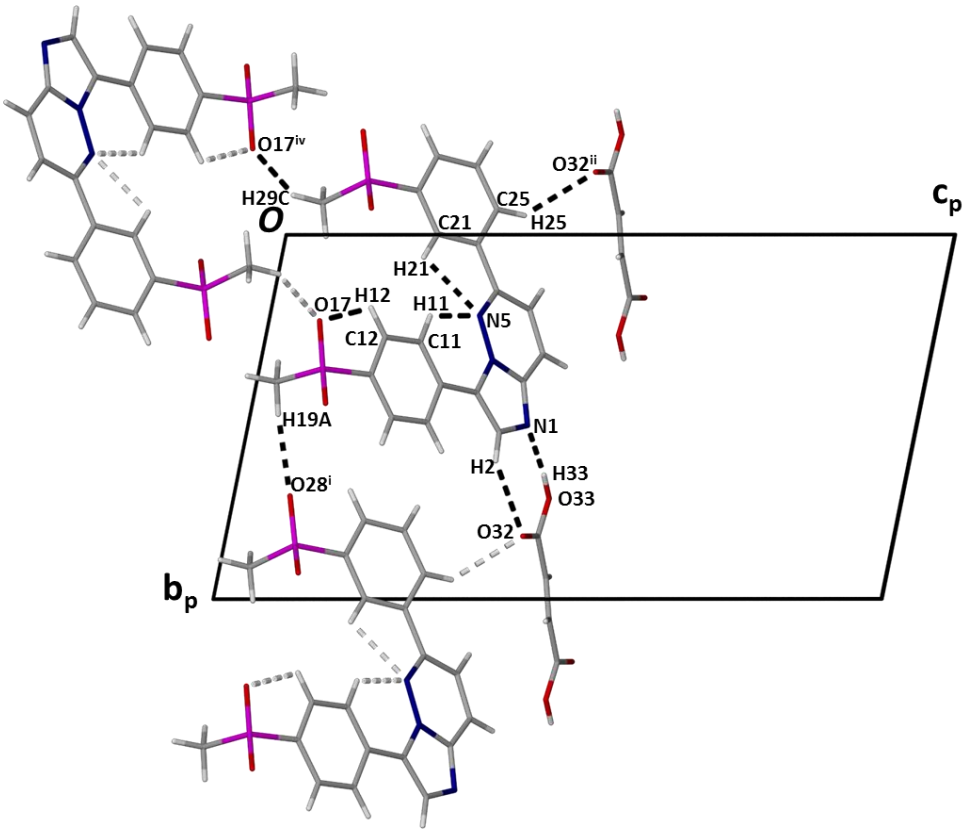

Fig. 4.2.86 Hydrogen bonding interactions found in the structure of MMVFUM viewed along [100] showing the interactions connecting molecules in the same layer.

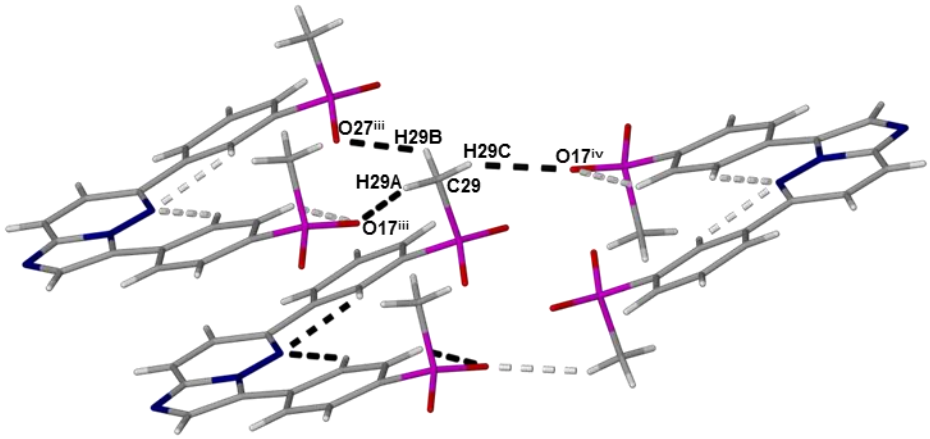

Fig. 4.2.87 Hydrogen bonding interactions found in the structure of MMVFUM.

As was the case with MMVSUCC1, discrete ribbons ($D_2^2(10)$) formed by two MMV molecules hydrogen bonded as a dimer ($R_2^2(7)$) to each end of the dicarboxylic fumaric acid molecules are present in this

structure (Figs. 4.2.86 and 4.2.88). These discrete ribbons are connected by intermolecular interactions between MMV molecules by C29-H29C···O17′ ($R_2^2(32)$) to form infinite ribbons (Fig. 4.2.89).

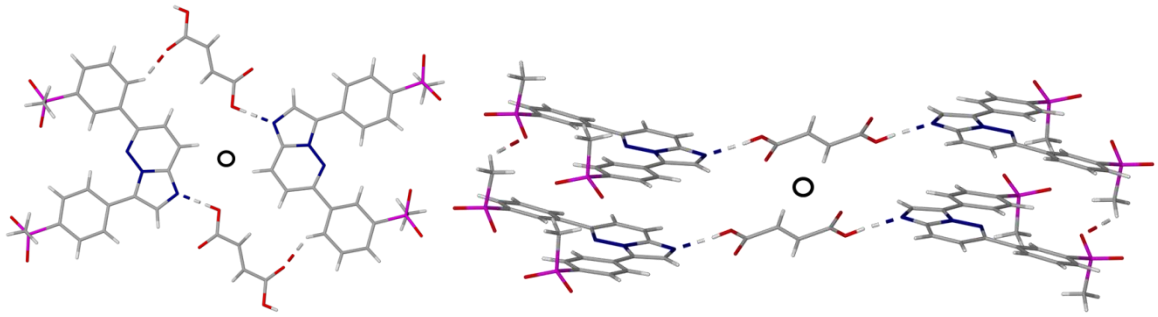

Fig. 4.2.88 Interactions that play a role in linking the infinite ribbons to form stepped layers. The interactions C25-H25···O32′ and C29-H29B···O27′ connect different layers and together with O33-H33···N1′ form rings described by $R_4^4(30)$ (left) and $R_6^6(58)$ (right).

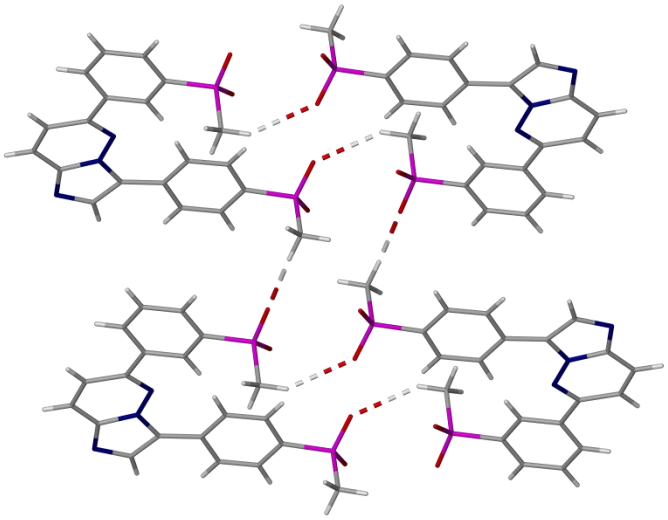

Fig. 4.2.89 Ring interactions connecting adjacent MMV molecules in MMVFUM. Showing C29-H29C···O17′ ($R_2^2(32)$) and C29-H29C···O17′ with C19-H19A···O28′ ($R_4^4(16)$).

This co-crystal packs in stepped layers, the topology and packing of which are shown in Figs. 4.2.90 and 4.2.91. The stepped layers are made up of infinite ribbons that are packed in a stepwise fashion. The ribbons are indirectly connected to other infinite ribbons in the same layer through interactions with molecules above and below the planes of these ribbons. The interactions connecting these layers are C19-H19A···O28′, C25-H25···O32′, and C29-H29B···O27′. These interactions and the rings which they generate are presented in Figs. 4.2.86 and 4.2.87.

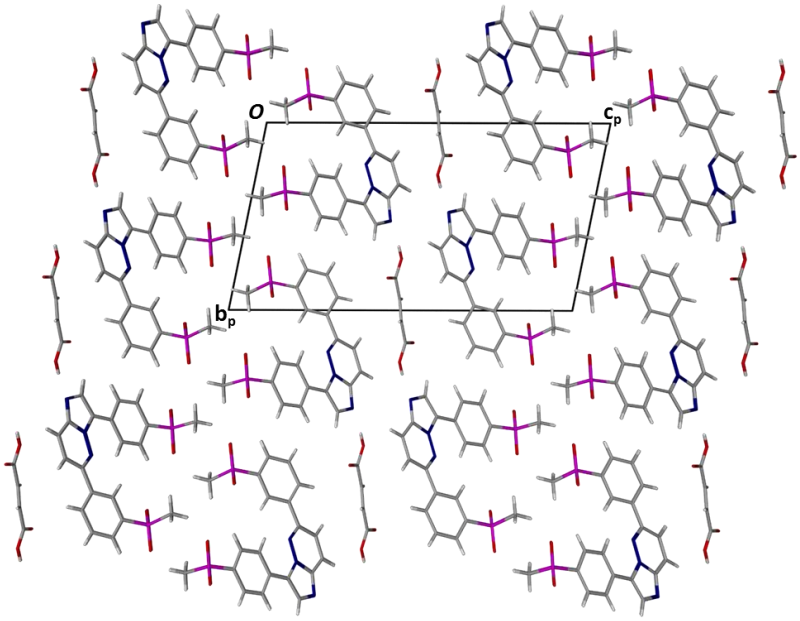

Fig. 4.2.90 Packing of MMVFUM viewed along [100].

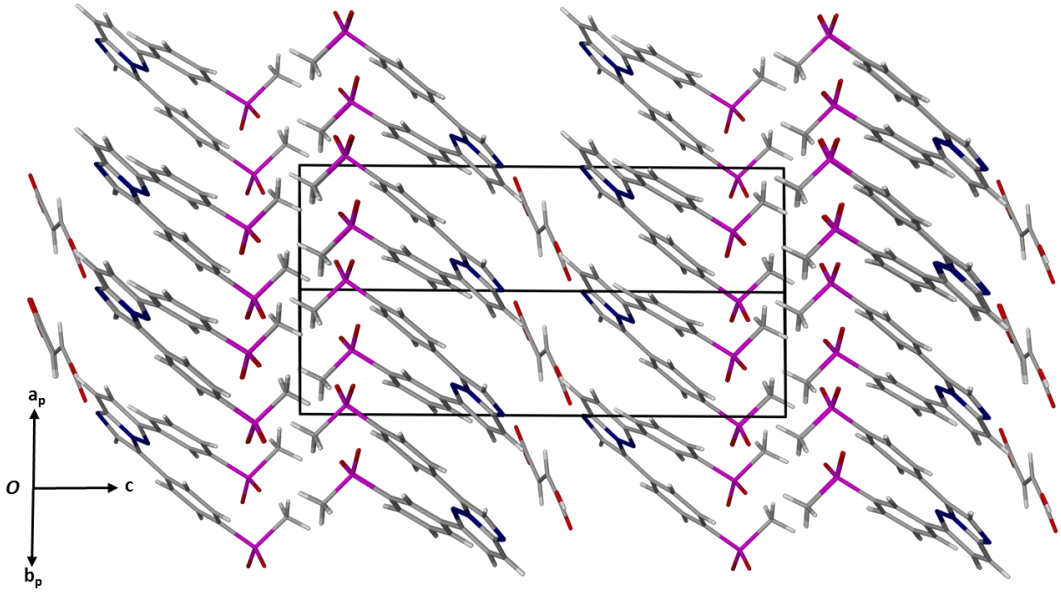

Fig. 4.2.91 Packing of MMVFUM showing layers viewed along [110].

Other interactions connecting the stacked layers are π-π interactions between the rings N1-C2-C3-N4-C9 (with centroid Cg(A)) and C10-C11-C12-C13-C14-C15 (with centroid Cg(C)) and the rings N4-N5-C6-C7-C8-C9 (with centroid Cg(B)) and C10-C11-C12-C13-C14-C15 (with centroid Cg(C)) (Fig. 4.2.92). The rings are orientated in a moderately offset face-to-face manner in both cases and are

related by the symmetry operator -1+x,y,z. The centroid-to-centroid distances are 3.647(1) Å for Cg(A)···Cg(C) and 3.540(1) Å for Cg(B)···Cg(C), the shortest contact distances between atoms being 3.318 Å (C9···C10), common for Cg(A)···Cg(C) and Cg(B)···Cg(C), and 3.361 Å (C8···C10) for Cg(B)···Cg(C).

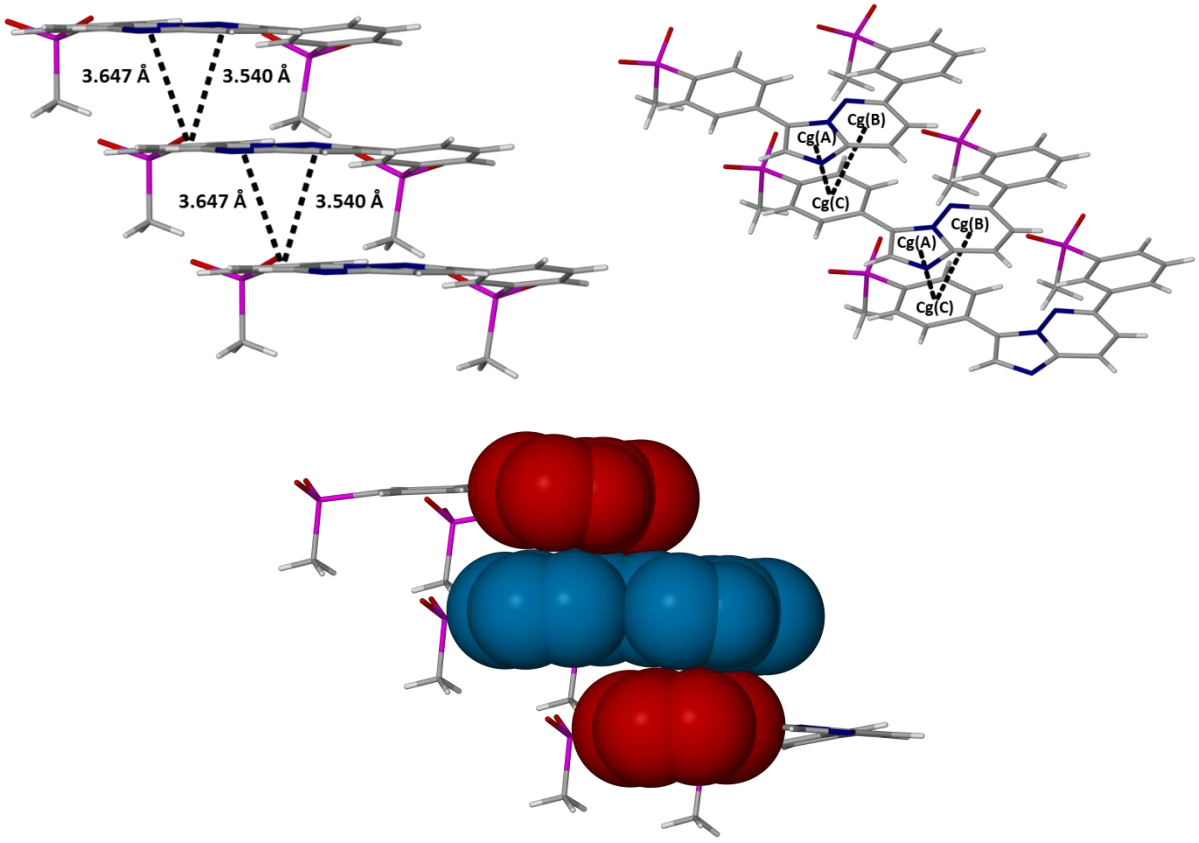

Fig. 4.2.92 π-π interactions connecting layers viewed from different perspectives showing centroids and offset centroid-to-centroid distances between them. Ring atoms are drawn with van der Waals radii to illustrate the overlap in the case of Cg(A)···Cg(C) and Cg(B)···Cg(C).

PXRD

A calculated PXRD trace for MMVFUM from the solved crystal structure is compared to a PXRD trace experimentally produced in the analysis of MMVFUM prepared by LAG with acetonitrile (Fig. 4.2.93). The correlation shows that this method could be used to produce this phase for further characterisation by other techniques. As expected, this trace also matches that obtained for MMVSUCC1 due to isostructurality (the PXRD traces are compared in Fig. A4.2.21 in Appendix A).

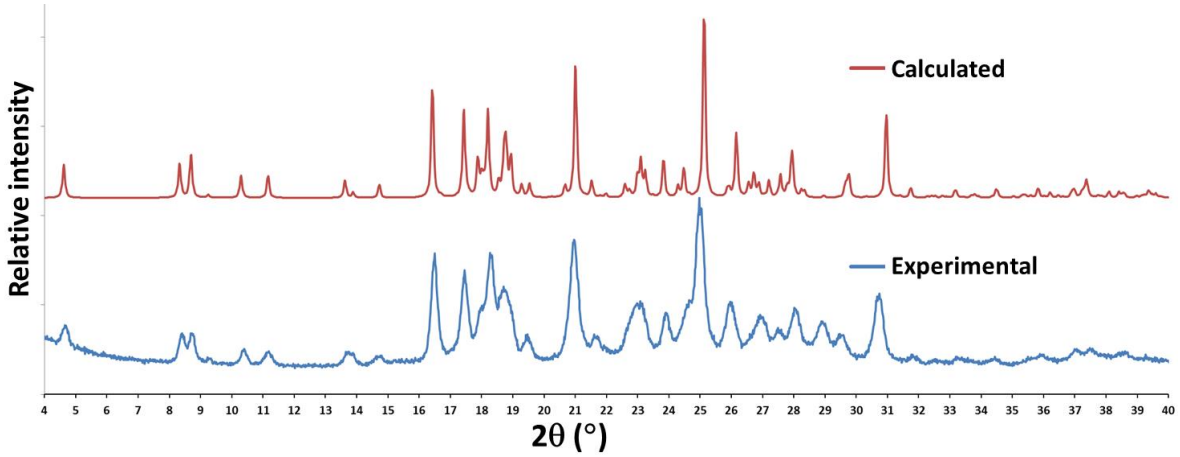

Fig. 4.2.93 PXRD traces collected for the bulk product produced by LAG (MMV, fumaric acid and acetonitrile) and a trace computationally generated from the single crystal X-ray structure of MMVFUM.

Thermal analysis

The HSM results for MMVFUM are shown in Fig. 4.2.94. As can be seen in the micrographs, by 220 °C the crystal has started to melt and by 240 °C the crystal has completely melted.

Fig. 4.2.94 Representative HSM photographs of MMVFUM at various temperatures.

The fumaric acid starting material does not have a clear melting point, but appears to begin to sublime around 200 °C in the DTA experimental result (Fig. 4.2.95). This value matches that reported in literature.[24] The MMVFUM sample had an endothermic event with an onset of 222.5 ± 0.93 °C (n = 3) and a peak at 231.17 ± 0.09 °C (n = 3). The temperature of the event seen in the DTA result is similar to that at which melting was observed with HSM. The difference in melting and decomposition temperatures observed between the starting materials and MMFUM support the supposition that a different phase has been produced.

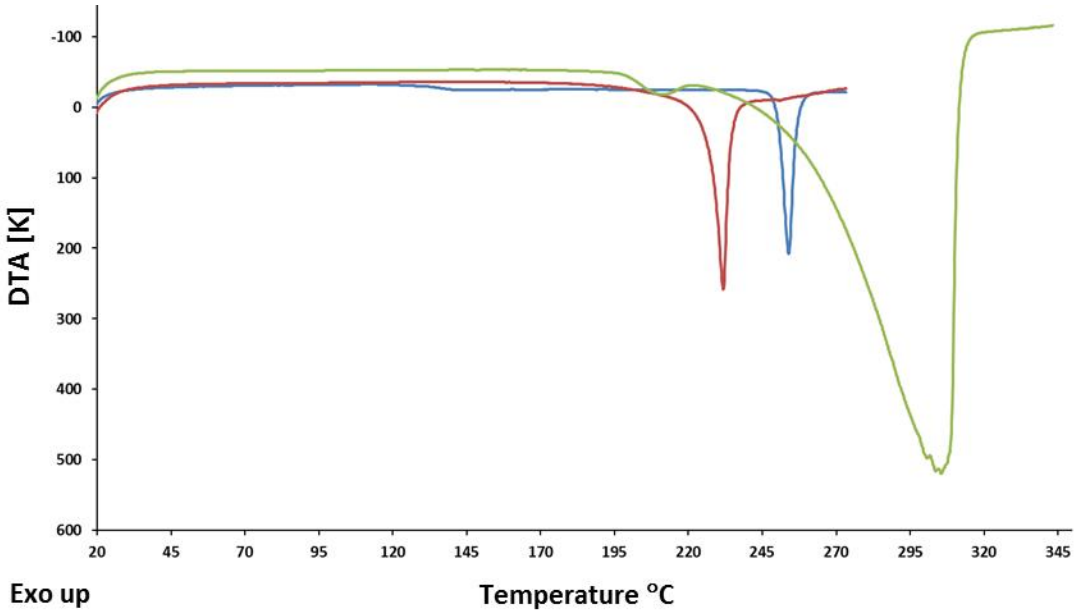

Fig. 4.2.95 Representative DTA traces of MMV (Blue) and fumaric acid (Green) starting materials and for MMVFUM (Red).

The mass loss of 11.5 ± 0.4 % (n = 3) observed through TGA (Fig. 4.2.96) equates to one molecule of fumaric acid for every two molecules of MMV (theoretical percentage 12.0). This matches the ratio seen in the SCXRD and NMR results. The first stepped mass loss had an onset temperature of 215.7 ± 0.5 °C (n = 3). This value does not precisely match the onset seen in the DTA result, but is relatively close.

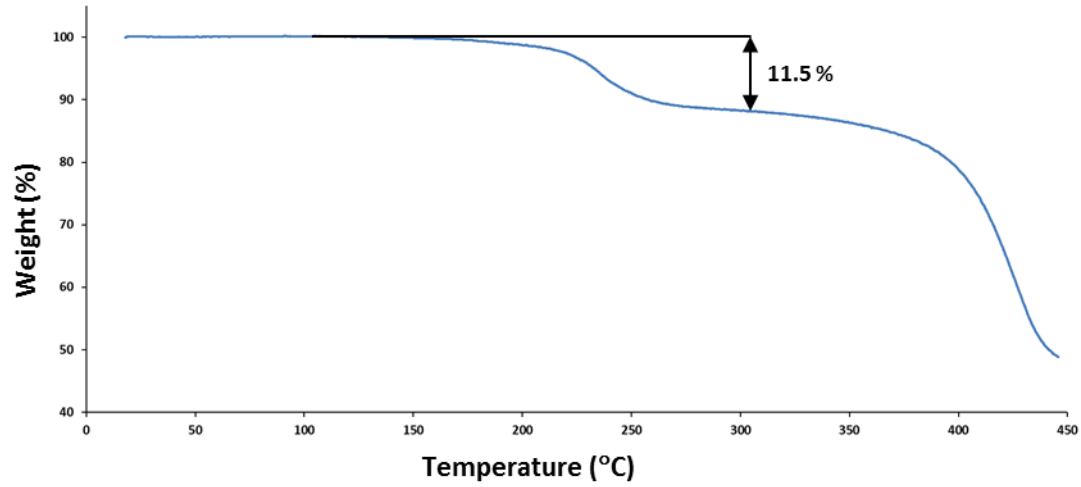

Fig. 4.2.96 Representative TGA trace of MMVFUM.

Solubility test

The same method as described in previous sections was employed; only deviations from it are pointed out here. A total of 28.39 mg of MMVFUM (equivalent to 25.00 mg of pure MMV) was added to 50 cm^3 of FaSSIF at a temperature of 37.5 ± 0.5 °C while being stirred at 500 rpm. The result is presented in Fig. 4.2.97. An S_{max} of 19.5 ± 1.8 µg. cm^{-3} (n = 3) was obtained at 10 min (a factor of over 5 times the S_0) and after this time the concentration dropped to 15.3 ± 0.4 µg. cm^{-3} (n = 3) by 15 min. The general trend after this point was one of steady decrease and plateauing after three hours and remaining within a range of 8.3-9.2 µg. cm^{-3} from there onward. This result epitomises the "spring and parachute" effect.[19]

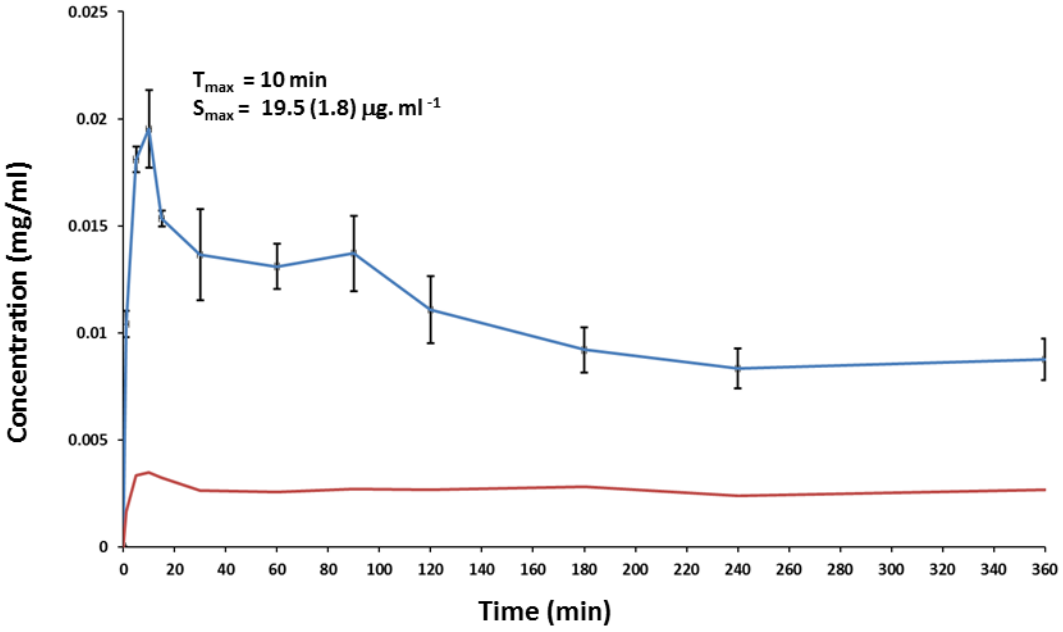

Fig. 4.2.97 Powder dissolution profile of MMV (Red) compared to MMVFUM (Blue) in FaSSIF at 37.5 ± 0.5 °C.

MMV-malonate salt (MMVMAL)

5 mg of MMV was ground with a mortar and pestle with an equimolar amount of malonic acid for 15 min while adding acetone in small drops. The product was then analysed with PXRD and the resulting trace was compared to those of the starting materials of MMV and the coformer. The results are shown in Fig. 4.2.98. There are various new peaks visible in the trace of the LAG product, the most noticeable being at °2θ of 15.4 and 30.0.

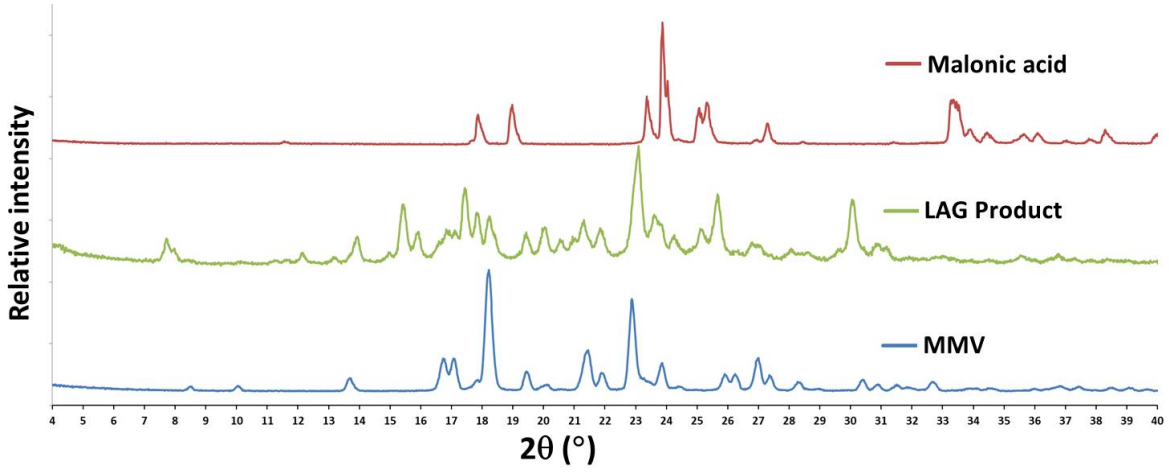

Fig. 4.2.98 Recorded PXRD traces for the product of a LAG experiment and the starting materials, MMV and malonic acid.

Infrared spectroscopy

The FTIR spectra of MMV, malonic acid and MMVMAL are compared in Fig. 4.2.99. The common features for dicarboxylic acids that were observed in the previous FTIR results presented in this chapter are visible in the spectrum of malonic acid as well. The broad O-H stretching band is seen between 2500 and 3400 cm^{-1}. In this case the most intense peak was again due to the carbonyl stretch at 1695 cm^{-1}. The in-plane O-H bending band can be seen around 1400 cm^{-1} and a broad band with moderate intensity representing out-of-plane O-H bending has a peak around 900 cm^{-1}.

As was the case for the previous FTIR results presented in this chapter, there is a great deal of overlap in the spectra of MMV and MMVMAL. The carbonyl stretching band is clearly visible in MMVMAL at 1734 cm^{-1} and at first glance this would appear to be an indication that MMVMAL is a co-crystal. Lee and Wang stated that a band between 1690 and 1740 cm^{-1} is a sign that the product is a co-crystal and reported a carbonyl stretching band at 1736 cm^{-1} for their co-crystal consisting of cytosine and malonic acid.[25] Aakeröy *et al.* stated that in the case of co-crystals of this nature the carbonyl stretch will always be observed above 1675 cm^{-1}.[7] In the case of other carboxylic acids such as benzenecarboxylic acids, Brittain designated a large shift in frequency of a vibrational mode from 1558 cm^{-1} to 1691 cm^{-1} to be due to deprotonation of the carboxylic acid group.[26] As there exist two carboxylic acid moieties in each malonic acid molecule, the presence of a carbonyl stretching band, though indicating that at least one of the carboxylic carbonyl groups is interacting in the neutral state, does not rule out the possibility that proton exchange occurred in the other carboxylic acid moiety. An example of such a case was reported

by Sarma *et al.* in a mirtazipinium hydrogen malonate salt where proton exchange had occurred at one terminus of the malonate anion with the other carboxylic acid moiety interacting to form an intramolecular H-bond (the carbonyl stretching band was present at 1709 cm^{-1}).[27] They had, however, ascribed this to the carbonyl stretch of the carboxylate moiety. Matulková et al. reported another example with a guanazole hydrogen malonate salt (the carbonyl stretching band was present at 1690 cm^{-1}).[28] An example where the carbonyl stretching band peak had shifted down to 1650 cm^{-1} is that of a riluzole malonate salt and this shift was ascribed to the formation of a carboxylate anion.[23] The peak of the band was visible at 1650 cm^{-1}, though the band was arguably rather wide spanning a range well beyond 1700 cm^{-1}.

These results reinforce the statement made before that FTIR results alone might be insufficient to confidently assign samples as being salts or co-crystals and one should be careful to avoid treating any of the guidelines used for screening as strict rules.

The broad bands observed in the other examples centred around 1920 and 2450 cm^{-1} due to the O-H···N stretching of the acid-imidazole absorption are absent in this case. The in-plane O-H bending band and the broad band representing out-of-plane O-H bending are also absent in MMVMAL.

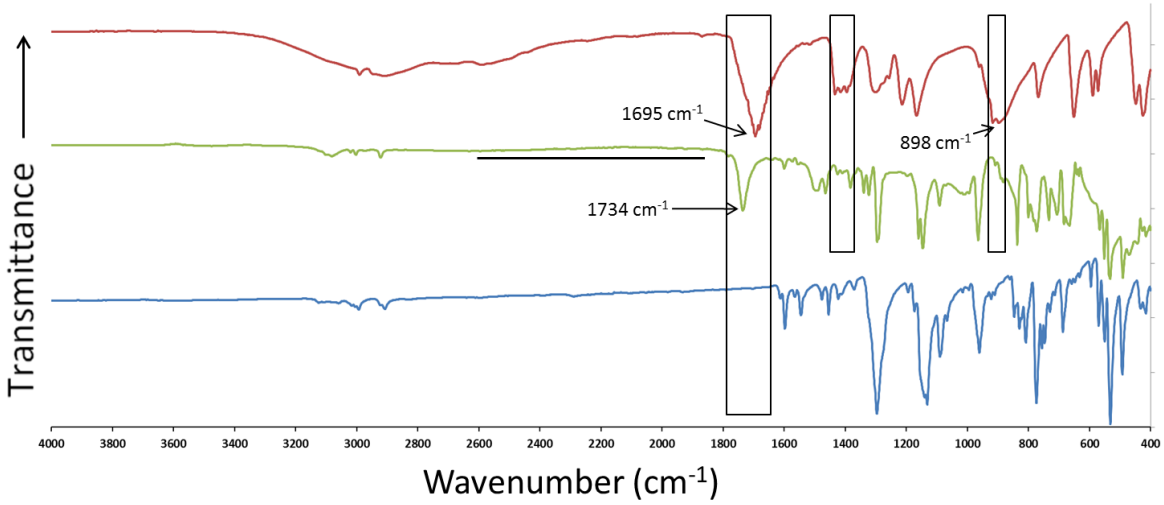

Fig. 4.2.99 FTIR spectra of MMV (blue), MMVMAL (green), and malonic acid (red).

Preparation of single crystals

Single crystals were obtained by co-precipitation of 5 mg of MMV with about 10 times the molar amount of malonic acid (12 mg) dissolved in 1 cm^3 of acetone, heated to 50 °C while stirring and filtering

through a 0.45 µm nylon filter into a clean vial and placing on a benchtop after covering the vial with Parafilm™.

Stoichiometry determination by ^{1}H – NMR spectroscopy

Single crystals of MMVMAL obtained by co-precipitation were dissolved in DMSO-d_6 and analysed by ^{1}H-NMR spectroscopy to determine the stoichiometric ratio of the individual components. The proton labelling schemes and the ^{1}H-NMR spectrum are shown in Fig. 4.2.100. The integration values are presented in Table 4.2.16. Due to slight overlap of peaks (water peak, methyl group of MMV labelled i, and the malonic acid proton labelled l) the integration values are compromised. The ratio was determined to be 1:1.15 (1:1) of MMV to malonic acid. This could be a result of the sample analysed containing some of the pure coformer that had precipitated from solution due to its being present in excess in the vial in which the co-precipitation experiment was performed.

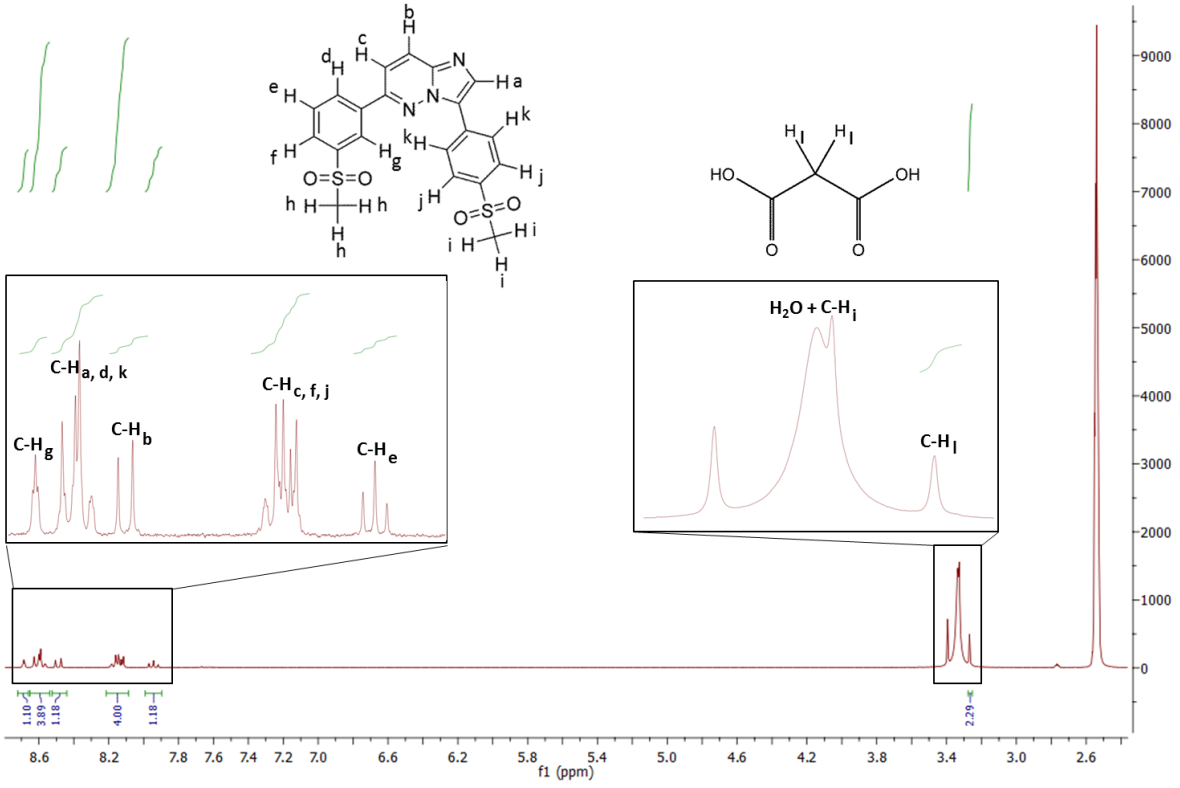

Fig. 4.2.100 ^{1}H-NMR spectrum of MMVMAL in DMSO-d_6 for determination of stoichiometry.

Table 4.2.16 Integrals of protons for individual components to determine stoichiometry of MMVMAL.

Proton – [Number of protons]	δ (ppm)	Integration	Experimental/ Theoretical
MMV			
C-$H_{c,f,j}$– [4]	8.09-8.22	4.00*	1.00
C-H_g – [1]	8.66-8.72	1.10	1.10
C-$H_{a,d,k}$– [4]	8.54-8.65	3.89	0.97
C-H_b – [1]	8.44-8.52	1.18	1.18
C-H_e – [1]	7.90-7.99	1.18	1.18
Malonic acid			
C-H_l – [2]	3.25-3.28	2.29	1.15

*** Reference integral**

Crystal structure analysis

Data-collection and space group determination

The single-crystal X-ray intensity data collection was performed on a Bruker Kappa Apex II Duo diffractometer at 173(2) K. The triclinic crystal system was indicated by $\bar{1}$ Laue symmetry shown by the X-ray diffraction pattern. The program XPREP[9] was used to determine a mean $|E^2-1|$value. The calculated value was 0.980 and this corresponds to centrosymmetry. Hence, the space group selected was $P\bar{1}$.

Structure solution and refinement

Crystallographic data, parameters for collection of intensity data and refinement details are in Table 4.2.17. The method for data reduction, unit cell refinement and structure elucidation was the same as that described for MMVADIP.

The means of defining MMVMAL as a salt or co-crystal was done by inspecting the Fourier difference map to seek the actual location of the H atoms originally present in the –COOH groups of the coformer. The Fourier difference map showed that a proton was present on the imidazole nitrogen moiety of the MMV molecule. One malonic acid –COOH group having lost a proton had thus become a carboxylate group with similar C-O bond lengths of 1.269(2) Å and 1.247(2) Å. These do not match common lengths of either single or double C-O bonds, but fall in the middle of the range.[12,13] The position of the proton from the Fourier difference map and the C-O bond lengths provided unequivocal evidence that proton exchange had occurred and that the product is a salt. Through further inspection of the Fourier electron density difference map, the position of the second carboxyl proton of the malonic acid molecule was determined to be present in the –COOH group at the other terminus. This group presents the unusual

anti-arrangement, the –OH group forming an intramolecular hydrogen bond with an oxygen atom of the carboxylate group. The distinct C-O bond lengths of this carboxyl functional group were 1.211(2) Å and 1.319(2) Å. This is indicative of double and single C-O bonds respectively.[12,13] All hydrogen atoms were found in difference electron density maps and placed in idealised positions in a riding model and refined with thermal parameters 1.2-1.5 times the U_{iso} values of their parent atoms.

Table 4.2.17 Data-collection and refinement parameters for MMVMAL

Molecular formula	$(C_{20}H_{17}N_3O_4S_2)^+ \cdot (C_3H_3O_4)^-$
Formula weight (g mol^{-1})	531.55
Crystal system	Triclinic
Space group	$P\ \bar{1}$
a (Å)	8.7754(7)
b (Å)	11.2994(10)
c (Å)	11.7979(10)
α (°)	86.811(2)
β (°)	79.565(2)
γ (°)	82.112(2)
V (Å)^3	1139.04(17)
Z	2
D_c (g cm^{-3})	1.550
μ (Mo Kα) (mm^{-1})	0.292
F(000)	552
Data-collection temp. (K)	173(2)
Crystal size (mm^3)	0.19 x 0.18 x 0.15
Range scanned θ (°)	1.75 – 28.38
Index ranges ±*h*, ±*k*, ±*l*	-11, 11; -15, 15; -15, 15
Reflections (total)	23 261
Independent reflections	5691
Reflections with I>2σ(I)	4394
Number of parameters	327
R_{int}	0.0589
S	1.044
R_1 [*I*>2σ(*I*)]	0.0445
Reflections omitted	4
wR_2	0.1165
a, b in w = 1/[$\sigma^2(F_o^2)$+(aP)^2+(bP)]	a = 0.0468; b = 0.4078
$(\Delta/\sigma)_{mean}$	< 0.001
$\Delta\rho_{min,max}$ (e Å^{-3})	-0.463, 0.393

Molecular structure

The asymmetric unit and labelling scheme of MMVMAL are shown in Fig. 4.2.101.

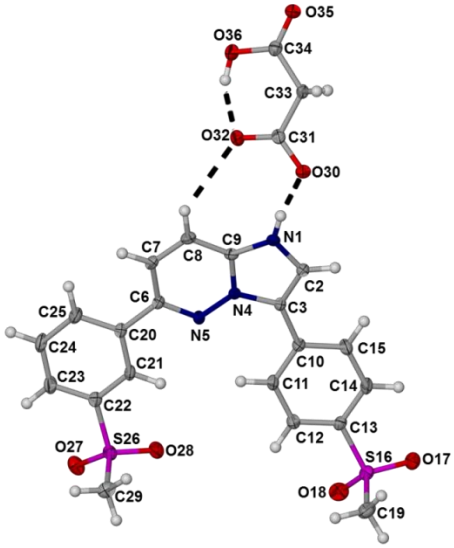

Fig. 4.2.101 The asymmetric unit and numbering scheme of MMVMAL with thermal ellipsoids shown at the 50% probability level.

Crystal packing and hydrogen bonding

The relevant symmetry information for MMVMAL is listed in Table 4.2.18.

Table 4.2.18 Hydrogen bonds in MMVMAL[a].

	D–H···A	*d*(D–H), Å	*d*(H···A), Å	*d*(D···A), Å	∠(DHA), deg.
	N1-H1···O30	0.88	1.66	2.536(2)	170
	C8-H8···O32	0.95	2.66	3.362(2)	132
Intra	O36-H36···O32	0.84	1.74	2.524(2)	154
	C2-H2···O35$^{i\,(2)}$	0.95	2.35	3.288(2)	170
	C7-H7···O17^{ii}	0.95	2.28	3.224(2)	170
Intra	C11-H11···N5	0.95	2.34	2.988(2)	125
Intra	C14-H14···O17	0.95	2.50	2.886(2)	104
	C15-H15···O35^{i}	0.95	2.52	3.402(2)	154
	C19-H19A···O35^{iii}	0.98	2.51	3.398(3)	151
	C19-H19B···O27^{iv}	0.98	2.50	3.353(3)	145
Intra	C21-H21···O28	0.95	2.53	2.901(2)	103
	C29-H29A···O18^{iv}	0.98	2.58	3.362(3)	136
	C29-H29C···O28^{iv}	0.98	2.49	3.328(2)	144
	C33-H33A···O28^{v}	0.99	2.59	3.489(2)	151
	C33-H33B···O30^{i}	0.99	2.50	3.403(2)	151
Intra	C21-H21···N5	0.95	2.37	2.702(2)	100
Intra	C23-H23···O27	0.95	3.01	2.699(2)	100

[a] Symmetry transformations used to generate equivalent atoms: *[i]: -x,-y,1-z; [ii]: -1+x,y,1+z; [iii]: 1+x,1+y,-1+z; [iv]: 1-x,2-y,1-z; [v]: -1+x,-1+y,z.*

The carboxylate group of the malonate anion is connected to the MMV cation *via* the charge-assisted H-bonds $N1^{+}$-H1···$O30^{-}$ and C8-H8···$O32^{-}$ while the carboxylic acid group of the malonate anion is intramolecularly H-bonded (O36-H36···O32), as can be seen in Figs. 4.2.101 and 4.2.102.

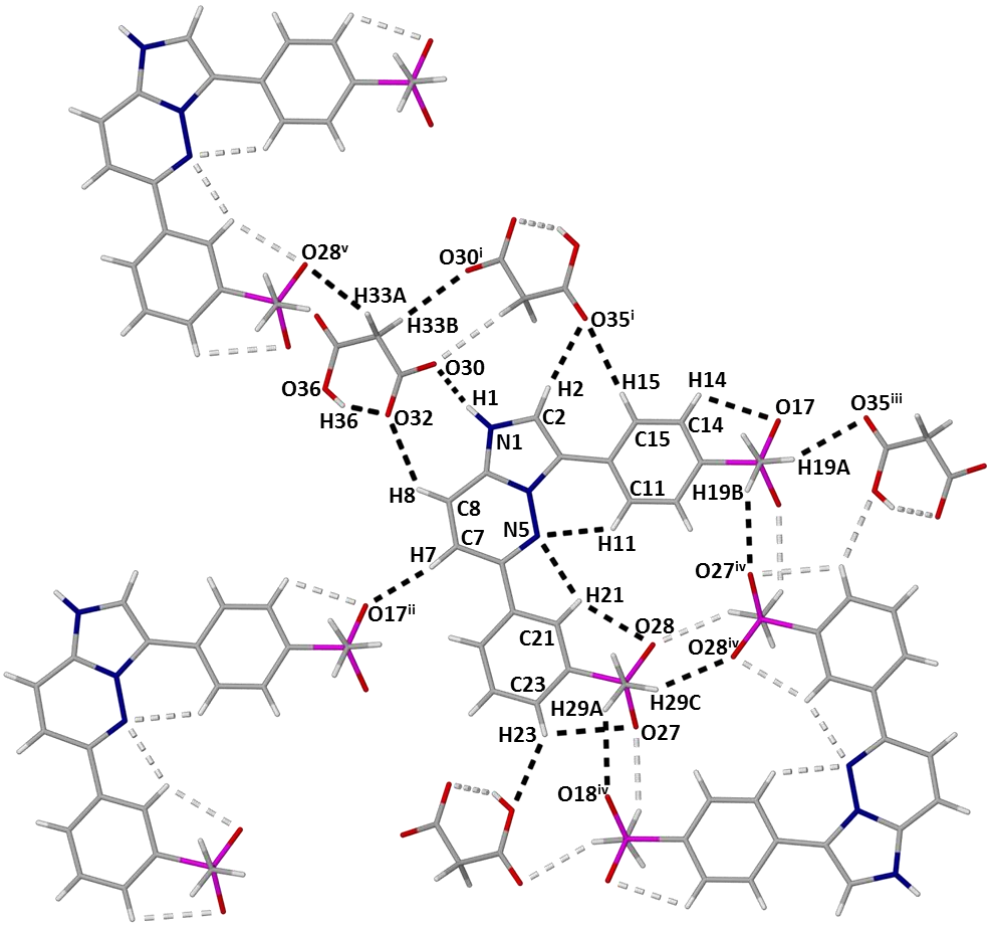

Fig. 4.2.102 Hydrogen bonding present in MMVMAL, showing the topology of a layer.

This malonate salt is packed into stacked layers as is visible in Fig. 4.2.103. The hydrogen and ionic bonds connecting the ions as well as the topology of such a layer is shown in Fig. 4.2.102. The layers are formed by alternating π-stacked MMV cations (Fig. 4.2.104) connected to other π-stacked molecules by the rings described by C29-H29C···O28′ ($R_2^2(8)$), C29-H29A···O18′ ($R_2^2(32)$), C19-H19B···O27′ ($R_2^2(32)$), and C19-H19B···O27′ with C7-H7···O17′ ($R_4^4(24)$) and ($R_4^4(56)$) (Fig. 4.2.105). The packing of these layers is shown in Fig. 4.2.103. The π-π interactions occur between the rings N1-C2-C3-N4-C9 (Cg(A)) and N4-N5-C6-C7-C8-C9 (Cg(B)) with offset face-to-face centroid-to-centroid distances of 3.341(1) Å

(Cg(A)···Cg(A) related by the symmetry operator -x,1-y,1-z) and 3.630(1) Å (Cg(A)···Cg(B) related by the symmetry operator -x,1-y,1-z) (Fig. 4.2.104).

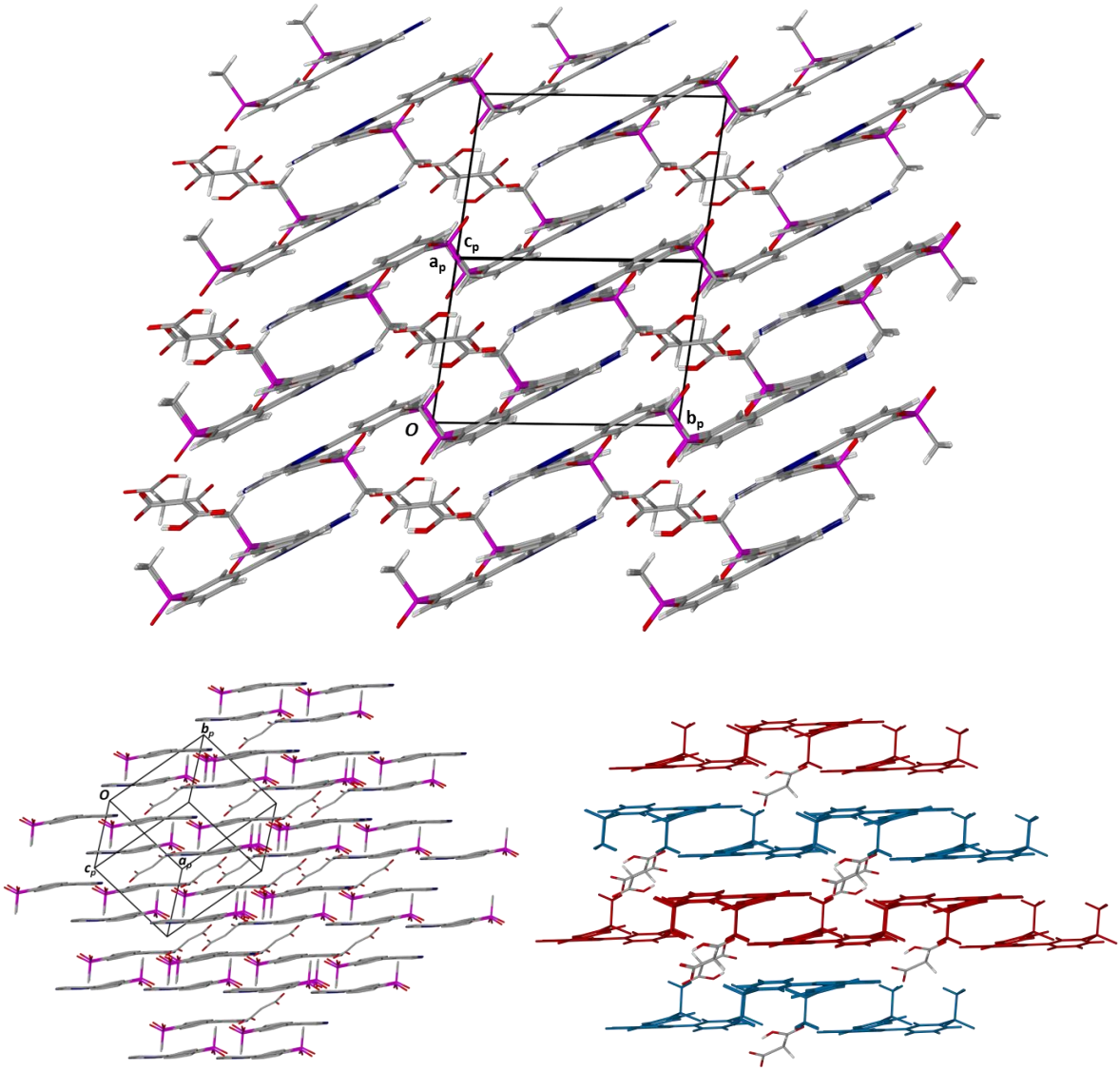

Fig. 4.2.103 Packing of MMVMAL showing the stacked layers.

The closest mutual atom-to-atom contact distance between these rings is 3.280 Å (C3···C9′). A ring interaction found between adjacent malonate anions is the H-bond C33-H33B···O30′ ($R_2^2(8)$) and is visible in Fig. 4.2.102. The stacked layers are also connected by rings between MMV and malonate ions, specifically N1-H1···O30 and C8-H8···O32 ($R_2^2(8)$), C2-H2···O35′ and C8-H8···O32 ($R_4^4(22)$), C2-H2···O35′

and N1-H1···O30 ($R_4^4(18)$), C15-H15···O35′ and N1-H1···O30 ($R_4^4(24)$), C15-H15···O35′ and C2-H2···O35′ ($R_2^1(7)$), C19-H19A···O35′ and C2-H2···O35′ ($R_4^2(22)$) (Fig. 4.2.106).

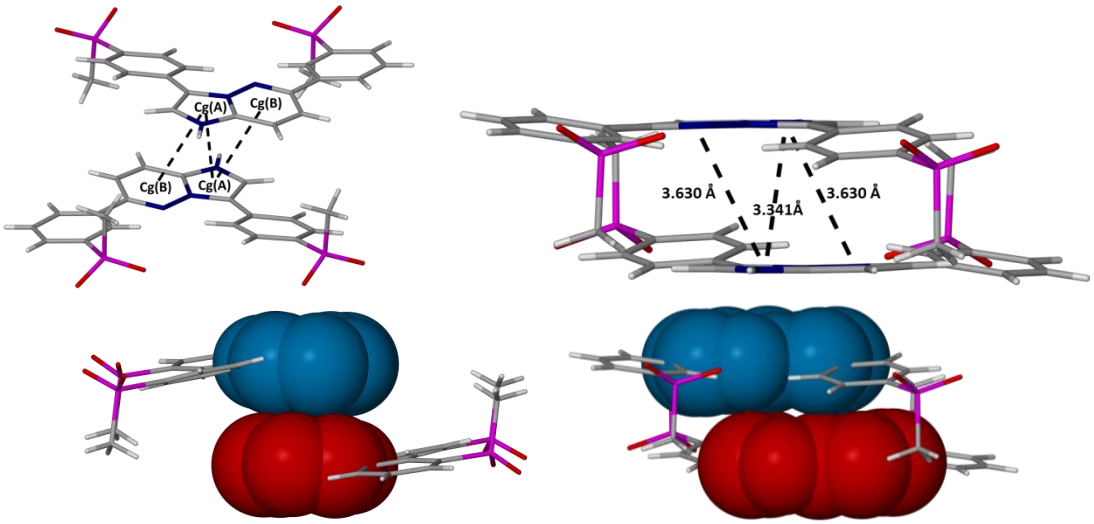

Fig. 4.2.104 π-π interactions connecting stacked molecules in MMVMAL viewed from different perspectives showing centroids and offset centroid-to-centroid distances between them. Ring atoms are drawn with van der Waals radii to illustrate the overlap in the case of Cg(A)···Cg(A) and Cg(A)···Cg(B).

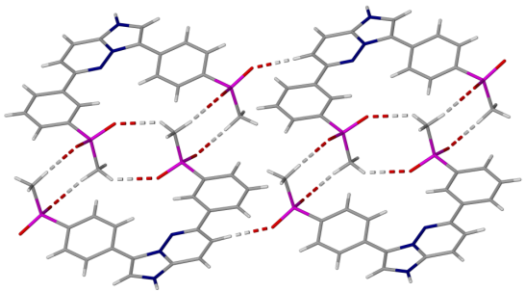

Fig. 4.2.105 Interactions connecting adjacent MMV molecules. Rings: C29-H29C···O28′ ($R_2^2(8)$); C29-H29A···O18′ ($R_2^2(32)$); C19-H19B···O27′ ($R_2^2(32)$); C19-H19B···O27′ and C7-H7···O17′ ($R_4^4(24)$) and ($R_4^4(56)$).

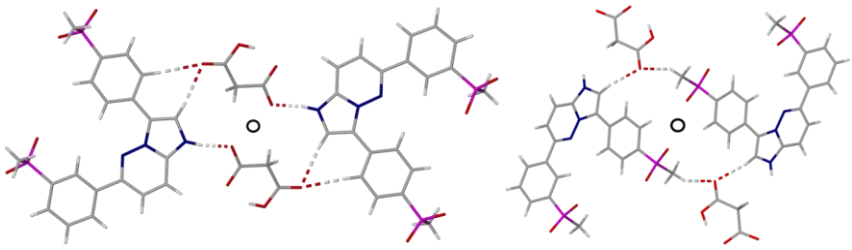

Fig. 4.2.106 Ring interactions connecting MMV and malonate ions in MMVMAL: C2-H2···O35′ and N1-H1···O30 ($R_4^4(18)$); C15-H15···O35′ and N1-H1···O30 ($R_4^4(24)$); C15-H15···O35′ and C2-H2···O35′ ($R_2^1(7)$) (left) C19-H19A···O35′ and C2-H2···O35′ ($R_4^2(22)$) (right).

PXRD

A calculated PXRD trace from the solved crystal structure of MMVMAL is compared to an experimentally produced trace of MMVMAL prepared by LAG in Fig. 4.2.107. The correlation between the traces would suggest that this method produces the same phase and the LAG product could thus be used for further characterisation. The second most intense peak in the PXRD trace found at 30.3 °2θ corresponds to the (2 -2 2) planes with a d-spacing of 2.949 Å and this coincides with the interlayer distance observed in Fig. 4.2.103.

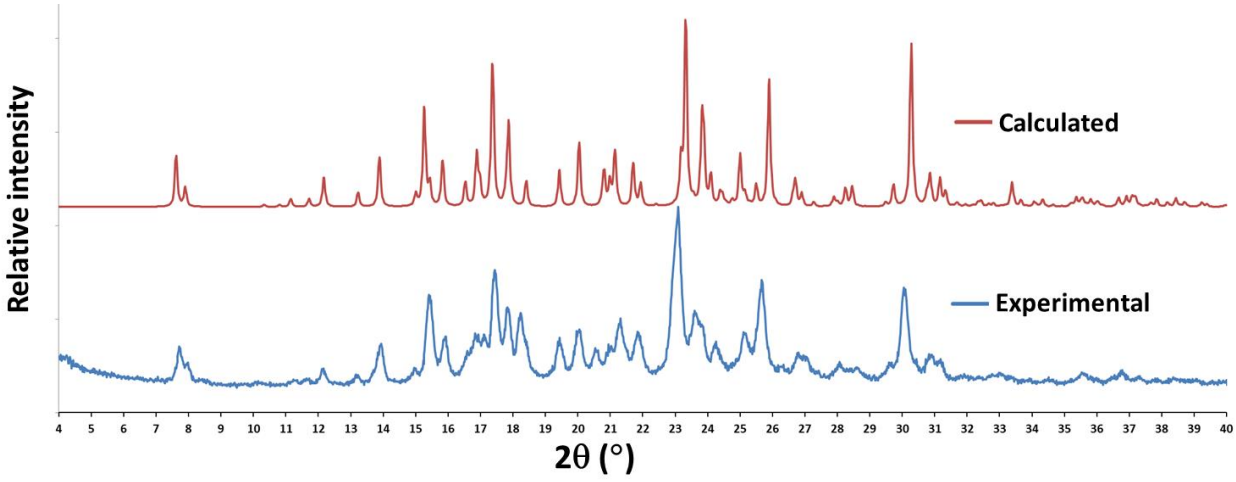

Fig. 4.2.107 PXRD traces collected for the bulk product produced by LAG and a trace computationally generated from the single crystal X-ray structure of MMVMAL.

Thermal analysis

A HSM experiment was carried out on a crystal of MMVMAL and the resulting micrographs are shown in Fig. 4.2.108. A gradual colour change was observed from faint pink to a yellow tinge as is visible in the contrast of the micrographs recorded at 25 and 175 °C. The crystal became opaque and its shape contorted between the micrographs taken at 175 and 194 °C. The bulk of the sample started to melt around 250 °C and was completely melted by 263 °C.

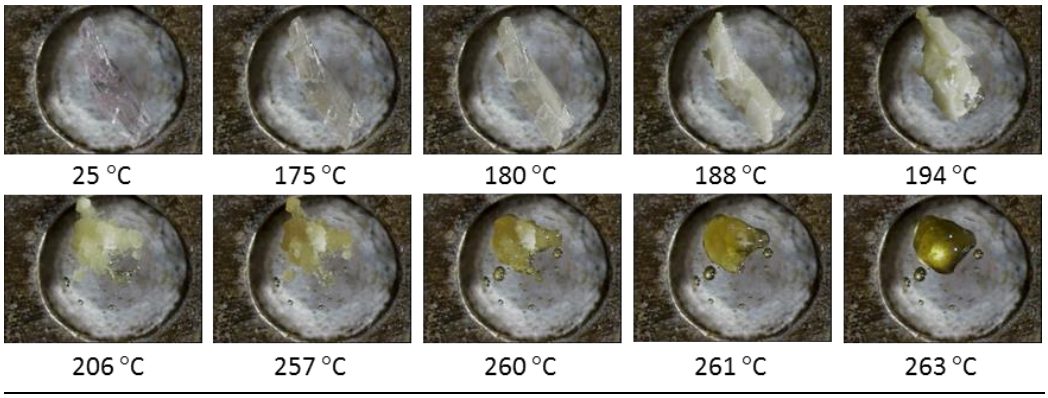

Fig. 4.2.108 Representative HSM photographs of MMVMAL at various temperatures.

In a DTA experiment (Fig. 4.2.109) the malonic acid starting material melted with an onset at 131.5 °C and a peak at 133 °C. A reported melting point value is 135(1) °C.[15] MMVMAL showed two separate events in the DTA result. The first had an onset at 165.4 ± 2.47 °C (n = 3) and a peak at 182.93 ± 0.12 °C (n = 3). The second onset was seen at 243.6 ± 0.65 °C (n = 3), with a peak at 249.87 ± 0.12 °C (n = 3). These temperatures are similar to the temperatures at which changes were visible in the HSM results.

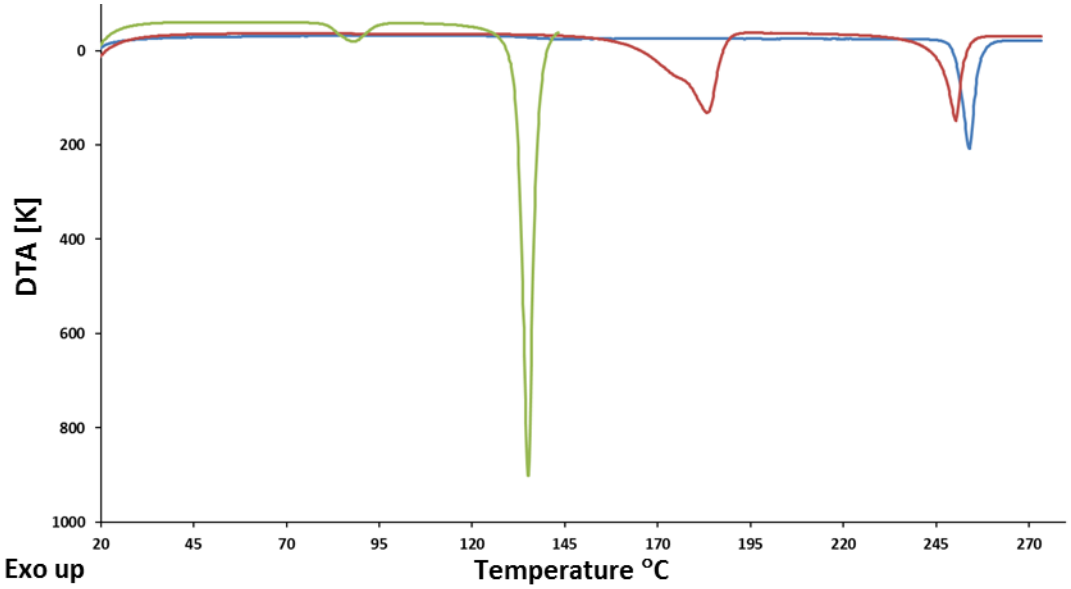

Fig. 4.2.109 Representative DTA thermogram traces of MMV (blue) and malonic acid (green) starting materials and for MMVMAL (red).

The mass loss of 20.3 ± 0.3 % (n = 3) observed from 100 – 200 °C through TGA (Fig. 4.2.110) equates to one molecule of malonic acid for every molecule of MMV (theoretical percentage 19.6). This matches the ratio seen in the SCXRD and NMR results. The onset temperature of the first stepped mass loss is 160.8 ± 0.2 °C (n = 3). The TGA result corresponds to the HSM and DTA results and the conclusion can be drawn that the first event is the loss of the coformer from the crystal structure. A possible phase change to the higher melting MMV polymorph takes place after the loss of the coformer as the next event is observed at a temperature close to the melting temperature of MMV Form 1.

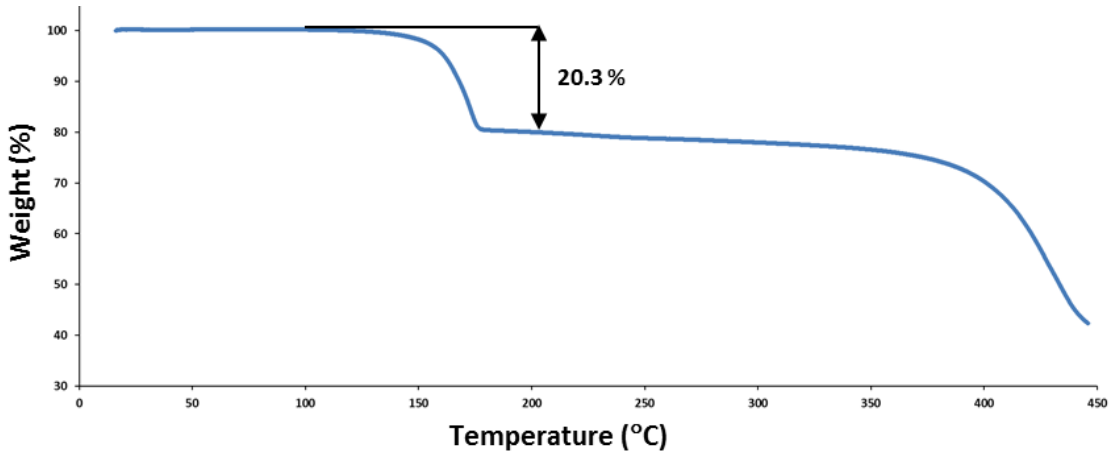

Fig. 4.2.110 Representative TGA trace of MMVMAL.

Solubility test

A sample mass of 31.09 mg of MMVMAL (equivalent to 25.00 mg of pure MMV) was added to FaSSIF and all further details were the same as the method described in previous sections. The measured concentrations of the samples taken (Fig 4.2.111) showed a rapid increase until a maximum concentration was reached after 10 min with a value of 18.9 ± 1.5 µg. cm^{-3} (n = 2), a factor of more than 5 times the S_0. After the 10 min mark the concentration started decreasing. The rate of decrease slowed after the 30 min mark and from the one hour mark onward the concentration fluctuated within a narrower range (8.8 to 11.7 µg. cm^{-3}) and the general trend indicates plateauing. This result also shows the "spring and parachute" effect[19]. The solution was centrifuged and the resulting solid product was analysed by PXRD and determined to most closely resemble the PXRD pattern of MMV monohydrate (Appendix A, Fig. A4.2.27).

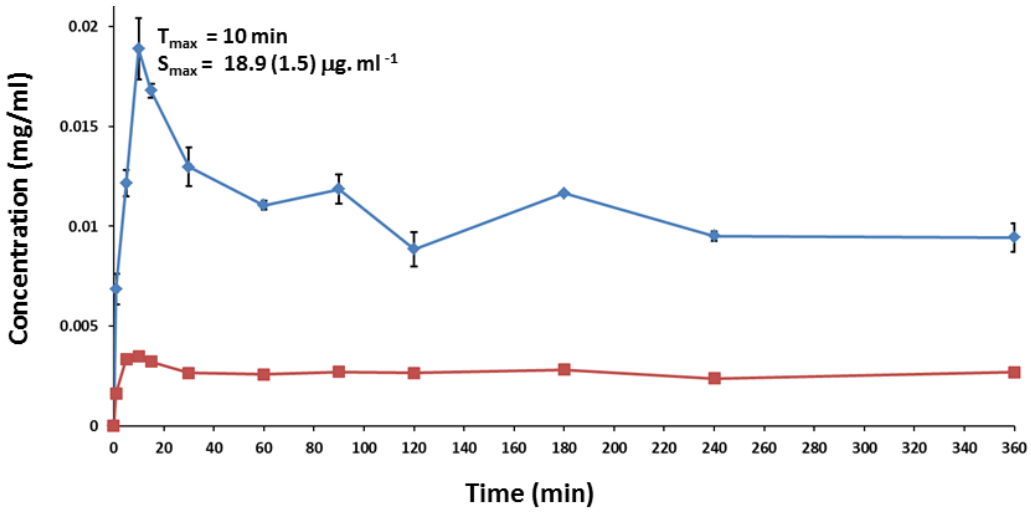

Fig. 4.2.111 Powder dissolution profile of MMV (red) compared to MMVMAL (blue) in FaSSIF at 37.5 ± 0.5 °C.

Conformations

The various conformers of MMV found in the multi-component crystal structures described in this chapter are presented in Fig. 4.2.112 and values for torsion angles between rotatable bonds are summarised in Table 4.2.19. At a glance the similarities of most of the conformers are self-evident. As was the case for the polymorphs of pure MMV, there are various intramolecular interactions playing a role in keeping the rings in most of these conformers coplanar. The obvious exception is the MMV conformer found in MMVSUCC3 and another, with smaller deviation, is MMVADIP. The MMV conformer in MMVADIP differs from the others in the torsion angle between the atoms N5-C6-C20-C21 by roughly 30 ° and the phenyl ring (C20-C21-C22-C23-C24-C25) and the attached methylsulfonyl group are in different orientations from those in the others. The difference in the case of MMVSUCC3 is even greater with the deviation of this same torsion angle (N5-C6-C20-C21) being more than 140°. This indicates adoption of a completely different conformation for the MMV molecule in the structure of MMVSUCC3.

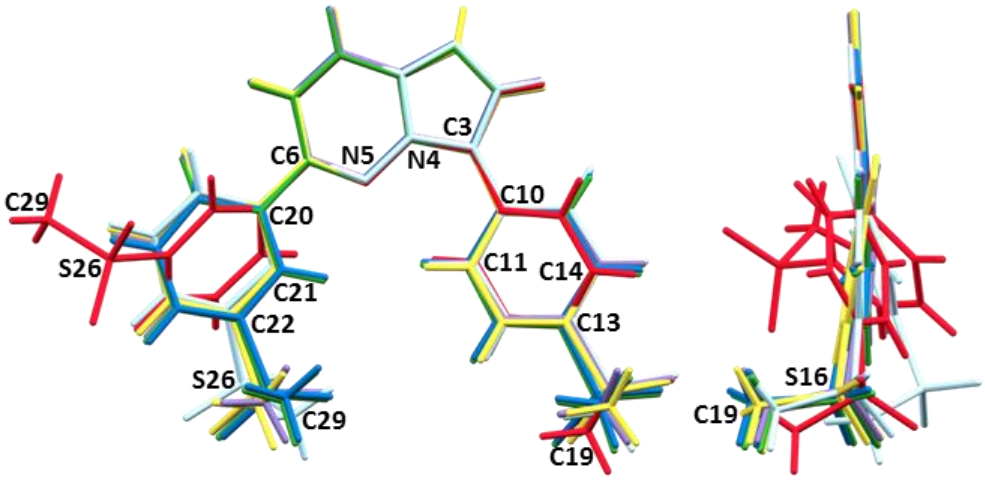

Fig. 4.2.112 Overlay of the different conformers of MMV occurring in the various co-crystal and salt forms viewed roughly normal (left) and parallel (right) to the imidazopyridazine ring [MMVADIP : light blue; MMVGLUT : purple; MMVSUCC1 : green; MMVSUCC3 : red; MMVFUM : blue; MMVMAL : yellow].

Table 4.2.19 Primary torsion angles for the conformers of MMV found in the various multi-component crystals.

Structure	Torsion angle N4-C3-C10-C11 (°)	Torsion angle N5-C6-C20-C21 (°)	Torsion angle C14-C13-S16-C19 (°)	Torsion angle C21-C22-S26-C29 (°)
MMVADIP	-1.5(3)	-18.4(3)	100.7(2)	63.9(2)
MMVGLUT	2.4(3)	10.4(3)	98.1(2)	88.7(2)
MMVSUCC1	2.0(3)	15.0(3)	86.3(2)	80.4(2)
MMVSUCC3	-27.8(3)	-132.1(2)	88.1(2)	96.4(2)
MMVFUM	-2.2(3)	14.4(2)	87.0(2)	81.7(2)
MMVMAL	-9.1(3)	12.0(2)	102.5(2)	90.0(2)

Hirshfeld plots

Two-dimensional fingerprint plots were generated from three-dimensional Hirshfeld surfaces of the MMV moiety in each of the multi-component crystal structures by making use of the program CrystalExplorer[29] and they are presented in Fig. 4.2.113. The plots represent the intermolecular interactions found in each of these systems and are used to facilitate their comparison. The quantified relative contributions are presented in Fig. 4.2.114. A common feature that appears in all the plots except the MMVMAL plot is the result of the shortest contact distance being N···H, where the nitrogen atom is a hydrogen acceptor bonded to a donor atom of the conformer and in each case ($d_i > d_e$). The reason why this feature is absent in MMVMAL is that proton exchange had occurred in that case and the nitrogen atom is protonated. In the case of MMVMAL the shortest contact is an O···H interaction where

the protonated nitrogen atom of the MMV molecule plays a role as the hydrogen donor ($d_i < d_e$). This difference can also be noted in the higher O···H and lower N···H values compared to the other systems described in the Fig. 4.2.114.

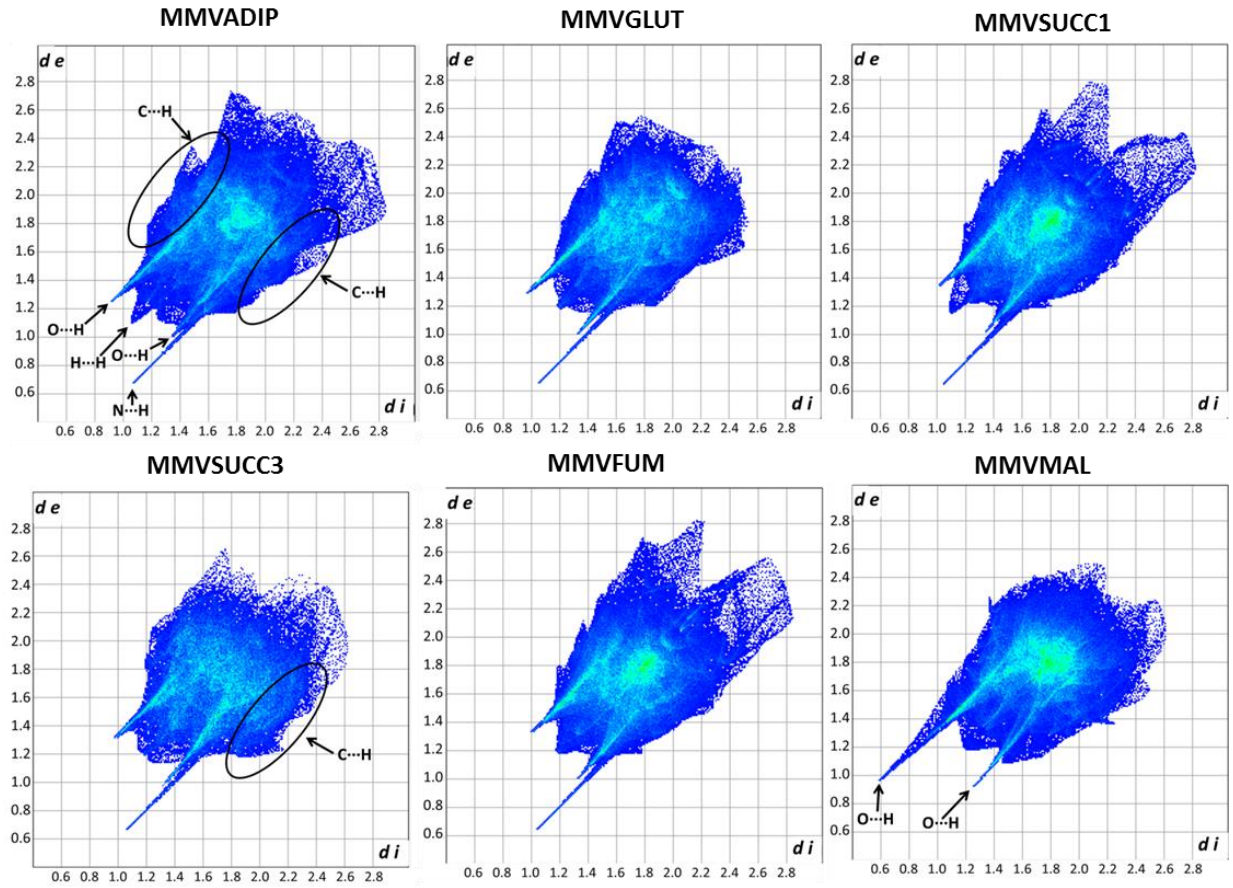

Fig. 4.2.113 Two-dimensional fingerprint plots for MMV moieties of the various multi-component crystal structures. Parameters d_e and d_i are the distances from a point on the surface to the nearest atom nucleus exterior and interior to the surface. Representative characteristic interactions are shown in the first image and other features of note are highlighted where appropriate.

Common features for all the plots are the symmetrical O···H interactions being among the shortest contact distances and arising from interactions with the sulfone oxygen atoms of the MMV molecules. A feature more prominent in some plots than others is that of the 'wings' caused by C···H interactions. The plots with narrower spreads in terms of the diagonal direction from the top left to the bottom right of the plot have less prominent C···H interactions. The MMVADIP has noticeable 'wings' and MMVSUCC3 has prominent 'wings' as a result of short X-H···π distances (an example is that of the relatively short

distance designated '···' in O30-H30B···(C10-C11-C12-C13-C14-C15) (visible at $d_i > d_e$ due the MMV molecule being the H-acceptor) in MMVSUCC3 (shown in Fig. A4.2.24 in Appendix A). Another notable feature is the higher intensity of colour at $d_i = d_e \approx 1.8$ Å in the cases of MMVSUCC1, MMVFUM, and MMVMAL than in the cases of MMVADIP, MMVSUCC3 and MMVGLUT. This is a result of π-π interactions present in the former structures showing up as C···C or N···C interactions (where nitrogen atoms form part of the interacting rings) at this distance. The difference in contributions of π-π and X-H···π interactions visualised by the 'wings' and higher or lower intensities at $d_i = d_e \approx 1.8$ Å can also be quantified for ease of comparison by considering the ratios of C···H/ C···C and C···H/ (C···C + C···N) (due to the presence of nitrogen atoms in some of the MMV rings).[30] These values are reported in Table 4.2.20. MMVSUCC3 has by far the highest C···H/ C···C and C···H/ (C···C + C···N) values and this is indicative of high X-H···π contribution present in its crystal structure as was also visible in the prominent 'wings' in Fig. 4.2.113. MMVFUM and MMVSUCC1 have lower comparative C···H/ C···C and C···H/ (C···C + C···N) values and higher intensities in Fig. 4.2.113 at $d_i = d_e \approx 1.8$ Å and this indicates higher contributions of π-π interactions. MMVMAL has a relatively low C···H/ (C···C + C···N) value and a relatively high intensity at $d_i = d_e \approx 1.8$ Å with a larger contribution from C···N. In general one can deduce that MMVSUCC1, MMVFUM, and MMVMAL have relatively higher π-π contributions, MMVADIP and MMVGLUT have contributions from both π-π and X-H···π, with MMVSUCC3 having much higher contributions from X-H···π.

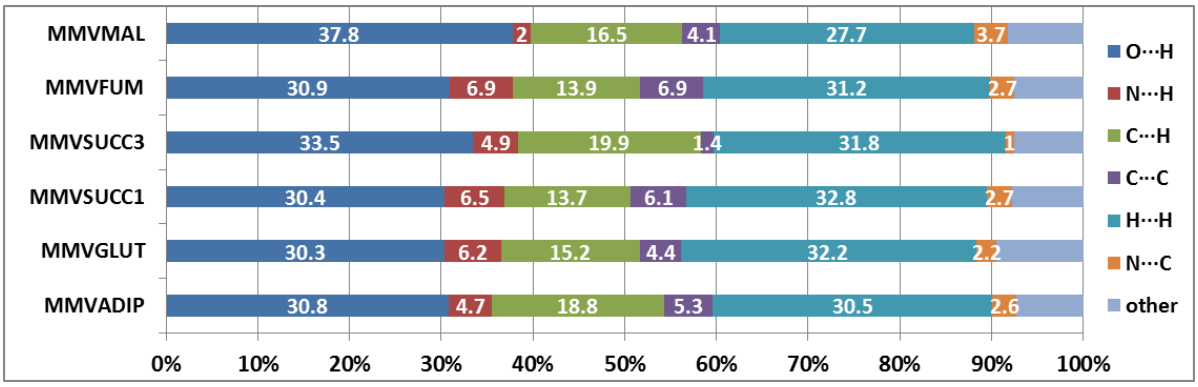

Fig. 4.2.114 Hirshfeld surface contributions for the close intermolecular contacts of MMV in the various multi-component crystal systems.

Table 4.2.20 Ratios of Hirshfeld surface contributions for the close intermolecular contacts of MMV to illustrate relative contributions of π-π and X-H···π interactions.

	C···H/ C···C	**C···H/ (C···C + C···N)**
MMVADIP	3.5	2.4
MMVGLUT	3.5	2.3
MMVSUCC1	2.2	1.6
MMVSUCC3	14.2	8.3
MMVFUM	2.0	1.4
MMVMAL	4.0	2.1

Hirshfeld plots of the asymmetric units

The two-dimensional fingerprint plots of the asymmetric units (in cases where only half of the coformer was part of the asymmetric unit, the fragment was completed for generation of the plots) of the various multi-component MMV crystal structures are presented in Fig. 4.2.115. The plots for MMVADIP, MMVSUCC1, MMVSUCC3, and MMVFUM are very similar in appearance whereas the plots for MMVGLUT and MMVMAL are slightly different. The N···H contacts are the shortest contacts in the cases of MMVADIP, MMVSUCC1, MMVSUCC3, and MMVFUM where the carboxylic acid oxygen of the coformer plays the role of the hydrogen donor in each of these cases ($d_i < d_e$). The O···H contacts are similar for these forms and are a result of intermolecular interactions with the oxygen atoms of the MMV sulfone moieties and of the coformer carbonyl oxygens. The relatively short H···H interactions that are common for all these plots are due to the inevitable close proximity of some hydrogen atoms in adjacent molecules. The short H···H distance in the case of MMVGLUT is a result of the hydrogen atoms taking part in the formation of a dicarboxylic acid homo-dimer between two glutaric acid molecules being in close proximity. This cyclic dimer is also the reason why the symmetrical O···H interactions are present in the plot of MMVGLUT. The 'wings' mentioned in the previous section due to C-H···π interactions are prominently present again in the case of MMVSUCC3. MMVMAL shows no N···H spikes due to the imidazole nitrogen being protonated and the N-H···X interactions do not contribute to the Hirshfeld surface as N···H interactions. The π-π interactions present in MMVSUCC1, MMVFUM, and MMVMAL show up in this case as well as more intense colours at $d_i = d_e \approx 1.8$ Å.

The relative Hirshfeld surface contributions for the close intermolecular contacts of the asymmetric units are presented in Fig. 4.2.116. MMVMAL displays higher O···H and lower N···H due to the imidazole nitrogen being protonated. MMVSUCC3 displays higher C···H and lower C···C and C···N contributions as a result of more C-H···π interactions. MMVFUM shows a slightly higher value for C···C contributions than the other systems, due to shorter distances between carbon atoms of the fumaric acid molecules and carbon atoms of adjacent MMV molecules than those observed in the other coformers. The carbons are sterically less available for π-π interactions as a result of being saturated in the case of MMVSUCC1 for instance.

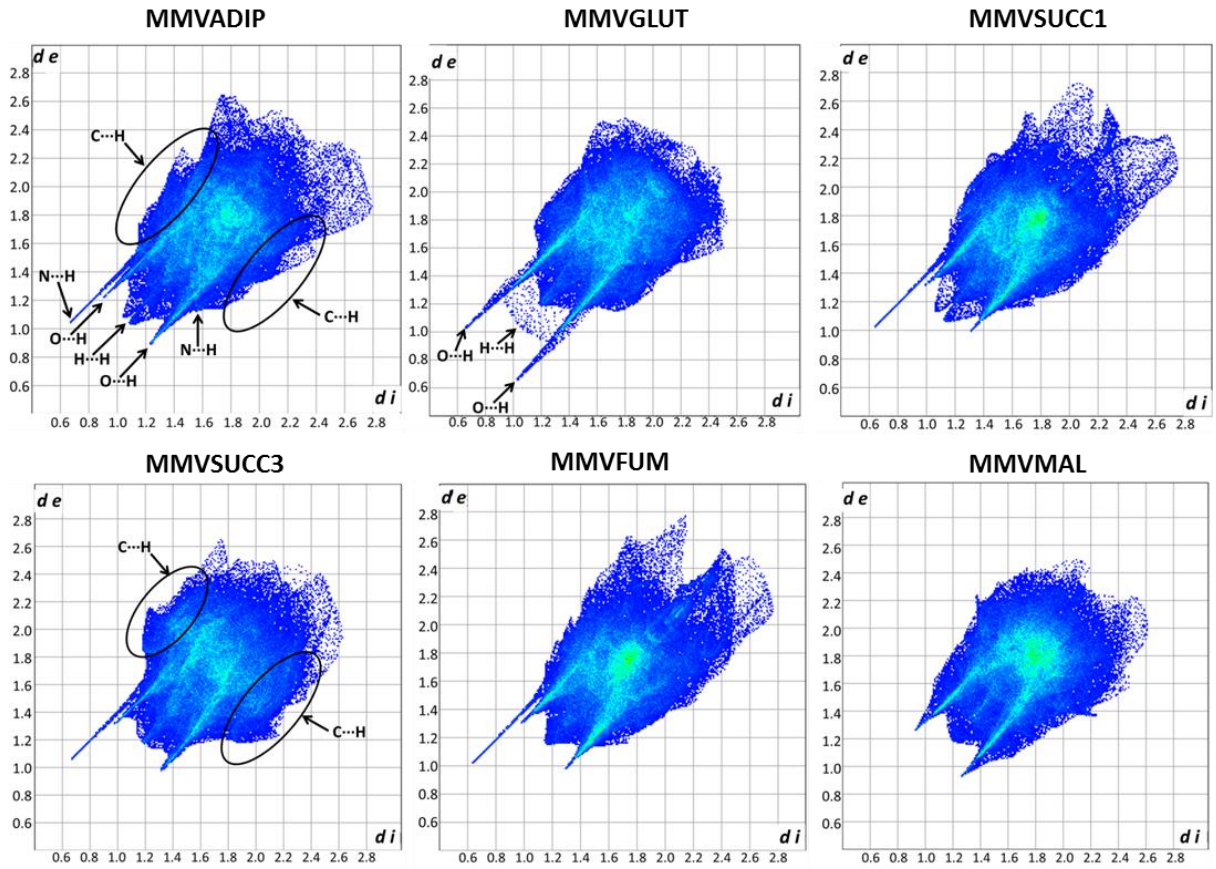

Fig. 4.2.115 Two-dimensional fingerprint plots for asymmetric units of the various multi-component crystal structures of MMV. (In cases where the asymmetric units consisted of incomplete fragments, the fragments were completed before generation of the fingerprint plots). Parameters d_e and d_i are the distances from a point on the surface to the nearest atom nucleus exterior and interior to the surface. Representative characteristic interactions are shown in the first image and other features of note are highlighted where appropriate.

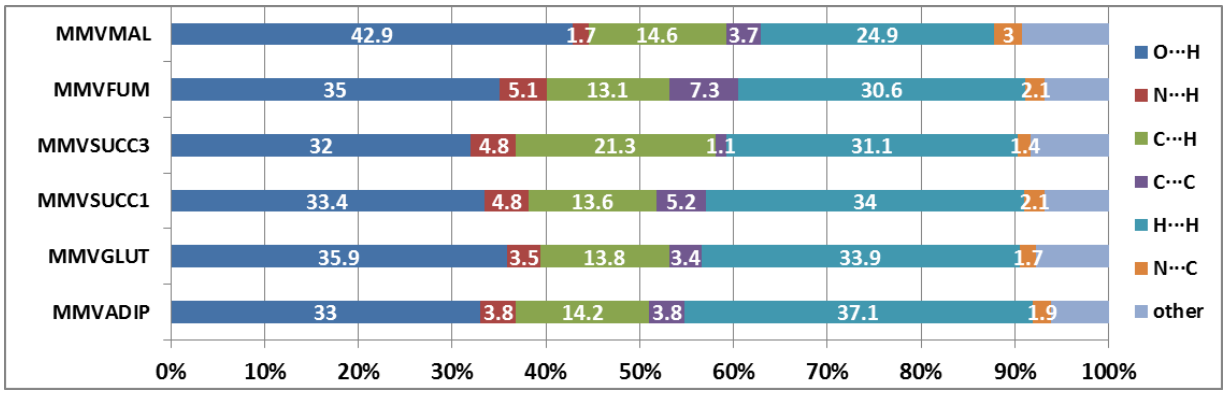

Fig. 4.2.116 Hirshfeld surface contributions for the close intermolecular contacts of the asymmetric units in the various multi-component crystal systems. In cases where the asymmetric units consisted of incomplete fragments, the fragments were completed before calculation of relative contributions.

Comparison of bonding motifs present in the various MMV multi-component crystal structures

The synthons most commonly used in the formation of co-crystals are shown in Fig. 4.2.117. The CSD[31] was searched by making use of the program Conquest[32] to obtain statistics of the frequency of occurrence of the various homo-and hetero-synthons and bonding motifs observed in the structures of the MMV multi-component crystal systems. If the parameters are too specific, hardly any search results appear and for this reason a broader, less definitive search was done at first, followed by a more specific search. The following filters were added: Organics only, with 3D coordinates determined, an R factor of less than 0.075; contact distances were set to less than or equal to the sum of van der Waals radii and no refcode restrictions were applied.

The broader search with less-refined parameters is similar to work reported by Weyna *et al.*[33] In the case of the present study the conditions were that both an endocyclic nitrogen and either a carboxyl or carboxylate moiety is required to be present in a structure to constitute a hit. A search with only these parameters resulted in 10 179 hits. It was then determined in how many of these cases an interaction was observed between the carboxyl moiety and the endocyclic nitrogen and in how many cases proton exchange had occurred where there was an interaction between the carboxylate moiety and the protonated endocyclic nitrogen (Fig. 4.2.117). In 2458 cases a neutral H-bond (labelled **a** in Fig. 4.2.117) was present and in 2493 cases an ionic bond was observed where proton exchange had taken place (labelled **b** in Fig. 4.2.117). These results show that these are common synthons and that neither shows a significant preference.

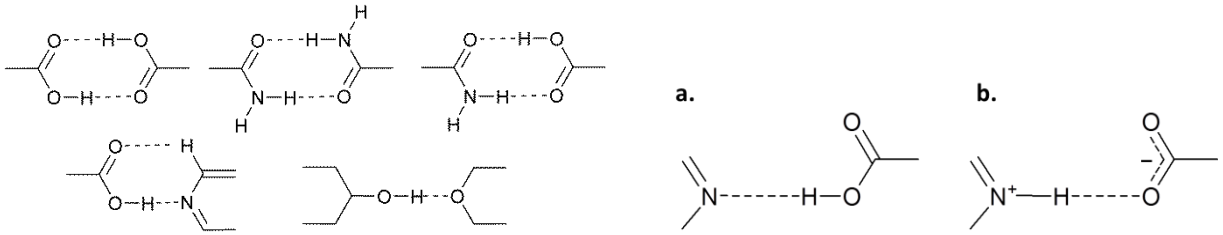

Fig. 4.2.117 Most common synthons found in co-crystals (left) and relevant supramolecular synthons in MMV multi-component systems (right).

Bonding motifs found in the MMV structures are shown in Fig. 4.2.118 and used to illustrate the motifs searched for in this study. In a search for structures containing both a 9-membered ring with a nitrogen in the position labelled N1 and hydrogens attached to C2 and C8 (following the labelling scheme used throughout this chapter) and either a carboxyl or carboxylate moiety, the result was 488 hits. Queries were combined to determine how many of these structures contained the motifs depicted in Fig. 4.2.118. The $R_2^2(8)$ motif labelled **a** in Fig. 4.2.118 (observed in MMVADIP and MMVSUCC3) was present in only 5 cases. The motif labelled **b** (where **a** and **d** were absent) (present in MMVGLUT) also occurred only 5 times. The cyclic $R_2^2(8)$ homodimer between carboxyl moieties labelled **c** (present in MMVGLUT) was present in 55 instances. The $R_2^2(7)$ dimer labelled **d** (present in MMVSUCC1 and MMVFUM) was only observed in 3 structures. The ionic $R_2^2(8)$ dimer labelled **e** (as is present in MMVMAL) was not present in any of the structures in this search; however, a more general search for a similar interaction of a carboxylate moiety with a positively charged protonated endocyclic nitrogen resulted in 2 hits. (The specifications of the search parameters are presented in more detail in the Appendix). As more structures are constantly being deposited in the database, more structures with similar bonding motifs will inevitably be added that will aid in prediction of potential interactions and facilitate the selection process of coformers with the highest probabilities of co-crystal formation. An inherent limitation of searches such as those employed here is that the statistics of occurrence frequencies of certain H-bonding motifs does not factor in the countless failed attempts by researchers to produce such multi-component systems, but merely reflects the percentages in successful efforts. Nevertheless these tools are useful and continuously growing in sophistication, quickly becoming indispensable for comprehensive crystal engineering.

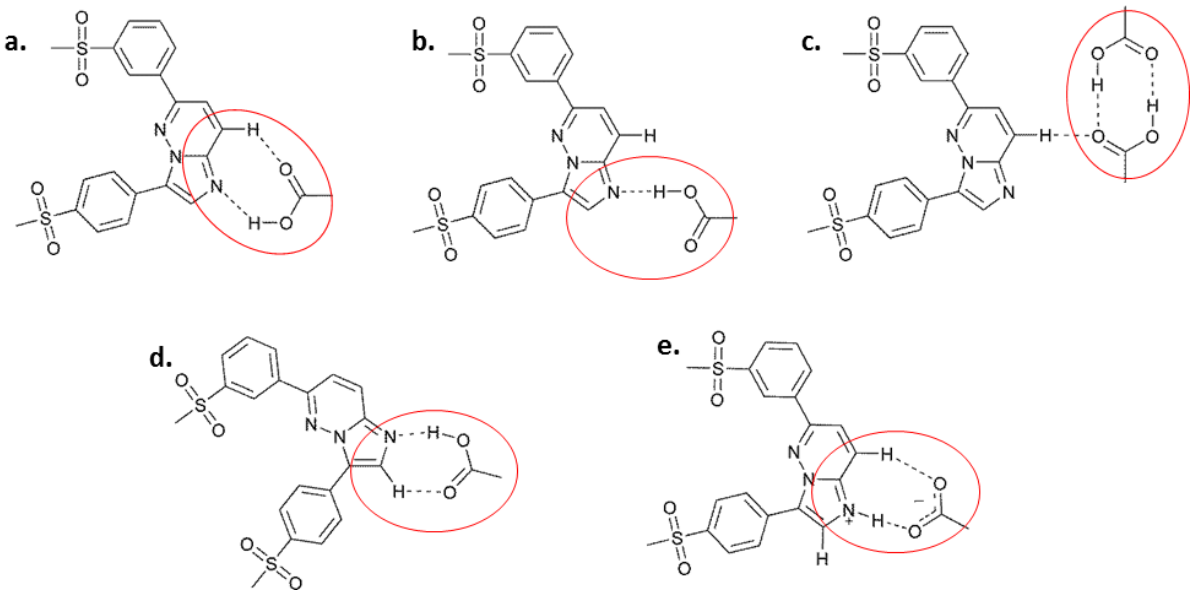

Fig. 4.2.118 Hydrogen bonding motifs found in the multi-component MMV crystal structures.

Comparison of physicochemical properties

Some of the physicochemical properties of the various multi-component forms of MMV as well as the corresponding coformers are presented in Table 4.2.21. The ΔpK_a between the drug candidate and the coformer usually gives a good indication of whether or not proton exchange will occur and result in the formation of a co-crystal or a salt, as was described in the introductory chapter of this thesis. It is suggested that if the difference pK_a(base)-pK_a(acid) is higher than 3, a salt will form; if the difference is less than 0, a co-crystal will form; anything in between will be either a salt or a co-crystal.[12,34] In this case, all the combinations involved ΔpK_a values below 0, this difference for MMV and malonic acid being the least negative. The measured pK_a of MMV might not be accurate and the ΔpK_a values are more approximate figures. However, despite these limitations, the so-called 'rule' held true for all the other combinations and only the combination MMV with malonic acid resulted in the formation of a salt.

The melting points of the various multi-component systems are reported in Table 4.2.21 and a comparison is made with those of the respective coformers and the common drug candidate in Fig. 4.2.119. The actual melting points were not used, but the onset of melting detected by DSC and in cases where the coformer underwent sublimation before a clear melt onset, this onset temperature was used. The observed trend of the multi-component systems melting at a temperature between the

melting points of the coformer and drug candidate as well as the correlation of higher melting points observed for coformers with higher melting points is a commonly observed occurrence.[16,35-38]

Table 4.2.21 Summary of physicochemical properties of multi-component MMV forms.

Co-crystal	pK_a	pK_a[a]	ΔpK_a	Experimental melting onset (°C)[b]			TGA mass loss %	Molar ratio
	MMV (free base)[39]	Coformer[15]		Coformer	Co-crystal	MMV		
MMVADIP	2.7	4.41	-1.71	150	215.5	245	15	2:1
MMVGLUT	2.7	4.32	-1.62	91.7	160.17	245	25	1:1
MMVSUCC1	2.7	4.21	-1.51	188.6	205.8	245	12.4	2:1
MMVSUCC3	2.7	4.21	-1.51	188.6	226.7	245	10.9	2:1
MMVFUM	2.7	3.02	-0.32	215.7	222.5	245	14.5	2:1
MMVMAL	2.7	2.85	-0.15	131.5	165.4	245	20	1:1

[a] pK_a at room temperature in water; [b] in cases where an onset of sublimation was observed before a melting onset this value was used.

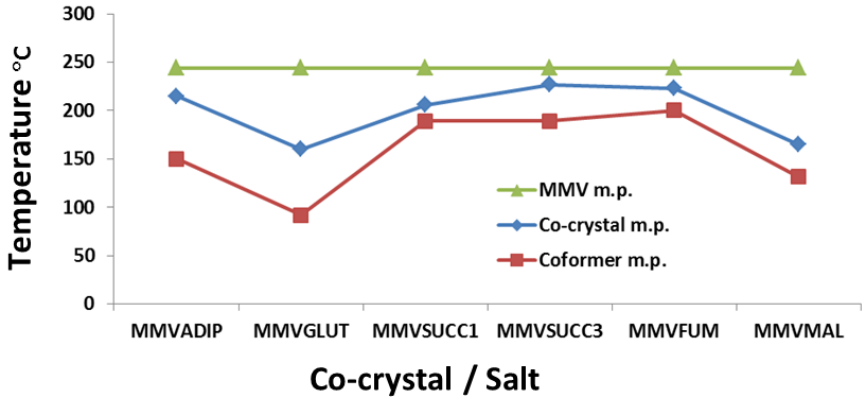

Fig. 4.2.119 Melting point comparison of MMV, the various multi-component MMV forms and the corresponding coformers.

Solubility comparison

The results obtained for the numerous solubility experiments with the various multi-component forms of MMV are overlayed in Fig. 4.2.120 for ease of comparison. (The results are listed in Table A4.2.3 in the appendix A). All the co-crystal forms as well as the salt form displayed greatly improved solubility profiles compared to pure MMV. A common feature for all the derivatised forms, except MMVADIP, was

the previously mentioned “spring and parachute” effect. The MMVADIP showed a “spring” effect with the highest concentration measured of all the forms tested at the 1 min mark, but the “parachute” effect was absent. Another aspect that was common for all the derivatised forms that were tested is that the maximum MMV concentrations were attained within the first 15 min of each experiment. The maximum concentrations measured for each form were not very significantly different if the standard deviations of the measurements are considered, though MMVMAL and MMVFUM had slightly higher values than the rest. In aqueous solutions it is expected that salt forms will show greater solubility improvements than co-crystals, though in this case the experiment was carried out in FaSSIF and this environment can significantly affect solubility. The potential increase in the bioavailability for these derivatised forms, as mentioned in previous sections, lies not only in the overall improved dissolution rate and higher solubility in a medium mimicking that found in the human body, but also in the consequent increase in the amount of MMV reaching the bloodstream due to the expected high permeability of membranes such as the intestinal epithelium, and the prevention of the eventual precipitation of MMV or MMV monohydrate due to increased concentrations. The compound has a reported partition coefficient (log D) value of 2.5,[39] theoretically placing it in Class 2 of the Biopharmaceutics Classification System (having poor solubility and high permeability).[40]

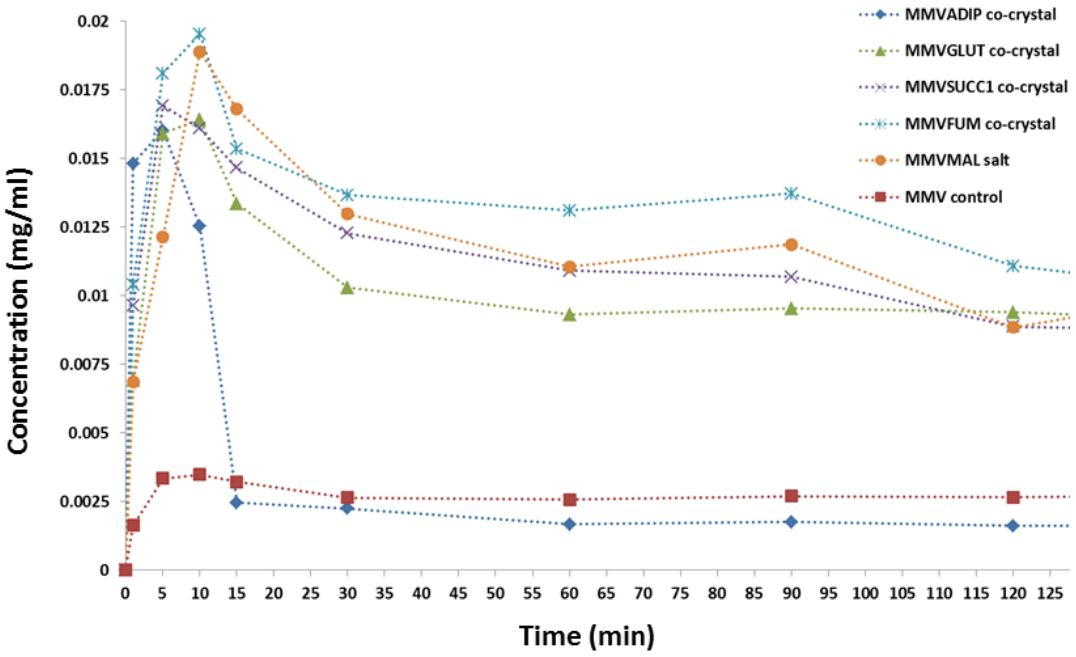

Fig. 4.2.120 Overlayed powder dissolution profile of MMV compared to those of various multi-component solid-state forms of MMV in FaSSIF at 37.5 ± 0.5 °C (Only the results of the first 120 min are shown here for clarity).

Conclusion

A multitude of novel solid-state forms of the antimalarial drug candidate MMV652103 ('MMV') were produced.

Four polymorphic forms of the drug candidate were created and characterised in terms of crystal structures and physicochemical properties, including solubility and stability rankings. MMV Form 1 crystallised in the space group $P2_12_12_1$ and MMV Form 2 in $P2_1/c$. Methods were developed to reproducibly scale up each form and quickly identify it by FTIR or PXRD. The amorphous MMV Form 4 displayed a great improvement (a factor of 3 to 4 times the concentration at 1 h of stirring) in the dissolution rate compared to the crystalline polymorphs. A monohydrated form of MMV was produced and characterised. This form might not be the preferred one to use in formulation of a drug product, though the knowledge of its existence, references for PXRD and FTIR comparison and understanding of measures required to prevent its formation during processing of other forms is essential.

A total of seven other multi-component solid-state forms of MMV were produced. At least five of these were co-crystals and one was a salt. All of these phases were produced with GRAS[1] dicarboxylic acids as coformers. This would suggest that the coformers should be safe for use in the formulation of drug products. The crystal structures of all but one of these seven multi-component crystals were solved and refined. All of these crystals belonged to the very common space group $P\bar{1}$. The main interaction in all the co-crystals was that of a hetero-synthon, O-H···N, though a variety of H-bonding motifs were observed. Three distinct phases were produced with the combination of MMV and succinic acid. Two of these were proven to be conformational co-crystal polymorphs and the third is believed to be a co-crystal with a different stoichiometric ratio of the same components. These polymorphs were ranked by stability and it was determined that MMVSUCC3 and MMVSUCC1 are monotropically related, with MMVSUCC3 being the more stable form. Methods were developed to reproducibly prepare the various multi-component forms and rapidly ascertain which form is present. Each form was characterised by HSM, DTA/DSC, TGA, FTIR spectroscopy, ^{1}H-NMR spectroscopy, PXRD, single-crystal XRD and in some cases variable-temperature PXRD. Solubility experiments were carried out in fasted state simulated intestinal fluid to determine the most likely solubility profiles in the human intestine. A comparison was made between the melting points and solubilities of the various forms. A positive correlation was observed in the melting points of the co-crystals being higher in cases where the relevant coformers had relatively higher melting points.

The main aim of the project concerning MMV was to produce new solid-state forms of this compound with improved physicochemical properties, the most important of which being improved solubility, to be used in the formulation of new drug products. This goal was accomplished.

Future work

Accelerated stability testing under elevated temperature and humidity will have to be carried out on the MMV polymorphs to determine if they have adequate stability to be kept under standard storage conditions before a particular form can be selected for formulation. The products generated will also have to be analysed to confirm that no transitions take place during the manufacturing processes involved. The stability of the glass form (MMV Form 4) will also have to be comprehensively characterised in terms of β- and γ-relaxations to determine if the products would remain stable for periods considered acceptable for the shelf life of a drug product. *In vivo* pharmacokinetic experiments need to be carried out in order to determine if the novel forms show improvement in the bioavailability and rate of uptake of MMV. The ultimate test would be that of the efficacy of the various derivatised forms in the treatment of Plasmodium falciparum *in vivo* in laboratory animals and eventually in clinical trials in humans. Efficacy testing is planned to be carried out in Plasmodium berghei mouse models and, depending on the outcome, in Plasmodium falciparum mouse models and eventually in humans.

Future work could involve further attempts to produce co-crystals by making use of the other coformers that resulted in new phases in the LAG experiments (presented in appendix A (Table A4.2.1 and Figs. A4.2.1-A4.2.7)). Growing single crystals for structural elucidation by X-ray diffraction of MMVSUCC2 could also be pursued.

References

1. U.S. Food and Drug Admistration, *FDA Generally Recognized as Safe (GRAS)*, http://www.fda.gov/Food/IngredientsPackagingLabeling/GRAS/ (accessed January 2018).
2. B. C. Smith, *Infrared spectral interpretation: a systematic approach*, CRC press, 1998.
3. S. Brandán, F. M. Lopez, M. Montejo, J. L. Gonzalez and A. B. Altabef, *Spectrochim. Acta A*, 2010, **75**, 1422-1434.
4. A. Mukherjee, S. Tothadi, S. Chakraborty, S. Ganguly and G. R. Desiraju, *CrystEngComm*, 2013, **15**, 4640-4654.
5. C. B. Aakeröy, T. K. Wijethunga and J. Desper, *New J. Chem.*, 2015, **39**, 822-828.
6. S. Kong, I. G. Shenderovich and M. V. Vener, *J. Phys. Chem. A*, 2010, **114**, 2393-2399.
7. C. B. Aakeröy, S. V. Panikkattu, B. DeHaven and J. Desper, *Cryst. Growth Des.*, 2012, **12**, 2579-2587.
8. H. G. Brittain, *Cryst. Growth Des.*, 2012, **12**, 1046-1054.
9. XPREP, *Data Preparation and Reciprocal Space Group Exploration*, Version 2008/2, © Bruker AXS Inc., Madison, Wisconsin, USA, **2008**.
10. Program SAINT, Version 7.60a, Bruker AXS Inc., Madison, Wisconsin, USA, **2008**.
11. G. M. Sheldrick, *Acta Cryst. A*, 2008, **64**, 112-122.
12. S. L. Childs, G. P. Stahly and A. Park, *Mol. Pharm.*, 2007, **4**, 323-338.
13. C. B. Aakeröy, I. Hussain and J. Desper, *Cryst. Growth Des.*, 2006, **6**, 474-480.
14. M. C. Etter, J. C. MacDonald and J. Bernstein, *Acta Cryst. B*, 1990, **46**, 256-262.
15. W. M. Haynes, Ed., *CRC Handbook of Chemistry and Physics*, CRC Press/Taylor and Francis, Boca Raton, FL, 96th edn., 2016.
16. M. K. Stanton and A. Bak, *Cryst. Growth Des.*, 2008, **8**, 3856-3862.
17. D. P. McNamara, S. L. Childs, J. Giordano, A. Iarriccio, J. Cassidy, M. S. Shet, R. Mannion, E. O'Donnell and A. Park, *Pharm. Res.*, 2006, **23**, 1888-1897.
18. S. L. Childs, L. J. Chyall, J. T. Dunlap, V. N. Smolenskaya, B. C. Stahly and G. P. Stahly, *J. Am. Chem. Soc.*, 2004, **126**, 13335-13342.
19. M. L. Cheney, N. Shan, E. R. Healey, M. Hanna, L. Wojtas, M. J. Zaworotko, V. Sava, S. Song and J. R. Sanchez-Ramos, *Cryst. Growth Des.*, 2009, **10**, 394-405.
20. D. P. Elder, R. Holm and H. L. de Diego, *Int. J. Pharm.*, 2013, **453**, 88-100.
21. M. K. Stanton, R. C. Kelly, A. Colletti, M. Langley, E. J. Munson, M. L. Peterson, J. Roberts and M. Wells, *J. Pharm. Sci.*, 2011, **100**, 2734-2743.
22. M. Perera, J. Desper, A. Sinha and C. Aakeröy, *CrystEngComm*, 2016, **18**, 8631-8636.
23. P. K. Mondal, V. Rao, S. Mittapalli and D. Chopra, *Cryst. Growth Des.*, 2017, **17**, 1938-1946.
24. The National Institute for Occupational Safety and Health (US), https://www.cdc.gov/niosh/ipcsneng/neng1173.html, (accessed January 2018).
25. T. Lee and P. Y. Wang, *Cryst. Growth Des.*, 2010, **10**, 1419-1434.
26. H. G. Brittain, *Cryst. Growth Des.*, 2010, **10**, 1990-2003.
27. B. Sarma, R. Thakuria, N. K. Nath and A. Nangia, *CrystEngComm*, 2011, **13**, 3232-3240.
28. I. Matulková, I. Císařová, P. Němec, J. Kroupa, P. Vaněk, N. a. Tesařová and I. Němec, *J. Mol. Struct.*, 2013, **1044**, 239-247.
29. CrystalExplorer, Version 3.1, S. K. Wolff, D. J. Grimwood, J. J. McKinnon, M. J. Turner, D. Jayatilaka and M. A. Spackman, University of Western Australia, Perth, Australia, **2012.**

30. L. Loots and L. J. Barbour, in *The Importance of Pi-Interactions in Crystal Engineering*, eds. E. R. T. Tiekink and J. Zukerman-Schpector, John Wiley & Sons, Chichester, UK, **2012**, pp. 109-124.
31. C. R. Groom, I. J. Bruno, M. P. Lightfoot and S. C. Ward, *Acta Cryst. B*, 2016, **72**, 171-179.
32. I. J. Bruno, J. C. Cole, P. R. Edgington, M. Kessler, C. F. Macrae, P. McCabe, J. Pearson and R. Taylor, *Acta Cryst. B*, 2002, **58**, 389-397.
33. D. R. Weyna, T. Shattock, P. Vishweshwar and M. J. Zaworotko, *Cryst. Growth Des.*, 2009, **9**, 1106-1123.
34. A. Lemmerer, S. Govindraju, M. Johnston, X. Motloung and K. L. Savig, *CrystEngComm*, 2015, **17**, 3591-3595.
35. M. R. Caira, S. A. Bourne, H. Samsodien, E. Engel, W. Liebenberg, N. Stieger and M. Aucamp, *CrystEngComm*, 2012, **14**, 2541-2551.
36. C. B. Aakeröy, S. Forbes and J. Desper, *J. Am. Chem. Soc.*, 2009, **131**, 17048-17049.
37. M. K. Stanton and A. Bak, *Cryst. Growth Des.*, 2008, **8**, 3856-3862.
38. C. B. Aakeröy, S. Forbes and J. Desper, *CrystEngComm*, 2014, **16**, 5870-5877.
39. C. Le Manach, D. Gonzàlez Cabrera, F. Douelle, A. T. Nchinda, Y. Younis, D. Taylor, L. Wiesner, K. L. White, E. Ryan, C. March, S. Duffy, V. M. Avery, D. Waterson, M. J. Witty, S. Wittlin, S. A. Charman, L. J. Street and K. Chibale, *J. Med. Chem.*, 2014, **57**, 2789-2798.
40. U.S. Food and Drug Admistration, *FDA Biopharmaceutics Classification System (BCS)*, https://www.fda.gov/aboutfda/centersoffices/officeofmedicalproductsandtobacco/cder/ucm128219.htm (accessed March 2018).

Chapter 5:

Inclusion of the antioxidant (±)-α-lipoamide in cyclodextrins

Characterisation of inclusion complexes with the bioactive compound (±) α-lipoamide (α-LA) (Scheme 5.1) and various cyclodextrins [α-cyclodextrin (α-CD), β-cyclodextrin (β-CD), γ-cyclodextrin (γ-CD), hexakis(2,3,6-tri-*O*-methyl)-α-cyclodextrin (TRIMEA), heptakis(2,6-di-*O*-methyl)-β-cyclodextrin (DIMEB) and heptakis(2,3,6-tri-*O*-methyl)-β-cyclodextrin (TRIMEB)] is presented in this chapter. Phase-solubility experiments were carried out to determine the association constants of some of these complexes as well as the effect of cyclodextrin addition on the aqueous solubility of α-LA. The native CDs, α-CD, β-CD and γ-CD as well as the derivatised CDs hydroxypropyl-β-CD (HP-β-CD), sulfobutylether β-CD (SE-β-CD) and randomly methylated β-CD (RAMEB) were used for these studies.

The guest: (±)-α-lipoamide

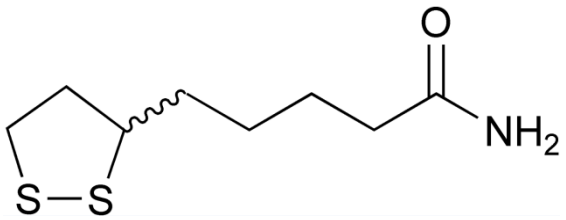

Scheme 5.1 Structure of (±)-α-lipoamide.

α-Cyclodextrin inclusion complex with (±)-α-lipoamide (ACDALA)

Preparation of complex

A screening experiment was carried out by kneading equimolar amounts (10 mg of α-LA ≈ 0.049 mmol) of the host and guest. The PXRD trace of the product was then compared to traces of each individual component as well as traces generated from crystal structures in the CSD[1] of various hydrates of the host and isostructural series of other inclusion complexes with the host.[2] Though the trace did not match any of the mentioned traces, it did match a generated trace of a complex between (R)-α-lipoic acid and α-CD.[3] The isostructurality implies that the packing arrangement of the host-guest inclusion complex is very similar to that of the (R)-α-lipoic acid complex with α-CD and serves as proof of inclusion of the guest in the host molecule (Fig. 5.1). A PXRD trace for a complex of (R)-α-lipoic acid with α-CD was also reported by Ikuta *et al*. with characteristic peaks observed at the °2θ positions 5.5, 11.0, and 19.0.[4] The highest intensity peaks observed for the putative kneading product ACDALA has peaks at 4.8, 9.5, and 19.8 °2θ. These peaks show very good correlation with

those reported for the complex of (R)-α-lipoic acid with α-CD when considering that minor shifts are possibly due to the X-ray analyses being carried out at different temperatures.

PXRD

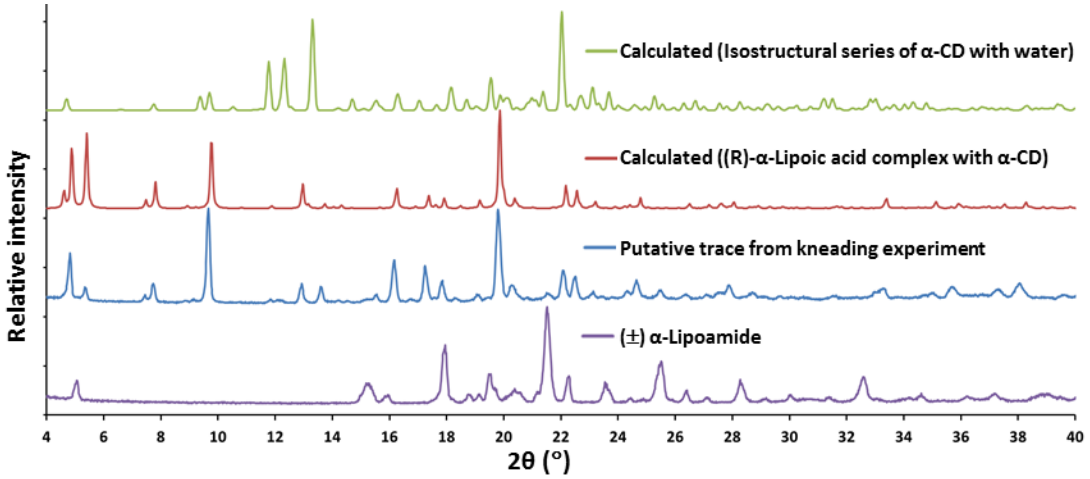

Fig. 5.1 Calculated PXRD traces of an inclusion complex of (R)-α-lipoic acid with α-CD,[3] uncomplexed α-LA and α-CD (complexed with water only), and the experimental trace of the putative complex obtained by kneading α-CD with α-LA.

Preparation of single crystals

The procedure used to prepare crystals was as follows: α-CD (26.4 mg, ≈ 0.025 mmol) was dissolved in 3 cm^{-3} of water by stirring the solution at an elevated temperature of 70 °C for one minute. The guest, α-LA, was then added incrementally over a period of about 10 minutes until a total of 5.0 mg (≈ 0.025 mmol) had been added. The solution was left to stir for an hour and then filtered while hot through a 0.45 µm nylon filter into a clean vial. This vial was capped and placed in an oven at 60 °C to avoid precipitation of the supersaturated solution. After a period of several months small hexagonally-shaped crystals had formed in the vial. Other variants of this method were attempted at different temperatures, concentrations and rates of solvent loss, with no other cases resulting in the formation of clear single crystals. Due to the limited mass of crystals produced as well as the time required for the crystals to be produced, full characterisation was not carried out. A single-crystal X-ray data collection was, however, carried out with one of these crystals and the results are reported in the following section.

Crystal structure analysis

Data-collection and space group determination

The X-ray intensity data for the complex ACDALA were collected on a Bruker Kappa Apex II Duo diffractometer at 173(2) K. The crystal was found to belong to the trigonal system with Z = 6. Due to

the chirality of the host, only chiral space groups were considered. This left the possibility of the space groups *R*3 and *R*32 as the other space groups with the same conditions limiting possible reflections (*R* $\bar{3}$, *R* $\bar{3}m$, and *R*3*m*) are non-chiral. The diffraction showed $\bar{3}$m Laue symmetry indicating that the correct choice of space group is *R*32.

The crystal was twinned and the program Cell_now[5] was used to index the twin data set and yielded a BASF factor of 0.30 for the minor component after the initial refinement. The program SAINT[6] was used for unit cell refinement and data reduction. Absorption correction and scaling of data was performed with the program TWINABS.[7]

Structure solution and refinement

Crystallographic data and parameters for collection of intensity data are reported in Table 5.1. No complexes with sufficiently similar structures for isomorphous replacement were found in a search of the CSD.[1] The host molecule of the complex of (R)-α-lipoic acid with α-CD[3] referred to earlier did, however, have a very similar structure and this was used for isomorphous replacement.[8] The co-ordinates of the non-hydrogen atoms making up the host glucose rings that form the skeletal framework of the host were used as a trial model. Due to the symmetry of this structure, three separate glucose 'dimers' were observed around the crystallographic threefold axis that, when expanded to show the threefold symmetry, result in three independent α-CD molecules (Fig. 5.2). The glucopyranose subunits making up the asymmetric unit were labelled G1 to G6 as shown in Fig. 5.2. The oxygens of the hydroxyl groups attached to the host were added after subsequent refinement steps when observed in the difference electron density maps. The host was resolved with minor disorder of hydroxyl groups at the primary rims of G1 and G5. Each of these had hydroxyl groups disordered over two positions and the respective major and minor components were assigned s.o.f.s. of *x* and *1-x* in both instances. The comprising disordered atoms were isotropically refined and the final *x* values after refinement were 0.75(1) for the disordered components at G1 and 0.55(1) for G5. The HKLF 5 file generated by the program TWINABS[7] was used in subsequent refinement cycles. After all the non-hydrogen host atoms were found in the difference Fourier map and placed, hydrogen atoms were placed in idealised positions in a riding model and refined with U_{iso} values of 1.2 to 1.5 times those of the parent atoms assigned. Most of these hydrogen atoms were placed in logical positions where hydrogen bonds were deemed likely. The reported redundancy (R_{int} value of 0) was a result of the strategy used where only one hemisphere was collected due to the twinning of the crystals.

A number of factors contributed to difficulties in the successful modelling of the α-lipoamide guest molecule. These included the fact that it was present as a racemic mixture, the data to parameter

ratio of ~7 was low and the crystal used for data-collection was twinned. The highest intensity peaks of the guest were, however, placed and refined and the result resembles the arrangement observed in the structure of the complex of (R)-α-lipoic acid with α-CD.[3] The correlation between the two structures led to the conclusion that these packing arrangements are analogous. An important point to note is that in the case of the complex of (R)-α-lipoic acid with α-CD[3], the guest had undergone partial decomposition to dihydro-(R)-α-lipoic acid. The possibility exists that analogous guest decomposition could have occurred during the course of co-precipitation of ACDALA, while the sample was kept at an elevated temperature for an extended period of time.

High intensity electron density peaks that appeared not to be part of the host or the guest were assigned as water oxygens and most of these were found to be in positions where hydrogen bonding to the host was present.

Table 5.1 Data-collection and refinement parameters for ACDALA.

Molecular formula	$3(C_{36}H_{60}O_{30})\cdot 2(C_8H_{15}NOS_2)\cdot 30(H_2O)$*
Formula weight (g mol^{-1})	3815.47
Crystal system	Trigonal
Space group	*R*32
a = b (Å)	23.576(2)
c (Å)	54.128(4)
α = β (°)	90
γ (°)	120
V (Å)^3	26055(5)
Z	6
D_c (g cm^{-3})	1.459
μ (Mo Kα) (mm^{-1})	0.176
F(000)	12 180
Data-collection temp. (K)	173(2)
Crystal size (mm^3)	0.34 x 0.20 x 0.07
Range scanned θ (°)	1.25 – 25.08
Index ranges ±*h*, ±*k*, ±*l*	-24, 0; 0, 28; 0, 64
Reflections (total)	5567
Independent reflections	5567
Reflections with I>2σ(I)	4597
Number of parameters	681
R_{int}	0
S	1.219
R_1 [*I*>2σ(*I*)]	0.1174
Reflections omitted	4
wR_2	0.2853
a, b in w = 1/[$\sigma^2(F_o^2)$+(aP)^2+(bP)]	a = 0.2000; b = 0
$(\Delta/\sigma)_{mean}$	0.121
$\Delta\rho_{min,max}$ (e Å^{-3})	-0.82, 1.31

*The stated molecular formula is nominal and the actual formula is unknown as the composition was not verified by complementary methods due to the paucity of the single crystal sample.

Due to the disorder and low accuracy of the crystal structure, the appended crystallographic data files (Appendix B) are limited to what is deemed necessary.

Molecular structure

The molecular structure of the host is displayed with the main peaks of the highly disordered guest represented in Fig. 5.2 as a space-filling model visible in the channel formed by consecutive CD molecules.

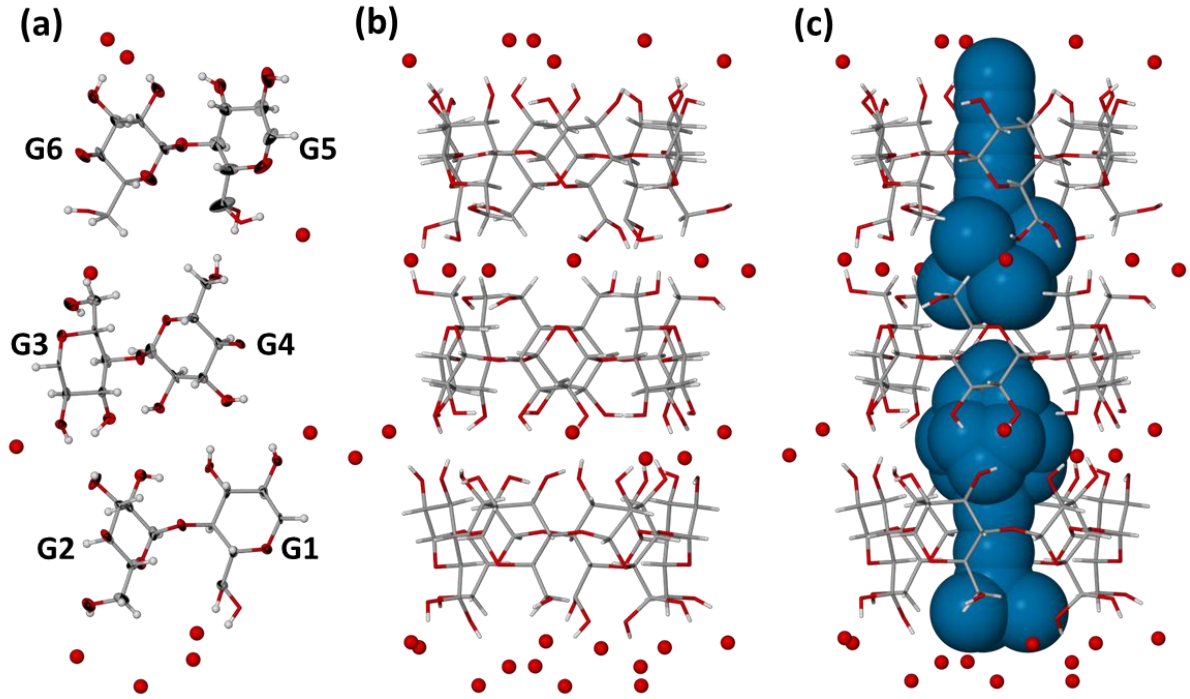

Fig. 5.2 (a) The asymmetric unit of ACDALA and numbering scheme of the host glucopyranose subunits with thermal ellipsoids shown at the 50% probability level for anisotropic atoms (water hydrogen atoms and guest molecules are omitted and the minor and major disorder components of the hydroxyl moieties at G1 and G5 are represented as stick models); (b) the symmetry-generated atoms that make up the rest of each of the host molecules; (c) the highest intensity peaks representing the disordered guest molecules are shown in blue as space-filling models.

Application of the twofold rotation axis normal to the c-axis in the z-direction results in three more CD molecules that line up with the channel observed in Fig. 5.2 to form a continuous channel along the c-axis. There exists a gap between the three host molecules of the asymmetric unit and that of the symmetry-generated host molecules that is filled with interstitial water molecules. These water molecules form hydrogen bonds that connect the sequential host assemblies to form an infinite column (Fig. 5.3).

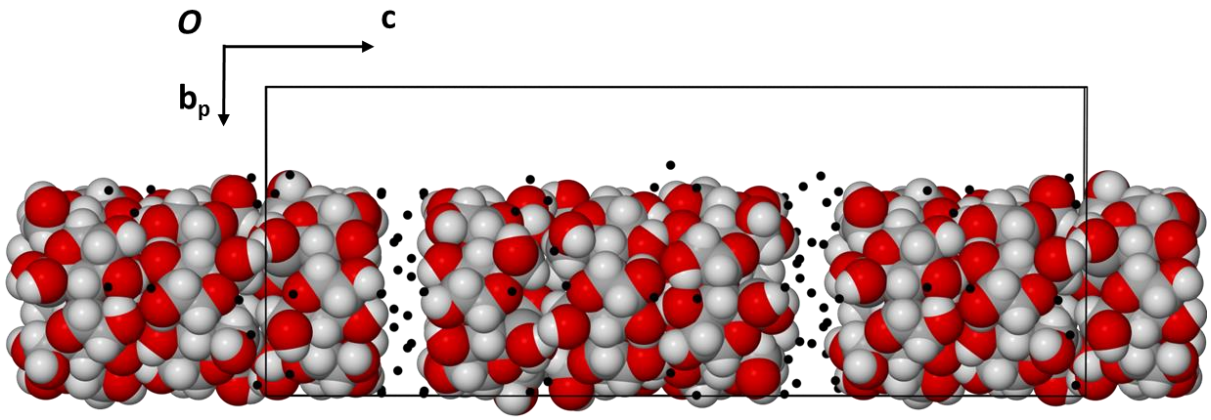

Fig. 5.3 Continuous columns formed by sequential host molecules along the c-axis (viewed along [100]). The host is shown as space-filling model with water oxygens represented as black dots.

Geometrical analysis of ACDALA

Conformation of the host

As described previously, three crystallographically independent α-CD molecules each consisting of two glucose units, repeated by symmetry are found in ACDALA. The geometrical parameters described by Harata[9] and Saenger[10] that were described in the introductory chapter of this thesis are presented for ACDALA in Tables 5.2 and 5.3. Due to the repetition of the glucose units through symmetry, only the two unique glucose units of each independent α-CD molecule are characterised and these molecules are labelled A, B and C. They are displayed in Fig. 5.4 and are also overlayed with the isostructural complex of (R)-α-lipoic acid with α-CD[3] for ease of visual comparison.

The O5-C5-C6-O6 dihedral angles (ω) of the major components all have negative values indicating that the hydroxyl groups on the primary rim of the CDs are pointed away from the cavity and the hydroxyl groups on the secondary rims are also directed away from the cavity leaving the continuous channel open on both sides of each macrocycle. The values of the parameters *l* (distance from O4 to generated centroid of the O4-hexagon), *D* (O4···O4′ distance) and ϕ (O4···O4′···O4′′ angle) are very similar for the three independent α-CD molecules and this shows that the inclusion of the guest did not have a significant effect on the conformation of the host molecules and they maintain a typical symmetrical truncated-cone shape.

The positive values for the parameter τ_2 (angle between the mean plane through all the O4 atoms of the host and the plane through the atoms O4, C4, C1 and O4′ of each respective glucopyranose residue) indicate that the glucopyranose units are inclined, with the primary hydroxyl side tilting inward towards the cavity. The values range from 2.01(2) to 11.2(2)° and are considered typical for α-CD.

Table 5.2 Torsion angles O5-C5-C6-O6 (ω) of the host α-CD molecules in ACDALA.

Molecule	Glucopyranose residue	Torsion angle ω (°)	(+) or (-) – gauche conformation	Torsion angle ω (°) of the minor disorder component	(+) or (-) – gauche conformation
A	G1	-63(2)*	(-)	70(2)	(+)
	G2	-74(1)	(-)		
B	G3	-63(1)	(-)		
	G4	-61(2)	(-)		
C	G5	-58(2)*	(-)	31(2)	(+)
	G6	-68(2)	(-)		

*Major disorder component

Table 5.3 Geometric parameters describing the α-CD host molecules in ACDALA.

Molecule	Residue	*l* (Å)	*D* (Å)	ϕ (°)	*d* (°)	τ_2 (°)
A	G1	4.211	4.252	119.3	0.5	11.2(2)
	G2	4.241	4.201	120.7	-0.5	8.1(2)
B	G3	4.210	4.175	120.2	-0.5	2.01(2)
	G4	4.204	4.239	119.9	0.5	8.0(2)
C	G5	4.234	4.215	120.3	-5.4	10.7(3)
	G6	4.220	4.241	119.6	5.4	2.8(1)

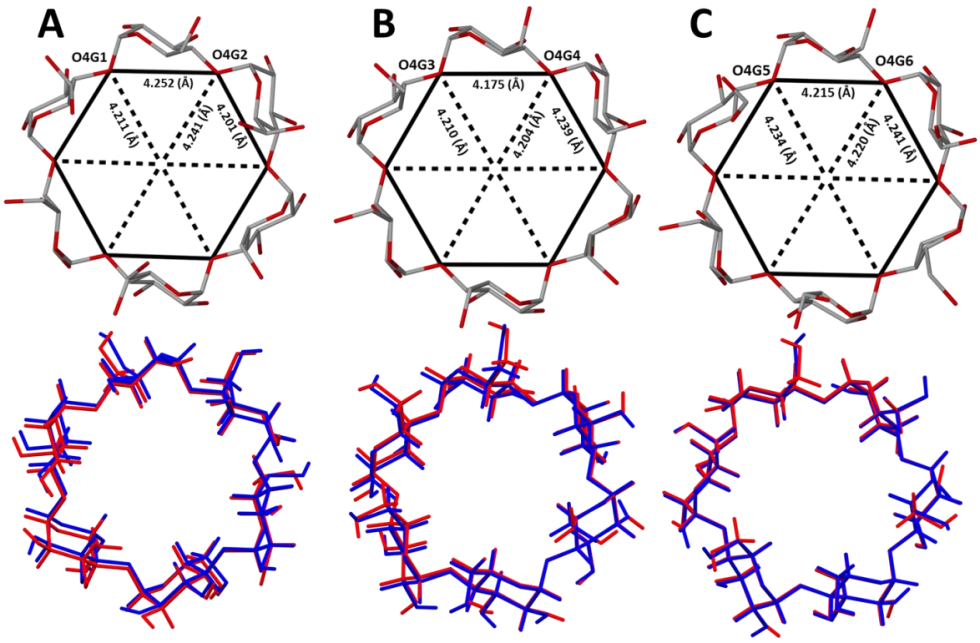

Fig. 5.4 The independent host molecules are displayed as sticks viewed from the primary rim side with hydrogen omitted for clarity. Solid lines connect the respective O4 atoms of the various glucopyranose residues to show the symmetrical O4-hexagon and dotted lines connect the O4 atoms with a generated centroid. The values for the parameters *l* and *D* are presented in this figure (top). Overlayed ACDALA (blue) with an isostructural complex of (R)-α-lipoic acid with α-CD[3] (red) (bottom).

Crystal packing and hydrogen bonding

ACDALA has a channel-type packing of the host with infinite columns running along the c-axis (Fig. 5.5). These columns form layers that run in a direction along the plane [110]. The CD molecules are arranged in a head-to-head and tail-to-tail manner (Fig. 5.6). Various hydrogen bonding interactions connect the host α-CD molecules with adjacent CD molecules as well as with water molecules. Many of these water molecules are found in the gaps between sets of three connected α-CD molecules and play roles as linkers connecting these sets to the consecutive sets in both directions along the c-axis. There are also water molecules to be found in the interstitial spaces between the columns and these are connected to hydroxyl groups of the host molecules. Due to the disorder of the guest molecules the interactions involving these will not be discussed in any detail.

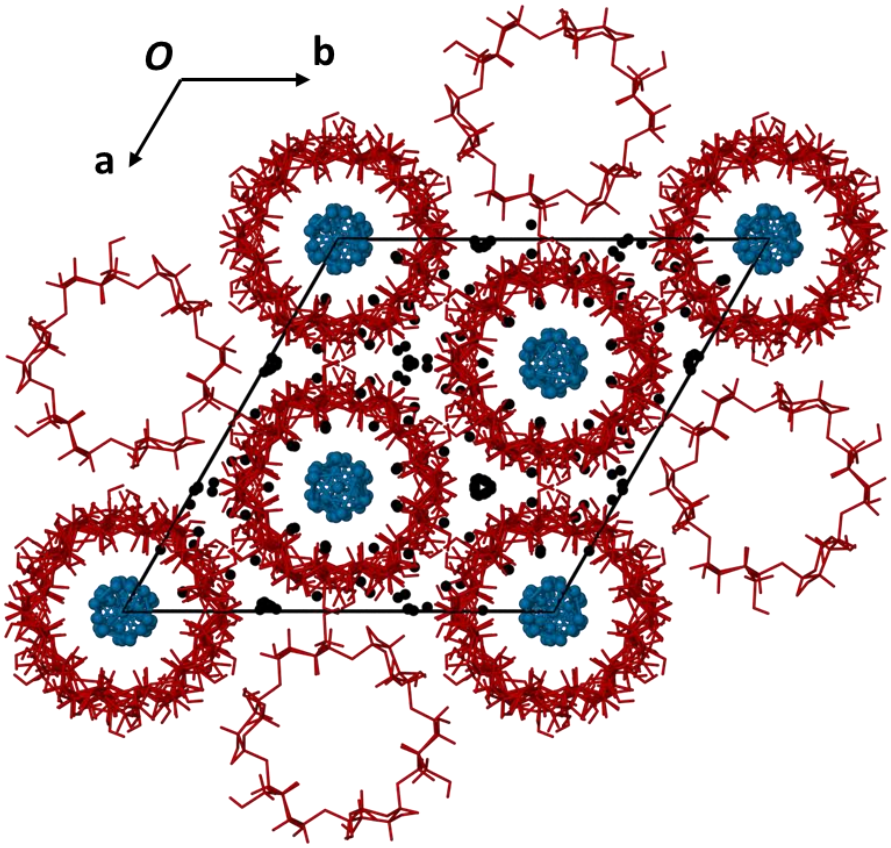

Fig. 5.5 Packing of ACDALA viewed along [001] showing infinite channels with the host in red, main peaks of the disordered guest in blue, and water oxygens in black.

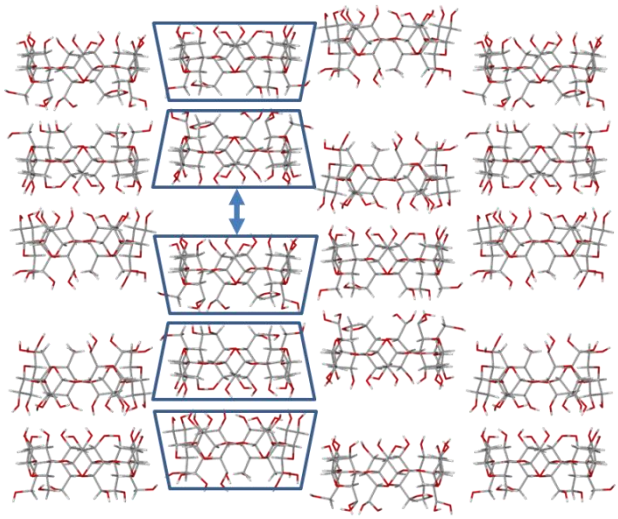

Fig. 5.6 Topology of a layer formed by aligned columns viewed along [110] highlighting tail-to-tail and head-to-head packing of the host molecules and showing the water-filled space between sets of CD molecules.

A PXRD trace collected for the product of a kneading experiment with α-CD and α-LA is compared to one calculated from the solved single crystal X-ray structure of ACDALA in Fig. 5.7. Preferred orientation effects aside, the correspondence is unmistakable, with the positions of the highest intensity peaks closely matching, showing that the product obtained by kneading matches the product produced by co-precipitation.

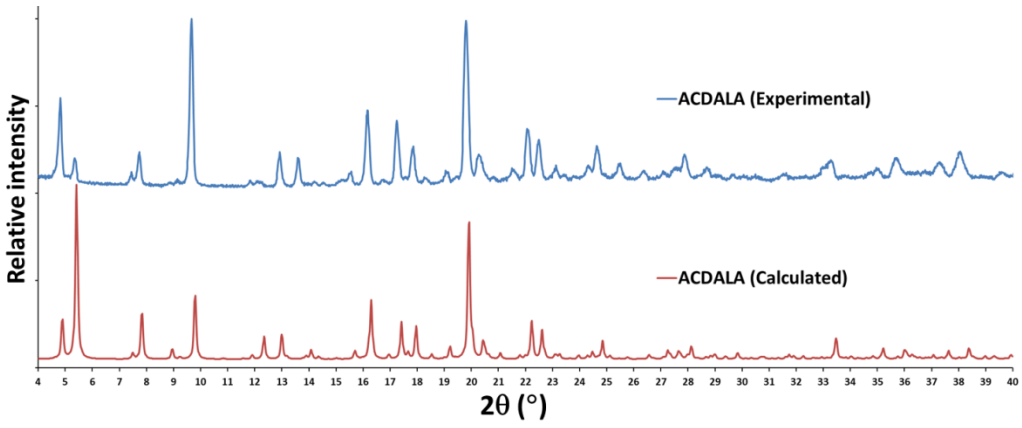

Fig. 5.7 PXRD traces collected for the product of a kneading experiment (α-CD and α-LA) and a trace computationally generated from the single crystal X-ray structure of ACDALA.

The unit cell data of an isostructural complex of ACDALA and those of ACDALA are summarised in Table 5.4. No other isostructural complexes were found in a search of the CSD.[1]

Table 5.4 Comparison of structural parameters of ACDALA with a known structure.

Space group	H:G:W*	a=b (Å)	c (Å)	α=β (°)	γ (°)	Guest	CSD Refcode	Ref.
*R*32	3:2:30	23.576(2)	54.128(4)	90	120	α-LA	ACDALA‡	NA
*R*32	3:2:27	23.633(2)	54.276(7)	90	120	(R)-α-lipoic acid	Ref 3‡	3

***Ratio of host : guest : water; ‡The crystallographic data have not been submitted to the Cambridge Crystallographic Data Centre yet and the compound codes are those used throughout this thesis.**

β-Cyclodextrin inclusion complex with (±)-α-lipoamide (BCDALA)

A literature search resulted in some reported complexes of (±)-α-lipoamide with β-CD, though no mention is made of single crystal X-ray structures.[11,12]

Preparation of complex

Kneading of equimolar quantities (10 mg of α-LA ≈ 0.049 mmol) of the host and guest was done in a mortar with a pestle for 20 min. During this period, small drops of distilled water were added to maintain a paste-like consistency. The product was then analysed by PXRD to compare the trace with the patterns of the starting materials, existing isostructural series of inclusion complexes and traces of the host with only water as guest generated from known crystal structures. The resulting trace bears some resemblance to that of one of the isostructural series complexes termed B7 by S. Lubhelwana[2] (Fig.5.8).

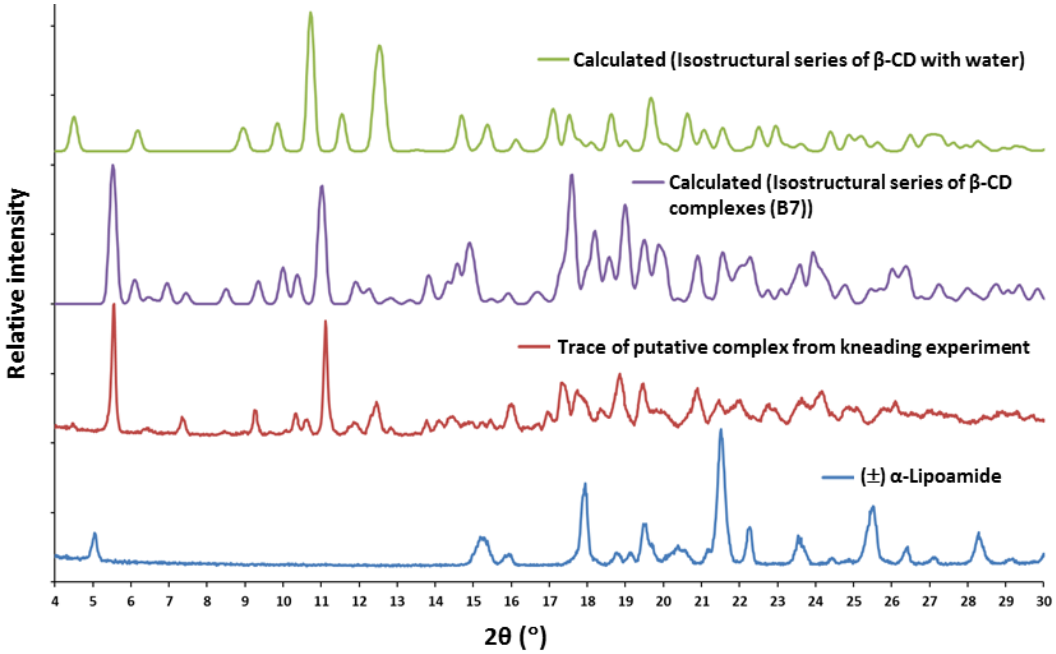

Fig. 5.8 The calculated PXRD traces for an isostructural series of β-CD inclusion complexes termed B7,[2] for uncomplexed α-LA and α-CD (complexed with water only), and the experimental trace for the putative complex obtained by kneading β-CD with α-LA.

Preparation of single crystals

Single crystals were prepared by the following method. 27.5 mg of β-CD (≈ 0.0243mmol) was dissolved in 3 cm^{-3} of water and 5.0 mg of α-LA (≈ 0.0243mmol) was incrementally added while the solution was stirred at an elevated temperature between 45 and 50 °C. The solution was stirred for a total of three hours before it was filtered while hot through a 0.45 µm nylon filter into a clean vial. The vial was capped and placed in a Dewar flask that was initially at 60 °C and left for a period of one week for slow cooling. No crystals had formed after this time and the vial was then left on a benchtop for several weeks before block-like crystals were visible in the vial.

Stoichiometry determination of BCDALA by ^{1}H – NMR spectroscopy

Crystals obtained by co-precipitation of the host with the guest were dissolved in DMSO-d_6 and analysed with ^{1}H-NMR spectroscopy. The proton labelling schemes for the host and guest as well as the spectrum obtained are shown in Fig. 5.9. The integration values for selected protons are reported in Table 5.5. The C-H_1 proton signal integration of β-CD was used as the reference integral. From the integration values a host to guest ratio of 1:1 was determined.

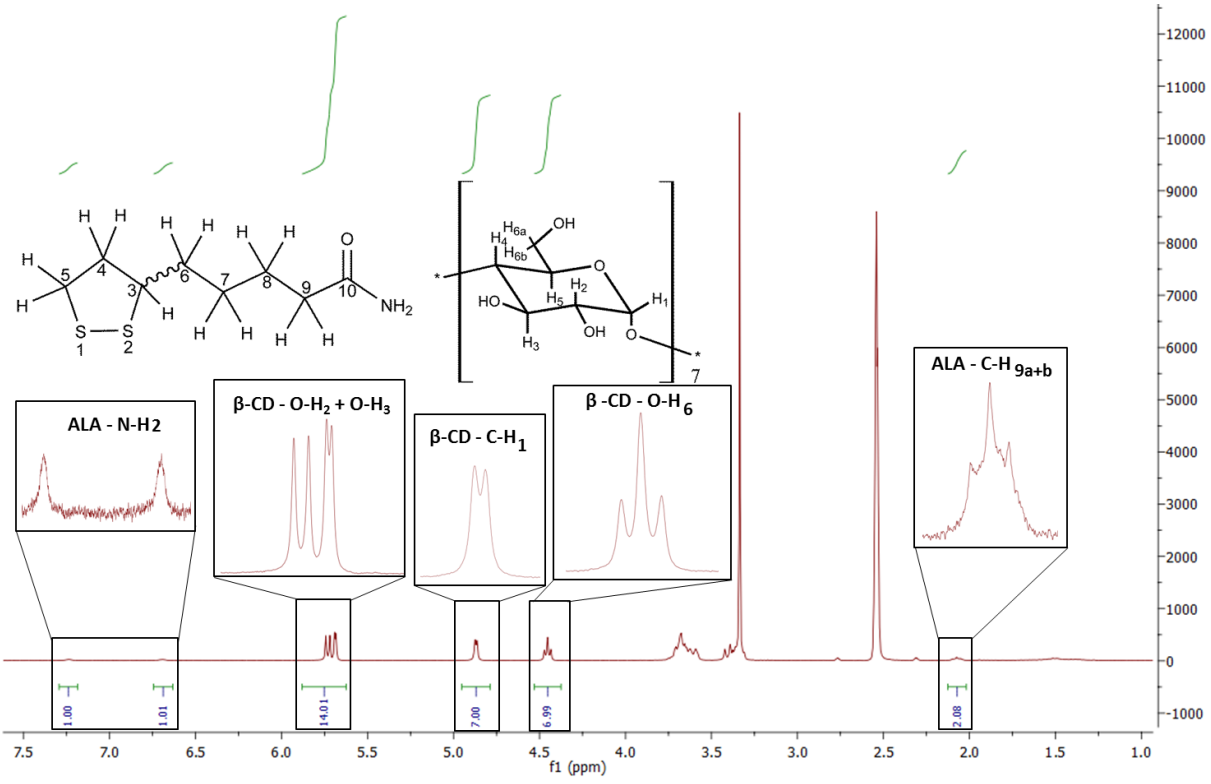

Fig. 5.9 ^{1}H-NMR spectrum of BCDALA in DMSO-d_6 for determination of stoichiometry.

Table 5.5 Integrals of protons for individual components to determine stoichiometry of BCDALA.

Proton – [Number of protons]	δ (ppm)	Integration	Experimental/ Theoretical
β-CD			
C-H_1 – [7]	4.79-4.95	7.00*	1.00
O-H_6 – [7]	4.37-4.53	6.99	1.00
O-H_2 + O-H_3 – [14]	5.62-5.88	14.01	1.00
α-LA			
C-H_{9a+b} – [2]	2.02-2.12	2.08	1.04
N-H – [1]	6.63-6.74	1.01	1.01
N-H – [1]	7.24	1.10	1.10

*** Reference integral**

Crystal structure analysis

Data-collection and space group determination

An X-ray intensity data-collection was initially performed at 173(2) K with a Bruker Kappa Apex II Duo diffractometer. Poor resolution of the included guest molecule based on a full X-ray analysis with these data indicated that another collection was warranted. The diffraction pattern of the second collection, with the crystal cooled to 135(2) K, showed $\bar{1}$ Laue symmetry, indicating that this crystal was triclinic. The space group *P*1 was the obvious choice because of the chirality of the host. The asymmetric unit consists of 2 unique β-CD molecules with 2 α-LA molecules and 22 waters in a ratio of 1:1:11.

Structure solution and refinement

Crystallographic data, parameters for collection of intensity data and refinement parameters are reported in Table 5.6. Unit cell refinement and data reduction including Lorentz-polarisation corrections were carried out by making use of the program SAINT.[6] A multi-scan method was used for absorption correction of data through the use of the program SADABS.[13] The program SHELXD[14] was used to solve the structure by *ab initio* direct methods.[15] An initial run with SHELXD[14] resulted in a sufficient starting point from which the assignment of host atoms and their refinement followed using SHELXL.[14] Each of the unique host molecules was labelled by its glucopyranose subunits from 1 to 7, the respective molecules having ~~a~~ suffixes A and B. One hydroxyl group on each of the host molecules (C6 and O6 of A7 and B4) were found to be disordered over two positions. The major and minor components in each case were assigned the s.o.f.s. *x* and *1-x* respectively and the comprising atoms were refined isotropically. The final *x* values after refinement were 0.68(1) for A7 and 0.52(1) for B4. Apart from these disordered atoms all other non-hydrogen host atoms were refined anisotropically. Hydrogen bonding between the host molecules of the dimer was apparent and the hydrogen atoms taking part in these interactions were placed in idealised positions in a riding model

and refined with thermal parameters 1.2-1.5 times the U_{iso} values of their parent atoms. By selecting high intensity peaks from the Fourier difference map a total of twenty-five water oxygen atoms were observed and assigned as these peaks did not appear to be covalently bound to the host or the guest molecules. These atoms were found to be in positions where probable hydrogen bonding to other water molecules and to the host molecules was indicated by the relevant distances (typical O···O range 2.6-3.0 Å). In some cases where hydrogen bonding was apparent constraints were applied to maintain the correct geometry. All other host hydrogen atoms were placed in idealised positions in a riding model and refined with thermal parameters 1.2-1.5 times the U_{iso} values of their parent atoms. Attempts at modelling the guest molecules proved unsuccessful. The highest intensity peaks believed to be those of the guest were placed and refined isotropically. A great deal of unresolved electron density remained within the host cavity after the final refinement was performed.

Table 5.6 Data-collection and refinement parameters for BCDALA.

Molecular formula	$C_{42}H_{70}O_{35} \cdot C_8H_{15}NOS_2 \cdot 11(H_2O)$
Formula weight (g mol^{-1})	1565.53
Crystal system	Triclinic
Space group	*P*1
a (Å)	15.355(1)
b (Å)	15.383(1)
c (Å)	17.794(1)
α (°)	99.160(2)
β (°)	113.190(2)
γ (°)	103.471(2)
V (Å)^3	3606.1(9)
Z	2
D_c (g cm^{-3})	1.4416
μ (Mo Kα) (mm^{-1})	0.183
F(000)	1674
Data-collection temp. (K)	135(2)
Crystal size (mm^3)	0.14 x 0.19 x 0.26
Range scanned θ (°)	1.29 – 27.18
Index ranges ±*h*, ±*k*, ±*l*	-19, 19; -19, 19; -22, 22
Reflections (total)	61 800
Independent reflections	31 796
Reflections with I>2σ(I)	23 639
Number of parameters	1616
R_{int}	0.0372
S	1.157
R_1 [*I*>2σ(*I*)]	0.1283
Reflections omitted	6
wR_2	0.3076
a, b in w = 1/[$\sigma^2(F_o^2)$+(aP)^2+(bP)]	a = 0.2000; b = 0
$(\Delta/\sigma)_{mean}$	< 0.001
$\Delta\rho_{min,max}$ (e Å^{-3})	-0.69, 1.23

Due to the disorder and low accuracy of the crystal structure, the appended crystallographic data files (Appendix B) are limited to what is deemed necessary.

Molecular structure

The asymmetric unit of BCDALA consisting of a hydrated 1:1 host:guest complex as well as the labelling scheme for the unique host molecules are shown in Fig. 5.10. The guest molecules are thought to be two independent non-interpenetrating molecules each with a s.o.f. of 1.0 with the dithiolane rings of each guest situated at the centre of the cavity with the amide groups of each guest at the primary rims of the host molecules.

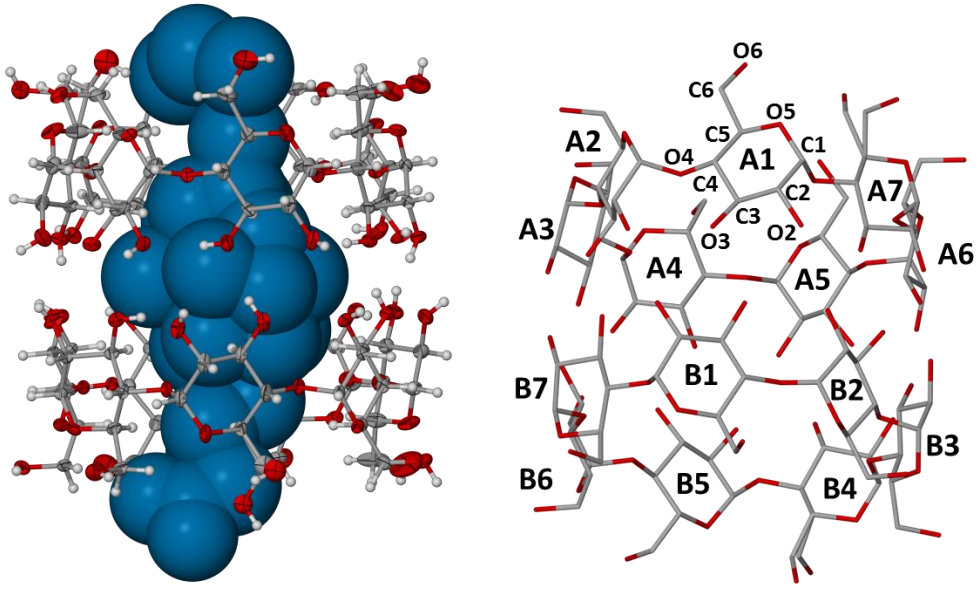

Fig. 5.10 The asymmetric unit of BCDALA showing the host atoms as thermal ellipsoids at the 50 % probability level, the main peaks of the highly disordered guest in space-filling representation (left) and the numbering scheme of the host glucopyranose rings (right).

Geometrical analysis of BCDALA

Conformation of the host

One of the parameters routinely used to describe the conformation of CDs is that of the O5-C5-C6-O6 dihedral angle (ω). This torsion angle shows whether the hydroxyl groups on the primary rim of the CD (C6-O6) are pointed towards or away from the CD cavity. The ω values for BCDALA are listed in Table 5.7. In this case all the O5-C5-C6-O6 (ω) torsion angles except for two (at A1 and A5) had negative values indicating that they were pointed away from the cavity. The minor disorder components at A7 and B4 also showed positive ω values. The resulting channels are thus left open at the primary rims of the host molecules. A cage is however formed by adjacent host molecules as the channels are not continuous, but slightly offset.

Table 5.7 Torsion angles O5-C5-C6-O6 (ω) of the host β-CD molecules in BCDALA.

Glucopyranose residue	Torsion angle ω (°)	(+) or (-) – gauche conformation	Torsion angle ω (°) of the minor disorder component	(+) or (-) – gauche conformation
A1	66(1)	(+)		
A2	-72(1)	(-)		
A3	-69(1)	(-)		
A4	-62(1)	(-)		
A5	72(1)	(+)		
A6	-65(1)	(-)		
A7	-56(1)*	(-)	57.5	(+)
B1	-63(1)	(-)		
B2	-65(1)	(-)		
B3	-61(1)	(-)		
B4	-60(2)*	(-)	65.4	(+)
B5	-67(1)	(-)		
B6	-67(1)	(-)		
B7	-64(1)	(-)		

*Major disorder component

The conformations of the β-CD host molecules in BCDALA are characterised by making use of geometrical parameters as described by Harata[9] and Saenger[10] that were presented in the introductory chapter of this thesis. These parameters are reported in Table 5.8. A common feature of β-CD complexes is that the host molecules form rigid rings by hydrogen bonding interactions on the secondary rim side of the host. Bonding occurs between the O3-H group on one glucopyranose subunit and the O2 atom of the next subunit. This results in the host molecules having a 'round' shape with low deviation of the descriptor values *l* (distance from O4 to generated centroid of the O4-hexagon), *D* (O4···O4′ distance), and ϕ (O4···O4′···O4″ angle). This feature was observed in both host molecules in the structure of BCDALA. As is evident from Table 5.8, the (*l*), (*D*), and (ϕ) values are similar when compared to the values in the glucopyranose subunits of the same molecule, but also when compared to those in the other host molecule. The *d* torsion angles (O4···O4′···O4″···O4‴) are small and illustrate that the deviation of O4 atoms from their respective O4 least-squares planes are low. The tilt angles (τ_2) (angle between the mean plane through all the O4 atoms of the host and the plane through the atoms O4, C4, C1 and O4′ of each respective glucopyranose residue) are positive and indicate a slight tilt of the primary rim of each host molecule towards the cavity. All the geometrical parameters of the host molecules in BCDALA are normal for β-CD and indicate that the conformation matches its standard truncated, cone-like shape.

Table 5.8 Geometric parameters describing the β-CD host molecules in BCDALA.

Residue	*l* (Å)	*D* (Å)	ϕ (°)	*d* (°)	τ_2 (°)
A1	5.232	4.326	132.0	-2.4	7.4(2)
A2	4.912	4.462	130.3	1.2	11.9(1)
A3	4.935	4.322	125.7	-1.0	10.0(2)
A4	5.168	4.359	127.7	1.4	9.7(4)
A5	5.082	4.337	131.7	-0.7	5.4(3)
A6	4.881	4.461	128.9	-1.1	8.4(2)
A7	5.038	4.332	123.7	2.6	8.5(1)
B1	5.044	4.350	128.5	0.9	5.1(1)
B2	5.012	4.368	129.7	-0.1	5.9(2)
B3	4.986	4.389	127.3	-0.5	11.4(1)
B4	5.080	4.318	128.2	0	7.3(1)
B5	5.039	4.413	130.0	0.6	10.4(3)
B6	4.968	4.332	127.9	-0.3	8.0(4)
B7	5.045	4.355	128.4	-0.7	9.8(4)

Crystal packing and hydrogen bonding

BCDALA crystallised in the space group *P*1 and the packing motif is classified as an 'intermediate-type packing' with a dimeric, cage-type arrangement. Two unique β-CD host molecules are stacked head-to-head with the secondary rims connected by several O-H···O hydrogen bonds to form a channel that runs parallel to the *c*-axis (Figs. 5.11 and 5.12). The openings on the primary sides of each host molecule are marginally offset in comparison to those of the host molecules making up the following dimeric layers. This results in what is described by Saenger[10] as 'cage-like' packing where the channels formed by the host cavities are interrupted to form isolated cages.

BCDALA is highly connected via intra- and intermolecular host-host interactions. Due to the high level of disorder observed in the guest structure the interactions involving the guest are not described in detail. As was mentioned earlier, hydrogen bonding occurs between O3-H and the O2 atom on the contiguous glucopyranose subunit on the secondary rim side of each host molecule. Some of these O3-H hydroxyl moieties form intermolecular connections with acceptor atoms on the secondary rim of the other host molecules forming the dimeric complex. Many of the O2-H hydroxyl moieties on the secondary rim of the host are bonded to water molecules found in the interstitial spaces between adjacent CD molecules.

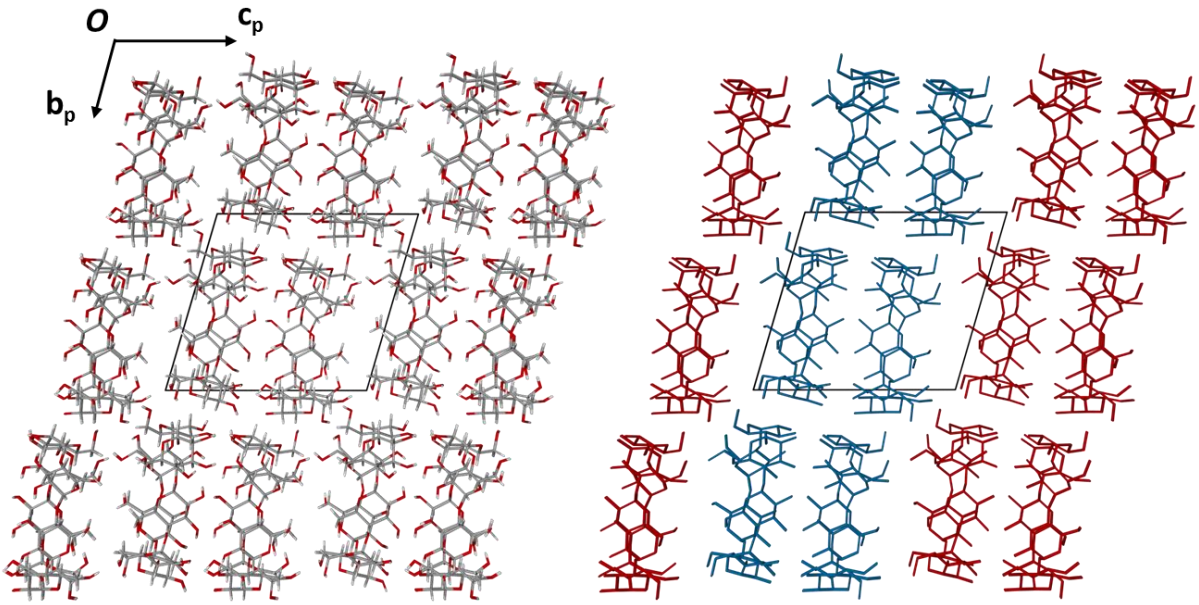

Fig. 5.11 Packing of BCDALA viewed along [100] displaying the offset dimeric layers forming isolated cages.

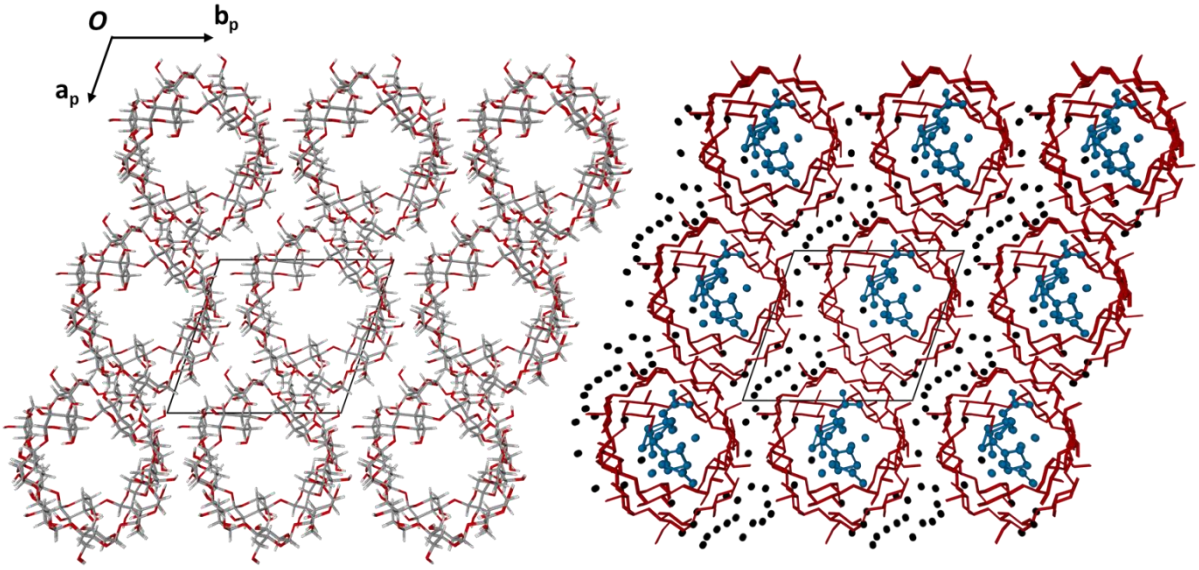

Fig. 5.12 Packing of BCDALA viewed along [001]. Water oxygen atoms shown in black with host atoms in red and the highest intensity peaks of the disordered guest in blue with hydrogen atoms omitted for clarity.

A comparison of an experimental PXRD trace for the product of kneading β-CD with α-LA and that of a trace calculated from the crystal structure of BCDALA is shown in Fig. 5.13. The positions of the peaks coincide and this confirms that the product generated by the kneading experiment matches that obtained in the co-precipitation experiment.

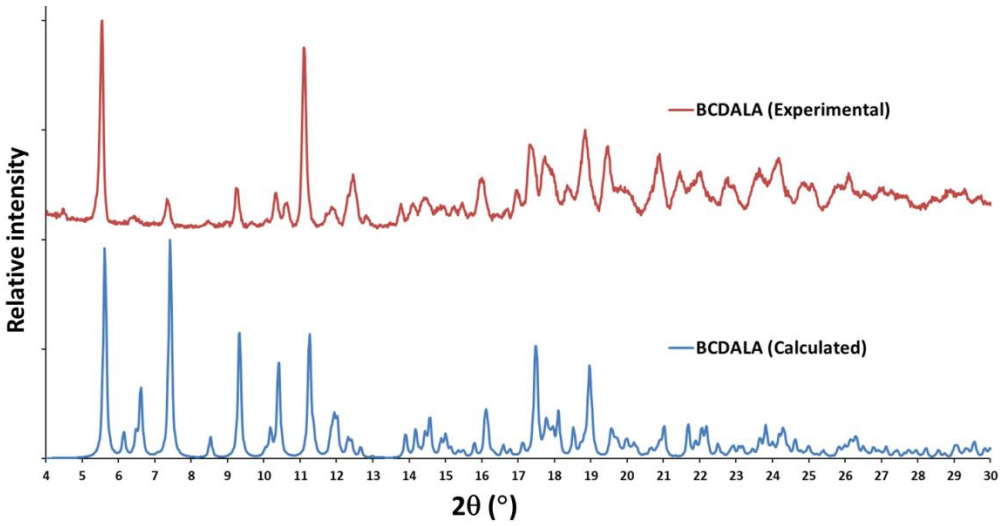

Fig. 5.13 PXRD traces collected for the product of a kneading experiment (β-CD and α-LA) and a trace computationally generated from the single crystal X-ray structure of BCDALA.

The unit cell data of isostructural complexes found in a CSD[1] search with a search tolerance of 1.5 % of the longest cell dimension and three-dimensional coordinates determined of BCDALA are summarised in Table 5.9. The high frequency of occurrence of the IM-type packing arrangement for β-CD complexes is evident from the data below.

Table 5.9 Comparison of structural parameters of BCDALA with known structures.

Space group	H:G:W*	a (Å)	b (Å)	c (Å)	α (°)	β (°)	γ (°)	Guest	CSD Refcode	Ref.
*P*1	1:1:11	15.355(1)	15.383(1)	17.794(1)	99.2	113.2	103.5	α-LA	BCDALA‡	NA
*P*1	1:1:10.5	18.15(6)	15.47(6)	15.41(6)	103.5	113.7	98.7	N-acetyl-D-phenylalanine	AGAZUD	16
*P*1	2:1:17.5	18.186(3)	15.486(2)	15.392(2)	102.8	113.6	99.7	ethyl cinnamate	BIDMOQ	17
*P*1	1:1:15	17.747(5)	15.255(5)	15.491(5)	102.5	113.5	98.9	1-adamantane-carboxylic acid	BOGCAB	18
*P*1	1:1:13.4	18.244(3)	15.476(3)	15.417(2)	102.9	113.1	99.7	4-t-butylbenzoic acid	HEGXUM	19
*P*1	2:1.6:23.9	18.056(3)	15.446(2)	15.452(2)	103.2	113.0	99.4	nonanoic acid	TEJHAR	20
*P*1	2:1:29	17.926(4)	15.399(3)	15.416(3)	103.4	113.4	98.9	1,12-dodecanediol	TAFZIK	21
*P*1	1:1:9.5	18.115(3)	15.497(3)	15.364(3)	103.0	113.2	99.5	4,4'-dipyridine	UKAGOC	22
*P*1	2:2:23.35	18.129(2)	15.411(2)	15.585(2)	104.0	112.9	98.8	N-acetyl-L-phenylalanine methyl ester	DOCVUM04	23
*P*1	2:1:22.18	18.207(6)	15.510(5)	15.280(6)	103.0	113.1	99.8	1,13-tridecanedioic acid, ethanol	LONGIE	24
*P*1	2:2:23	18.12(6)	15.40(6)	15.53(6)	103.2	112.9	99.2	N-acetyl-L-phenylalanine amide	VOQDOU	23
*P*1	2:2:21.85	18.30(6)	15.50(6)	15.31(6)	102.8	112.7	99.5	N-acetyl-*p*-methoxy-L-phenylalanine methyl ester	VOQDUA	25
*P*1	2:1:27.46	18.153(7)	15.456(8)	15.251(4)	102.8	113.1	99.9	1,12-dodecanedioic acid, ethanol	WISREV	26
*P*1	1:1:14	18.019(3)	15.343(4)	15.414(3)	103.5	113.1	99.3	methyl-4-hydroxybenzoate	AJUVAC	27
*P*1	2:1:21.86	18.242(1)	15.492(1)	15.436(1)	102.8	113.0	99.8	1,14-tetradecanedioic	CACPOM	28

								acid, ethanol		
*P*1	1:1:12	17.890(6)	15.390(6)	15.390(6)	102.8	113.4	99.3	N-acetyl-L-phenylalanine	AGAZOX	16
*P*1	1:1:11.25	18.01(6)	15.53(6)	15.37(6)	103.4	113.2	99.5	7-hydroxy-4-methylcoumarin	MASBIR	29
*P*1	2:1:22.5	18.133(4)	15.479(4)	15.401(3)	102.9	113.4	99.5	4,7-dimethylcoumarin	MASBOX	29
*P*1	2:2:1:23.3	19.777(5)	15.247(3)	15.475(4)	102.6	112.7	99.9	aspirin, salicylic acid	DIFHOP	30
*P*1	1:1:12	18.06(6)	15.44(6)	15.53(6)	103.4	113.0	99.0	N-acetyl-L-phenylalanine	AGAZIR	16
*P*1	2:0.5:23.5	15.224(1)	15.486(1)	18.032(1)	99.6	113.3	102.9	4,4'-vinylenedipyridine, ethanol	BOSZEP	31
*P*1	1:1:12.5	15.216(2)	15.514(2)	17.791(2)	99.3	112.6	103.0	4,4'-ethylenedipyridine, ethanol	BOSZIT	31
*P*1	1:1:10	15.281(1)	15.404(1)	17.890(1)	99.7	113.4	102.5	4,4'-dithiodipyridine	BOSZOZ	31
*P*1	2:1:X	15.277(2)	15.471(2)	17.963(2)	99.6	113.4	102.8	N-methylanthranilic acid, isopropanol	CUPYOC	32
*P*1	1:1:11.5	15.404(1)	15.281(1)	17.890(1)	99.7	113.4	102.5	pyranocoumarin/ aegelinol	EQENEV	33
*P*1	1:1:13.5	17.945(4)	15.449(1)	15.232(3)	103.2	113.3	99.7	7-hydroxycoumarin	EYAQAX	34
*P*1	1:1.5:9.5	17.958(3)	15.407(1)	15.296(1)	102.5	113.4	99.4	4-hydroxycoumarin	EYAQEB	34
*P*1	1:1:8	15.440(2)	15.483(2)	17.971(3)	112.9	99.1	103.3	4-hydroxyazobenzene	FODBEG	35
*P*1	1:1:11	15.281(3)	15.431(3)	17.911(4)	99.6	113.1	102.5	4-phenyl-pyridine-N-oxide	GOTMOT	36
*P*1	2:1:23	15.435(3)	15.466(2)	17.949(3)	99.3	113.2	103.1	(1,10-bis(imidazol-1-yl)decane)-pseudorotaxane	HAHVES	37
*P*1	1:1:11	17.842(4)	15.394(2)	15.463(4)	103.1	113.3	99.2	biphenyl-4-ylacetic acid/ felbinac	HAKPUG	38
*P*1	1:1:14.25	15.260(2)	15.434(2)	17.950(2)	99.2	113.2	103.3	4-nitrobenzoic acid	NILQUV	39
*P*1	2:1.5:19	15.430(1)	15.455(1)	17.996(1)	99.3	113.2	103.0	ethanol	OFOWIQ	40
*P*1	2:1:30	17.824(3)	15.373(2)	15.380(1)	103.3	113.4	99.0	quinolin-8-ol, ethanol	UJEFEV	41
*P*1	2:3:23	15.249(2)	15.300(2)	17.853(3)	99.6	113.4	101.9	o-aminobenzoic acid	VOFJIK	42
*P*1	1:1:10.5	15.343(1)	15.405(1)	17.764(1)	113.6	99.4	102.1	geraniol	VUYGUT	43
*P*1	1:1:11.22	15.166(2)	15.486(2)	17.908(2)	113.3	99.2	102.4	(-)-isopulegol	PAKRAX	44
*P*1	1:1:12.38	15.257(4)	15.351(4)	17.794(4)	113.2	99.1	102.1	(+)-isopulegol	PAKREB	44
*P*1	1:1:13	15.340(5)	15.393(4)	17.913(5)	98.8	113.4	103.2	3-(4-hydroxyphenyl)-2H-1-benzopyran-7-ol	XAMDEX	45

***Ratio of host : guest : water and in applicable cases a second guest or solvent; ‡The compounds have not been submitted to the Cambridge Crystallographic Data Centre yet and the compound codes are those used throughout this thesis.**

Thermal analysis

The HSM result for BCDALA is displayed in Fig. 5.14. The evolution of bubbles from the crystals was observed during heating. A gradual but noticeable change in opacity and colour occurred during heating and by 320 °C darkening of the crystals was visible.

Differential thermal analysis results for BCDALA are presented in Fig. 5.15. A broad endotherm spanning the temperature range from the onset of heating up to around 130 °C is visible. This event is most likely due to the evolution of water from the crystals that was also seen in the HSM result. Another less pronounced exothermic event is visible with an onset at 263.1 ± 5.6 °C (n = 3) and a peak at 273.3 ± 2.5 °C (n = 3). This event leads into a small endothermic event. Though a change in colour and opacity was observed in the HSM result, there was no clear distinct change that occurred

at this specific temperature. An explanation for this event could be that the host undergoes restructuring after loss of the guest. The next event is the decomposition of the sample with an onset at 333.0 ± 1.8 °C (n = 3) that was also evident in the HSM result.

The TGA result for BCDALA is shown in Fig. 5.16. A large mass loss step is seen with an onset at commencement of heating and continues to above 100 °C. The mass loss of this step was 12.48 ± 0.40 % (n = 3) of the total starting sample mass. A second step is observed with an onset at 232.1 ± 1.5 °C (n = 3) that continues up to a temperature that overlaps with a third event and has a mass loss of 11.91 ± 0.03 % (n = 3). This calculation was for the mass loss from 200 to 325 °C and is most likely due to guest loss. A third event with an onset temperature of 330.1 ± 1.5 °C (n = 3) and a mass loss of 61.97 ± 0.80 % (n = 3) is thought to be due to the decomposition of the host. The results match those observed in the DTA and HSM results. The calculated ratio of water to guest to host from these results is 10.6 ± 0.3:0.9 ± 0.1: 1.0 and this matches the ratio of host to guest observed in the NMR results. The water to host ratio does not precisely match what was modelled in the single-crystal X-ray results, though this result is unsurprising considering the level of disorder observed.

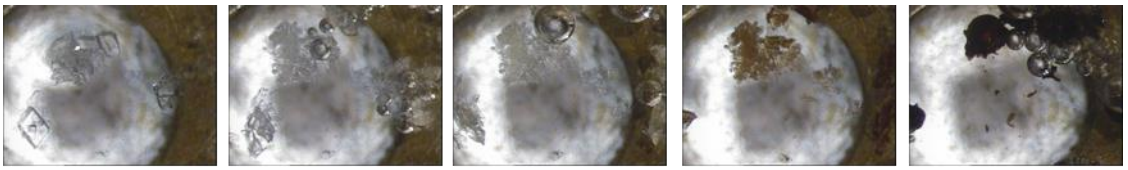

Fig. 5.14 Representative HSM photographs of BCDALA at various temperatures.

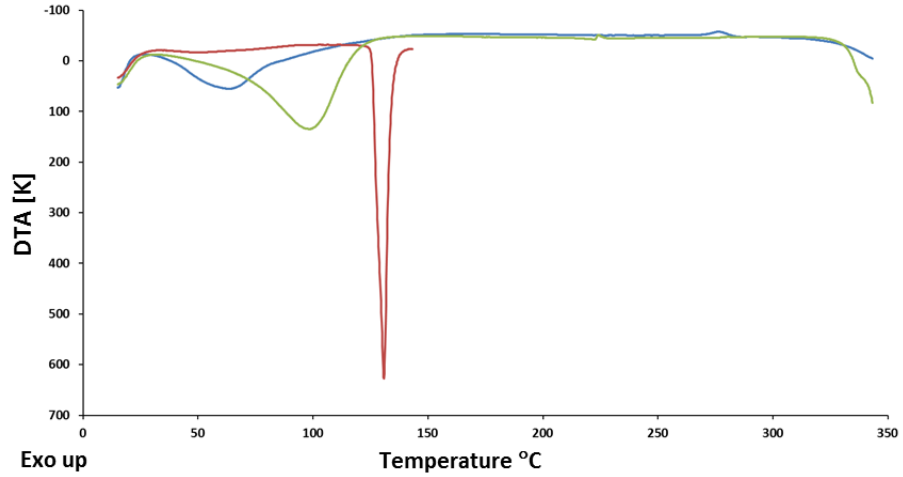

Fig. 5.15 Representative DSC trace for BCDALA (blue), α-LA (red) and β-CD (green).

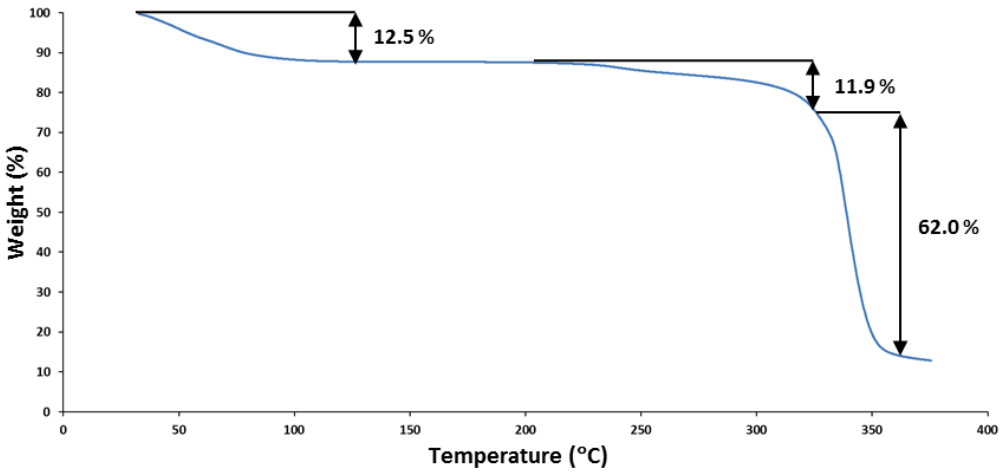

Fig. 5.16 Representative TGA trace of BCDALA.

γ-Cyclodextrin inclusion complex with (±)-α-lipoamide (GCDALA)

Preparation of complex

A screening experiment was carried out by kneading equimolar amounts (10 mg of α-LA ≈ 0.049 mmol) of the host and guest for 20 minutes.

PXRD

The kneading product was analysed by PXRD (Fig. 5.17) and the putative trace was compared to one generated from an isostructural series of inclusion complexes with γ-CD[2] and that of the host complexed with water alone. The result matched that of the series demonstrating that a complex had been formed. From this match it can be deduced that the complex is tetragonal, crystallizing in the space group $P42_12$.[2]

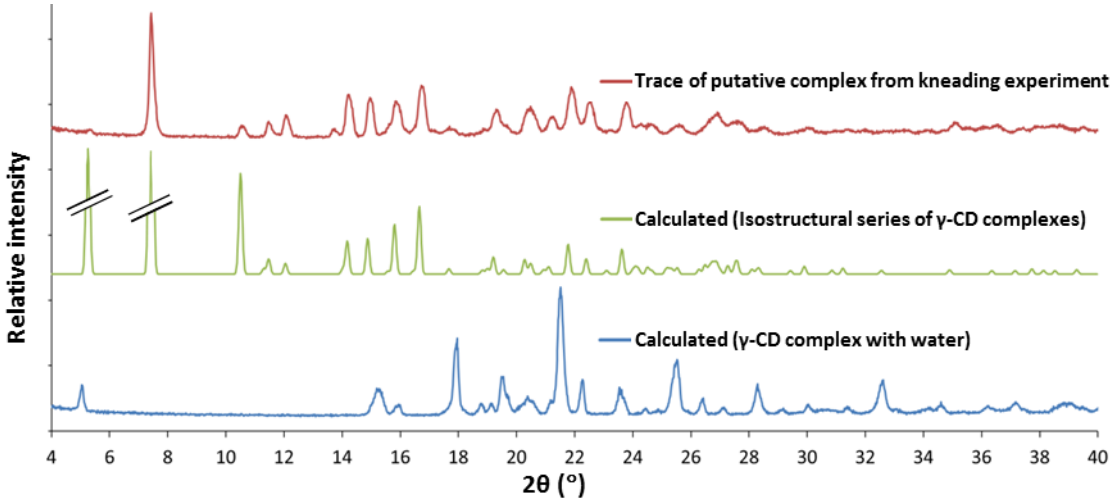

Fig. 5.17 Calculated trace for a series of γ-CD inclusion complexes, uncomplexed γ-CD and the putative complex obtained by kneading with α-LA.

Preparation of single crystals

Crystals of the complex were prepared by co-precipitation of equimolar amounts of the host and guest from distilled water (5 mg of α-LA ≈ 0.025 mmol). The CD was dissolved in 3 cm^{-3} of water before incrementally adding the guest while continuously stirring at a temperature between 45 and 50 °C. The solution was filtered through a nylon filter into a clean vial. The vial was capped with a lid with small perforations and left on a benchtop. Block-like crystals started appearing after a few weeks. Unit cell checks performed on the crystals showed that the parameters matched those of other complexes formed with this host (found in a search of the CSD)[1] having dimensions of a ~ b ~ 23.8, c ~ 23.2 Å and α= β= γ= 90° (summarised in Table 5.10). The packing of complexes with a number of guest molecules and this host has been reported as having the symmetry of the uncommon tetragonal space group $P4_12$. An example where this packing is described is in the case of a hydrated γ-CD-methanol complex reported by Steiner and Saenger.[46] The way in which these complexes generally tend to pack is interesting in that their asymmetric units consist of three distinct pairs of glucose residues which result in three independent γ-CD molecules generated by a four-fold axis and stacked into infinite columns, the cavities of which link up to form infinite channels running parallel to the tetragonal *c*-axis (Fig. 5.18). Another result of this packing is that a large cavity is formed in the interstitial spaces between these columns and these are usually filled with water or other solvent molecules. There exist strong intermolecular interactions (O–H···O) between the faces of the stacked γ-CD molecules that result in the formation of a robust framework by head-to-head (A), tail-to-tail (B) and head-to-tail (C) connections (Fig. 5.18). The ultimate consequence of this interesting and highly symmetrical packing arrangement is that the guest requires fourfold symmetry to be adequately modelled. Another complication is that the stoichiometric ratio often differs from 1:1. It is for this reason that no data-collections and subsequent structural elucidation were attempted for the crystals of GCDALA.

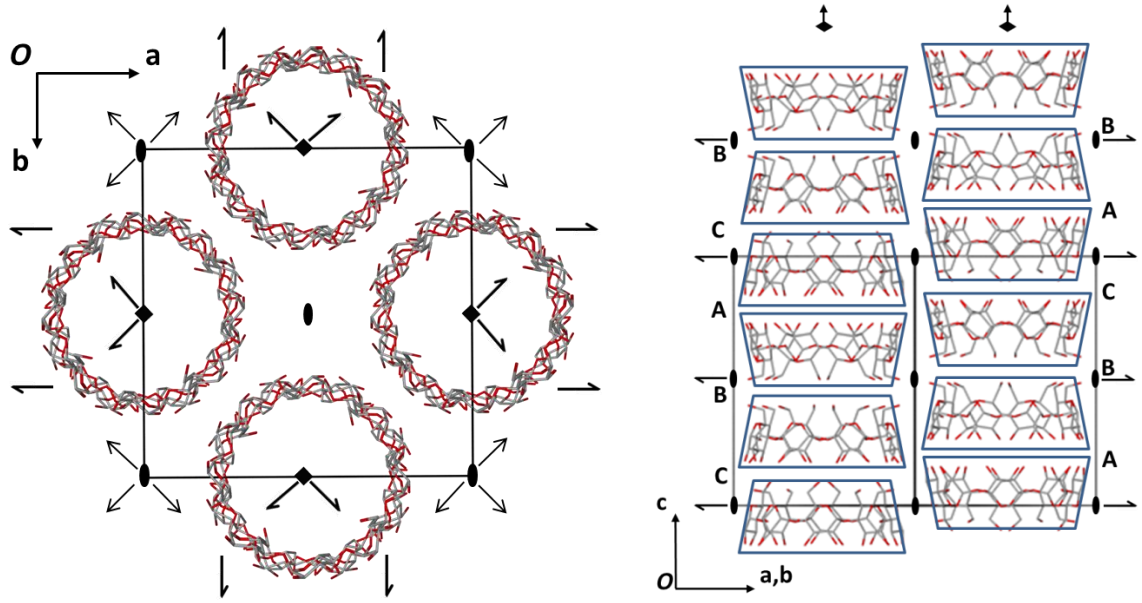

Fig. 5.18 Representative packing of γ-CD complexes of the tetragonal space group $P42_12$, showing symmetry elements viewed down the infinite channels along the c-axis (left) and the stacking sequence and the lateral connections viewed down a diagonal plane (right).

The unit cell data of isostructural complexes found in a CSD[1] search (selected with the same criteria as described for those used for BCDALA) of GCDALA are summarised in Table 5.10. This is a very common packing arrangement, though the general difficulty in obtaining a satisfactory model of an unsymmetrical guest molecule, described earlier, is the reason for the limited number of matching structures found in the CSD.

Table 5.10 Comparison of structural parameters of GCDALA with known structures.

Space group	H:G:W*	a=b (Å)	c (Å)	Guest	CSD Refcode	Ref.
$P42_12$	NA	23.8	23.2	α-LA	GCDALA‡	NA
$P42_12$	1:X:X	23.808(4)	23.140(3)	methanol	NUNRIX	14
$P42_12$	1:1:17	23.840(5)	23.227(6)	1-propanol	SIBJAO	47
$P42_12$	1:1:17.12	23.809(1)	23.207(1)	1-propanol	SIBJES	47
$P42_12$	1:1:X	23.759(7)	23.069(7)	1-propanol	CYDXPL	48
$P42_12$	1:1:9	23.808(2)	23.175(2)	12-crown-4	DOCYID	49
$P42_12$	3:1:1:23.1	23.75(2)	22.92(3)	12-crown-4-lithium, 12-crown-4 isothiocyanate	FEJFIJ	50
$P42_12$	3:1:1:27	23.842(2)	23.132(2)	12-crown-4-potassium, 12-crown-4 chloride	FEJFOP	50
$P42_12$	3:1:1:23.1	23.816(3)	23.072(3)	bis(12-crown-4)-sodium, tris 12-crown-4 chloride	SAJNAS	51
$P42_12$	3:1:1	23.697(1)	22.893(1)	potassium, tetrachloro-gold(iii)	YIHHUU	52

***Ratio of host : guest : water and in applicable cases a second guest or solvent; ‡The structure has not been submitted to the Cambridge Crystallographic Data Centre and the compound codes are those used throughout this thesis.**

Stoichiometry determination of GCDALA by ^{1}H – NMR spectroscopy

^{1}H-NMR spectroscopy with DMSO-d_6 as solvent was used to determine the stoichiometry of crystals obtained by co-precipitation of the host with the guest. The spectrum obtained as well as the labelling schemes for the host and guest molecules are shown in Fig. 5.19. Table 5.11 summarises the values of integration and spectral assignments. The C-H_1 proton signal integration of γ-CD was used as the reference integral. The NMR results indicate a host to guest ratio of 3:4.

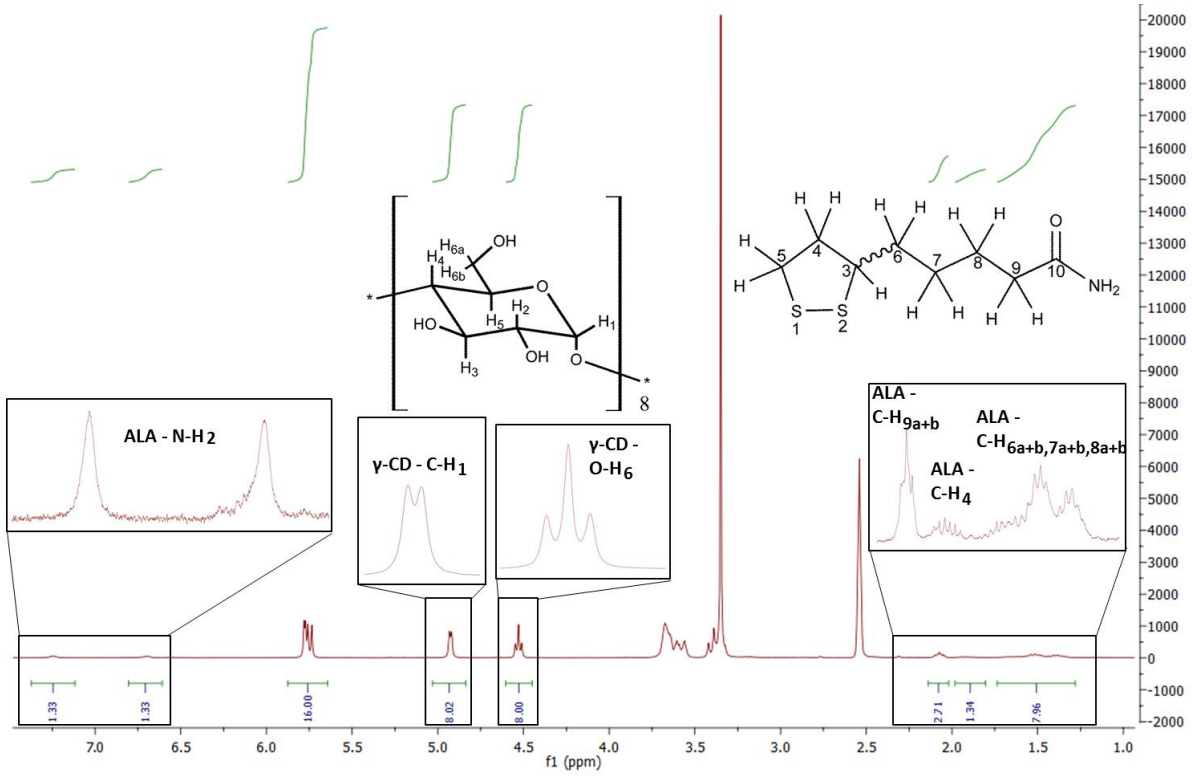

Fig. 5.19 ^{1}H-NMR spectrum of GCDALA in DMSO-d_6 for determination of stoichiometry.

Table 5.11 Integrals of protons for individual components to determine stoichiometry of GCDALA.

Proton – [Number of protons]	δ (ppm)	Integration	Experimental/ Theoretical
γ-CD			
C-H_1 – [8]	4.45-4.60	8.00*	1.00
O-H_6 – [8]	4.84-5.03	8.02	1.00
O-H_2 + O-H_3 – [16]	5.64-5.88	16.00	1.00
α-LA			
C-H_{9a+b} – [2]	2.02-2.14	2.71	1.36
C-H_{6a+b} + C-H_{7a+b} + C-H_{8a+b} – [6]	1.28-1.74	7.96	1.33
C-H_4 – [1]	1.80-1.98	1.34	1.34
N-H – [1]	6.61-6.80	1.33	1.33
N-H – [1]	7.12-7.37	1.33	1.33

*** Reference integral**

Thermal analysis

The HSM analysis of GCDALA (Fig. 5.20) did not display any noticeable evolution of bubbles between the commencement of heating to a temperature of 100 °C. The crystals did, however, undergo a discernible change in this temperature range from clear individual crystals to a more opaque amalgamation. Gradual changes occurred in the temperature range from 100 to 250 °C with clear decomposition visible at higher temperatures.

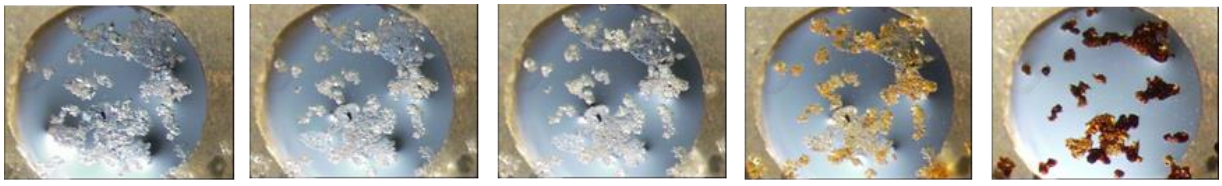

Fig. 5.20 Representative HSM micrographs of GCDALA at various temperatures.

The DSC results for GCDALA (Fig. 5.21) exhibited a broad endotherm spanning from the onset of heating up to just above 100 °C. A second event was observed with an onset temperature of 130.1 ± 1.2 °C (n = 3) and a peak at 131.3 ± 0.9 °C (n = 3). An exothermic event was visible with an onset temperature of 199.5 ± 1.8 °C (n = 3) and a peak at 209.3 ± 1.2 °C (n = 3). The first broad endotherm is typical for water loss from inclusion complexes. The second endothermic event very closely matches the melting temperature of the guest and this indicates that the complexation with γ-CD did not result in significant improvement in the thermal stability of the guest. The third event could possibly be the host recrystallising into a more stable form before eventual decomposition starts above 280 °C.

The TGA results for GCDALA (Fig. 5.22) displayed a mass loss of 14.08 ± 0.35 % (n = 3) with an onset from commencement of heating up to above 100 °C, most likely due to water loss. Another stepped mass loss, interpreted as the guest loss, is seen with an onset at 227.8 ± 7.8 °C (n = 3) and continues past the onset of a third stepped mass loss and overlaps with this event, having an onset near 329.8 ± 0.5 °C (n = 3). Due to this overlap of mass loss steps it was not possible to determine an accurate value for each event individually. The host to guest ratio is thus more of an estimate than an exact value. The calculated host to guest ratio was roughly 3:4 and matches that seen in the NMR results. The water to CD ratio is roughly 14:1.

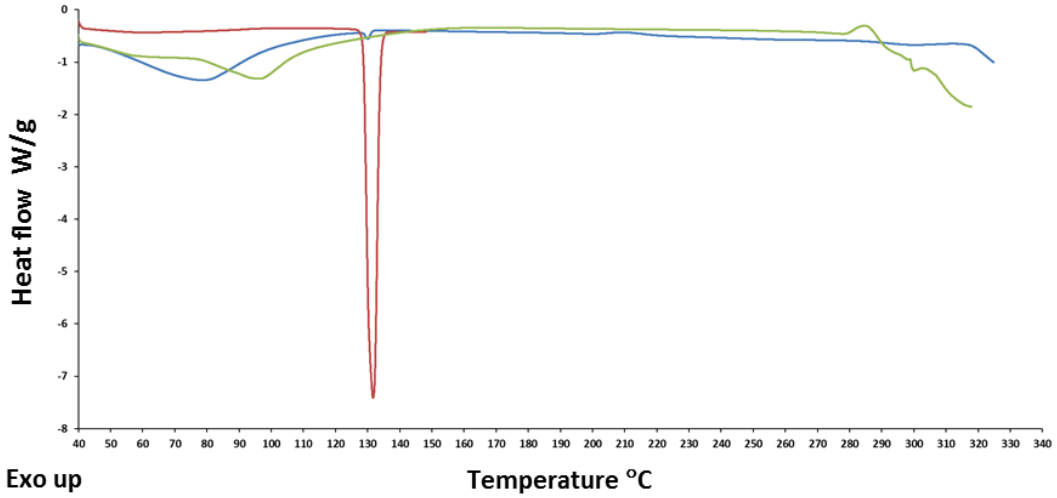

Fig. 5.21 Representative DSC trace for GCDALA (blue), α-LA (red) and γ-CD (green).

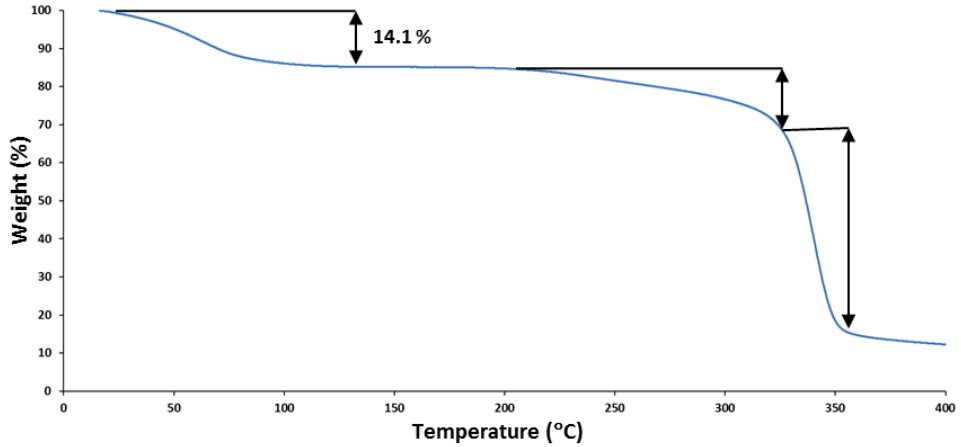

Fig. 5.22 Representative TGA trace of GCDALA.

Although X-ray analysis was not pursued for reasons stated earlier, the proven isostructurality with known γ-CD complexes indicates genuine inclusion complexation of α-LA. The NMR and thermal analyses yielded a host to guest ratio for the complex of 3:4.

TRIMEA inclusion complex with (±)-α-lipoamide (TMAALA)

Preparation of complex

For the preparation of this complex an equimolar amount of α-LA (10 mg ≈ 0.049 mmol) was added to an aqueous solution of TRIMEA (0.049 mmol in 5 cm^{-3}) and the solution was stirred during heating and cooling cycles at a minimum of -8 °C to a maximum of 50 °C. The solution went clear during the cooling cycle and after stirring for a total of three hours it was filtered through a 0.45 µm nylon filter into a clean vial. This vial was capped and placed in an oven at 60 °C. After a few days block-like crystals had formed.

Stoichiometry determination of TMAALA by ^{1}H – NMR spectroscopy

Single crystals obtained by co-precipitation of the host and guest were dissolved in DMSO-d_6 and analysed with ^{1}H-NMR spectroscopy. The result is shown together with the proton labelling schemes of the host and guest molecules in Fig. 5.23. The integration values are reported in Table 5.12. As was the case for the previous proton NMR analyses with cyclodextrin complexes described in this chapter, the C-H_1 proton signal integration of TRIMEA was used as the reference integral. The host to guest ratio was determined to be 1:1.

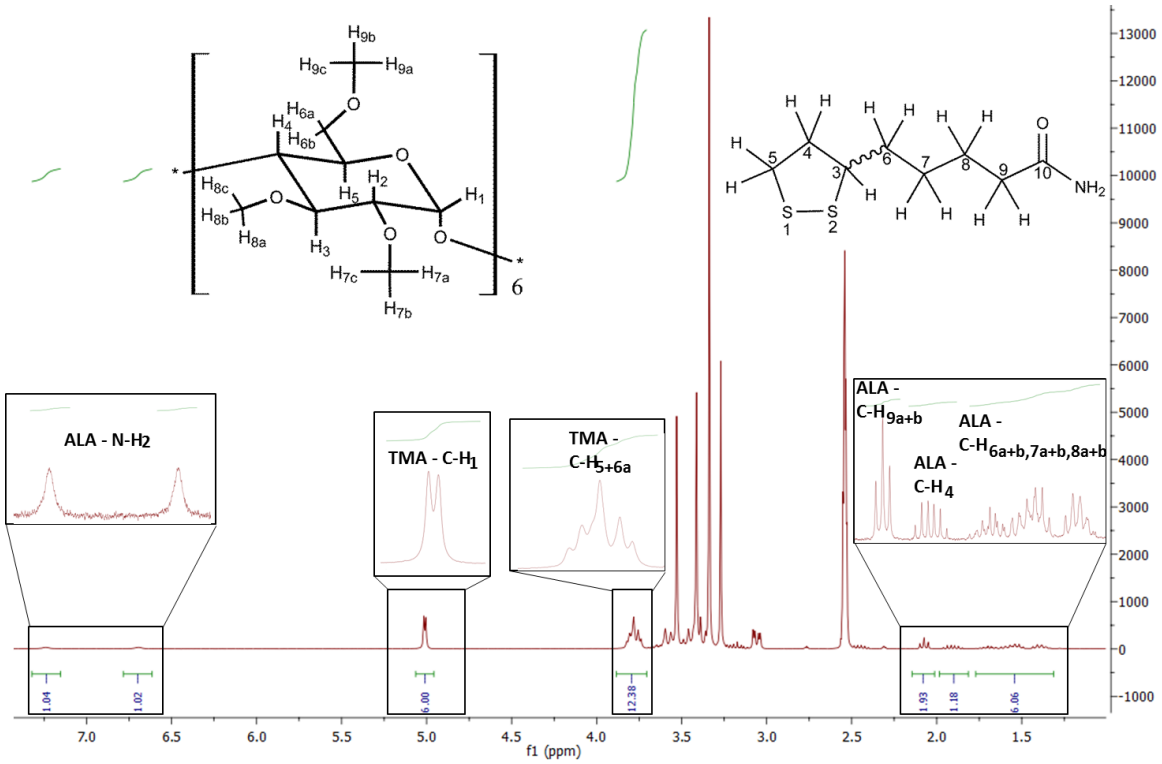

Fig. 5.23 ^{1}H-NMR spectrum of TMAALA in DMSO-d_6 for determination of stoichiometry.

Table 5.12 Integrals of protons for individual components to determine stoichiometry of TMAALA.

Proton – [Number of protons]	δ (ppm)	Integration	Experimental/ Theoretical
TRIMEA			
C-H_1 – [6]	4.96-5.06	6.00*	1.00
C-H_5 + C-H_{6a} – [12]	3.71-3.88	12.38	1.03
α-LA			
C-H_{9a+b} – [2]	2.01-2.15	1.93	0.965
C-H_{6a+b} + C-H_{7a+b} + C-H_{8a+b} – [6]	1.39-1.70	6.06	1.01
C-H_4 – [1]	1.81-1.98	1.18	1.18
N-H – [1]	6.61-6.78	1.02	1.02
N-H – [1]	7.15-7.32	1.04	1.04

*** Reference integral**

Crystal structure analysis

Data-collection and space group determination

The X-ray intensity data of a TMAALA monocrystal were collected on a Bruker Kappa Apex II Duo diffractometer at 173(2) K. The X-ray diffraction pattern displayed *mmm* Laue symmetry and this indicates that the crystal belongs to the orthorhombic crystal system. The conditions limiting possible reflections were *hkl: none, h00: h = 2n, 0k0: k = 2n, 00l: l = 2n*. The space group was thus determined to be $P2_12_12_1$. The asymmetric unit of TMAALA was found to consist of one TRIMEA molecule, one α-LA molecule and five water molecules.

Structure solution and refinement

Crystallographic data and parameters for collection of intensity data and structure refinement are reported in Table 5.13. Unit cell refinement and data reduction were performed with the program SAINT.[6] Absorption correction of the data was done by making use of the program SADABS[13] with a multi-scan method. No suitable structures for isomorphous replacement were found in a CSD[1] search and the program SHELXD[14] was used to solve the structure by *ab initio* direct methods.[15] An acceptable solution was obtained by making use of direct methods and after this step the atoms of the host molecule were assigned and refined by making use of SHELXL.[14] Once the atoms of the glucopyranose backbone of the host molecule were assigned and refined, the glucopyranose subunits were labelled G1-G6. A single primary methoxymethyl group on the glucopyranose unit labelled G2 was found to be disordered over two positions in the host structure. The major and minor components were assigned the s.o.f.s. *x* and *1-x* respectively and the comprising atoms were refined isotropically. The final *x* value after refinement was 0.54(1). All other non-hydrogen host atoms were refined anisotropically. The hydrogen atoms of the host molecule were evident in successive difference electron density maps and these were placed in idealised positions in a riding model and refined with thermal parameters 1.2-1.5 times the U_{iso} values of their parent atoms.

The atoms of the guest molecule were observed in the difference electron density maps with some disorder observed at the 1,2-dithiolane ring. This is due to the guest being a racemic mixture and packing with a certain fraction of the complexes forming with one enantiomer and the rest with the other. The 1,2-dithiolane ring as well as the first carbon of the chain linking it to the amide moiety were assigned s.o.f.s. *x* and *1-x* respectively to represent each enantiomer and were refined isotropically. The rest of the carbon chain and amide moiety of the guest were shared between the respective enantiomers and were refined anisotropically. The final *x* value after refinement was 0.58(1), indicating that the enantiomeric selectivity is low for the crystal selected. The hydrogens attached to the guest molecules were apparent in the difference electron density maps and all

(except for those attached to the amide nitrogen) were placed in idealised positions in a riding model and refined with thermal parameters 1.2-1.5 times the U_{iso} values of their parent atoms. The hydrogen atoms connected to the amide nitrogen were freely refined.

A total of five water molecules were visible in the Fourier difference map. The oxygen atoms of four of these molecules were initially refined isotropically and subsequently anisotropically and the attached H atoms were found in the difference electron density maps and refined after applying reasonable constraints on the bond lengths and thermal parameters. One of the water molecules was not satisfactorily refined and was instead refined isotropically as two separate components with s.o.f.s. of *x* and *1-x* assigned to each respectively. The final *x* value after refinement was 0.52(1) and no hydrogens were assigned to these atoms.

Table 5.13 Data-collection and refinement parameters for TMAALA.

Molecular formula	$C_{54}H_{96}O_{30} \cdot C_8H_{15}NOS_2 \cdot 5(H_2O)$
Formula weight (g mol^{-1})	1518.69
Crystal system	Orthorhombic
Space group	$P2_12_12_1$
a (Å)	15.1645(17)
b (Å)	21.7099(24)
c (Å)	23.5658(25)
α = β = γ (°)	90
V (Å)^3	7758.3(3)
Z	4
D_c (g cm^{-3})	1.300
μ (Mo Kα) (mm^{-1})	0.157
F(000)	3272
Data-collection temp. (K)	173(2)
Crystal size (mm^3)	0.19 x 0.32 x 0.34
Range scanned θ (°)	1.59 – 27.90
Index ranges ±*h*, ±*k*, ±*l*	-19, 19; -28, 26; -30, 22
Reflections (total)	120 686
Independent reflections	18 469
Reflections with I>2σ(I)	16 086
Number of parameters	954
R_{int}	0.0479
S	1.014
R_1 [*I*>2σ(*I*)]	0.0488
Reflections omitted	5
wR_2	0.1237
a, b in w = 1/[σ^2(F_o^2)+(aP)^2+(bP)]	a = 0.0549; b = 4.9961
$(\Delta/\sigma)_{mean}$	< 0.001
$\Delta\rho_{min,max}$ (e Å^{-3})	-0.95, 0.77

Molecular structure

The asymmetric unit and labelling scheme of TMAALA are shown in Figs. 5.24 and 5.25.

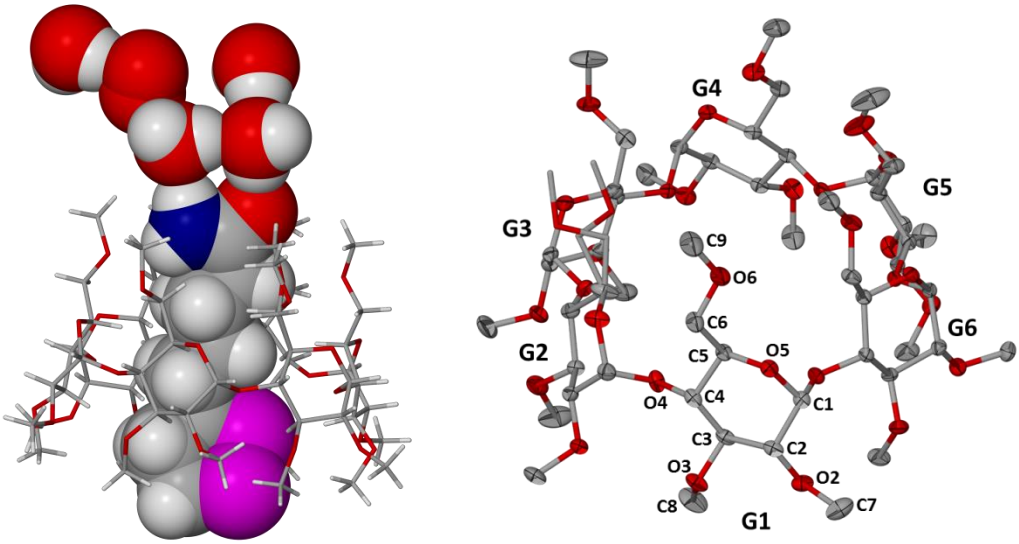

Fig. 5.24 The asymmetric unit of TMAALA (left) and numbering scheme of the host molecule with thermal ellipsoids shown at the 50 % probability level for anisotropic atoms (right). The minor and major disorder components of the methoxymethyl moiety at G2 are represented as stick models.

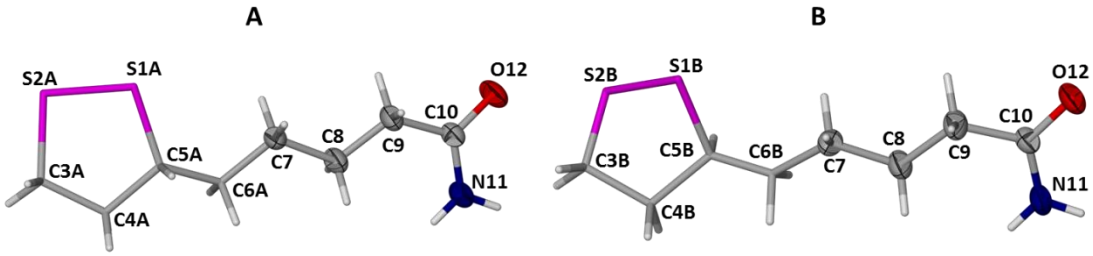

Fig. 5.25 The numbering scheme of the guest molecules with the respective enantiomers labelled A and B, with thermal ellipsoids shown at the 50 % probability level for anisotropic atoms.

Geometrical analysis of TMAALA

Conformation of the host

A descriptor used for the methoxymethyl groups on the primary rim of the host TRIMEA molecule is the torsion angle O5-C5-C6-O6 (ω). This descriptor will indicate the orientation of the C6-O6 bonds and this will show if the methoxymethyl groups are pointed toward or away from the CD cavity.

The ω values observed in TMAALA are reported in Table 5.13. In the case of TMAALA, the glucose residues G1, G4, G5, G6 and the minor disorder component of G2 of the host TRIMEA molecule have positive values for ω. This indicates a (+)-gauche conformation with the methoxymethyl groups

pointing inward, towards the CD cavity. G3 and the major disorder component of G2 have negative values for ω and this indicates (-)-gauche conformation and that the methoxymethyl groups are directed away from the CD cavity. In many cases the methoxymethyl groups on the primary rim of TRIMEA molecules of CD complexes serve as a 'lid' that closes off the CD cavity to form a 'cage' to enclathrate a guest. In the case of TMAALA the CD cavity is partially open forming a narrow channel from which the guest slightly protrudes (Fig. 5.26). This occurrence is an example where the standard descriptors should not simply be taken at face value as even though most of the methoxymethyl groups point towards the CD cavity, the cavity is not closed off. The O6 atoms of the various glucose residues interact in a variety of ways including via interactions with extrastitial waters, guest molecules as well as being involved in intra- and intermolecular interactions of the host molecules.

Table 5.13 Torsion angles O5-C5-C6-O6 (ω) of host TRIMEA in TMAALA.

Glucopyranose residue	Torsion angle ω (°)	(+) or (-) – gauche conformation	Torsion angle ω (°) of the minor disorder component	(+) or (-) – gauche conformation
G1	69.5(3)	(+)		
G2	-70.2(5)*	(-)	73.7	(+)
G3	-57.9(3)	(-)		
G4	68.9(3)	(+)		
G5	67.5(3)	(+)		
G6	56.2(3)	(+)		

*Major disorder component

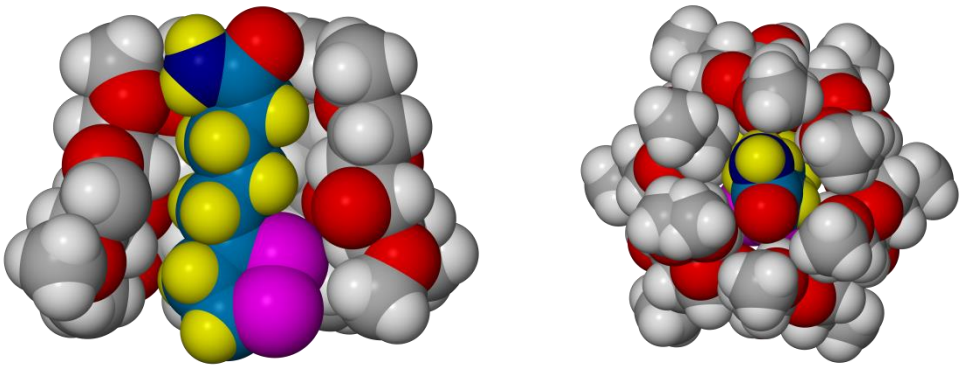

Fig. 5.26 Space-filling models of the inclusion of the guest in the host TMAALA as a cross-sectional view (left) and a view from the primary rim of the host molecule (right).

The geometrical parameters as described respectively by Harata[9] and Saenger[10] that were discussed in the introductory chapter used to define the host TRIMEA molecule are reported for TMAALA in Table 5.14. A slight ellipticity is indicated by the parameters *l* (distance from O4 to generated centroid of O4-hexagon), *D* (O4···O4′ distance) and ϕ (O4···O4′···O4′′ angle) values and can be observed in the O4-hexagon presented in Fig. 5.27. A comparison of the transannular distance O4G2···O4G5 (8.252 Å) (with direction roughly normal to the face of the included 5-membered ring) and O4G1···O4G4 (8.816 Å) or O4G3···O4G6 (8.735 Å) (with direction roughly parallel to the face of the included 5-membered ring) shows minor differences of 0.564 and 0.483 Å respectively. The ϕ values for G1 and G4 are larger than all the other ϕ angles and also indicates that the shape of the hexagon is irregular. These differences indicate how the shape of the host ring is slightly distorted to accommodate the guest molecule. There are many examples of similar occurrences and these are often explained as being the resultant of the phenomenon of 'mutual induced fit', where the conformations of smaller guest molecules induce a conformational change of the host and alter the eventual packing of the host, instead of only being influenced by the larger macromolecules.[53,54]

The τ_2 tilt angles all have positive values for TRIMEA in TMAALA and this indicates that all the glucopyranose rings are tilted inward towards the cavity on the primary methoxymethyl side. The combined (+)-gauche orientations of the C6-O6 bonds and the inward tilting of the glucose rings on the primary methoxymethyl side all indicate that the opening on this side of the host molecule is sterically congested, though it is observed that the guest molecule protrudes through this opening to interact with water molecules in the interstitial spaces in this structure.

Table 5.14 Geometric parameters describing the TRIMEA host molecule in TMAALA.

Residue	*l* (Å)	*D* (Å)	ϕ (°)	*d* (°)	τ_2 (°)
G1	4.427	4.365	124.0	2.0	23.0(1)
G2	4.139	4.412	118.5	-4.0	14.9(1)
G3	4.369	4.109	117.6	5.1	17.5(1)
G4	4.389	4.391	124.5	-3.5	7.7(1)
G5	4.113	4.298	118.6	1.0	16.4(1)
G6	4.366	4.238	116.6	-0.4	13.1(1)
Mean	4.30	4.30	120.0	0.0	15.4

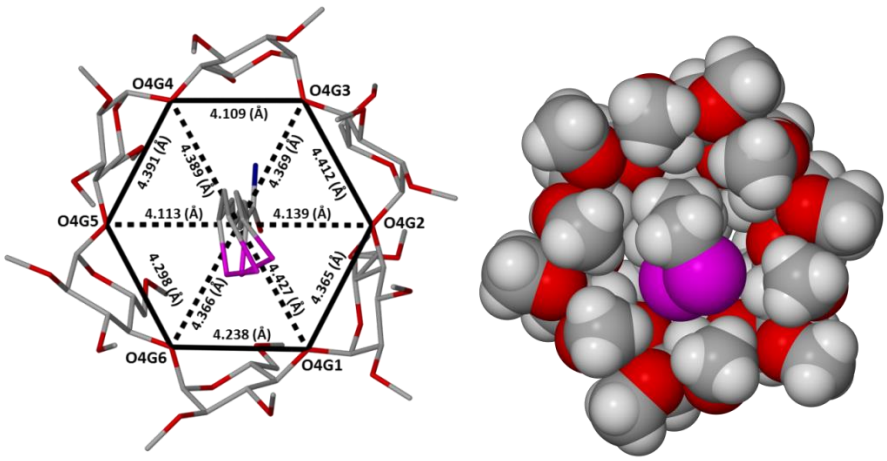

Fig. 5.27 The host molecule is displayed viewed from the secondary rim with the guest moiety visible as sticks with hydrogens omitted for clarity (left) and as space-filling model (right). Solid lines connect the respective O4 atoms of the various glucopyranose residues to show the slight ellipticity of the O4-hexagon and dotted lines connect the O4 atoms with a generated centroid. The values for the parameters *l* and *D* are presented in this figure.

Extended conformation of the aliphatic chain of the guest

The guest α-LA molecules maintain a linear conformation with the 1,2-dithiolane rings found at the secondary methoxyl rim of the host molecule and the amide moiety slightly protruding from the primary methoxymethyl rim. The five-membered rings of the major and minor disorder components are in envelope and twisted conformations respectively. The conformations of the guest components are overlayed in Fig. 5.28.

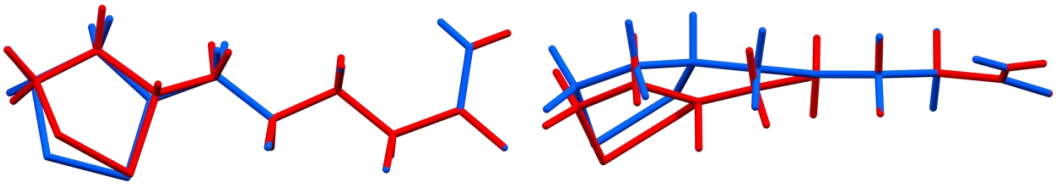

Fig. 5.28 Overlay of conformations of the major (blue) and minor (red) guest components representing the enantiomers of the guest in TMAALA viewed roughly normal to the 1,2-dithiolane rings (left) and roughly parallel to the rings (right).

Crystal packing and hydrogen bonding

The relevant symmetry information for TMAALA is listed in Table 5.15.

Table 5.15 Hydrogen bonds in TMAALA[a].

D–H···A	*d*(D–H), Å	*d*(H···A), Å	*d*(D···A), Å	∠(DHA), deg.
O1-H1A···O2	0.82(2)	2.05(2)	2.843(4)	165(4)
O1-H1B···O6G6 [i]	0.83(3)	2.06(3)	2.864(5)	165(4)
O2-H2A···O12	0.82(3)	1.97(3)	2.786(4)	177.4(8)
O2-H2B···O3G1 [ii]	0.82(2)	2.02(2)	2.833(4)	171(3)
O4-H4A···O2	0.81(3)	2.06(3)	2.868(4)	175(2)
O4-H4B···O6G3 [iii]	0.82(4)	2.12(4)	2.932(4)	170(4)
N11-H11A···O1	0.85(6)	2.19(6)	3.031(5)	174(6)
N11-H11B···O6G4	0.81(6)	2.36(5)	3.080(5)	148(5)
O5-H5A1···O3A	0.82(3)	1.96(2)	2.774(6)	171(4)
O5-H5B1···O3G4 [iv]	0.82(4)	2.29(4)	3.036(4)	151(4)
C6G3-H2···O5G4	0.99	2.53	3.357(4)	141
C6G1-H3···O5G2	0.99	2.35	3.260(4)	153
C9-H9A···O6G6	0.99	2.48	3.431(5)	161
C7G6-H13···O3G3 [v]	0.98	2.60	3.413(4)	140
C6G6-H6G1···O5G1	0.99	2.49	3.326(4)	142
C2G2-H2G2···O5G4 [vi]	1.00	2.58	3.569(4)	169
C3G1-H3G1···S1A	1.00	2.83	3.822(3)	171
C5G3-H5G3···O4G2	1.00	2.46	2.828(4)	101
C2G1-H2G1···O5G5 [vii]	1.00	2.55	3.388(4)	141
C9G6-H9G1···O6G1	0.98	2.58	3.504(5)	157
C2G4-H2G4···O6G2 [viii]	1.00	2.58	3.425(6)	142
C1G5-H1G5···O5 [ix]	1.00	2.55	3.493(5)	157
C6G5-H6G3···O5G6	0.99	2.53	3.431(4)	151
C6G4-H6G5···O5G5	0.99	2.52	3.430(4)	153
C2G5-H2G5···O5G1 [x]	1.00	2.38	3.339(4)	159
C5G2-H5G2···O4G1	1.00	2.43	2.849(5)	105
C8G4-H8G9···O2G4	0.98	2.51	3.105(5)	119
C7G3-H7G9···O3G6 [xi]	0.98	2.39	3.342(5)	164

[a] Symmetry transformations used to generate equivalent atoms: *[i]: -1/2+x,1/2-y,1-z;*

[ii]: 1-x,-1/2+y,1/2-z; [iii]: 1/2+x,1/2-y,1-z; [iv]: 1-x,-1/2+y,3/2-z; [v]: 1+x,y,z; [vi]: 1/2-x,1-y,-1/2+z; [vii]: 3/2-x,1-y,-1/2+z; [viii]: 1/2-x,1-y,1/2+z; [ix]: 1-x,1/2+y,3/2-z; [x]: 3/2-x,1-y,1/2+z; [xi]: -1+x,y,z.

The host molecules of TMAALA are packed into a cage-type monomeric brickwork arrangement (Fig. 5.29) where the individual cages are connected to form flat layers in the *ac*-plane.

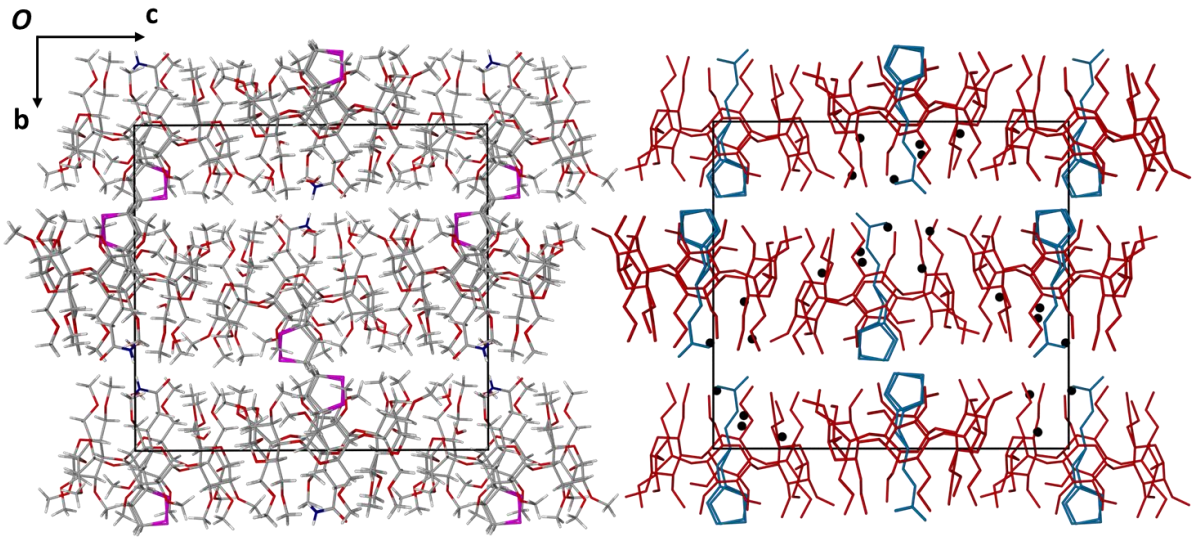

Fig. 5.29 Packing of TMAALA viewed along [100] showing water oxygens in black, host atoms in red and guest atoms in blue.

These layers are highly connected by intermolecular interactions between the host molecules. The topology of these layers as well as some of the interactions connecting host molecules in the same layers are presented in Fig. 5.30 (these interactions include: C7G6-H13···O3G3′; C2G2-H2G2···O5G4′; C2G1-H2G1···O5G5′; C2G4-H2G4···O6G2′; C2G5-H2G5···O5G1′; C7G3-H7G9···O3G6′). Many intramolecular host-host interactions can also be found and are shown in Fig. 5.30. Adjacent layers are shifted by *b*/2 + *c*/2 as is visible in Fig. 5.29 and 5.31.

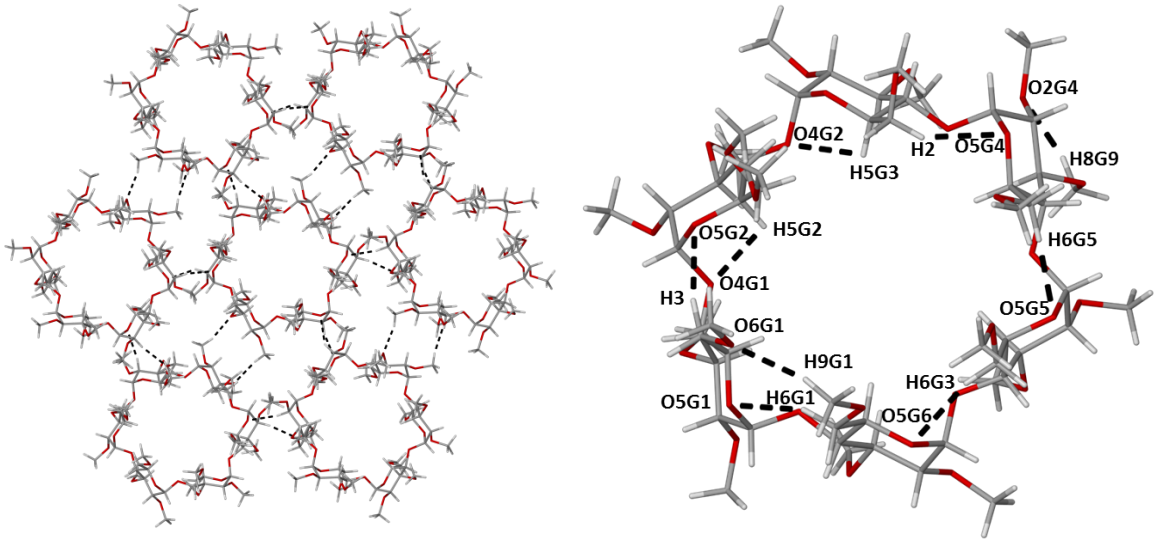

Fig. 5.30 Topology of a portion of a single layer of host molecules showing intermolecular host-host interactions (left). Intramolecular interactions of host molecule found in TMAALA (right).

The packing of TMAALA is shown viewed along [100] in Fig. 5.29, along [010] in Fig. 5.31 and along [001] in Fig. 5.32.

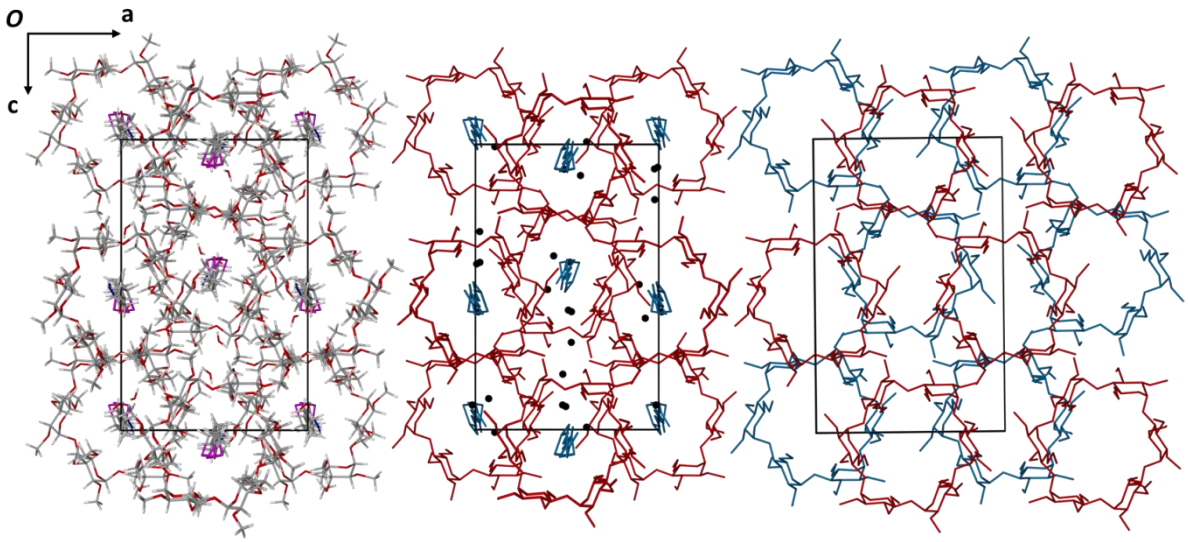

Fig. 5.31 Packing of TMAALA viewed along [010] showing water oxygens in black, host atoms in red and guest atoms in blue and staggered adjacent layers.

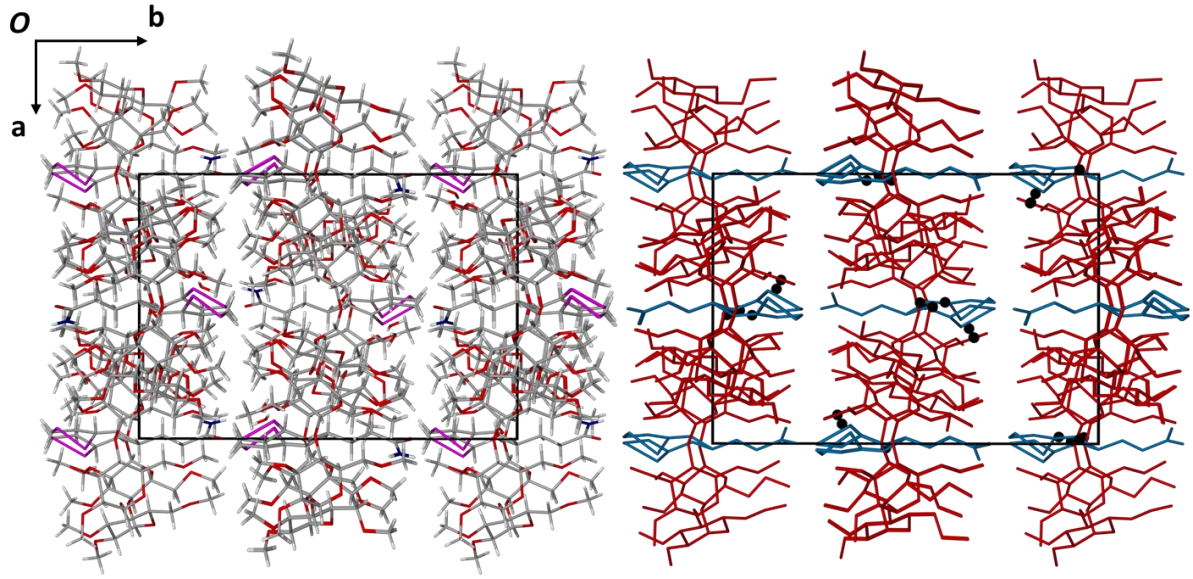

Fig. 5.32 Packing of TMAALA viewed along [001] showing water oxygens in black, host atoms in red and guest atoms in blue.

The way in which the guest molecules fit into the host cavities has been presented in earlier sections of this chapter in Figs. 5.24, 5.26 and 5.27. The narrow TRIMEA cavity firmly holds the α-LA guest with interactions including the following: a hydrogen bond connecting the amide moiety of the guest with a methoxyl oxygen atom at the primary rim of the host (N11-H11B···O6G4′), a host-guest interaction C9-H9A···O6G6′ and a host-guest interaction C3G1-H3G1···S1A′ (Fig. 5.33). The primary methoxymethyl rim of the host molecule has a narrow opening from which the amide moiety of the guest protrudes and interacts with water molecules situated in the interstitial space between the adjacent layers of the host (Fig. 5.33).

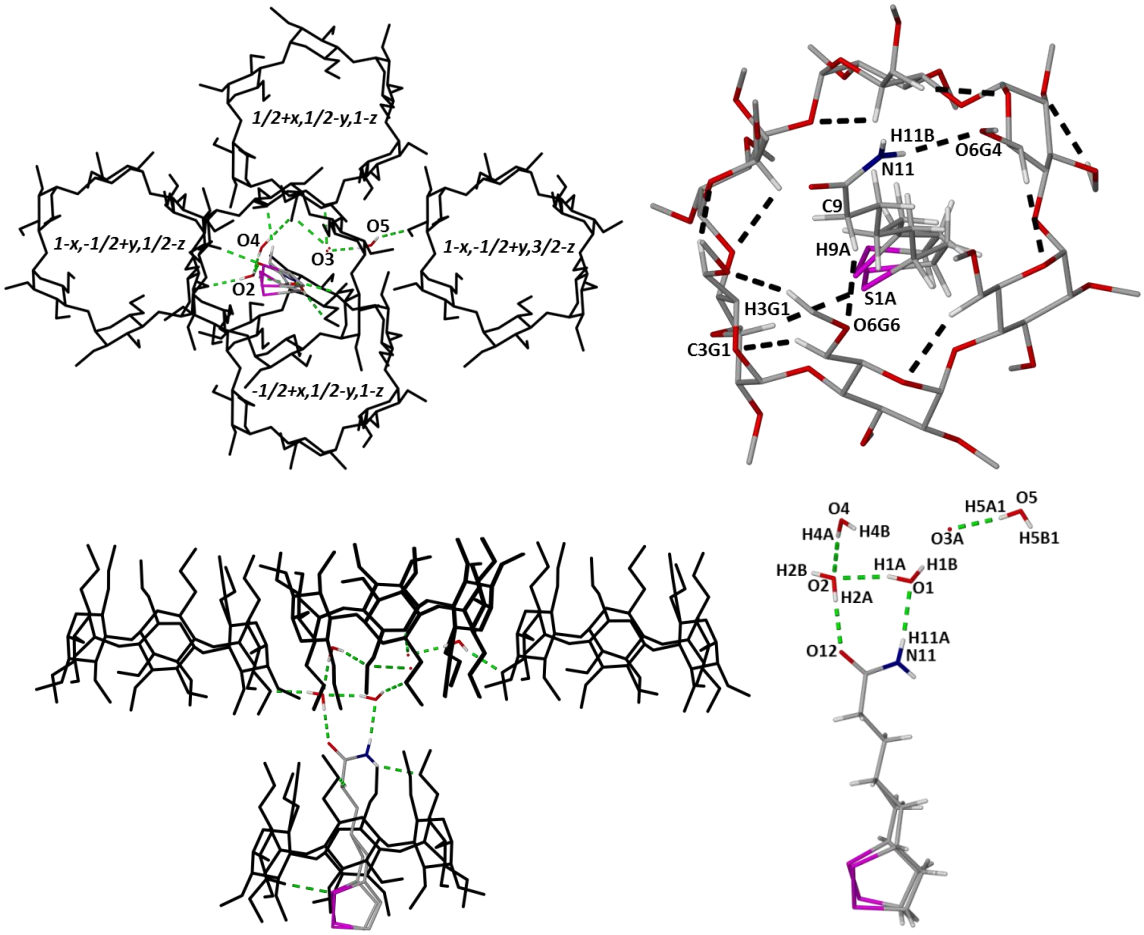

Fig. 5.33 Clockwise starting from top left: water-host, water-water and water-guest interactions connecting adjacent layers of host molecules, showing symmetry operations viewed from the secondary rim of the host in the asymmetric unit; host-guest interactions (non-interacting hydrogens of host omitted for clarity); intermolecular interactions connecting adjacent layers (side-view); water-guest and water-water interactions.

The water molecules form water-guest, water-host and water-water connections. The guest molecule is connected to two water molecules by the H-bonds N11-H11A···O1′ and O2-H2A···O12′. These water molecules are in turn H-bonded to host molecules forming the next layer of host molecules by the interactions O1-H1B···O6G6′ and O2-H2B···O3G1′. A water molecule containing the atom labelled O4 is H-bonded to the water molecule O2 (O4-H4A···O2′) and another host molecule of an adjacent layer (O4-H4B···O6G3′). Due to disorder of one water molecule, the oxygen atom components O3A and O3B were refined isotropically and no hydrogens were placed on these atoms. The atoms are situated at positions where H-bonding to surrounding molecules is feasible with atom to atom distances of O3B···O6G3 = 2.976 Å; O3A···O5G3 = 2.918 Å and an H-bond connecting another water molecule (O5-H5A1···O3A′). The water molecule containing the oxygen atom O5 also connects to an adjacent host molecule (O5-H5B1···O3G4′). These interactions with water molecules clearly play an important role in the formation of the complex and maintenance of its stability.

The unit cell data of complexes with similar packing found in a CSD[1] search of TMAALA and those of TMAALA are summarised in Table 5.16. In this instance the search criteria used for the other structures retrieved only one 'hit' and they were relaxed in order to find more complexes with similar packing. The lack of complexes with matching parameters highlights the rarity of this packing arrangement. A PXRD trace calculated from the single crystal structure of TMAALA is compared to a trace calculated from a structure with matching unit cell dimensions (a complex of TRIMEA with (R)-α-lipoic acid)[55] in Fig. 5.34. The PXRD traces show a striking resemblance and proves that these structures are isostructural in their packing.

Table 5.16 Comparison of structural parameters of TMAALA with known structures.

Space group	H:G:W*	a (Å)	b (Å)	c (Å)	Guest	CSD Refcode	Ref.
$P2_12_12_1$	1:1:5	15.165(2)	21.710(2)	23.566(3)	α-LA	TMAALA‡	NA
$P2_12_12_1$	1:1:6	15.189(1)	21.743(1)	23.458(1)	(R)-α-lipoic acid	CCDC 1524720	55
$C222_1$	1:1:3	15.571	21.116	23.187	(S)-mandelic acid	CECMAY11	56
$P2_12_12_1$	1:1:5.1	14.636(8)	21.637(1)	23.450(3)	(R)-1,7-dioxaspiro(5.5)undecane	QOYLEV	57

***Ratio of host : guest : water; ‡The compounds have not been submitted to the Cambridge Crystallographic Datacentre yet and the compound codes are those used throughout this thesis.**

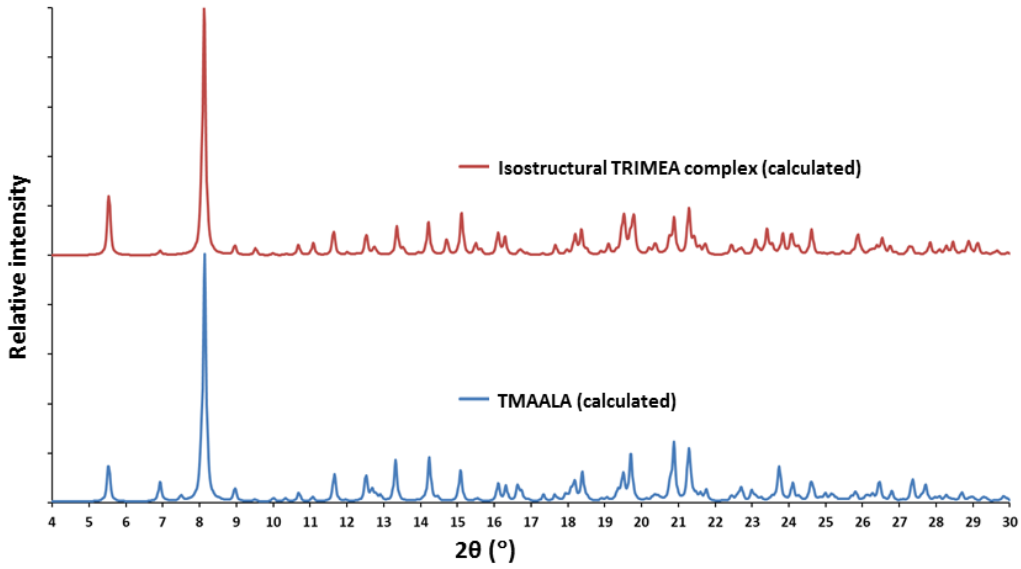

Fig. 5.34 Comparison of PXRD traces calculated from the single crystal structures of TMAALA and that of a complex with matching unit cell dimensions.

Thermal analysis

The HSM result for TMAALA is presented in Fig. 5.35. Bubbles were visible above 80 °C. A wide endotherm is visible in the DTA result (Fig 5.36) starting near the onset of heating and continues up to around 80 °C. This is most likely due to the loss of water from the crystal structure and correlates with the HSM result where bubbles were visible around the same temperature. Another endothermic event is visible with an onset of 117.1 ± 0.1 °C (n = 3) and a peak at 120.8 ± 0.4 °C (n = 3). Near this temperature the crystals in the HSM analysis had become opaque. The next endothermic event visible in the DTA trace has an onset of 174.5 ± 1.8 °C (n = 3) and a peak at 183.4 ± 0.4 °C (n = 3). This event is most likely due to the melting of TMAALA. The temperature at which the crystals in the HSM analysis appeared to melt was slightly higher than this temperature, where it only visibly started to melt at 200 °C and completely melted at 220 °C. The measured melt onset of TMA was 220.5 °C.

Fig. 5.35 Representative HSM micrographs of TMAALA at various temperatures.

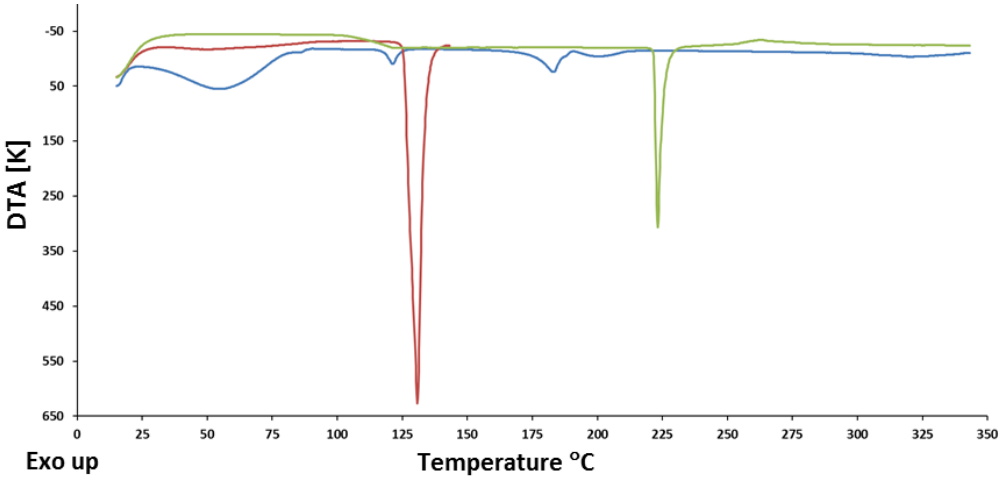

Fig. 5.36 Representative DTA thermograms of TMAALA (blue), TMA (green) and ALA (red).

The mass losses determined in the TGA experiments with TMAALA (Fig. 5.37) were as follows: for the first observed step from 20 to 100 °C, 5.74 ± 0.45 % (n = 3) with an onset temperature of 69.0 ± 2.7 °C (n = 3); for the second step from 180 to 300 °C, 13.41 ± 0.34 % (n = 3) with an onset temperature of 232.7 ± 4.8 °C (n = 3); for the third step from 300 to 400 °C, 77.25 ± 0.38 % (n = 3) with an onset temperature of 354.4 ± 4.4 °C (n = 3). The first mass loss matches the results recorded in the HSM and DTA analyses and is attributed to water loss. The second mass loss is most likely due to the gradual loss of the guest and the third step to the decomposition of the host. The values equate to a stoichiometric ratio of 4.8 ± 0.4:1.0 ± 0.1:1.0 of water to guest to host. This matches the host to guest ratio observed in the proton NMR (within experimental error) and single-crystal XRD results.

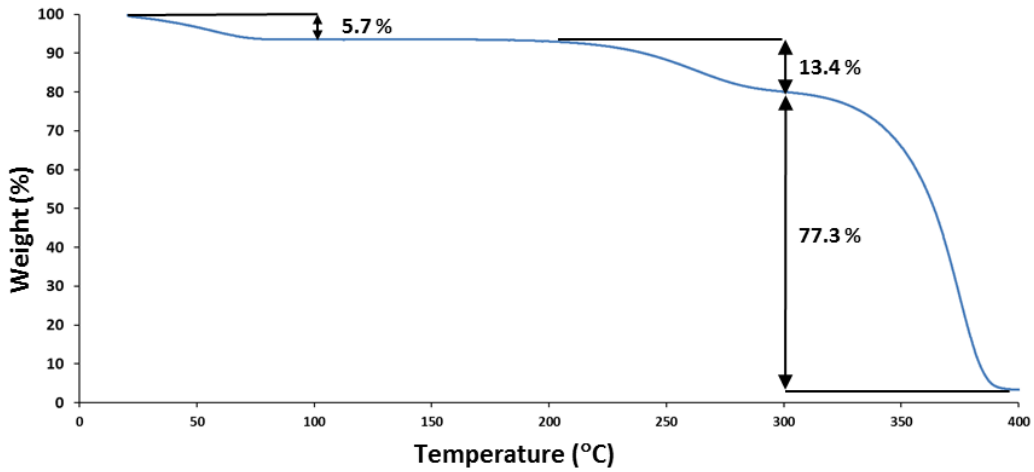

Fig. 5.37 Representative TGA trace of TMAALA.

DIMEB inclusion complex with (±) α-Lipoamide (DMBALA)

Single crystals of DMBALA were prepared by the following method. 5.000 mg of α-LA (≈ 0.024 mmol) was dissolved in 0.5 cm^{-3} of ethanol and an equimolar amount of DIMEB (32.722 mg ≈ 0.024 mmol) was dissolved in 2 cm^{-3} of distilled water. The solution of α-LA was added to the DIMEB solution and the resultant solution was stirred at room temperature for an hour before being filtered through a 0.45 µm nylon filter into a clean vial. The vial was placed in an oven at 60 °C and left uncapped for 45 minutes. After this time a cap was placed on the vial and the vial was left in an oven at 60 °C for several months before small crystals were observed. A representative specimen was selected for single-crystal X-ray data collection. Due to the limited amount of crystals produced and the time required for these crystals to form no thermal experimentation was carried out with DMBALA. The results of the crystal structure analysis will be described in the following section.

Crystal structure analysis

Data-collection and space group determination

X-ray intensity data for DMBALA were collected on a Bruker Kappa Apex II Duo diffractometer. The collection was carried out at a lower than usual temperature of 113(2) K to avoid deterioration of the crystal over a long period of exposure and also to minimise thermal motion of atoms during the collection. Laue symmetry *mmm* was observed, indicating that the crystal is orthorhombic. The space group was determined to be $P2_12_12_1$ from the conditions limiting possible reflections, namely *hkl: none, h00: h = 2n, 0k0: k = 2n, 00l: l = 2n*). The asymmetric unit contains one DIMEB molecule and a disordered α-LA molecule in a 1:1 ratio (Fig. 5.38).

Structure solution and refinement

Crystallographic data and parameters for collection of intensity data are reported in Table 5.17. The same method for structure solution and refinement that was described for BCDALA was used for DMBALA. After the initial refinement with SHELXD[14] the host atoms forming the backbone of the framework were made anisotropic and refined. Some of these atoms displayed a relatively high degree of thermal motion. The methoxy and hydroxyl groups of the host that were found in the Fourier difference map were placed and anisotropically refined. It was noticed that some atoms showed high thermal motion and these atoms were reverted to being isotropically refined. The glucopyranose subunits were labelled G1 to G7 (Fig. 5.38). A methyl group connected on the primary

rim of the host to the atom O6G3 was found to be disordered over two positions and isotropically refined (the major component showed a s.o.f. of 0.66(1)). Guest atoms showing the highest intensity were placed and refined, though the guest could not adequately be modelled due to a high degree of disorder. Host hydrogens that were observed in the difference electron density maps were placed in idealised positions using a riding model with isotropic temperature factors of 1.2 to 1.5 times that of the respective parent atoms.

Table 5.17 Data-collection and refinement parameters for DMBALA.

Molecular formula	$C_{56}H_{96}O_{35} \cdot C_8H_{15}NOS_2$*
Formula weight (g mol^{-1})	1534.65
Crystal system	Orthorhombic
Space group	$P2_12_12_1$
a (Å)	10.288(2)
b (Å)	15.325(3)
c (Å)	51.300(8)
α = β = γ (°)	90
V $(Å)^3$	8088(3)
Z	4
D_c (g cm^{-3})	1.260
μ (Mo Kα) (mm^{-1})	0.151
F(000)	3288
Data-collection temp. (K)	113(2)
Crystal size (mm^3)	0.08 x 0.18 x 0.21
Range scanned θ (°)	1.78 – 24.89
Index ranges ±*h*, ±*k*, ±*l*	-10, 12; -18, 9; -60, 60
Reflections (total)	34 936
Independent reflections	13 041
Reflections with I>2σ(I)	4933
Number of parameters	2257
R_{int}	0.1323
S	1.167
R_1 [*I*>2σ(*I*)]	0.1502
Reflections omitted	7
wR_2	0.4318
a, b in w = $1/[\sigma^2(F_o^2)+(aP)^2+(bP)]$	a = 0.2000; b = 0
$(\Delta/\sigma)_{mean}$	< 0.001
$\Delta\rho_{min,max}$ (e $Å^{-3}$)	-0.46, 0.97

*The molecular formula used is a nominal formula and the actual formula is unknown as the composition was not verified by complementary methods.

Due to the disorder and low accuracy of the crystal structure, the appended crystallographic data files (Appendix B) are limited to what is deemed necessary.

Molecular structure

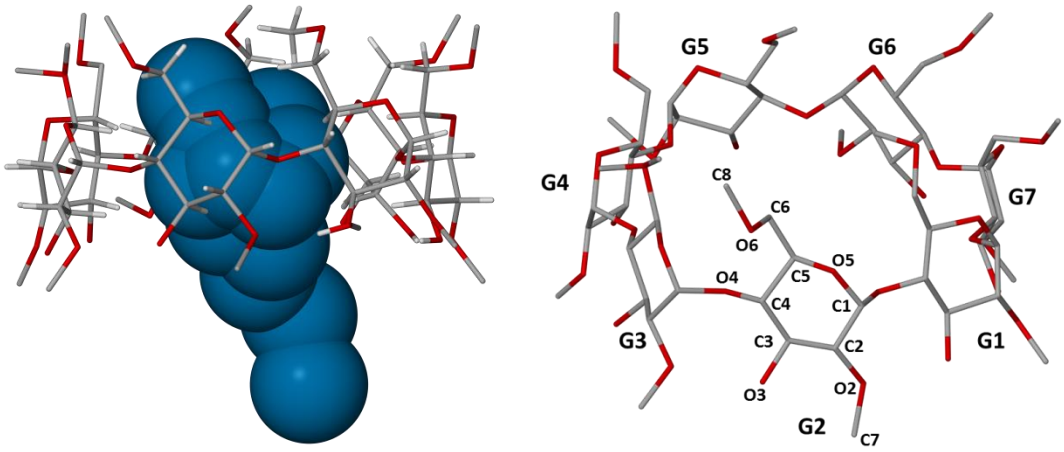

Fig. 5.38 The asymmetric unit of DMBALA showing the main peaks of the highly disordered guest as space-filling model in blue (left) and numbering scheme of the host molecule (right).

Geometrical analysis of DMBALA

Conformation of the host

The O5-C5-C6-O6 torsion angles (ω) of DIMEB in DMBALA are presented in Table 5.18. The ω values are negative for all but two of the glucopyranose units. This shows that only the methoxyl groups on units G1 and G5 (and the minor disorder component of G3) are pointed toward the cavity of the macrocycle with all the others pointed away. The result is that the aperture on the primary side of the host molecule is left mostly open. All of the O2-C7 methoxyl groups on the secondary rim are directed outward, away from the cavity. The other geometrical parameters describing the host configuration are summarised in Table 5.19. The *l, D* and ϕ values are all within narrow ranges indicating that the shape is roughly round and symmetrical, as is common for the somewhat rigid DIMEB host. A factor that is usually predominantly responsible for the symmetrical, rigid, round shape is the O3-H···O2′ hydrogen bonding interactions that connect contiguous glucose units. A high degree of thermal motion was observed, as is visible in Fig. 5.39 showing the thermal ellipsoids at the 50% probability level for anisotropic atoms. The observed thermal motion raises doubt in the accuracy of the described geometrical parameters, though the general conformational description should be true. The structure proved to be isostructural with a DIMEB complex containing the phenylurea herbicide cycluron[58] and the respective host molecules are overlayed to facilitate comparison in Fig. 5.39. Some differences in the conformations are visible.

Table 5.18 Torsion angles O5-C5-C6-O6 (ω) of host DIMEB in DMBALA.

Glucopyranose residue	Torsion angle ω (°)	(+) or (-) – gauche conformation	Torsion angle ω (°) of the minor disorder component	(+) or (-) – gauche conformation
G1	64.3(2)	(+)		
G2	-64(2)	(-)		
G3	-64(3)*	(-)	21.5	(+)
G4	-77(2)	(-)		
G5	71(2)	(+)		
G6	-69.6(2)	(-)		
G7	-66.2(2)	(-)		

*Major disorder component

Table 5.19 Geometric parameters describing the DIMEB host molecule in DMBALA.

Residue	*l* (Å)	*D* (Å)	ϕ (°)	*d* (°)	τ_2 (°)
G1	5.024	4.362	127.7	-3.1	14(1)
G2	5.065	4.264	129.4	6.9	11(1)
G3	4.976	4.510	128.7	1.0	8(1)
G4	5.012	4.348	126.0	-10.1	27(1)
G5	5.131	4.343	129.4	7.9	12(1)
G6	4.989	4.399	129.3	2.1	4.7(5)
G7	4.959	4.305	128.5	-4.3	22.5(6)

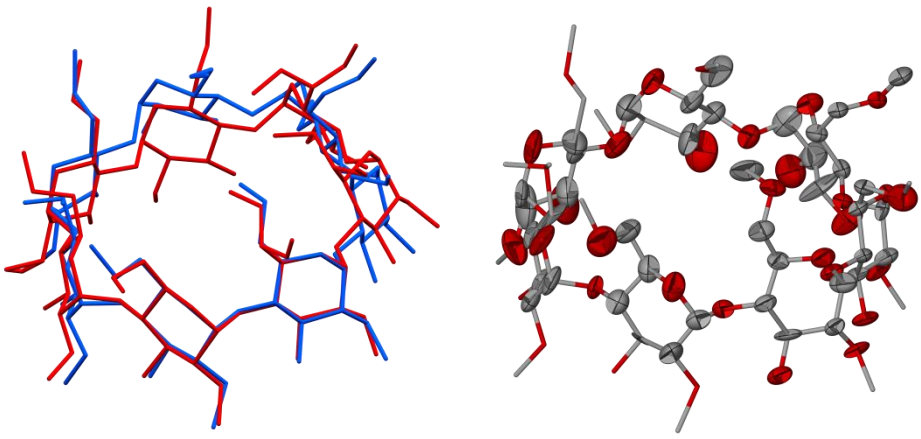

Fig. 5.39 Comparison of conformation of the DIMEB host in DMBALA (blue) and an isostructural complex from the CSD[1] (CSD refcode: OYAPAG)[58] (red) (left) and the thermal ellipsoids shown at the 50% probability level for anisotropic atoms of the host DIMEB molecule of DMBALA indicating high thermal motion (right).

Crystal packing and hydrogen bonding

DMBALA has a monomeric, herringbone-type packing arrangement of the host (Fig. 5.40). Infinite columns running along the a-axis are formed by DIMEB molecules packed in a head-to-tail manner (Fig. 5.40 and 5.41). The columns line up to form sheets parallel to the [001] plane (Fig. 5.42). A closed off cage is formed for each guest molecule due to the O4-planes of the host molecules being inclined to the direction of the a-axis causing the opening on the primary and secondary sides of the host to align with the rim of the next CD molecule in the column in either direction. The cavity is thus mostly closed off by adjacent host molecules.

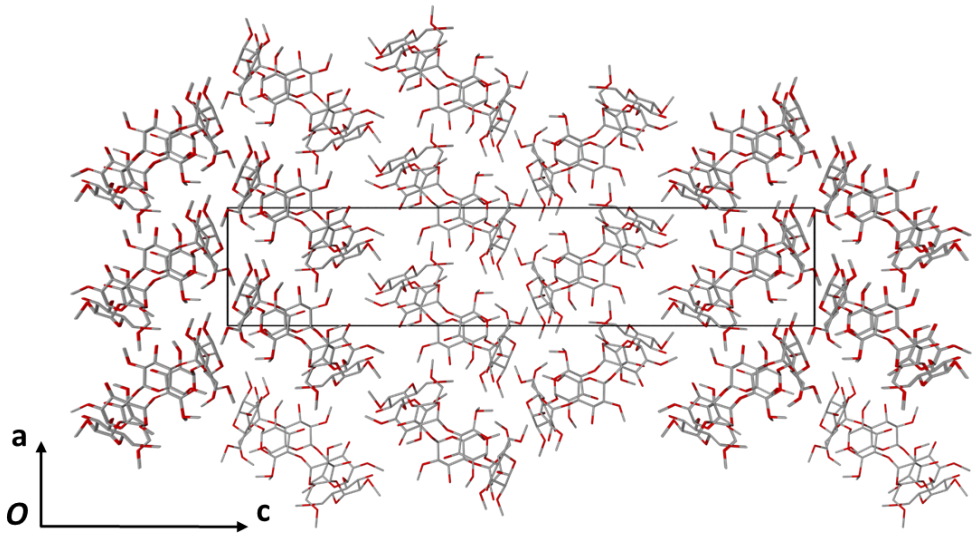

Fig. 5.40 Packing of DMBALA viewed along [010] showing the herringbone-type packing arrangement of the host (guest omitted).

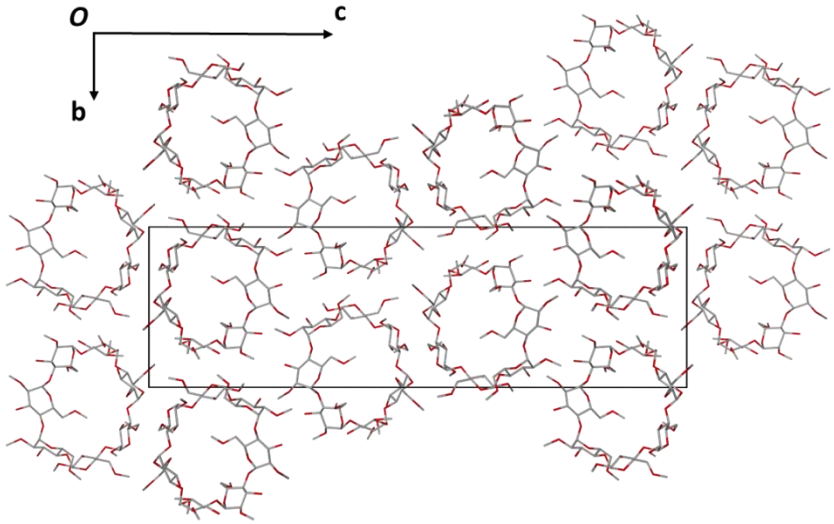

Fig. 5.41 Packing of DMBALA viewed along [100] showing infinite columns running parallel to the a-axis (guest omitted).

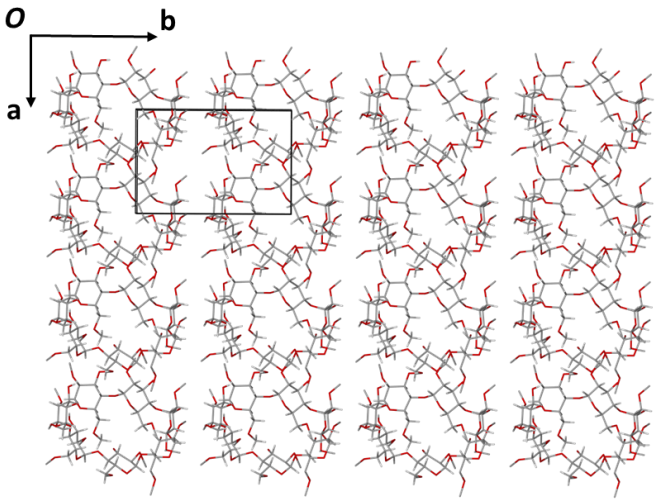

Fig. 5.42 Packing of DMBALA viewed along [001] showing a single sheet running parallel to the [001] plane made up of adjacent columns (guest omitted).

The unit cell data of isostructural complexes found in a CSD[1] search (with the same criteria as described for those used for BCDALA) of DMBALA are summarised in Table 5.20. This packing arrangement is also fairly uncommon. PXRD traces were calculated from the complexes in Table 5.20 and compared to the PXRD trace calculated from the single crystal structure of DMBALA and are presented in Fig. 5.43. The main peaks match, though there are clear differences. It is important to keep in mind that the traces of the other four complexes are with different guests and hence some differences are to be expected.

Table 5.20 Comparison of structural parameters of DMBALA with a known structures.

Space group	H:G:W*	a (Å)	b (Å)	c (Å)	Guest	CSD Refcode	Ref.
$P2_12_12_1$	1:1:0	10.288(2)	15.325(3)	51.300(8)	α-LA	DMBALA‡	NA
$P2_12_12_1$	1:1:2.9	10.387(2)	15.092(3)	51.862(1)	cycluron	OYAPAG	58
$P2_12_12_1$	1:1:3.7	10.601(1)	15.476(2)	48.244(6)	methyl paraben	VOFJUW	59
$P2_12_12_1$	1:1:4	10.656(1)	15.307(1)	49.042(1)	ethyl paraben	VOFKAD	59
$P2_12_12_1$	1:1:1	10.776(1)	15.108(4)	49.029(1)	n-butylacrylate	QAZYEV	60

***Ratio of host : guest : water; ‡The compounds have not been submitted to the Cambridge Crystallographic Datacentre and the compound codes are those used throughout this thesis.**

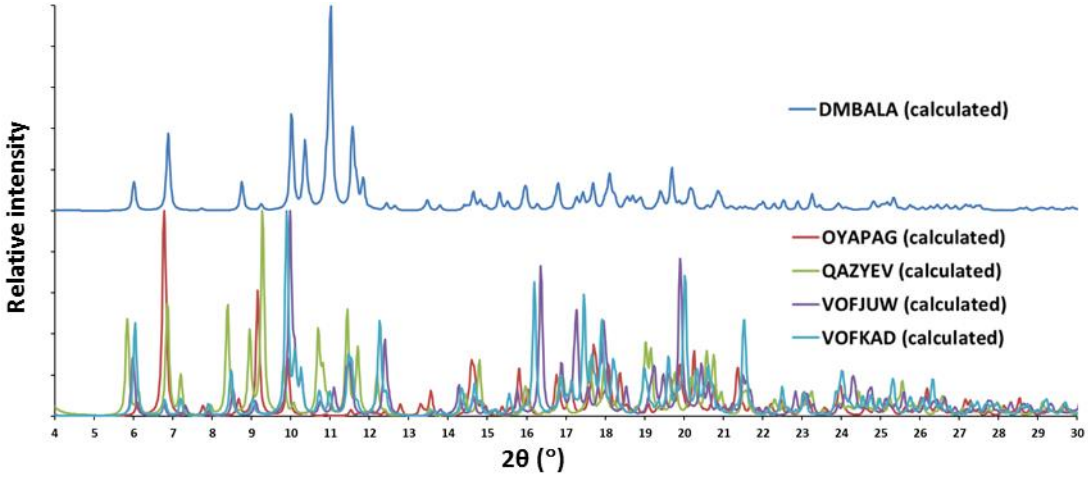

Fig. 5.43 Comparison of PXRD traces calculated from the single crystal structure of DMBALA and of a series of DIMEB inclusion complexes.

TRIMEB inclusion complex with (±)-α-lipoamide (TMBALA)

Preparation of complex

The same method of co-precipitation was employed as that used for obtaining the TMAALA complex. The only difference was that the solution was filtered after the heating cycle instead of after cooling. Block-like crystals formed after a few weeks.

Stoichiometry determination of TMBALA by ^{1}H – NMR spectroscopy

^{1}H-NMR spectroscopy was employed to determine the stoichiometric ratio of host to guest in single crystals of TMBALA. The labelling schemes of the individual components are presented with the resulting spectrum in Fig. 5.44. The integration values are reported in Table 5.21. The C-H_1 proton signal integration of TRIMEB was used as the reference integral and the host to guest ratio was determined to be 1:1.

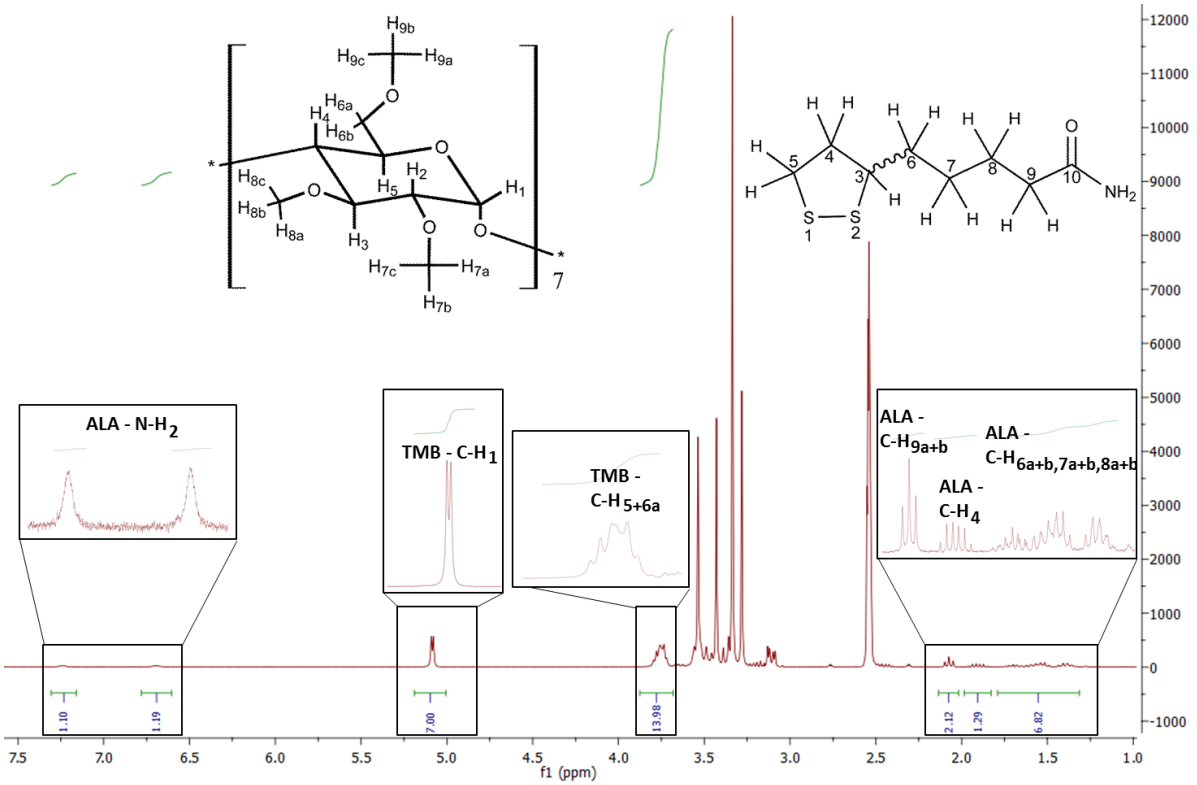

Fig. 5.44 ^{1}H-NMR spectrum of TMBALA in DMSO-d_6 for determination of stoichiometry.

Table 5.21 Integrals of protons for individual components to determine stoichiometry of TMBALA.

Proton – [Number of protons]	δ (ppm)	Integration	Experimental/ Theoretical
TRIMEB			
C-H_1 – [7]	5.00-5.19	7.00*	1.00
C-H_5 + C-H_{6a} – [14]	3.68-3.87	13.98	1.00
α-LA			
C-H_{9a+b} – [2]	2.02-2.13	2.12	1.06
C-H_{6a+b} + C-H_{7a+b} + C-H_{8a+b} – [6]	1.31-1.79	6.82	1.14
C-H_4 – [1]	1.83-1.98	1.29	1.29
N-H – [1]	6.60-6.78	1.19	1.19
N-H – [1]	7.16-7.31	1.10	1.10

*** Reference integral**

Crystal structure analysis

Data-collection and space group determination

The X-ray intensity data for the complex TMBALA were collected on a Bruker Kappa Apex II Duo diffractometer at 173(2) K. The X-ray diffraction displayed *mmm* Laue symmetry signifying that the crystal belongs to the orthorhombic crystal system. The space group was determined to be $P2_12_12_1$ from the systematic absences *hkl: none, h00: h = 2n + 1, 0k0: k = 2n +1, 00l: l = 2n +1*). The asymmetric unit contains TRIMEB and α-LA molecules in a 1:1 ratio and two water molecules.

Structure solution and refinement

Crystallographic data, parameters for collection of intensity data and refinement details are reported in Table 5.22. The method of isomorphous replacement[8] was used to solve the structure of TMBALA. The host co-ordinates of an isostructural complex found in the CSD[1] (Refcode: RONWOG)[61] were used as a skeletal framework for a trial model. The primary methoxy and secondary methyl groups of the host molecule were omitted before the initial refinement was performed. After subsequent refinement steps the atoms of these groups were found in the difference electron density maps and placed in these positions. The non-hydrogen atoms of the host were labelled from G1 to G7 for the comprising glucopyranose units as shown in Fig. 5.44. All the non-hydrogen host atoms were then refined anisotropically. Host hydrogens that were observed in the difference electron density maps were placed in idealised positions using a riding model with isotropic temperature factors of 1.2 to 1.5 times those of the respective parent atoms. The guest atoms that were visible in the Fourier difference map were added in a piecemeal fashion starting from the pentanamide chain of the guest molecule. The 1,2-dithiolane ring and the first carbon connecting it to the pentanamide chain of the guest was found to be disordered over two positions and for this reason was split into different parts with s.o.f.s of *x* and *1-x* assigned to the respective major and minor disorder components. The other guest atoms from C7 to O12 (see Fig. 5.44 for labelling scheme) were shared between the different components and were refined anisotropically. In order to maintain reasonable geometry of the 1,2-dithiolane rings, some distance constraints were applied. Hydrogen atoms were then added to the guest molecule in idealised positions using a riding model with isotropic temperature factors of 1.2 to 1.5 times those of the respective parent atoms. The final *x* value for the major disorder component after refinement was 0.59(1). The major and minor components represent the (R)- and (S)-enantiomers of the guest respectively, indicating low enantiomeric selectivity. Two positions showed residual electron density in the Fourier electron density maps that were not related to the host or guest molecules and the peaks were assigned as oxygen atoms as these were presumed to

be water molecules, based on their distances from the host molecule. One of these oxygen atoms (O1) was refined anisotropically and the hydrogens that were observed in the electron density maps in H-bonded positions were placed with distance constraints applied. The other oxygen atom (O2) was refined isotropically. One of the hydrogens was found in the Fourier difference map and placed whereas the other hydrogen was not observed in the difference map, but placed in a position where H-bonding was most likely. The O2 water oxygen atom was at a donor-to-acceptor distance of 3.114(9) Å from the atom O5G3. Distance constraints were applied to these hydrogens and after refinement the final H-O-H angle was 111° with a donor-hydrogen-acceptor angle of 170(5)° and a O2-H2A···O5G3 distance of 2.31(4) Å. Water hydrogens were assigned thermal parameters of 1.2 times the thermal displacement values of their parent oxygen atoms.

Table 5.22 Data-collection and refinement parameters for TMBALA.

Molecular formula	$C_{63}H_{112}O_{35} \cdot C_8H_{15}NOS_2 \cdot 2(H_2O)$
Formula weight (g mol^{-1})	1670.88
Crystal system	Orthorhombic
Space group	$P2_12_12_1$
a (Å)	15.217(2)
b (Å)	20.663(2)
c (Å)	27.814(3)
α = β = γ (°)	90
V (Å)^3	8745.4(2)
Z	4
D_c (g cm^{-3})	1.269
μ (Mo Kα) (mm^{-1})	0.147
F(000)	3600
Data-collection temp. (K)	173(2)
Crystal size (mm^3)	0.42 x 0.47 x 0.60
Range scanned θ (°)	1.22 – 27.99
Index ranges ±*h*, ±*k*, ±*l*	-20, 20; -27, 27; -36, 36
Reflections (total)	18 9877
Independent reflections	20 913
Reflections with I>2σ(I)	17 661
Number of parameters	1032
R_{int}	0.0419
S	1.019
R_1 [$I > 2\sigma(I)$]	0.0603
Reflections omitted	2
wR_2	0.1777
a, b in w = 1/[$\sigma^2(F_o^2)$+(aP)^2+(bP)]	a = 0.1084; b = 4.7017
$(\Delta/\sigma)_{mean}$	< 0.001
$\Delta\rho_{min,max}$ (e Å^{-3})	-1.02, 1.01

Molecular structure

The asymmetric unit and labelling scheme of TMBALA are shown in Fig. 5.44.

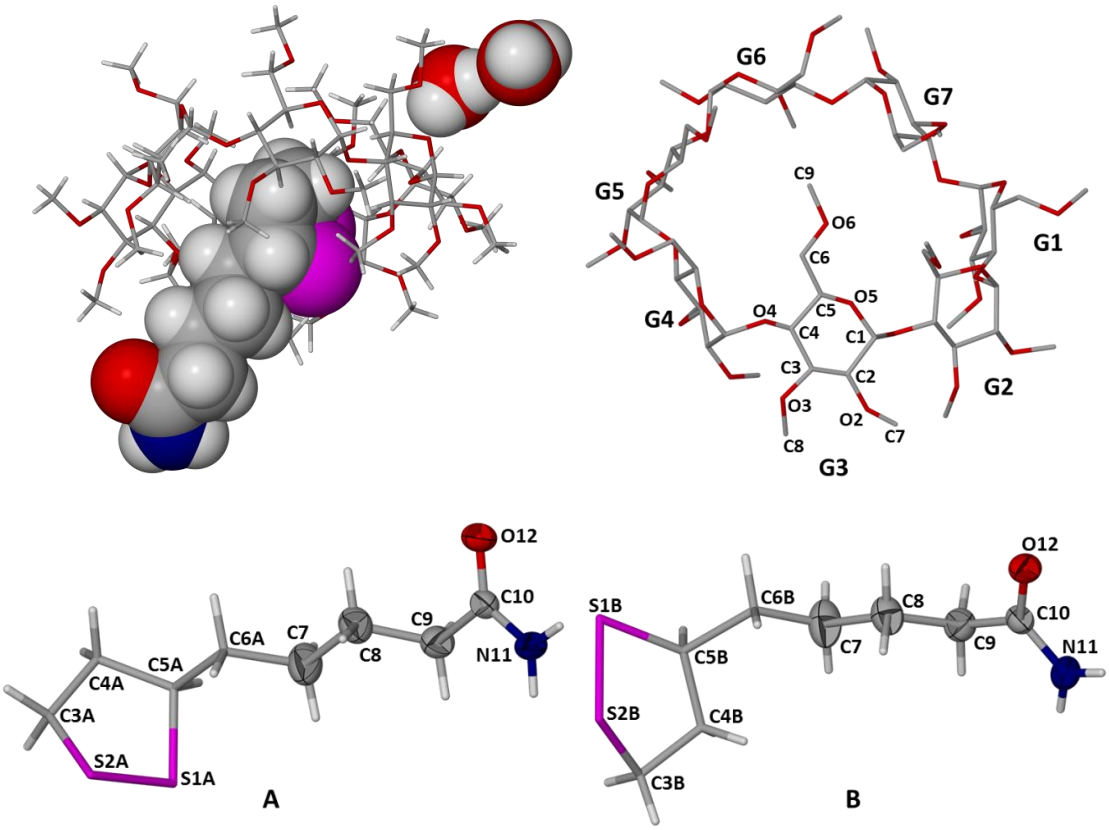

Fig. 5.44 The asymmetric unit of TMBALA (left) and numbering scheme of the host molecule (right). The numbering scheme of the guest molecules with the respective enantiomers (R)- and (S)- labelled A and B respectively with thermal ellipsoids shown at the 50% probability level for anisotropic atoms (bottom).

Geometrical analysis of TMBALA

Conformation of the host

The torsion angles O5-C5-C6-O6 (ω) representing (+) or (-)–gauche relationship of the C5-O5 and C6-O6 bonds of the methoxymethyl groups on the primary rim of the TRIMEB host molecules are reported in Table 5.23. The glucose residues G3 and G5 have positive ω values indicating a (+)–gauche conformation and hence that the methoxymethyl groups are pointed inward, towards the host cavity. All the other glucose residues (G1, G2, G4, G6 and G7) show a (-)–gauche conformation with the methoxymethyl groups pointing away from the host cavity. A space-filling model of the guest included within the host is shown in Fig. 5.45. This figure shows that the host cavity is closed off on the side of the primary rim by the methoxymethyl groups. The methoxymethyl

groups form a concave hydrophobic 'lid' that holds the 1,2-dithiolane ring of the guest at the primary rim side of the host.

Table 5.23 Torsion angles O5-C5-C6-O6 (ω) of host TRIMEB in TMBALA.

Glucopyranose residue	Torsion angle ω (°)	(+) or (-)–gauche conformation
G1	-79.3(4)	(-)
G2	-75.8(3)	(-)
G3	81.9(4)	(+)
G4	-62.2(4)	(-)
G5	75.5(4)	(+)
G6	-74.9(4)	(-)
G7	-66.6(4)	(-)

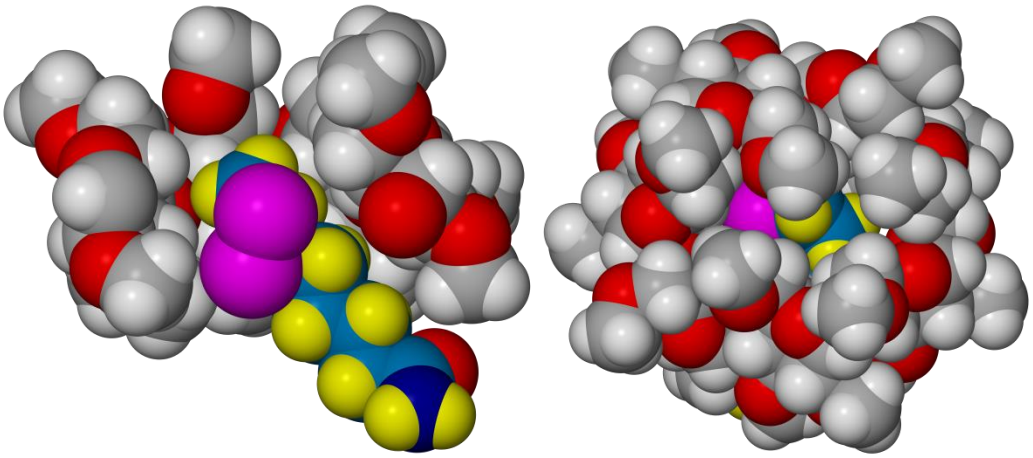

Fig. 5.45 Sapce-filling models of the guest inclusion mode in the host of TMBALA as a cross-sectional view (left) and a view from the primary rim of the host molecule (right).

The geometrical parameters used to describe the conformation of TRIMEB in TMBALA are reported in Table 5.24 and are represented in Fig. 5.46. The glucopyranose units are tilted in relation to the heptagonal O4 plane as revealed by the variation in torsion angles (*d*) and large tilt angles (τ_2). The tilting of the glucopyranose residues along with wide variation in the other parameters such as the O4···O4′···O4″ angles (ϕ) (119.2 – 140.9°), the O4···O4′ distance (*D*) (4.305 – 4.517 Å) and the distance from O4 to the generated centroid of the O4 atoms (*l*) (4.537 – 5.305 Å) results in the host having a saddle-like curvature. The positive τ_2 values also indicate that the gluopyranose residues are tilted in such a way that the primary rim of the host is inclined towards the cavity, resulting in the closing off of this end of the cavity to form the 'lid' described previously.

The conformation of TRIMEB in TMBALA is in good agreement with that of TRIMEB in the isostructural complex used for isomorphous replacement (CSD[1] refcode: RONWOG)[61] as can be seen

in Fig. 5.47 where these structures are overlayed. There are clear differences between the conformation of the host complexed with water alone and the conformation of the host in TMBALA. The conformation of 'free' TRIMEB, i.e. TRIMEB complexed with water alone as a monohydrate, is described as having a somewhat collapsed structure.[62] The same differences were observed and described for the isostructural complexes of TRIMEB with the drug ibuprofen[61] and TRIMEB with the drug (S)-naproxen.[63] In these examples as well as for TMBALA the glucopyranose residues were in the $^4C_1$ chair conformation, whereas in the case of the 'free' host, one of these residues was in the $^1C_4$ conformation. The result is that for the 'free' host the hydrophobic cavity is collapsed in order to minimise the free space that would be taken up by a hydrophobic guest in the case of complexes with larger guest molecules.

Table 5.24 Geometric parameters describing the TRIMEB host molecule in TMBALA.

Residue	*l* (Å)	*D* (Å)	ϕ (°)	*d* (°)	τ_2 (°)
G1	5.239	4.368	119.2	-17.8	36.5(1)
G2	5.238	4.350	140.9	-12.7	45.3(1)
G3	4.537	4.517	122.3	19.9	10.7(1)
G4	5.113	4.305	122.7	6.1	17.9(1)
G5	5.305	4.406	127.9	-30.5	28.7(1)
G6	4.904	4.451	134.3	9.7	46.0(1)
G7	4.685	4.318	122.9	19.8	10.1(1)
Mean	5.00	4.39	127.2	-0.8	27.9

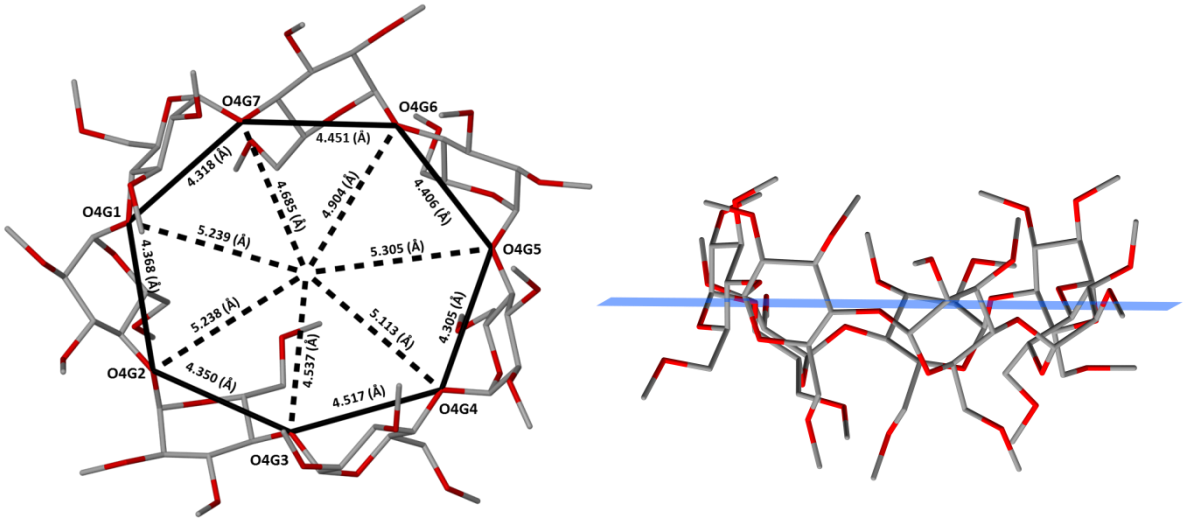

Fig. 5.46 The host TRIMEB molecule in TMBALA is displayed viewed from the secondary face with hydrogens omitted for clarity. Solid lines connect the respective O4 atoms of the various glucospyranose residues to show an O4-heptagon and dotted lines connect the O4 atoms with a generated centroid showing *l* and *D* values (left). The saddle-like shape of this molecule can be seen and the mean O4 plane is shown to illustrate the deviations of the O4 atoms of TRIMEB in TMBALA from this plane (right).

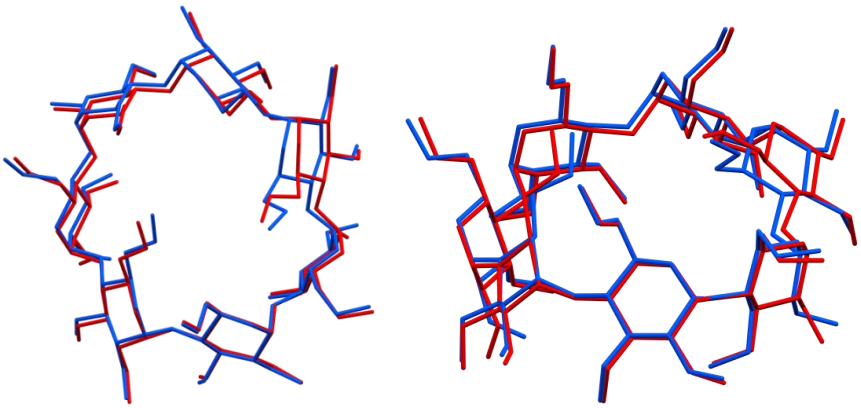

Fig. 5.47 Comparison of the conformation of the TRIMEB host in TMBALA (blue) and in a complex used for isomorphous replacement (CSD[1] refcode: RONWOG)[61] (red) viewed roughly from the primary face (left) and roughly side-on (right).

Extended conformation of the aliphatic chain of the guest

The solved crystal structure of TMBALA showed that the respective (R)- and (S)- α-LA enantiomers were included in the complex with low enantiomeric selectivity. The conformations of the components of the disordered guest molecule are presented in Fig. 5.48. The pentanamide chains are reasonably linear with the 1,2-dithiolane moieties bent away from this line resulting in the shape of the guest being slightly more contorted than in the case of TMAALA. The torsion angles C7-C6A-C5A-S1A and C7-C6B-C5B-S1B are 80.3(2)° and -169.6° respectively for the guests in TMBALA. The torsion angles in the case of TMAALA were 27.8(8)° for C7-C6A-C5A-S1A and 6.6° for C7-C6B-C5B-S1B. The puckered conformations of the 1,2-dithiolane rings showed a twisted conformation on S1A-S2A and an envelope in the case of S1B-S2B.

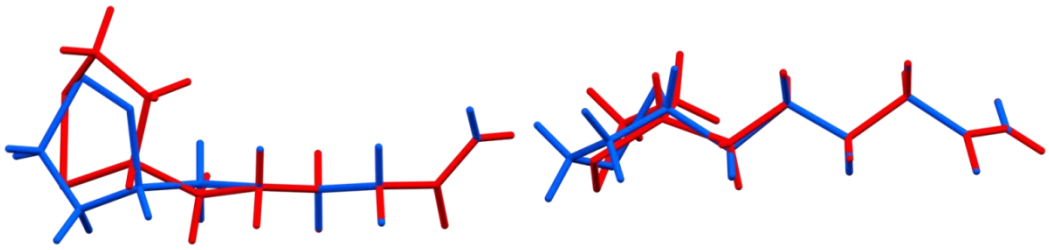

Fig. 5.48 Overlay of conformations of the major (blue) and minor (red) guest components representing the (R)- and (S)-enantiomers of the guest in TMBALA viewed roughly normal to the 1,2-dithiolane rings (left) and roughly parallel to the rings (right).

Crystal packing and hydrogen bonding

The relevant symmetry information for TMBALA is listed in Table 5.25.

Table 5.25 Hydrogen bonds in TMBALA[a].

D–H···A	*d*(D–H), Å	*d*(H···A), Å	*d*(D···A), Å	∠(DHA), deg.
N11-H11A···O6G7 [i]	0.88	2.15	3.000(5)	163
N11-H11B···O5G4 [ii]	0.88	2.25	3.029(5)	147
O1-H1A···O12 [iii]	0.82(3)	1.99(4)	2.808(6)	170(8)
O1-H1B···O3G5 [iv]	0.82(5)	2.01(4)	2.808(5)	165(6)
O2-H2A···O5G3	0.82(5)	2.31(4)	3.114(9)	170(5)
O2-H2B···O1	0.82(3)	2.063(2)	2.878(9)	173(9)
C1G1-H1G1···O3G7	1.00	2.48	3.134(4)	123
C4G1-H4G1···O6G1	1.00	2.58	2.940(4)	101
C8G7-H6···O2G7	0.98	2.40	3.044(5)	122
C6G1-H6G8···O5G2	0.99	2.37	3.163(5)	137
C9G1-H10···O5G1	0.98	2.50	3.137(6)	122
C9G1-H10···O3G3 [v]	0.98	2.49	3.098(6)	120
C8G1-H8G7···O4G1	0.98	2.55	3.133(5)	118
C1G2-H1G2···O6G1	1.00	2.44	3.232(4)	136
C2G2-H2G2···O6G6 [vi]	1.00	2.33	3.294(5)	161
C4G2-H4G2···O6G2	1.00	2.39	2.782(4)	102
C6G2-H20···O5G3	0.99	2.38	3.085(4)	128
C6G2-H20···O6G3	0.99	2.47	3.407(5)	157
C6G5-H21···O5G6	0.99	2.44	3.370(5)	156
C5G3-H5G3···O4G2	1.00	2.46	2.810(4)	100
C6G3-H6G9···O4G3	0.99	2.57	2.967(5)	104
C8G3-H8G6···O2G3	0.98	2.55	3.049(6)	111
C1G4-H1G4···O3G3	1.00	2.36	3.031(5)	124
C2G4-H2G4···O3G7 [vii]	1.00	2.56	3.511(5)	159
C6G4-H6G2···O5G5	0.99	2.28	3.145(5)	146
C7G4-H7GC···O4G3	0.98	2.59	3.16(1)	117
C8G4-H8GX···O2G5	0.98	2.50	3.261(7)	134
C5G5-H5G5···O4G4	1.00	2.45	2.812(4)	100
C7G5-H7G5···O2G6 [viii]	0.98	2.59	3.514(7)	158
C1G6-H1G6···O6G1 [ix]	1.00	2.53	3.502(4)	164
C2G6-H2G6···O5G2 [ix]	1.00	2.55	3.424(4)	145
C5G6-H5G6···O4G5	1.00	2.40	2.783(4)	102
C6G6-H6G4···O5G7	0.99	2.37	3.086(5)	129
C1G7-H1G7···O6G6	1.00	2.56	3.156(5)	118
C2G7-H2G7···O6G4 [v]	1.00	2.53	3.528(5)	175
C5G7-H5G7···O4G6	1.00	2.33	2.769(5)	105
C9G7-H9G2···O12 [x]	0.98	2.56	3.411(7)	145
C8-H8A···O2G1	0.99	2.57	3.560(6)	174

[a] Symmetry transformations used to generate equivalent atoms: *[i]: 1-x,-1/2+y,1/2-z;*

[ii]: 2-x,-1/2+y,1/2-z; [iii]: 2-x,1/2+y,1/2-z; [iv]: 5/2-x,1-y,-1/2+z; [v]: -1+x,y,z; [vi]: 3/2-x,1-y,-1/2+z; [vii]: 1+x,y,z; [viii]: 1/2+x,1/2-y,1-z; [ix]: 3/2-x,1-y,1/2+z; [x]: 1-x,1/2+y,1/2-z.

As was described in previous sections, the 1,2-dithiolane rings of the guest molecules are situated in the hydrophobic cavities of the host molecules with the primary rim closed off to form a 'lid'. The other end of the guest extends past the secondary rim of the host molecule and forms connections with adjacent host molecules (N11-H11A···O6G7′ and N11-H11B···O5G4′) and a water molecule (O1-H1A···O12′) (Fig. 5.49). The guest is linked to the host molecule of the asymmetric unit by C8-H8A···O2G1′ (Fig. 5.50).

The water molecules situated in the interstitial spaces between the host molecules are H-bonded to each other (O2-H2B···O1′) to host molecules (O2-H2A···O5G3′) and the guest (O1-H1A···O12′) (Figs. 5.49 and 5.50).

The host molecules are highly interconnected by intermolecular interactions (listed in Table 5.25 and displayed in Fig. 5.51) and the structure of each host molecule is reinforced by many intramolecular interactions (Fig. 5.50).

The packing arrangement of TMBALA matches that observed in the majority of monomeric TRIMEB complexes reported to date. The host molecules stack head-to-tail to form infinite columns that pack in a screw channel mode that runs nearly parallel to the direction of the *b*-axis (Figs. 5.52 and 5.53).

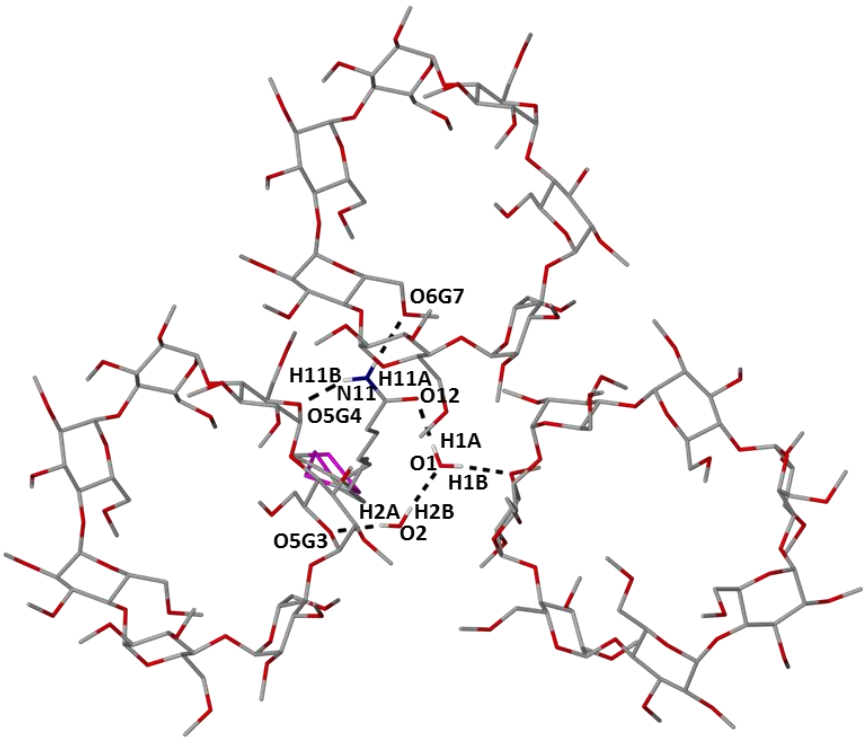

Fig. 5.49 Various intermolecular interactions found in TMBALA.

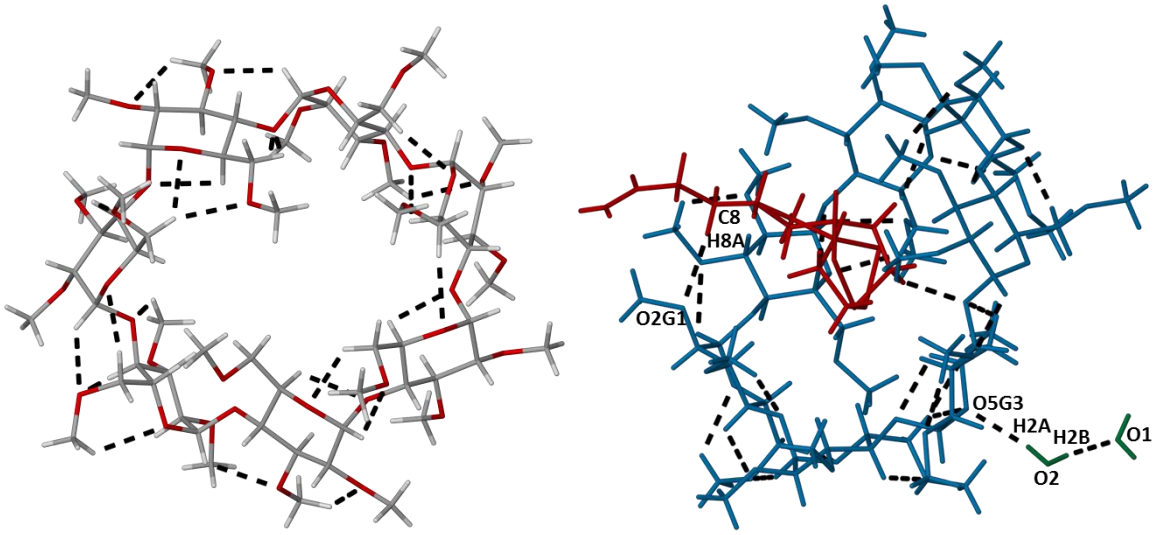

Fig. 5.50 Intramolecular host-host interactions (left) and intermolecular host-guest, water-water, and host-guest interactions of molecules in the asymmetric unit of TMBALA (right).

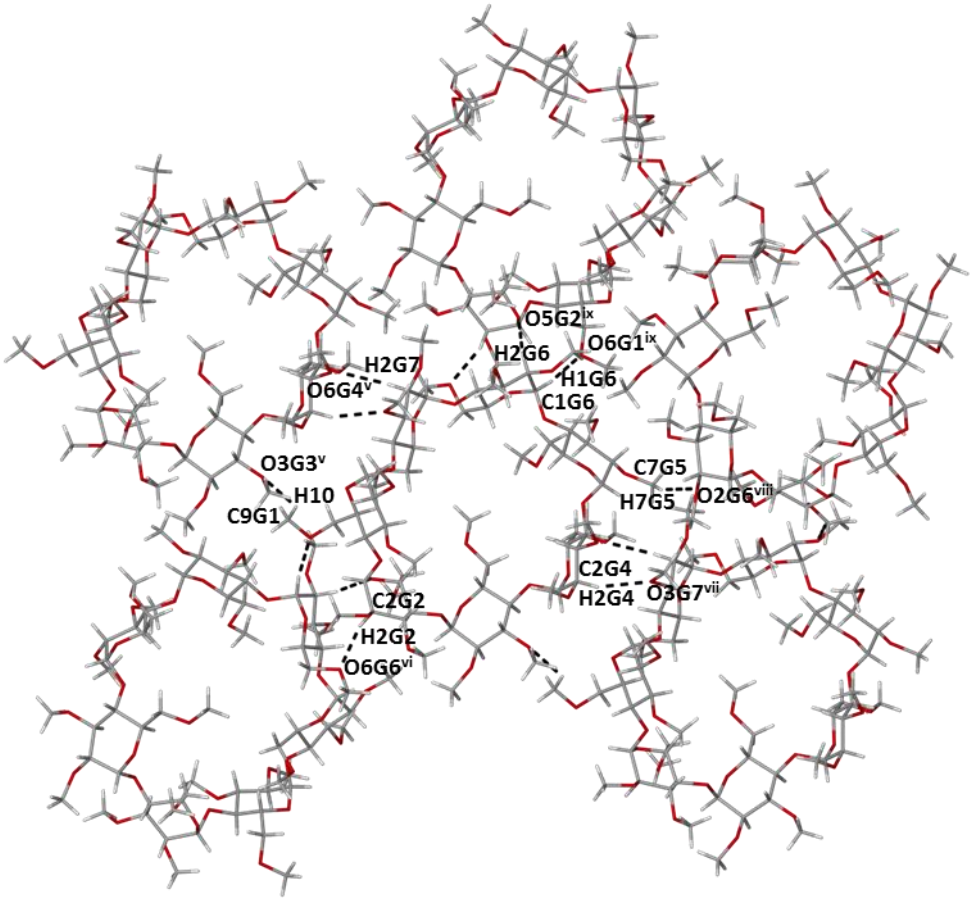

Fig. 5.51 Host-host intermolecular interactions in TMBALA. Guest and water molecules omitted for clarity.

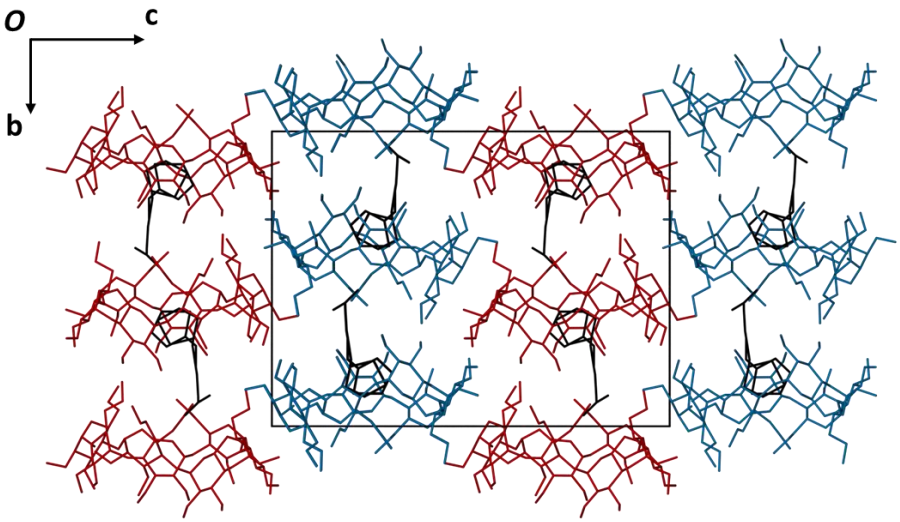

Fig. 5.52 Packing of TMBALA viewed along [100] showing the infinite columns that pack in a screw channel mode in the direction of the *b*-axis. Hydrogens have been omitted for clarity.

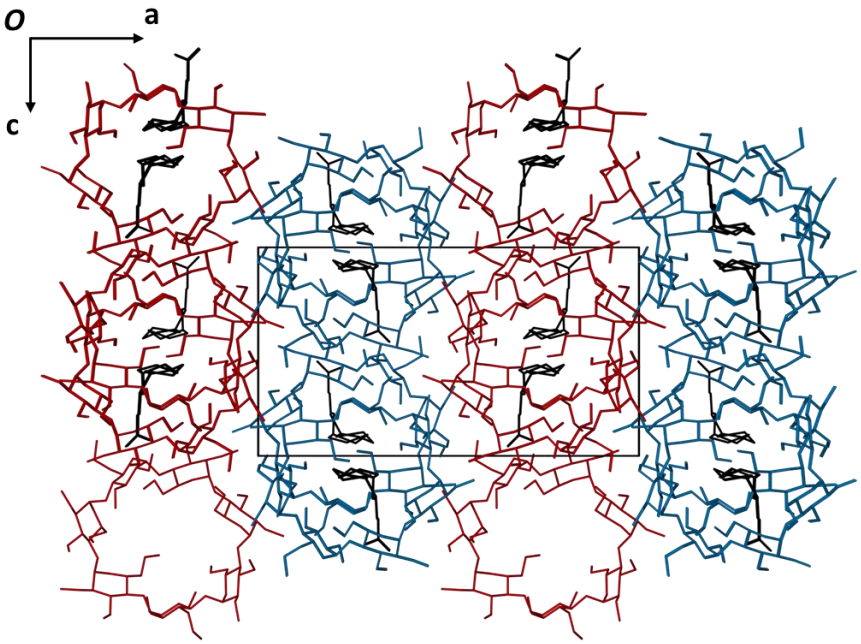

Fig. 5.53 Packing of TMBALA viewed along [010] showing the infinite columns that pack in a screw channel mode in the direction of the *b*-axis. Hydrogens have been omitted for clarity.

The unit cell data of isostructural complexes found in a CSD[1] search (with the same criteria as described for BCDALA) of TMBALA are summarised in Table 5.26. This packing arrangement is fairly common, though a difference in the b-axis length of TMBALA with the series is observed. In order to confirm isostructurality, the PXRD trace calculated from the single crystal structure of TMBALA was compared to a trace of a calculated average of the structures of the isostructural series found in Table 5.26. The result is shown in Fig. 5.54.

Table 5.26 Comparison of structural parameters of TMBALA with known structures.

Space group	H:G:W*	a (Å)	b (Å)	c (Å)	Guest	CSD Refcode	Ref.
$P2_12_12_1$	1:1:2	15.217(2)	20.663(2)	27.814(3)	α-LA	TMBALA‡	NA
$P2_12_12_1$	1:1:4	14.997(2)	21.368(2)	28.205(3)	*p*-iodophenol	CAMPIP	64
$P2_12_12_1$	1:1:1	15.092(2)	21.714(3)	28.269(4)	(R)-flurbiprofen	COYXAP10	65
$P2_12_12_1$	1:1:0	15.271(2)	21.451(3)	27.895(3)	(S)-flurbiprofen	COYXET20	65
$P2_12_12_1$	1:1:1	14.890(3)	21.407(5)	28.540(6)	4-biphenylacetic acid	PAFSOE	66
$P2_12_12_1$	1:1:0	15.232(7)	21.327(7)	27.597(7)	(S)-ibuprofen	RONWOG	61
$P2_12_12_1$	1:1:0	15.179(4)	21.407(5)	27.670(1)	(S)-naproxen	ZIFQOU	63
$P2_12_12_1$	1:1:1.92	14.796(2)	22.444(6)	27.720(8)	ethyl laurate	PINMAA	67
$P2_12_12_1$	1:1:0	14.854(1)	21.383(1)	28.509(1)	(-)-(R)-5-methyl-5-(p-tolyl)hydantoin	CETKUI	68
$P2_12_12_1$	1:1:0.91	14.887(1)	21.244(1)	27.933(1)	cycluron	OYAPIO	58
$P2_12_12_1$	1:1:0	14.775(1)	21.333(1)	27.872(1)	(S)-p-methoxyphenyl propylthiosulfinate	SIBSIG	69

***Ratio of host : guest : water; ‡The compounds have not been submitted to the Cambridge Crystallographic Datacentre yet and the compound codes are those used throughout this thesis.**

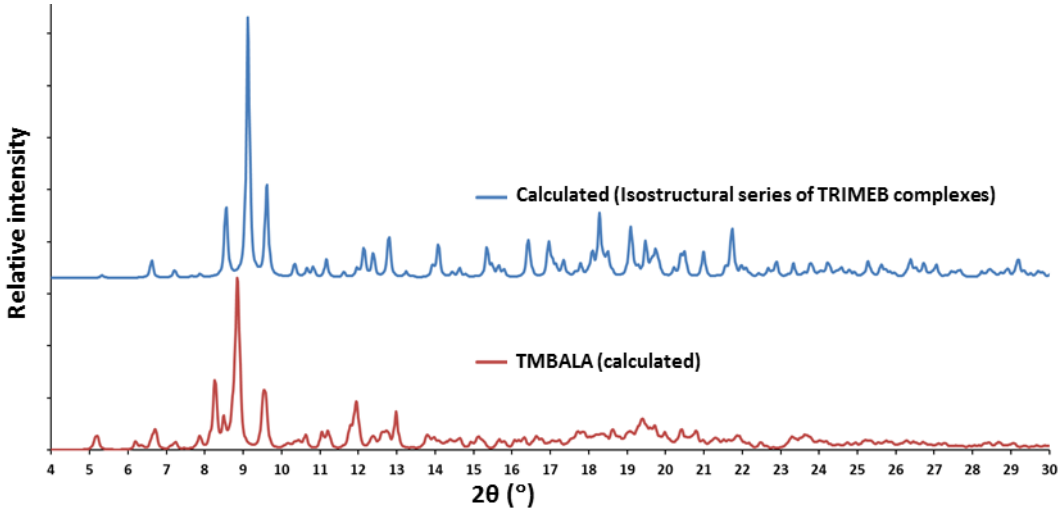

Fig. 5.54 The PXRD trace calculated from the single crystal X-ray structure of TMBALA and that obtained by averaging the traces for several complexes in the same isostructural series.

Thermal results

The HSM result for TMBALA is presented in Fig. 5.55. The crystals started to melt from the edges nearest to the heating block first. This was visible at a temperature of about 140 °C. By 146 °C the crystals had almost completely melted. The same experiment was carried out with the crystals submerged in silicone oil in order to observe the evolution of water from the crystals (Fig. 5.56). The crystals appeared to melt in the same temperature range as the crystals that were not submerged in oil. A clear difference is that immersed in oil the formation of bubbles was visible during most of the heating process, indicating potential loss of water and at higher temperatures loss of the guest.

Fig. 5.55 Representative HSM photographs of TMBALA at various temperatures.

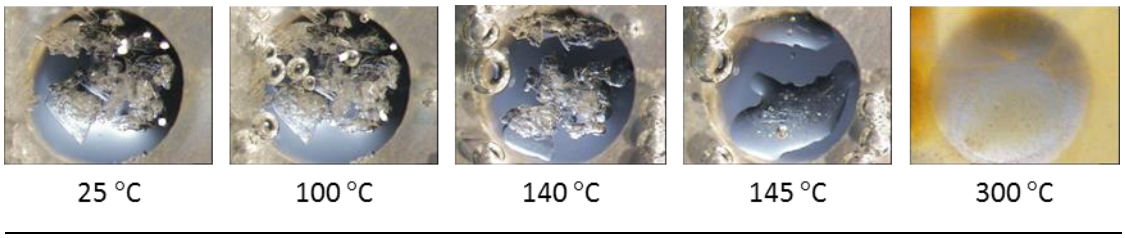

Fig. 5.56 Representative HSM photographs of TMBALA at various temperatures taken with sample submerged in silicone oil.

The DTA result for TMBALA is shown in Fig. 5.57. A small, but broad endothermic event is visible spanning the temperature range from the onset of heating up to around 75 °C. After the first event a single endotherm is observed with an onset at 131.0 ± 1.8 °C (n = 3) and a peak at 135.8 ± 0.4 °C (n = 3). This temperature is very close to, but slightly higher than, the melting temperature observed for α-LA with an onset at 125.7 ± 0.1 °C (n = 3) and a peak at 129.6 ± 0.3 °C (n = 3). The event occurs at a temperature close to the melting temperature observed in the HSM result and appears implicit that this event is the melting of TMBALA. The melt occurs well below the melting point of TMB which displays an onset at 156.4 °C and a peak at 160.2 °C. A reported melting point for a polymorph of TMB is 157 °C.[70]

The TGA result for TMBALA is presented in Fig. 5.58. A small drop in the sample mass is observed from the onset of the experiment up to a temperature of 100 °C (1.29 ± 0.17 % (n = 3)). This is believed to be due to loss of water and the bubbles observed in the HSM as well as the broad endotherm observed in the DTA experiment support this assumption. The next mass loss step with an onset at 231.4 ± 6.0 °C (n = 3) is more substantial, having the value 11.36 ± 0.07 % (n = 3). The final step has an onset temperature of 358.7 ± 1.7 °C (n = 3) and a mass loss of 82.08 ± 0.78 % (n = 3). The most likely explanation for the three observed steps is that the first mass loss is a result of the evaporation of water followed by the loss of the guest and finally the decomposition of the host. The mass loss percentages equate to a ratio of 1.2 ± 0.2:0.9 ± 0.1:1 of water to guest to host.

This confirms the host-guest stoichiometric ratio observed in the proton NMR result and the structure determined by single-crystal X-ray diffraction. There is a slight discrepancy between the water content of the solved crystal structure and that observed in the TGA result namely 2 vs 1.2 ± 0.2. Most of the TMBALA crystals tended to form on the side of a vial kept in an oven at 60 °C. These crystals showed no water loss during TGA experiments. In an attempt to obtain an accurate measurement of crystallisation water lost, care was taken to only use only crystals that were still submerged in the mother liquor. Some crystals might, however, have inadvertently fallen from the sides during handling and re-uptake of water into these crystals might have been incomplete or not have taken place.

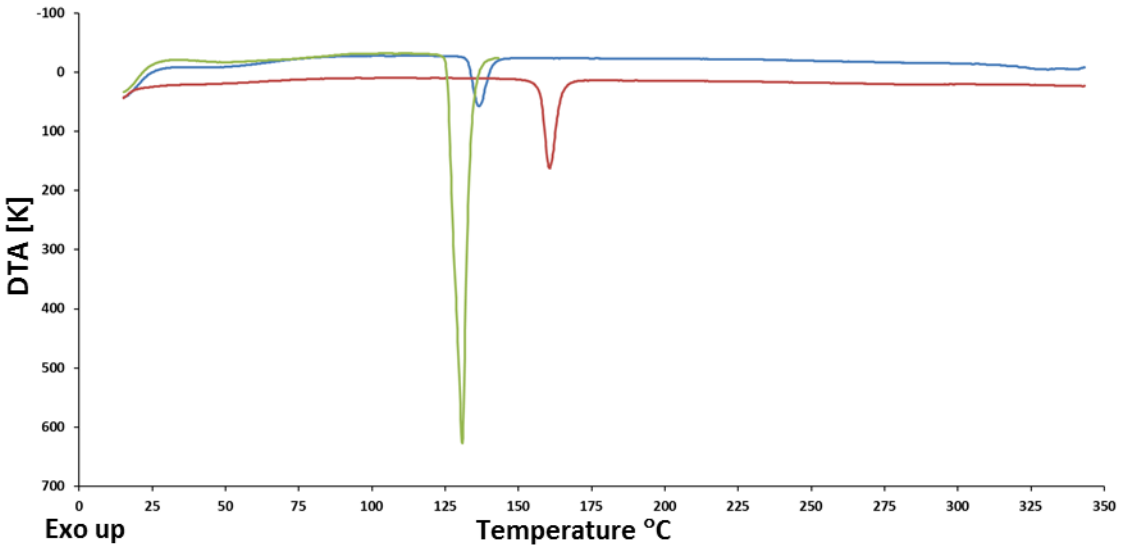

Fig. 5.57 Representative DTA thermograms of TMBALA (blue), ALA (green) and TMB (red).

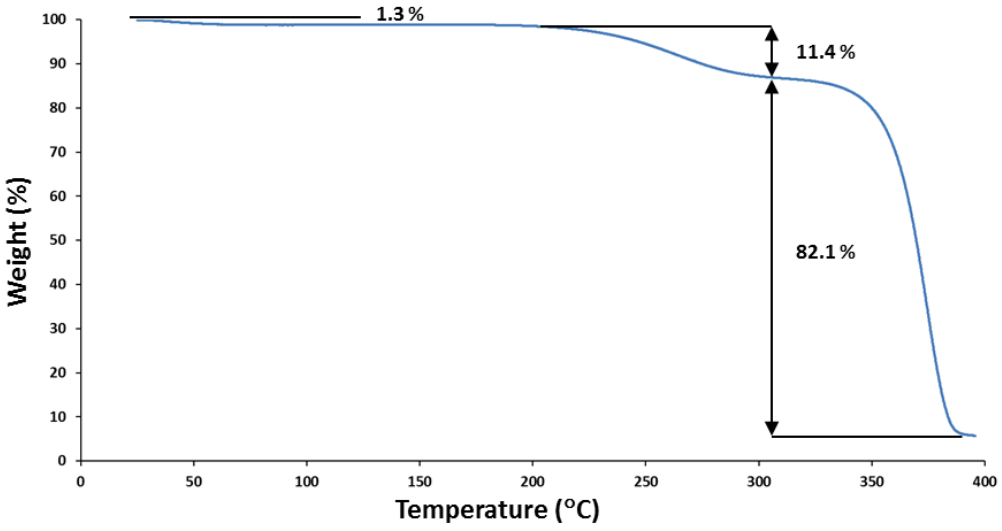

Fig. 5.58 Representative TGA trace of TMBALA.

Phase solubility studies

Phase solubility studies were carried out with the native CDs, α-, β- and γ-CD, and some selected derivatised CDs (HP-β-CD, SEBCD and RAMEB) according to the method of Higuchi and Connors[71] by making use of UV-Vis spectrophotometry in this case, as was described in Chapter 2. To determine the solubility of α-LA in the absence of CD i.e. the S_0 value, an excess of the compound was added to pure water and exposed to the same conditions as those for the CD-containing vials described in Chapter 2. S_0 was determined to be 3.101 x 10^{-3} M at 25 ± 0.5 °C. The results of this phase solubility study are reported in the following section.

Phase solubility analysis using α-, β- and γ-CD

The curves showing the phase solubility of α-Lipoamide with the respective CDs, α-, β- and γ-CD, are shown in Fig. 5.59. The curve of α-Lipoamide with α-CD displays a B-type phase solubility profile and is indicative of a complex with limited solubility in water. From the graph it is evident that the solubility of α-LA was increased when low concentrations of α-CD were present up to a CD concentration of 5 mM. This was the value that displayed the greatest improvement in solubility for α-LA in the experimental range with a value of 5.44 mM (a 1.8-fold increase compared to S_0). With higher concentrations the solubility improvement decreased. At an α-CD concentration of 20 mM the solubility of α-LA was lower than for the compound in the absence of the CD. The association constant was determined from the linear part of the graph described by y= 0.4673x + 3.1959 (R^2 of 0.9806) from an α-CD concentration of 0 – 5 mM. The K_c value was determined to be 283 M^{-1} which is considered relatively low and is indicative of weak host-guest binding in solution. This value is somewhat higher than the mean of 130 M^{-1} reported for α-CD complexes by Connors,[72] or 123 M^{-1} obtained by Burnette and Connors.[73]

The curve for α-LA with β-CD shows an A-type phase solubility profile and is indicative of an increase of the water solubility of the α-LA with an increase in the concentration of β-CD. The increase is linear and the maximum measured concentration in the experimental range was 19.2 mM at a β-CD concentration of 20 mM. This is a 6.2 fold increase compared to the S_0.The reason why in this case the experiment was only taken up to a concentration of 20 mM for this CD is because of the lower water solubility of the CD in the absence of guest in comparison to the others tested. The K_c value was determined to be 1067 M^{-1} from the slope of the line described by y = 0.7679x + 3.6449 (R^2 = 0.993). The range 0 – 20 mM was used to determine this value. This K_c value indicates

moderate host-guest binding. The K_c value is higher than the mean of 490 M^{-1} reported for β-CD complexes.[72,73]

Higher concentrations of γ-CD show a slight increase in the solubility of α-LA in the curve for γ-CD with α-LA. The phase solubility profile is an A-type profile and shows a linear increase with higher CD concentrations in the experimental range. The maximum measured concentration of α-LA was 7.6 mM at a γ-CD concentration of 30 mM. A 2.5 fold increase compared to the S_0 for α-LA. The K_C value was determined to be 58 M^{-1} from the line described by y = 0.1517x + 2.9699 (R^2 = 0.9947). This K_C value is very low and would suggest that the host and guest readily dissociates with weak binding interactions in solution. The K_C value is lower than the average reported for γ-CD complexes of 350 M^{-1} or 525 M^{-1}.[72,73]

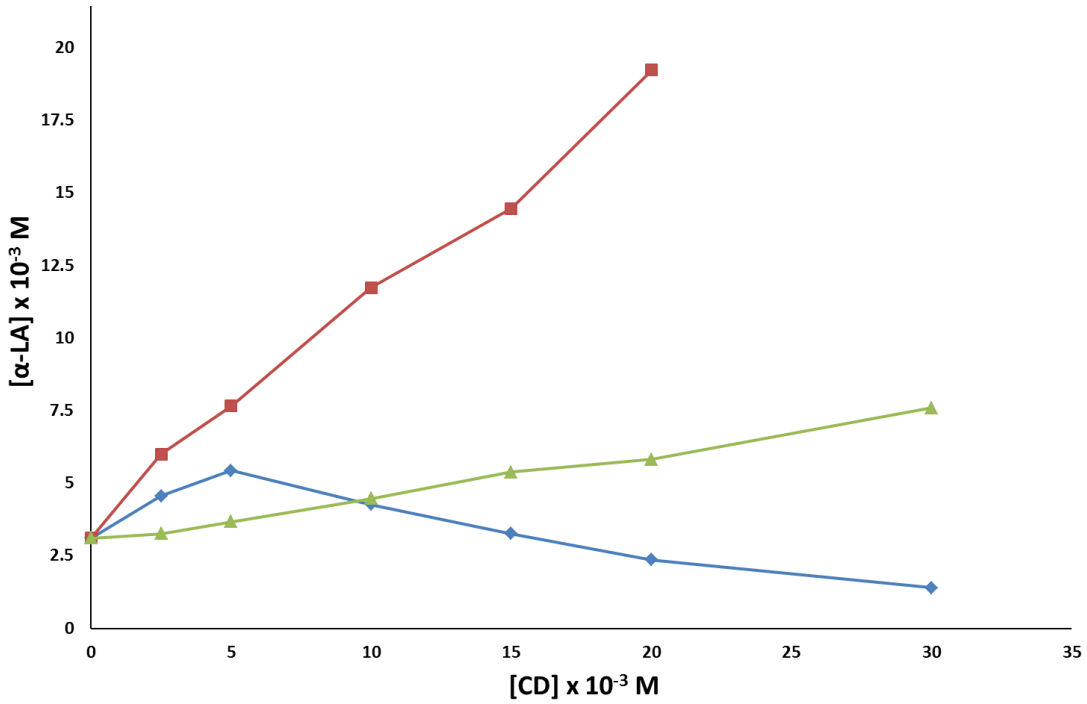

Fig. 5.59 Solubility of α-LA as a function of α-CD (blue), β-CD (red) and γ-CD (green) at 25 ± 0.5 °C.

Phase solubility analysis using RAMEB, HP-β-CD and SE-β-CD

The curves for RAMEB, HP-β-CD and SE-β-CD with α-LA are shown in Fig. 5.60. The curves all show A-type phase solubility profiles where the solubility of α-LA increases linearly with an increase of CD concentration.

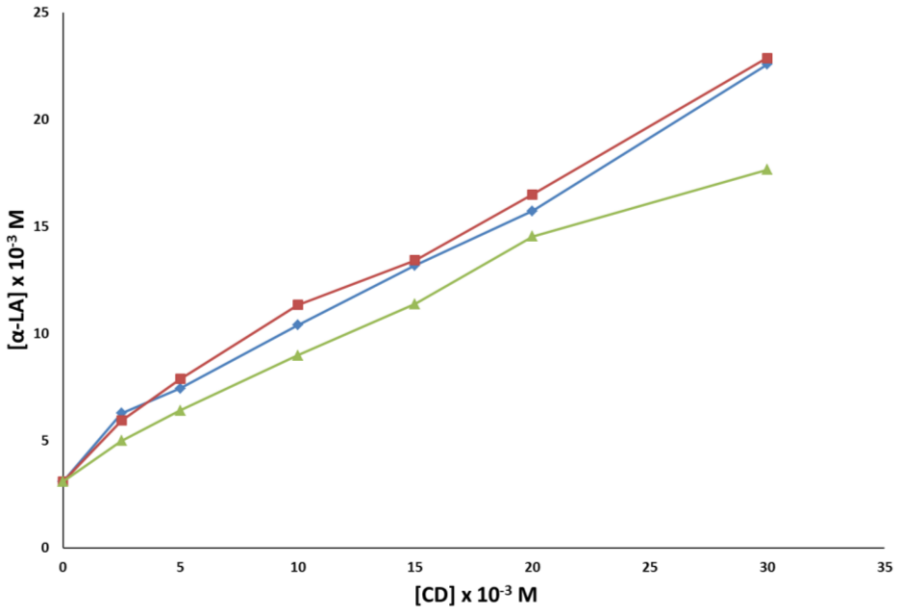

Fig. 5.60 Solubility of α-LA as a function of HP-β-CD (blue), RAMEB (red) and SE-β-CD (green) at 25 ± 0.5 °C.

The experimental phase solubility results are summarised in Table 5.27. The K_C value for RAMEB with α-LA was determined to be 545 M^{-1} from the line described by y = 0.6284x + 4.1717 (R^2 = 0.9912) making use of the range 0 – 30 mM of RAMEB. The K_C value indicates weak to moderate host-guest binding. The K_C for HP-β-CD with α-LA was calculated to be 509 M^{-1} from the line described by y = 0.6122x + 4.029 (R^2 = 0.9927) making use of the values on the graph from 0 – 30 mM of HP-β-CD. The K_C value in this instance is relatively low as HP-β-CD complexes are often found to be much higher with values generally being several thousand M^{-1}.

The calculated K_C value for SE-β-CD with α-LA is 395 M^{-1} from the line described by y = 0.5504x + 3.4178 (R^2 = 0.9966), using the range of 0 – 30 mM of SE-β-CD. This K_C value indicates weak binding in solution.

Table 5.27 Solubility increase and K_C values for 1:1 complexes between α-LA and various CDs.

CD	Solubility increase factor	K_C (M^{-1})
α-CD	1.8	283
β-CD	6.2	1067
γ-CD	2.5	58
HP-β-CD	7.3	509
RAMEB	7.4	545
SEBCD	5.7	395

Conclusion

In an attempt to generate new solid-state forms of the antioxidant (±)-α-lipoamide, various inclusion complexes were successfully synthesised with the native cyclodextrins α-, β-, and γ-CD as well as the derivatised CDs, TRIMEA, DIMEB and TRIMEB. The solved crystal structures of TMAALA and TMBALA indicated low enantioselectivity with roughly equal representation of each enantiomer in both cases.

^{1}H – NMR spectroscopy was employed to determine the host-guest stoichiometries of the complexes. A 1:1 ratio of host to guest was observed in BCDALA, TMAALA and TMBALA, and a 3:2 ratio for GCDALA. The same ratios were observed in the crystal structures for TMAALA and TMBALA and the TGA results for BCDALA, GCDALA, TMAALA and TMBALA.

Various thermal analyses were carried out to determine water composition, melting points and thermal stability in terms of decomposition and guest loss temperatures of the complexes. The amounts of water present in the complexes were determined to be 11, 5 and 2 water molecules for every 1:1 host-guest complex in the case of BCDALA, TMAALA and TMBALA respectively. GCDALA indicated a water to host ratio of roughly 14:1. The inclusion of the guest in TRIMEA and TRIMEB did not make a significant difference in the apparent thermal stability of the included guest compared to the unaltered starting material as the complex appeared to melt or lose the guest upon heating at temperatures close to those at which the guest starting material melted. In the case of BCDALA the complex did not melt and the loss of the guest upon heating occurred at a higher temperature than that observed for the guest starting material, a result which could have a significant positive impact on the stability of the complex.

The single crystal structures of the inclusion complexes were elucidated by X-ray diffraction. Comparisons of the structural parameters of the complexes reported in this chapter with those of known structures were presented. BCDALA, GCDALA and TMBALA were each found to be packed in ways that are common for inclusion complexes with these hosts. These structures match those of other structures in the CSD[1] forming part of isostructural series.[2] ACDALA crystallizes in an uncommon packing arrangement and has only one known isostructural complex, that of (R)-α-lipoic acid with α-CD.[3] DMBALA also crystallizes in a less common packing arrangement, but as mentioned earlier matches that of a known complex of DIMEB with the phenylurea herbicide cycluron.[58] The packing arrangement observed in TMAALA is rare, though other complexes with this host have been found to self-assemble in a similar fashion and one known structure is isostructural (Table 5.16).

Phase solubility experiments were carried out to measure the solubility enhancement effect of addition of CDs on α-LA and to determine stability constants of complexes in solution. The

experiments were limited to CDs that were available at the time of experimentation due to the high cost of other chemically modified CD hosts. The solubility enhancement effected by the CDs in this experiment ranged from a 1.8-fold increase with α-CD to a 7.4-fold increase with RAMEB. Though the improvement is evident, the degree of improvement is relatively low. The experimental K_C values ranged from 58 to 1067 M^{-1}, indicating weak to moderate binding in solution and they fall in the normal range for drug-CD complex binding constants (10 – 2000 M^{-1}).[74]

Novel solid-state forms of α-LA in the form of CD inclusion complexes were produced that exhibited enhanced aqueous solubility properties compared to the unaltered starting material. It was also shown that CD inclusion took place in solution with other derivatised CDs and that these effected solubility enhancement on α-LA. Any of these forms could be used to formulate new products with improved physicochemical properties and the reported results will be useful in planning for future developments.

Future work

The phase solubility experiments carried out to date are useful in giving an indication of solubility enhancement, though the true value can only be defined by experiments in which the bioavailability is measured such as *in vivo* pharmacokinetic experiments. The logical next step in the development of new products would thus be to carry out such experiments.

Stability improvements were observed in the thermal analyses carried out on BCDALA and formulation with this form could result in an improvement of the shelf life of products. The impact will have to be determined through more thorough chemical and thermal stability testing under heightened humidity and temperature for extended periods.

In attempts to produce inclusion complexes comprising α-LA with each of the respective hosts, α-CD and DIMEB, new phases were produced. Limited amounts of each of these forms were initially produced as a screening step for growth of crystals of adequate size and quality for single-crystal X-ray diffraction. Due to time constraints the full characterisation of each of these complexes was not completed as the growth of the crystals was a lengthy process. Both of these complexes were formed in an oven kept at 60 °C over a period of several months and the integrity of the guest will need to be verified. Future work will thus entail the reproduction of each of these forms in sufficient quantities for full characterisation.

References

1. Cambridge Structural Database and Cambridge Structural Database System, Version 5.39 (February 2018 update), Cambridge Crystallographic Data Centre, University Chemical Laboratory, Cambridge, England, 2018.
2. S. Lubhelwana, MSc Dissertation, *Crystal Isostructurality and X-ray Diffraction studies of Cyclodextrin Inclusion Compounds*, University of Cape Town, South Africa, **2005**.
3. Poster presentation MS67.P05.B203: *Cyclodextrin inclusion complexes of the antioxidant a-lipoic acid*, M. R. Caira, S. A. Bourne, B. Mzondo, 23rd Congress and General Assembly of the International Union of Crystallography, Montrèal, Quèbec, Canada, August 5-12, 2014. Also published as: M. Caira, S. Bourne and B. Mzondo, *Acta Crystallogr.*, 2014, **70**, C992.
4. N. Ikuta, T. Endo, S. Hosomi, K. Setou, S. Tanaka, N. Ogawa, H. Yamamoto, T. Mizukami, S. Arai and M. Okuno, *Int. J. Mol. Sci.*, 2015, **16**, 24614-24628.
5. Program cell_now, Bruker AXS Inc., Madison, WI, USA, **2008**.
6. Program SAINT, Version 7.60a, Bruker AXS Inc., Madison, Wisconsin, USA, **2008**.
7. G. M. Sheldrick, Program TWINABS, University of Göttingen, Germany, **2001**.
8. M. R. Caira, *Rev. Roum. Chim.*, 2001, **46**, 371-386.
9. K. Harata, *Chem. Rev.*, 1998, **98**, 1803-1828.
10. W. Saenger, in *Inclusion compounds*, eds. J. L. Atwood, J. E. D. Davies and D. D. MacNicol, Oxford University Press, London, **1984**, vol. 2, ch. 8.
11. S. V. Klinov, N. I. Klinova, B. I. Kurganov, N. P. Sugrobova, A. A. Poznanskaya, T. N. Klementyeva and V. M. Avakumov, *Khim.-Farm.*, 1991, **25**, 45-47.
12. L. Yunqing; L. Xiying; L. Wei and L. Tong, Faming Zhuanli Shenqing, 2002, CN 1379047 A 20021113.
13. G. M. Sheldrick, SADABS, *program for empirical absorption correction of area detector data*, University of Göttingen, Göttingen, Germany, **1997**.
14. G. M. Sheldrick, Acta Crystallogr., Sect. A: Found. Crystallogr., 2008, **64**, 112-122.
15. G. M. Sheldrick, *Direct Methods for Solving Macromolecular Structures*, ed. S. Fortier, Dordrecht: Kluwer Academic Publishers, **1998**, 401-411.
16. J. M. Alexander, J. L. Clark, T. J. Brett and J. J. Stezowski, *Proc. Natl. Acad. Sci. U. S. A.*, 2002, **99**, 5115-5120.
17. M. B. Hursthouse, C. Z. Smith, M. Thornton-Pett and J. H. Utley, *J. Chem. Soc., Chem. Commun.*, 1982, 881-882.
18. J. Hamilton and M. Sabesan, *Acta Crystallogr., Sect. B: Struct. Crystallogr. Cryst. Chem.*, 1982, **38**, 3063-3069.
19. A. Rontoyianni, I. M. Mavridis, E. Hadjoudis and A. J. Duisenberg, *Carbohydr. Res.*, 1994, **252**, 19-32.
20. A. Rontoyianni and I. M. Mavridis, *Acta Crystallogr., Sect. C: Cryst. Struct. Commun.*, 1996, **52**, 2277-2281.
21. T. Bojinova, H. Gornitzka, N. Lauth-de Viguerie and I. Rico-Lattes, *Carbohydr. Res.*, 2003, **338**, 781-785.
22. Y. Liu, Y. L. Zhao, H. Y. Zhang and H. B. Song, *Angew. Chem.*, 2003, **115**, 3382-3385.
23. J. L. Clark and J. J. Stezowski, *J. Am. Chem. Soc.*, 2001, **123**, 9880-9888.
24. S. Makedonopoulou, A. Tulinsky and I. M. Mavridis, *Supramol. Chem.*, 1999, **11**, 73-81.
25. J. L. Clark, B. R. Booth and J. J. Stezowski, *J. Am. Chem. Soc.*, 2001, **123**, 9889-9895.
26. S. Makedonopoulou and I. M. Mavridis, *Acta Crystallogr., Sect. B: Struct. Sci.*, 2000, **56**, 322-331.

27. M. R. Caira, E. J. De Vries and L. R. Nassimbeni, *Chem. Commun.*, 2003, 2058-2059.
28. S. Makedonopoulou and I. M. Mavridis, *Carbohydr. Res.*, 2001, **335**, 213-220.
29. T. J. Brett, J. M. Alexander and J. J. Stezowski, *J. Chem. Soc., Perkin Trans. 2*, 2000, 1105-1111.
30. F. Nishioka, I. Nakanishi, T. Fujiwara and K.-i. Tomita, *J. Inclusion Phenom.*, 1984, **2**, 701-714.
31. Y. L. Zhao, D. Benítez, I. Yoon and J. F. Stoddart, *Chem.–Asian J.*, 2009, **4**, 446-456.
32. N. Lien and J. Telford, *Carbohydr. Res.*, 2009, **344**, 2606-2608.
33. K. Elasaad, R. Alkhatib, T. Hennebelle, B. Norberg and J. Wouters, *Crystals*, 2012, **2**, 1441-1454.
34. E. Wang, G. Chen and C. Han, *Chin. J. Chem.*, 2011, **29**, 617-622.
35. Y. Liu, Y.-L. Zhao, Y. Chen and D.-S. Guo, *Org. Biomol. Chem.*, 2005, **3**, 584-591.
36. J. A. Fernandes, A. I. Ramos, P. Ribeiro-Claro, F. A. A. Paz and S. S. Braga, *CrystEngComm*, 2015, **17**, 937-946.
37. X.-J. Shen, H.-L. Chen, F. Yu, Y.-C. Zhang, X.-H. Yang and Y.-Z. Li, *Tetrahedron Lett.*, 2004, **45**, 6813-6817.
38. E. Wang, G. Chen and H. Liu, *Chin. J. Chem.*, 2009, **27**, 2097-2101.
39. Z. Fan, C.-H. Diao, M.-J. Guo, R.-J. Du, Y.-F. Song, Z.-L. Jing and M. Yu, *Carbohydr. Res.*, 2007, **342**, 2500-2503.
40. T. Aree and N. Chaichit, *Carbohydr. Res.*, 2008, **343**, 2285-2291.
41. E. Wang, G. Chen, C. Han, *Huaxue Xuebao*, 2009, **67**, 2527.
42. Y. Zhang, S. Yu and F. Bao, *Carbohydr. Res.*, 2008, **343**, 2504-2508.
43. M. Ceborska, K. Szwed, M. Asztemborska, M. Wszelaka-Rylik, E. Kicińska and K. Suwińska, *Chem. Phys. Lett.*, 2015, **641**, 44-50.
44. M. Ceborska, K. Szwed and K. Suwinska, *Carbohydr. Polym.*, 2013, **97**, 546-550.
45. E. M. Yee, J. M. Hook, M. M. Bhadbhade, O. Vittorio, R. P. Kuchel, M. B. Brandl, R. D. Tilley, D. S. Black and N. Kumar, *Carbohydr. Polym.*, 2017, **165**, 444-454.
46. T. Steiner and W. Saenger, *Acta Crystallogr., Sect. B: Struct. Sci.*, 1998, **54**, 450-455.
47. J. Ding, T. Steiner and W. Saenger, *Acta Crystallogr., Sect. B: Struct. Sci.*, 1991, **47**, 731-738.
48. K. Lindner and W. Saenger, *Biochem. Biophys. Res. Commun.*, 1980, **92**, 933-938.
49. S. Kamitori, K. Hirotsu and T. Higuchi, *J. Chem. Soc., Chem. Commun.*, 1986, 690-691.
50. S. Kamitori, K. Hirotsu and T. Higuchi, *J. Am. Chem. Soc.*, 1987, **109**, 2409-2414.
51. S. Kamitori, K. Hirotsu and T. Higuchi, *Bull. Chem. Soc. Jpn.*, 1988, **61**, 3825-3830.
52. Z. Liu, M. Frasconi, J. Lei, Z. J. Brown, Z. Zhu, D. Cao, J. Iehl, G. Liu, A. C. Fahrenbach and Y. Y. Botros, *Nat. Commun.*, 2013, **4**, 1855.
53. T. Sawada, H. Hisada and M. Fujita, *J. Am. Chem. Soc.*, 2014, **136**, 4449-4451.
54. A. Cooper, M. Nutley, E. J. MacLean, K. Cameron, L. Fielding, J. Mestres and R. Palin, *Org. Biomol. Chem.*, 2005, **3**, 1863-1871.
55. M. R. Caira, S. A. Bourne and B. Mzondo, *Molecules*, 2017, **22**, 866.
56. R. E. Marsh, M. Kapon, S. Hu and F. H. Herbstein, *Acta Crystallogr., Sect. B: Struct. Sci.*, 2002, **58**, 62-77.
57. S. Makedonopoulou, K. Yannakopoulou, D. Mentzafos, V. Lamzin, A. Popov and I. M. Mavridis, *Acta Crystallogr., Sect. B: Struct. Sci.*, 2001, **57**, 399-409.
58. D. L. Cruickshank, S. A. Bourne and M. R. Caira, *ARKIVOC*, 2011, **12**, 103-107.
59. E. J. de Vries and M. R. Caira, *Carbohydr. Res.*, 2008, **343**, 2433-2438
60. P. Glockner, H. Ritter, D. Schollmeyer, CCDC 153137: Experimental Crystal Structure Determination, 2000, DOI:10.5517/cc54bxj.

61. G. R. Brown, M. R. Caira, L. R. Nassimbeni and B. Van Oudtshoorn, *J. Inclusion Phenom. Mol. Recognit. Chem.*, 1996, **26**, 281-294.
62. M. R. Caira, V. J. Griffith, L. R. Nassimbeni and B. van Oudtshoorn, *J. Chem. Soc., Perkin Trans. 2*, 1994, 2071-2072.
63. M. R. Caira, V. J. Griffith, L. R. Nassimbeni and B. Van Oudtshoorn, *J. Inclusion Phenom. Mol. Recognit. Chem.*, 1994, **20**, 277-290.
64. K. Harata, K. Uekama, M. Otagiri and F. Hirayama, *Bull. Chem. Soc. Jpn.*, 1983, **56**, 1732-1736.
65. K. Harata, K. Uekama, T. Imai, F. Hirayama and M. Otagiri, *J. Inclusion Phenom.*, 1988, **6**, 443-460.
66. K. Harata, F. Hirayama, H. Arima, K. Uekama and T. Miyaji, *J. Chem. Soc., Perkin Trans. 2*, 1992, 1159-1166.
67. D. Mentzafos, I. M. Mavridis and H. Schenk, *Carbohydr. Res.*, 1994, **253**, 39-50.
68. L. Ferron, F. Guillen, S. Coste, G. Coquerel and J. C. Plaquevent, *Chirality*, 2006, **18**, 662-666.
69. N. Stellenboom, R. Hunter, M. R. Caira, S. A. Bourne, K. Cele, T. Qwebani and T. Le Roex, *ARKIVOC*, 2007, **9**, 53-63.
70. M. R. Caira, S. A. Bourne, W. T. Mhlongo and P. M. Dean, *Chem. Commun.*, 2004, 2216-2217.
71. T. Higuchi and A. Connors, *Adv. Chem. Instrum.*, 1965, **4**, 212–217.
72. K. A. Connors, *Chem. Rev.*, 1997, **97**, 1325-1358.
73. R. R. Burnette and K. A. Connors, *J. Pharm. Sci.*, 2000, **89**, 1389-1394.
74. T. Loftsson and M. E. Brewster, *J. Pharm. Pharmacol.*, 2010, **62**, 1607-1621.

Chapter 6

Conclusion

Summary

Clevudine

Aim

The main aim concerning this chiral antiviral drug, indicated and in widespread and ongoing use in the treatment of chronic hepatitis B virus infection, was to prepare new solid-state forms that could potentially be used in the formulation of new completed products. The secondary aim was to fully characterise a novel polymorph of this API and to compare the relative thermodynamic stabilities and solubilities of the different forms.

Results

A third polymorphic form was discovered in the process of characterisation of the other forms and a combination of complementary methods was utilised to facilitate the construction of an energy-temperature diagram incorporating all three clevudine crystal forms. These methods included HSM, DSC, VTPXRD, and solvent-mediated phase transformation experiments. Further characterisation was accomplished through kinetic solubility experiments, single-crystal X-ray diffraction, PXRD and FTIR spectroscopy. The stability and solubility ranking of the various forms were established and the crystal structures of each form elucidated. A degree of conformational flexibility resulted in Form 1 and Form 3 packing in layers and Form 2 in a helical hydrogen bonded motif, though all three forms crystallise in the space group $P2_1$. The Z' values differed for each form with Form 1, 2 and 3 having values of 2, 1 and 4 respectively.

Significance of results

The determined thermal stability ranking at 25 °C (Form 2 > Form 1 > Form 3) indicates that the starting material as purchased corresponds to a metastable form at room temperature. Moreover this metastable form was also found to transform into a more stable form during LAG with acetonitrile. A phase transition could thus potentially occur in the marketed products during the course of

manufacturing processes or storage over extended periods. This information is crucial for quality control of existing and future marketed products containing this active pharmaceutical ingredient.

The challenges in the prediction of crystal structures with multiple Z' values[1] make this series of polymorphs a noteworthy test case.

A rapid and simple means of differentiation of the various forms via PXRD and FTIR spectroscopy has been developed.

MMV

Aim

For this novel drug candidate, developed for use as an antimalarial drug, the aim was to produce new solid-state forms with improved physicochemical properties, the most essential of which being the aqueous solubility. The next step would be to compare the properties of the novel solid-state forms with those of the starting material and if improvement were to be observed these forms could be used in the further development of a new antimalarial drug product.

Results

A number of novel solid-state forms including four polymorphs, a hydrate and seven other multi-component forms were produced, and characterised.

The polymorphs were characterised in terms of their crystal structures and physicochemical properties including solubility and stability rankings. Form 1 and Form 2 crystallised in the space groups $P2_12_12_1$ and $P2_1/c$ respectively, but no single crystals of the metastable Form 3 of adequate size and quality were obtained for single-crystal X-ray data-collection, and Form 4 is amorphous. In kinetic solubility experiments with the polymorphs, Form 4 displayed a significant improvement in dissolution rate compared to the crystalline forms (a factor of 3 to 4 times the concentration at 1 h of stirring at 25 ± 0.5 °C). The determined thermal stability ranking at 25 °C is Form 2 > Form 1 > Form 3 > Form 4. Forms 1 and 2 proved to be enantiotropically related with Form 2 being the stable form up to a temperature between 75 and 100 °C, above which Form 1 is the stable form. All the other pairwise combinations are monotropically related.

At least five of the multi-component forms are co-crystals and one is a salt. Crystal structures were elucidated by single-crystal X-ray diffraction for all but one of the seven multi-component systems.

Though all of these compounds crystallised in the very common space group $P\bar{1}$, with an O-H···N hydrogen bond being the main intermolecular interaction in all of the co-crystals, the specific hydrogen bonding motifs were varied. The combination of MMV with succinic acid resulted in the formation of three distinct phases of which two (MMVSUCC1 and MMVSUCC3) were unequivocally determined to be conformational synthon co-crystal polymorphs[2,3] while the third (MMVSUCC2) is believed to be a co-crystal with a different stoichiometric ratio. No single crystals of MMVSUCC2 having adequate size and quality for X-ray analysis were obtained. Isostructurality[4,5] was observed in the case of MMVSUCC1 and MMVFUM. The stability ranking of the three polymorphs showed that MMVSUCC1 and MMVSUCC3 are monotropically related, MMVSUCC3 being the most stable form. Each of the multi-component systems was characterised by HSM, DTA/DSC, TGA, FTIR, ^{1}H-NMR spectroscopy, PXRD, single-crystal XRD techniques and in some cases variable-temperature PXRD. In order to mimic the environment of the human intestine, solubility experiments were carried out in fasted state simulated intestinal fluid to determine the most likely solubility profiles of the novel forms in this medium. The maximum concentrations of free drug measured during these solubility experiments for the salt and co-crystal forms were four to well over five times as high as that recorded for the untreated MMV.

Significance of results

Methods were developed to reproducibly scale up as well as quickly identify each of the novel solid-state forms mentioned previously.

The monohydrated form of MMV was determined to be a less viable option to be used in the formulation of a drug product, though the knowledge of the existence of this form and how to avoid transition to this form is vital in quality control during storage and manufacturing of any future products containing MMV.

The various polymorphs have different aqueous solubilities and thermodynamic stabilities. These forms could be used for formulation of pharmaceutical products and the knowledge of their existence as well as the conditions required to produce pure phases and avoid transitions to other forms during storage and processing is important for quality control.

All of the multi-component phases were produced with GRAS[6] dicarboxylic acids as coformers. Formulation of products with any of these novel forms should thus be pharmaceutically acceptable. Each of the co-crystals displayed a significant improvement in the dissolution rate of MMV and could

potentially provide the needed improvement in bioavailability and efficacy to advance this drug candidate to the clinical trial stage.

(±)-α-Lipoamide

Aim

The aim was to produce and characterise CD inclusion complexes with the antioxidant (±)-α-lipoamide with improved stability and solubility for potential use in the formulation of new drug products.

Results

Inclusion complexation was successful with each combination of (±)-α-lipoamide with native α-, β-, and γ-CD as well as the derivatised CDs, TRIMEA, DIMEB and TRIMEB.

A combination of TGA and ^{1}H – NMR spectroscopy was employed to determine the host-guest stoichiometry of the complexes. Melting points, water loss and decomposition temperatures were determined by HSM, DTA and TGA. The β-CD complex displayed an improvement in stability compared to the starting material in that the complex did not melt and the loss of the guest upon heating occurred at a higher temperature. The single crystal X-ray structures of the inclusion complexes were elucidated by X-ray diffraction and the host conformations were compared to those of known structures from the CSD[7] and the known isostructural complexes were summarised in tables. The complex with α-CD crystallised in a very rare packing arrangement with the space group *R*32 and has only one known isostructural counterpart in which the guest molecule is α-lipoic acid.[8] The complexes with DIMEB and TRIMEA also feature rare packing arrangements, while the β-CD, γ-CD and TRIMEB complexes are packed in common arrangements. The effects on solubility enhancement as well as stability constants of complexes in solution realised by addition of CDs were determined by phase solubility experiments. The range of solubility enhancement was from a 1.8 fold increase in the case of α-CD to an increase of 7.4 times with RAMEB. Weak to moderate complex stabilities were reflected in the observed stability constant values which ranged from 58 to 1067 M^{-1}.

Significance of results

Novel cyclodextrin inclusion complexes with (±)-α-lipoamide displaying improved aqueous solubility and in some cases improved thermal stability were produced that can be used in the formulation of new

drug products. The efficacy in the numerous nutraceutical and therapeutic applications of this antioxidant can thus potentially be greatly improved.

Future work

Clevudine

An aspect that was not studied was the compression shear strength of this compound and potential consequential benefits to tabletting ability that could reasonably be expected considering the differences in the packing arrangements of the various polymorphs. Intrinsic dissolution rates, *in vivo* pharmacokinetic and efficacy testing and stability under increased humidity and temperature over extended periods could also be measured and compared for the various polymorphs in order to determine whether any other polymorphic form could be a viable alternative option for formulation of new products.

MMV652103

Many screening liquid-assisted grinding experiments with other coformers produced "hits" on which no further characterisations have been carried out and no single crystal structures have been solved. These materials present future avenues to explore along with combinations with other potential coformers possessing similar functional groups.

Stability testing under elevated temperature and humidity will have to be carried out on the MMV polymorphs and multi-component systems to determine if they have adequate stability to be kept under standard storage conditions before a particular form can be selected for formulation. The amorphous form (MMV Form 4) will require rigorous stability testing and will necessitate characterisation in terms of β- and γ-relaxations before it could be formulated into a completed product. The formulated products would have to be screened to verify that no transitions occurred during processing.

During the course of the present study, pharmacokinetic *in vivo* experiments in mice involving the application of the various novel solid-state forms of MMV as enteric coated capsules were carried out. The method was not perfected and it was concluded that a great deal of further method development is required before these experiments could be repeated as the results obtained were extremely erratic.

The ultimate test that remains to be carried out is that of the efficacy of the various derivatised forms in the treatment of Plasmodium falciparum *in vivo* in laboratory animals and eventually in clinical trials in humans.

(±)-α-lipoamide

In order to determine the effect of the solubility enhancement of (±)-α-lipoamide produced by the various CDs on the bioavailability of this bioactive compound, *in vivo* pharmacokinetic experiments will need to be carried out. The extent of stability improvement from CD complexation can be determined by carrying out chemical and thermal stability testing under elevated humidity and temperature for extended periods. Full characterisation of the α-CD and DIMEB complexes can be completed.

Final comments

The immeasurable importance of supramolecular beneficiation in the pharmaceutical field has been highlighted and these methods were utilised in producing many novel solid-state forms of bioactive compounds. In this study the application of various complementary analytical methods was shown to be invaluable in the determination of thermal stability rankings of polymorphs with a narrow range of melting/transition temperatures. The application of crystal engineering in the selection of ideal coformers was proven to be a valuable means of expediting the experimental process of producing co-crystals. Application of empirical due diligence in polymorph/pseudopolymorph screening proved to be imperative in preformulation, with many novel polymorphs discovered throughout this study. The value of inclusion complexation with cyclodextrins was evidenced in the improved physicochemical properties of the complexes formed. All the results presented in this thesis are of significance in future developments involving any of the bioactive compounds studied.

References

1. S. L. Price, *Chem. Soc. Rev.*, 2014, **43**, 2098-2111.
2. J. A. Bis, P. Vishweshwar, R. A. Middleton and M. J. Zaworotko, *Cryst. Growth Des.*, 2006, **6**, 1048-1053.
3. S. Li, J.-M. Chen and T.-B. Lu, *CrystEngComm*, 2014, **16**, 6450-6458.
4. M. R. Caira, in *Encyclopaedia of Supramolecular Chemistry*, ed. J. L. Atwood and J. W. Steed, Marcel Dekker, Inc., **2004**, vol. 1, pp. 767-775.
5. A. Kalman, L. Párkányi and G. Argay, *Acta Crystallogr., Sect. B: Struct. Sci.*, 1993, **49**, 1039-1049.
6. U.S. Food and Drug Admistration, *FDA Generally Recognized as Safe (GRAS)*, http://www.fda.gov/Food/IngredientsPackagingLabeling/GRAS/ (accessed January 2018).
7. Cambridge Structural Database and Cambridge Structural Database System, Version 5.39 (February 2018 update), Cambridge Crystallographic Data Centre, University Chemical Laboratory, Cambridge, England, 2018.
8. Poster presentation MS67.P05.B203: *Cyclodextrin inclusion complexes of the antioxidant α-lipoic acid*, M. R. Caira, S. A. Bourne, B. Mzondo, 23rd Congress and General Assembly of the International Union of Crystallography, Montrèal, Quèbec, Canada, August 5-12, 2014.